Dye-based coordination cages

This dissertation is submitted for the degree of

“Doctor rerum naturalium”

TU Dortmund

Fakultät für Chemie und Chemische Biologie

Irene Regeni

To my brother Giulio

Eidesstattliche Versicherung (Affidavit)

_____ _____

Name, Vorname
(Surname, first name)

Matrikel-Nr.
(Enrolment number)

Belehrung:

Wer vorsätzlich gegen eine die Täuschung über Prüfungsleistungen betreffende Regelung einer Hochschulprüfungsordnung verstößt, handelt ordnungswidrig. Die Ordnungswidrigkeit kann mit einer Geldbuße von bis zu 50.000,00 € geahndet werden. Zuständige Verwaltungsbehörde für die Verfolgung und Ahndung von Ordnungswidrigkeiten ist der Kanzler/die Kanzlerin der Technischen Universität Dortmund. Im Falle eines mehrfachen oder sonstigen schwerwiegenden Täuschungsversuches kann der Prüfling zudem exmatrikuliert werden, § 63 Abs. 5 Hochschulgesetz NRW.

Die Abgabe einer falschen Versicherung an Eides statt ist strafbar.

Wer vorsätzlich eine falsche Versicherung an Eides statt abgibt, kann mit einer Freiheitsstrafe bis zu drei Jahren oder mit Geldstrafe bestraft werden, § 156 StGB. Die fahrlässige Abgabe einer falschen Versicherung an Eides statt kann mit einer Freiheitsstrafe bis zu einem Jahr oder Geldstrafe bestraft werden, § 161 StGB.

Die oben stehende Belehrung habe ich zur Kenntnis genommen:

Official notification:

Any person who intentionally breaches any regulation of university examination regulations relating to deception in examination performance is acting improperly. This offence can be punished with a fine of up to EUR 50,000.00. The competent administrative authority for the pursuit and prosecution of offences of this type is the chancellor of the TU Dortmund University. In the case of multiple or other serious attempts at deception, the candidate can also be unenrolled, Section 63, paragraph 5 of the Universities Act of North Rhine-Westphalia.

The submission of a false affidavit is punishable.

Any person who intentionally submits a false affidavit can be punished with a prison sentence of up to three years or a fine, Section 156 of the Criminal Code. The negligent submission of a false affidavit can be punished with a prison sentence of up to one year or a fine, Section 161 of the Criminal Code.

I have taken note of the above official notification.

_____ _____

Ort, Datum
(Place, date)

Unterschrift
(Signature)

Titel der Dissertation:
(Title of the thesis):

_____

_____

_____

Ich versichere hiermit an Eides statt, dass ich die vorliegende Dissertation mit dem Titel selbstständig und ohne unzulässige fremde Hilfe angefertigt habe. Ich habe keine anderen als die angegebenen Quellen und Hilfsmittel benutzt sowie wörtliche und sinngemäße Zitate kenntlich gemacht.
Die Arbeit hat in gegenwärtiger oder in einer anderen Fassung weder der TU Dortmund noch einer anderen Hochschule im Zusammenhang mit einer staatlichen oder akademischen Prüfung vorgelegen.

I hereby swear that I have completed the present dissertation independently and without inadmissible external support. I have not used any sources or tools other than those indicated and have identified literal and analogous quotations.

The thesis in its current version or another version has not been presented to the TU Dortmund University or another university in connection with a state or academic examination.*

*Please be aware that solely the German version of the affidavit ("Eidesstattliche Versicherung") for the PhD thesis is the official and legally binding version.

_____ _____

Ort, Datum
(Place, date)

Unterschrift
(Signature)

Abstract

Synthetic organic dyes find broad use in industry (e.g. as colorizing agents and laser materials), medicine (e.g. as diagnostic tools and drugs) and research (e.g. in fluorescence microscopy, FRET setups and as photosensitizers). All the applications originate from the typical interaction that these chromophores have with visible light. However, while a number of these dyes is produced on a multi ton scale since decades, their implementation into complex chemical systems and nano structures still offers unexploited potential for the development of novel functional devices and materials. In particular, their synthetic incorporation into self-assembled supramolecular systems is rather rarely found. The combination of the two concepts would lead to functional architectures with interesting photophysical and redoxchemical properties that could be utilized for diagnostic and catalytic applications.

Hence, this thesis aims at delivering an unprecedented design and implementation of organic dyes into nano-sized coordination cages to enrich them with the feature to strongly interact with visible light. New bis-monodentate ligands were designed based on a selection of dyes, namely diketopyrrolopyrroles (DPP) and members of the coal-tar dye family: Michler's ketone, rhodamine B, methylene blue and crystal violet. The incorporation of these dye functionalities into metallo-supramolecular architectures was achieved through coordination of the newly developed ligands to Pd(II) cations. Structural and optical properties of the assemblies were evaluated and fully characterized with a wide range of spectroscopic, spectrometric and diffraction techniques. Interesting optical features were found for DPP-based homoleptic and heteroleptic assemblies. From the structural point of view, a new topology of a homoleptic [Pd_2L_4] cage was revealed and characterized by an atypical arrangement of the four ligands around the Pd-axis in order to promote π-stacking of the four chromophores. Furthermore, cage-to-cage transformations were observed for a combination of three different ligands (DPP-based, carbazole-based and dimethylfluorene-based as optically relevant moieties).

The introduction of the coal-tar dyes moieties into bis-pyridine or bis-isoquinoline ligands required a careful design to allow retainment of their specific absorption properties. Typical alkyne bridges between donor groups and backbones would have hampered the electronic structure of the parental dyes. Therefore, the new ligand design used in this thesis exploited piperazine linkers. By coordination to the square planar metal cations, lantern-shaped and helically twisted, visible light-absorbing [Pd_2L_4] cages were obtained. Their remarkable absorption properties were exploited for the recognition of small chiral molecules. Encapsulation or even only external association caused the chromophore-based cages to populate a chiral conformation and the effect was measured with CD spectroscopy. Moreover, some promising results were obtained in the recognition of bio-relevant anionic molecules where one specific lantern-shaped cage, based on the rhodamine B dye, exhibited impressive ellipticities.

Important results were obtained in the field of supramolecular DNA recognition by employing the newly synthesized methylene blue-based Pd-helicate. Besides the preferential interaction of double-stranded DNA for one helical handedness of the artificial binding agent, focus was set on the class of G-quadruplexes. Several different topologies were analysed in combination with the helicate to understand the origin of selective structural recognition. A notable selectivity was found for the sequence *c-Myc27*, part of the promoter region of oncogene c-MYC, and its derivatives. Even if the recognition process was not yet elucidated in atomistic detail, the new findings spur its application potential.

The implementation of organic dye functionalities was proven to be a successful strategy to expand cage properties that arise from the interaction with visible light. New structural motifs, with interesting optical properties and applicability in chiral recognition of both small molecules and DNA have been developed. This work opens new possibilities of exploring light-driven processes such as photoinduced energy or electron transfer and their application in the field of photo-redox supramolecular catalysis.

Zusammenfassung

Organische Farbstoffe sind weithin für ihre breite Anwendung in der Industrie (z.B. als Färbungsmittel und Lasermaterialien), der Medizin (z.B. als Diagnosewerkzeug und Wirkstoff) und in der Forschung (z.B. in der Fluoreszenzmikroskopie, in FRET-Setups und als Photosensibilisatoren) bekannt. Alle Anwendungen beruhen auf der typischen Interaktion dieser Chromophore mit sichtbarem Licht. Während die Farbstoffe im Tonnenmaßstab hergestellt werden, bietet ihre Implementierung in komplexe chemische Systeme und Nanostrukturen noch nicht ausgeschöpftes Potenzial in der Entwicklung neuer funktionaler Systeme und Materialien. Insbesondere ihr synthetischer Einbau in selbstassemblierte supramolekulare Systeme ist noch weitgehend unerforscht. Die Kombination beider Konzepte würde zu funktionalen Konstrukten mit interessanten photophysikalischen und redoxchemischen Eigenschaften führen, die für diagnostische und katalytische Anwendungen genutzt werden könnten.

Das Ziel dieser Arbeit ist daher der Einbau organischer Farbstoffe in nanogroße Koordinationskäfige, um diese mit der Fähigkeit zur Interaktion mit sichtbarem Licht auszustatten. Neue bis-monodentate Liganden wurden auf Basis ausgewählter Diketopyrrolopyrrolfarbstoffe (DPPs) und der Teerfarbstoffe Michlers Keton, Rhodamin B, Methylenblau und Kristallviolett entworfen. Der Einbau dieser Farbstofffunktionalitäten in metallbasierte supramolekulare Strukturen wurde durch die Koordination der neu entwickelten Liganden an Pd(II)-Kationen erreicht. Die strukturellen und optischen Eigenschaften dieser Konstrukte wurden mit einer breiten Palette an Spektroskopie-, Spektrometrie- und Beugungsmethoden untersucht und vollständig charakterisiert. Für DPP-basierte homo- und heteroleptische Strukturen wurden interessante optische Merkmale gefunden. Die neue Topologie eines homoleptischen $[Pd_2L_4]$-Käfigs wurde aufgedeckt, welche eine untypische Anordnung der vier Liganden um die Pd-Achse aufweist, um die π-π-Stapelung der vier Chromophore zu ermöglichen. Außerdem wurden Käfig-zu-Käfig-Umwandlungen bei Kombination von drei unterschiedlichen Liganden (mit DPP-, Carbazol- und Dimethylfluoren-basierten optisch relevanten Gruppen) beobachtet.

Der Einbau der funktionellen Gruppen der Teerfarbstoffe in bis-Pyridin- oder bis-Isochinolinliganden erforderte ein durchdachtes Design, um die Erhaltung der Absorptionseigenschaften zu gewähren. Typische Alkinbrücken zwischen den Donorgruppen und den Grundgerüstbausteinen hätten die elektronische Konfiguration des ursprünglichen Farbstoffs gestört. Deshalb wurden in dieser Arbeit Piperazinlinker verwendet. Durch Koordination an die quadratisch planaren Metallkationen wurden laternenförmige oder helikal verdrehte $[Pd_2L_4]$-Käfige erhalten, die sichtbares Licht absorbieren. Die bemerkenswerten Absorptionseigenschaften wurden bei der Erkennung kleiner, chiraler Moleküle ausgenutzt. Deren Bindung im Käfiginnern oder an der Peripherie führte dazu, dass die chromophorbasierten Käfige eine chirale Konformation einnahmen, was mit CD-Spektroskopie gemessen wurde. Des Weiteren wurden einige vielversprechende Ergebnisse bei der Erkennung biorelevanter anionischer Gäste erzielt, wobei ein spezieller laternenförmiger Käfig, der auf Rhodamin B basiert, beeindruckende Elliptizitäten zeigte.

Wichtige Ergebnisse wurden durch Verwendung des neu synthetisierten, Methylenblau-basierten Pd-Helikats auch auf dem Feld der supramolekularen DNA-Erkennung erhalten. Neben der bevorzugten Interaktion von doppelsträngiger DNA mit einer der beiden möglichen helikalen Orientierungen des künstlichen Bindungspartners wurde der Fokus auf die Klasse der G-Quadruplexe gelegt. Mehrere unterschiedliche Topologien wurden in Kombination mit dem Helikat analysiert, um den Ursprung der verschiedenen und selektiven strukturellen Erkennung zu verstehen. Eine auffallende Selektivität wurde für die Sequenz c-Myc27, welche Teil der Promotorregion des c-MYC-Onkogens ist, und deren Derivaten gefunden. Auch wenn der genaue Erkennungsprozess nicht vollständig aufgeklärt werden konnte, wurde ein erheblicher Fortschritt in diese Richtung gemacht.

Es wurde gezeigt, dass der Einbau organischer Farbstofffunktionalitäten eine erfolgreiche Strategie darstellt, um Käfigeigenschaften um die Interaktion mit sichtbarem Licht zu erweitern. Neue Strukturmotive mit interessanten optischen Eigenschaften und Anwendbarkeit in chiraler Erkennung von kleinen Molekülen und auch von DNA wurden entwickelt. Diese Arbeit eröffnet neue Möglichkeiten bei der Nutzung von lichtgesteuerten Prozessen wie photoinduziertem Energie- oder Elektronentransfer und deren Anwendung auf dem Feld der supramolekularen Photoredoxkatalyse.

Awards and Scholarships

2020 Poster Prize at the Twitter Poster Session of ISMSC2020.

2020 Chosen participant of the 70th Lindau Nobel Laureate Meeting (Interdisciplinary).

2019 IUCr Travel bursary to visit the ISMSC2019 in Lecce, Italy.

2019 Poster Prize at SupraChem2019 offered from Springer in the category "Molecular Cages, Switches and Machines".

2018 Poster Prize at Supra@Lyon2018 offered from Wiley with the book "The Nature of the Mechanical Bond: From Molecules to Machines".

2017 Kekulé Mobility PhD Fellowship offered by the Fonds der Chemischen Industrie (FCI).

Conferences and Contributions

Poster presentation	Aug 2020	Twitter Poster Session for ISMSC2020
	Sep 2019	IMBP in Dortmund, Germany
	Sep 2019	ISCCC in Bochum, Germany
	Jun 2019	14th ISMSC in Lecce, Italy
	Feb 2019	SupraChem 2019 in Würzburg, Germany
	Dec 2018	Supra@Lyon in Lyon, France
	Mar 2018	9th MSCEC in Münster, Germany
	Aug 2017	9th KOPO in Bad Honnef, Germany
	Jul 2017	13th ISMSC in Cambridge, United Kingdom
	Feb 2017	SupraChem 2017 in Aachen, Germany
Oral presentation	Nov 2020	Invited talk 2nd SEEDS4CD Virtual Seminar
	Jun 2020	Invited talk from group of Prof. Prato – Trieste University
	Feb 2020	Tag der Chemie, TU Dortmund
	May 2018	FCI fellows meeting, Bochum, Germany

Publications

- "Coal-Tar Dye-based Coordination Cages" I. Regeni, B. Chen, M. Frank, A. Baksi, J. J. Holstein, G. H. Clever, *Angew. Chem. Int. Ed.* **2020,** accepted, DOI: 10.1002/anie.202015246.
- "Bifunctional Behavior of a Porphyrin in Hydrogen-Bonded Donor-Acceptor Molecular Chains on a Gold Surface" Z. Feng, S. Velari, C. Dri, A. Goldoni, L. L. Patera, I. Regeni, C. Forzato, F. Berti, M. Peressi, A. De Vita, G. Comelli, *J. Phys. Chem. C* **2019**, *123*, 7088.
- "Catenation and Aggregation of Multi-Cavity Coordination Cages" R. Zhu*, I. Regeni*, J. J. Holstein, B. Dittrich, M. Simon, S. Prévost, M. Gradzielski, G. H. Clever, *Angew. Chem. Int. Ed.* **2018**, *57*, 13652. (* these authors contributed equally to this work)
- "Structure relationships between bis-monodentate ligands and coordination driven self-assemblies" S. Saha, I. Regeni, G. H. Clever, *Coord. Chem. Rev.* **2018**, *374*, 1.
- "Rapid structure determination of microcrystalline molecular compounds using electron diffraction" T. Gruene, J. T. C. Wennmacher, C. Zaubitzer, J. J. Holstein, J. Heidler, A. Fecteau-Lefebvre, S. De Carlo, E. Müller, K. N. Goldie, I. Regeni, T. Li, G. Santiso-Quinones, G. Steinfeld, S. Handschin, E. van Genderen, J. A. van Bokhoven, G. H. Clever, R. Pantelic, *Angew. Chem. Int. Ed.* **2018**, *57*, 16313.

Table of Contents

1. General introduction

1. General introduction

1.1 Organic Dyes

1.1.1 Historical and cultural background of synthetic organic dyes

In the middle of the 19th century, coal gas and solid coke had replaced candles, animal oils, and wood as the most important source of light, heat and cooking fuel in European and American cities. Coal gas and coke were obtained by burning coal at high temperature in absence of oxygen. The process left behind a thick, smelly, brown liquid – coal tar, the first large-scale industrial waste. August Wilhelm von Hofmann, member of the Royal College of Chemistry in London, was convinced that coal tar could be employed for something useful, and spent years separating the various components by vaporizing them at different temperatures. The new compounds were then studied for the synthesis of drugs for medical treatments, otherwise difficult and expensive to obtain from natural sources. It was in 1856, in a failed attempt to synthetize quinine, the only effective drug against malaria, that William Henry Perkins, an 18-year old student of Hofmann, obtained accidentally the first synthetic dye, Mauveine, starting from a mixture of aniline and toluidine.[1]

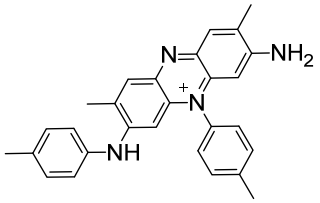

Figure 1.1: Perkin's Mauveine.

In the following years, the industry rapidly expanded around Perkin's discovery. An important decision was to follow the instinct of Hofmann by finding uses for all the coal-tar constituent parts, not just aniline. After the aniline dyes, derived from benzene, came magentas made from toluene, reds from anthracene, pinks from phenol and indigos from naphthalene. In these years, dyes like methylene blue, crystal violet, malachite green, rhodamine B and many more were discovered. Dyes came first, soon followed by paints, solvents, drugs such as aspirin, sweeteners, laxatives, detergents, inks, anesthetics, cosmetics, adhesive, photographic materials, roofing, resins, and the first primitive plastics, all synthetic and all derived from coal tar, the fountainhead of commercial chemistry. The discovery of mauveine also led to developments within immunology and chemotherapy. In 1891, in his research for antiseptic substances that could be used to treat bacterial infections, Paul Ehrlich discovered that one of the dyes he used for staining his microscope slides actually killed bacteria. He found that the yellow dye flavine killed the germs responsible for abscesses. Ehrlich went on to use a compound to target syphilis, the first time a chemical was used in order to selectively kill bacteria in the body. He also used methylene blue to target the plasmodium responsible for malaria. Coal tar shampoos and soaps came too - and are still available in very diluted forms as approved treatments for psoriasis and head lice. Germany's Ruhr Valley, with its vast deposits of bituminous coal, became the industrial heartland of Europe and thus the world. By 1913, Germany was exporting about 135 000 tons of dyes.[2]

The British satirical magazine Punch, back in 1859 had lampooned "mauveine measles" as a fashion epidemic that should be treated with a "dose of ridicule". The same magazine, by 1888, was singing the praises of aniline chemistry, with only a tinge of sarcasm (here a small extract):[3]

Oil, and ointment, and wax and wine,
And the lovely coulours called aniline;
You can make anything from a salve to a star,
If you only know how to, from black Coal-tar.

The discovery of synthetic dyes revolutionized society as we know it, democratizing colors. New dyes kept being discovered and employed in all possible industrial applications. However, the developments of new

reactive dyes illustrate the general tendency of moving away from purely empirical synthesis of colorants towards studying the mechanisms of the dye/substrate interaction with already known chromogens. The discovery of the diketopyrrolopyrrole (**DPP**) pigment is a brilliant example of a new class of pigments found this way (for more details on **DPP**s see introduction of chapter 3).

1.1.2 Organic dyes in research

Besides their major aesthetic application for the coloring of objects such as textiles, cars, household items and food ingredients, organic dyes count endless applications in every conceivable field of research. Most of the functionalities arise from the typical interaction that such moieties have with the visible part of the electromagnetic spectrum of light. For example, depending on their chemical structure, they can function as indicators (Figure 1.2) since it is possible to dramatically change their maximum absorbance wavelength upon slightly changing environmental conditions (pH, redox environment, solvent polarity, temperature, concentration, etc).[2]

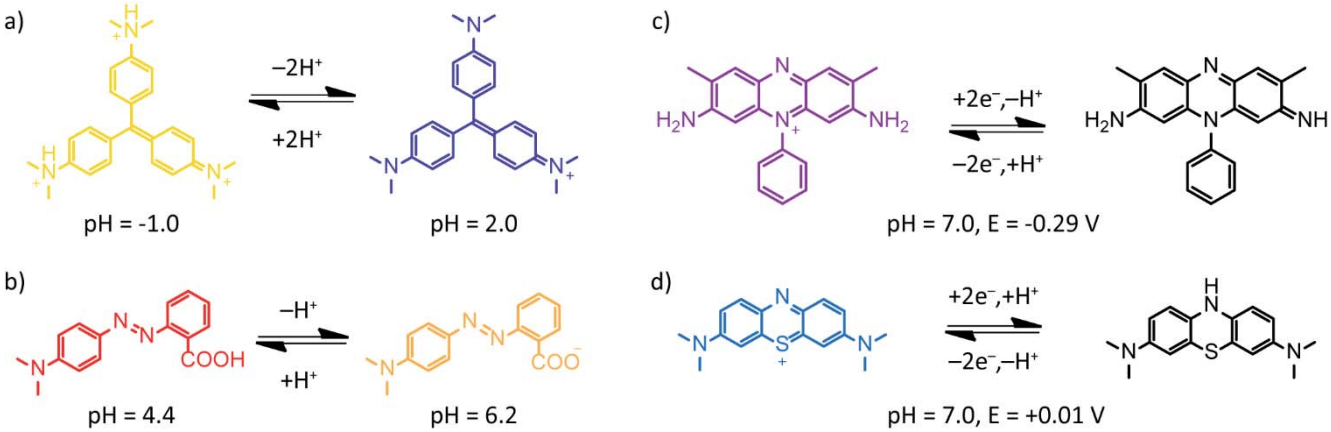

Figure 1.2: Examples of a), b) pH indicators and c), d) redox indicators. a) Crystal violet, b) methyl red c) safranin T, d) methylene blue.

Visible light photoredox catalysis is receiving an increasing attention in organic synthesis owing to milder conditions, unnecessary requirement of radical initiators or stoichiometric chemical oxidants or reductants, when compared to thermal reactions.[4] Organic dyes are considered as attractive metal-free organic photosensitizers in photoredox catalysis in view of their ready availability, sustainability, non-toxicity and ease of handling.[5,6] The reactivity afforded by many organic catalysts allows access to unique chemistries and a broad range of substrates that are unreactive in most synthetic contexts. Moreover, the diversity of these organic compounds can accomplish both reductive, oxidative as well as redox neutral transformations. For example, making use of Eosin Y, a fluorescent dye from the family of fluorescein, a number of reactions could be catalyzed like reductive deoxygenations[7] and desulfonation[8], oxidative transformation of phenylboronic acid to phenol[9], oxidative synthesis of aryl ketones[10] and many more.[11,12] For their photosensitizer abilities, multiple dyes have been exploited like methylene blue, [13,14] especially for its ability of promoting $^3O_2$ to $^1O_2$ enabling photooxygenation reactions.

Organic dyes are also employed in colorimetric sensors,[15] as well as in fluorescent receptors.[16] Their particular chromophoric nature is studied in medical contexts for photodynamic therapies (PDT) but also for their particular antibacterial activity, they are considered promising pharmaceuticals.[17] New laser technologies have also started to exploit the high quantum yield of colored organic compounds such as rhodamine 6G or malachite green. These dye-based lasers can provide ultra-short laser pulses down to 16 femtoseconds.[18] Furthermore, recent years have witnessed many fascinating applications of organic dyes as sensitizers in the development of dye-sensitized solar cells.[19]

1.1.3 Interaction of organic dyes with DNA

Certain organic dyes are particularly popular in medicine and biology and are found to strongly interact with biomolecules such as proteins and DNA. They are used as biological stains to highlight structures in biological tissues. The colored or fluorescent compounds are used to visualize more or less specifically certain types of components in samples such as proteins or DNA/RNAs in cells, bacteria, tissues or gels in different analytical techniques (microscopy, electrophoresis, …).[20] Crystal violet and safranin are used in Gram's stain, a staining technique used to classify bacteria in which a specimen is first stained with crystal violet, than treated with an iodine solution, decolorized with alcohol, and counterstained with safranine. Gram-positive bacteria retain the violet stain, gram-negative bacteria do not.

Focusing on their use in nucleic acid research, beside serving as biological stain (e.g. electrophoresis studies), they are investigated as potential DNA binders and drug candidates.[21–33] Crystal violet and methylene blue dyes are particularly popular in this field. Their cationic and planar structure allow multiple binding modes on secondary structures, such as groove binding and intercalation. Moreover, being chromophores, their interaction and properties can easier be assessed with optical spectroscopy. They are also well-known as binders for G-quadruplexes (a special kind of DNA secondary structure, see chapter 5 for more insights) binders with high stabilization effects in the overall structure. Their binding modes have been studied and postulated (Figure 1.3) by several research groups.[27,34,35] They are, however, still central topic of discussions in the field.

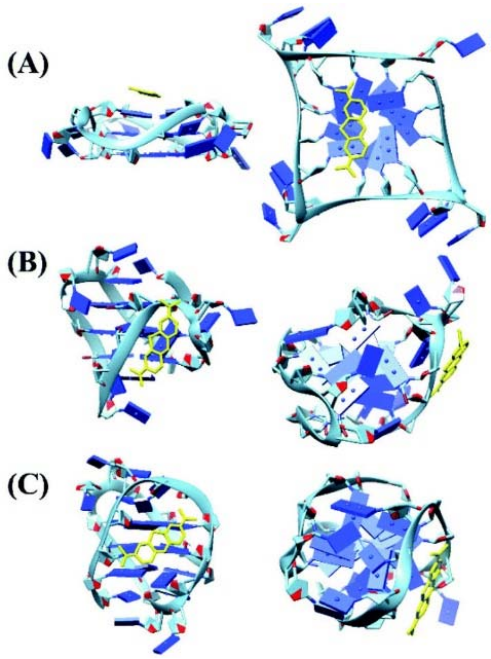

Figure 1.3: Docking results of interaction mechanisms between the methylene blue dye (in yellow) and human telomer G-quadruplexes with (A) parallel, (B) mixed hybrid and (C) antiparallel conformations. Left pictures are the side views of the G-quartets, and the right ones are top views. Reprint with permission from RSC.[35]

As briefly covered here, organic dyes have been known for more than a century and find countless applications in every conceivable field of research. However, their outstanding properties and reactivities have yet not fully been explored in the context of self-assembled supramolecular structures. This work aims at covering this gap (for more details see chapter 2, scope of the thesis). In order to provide the reader with the necessary background to frame and fully understand the reported research study, an essential introduction on supramolecular chemistry, coordination cages and already existing example of chromophore-based cages, will be presented in the following.

1.2 Origin and development of Supramolecular Chemistry

The key goal of chemical science in the nineteenth and twentieth century was to understand how atoms come together to form molecules trough chemical bonds. This understanding was critical and underlies the high standard of living that the world enjoys today. By the 1960s, non-covalent interactions like hydrogen bonds had already been recognized to be critical for biochemistry, for example playing a big role in holding proteins or DNA together. But non-covalency had yet to be accepted along with covalent bond formation as a tool of equal synthetic capability. That changed with the work of Lehn, Cram and Pederson that led them to the 1987 Nobel Prize in chemistry for "their development and use of molecules with structure specific interactions of high selectivity".[36]

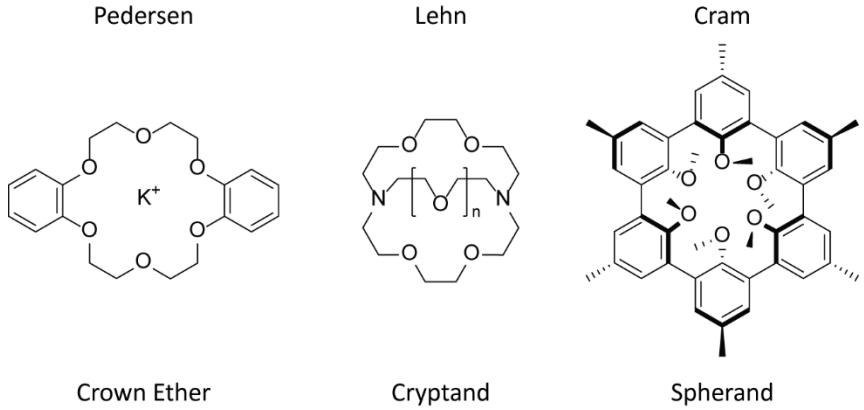

Figure 1.4: Macrocyclic compounds developed by 1987 Nobel prize laureates. Crown ethers were first reported by the group of Pedersen as an accidental discovery, cryptands from the group of Lehn and spherands by the group of Cram.

Their work on macrocyclic compounds with high affinity to metal cations led to the conception of a new field of chemistry. Lehn called the study of the structure and synthesis of compounds built from intermolecular interactions "Supramolecular Chemistry". Intermolecular forces comprise electrostatic attraction, hydrogen bonds, π-π stacking, Van-der-Waals forces, hydrophobic effects and, under certain conditions, metal coordination.

The development of host molecules such as crown ethers, cryptands and spherands, established the field of the so called "*host-guest*" chemistry. In this sector, a molecule, *host*, coordinates or binds through non-covalent interactions a smaller species, *guest*, to yield a host-guest adduct which represents the actual supramolecular system. Basic requirement for host and guest to interact effectively is complementarity from the electronical as well as the geometrical and dimensional point of view. A natural development of khas been to make use of the non-covalent interactions upstream, as the glue to hold together new supramolecular architectures, highly functional and usually in equilibrium with the basic components.

In the following years, the field of supramolecular chemistry experienced a rapid expansion and the number of supramolecular systems and unique structures increased continuously. With the rising interest and development of new analytical techniques, novel chemical systems with high diversity and complexity were developed. Work in modern supramolecular chemistry encompasses not just host-guest systems but also molecular devices and machines, molecular recognition, as well as the so called 'self-processes' such as self-assembly and self-organisation. Modern supramolecular chemistry interfaces with the emergence of complex matter and nanochemistry.

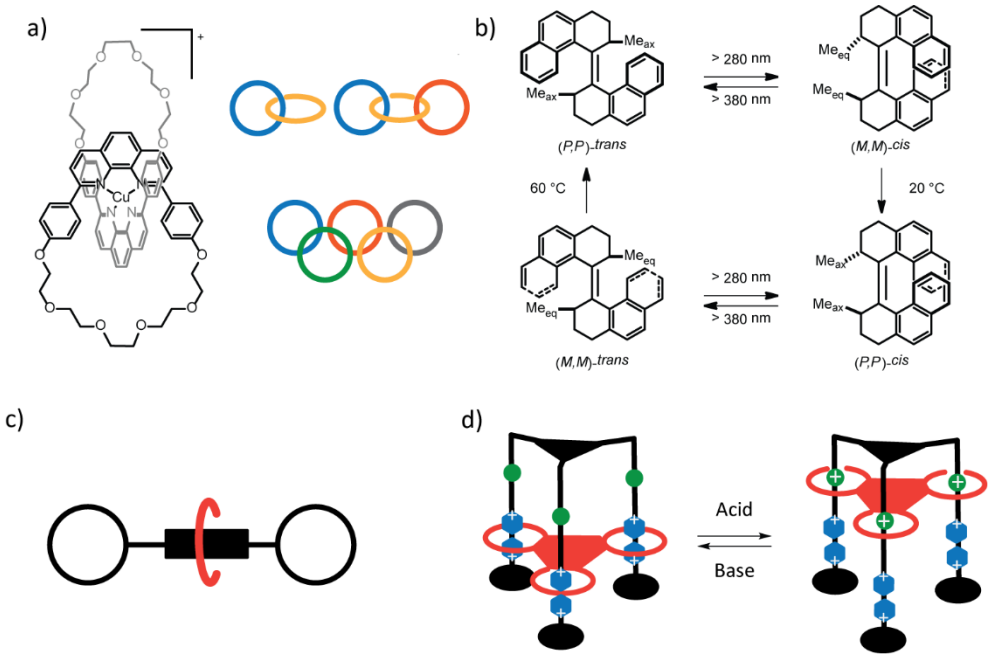

Figure 1.5: a) The first catenane developed by Sauvage and its simple representation together with the iconic [3]catenane and the so called olympiadane. b) The first molecular motor developed by Feringa. The paddles can rotate in two directions after breaking of the double bond via light irradiation for the *cis-trans* isomerization, but the thermal isomerization occurs only in one direction and therefore the full 360° rotation is only possible in the clockwise sense. c) Schematic illustration of a rotaxane with the macrocycle (in red) that can shuttle on different position along the axle (in black) but never leave because of the stoppers (white spheres). d) Molecular lift designed by Stoddart. The red triple macrocycle is designed to have higher affinity to the blue stop (bispyridinium units) than the green stop (secondary amines). But upon protonation, the ammonium cations are the strongest interaction partner and make the whole red part lift up along the structure. Upon deprotonation, the red part shifts down again.

In 2016 Stoddart, Feringa and Sauvage received the Nobel Prize for their work on mechanical bonding and nanomachines.[37] The development of catenanes, molecular interlocked rings, marked a new way to bind molecules. Transition metals like Cu(I) were used to template the catenanes and allowing high yield synthesis.[38] The concept was extended with a big variety of binding motifs to template the supramolecular assemblies allowing the formation of a vast number of topologies like a [3]catenane, a [5]catenane called olympiadane due to its similarity to the Olympic rings,[39] a chiral molecular trefoil knot[40] and many more (Figure 1.5 a).[41–43]

A further development led to the first molecular shuttles, the rotaxanes (Figure 1.5 c). In such mechanically interlocked molecules, a linear molecule is threaded through a macrocycle. The molecular cycle can be moved to certain positions on the axle and is hindered from leaving the axle by stoppers. The movement can be controlled by external stimuli such as light, temperature, solvent, chemical imputs and pH. Extending this concept, the first molecular "lift" was reported, which can move itself up and down upon changing of the external conditions (Figure 1.5 d).[44] Feringa et al. reported more than 50 molecular motors that allow a unidirectional turning.[45] Their first synthetic molecular motor, published in 1999, marked a turning point in the field. The motor was made out of a single molecule, that contained two chiral "paddle" units connected through a double bond and the turning could be controlled via thermal isomerization and photoisomerization (Figure 1.5 b).[46] The chirality of the paddles is necessary to dictate the direction of thermal isomerization to the energetically favored (*P*,*P*) isomers with the methyl groups in axial position.

The field of supramolecular chemistry is being vastly explored by research groups all around the word and new fascinating functional structures are published continuously. Supramolecular chemistry critically hinges on the phenomenon of self-assembly and self-organization that operates in an astonishing diversity of applications, from the action of detergents to the origin of life. The greatest advantage of non-covalent association is that, unlike most covalent bond formations (exceptions include dynamic covalent bonds), it

is reversible. Life as we know it would be impossible if molecules were kept bound to each other permanently.

1.1.4 Metal-mediated self-assembly

Among all the dynamic and reversible interactions, transition metal coordination takes a prominent role in the construction of functional architectures. Such approach takes the name "Metal-Mediated Self-Assembly".[47] In this approach, two kinds of building blocks are joint together to form the supramolecular structure. Electron pair acceptor building blocks can be defined as Lewis acids and usually comprise transition metal complexes or *naked* cations (metal cations coordinated by exclusively labile ligands). While electron pair donor building blocks, Lewis bases, typically consist of polytopic organic ligands of various geometrical design. In Figure 1.6, some examples of coordination compounds and organic polytopic ligands with the most commonly found donor groups are reported. The depicted structures are also associated to the schematic view of their inherent coordination geometry as electron accepting building blocks (in green) and their geometry as electron donating building blocks (in red). Depending on the nature and directionality of the metal nodes and the length, bending angle, choice of coordinating groups and denticity of the organic ligand, multiple topological arrangement can be obtained. Deterministic thinking and logics play a big role in designing the basic components. Their geometrical and electronical complementarity allow their simple combination in solution to result in the spontaneous formation of the desired product. However, occasionally this approach overcomes rationality and leads to unexpected and stimulating results.

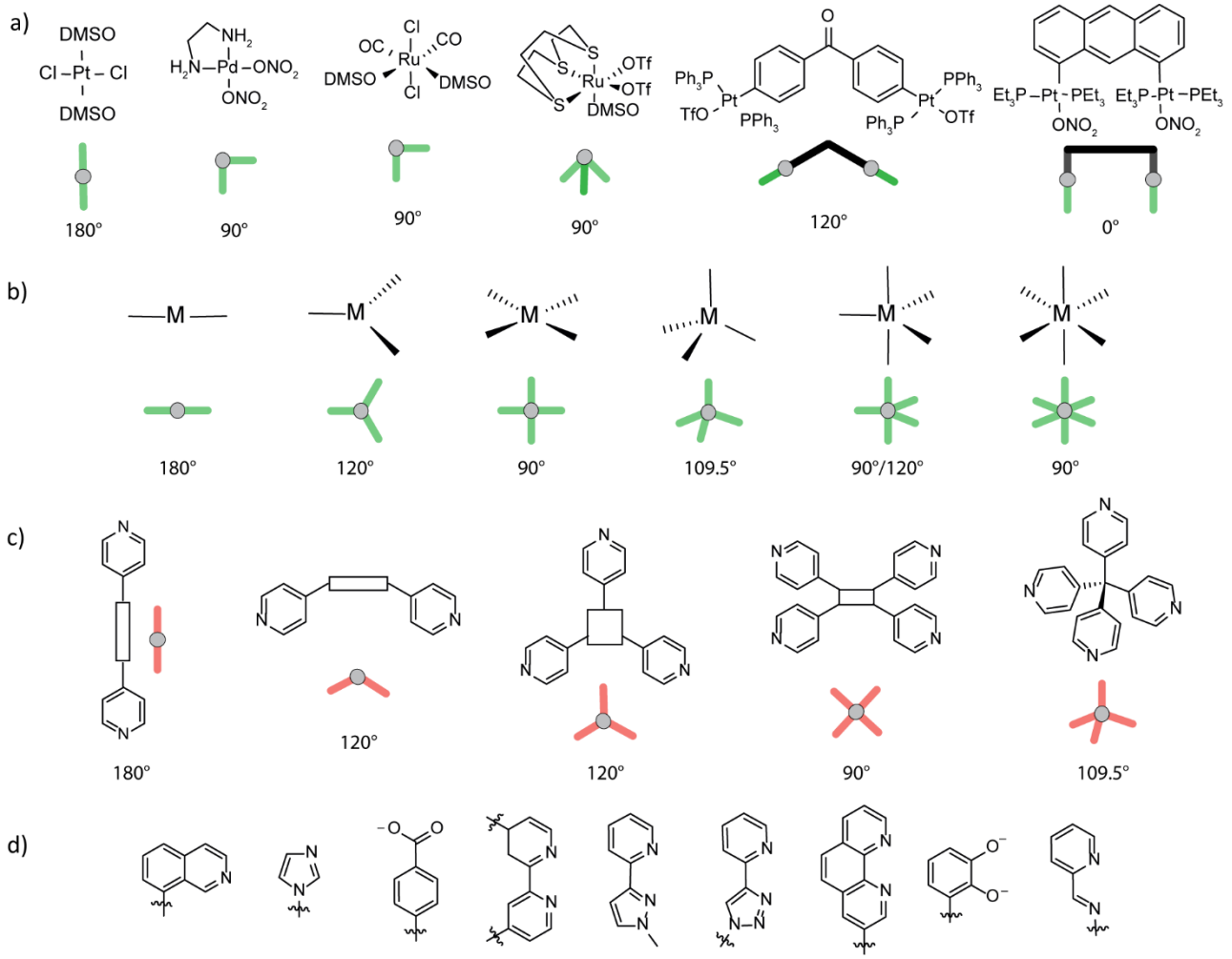

Figure 1.6: a), b) Some examples of electron acceptor building blocks. a) transition metal complexes with the weakly bound ligands determining the coordination geometry available for the supramolecular structure to form. b) Coordination geometries of transition metal cations if coordinated by exclusively labile ligands. c) Some examples of generic structures of electron donating building blocks. The pyridine donor groups can be substituted with d) other most commonly found coordinating groups.

The self-assembly of organic ligands with metal cations/coordination complexes, has proven to be a reliable recipe for the realization of mesmerizing supramolecular structures such as rings, helicates,[48] cages and capsules,[49–52] as well as knots and links.[42] Some of these assemblies were only synthetized in order to demonstrate the power and reliability of rational design in supramolecular chemistry. Other structures were prepared with the aim of encapsulating certain guest compounds with high selectivity, often projected towards the discovery of new receptors, sensors and molecular transporters.[53,54] An increasing number of systems are also showing the capability of stabilizing reactive compounds[55] and behaving as catalytic reaction chambers that can mimic enzyme functionalities.[56] Confining the reagents in a restricted environment has shown to dramatically enhance the reaction rate as well as to effect the regio- and stereoselectivity.[57,58]

1.1.5 Self-assembled systems based on bis-monodentate ligands

Among all the metals used in the construction of metallo-supramolecular cages, square-planar palladium(II) ions take a prominent role due to their highly directional and predictable coordination environment, convenient ligand exchange kinetics and diamagnetism. One of the most versatile ligand designs comprises bent or banana-shaped, bis-monodentate pyridine-based bridging ligands. Most of the ligands already reported, are composed of an aromatic core which is connected to the pyridine donors through rigid bridges such as alkynes or 1,4-phenylene linkers. Depending on the ligand length, bending angle, flexibility and other structural features as well as templating molecules, solvent effects and counter ions, a variety of discrete structures may be formed. Usually, these ligands form metal complexes in which they can afford to remain in their least constrained conformation, as strain often plays a key role amongst the factors that lead to the thermodynamically most stable structure. Thus, following general geometrical considerations, the ligand shape often determines the shape of the final product.[52]

In a 2D simplification of the real 3D geometric problem, the ligands can adopt conformations where the bonding vectors of the two pyridyl donors are divergent, collinear or convergent. Figure 1.7 classifies the ligands according to the 2D-approximated angles between the donating lone pairs of the widely used pyridine systems. The extreme cases, shown to the left and right, respectively, are linear ligands with 180° diverging donors, producing extended grids when mixed with *naked* square-planar metal nodes, and highly inward bent ligands with a -180° donor relation that can lead to the formation of unique mononuclear complexes *trans*-chelates.[60] Ligands with angles between these extremes form a variety of discrete structures and we name here a representative sample. For ligands highly inward pointing (< 0°), depending on the distance between the pyridine groups, a mononuclear butterfly structure [ML_2] may be formed when the two donor sites of the ligand come so close that they are able to chelate a single metal cation.[61] While, when they are more distant from each other, they usually form [M_2L_4] cages characterized by a high degree of helical twist around the metal-axis.[62] When the angle between the two vectors defined by the lone pair of the donor group is close to 0° (small deviations in both directions are also allowed) small [M_2L_4] cages and/or their interpenetrated dimers form.[63] As the angle increases, the size of the assembly and the number of components increases, too. For ligands that have an angle between 0° and 90° several topologies have been reported, often in equilibrium with each other. The most common ones are highly symmetrical rings [M_3L_6],[64,65] [M_4L_8][66] or even [M_5L_{10}], but also [M_4L_8] tetrahedrons and their dimers,[67] or [M_3L_6] rings with low symmetry.[68] For ligands that have a close proximity to 90°, the [M_6L_{12}] topological assembly, representing a perfect cubic box, has been shown by different groups.[69,70] While for larger angles, different size of large Archimedean solids form most of the times.[71] Some interesting evidence in the formation of Goldberg Polyhedra opened the field of chiral structure formations.[72] In the following chapters of this thesis, many of these structure will be encountered.

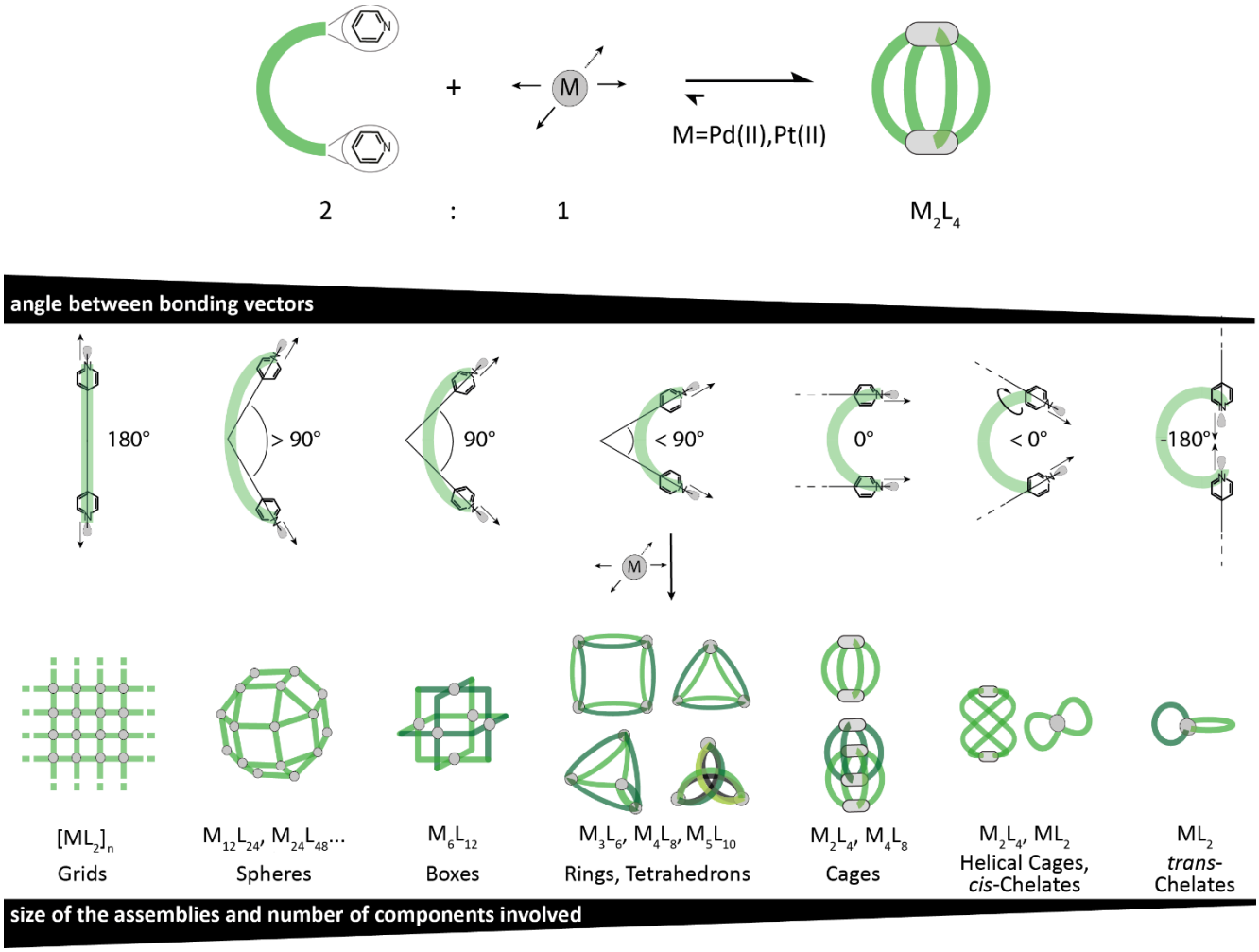

Figure 1.7: Formation of a M_2L_{2n} coordination cage by combination of a bent bis-pyridine ligand with square planar metal cation in the ratio 2:1. The product is in equilibrium with the single components. Formation of a variety of M_nL_{2n} coordination architectures from square-planar coordinated metal cations and different types of bis-monodentate ligands. The classification of the ligands is based on the angle between their two-donor electron lone pairs (here simplified in two dimensions by placing the donor vectors in a common plane. The definition of the angles between vectors in 3D, representing donors that have rotated out of plane, is less intuitive).

It should be noted that these rules of thumb may be overwritten by entropic effects and the action of further (de)stabilizing enthalpic contributions. The shown cartoon representations indeed do simplify the real situation since ligands may have flexible backbone structures and adopt different geometries in different assembly contexts. Furthermore, the three-dimensional shapes and conformational freedom of real ligands often allow them to yield structures whose formation may not be apparent upon visual inspection of the drawn ligand structures.

Most of the supramolecular assemblies have large openings that allow small guest molecules to enter and leave the cavity. Suitably functionalized members of this compound class have the potential to mimic natural binding pockets found in regulatory proteins and enzymes. Therefore, they promise to be employed in a wide variety of applications for the transport of molecular cargo and catalysis. For this reason, in more recent studies, the focus has shifted towards the design of ligands that, beside the structural role, bring additional functionality to the assemblies.

Two approaches were undertaken in the last years both aiming at achieving multifunctional system. On the one hand, new strategies to increase the structural complexity of metallo-supramolecular molecules were explored. On the other hand, ligands based on new functionalities were designed (Figure 1.8). In the first approach, carefully designed ligands are mixed together and, thanks to principles such as shape

complementarity, donor site engineering and secondary interactions, only one product is favored and arises from all the possible statistical ones.[73] Such method has been substantially successful and led to several heteroleptic $[Pd_2L^A{}_2L^B{}_2]$ cages with the two kind of ligands in *cis*-[62] or *trans*-[74] configuration in the structure. In the second approach, the expansion of functionality in the systems could be obtained either introducing endo- or exohedral-substituents in the cage[75,76], or by implementing known active molecular moieties into the backbone of the ligands and transferring their functionality to the whole cage assembly.

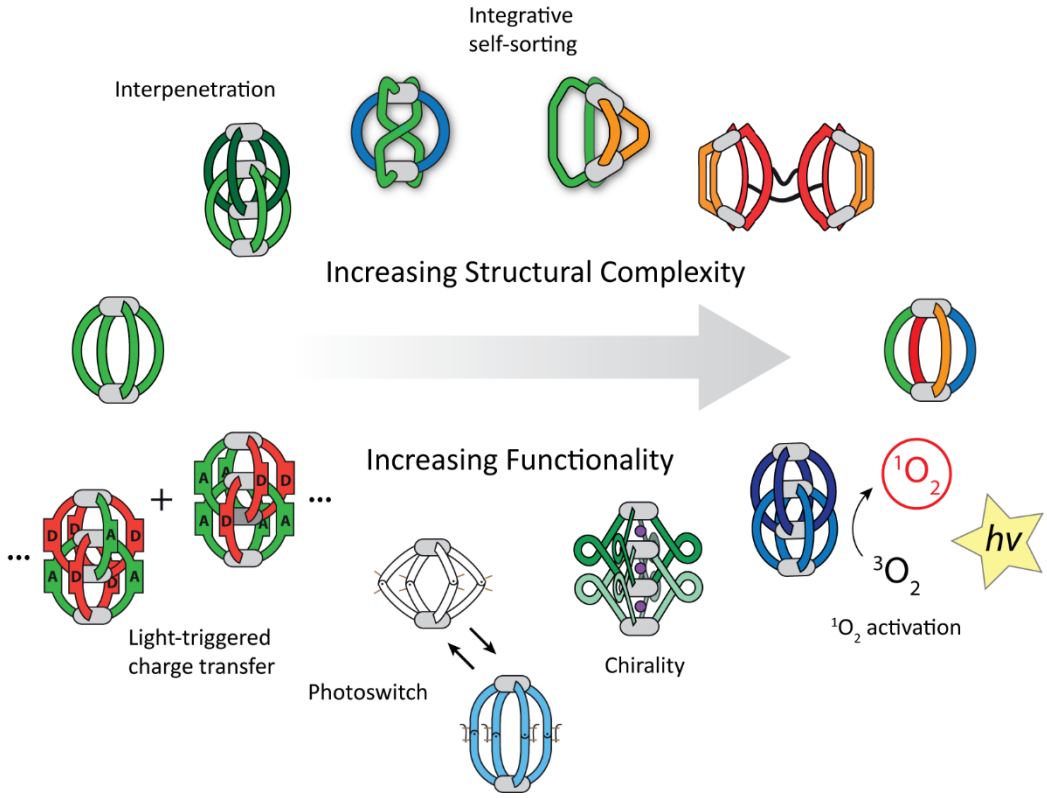

Figure 1.8: Increasing structural complexity and functionality of supramolecular coordination cages. Some iconic examples of our lab are presented.

The combination of structural complexity and new functionalities promises to lead to advanced applications in future research studies. In the context of bringing additional functionality to the supramolecular cages, particular focus is set in this work on those systems that have the inherent functionality of interacting with light and some examples are presented here.[77]

1.3 Chromophore-based coordination cages

Organic chromophores have been integrated into supramolecular architectures to equip them with various functions. Artificial mimics for solar energy conversion often use porphyrin arrays as light harvesting units, capable of energy transfer and charge separation.[78–80] Organic optical materials based on the non-covalent arrangement of compounds with specific photophysical properties have been proposed as active components for displays, light sources and optoelectronic circuits.[81,82] Moreover, numerous receptors with optical read-out, photoswitchable self-assemblies and light-controlled molecular machines have been reported.[83,84] Recently, photo-redox chemistry started to take advantage of the supramolecular organization of organic or metal-based chromophores into functional systems, e.g. for catalytic oxidation of alcohols[85] or cycloaddition reaction on anthracenes.[86] Dye-based assemblies have further been studied in the context of bio-imaging[87–89] and medicinal applications such as photodynamic therapy.[90–92]

With respect to discrete coordination cages with an accessible cavity, several different chromophores have been implemented in the ligand backbones to exploit the specific interaction that the functional groups have with light.[93–95] The resulting cages´ properties range from (chiro)optical sensing to charge separation

and energy transfer. Radical reactions have been realized in hosts where side-walls can be brought to excited states by irradiation with light.[96] Cages have also been used as photosensitizers for singlet O_2 generation,[97,98] and as reagents for photochemical hydrogen formation.[99–101] Most of the reported systems, however, are based on chromophores that absorb in the UV to short-wavelength visible region, giving rise to colorless or yellowish compounds. Exceptions include assemblies where highly colored charge-transfer complexes are part of metal nodes,[102] or metallo-ligands [103,104] and architectures based on photochromic diarylethenes (convertible between faint yellow and deep blue photoisomers)[105–108] or perylene units,[109–111] porphyrin-based boxes,[112] or BODIPY-functionalized assemblies.[113]

In view of the great importance of developing sensors for small molecules recognition, dye-based cages are very attractive candidates. Chromophore-based receptors own the characteristic inherent feature to allow diagnostics in the recognition event measurable with UV-Vis based spectroscopies. Multiple examples of this applications are reported in the literature and only few selected examples are reported here. The group of Nitschke recently reported a water-soluble tetrahedral capsule based on triazatriangulenium (TATA+) panels and Zn(II) cations (Figure 1.9 a).[114] TATA+ compounds are a class of organic dyes that feature a stable planar carbocation and an extended aromatic surface.[115,116] The subcomponent self-assembly of the TATA+ panels with tris(2-aminoethyl)amine and Zn(II), yielded a metal–organic container that is water soluble, stable at low concentrations, and enable to monitor the binding of biologically relevant species by fluorescence spectroscopy. The capsule was found to strongly interact with positively charged nucleotides, while no binding was encountered for neutral species. Upon anion recognition the fluorescence of the cage was quenched, and the color of the solution shifted from pink to orange, visible by eye.

In 2019, the Clever group, contributed with a helicene-based sensor for small anionic guests (Figure 1.9 b).[117] The Pd-based coordination cage features bis-pyridine organic ligands with the backbone based on enantiopure helicene moieties. The homochiral organization of the ligands in the assembly leads to hollow structures with distinctive CD signatures. Encapsulation of sulphonated guests causes a modulation of the helical pitch of the four helicenes (arranged as parallel springs around the Pd(II) cations) as the cage structure adapts to maximize the positive interaction with the guests. The effect of differently sized guests is measurable with CD spectroscopy. Furthermore, direct evidence for shrinking and expansion of the cages upon addition of the short and long guests, respectively, came from trapped ion mobility ESI-TOF mass spectrometry (timsTOF).

The group of Ward, reported a cubic cage featuring twelve naphthalene moieties as parts of bis(pyrazolyl-pyridine) ligands, wrapped around 8 Co(II) metal centers.[118–120] On the one hand, the cubic cage was found to have a high affinity for alkyl phosphonates such as chemical warfare agent simulants (Figure 1.9 c'). The guests' encapsulation was studied and monitored with fluorescence-based response.[121] On the other hand, exploiting the array of twelve naphthyl fluorophores built into the same self-assembled cage, it has been demonstrated how it can act as an antenna group, effecting photoinduced electron or energy transfer to bounded guests (Figure 1.9 c'' and c''') in the central cavity.[122,123]

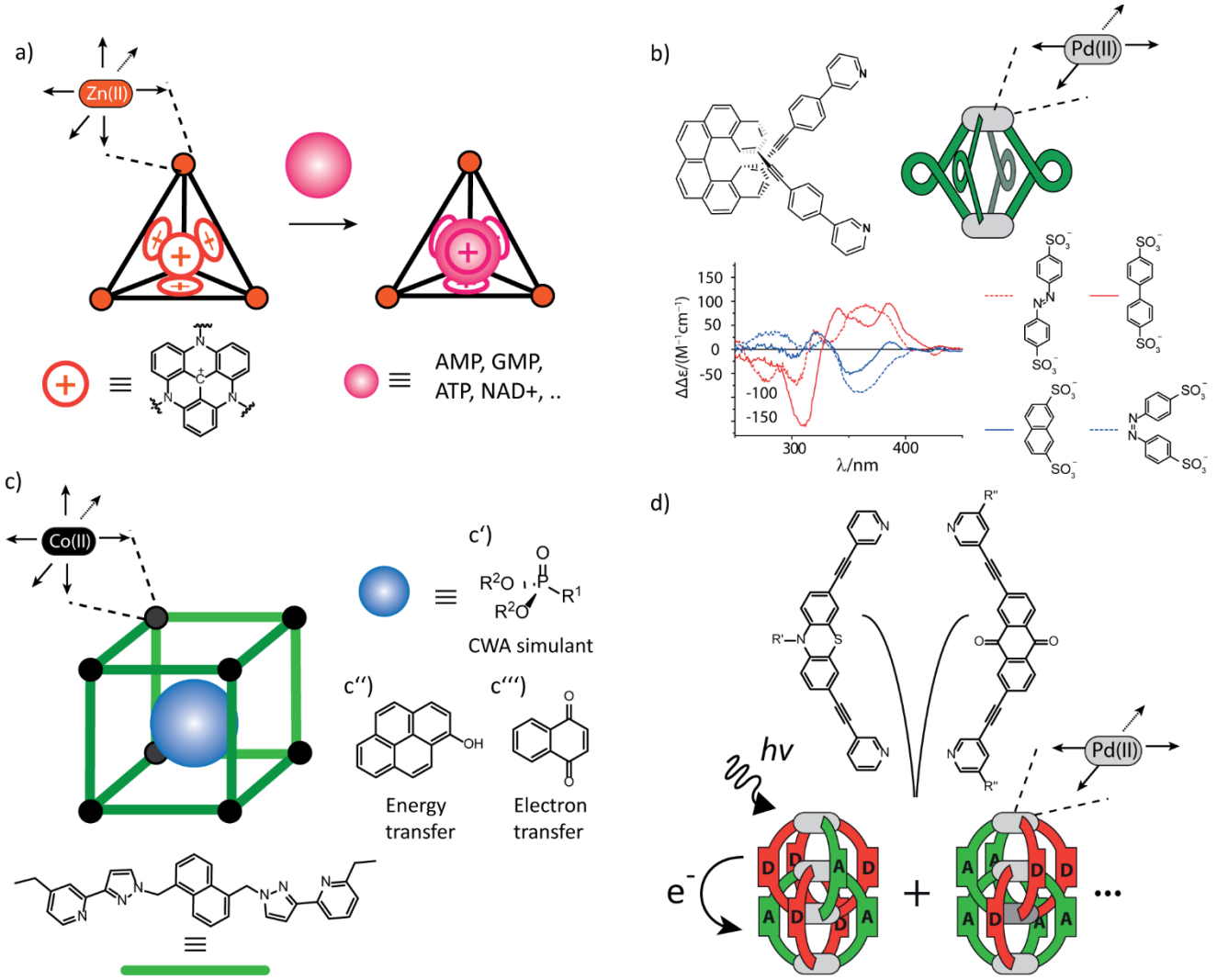

Figure 1.9: a) Water-soluble tetrahedral capsule based on triazatriangulenium (TATA+) panels and Zn(II) cations for emission spectroscopy monitoring binding of negatively charged nucleotides. b) Helicene-based Pd-cage as chiroptical sensor for small anionic guests. c) Cubic Co-cage featuring 12 naphthalene moieties for c') monitoring binding with CWA simulant with fluorescent response, c'') photoinduced energy transfer processes and c''') photoinduced electron transfer processes. d) Phenothiazine-based electron donor ligands and anthraquinone-based electron acceptor ligands are mixed to form interpenetrated Pd-double cages (all the possible products from the statistical combination of the two ligands in the topology are formed). Upon irradiation the cage undergoes charge separation.

Interpenetrated coordination cages that undergo charge separation upon irradiation, have been reported by the group of Clever.[124] By mixing two ligands, one consisting of an electron donor backbone and one of an electron acceptor backbone, closely packed interpenetrated double cages as statistical mixtures of all the possible combinations of the ligands formed. The spectroscopic and electrochemical properties of the homoleptic cages, mixtures of donor and acceptor cages and the mixed-ligand cages were characterized and compared by steady-state UV–vis and transient absorption spectroscopy, cyclic voltammetry and spectro-electrochemistry.[125] Interestingly, a close intra-assembly communication between donors and acceptors is only observed with the mixed-ligand cages as it shows the evolution of characteristic UV-Vis signatures of the donor radical cation and the acceptor radical anion upon irradiation.

The photosensitizing ability of chromophores as part of the supramolecular architectures has been exploited for visible-light photo-redox catalysis.[93,94,126–131] A strategy to construct supramolecular systems for the photocatalytic generation of hydrogen from water lies in encapsulating an organic dye molecule into the pocket of a redox-active metal–organic polyhedron (Figure 1.10 a).[128] The tetrahedral structure, consisting of four tridentate thiosemicarbazone NS chelator ligands and four cobalt(II) ions, exhibits a redox

potential suitable for electrochemical proton reduction. The close proximity between the redox site and the photosensitizer encapsulated in the pocket enables photoinduced electron transfer from the excited state of the photosensitizer to the cobalt-based catalytic sites via a powerful pseudo-intramolecular pathway. Photochemical hydrogen production was also achieved exploiting an inorganic chromophore-based octahedral structure reported by the group of Su (Figure 1.10 b).[127] The Pd(II)-based structure was formed by the coordination of tris-monodentate pyridine panels with the core consisting of a Ru(II) metal complex. Upon irradiation, the multiple metal centers undergo stepwise electron transfer processes from ruthenium-photocenters to catalytic palladium-centers as probed by ultrafast transient absorption spectroscopy. The proper organization of the metal centers results in the efficient hydrogen production. In a follow-up study, tetrathiafulvalene was encapsulated in the octahedral cavity to improve the overall electron transfer efficiency and led to the promotion of visible-light driven H_2 evolution.[131]

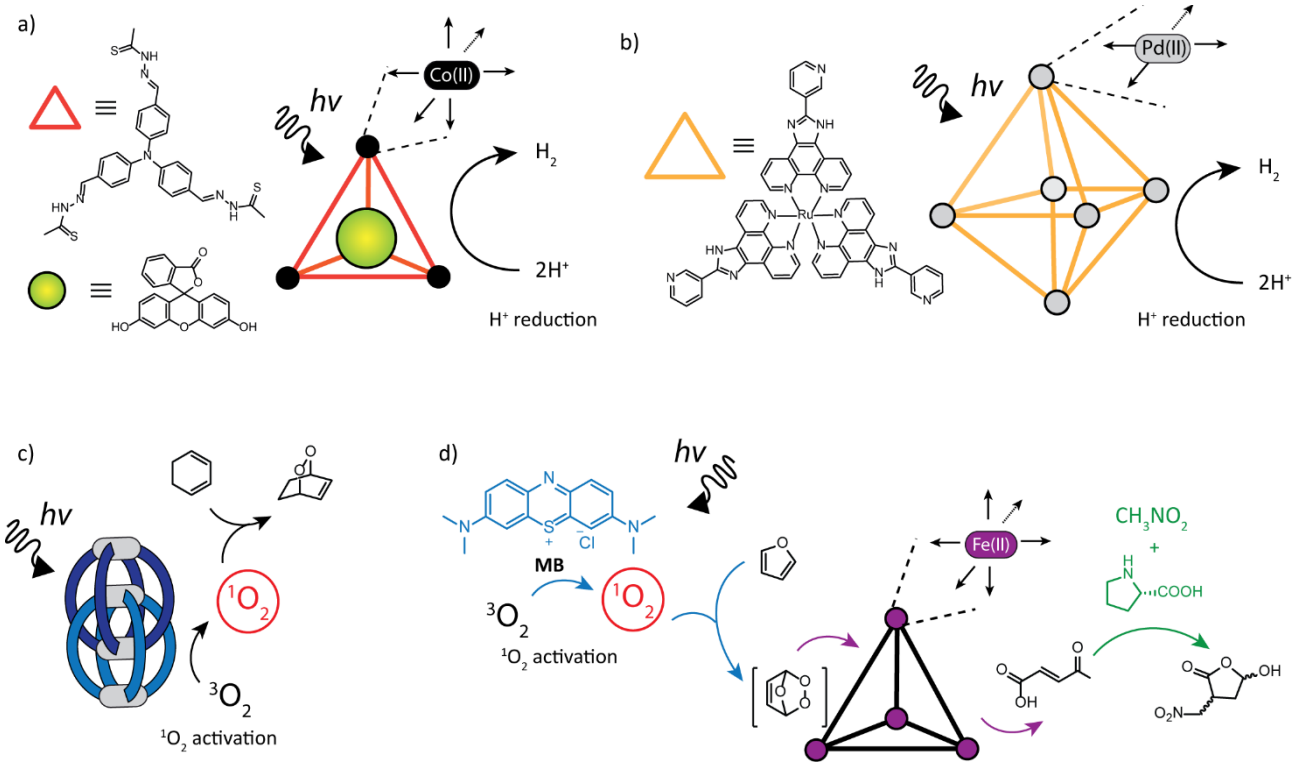

Figure 1.10: a) and b) H_2 evolving systems. c) and d) $^1O_2$ promotion systems for photooxygenation reactions.

The photosensitizer properties of the chromophores incorporated as ligand backbones have also been exploited for the activation of $^1O_2$. Recently, the Clever Lab reported that an interpenetrated double cage deriving from the coordination of acridone-based bis-monodentate ligand to Pd(II), upon irradiation, could promote the $^3O_2$ to its most reactive state by energy transfer (Figure 1.10 c). In the reported system, 1,3-cyclohexadiene was used in a model reaction to undergo [4+2] cycloaddition. Both the substrate encapsulated in the central pocket and the one in solution were converted. Organic dyes are known to photosensitize the conversion of $^3O_2$ to $^1O_2$, with methylene blue as one of the most known and efficient ones. The group of Nitschke, exploited this as the first step of a cascade reaction process (Figure 1.10 d). Furan reacting with the singlet oxygen gave the corresponding endoperoxide.[130] This high-energy intermediate was transformed into fumaraldehydic acid in the presence of a catalytic amount of a tetrahedral Fe(II)-cage that assembled *in situ* without interference from the other components within the mixture. The L-proline-catalyzed 1,4-addition of nitromethane afforded the final product.

Coordination cages with switches and motors implemented as ligands backbone increased the interest for light-driven transformation processes within the cage structure. The Clever Lab reported a photochromic coordination cage comprised of two square-planar coordinated Pd(II) ions and four bis-monodentate

pyridyl ligands based on a light switchable dithienylethene (DTE) backbone.[132] This DTE photoswitch can either exist in a colorless "open-ring" photo isomeric form (*o*-**L** in Figure 1.11), containing rotatable single bonds that render it very flexible, or in a deep blue "closed ring" (*c*-**L** in Figure 1.11) form which is shape-persistent and has nearly collinear donors. Upon UV-light irradiation, the flexible open-ring form quantitatively transforms into the structurally rigid closed-ring form. In reverse, the close form can be transformed back to the open form under the influence of 617 nm irradiation (or white light). Both form of the ligands self-assemble in presence of Pd(II) cations into Pd_2L_4 cages with the 'open form' cage characterized by higher structural flexibility than the 'closed' cage. As a result, the anion encapsulation abilities of both cage photoisomers are different. Since the response of the cages to irradiation is maintained also in presence of the guest, the light-triggered uptake and release of the molecular cargo becomes possible. Further insight on the mechanism were elucidated in a recent publication.[133] A slight variation of the backbone geometry of the DTE ligand was shown to lead to the formation of different assembly sizes, depending on the photoisomeric state of the ligand.[134] The open form isomer formed $[Pd_3\mathbf{L}_6]$ three-rings (and depending on the solvent also some $[Pd_4\mathbf{L}_8]$ four-rings) whereas the closed form isomer forms $[Pd_{24}\mathbf{L}_{48}]$ spheres with an impressive diameter of about 7 nm.

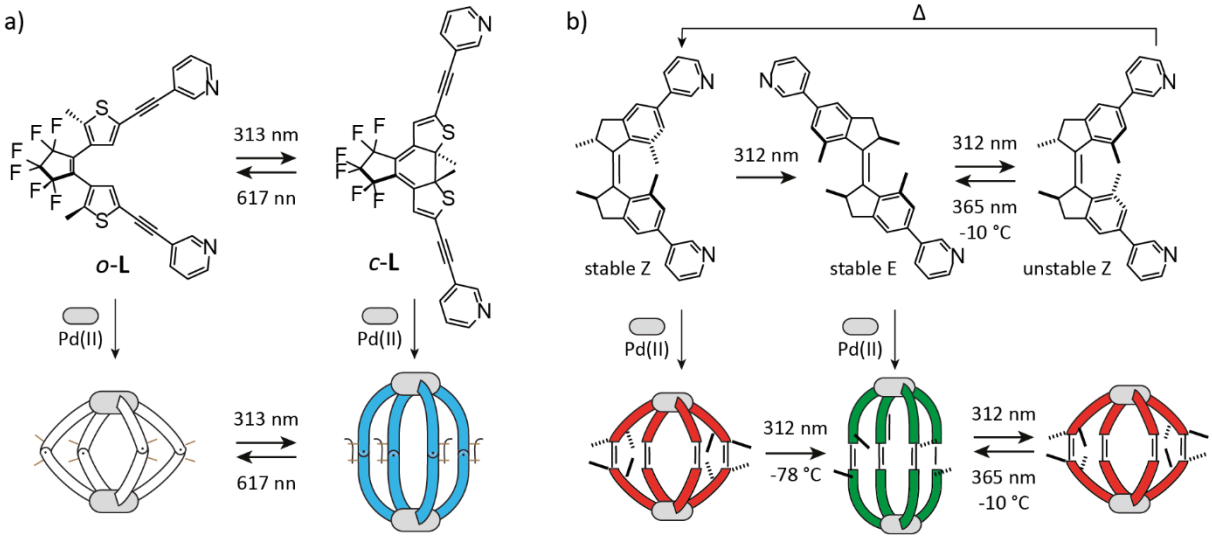

Figure 1.11 a) Light-triggered interconversion between the photoisomeric ligands *o*-**L** and *c*-**L**, which assemble into the corresponding $[M_2L_4]$ cages in the presence of Pd(II) cations. b) A chiral self-sorting photoresponsive coordination cage based on overcrowded alkenes.

The group of Feringa reported a photoresponsive coordination cage $[Pd_2L_4]$ with bidentate bispyridyl ligands based on a first-generation molecular motor.[135] The photochromic ligands can be switched between three states, forming separate discrete cage complexes, allowing cage-to-cage transformations. Interestingly, only homochiral cages are formed revealing that a chiral self-sorting process takes place. Although photoswitching affords a large geometric change of the ligands, only minor changes were observed in binding constants of the different cage structures to guest molecules. These results show that by incorporation of overcrowded alkenes into supramolecular coordination complexes, the geometry of cage structures can be controlled by light.

Despite the great number of chromphore-based coordination cages showing promising and inspiring applicability in many fields, organic-dyes, such as coal-tar dyes or diketopyrrolopyrroles have not been integrated yet as ligand backbones. Such functionalities have merely been used as additives as described.[128,130] The work presented in this thesis will focus on developing a design to include such moieties as architectural features of supramolecular molecules and study the outcoming properties.

The work will therefore be complementary to the previously reported light-switchable receptors and photo-excitable redox-cages by the Clever Lab and other groups by creating systems whose intense absorptions and emissions in the visible spectrum will be employed for analytical and reactivity purposes.

1.4 References

[1] I. Holme, *Color. Technol.* 2006, *122*, 235–251.
[2] Z. Heinrich, *Color Chemistry*, Wiley-VCH, 2003.
[3] D. Fagin, *Toms River: A Story of Science and Salvation Illustrated Edition*, Bantam, 2013.
[4] S. Ray, P. K. Samanta, P. Biswas, *Visible-Light-Active Photocatalysis: Nanostructured Catalyst Design, Mechanisms, and Applications,* Wiley-VCH, 2018, 393–419.
[5] N. A. Romero, D. A. Nicewicz, *Chem. Rev.* 2016, *116*, 10075–10166.
[6] D. Ravelli, M. Fagnoni, *ChemCatChem* 2012, *4*, 169–171.
[7] S. Gazi, R. Ananthakrishnan, *Appl. Catal. B* 2011, *105*, 317–325.
[8] D. Yang, Q. Meng, J. Zhong, M. Xiang, Q. Liu, L. Wu, *Eur. J. Org. Chem.* 2013, *2013*, 7528–7532.
[9] A. Paul, D. Chatterjee, Rajkamal, T. Halder, S. Banerjee, S. Yadav, *Tetrahedron Lett.* 2015, *56*, 2496–2499.
[10] L. Gu, C. Jin, J. Liu, *Green Chem.* 2015, *17*, 3733–3736.
[11] V. Srivastava, P. P. Singh, *RSC Adv.* 2017, *7*, 31377–31392.
[12] D. P. Hari, B. König, *Chem. Commun.* 2014, *50*, 6688–6699.
[13] D. A. Nicewicz, T. M. Nguyen, *ACS Catal.* 2014, *4*, 355–360.
[14] H. Zhang, Z. Zhan, Y. Lin, Y. Shi, G. Li, Q. Wang, Y. Deng, L. Hai, Y. Wu, *Org. Chem. Front.* 2018, *5*, 1416–1422.
[15] S. Suganya, S. Naha, S. Velmathi, *Chem* 2018, *3*, 7231–7268.
[16] J. F. Callan, A. P. de Silva, D. C. Magri, *Tetrahedron Lett.* 2005, *61*, 8551–8588.
[17] M. Wainwright, *Dyes Pigm.* 2008, *76*, 582–589.
[18] F. J. Duarte, L. W. Hillman, Eds., *Dye Laser Principles: With Applications*, Academic Press, 1990.
[19] K. Sharma, V. Sharma, S. S. Sharma, *Nanoscale Res. Lett.* 2018, *13*, 381.
[20] J. A. Kiernan, *Color. Technol.* 2006, *122*, 1–21.
[21] S. N. Letuta, G. A. Ketsle, L. V. Levshin, A. N. Nikiyan, O. K. Davydova, *Opt. Spectrosc.* 2002, *93*, 844–847.
[22] E. Bağda, E. Bağda, E. Yabaş, *J. Turk. Chem. Soc., Sect. A* 2017, *4*, 579-596.
[23] D. Sarkar, P. Das, S. Basak, N. Chattopadhyay, *J. Phys. Chem. B* 2008, *112*, 9243–9249.
[24] A. Głuszyńska, B. Juskowiak, B. Rubiś, *Molecules* 2018, *23*, 3154.
[25] M. Zama, S. Ichimura, *Biopolymers* 1970, *9*, 53–63.
[26] H. Asanuma, T. Fujii, T. Kato, H. Kashida, *J. Photochem. Photobiol. C* 2012, *13*, 124–135.
[27] D.-L. Ma, M. H.-T. Kwan, D. S.-H. Chan, P. Lee, H. Yang, V. P.-Y. Ma, L.-P. Bai, Z.-H. Jiang, C.-H. Leung, *Analyst* 2011, *136*, 2692.
[28] Z. Wujuan, X. Hongping, W. Shuqing, C. Xingguo, H. Zhide, *Analyst* 2001, *126*, 513–517.
[29] A. S. Jalilov, R. M. Young, S. W. Eaton, M. R. Wasielewski, F. D. Lewis, *Photochem. Photobiol.* 2014, *91*, 739–747.
[30] M. Hossain, G. S. Kumar, *Mol. Biosyst.* 2009, *5*, 1311.
[31] A. C. Bhasikuttan, J. Mohanty, H. Pal, *Angew. Chem. Int. Ed.* 2007, *46*, 9305–9307.
[32] B. Nordén, F. Tjerneld, E. Palm, *Biophys. Chem.* 1978, *8*, 1–15.
[33] E. M. Tuite, J. M. Kelly, *J Photochem. Photobiol. B* 1993, *21*, 103–124.
[34] D. S.-H. Chan, H. Yang, M. H.-T. Kwan, Z. Cheng, P. Lee, L.-P. Bai, Z.-H. Jiang, C.-Y. Wong, W.-F. Fong, C.-H. Leung, D.-L. Ma, *Biochimie* 2011, *93*, 1055–1064.
[35] T. Cao, F.-T. Zhang, L.-Y. Cai, Y.-L. Zhou, N. J. Buurma, X.-X. Zhang, *Analyst* 2017, *142*, 987–993.
[36] D. J. Cram, *Angew. Chem. Int. Ed.* 1988, *27*, 1009–1020.
[37] T. Clynes, *Nature* 2016, *538*, 152.
[38] C. O. Dietrich-Buchecker, J.-P. Sauvage, A. D. Cian, J. Fischer, *Chem. Commun.* 1994, *0*, 2231–2232.
[39] D. B. Amabilino, P. R. Ashton, A. S. Reder, N. Spencer, J. F. Stoddart, *Angew. Chem. Int. Ed.* 1994, *33*, 1286–1290.
[40] C. O. Dietrich-Buchecker, J. Sauvage, *Angew. Chem. Int. Ed.* 1989, *28*, 189–192.
[41] D. B. Amabilino, P. R. Ashton, A. S. Reder, N. Spencer, J. F. Stoddart, *Angew. Chem. Int. Ed.* 1994, *33*, 433–437.
[42] R. S. R. Forgan, J.-P. J. Sauvage, J. F. J. Stoddart, *Chem. Rev.* 2011, *111*, 5434 5464.
[43] F. M. Raymo, J. F. Stoddart, *Chem. Rev.* 1999, *99*, 1643–1664.
[44] C. Cheng, P. R. McGonigal, S. T. Schneebeli, H. Li, N. A. Vermeulen, C. Ke, J. F. Stoddart, *Nat. Nanotechnol.* 2015, *10*, 547–553.
[45] S. Kassem, T. van Leeuwen, A. S. Lubbe, M. R. Wilson, B. L. Feringa, D. A. Leigh, *Chem. Soc. Rev.* 2017, *46*, 2592–2621.
[46] N. Koumura, R. W. J. Zijlstra, R. A. van Delden, N. Harada, B. L. Feringa, *Nature* 1999, *401*, 152–155.
[47] R. Chakrabarty, P. S. Mukherjee, P. J. Stang, *Chem. Rev.* 2011, *111*, 6810–918.
[48] M. Albrecht, *Chem. Rev.* 2001, *101*, 3457–3498.
[49] G. H. Clever, P. Punt, *Acc. Chem. Res.* 2017, *50*, 2233–2243.
[50] M. Frank, M. D. Johnstone, G. H. Clever, *Chem. Eur. J.* 2016, *22*, 14104–14125.
[51] M. Han, D. M. Engelhard, G. H. Clever, *Chem. Soc. Rev.* 2014, *43*, 1848–1860.
[52] S. Saha, I. Regeni, G. H. Clever, *Coord. Chem. Rev.* 2018, *374*, 1–14.

[53] J. W. Steed, *Chem. Soc. Rev.* **2008**, *38*, 506–519.
[54] L. C. Palmer, Jr. J. Rebek, *Org. Biomol. Chem.* **2004**, *2*, 3051–3059.
[55] P. Mal, B. Breiner, K. Rissanen, J. R. Nitschke, *Science* **2009**, *324*, 1697–1699.
[56] C. J. Brown, F. D. Toste, R. G. Bergman, K. N. Raymond, *Chem. Rev.* **2015**, *115*, 3012–3035.
[57] J. Kang, J. Rebek, *Nature* **1997**, *385*, 50–52.
[58] Y. Fang, J. A. Powell, E. Li, Q. Wang, Z. Perry, A. Kirchon, X. Yang, Z. Xiao, C. Zhu, L. Zhang, F. Huang, H.-C. Zhou, *Chem. Soc. Rev.* **2019**, *48*, 4707-4730
[59] S. Saha, I. Regeni, G. H. Clever, *Coord. Chem. Rev.* **2018**, *374*, 1–14.
[60] T. R. Schulte, J. J. Holstein, L. Krause, R. Michel, D. Stalke, E. Sakuda, K. Umakoshi, G. Longhi, S. Abbate, G. H. Clever, *J. Am. Chem. Soc.* **2017**, *139*, 6863–6866.
[61] M. D. Johnstone, M. Frank, G. H. Clever, F. M. Pfeffer, *Eur. J. Org. Chem.* **2013**, *2013*, 5848–5853.
[62] W. M. Bloch, Y. Abe, J. J. Holstein, C. M. Wandtke, B. Dittrich, G. H. Clever, *J. Am. Chem. Soc.* **2016**, *138*, 13750–13755
[63] R. Zhu, J. Lübben, B. Dittrich, G. H. Clever, *Angew. Chem. Int. Ed.***2015**, *54*, 2796–2800.
[64] B. Roy, R. Saha, A. K. Ghosh, Y. Patil, P. S. Mukherjee, *Inorg. Chem.* **2017**, *56*, 3579–3588.
[65] D. Samanta, P. S. Mukherjee, *Chem. Eur. J.* **2014**, *20*, 12483–12492.
[66] W. M. Bloch, J. J. Holstein, W. Hiller, G. H. Clever, *Angew. Chem. Int. Ed.* **2017**, *56*, 8285–8289.
[67] W. M. Bloch, J. J. Holstein, B. Dittrich, W. Hiller, G. H. Clever, *Angew. Chem. Int. Ed.* **2018**, *57*, 5534–5538.
[68] D. M. Engelhard, S. Freye, K. Grohe, M. John, G. H. Clever, *Angew. Chem. Int. Ed* .**2012**, *51*, 4747–4750.
[69] K. Suzuki, M. Tominaga, M. Kawano, M. Fujita, *Chem. Commun.* **2009**, *0*, 1638–1640.
[70] M. Han, R. Michel, G. H. Clever, *Chem. Eur. J.* **2014**, *20*, 10640–10644.
[71] K. Harris, D. Fujita, M. Fujita, *Chem. Commun.* **2013**, *49*, 6703–6712.
[72] D. Fujita, Y. Ueda, S. Sato, N. Mizuno, T. Kumasaka, M. Fujita, *Nature* **2016**, *540*, 563.
[73] W. M. Bloch, G. H. Clever, *Chem. Commun.* **2017**, *53*, 8506–8516.
[74] W. M. Bloch, J. J. Holstein, W. Hiller, G. H. Clever, *Angew. Chem. Int. Ed.* **2017**, *56*, 8285–8289.
[75] S. Löffler, J. Lübben, A. Wuttke, R. A. Mata, M. John, B. Dittrich, G. H. Clever, *Chem. Sci.* **2016**, *7*, 4676–4684.
[76] M. Krick, J. Holstein, C. Würtele, G. H. Clever, *Chem. Commun.* **2016**, *52*, 10411–10414.
[77] A. J. Musser, P. P. Neelakandan, J. M. Richter, H. Mori, R. H. Friend, J. R. Nitschke, *J. Am. Chem. Soc.* **2017**, *139*, 12050–12059.
[78] J. Otsuki, *J. Mater. Chem. A* **2018**, *6*, 6710–6753.
[79] A. Prodi, C. Chiorboli, F. Scandola, E. Iengo, E. Alessio, R. Dobrawa, F. Würthner, *J. Am. Chem. Soc.* **2005**, *127*, 1454–1462.
[80] S. Durot, J. Taesch, V. Heitz, *Chem. Rev.* **2014**, *114*, 8542–8578.
[81] X. Lou, Y. Yang, *Adv. Opt. Mater* **2018**, *6*, 1800668.
[82] D. Li, J. Wang, X. Ma, *Adv. Opt. Mater* **2018**, *6*, 1800273.
[83] V. García-López, D. Liu, J. M. Tour, *Chem. Rev.* **2019**, *120*, 79–124.
[84] V. Balzani, A. Credi, M. Venturi, *Chem. Soc. Rev.* **2009**, *38*, 1542–1550.
[85] R. Cibulka, R. Vasold, B. König, *Chem. Eur. J.* **2004**, *10*, 6223–6231.
[86] T. Uchikura, M. Oshima, M. Kawasaki, K. Takahashi, N. Iwasawa, *Angew. Chem. Int. Ed.* **2020**, *59*, 7403–7408.
[87] N. Mehwish, X. Dou, Y. Zhao, C.-L. Feng, *Mater. Horiz.* **2018**, *6*, 14–44.
[88] S. Gnaim, A. Scomparin, A. Eldar-Boock, C. R. Bauer, R. Satchi-Fainaro, D. Shabat, *Chem. Sci.* **2019**, *10*, 2945–2955.
[89] S. S. Liow, H. Zhou, S. Sugiarto, S. Guo, M. L. S. Chalasani, N. K. Verma, J. Xu, X. J. Loh, *Biomacromolecules* **2017**, *18*, 886–897.
[90] X. Li, S. Lee, J. Yoon, *Chem. Soc. Rev.* **2018**, *47*, 1174–1188.
[91] R. Chang, E. Nikoloudakis, Q. Zou, A. Mitraki, A. G. Coutsolelos, X. Yan, *ACS Appl. Bio Mater.* **2019**, *3*, 2–9.
[92] H.-B. Cheng, Y. Cui, R. Wang, N. Kwon, J. Yoon, *Coord. Chem. Rev.* **2019**, *392*, 237–254.
[93] S. Yadav, P. Kannan, G. Qiu, *Org. Chem. Front.* **2020**, *7*, 2842–2872.
[94] X. Jing, C. He, L. Zhao, C. Duan, *Acc. Chem. Res.* **2018**, *52*, 100–109.
[95] A. J. McConnell, C. S. Wood, P. P. Neelakandan, J. R. Nitschke, *Chem. Rev.* **2015**, *115*, 7729–7793.
[96] M. Yoshizawa, S. Miyagi, M. Kawano, K. Ishiguro, M. Fujita, *J. Am. Chem. Soc.* **2004**, *126*, 9172–9173.
[97] S. Pullen, S. Löffler, A. Platzek, J. J. Holstein, G. H. Clever, *Dalton Trans.* **2020**, *49*, 9404–9410.
[98] C. Colomban, C. Fuertes-Espinosa, S. Goeb, M. Sallé, M. Costas, L. Blancafort, X. Ribas, *Chem. Eur. J.* **2018**, *24*, 4371–4381.
[99] S. Chen, K. Li, F. Zhao, L. Zhang, M. Pan, Y.-Z. Fan, J. Guo, J. Shi, C.-Y. Su, *Nat. Commun.* **2016**, *7*, 13169.
[100] M. S. Deshmukh, V. S. Mane, A. S. Kumbhar, R. Boomishankar, *Inorg. Chem.* **2017**, *56*, 13286–13292.
[101] X. Jing, Y. Yang, C. He, Z. Chang, J. N. H. Reek, C. Duan, *Angew. Chem. Int. Ed.* **2017**, *56*, 11759–11763.
[102] T. K. Ronson, S. Zarra, S. P. Black, J. R. Nitschke, *Chem. Commun.* **2012**, *49*, 2476–2490.
[103] S. M. Jansze, K. Severin, *Acc. Chem. Res.* **2018**, *51*, 2139–2147.
[104] K. Li, L.-Y. Zhang, C. Yan, S.-C. Wei, M. Pan, L. Zhang, C.-Y. Su, *J. Am. Chem. Soc.* **2014**, *136*, 4456–4459.
[105] R. Li, M. Han, J. Tessarolo, J. J. Holstein, J. Lübben, B. Dittrich, C. Volkmann, M. Finze, C. Jenne, G. H. Clever, *ChemPhotoChem* **2019**, *3*, 378–383.
[106] R.-J. Li, J. J. Holstein, W. G. Hiller, J. Andréasson, G. H. Clever, *J. Am. Chem. Soc.* **2019**, *141*, 2097–2103.

[107] M. Han, R. Michel, B. He, Y. Chen, D. Stalke, M. John, G. H. Clever, *Angew. Chem. Int. Ed.* **2013**, *52*, 1319–1323.
[108] M. Han, Y. Luo, B. Damaschke, L. Gómez, X. Ribas, A. Jose, P. Peretzki, M. Seibt, G. H. Clever, *Angew. Chem. Int. Ed.* **2015**, *55*, 445–449.
[109] X. Chang, S. Lin, G. Wang, C. Shang, Z. Wang, K. Liu, Y. Fang, P. J. Stang, *J. Am. Chem. Soc.* **2020**, *142*, 15950–15960.
[110] S. Ganta, D. K. Chand, *Inorg. Chem.* **2017**, *57*, 3634–3645.
[111] P. D. Frischmann, V. Kunz, F. Würthner, *Angew. Chem. Int. Ed.* **2015**, *54*, 7285–7289.
[112] S. Anderson, H. L. Anderson, A. Bashall, M. McPartlin, J. K. M. Sanders, *Angew. Chem. Int. Ed.* **1995**, *34*, 1096–1099.
[113] M. Käseborn, J. J. Holstein, G. H. Clever, A. Lützen, *Angew. Chem. Int. Ed.* **2018**, *57*, 12171–12175.
[114] A. J. Plajer, E. G. Percástegui, M. Santella, F. J. Rizzuto, Q. Gan, B. W. Laursen, J. R. Nitschke, *Angew. Chem. Int. Ed.* **2019**, *58*, 4200–4204.
[115] B. W. Laursen, F. C. Krebs, *Angew. Chem. Int. Ed.* **2000**, *39*, 3432 – 3434.
[116] C. Nicolas, J. Lacour, *Org. Lett.* **2006**, *8*, 4343–4346.
[117] T. R. Schulte, J. J. Holstein, G. H. Clever, *Angew. Chem. Int. Ed.* **2019**, *58*, 5562–5566.
[118] W. Cullen, M. C. Misuraca, C. A. Hunter, N. H. Williams, M. D. Ward, *Nat. Chem.* **2016**, *8*, 231–236.
[119] S. Turega, M. Whitehead, B. R. Hall, M. F. Haddow, C. A. Hunter, M. D. Ward, *Chem. Commun.* **2012**, *48*, 2752–2754.
[120] W. Cullen, K. A. Thomas, C. A. Hunter, M. D. Ward, *Chem. Sci.***2015**, *6*, 4025–4028.
[121] C. G. P. Taylor, J. R. Piper, M. D. Ward, *Chem. Commun.* **2016**, *52*, 6225–6228.
[122] J. R. Piper, L. Cletheroe, C. G. P. Taylor, A. J. Metherell, J. A. Weinstein, I. V. Sazanovich, M. D. Ward, *Chem. Commun.* **2016**, *53*, 408–411.
[123] J. S. Train, A. B. Wragg, A. J. Auty, A. J. Metherell, D. Chekulaev, C. G. P. Taylor, S. P. Argent, J. A. Weinstein, M. D. Ward, *Inorg. Chem.* **2019**, *58*, 2386–2396.
[124] M. Frank, J. Ahrens, I. Bejenke, M. Krick, D. Schwarzer, G. H. Clever, *J. Am. Chem. Soc.* **2016**, *138*, 8279–8287.
[125] J. Ahrens, M. Frank, G. H. Clever, D. Schwarzer, *Phys. Chem. Chem. Phys.* **2017**, *19*, 13596–13603.
[126] H. Yu, C. He, J. Xu, C. Duan, J. N. H. Reek, *Inorg. Chem. Front.* **2016**, *3*, 1256–1263.
[127] S. Chen, K. Li, F. Zhao, L. Zhang, M. Pan, Y.-Z. Fan, J. Guo, J. Shi, C.-Y. Su, *Nat. Commun.* **2016**, *7*, 13169.
[128] X. Jing, C. He, Y. Yang, C. Duan, *J. Am. Chem. Soc.* **2015**, *137*, 3967–3974.
[129] D. Preston, J. J. Sutton, K. C. Gordon, J. D. Crowley, *Angew. Chem. Int. Ed.* **2018**, *57*, 8659–8663.
[130] A. G. Salles, S. Zarra, R. M. Turner, J. R. Nitschke, *J. Am. Chem. Soc.* **2013**, *135*, 19143–19146.
[131] K. Wu, K. Li, S. Chen, Y. Hou, Y. Lu, J. Wang, M. Wei, M. Pan, C. Su, *Angew. Chem. Int. Ed.* **2020**, *59*, 2639–2643.
[132] M. Han, R. Michel, B. He, Y. Chen, D. Stalke, M. John, G. H. Clever, *Angew. Chem. Int. Ed.* **2013**, *52*, 1319–1323.
[133] R.-J. Li, J. J. Holstein, W. G. Hiller, J. Andréasson, G. H. Clever, *J. Am. Chem. Soc.* **2019**, *141*, 2097–2103.
[134] M. Han, Y. Luo, B. Damaschke, L. Gómez, X. Ribas, A. Jose, P. Peretzki, M. Seibt, G. H. Clever, *Angew. Chem. Int. Ed.* **2015**, *55*, 445–449.
[135] C. Stuckhardt, D. Roke, W. Danowski, E. Otten, S. J. Wezenberg, B. L. Feringa, *Beilstein J. Org. Chem.* **2019**, *15*, 2767–2773.

2. Scope of the thesis

The scope of this thesis is to extend the cage properties that result from the interaction with light by implementing popular organic dyes as ligand backbones. These molecules are widely known due to their broad use in industry (e.g. as laser materials and colorizing agents), medicine (e.g. as diagnostic tools and drugs) and research (e.g. in fluorescence microscopy, electron and energy transfer setups and as photosensitizers). All these applications originate from the strong electronic transition in the visible range of the electromagnetic spectrum of light that characterize them. However, while the parent dyes are produced on a multi ton scale, their use in self-assembled supramolecular systems is rather rarely found in literature. Hence, this thesis aims to the unprecedented combination of dyes with the concept of self-assembled supramolecular cages. The photophysical properties of the resulting 3-dimensional nanoscopic objects are aimed to be studied in the context of diagnostic of recognition events. Moreover, certain organic dyes are particularly popular in medicine and biology for imaging purposes and are often found to have high affinity to biomolecules. Supramolecular architectures bearing such functionalities and featuring optimal structural arrangement for the recognition of biopolymers, such as DNA, will be investigated. The interest is not only focused on the most commonly known DNA secondary structure, the double helix, but also on the class of DNA G-quadruplexes which gain rapidly growing attention in view of their regulation roles in gene expression as well as potential anticancer drug targets.

Based on the overall goal, the following main steps for this thesis can be outlined:

- Construction of the **dye-based coordination cages**: design and synthesis of bis-monodentate ligands based on the chemical structures of the dyes of interest. Incorporation of the dye functionalities in supramolecular architectures by coordination of the new ligands to Pd(II) cations. Study of the resulting topological arrangements with NMR, ESI-MS and X-ray diffraction techniques.

- When appropriate, combination of different ligands in the same architecture and study of their self-sorting properties with NMR and ESI-MS techniques.

- Characterization of the **optical properties** of the assemblies through UV-Vis absorption and emission spectroscopic techniques.

- Application of the dye-based cages in **chiroptical recognition** of small anionic molecules. Exploitation of the cavity of the cages for recognition of small anionic chiral molecules. The effects are studied with a variety of spectroscopic and spectrometric techniques, including CD spectroscopy.

- Interaction studies of the dye-based cages and different secondary structures of DNA. The **DNA supramolecular recognition** is studied mainly with UV-Vis absorption and CD spectroscopy. Preliminary docking studied have been carried out.

The functionalities of diketopyrrolopyrrole dyes and coal-tar dyes, Michler's ketone, rhodamine B, methylene blue and crystal violet, have been chosen. In the following chapters, their implementation into supramolecular coordination architectures is presented. In view of their different chemical structures and consequently alternative designs, this part of the thesis is divided into two chapters. The last chapter covers the DNA-cage interaction studies.

3. Ferrari red dye-based coordination cages

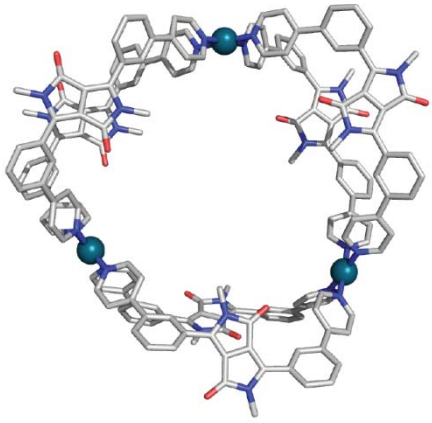

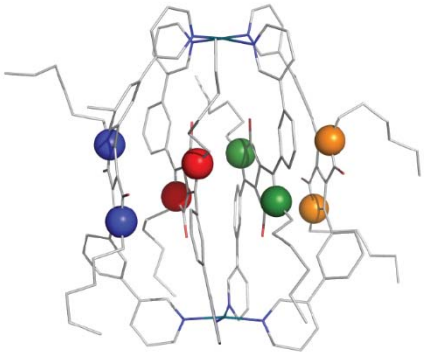

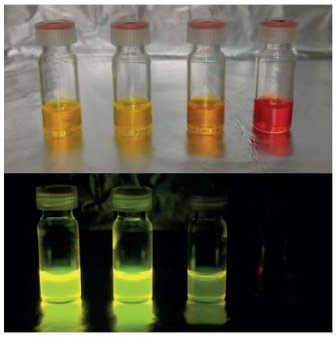

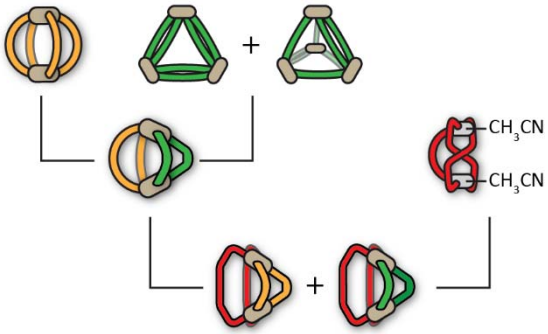

3.1 Diketopyrrolopyrrole dye

Diketopyrrolopyrroles (**DPP**s) are organic dyes based on the heterocyclic dilactam 2,5-dihydropyrrolo[3,4-*c*]pyrrole-1,4-dione (Figure 3.1). **DPP**s were initially used as pigments in the painting industry (e.g. automotive paints) due to their high resistance to photodegradation. More recently, **DPP** derivatives have been also investigated as promising fluorescent dyes for bioimaging applications, as well as in optoelectronics, because of their peculiar physicochemical properties.[1,2]

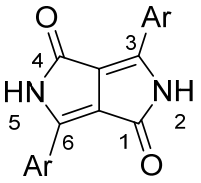

2,5-dihydropyrrolo[3,4-*c*]pyrrole-1,4-dione [IUPAC]

= diketopyrrolopyrrole (**DPP**)

Figure 3.1: Chemical structure and nomenclature of diketopyrrolopyrroles (**DPP**s).

In 1974, Donald Farnum's group attempted the synthesis of monocyclic β-lactams through a modified version of the Reformatskii reaction.[3] To their surprise, they got a mixture of products: a crystalline yellow compound and a nearly insoluble deep red compound that they obtained with low yields (Figure 3.2 a). The group characterized the latter as diketopyrrolopyrrole (**Ph-DPP**), a bicyclic dilactam. Farnum's group already observed some of the unusual photophysical properties of **DPP**s but did not investigate further. On the contrary, researchers from Ciba-Geigy AG (nowadays part of BASF) saw a great potential in **DPP**s as red pigments, both because of their structural similarity with already known pigments such as indigo (Figure 3.2 b) and because of their high stability against temperature and radiation, and started improving Farnum's synthesis route. They were successful and started selling **DPP**s as dyes in the late 80s, with Ferrari being the most prominent customer. This led to the commonly known nickname "*Ferrari Red dye*".[2]

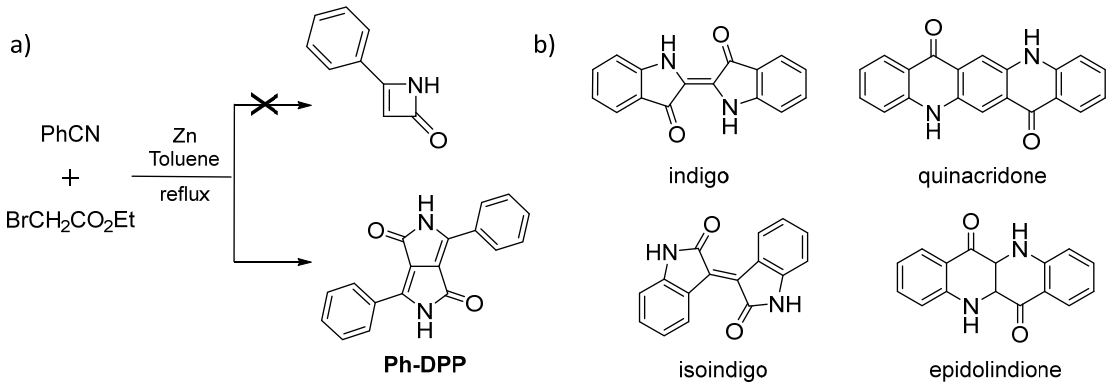

Figure 3.2: a) Farnum's group attempted the synthesis of monocyclic β-lactams through a modified version of the Reformatskii reaction leading to the **Ph-DPP**. b) Known pigments whose structure are similar to **DPP**s.

In recent years, **DPP** was rediscovered by many different research groups in view of the great physical properties of such moieties besides stability and red color. The base structure of **DPP** (Figure 3.1) is highly modifiable. Alkyl chains are often attached to the nitrogen atoms of the amide groups to overcome solubility issues. The insolubility of the compound originates from the combination of their π- π stacking and hydrogen bonding abilities. In Figure 3.3, the combination of such intermolecular forces is schematically shown. The N-H and carbonyl group on one side of the molecule interact with a second molecule to form a very strong 8-membered hydrogen-bondend ring. Not surprisingly, in order to improve the solubility of these compounds it became necessary to alkylate the nitrogen atom and break at least one of the two strong intermolecular forces.[4]

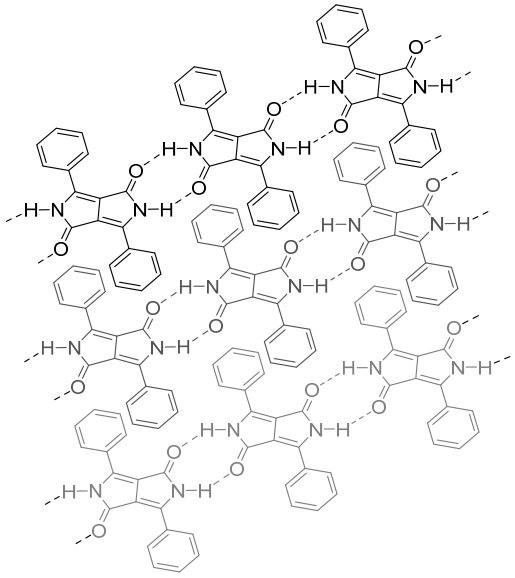

Figure 3.3: Schematic representation of the **Ph-DPP**'s packing to maximize hydrogen bond formation and π-stacking.

The aromatic nitrile used in the synthesis can also be varied in an enormous fashion to change the molecular properties to ones demands.[5,6] The bright and intense emission of **DPP** dyes can be ascribed to their high fluorescent quantum yield.[1] The ability to transform a great amount of light energy into chemical energy led to the development of **DPP**-based solar cells.[7–9] Its centro-symmetry also leads to a strong quadrupolar moment, a characteristic feature in fluorophores used in two-photon absorption.[10] Many other characteristics and possible applications are currently being investigated.[6,7,11–15] Joining the great optical properties of **DPP** dyes and the concept of metal-mediated self-assembly, promise to obtain functional architectures enriched with light-driven properties that can be utilized in the context of electron or energy transfer within the structures or with other substrates.

In the following sections, the implementation of the **DPP** dye functionality as backbone of bis-pyridine or bis-isoquinoline ligands is presented. The assembly properties of four new ligands with Pd(II) cations are investigated and different supramolecular architectures are constructed. The optical properties of the new structures are compared to the ones of the basic components. Moreover, some preliminary results in combining such functionalities with other known electron donor/acceptor moieties, like fluorene or carbazole derivatives, in the same structure through integrative self-sorting strategies are shown. Interesting cage-to-cage transformation effects are found and will be deeply analyzed in future research as well as their photoinduced abilities to transfer energy or electrons.

3.2 Ferrari Red dye-based assemblies

3.2.1 Ligand synthesis

Starting from succinic acid diisopropyl ester and the properly substituted nitriles, the **DPP** based ligands 2,5-dihexyl-3,6-di(pyridin-3-yl)-2,5-dihydropyrrolo[3,4-c]pyrrole-1,4-dione (**3P-DPP**), 2,5-dihexyl-3,6-bis(3-(pyridin-3-yl)phenyl)-2,5-dihydropyrrolo[3,4-c]pyrrole-1,4-dione (**3PM-DPP**), 2,5-dihexyl-3,6-bis(3-(pyridin-3-yl)phenyl)-2,5-dihydropyrrolo[3,4-c]pyrrole-1,4-dione (**4PM-DPP**) and 2,5-dihexyl-3,6-bis(4-(isoquinolin-8-yl)phenyl)-2,5-dihydropyrrolo[3,4-c]pyrrole-1,4-dione (**8QP-DPP**) were successfully synthesized. The schematic synthetic routes are reported in Figure 3.4. For the complete synthesis and characterization information, see the experimental part of this chapter, section 3.6.2.

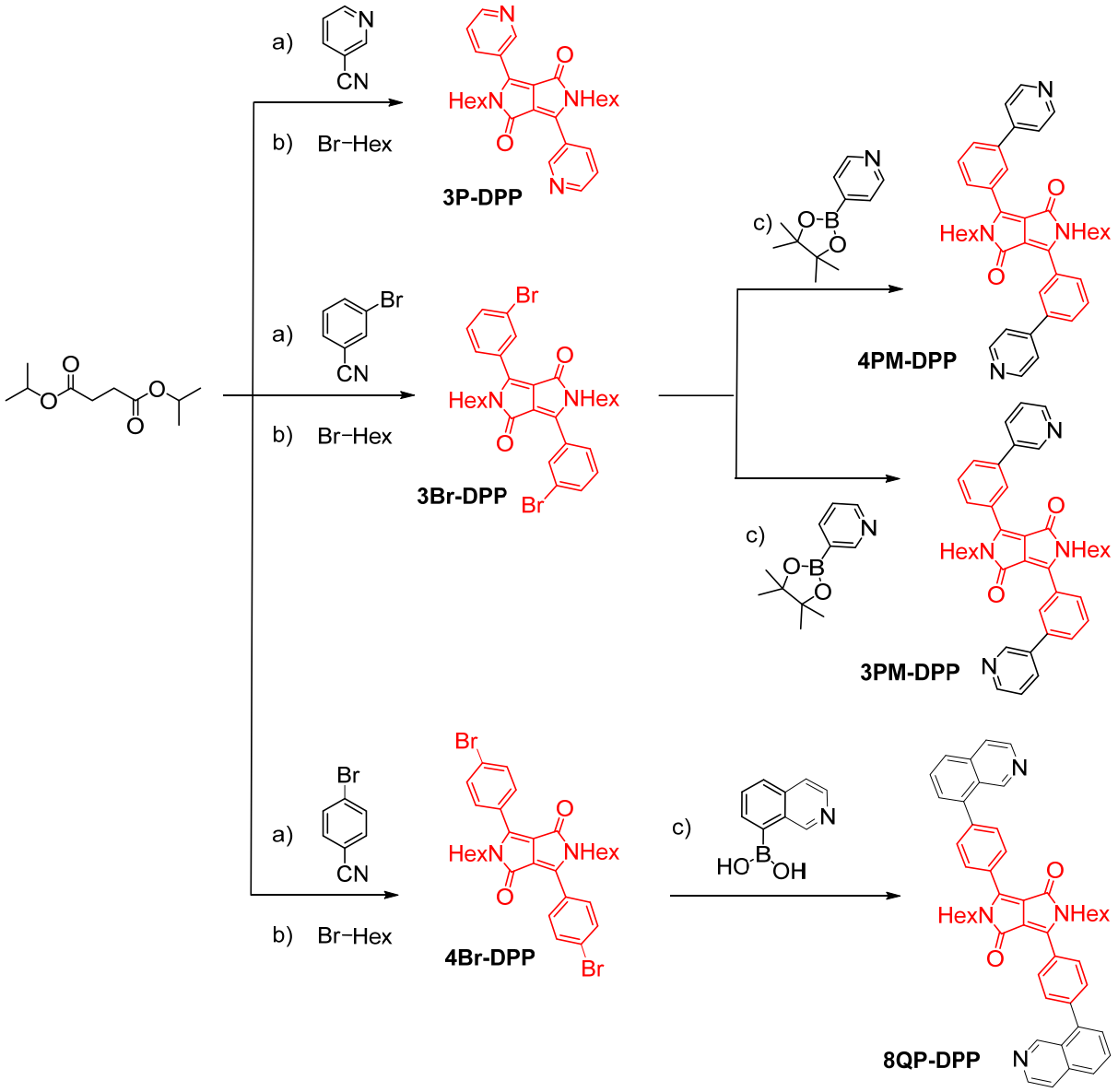

Figure 3.4: Synthesis of ligands **3P-DPP**, **3PM-DPP**, **4PM-DPP** and **8QP-DPP.** Reaction conditions: a) *tert*-amyl alcohol, Na, 90°C b) NMP, KO*t*-Bu, 60°C, c) 1,4-dioxan/H_2O (4:1), $K_3PO_4 \cdot H_2O$, $Pd(PPh_3)_4$, 90°C.

The first step common for all ligands is the ring closing addition of two nitriles to the succinic acid ester already developed by Ciba-Geigy AG in the 70s.[2] To this day, this reaction still represents the most commonly used method to synthesize diketopyrrolopyrrole backbones. In the first step of the reaction, the succinic acid ester is transformed into the corresponding nucleophilic enolate by deprotonation with a base. A nucleophilic attack follows on the nitrile function and the first ring closes by nucleophilic acyl substitution on the isopropyl ester group. Due to the symmetric structure of the ester this reaction occurs twice, leading to the formation of the **DPP** core. In the presented results, the used nitriles are pyridine-3-carbonitrile for the synthesis of **3P-DPP**, 3- bromobenzonitrile for **3PM-DPP** or **4PM-DPP** and 4-bromobenzonitrile for **8QP-DPP**. Despite the efforts of various groups over the last 50 years, the synthesis of **DPP** is still notorious for its bad yield, being only approx. 25%. Due to its poor solubility in nearly every available deuterated solvent, there are no NMR data available for the obtained compounds (appearing as reddish muddy powders). To overcome the poor solubility of the molecules (see section 3.1 for insights on insolubility), hexyl chains are attached to the nitrogen atoms through classic nucleophilic substitution with potassium *tert*-butoxide as a base. The reaction needs to be carried out in a potent polar aprotic solvent, *N*-methyl-2-pyrrolidone (NMP), to keep part of the starting material dissolved and lead to successive conversion. The yield of this reaction is difficult to determine due to

purification issues in the previous step. Additionally, a frequent further difficulty consists in separating the mono-converted product from the desired double-converted one. In the end, ligand **3P-DPP** and the compounds **3Br-DPP** and **4Br-DPP** were obtained in pure form by a combination of column chromatography and crystallization. Lastly, ligands **3PM-DPP**, **4PM-DPP** and **8QP-DPP** were formed by Suzuki-cross-coupling of the now readily soluble compounds **3Br-DPP** and **4Br-DPP** with the corresponding boronic ester or acid.

By cooling down a solution of ligand **3PM-DPP** in acetonitrile from 70 °C to room temperature (r.t.), deep red single-crystals were obtained. These crystals were measured with inhouse XRD and proved to be crystallized ligand. The preliminary crystal structure is shown in Figure 3.5. From the side views the almost perfectly flat structure of the ligand can be observed.

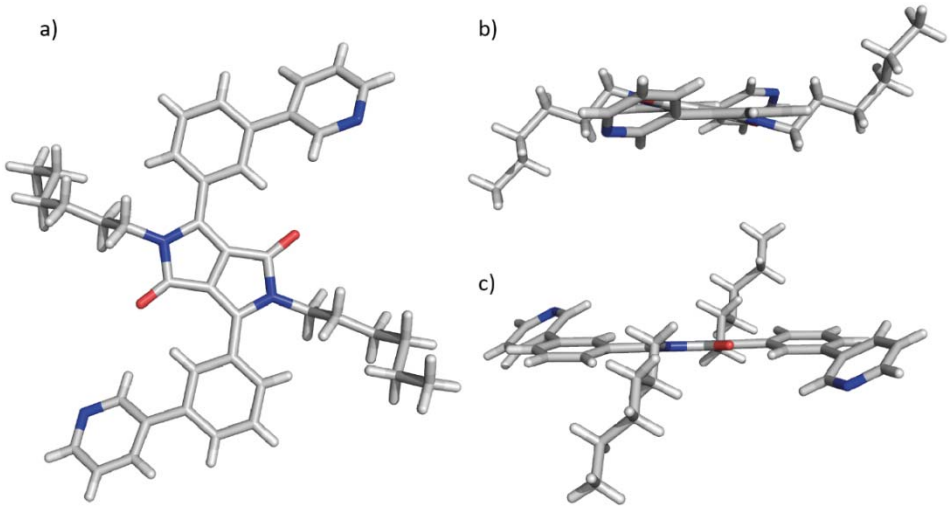

Figure 3.5: X-ray structure of ligand **3PM-DPP** a) top view, b) and c) side views.

3.2.2 3P-DPP

The first synthesized ligand, **3P-DPP**, is a short derivative of **DPP** where the pyridine donor groups are directly part of the basic core structure. The nitrogen atoms are in meta position and they form angles between the bonding vectors (see Introduction, section 1.2.2) which are larger than 0°. Hence, upon palladium addition, the expected assembly would be characterized by a topology Pd_xL_{2x} with x>2.

The assembly of the supramolecular architecture was tested both in dimethylsulfoxide-d_6 (DMSO-d_6) and acetonitrile-d_3 (CD_3CN) following the same procedure. Ligand **3P-DPP** was mixed in a 2:1 ratio with $[Pd(CH_3CN)_4](BF_4)_2$ and heated at 70 °C for 30 min. The resulting ^{1}H NMR spectra are reported in Figure 3.6. For better understanding, only the aromatic regions of the spectra are reported where only the pyridine signals are visible. Usually, a downfield shift of the signals indicates the coordination of the pyridines to the Pd(II). This effect is joined by a possible splitting in case of low symmetry of the resulting structure (e.g. when ligands are occupying different positions in the same structure).[16–19] As Figure 3.6 shows, in CD_3CN one signal shifts downfield but the rest of the spectrum is characterized by highly complicated splitting of the rest of the signals. This situation is typical for ligands that form multiple topologies coexisting in equilibrium in solution. On the other hand, in DMSO-d_6, the shift resulting from the addition of the Pd(II) is not as large and the signals are broadened. Similar ^{1}H NMR spectra are observed when the coordination of the ligands to the square metal coordinated cations form spheres Pd_xL_{2x} with x>6.[20] A technique that would provide great insight in the assembly process to assess what topologies form, is HR-ESI mass spectrometry. However, ESI-MS spectra of neither the CD_3CN or DMSO-d_6 solutions, with standard injection conditions or under cryo-ionization conditions, afforded *m/z* values corresponding to Pd_xL_{2x} with x=1-12 but only low charged fragmentation peaks. ^{1}H DOSY measurements proved efficient in providing a first estimation of the size of the assembly forming in DMSO-d_6 (a deeper discussion on diffusion order spectroscopy, DOSY, is presented in chapter 4, section 4.5.2). The

hydrodynamic radius extrapolated from the measurements is 12.2 Å. Such value indicates the formation of a supramolecular self-assembled structure, for more insights on the topology, further structural information is needed (e.g. X-ray crystal structure).

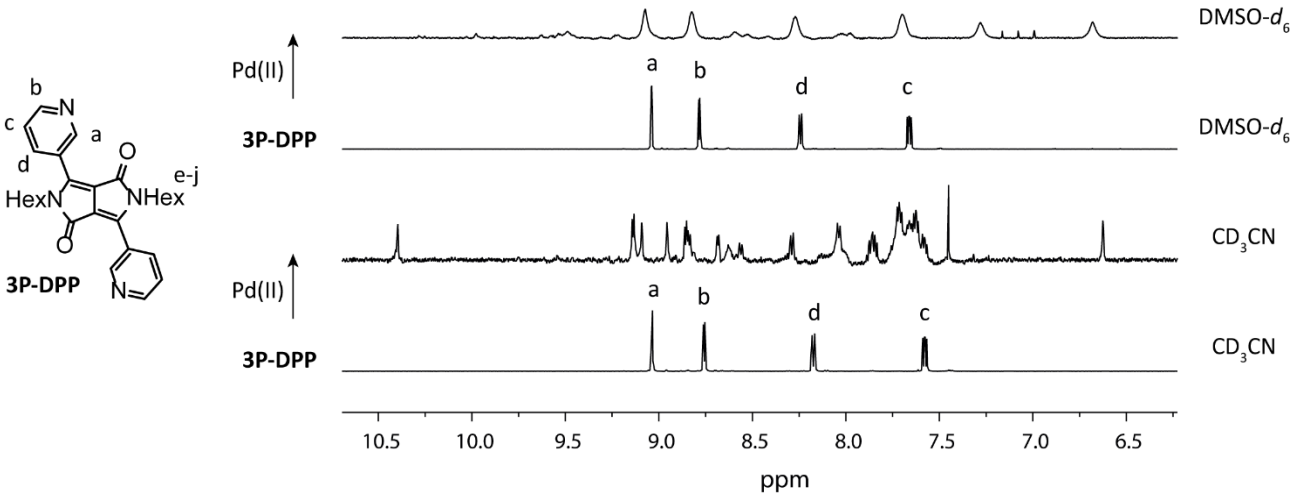

Figure 3.6: Stacked ^{1}H NMR spectra of ligand **3P-DPP** and upon addition of 0.5 equiv. Pd(II) cations in both DMSO-d_6 and CD_3CN.

The ESI-MS results might be explained with a low propensity of ligand **3P-DPP** to form stable supramolecular architectures when combined with Pd(II) cations. The very short design of the ligand, together with the long chain substitution to prevent insolubility issues, might lead to complications when the pyridines are brought in close proximity to coordinate to the metal cation.

For the above mentioned reasons, a longer version of **3P-DPP**, ligand **4PM-DPP** was designed, with one extra phenyl ring between the **DPP** core and the pyridine, however maintaining the angle (always in a two-dimensional approximation) formed by the two vectors defined by the lone-pair of the coordinating nitrogen atoms.

3.2.3 Ligand 4PM-DPP

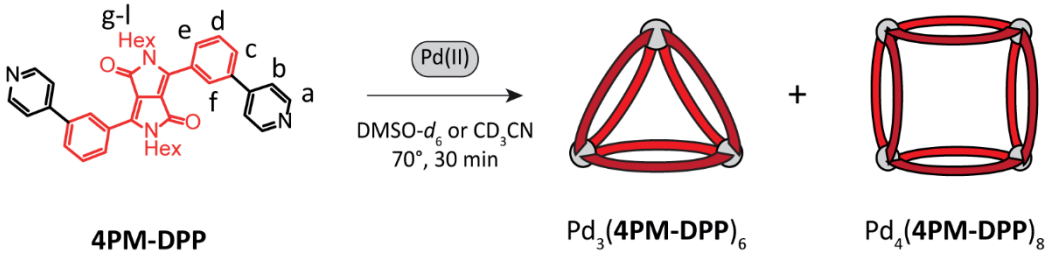

Figure 3.7: Formation of the [Pd_3(**4PM-DPP**)$_6$] + [Pd_4(**4PM-DPP**)$_8$] rings upon addition of Pd(II) cations to ligand **4PM-DPP**.

Ligand **4PM-DPP**, the elongated version of **3P-DPP**, is mixed in a 2:1 ratio with $[Pd(CH_3CN)_4](BF_4)_2$ in DMSO-d_6 solution and heated at 70 °C for 30 min. The stacked ^{1}H NMR spectra of the ligand and the assembly result are reported in Figure 3.8. From such spectra, the typical downfield shift of the ligand signals can be observed, indication of the coordination to the Pd(II) with the shift being larger the closer the correspondent protons are located to the coordination center. However, the spectrum is characterized by a splitting of the signals, signifying that either the symmetry of the resulting species is partially lost, when compared to the free ligand, or that multiple species form upon metal addition. HR-ESI mass spectrometry proved that indeed, coordination to the Pd(II) favors the formation of a mixture of stoichiometries [Pd_3L_6] and [Pd_4L_8] (Figure 3.9). [Pd_3L_6] topologies reported in the literature are mainly trinuclear rings where all the ligands occupy equivalent positions.[21] Exceptions include a highly entangled structure that can be described as two trefoil knots (composed of three intertwined ligands, each) that are joined by the three square-planar metal centers.[22] However, the low symmetry

is evident in the ^{1}H NMR spectrum, showing tremendous signal splitting effects, which is not the case here. On the other hand, [Pd_4L_8] could represent multiple topologies, from interpenetrated monomeric cages,[17–19,23] to tetrahedral structures[16] and tetranuclear rings.[24] Both interpenetrated and tetrahedral structures, lead to a split of the signals into two sets of equivalent integration. In the ^{1}H NMR spectrum in Figure 3.8, the signals have higher multiplicity compared to a single species, meaning that the actual chemical shift in both structures for all protons is similar and, since no further structural proof for the [Pd_4L_8] architecture was obtained, both species are assumed to be ring structures. Full assignment of the spectra was not possible.

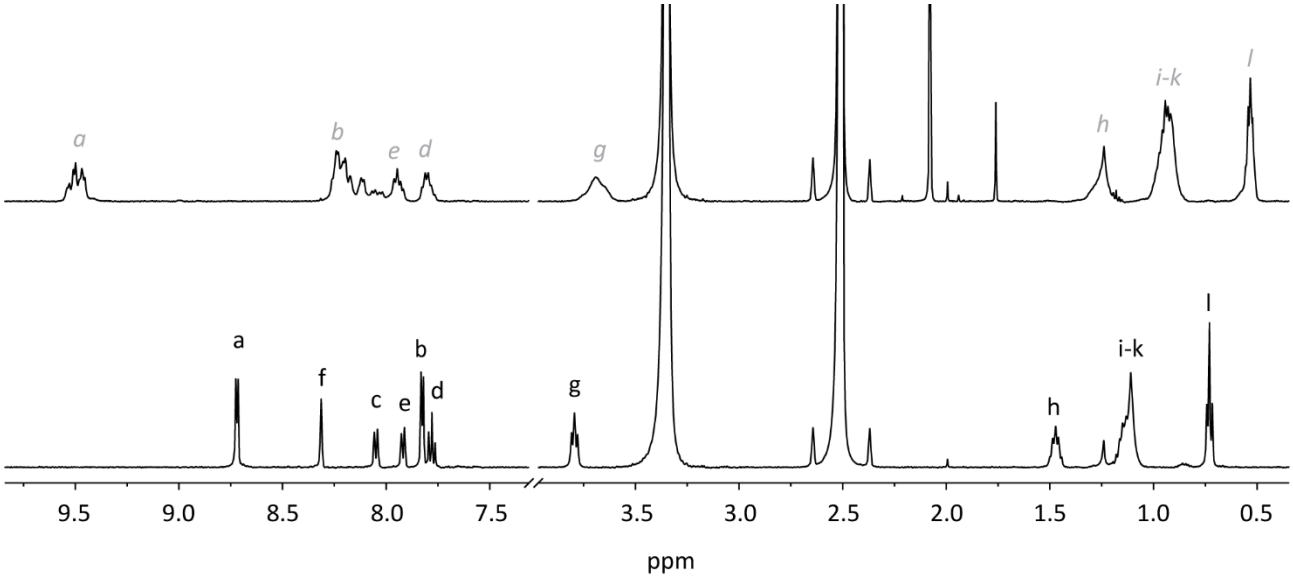

Figure 3.8: Stacked ^{1}H NMR spectra of ligand **4PM-DPP** and corresponding mixture solution of [Pd_3(**4PM-DPP**)$_6$] and [Pd_4(**4PM-DPP**)$_8$] rings upon addition of 0.5 equiv. of Pd(II) in DMSO-d_6. The assignment in grey derives from the analysis of the ^{1}H-^{1}H COSY NMR spectrum. For the chemical structure of **4PM-DPP** and the letter assignment, see Figure 3.7.

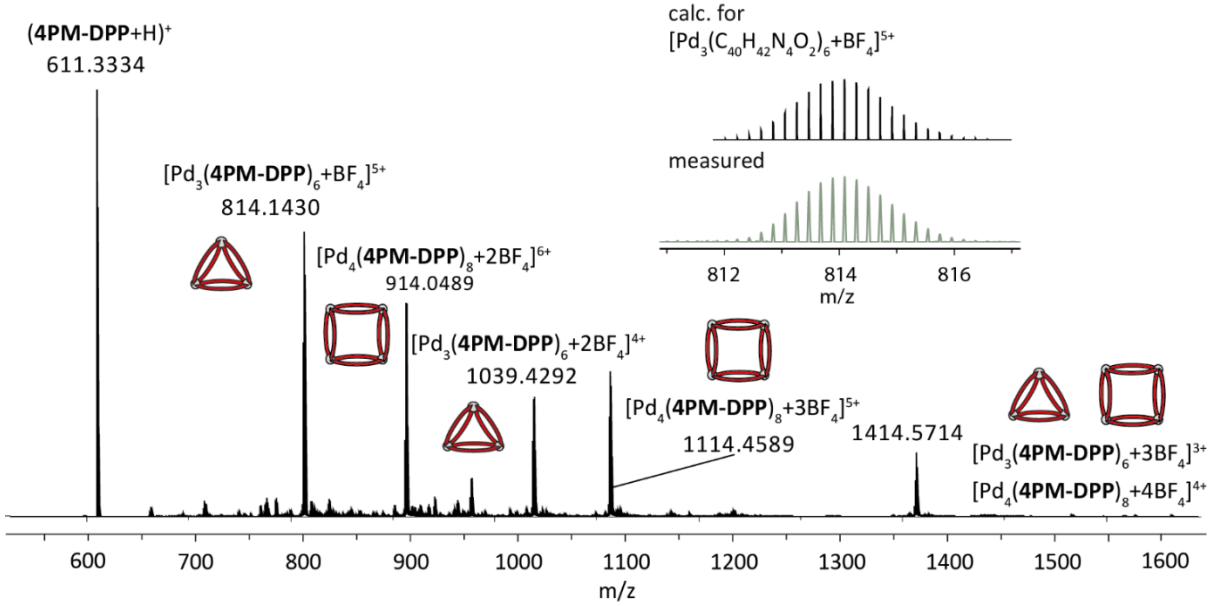

Figure 3.9: ESI-MS spectrum of [Pd_3(**4PM-DPP**)$_6$+nBF_4]$^{(6-n)+}$ with n=1-3 and [Pd_4(**4PM-DPP**)$_8$+nBF_4]$^{(8-n)+}$ with n=2-4. The observed and calculated isotopic patterns of [Pd_3(**4PM-DPP**)$_6$+BF_4]$^{5+}$ are shown in the inset.

By slow diffusion of diethyl ether in the acetonitrile solution of [Pd_3(**4PM-DPP**)$_6$] and [Pd_4(**4PM-DPP**)$_8$], orange crystals were obtained suitable for synchrotron X-ray diffraction. The obtained structure is reported in Figure 3.3.10 and represents the species [Pd_3(**4PM-DPP**)$_6$]. In the solid state, the structure

with lower nuclearity is favored as, besides being the entropically most probable product, might also be stabilized by packing effects.

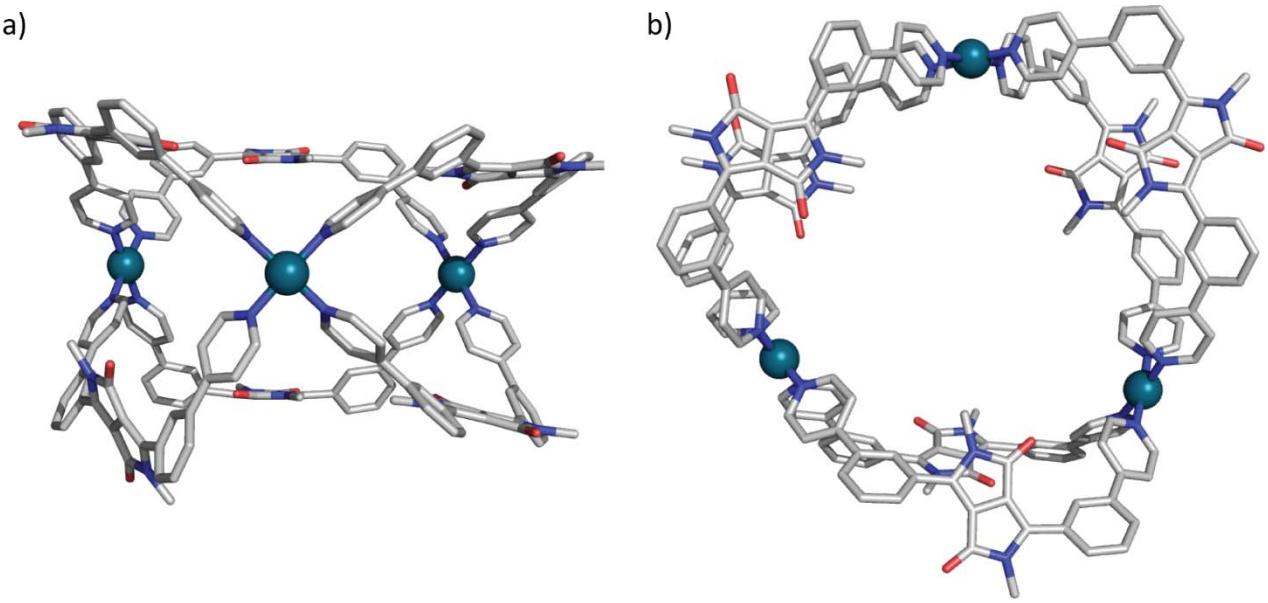

Figure 3.3.10: a) Side view and b) top view of the crystal structure of the [Pd_3(**4PM-DPP**)$_6$] ring. The hexyl chains have been omitted for clarity.

3.2.4 Ligand 3PM-DPP

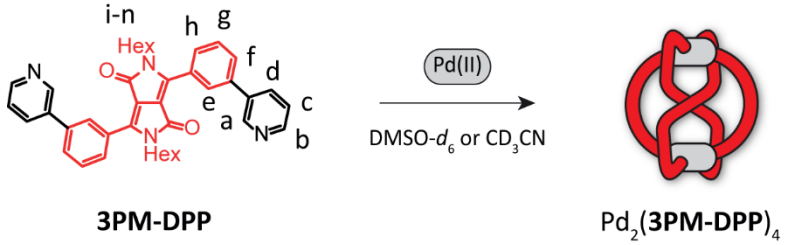

Figure 3.11: Formation of the cage *Fig8*-[Pd_2(**3PM-DPP**)$_4$] upon addition of Pd(II) cations to ligand **3PM-DPP**.

Ligand **3PM-DPP** differs from ligand **4PM-DPP** in the position of the nitrogen atom of the pyridine. The meta substituted pyridine affords ligands in which the angle between the bonding vectors is much narrower than the one in **4PM-DPP**. When ligand **3PM-DPP** is mixed with 0.5 equiv. of [$Pd(CH_3CN)_4$](BF_4)$_2$, a peculiar combination of ^{1}H NMR spectrum (Figure 3.12) and HR-ESI mass spectrum (Figure 3.13) is observed. In the NMR spectrum, the typical downfield shift of the signals indicating the coordination of the pyridine groups to the Pd(II) cation can be seen. Additionally, there is also a splitting of the signals into two sets with the same integration. Such observation is consistent with either the formation of two different self-assembled species that coexist in a 1:1 ratio or the formation of a single species in which two different chemical and magnetic environments for the ligands can be distinguished. Such situation is typically observed for interpenetrated dimer structures.[19] However, HR-ESI mass spectroscopy unequivocally proves the exclusive formation of a [Pd_2L_4] species. Several hypotheses came to mind in order to combine these two results: the interpenetrated dimer of monomeric cages decomposes under ionization conditions when attempting to measure its mass spectrum and only the monomeric component can be measured (however unlikely since usually interpenetrated double cages are more stable that the monomeric forms), or the ligands arrange themselves in a conformation that leads to a desymmetrization of the two halves of the ligands, or there actually is interpenetration but within the same cage structure – a self-penetrating structure.

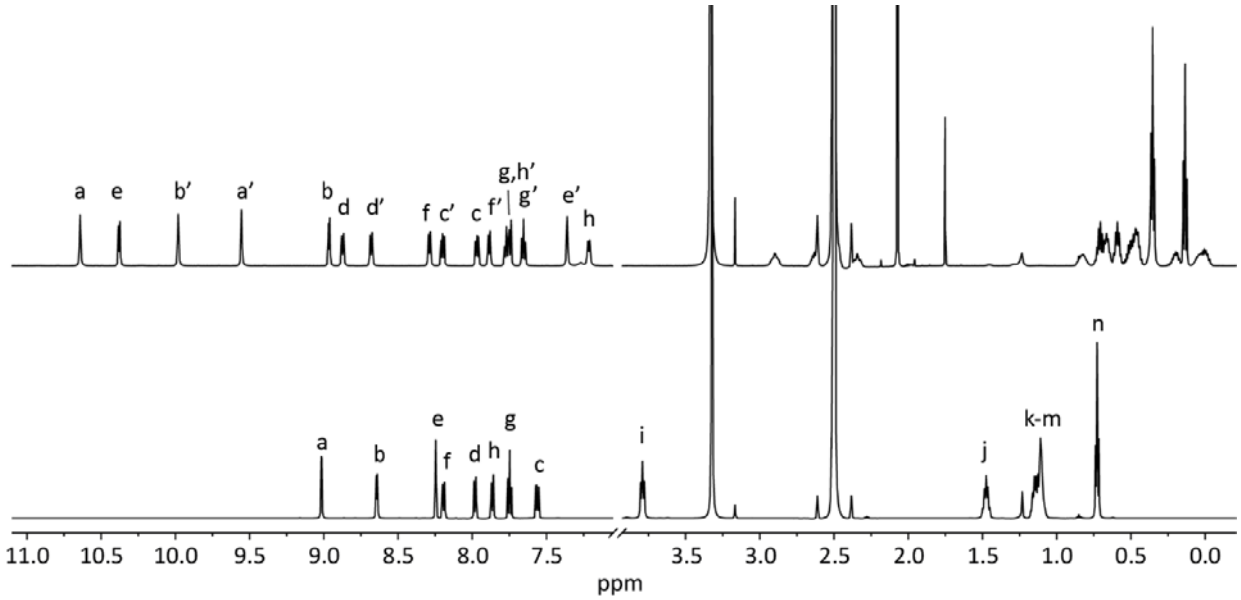

Figure 3.12: Stacked ^{1}H NMR spectra of ligand **3PM-DPP** (bottom) and corresponding $[Pd_2(\mathbf{3PM\text{-}DPP})_4]$ cage upon addition of 0.5 equiv. of Pd(II) (top) in DMSO-d_6. The assignment refers to Figure 3.11.

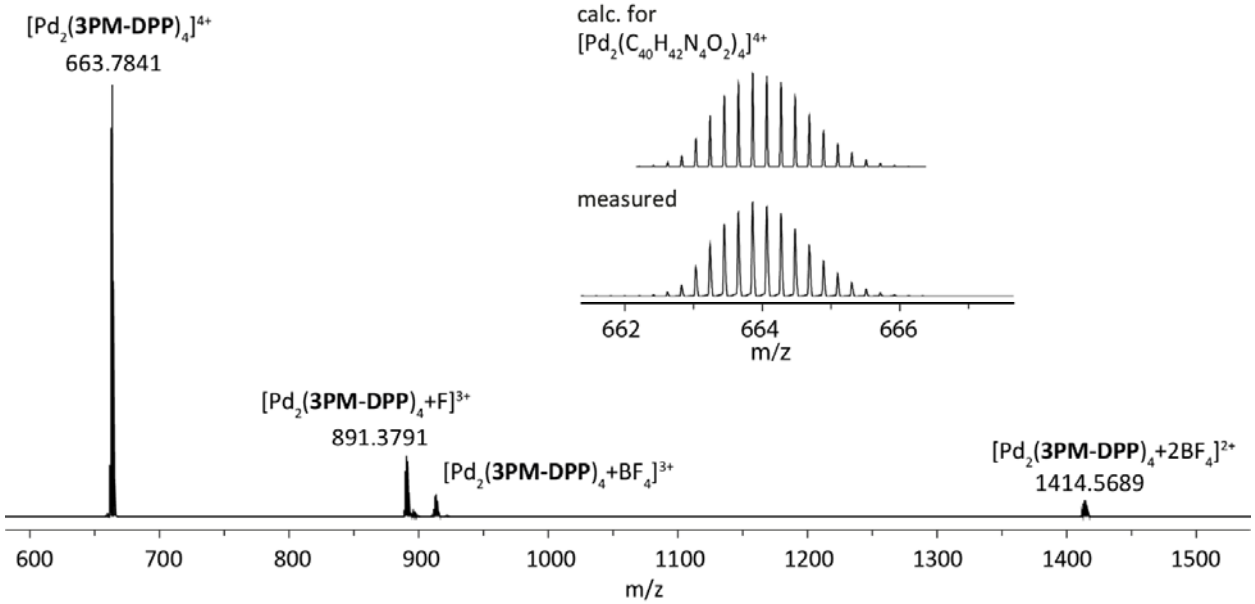

Figure 3.13: ESI-MS spectrum of $[Pd_2(\mathbf{3PM\text{-}DPP})_4{+}nBF_4]^{(4-n)+}$ with n=0-2. The observed and calculated isotopic patterns of $[Pd_2(\mathbf{3PM\text{-}DPP})_4]^{4+}$ are shown in the inset.

Single-crystal X-ray diffraction provided the ultimate proof which nicely merged all the puzzle pieces collected with the miscellaneous techniques. In the solid-state, the self-penetration of two ligands in the cavity of a $[Pd_2L_4]$ topological arrangement can be indeed observed. In other words, two ligands adopt the typical banana-shaped conformation and bridge the Pd(II) cations from outside the cavity and two ligands adopt an "*S*" conformation and cross in the middle of the cavity. A similar, however heteroleptic, organization of ligands around the Pd(II) centers, was reported by our group before.[25] In such an assembly, two carbazole-based bispyridin ligands bridge the Pd(II) centers from the outside, while the longer acridone-based bis-isoquinoline ligands cross in the middle of the cavity to form -as it has been named- a "Figure 8" structure. $[Pd_2(\mathbf{3PM\text{-}DPP})_4]$ is the first reported self-interpenetrating Pd_2L_4 structure and from now on it will be referred as *Fig8*-$[Pd_2L_4]$. The structure, being chiral, is present as a racemic

mixture in both enantiomeric forms. Such observation is supported by splitting of the signals assigned to the -CH_2 protons H_i (see spectrum in CD_3CN in Figure 3.52).

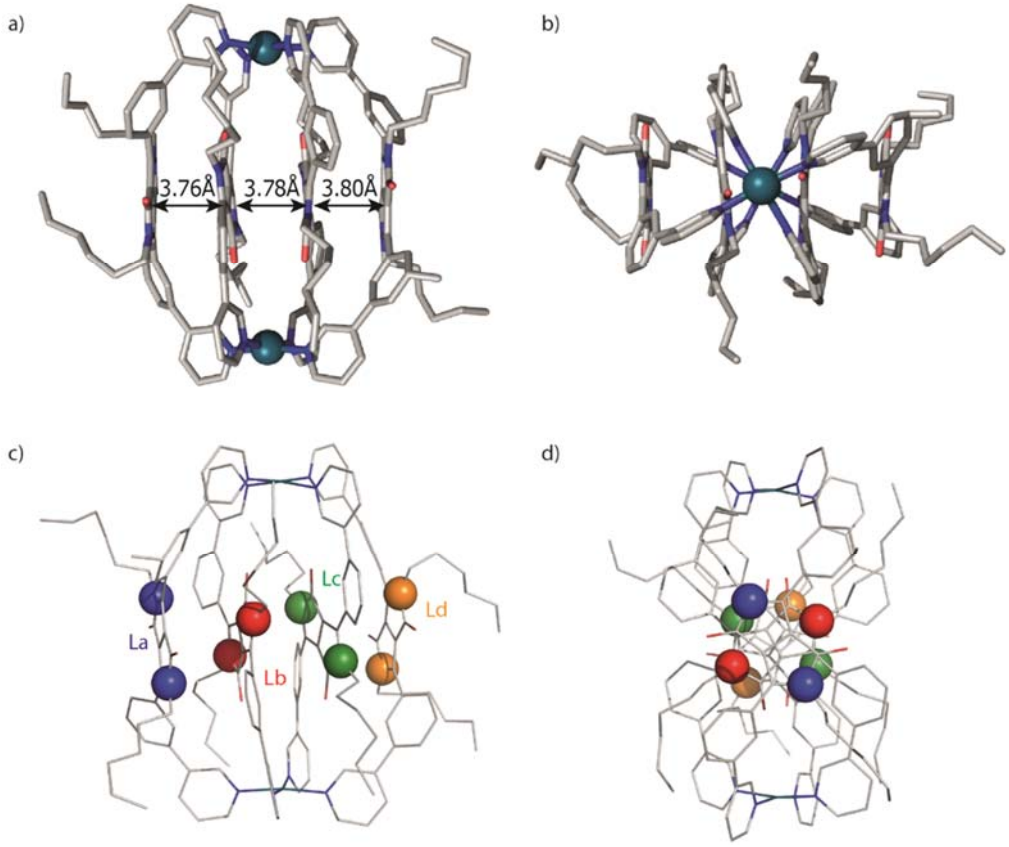

Figure 3.14: Crystal structure of *Fig8*-[Pd_2(**3PM-DPP**)$_4$]. a) Side view with indicated distances between the stacked chromophore units b) top view, c) and d) side views in which N atoms of different dye backbones are differently colored and labelled. The different colors serve the purpose of better highlighting the opposite alternate rotation of the dyes within the stack.

The overall structure is characterized by the π-π stacking of the four ligand backbones, the Ferrari Red dye functionalities, which are facing each other with an alternated rotation of roughly 90°. The mutual orientation of the dyes in the structure can be defined by the angles between the vectors defined by the N atoms of each diketopyrrolopyrrole moiety. The angles measured between each vector combination are listed in the following table (Table 3.1). Deviation from the perfect 90° stack can be due to restriction in view of the coordination to the Pd(II) ions as well as crystal packing effects.

Table 3.1: Angles between the vectors defined by the N atoms of each **DPP** moiety (pictured in different colors in Figure 3.14). The angles in bold along the diagonal of the tables refer to the orientation of two neighboring **DPP** units.

	Lb	Lc	Ld
La	**89.60°**	33.55°	63.81°
Lb	/	**57.32°**	27.07°
Lc	/	/	**84.39°**

In order to understand the solvent dependency on the formed topology, and if different solvents would favor different arrangement of the ligands around the Pd(II) coordination centers, the assembly was studied also in CD_3CN, acetone-d_6, tetrahydrofuran-d_8 (THF-d_8), nitromethane-d_3 ($MeNO_2$-d_3), *N,N*-dimethyformammide-d_7 (DMF-d_7) and methanol-d_4 (CD_3OD). The measured ^{1}H NMR spectra are reported in Figure 3.15 and show how in all solvents, except for CD_3OD where only the signals

corresponding to the free ligand are measured, the *Fig8*-[Pd_2L_4] forms, stabilized by the π-stacking of the chromophores.

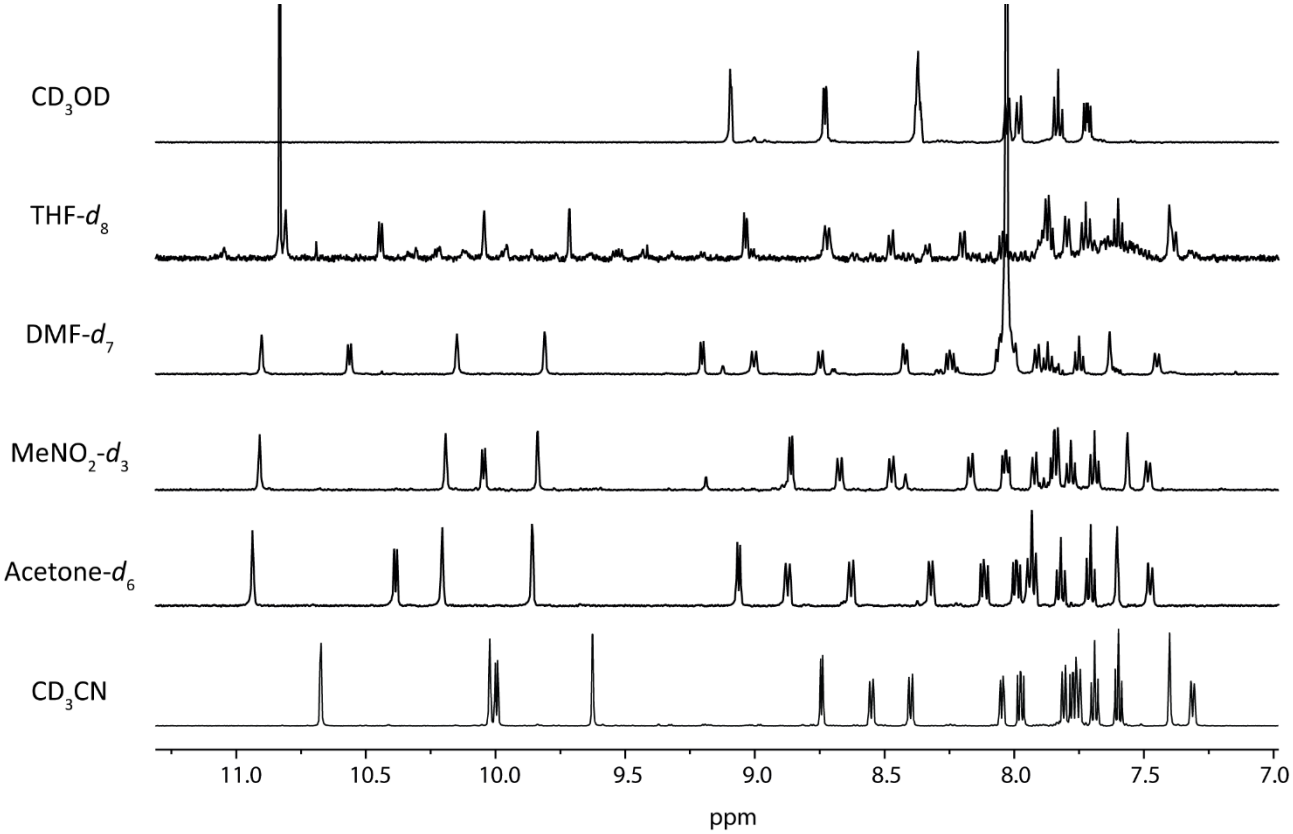

Figure 3.15: Stacked ^{1}H NMR spectra (25 °C) of cage *Fig8*-[Pd_2(**3PM-DPP**)$_4$] in the indicated different solvents.

The peculiar ability of such cage to organize the ligands in two different conformations arose questions around its applicability in host-guest chemistry. For a guest to access the cage cavity, at least two ligand-Pd bonds must brake to allow the two penetrating ligands to adopt a banana shape conformation and bridge the Pd(II) cations from the outside, like the other two ligands. In this way, the 'canonical' [Pd_2L_4] cage would form. The cage transformation was attempted with various guests, listed in Figure 3.16. The guests were chosen in order to either compete with the π-stacking ability of the ligands and replace them in the cage cavity, or, as anionic molecules, to maximize the electrostatic attraction with the Pd(II) cations. Hence, some neutral, planar and aromatic molecules were tested, as well as sulfonates and phosphates anions. Moreover, two clusters, [W_6I_{14}](Bu_4N)$_2$ and [Mo_6I_{14}](Bu_4N)$_2$, and fullerene C_{60} were combined with *Fig8*-[Pd_2(**3PM-DPP**)$_4$]. However, none of the small molecules created an interaction strong enough to transform the cage and accommodate in its cavity. In most cases, the resulting mixtures lead either to the mere superimposition of the single components in solution, or to abundant precipitation caused by unspecific aggregation effects. In some cases, cage decomposition to the free ligand was observed. In Figure 3.17, an example with the guest 1,4-disufonate benzene is reported. In order to slow down the cage formation process, ligand **3PM-DPP** and the guest were mixed together in DMSO-d_6 at 0°C and subsequently the Pd(II) solution was added, in order to exploit the guest as a template in the formation of the 'canonical' [Pd_2L_4] cage. The same experiment was performed without the guest as a comparison. In absence of the guest (Figure 3.17, first spectrum from the bottom on the right), already at 0°C, immediately after mixing the ligand with the Pd(II), the *Fig8*-[Pd_2L_4] is already forming. This result is a further indication of how strong the interaction within the stack of the four chromophores is and what a remarkable stability it grants to the supramolecular assembly. On the other hand, when the guest is present in solution, the formation of the cage is completely obstructed and neither waiting longer or heating helps the structure to form.

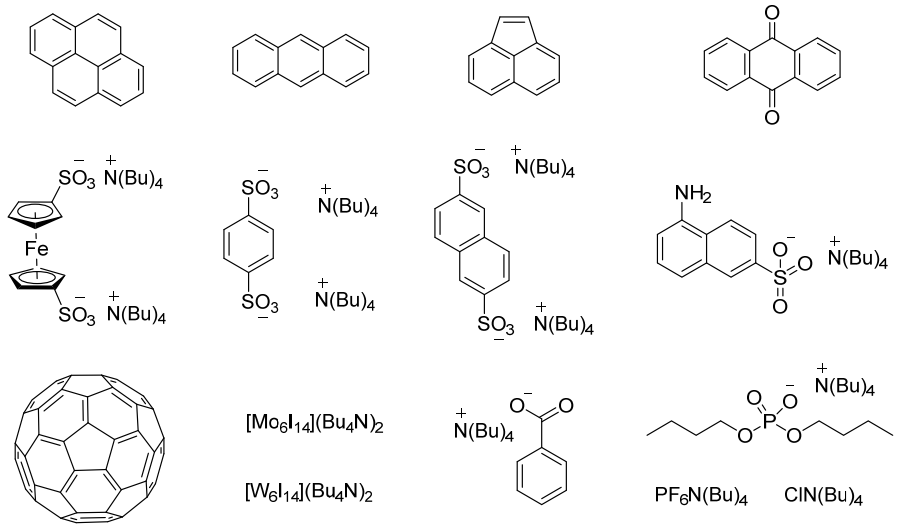

Figure 3.16: List of guests used for the (unsuccessful) transformation of *Fig8*-[Pd_2L_4] to the 'canonical' [Pd_2L_4]. For more details see Table 3.3.

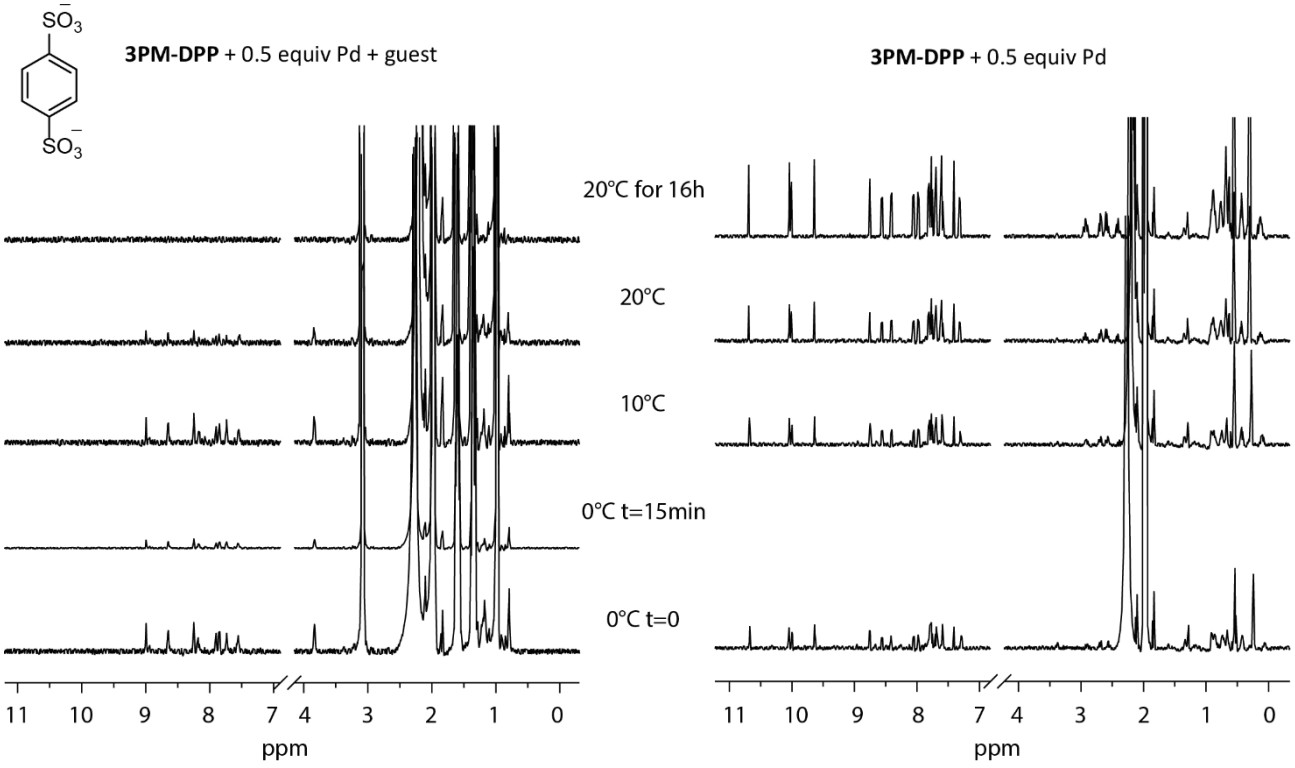

Figure 3.17: Stacked ^{1}H NMR spectra (DMSO-d_6 at the indicated temperature) of the (unsuccessful) templated formation of non-entangled [Pd_2L_4] with the guest depicted in the figure. On the right, the control without the guest is reported.

3.2.5 Ligand 8QP-DPP

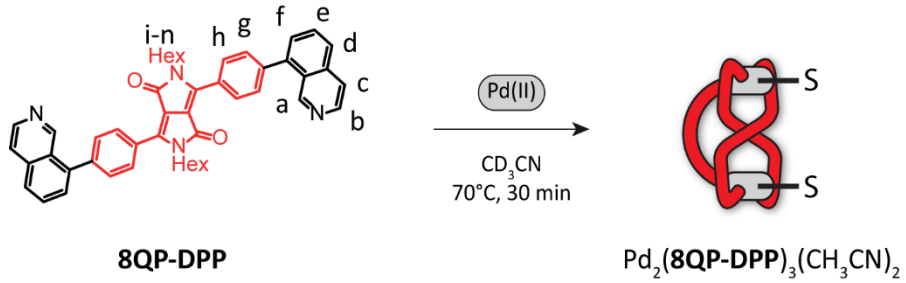

8QP-DPP Pd_2(**8QP-DPP**)$_3$(CH_3CN)$_2$

Figure 3.18: Formation of the assembly [Pd_2(**8QP-DPP**)$_3$(CH_3CN)$_2$] and depiction of possible topology. The S in the figure stands for a solvent molecule.

Ligand **8QP-DPP** is equipped with two isoquinoline donor groups which are attached in para position to the phenyl ring part of the **DPP** central core. The ligand owns a much more straight structure than the previously presented ones and coordination to the Pd(II) cations leads to a structure where only three ligands are coordinating two metal centers. Such architecture has already been defined in the literature as a bowl structure and arises from the steric hindrance of the isoquinoline donor groups around the Pd(II) centers. The steric repulsion does not allow the coordination of the fourth ligand, leaving one coordination site free for solvent molecules or small anions to saturate it. The assembly in CD_3CN leads to a ^{1}H NMR spectrum in which the ligands' signals split into 3 sets equally integrating (Figure 3.19). For other bowl structures[26,27] the signals split into two sets of integration 2:1 because two ligands, the external ones, are in the same chemical environment while the third one, the one in the middle, is in a different environment. The possible explanation for the splitting into 3 sets could lie in the ability of this ligand to form "Figure 8" π-stacks, similar to **3PM-DPP**, and decrease the symmetry of the overall structure (like depicted in Figure 3.18). However, such assumption would need further structural evidence to be proven, and for the rest of the chapter the structure is indicated simply as a bowl without further indications on the actual arrangement of the ligands. ESI-MS spectrum (Figure 3.20) confirms the [Pd_2(**8QP-DPP**)$_3$] topology. Furthermore, it shows that the coordination sphere of the Pd(II) is saturated by a molecule of solvent, in this case CD_3CN, or by a small anion such as F^-, Cl^-, Br^- or NO_3^-, BF_4^-.

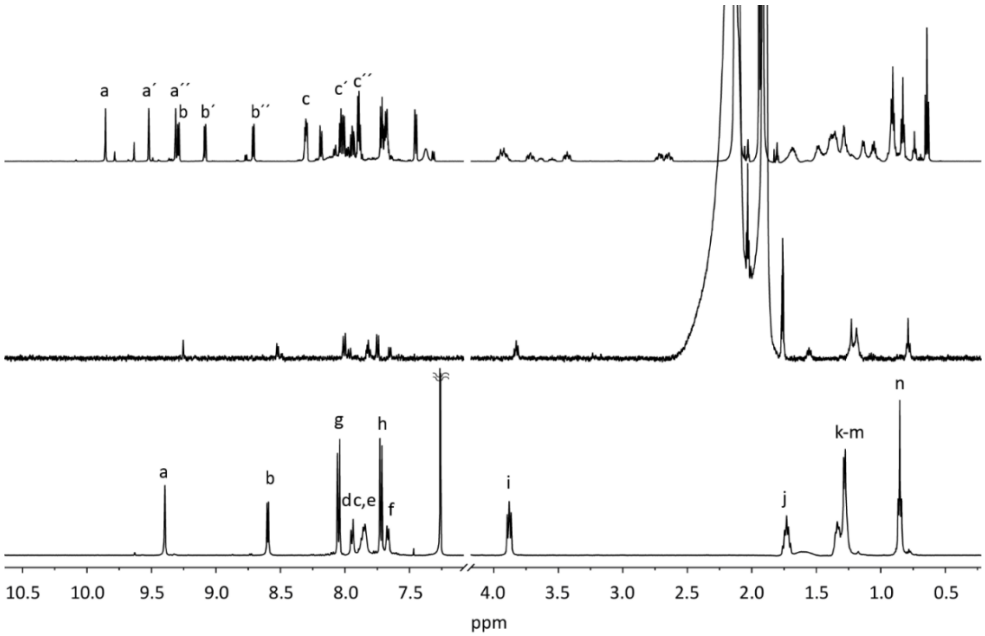

Figure 3.19: Stacked ^{1}H NMR spectra of ligand **8QP-DPP** in $CDCl_3$ (bottom), ligand **8QP-DPP** in CD_3CN (poorly soluble, middle) and ligand **8QP-DPP** in CD_3CN upon addition of 0.5 equiv. of Pd(II) and heating at 70 °C for 30 min (top). The assignment refers to Figure 3.18.

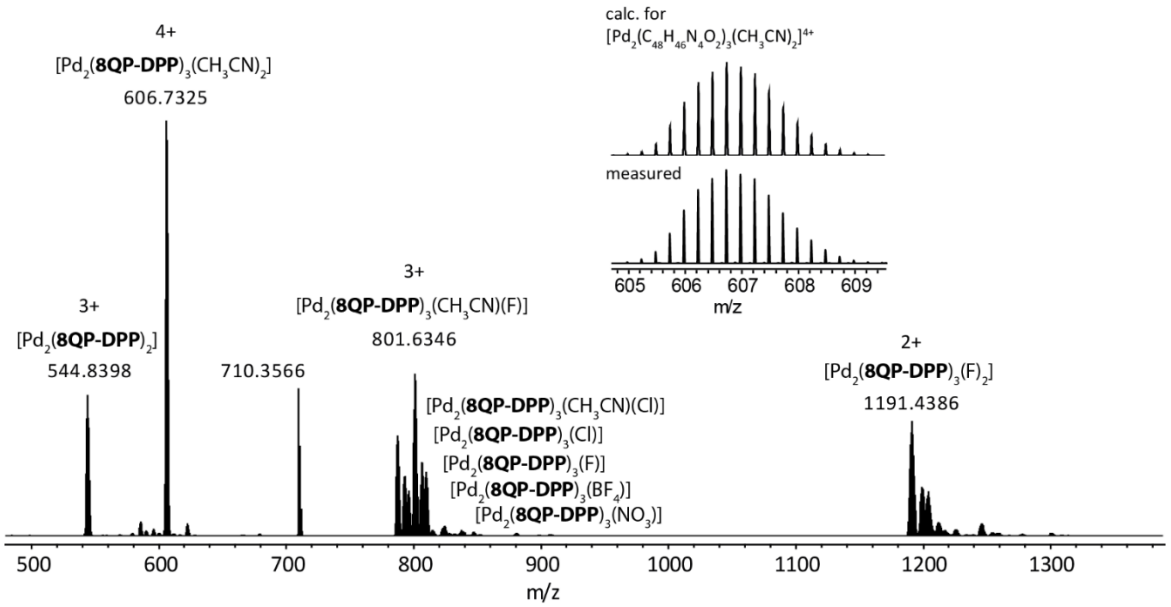

Figure 3.20: ESI-MS spectrum of $[Pd_2(\mathbf{8QP\text{-}DPP})_3(CH_3CN)_2{+}nBF_4]^{4-n+}$ with measured and simulated patterns for $[Pd_2(\mathbf{8QP\text{-}DPP})_3(CH_3CN)_2]^{4+}$ shown in the inset. Species in which the solvent molecules are exchanged for various anions are assigned in the spectrum.

The assembly in DMSO-d_6 leads to a very broadened spectrum (Figure 3.24 in red), but the formation of $[Pd_2(\mathbf{8QP\text{-}DPP})_3(solvent)_2]$ is unequivocally confirmed by ESI mass spectrometry (Figure 3.25).

3.3 Optical properties

The optical properties of the ligands and assemblies have been studied and the absorption and emission spectra in DMSO are reported in Figure 3.21.

Ligands **3PM-DPP** and **4PM-DPP** display extremely similar absorption and emission properties, as expected in view of their analogous structure, with an absorption band with a maximum at 474 nm and an intense emission band with a maximum at 539 nm. Ligand **8QP-DPP** is slightly red shifted, with an absorption maximum at 482 nm and an emission maximum at 558 nm, accordingly to the larger π system of the molecule. Upon Pd(II) addition, the assemblies show specific different behaviors, as it can already be appreciated from the pictures of the vials containing ligands **3PM-DPP** and **4PM-DPP** and their assemblies (Figure 3.21 d). While the ligands are bright yellow and emit even under day-light, the high emission property is partially quenched for the ring mixture, $[Pd_3(\mathbf{4PM\text{-}DPP})_6]$ and $[Pd_4(\mathbf{4PM\text{-}DPP})_8]$, with the solution being darker. Emission is completely lost for cage $[Pd_2(\mathbf{3PM\text{-}DPP})_4]$ whose solution is deep red. Indeed, the absorption spectrum of $[Pd_2(\mathbf{3PM\text{-}DPP})_4]$ is slightly red shifted and a second shoulder band appears around 540 nm. Such band could be attributed to the π-stacking of the dyes, coherent with the typical bathochromic shift for H-aggregates.[28] Further spectroscopic analysis must support this hypothesis. On the contrary, the absorption spectrum of $[Pd_3(\mathbf{4PM\text{-}DPP})_6]$ + $[Pd_4(\mathbf{4PM\text{-}DPP})_8]$ is almost identical to the one of **4PM-DPP**, only 4 nm blue-shifted while the emission spectrum shows a band at 545 nm of decreased intensity. Since such effect may result from residual free ligand in the equilibrium mixture, the emission spectrum of the rings was recorded in presence of an excess of Pd(II) cations, in order to shift the equilibrium to the completely assembled structures (violet line in Figure 3.21 b). From the experiment, it can reasonably be assumed that, even if decreased, the assembled structure still shows emission. Concerning the assembly deriving from ligand **8QP-DPP**, in the absorption spectrum, a blue shifted band, compared to the ligand, could be measured with a maximum at 488 nm (Figure 3.21 c). A remarkable feature of this system is the large increase in absorption intensity. Also for this assembly, the emission is completely quenched. Whether this could be an indication of a specific structural arrangement of the dyes in the structure, will be investigated in future research studies.

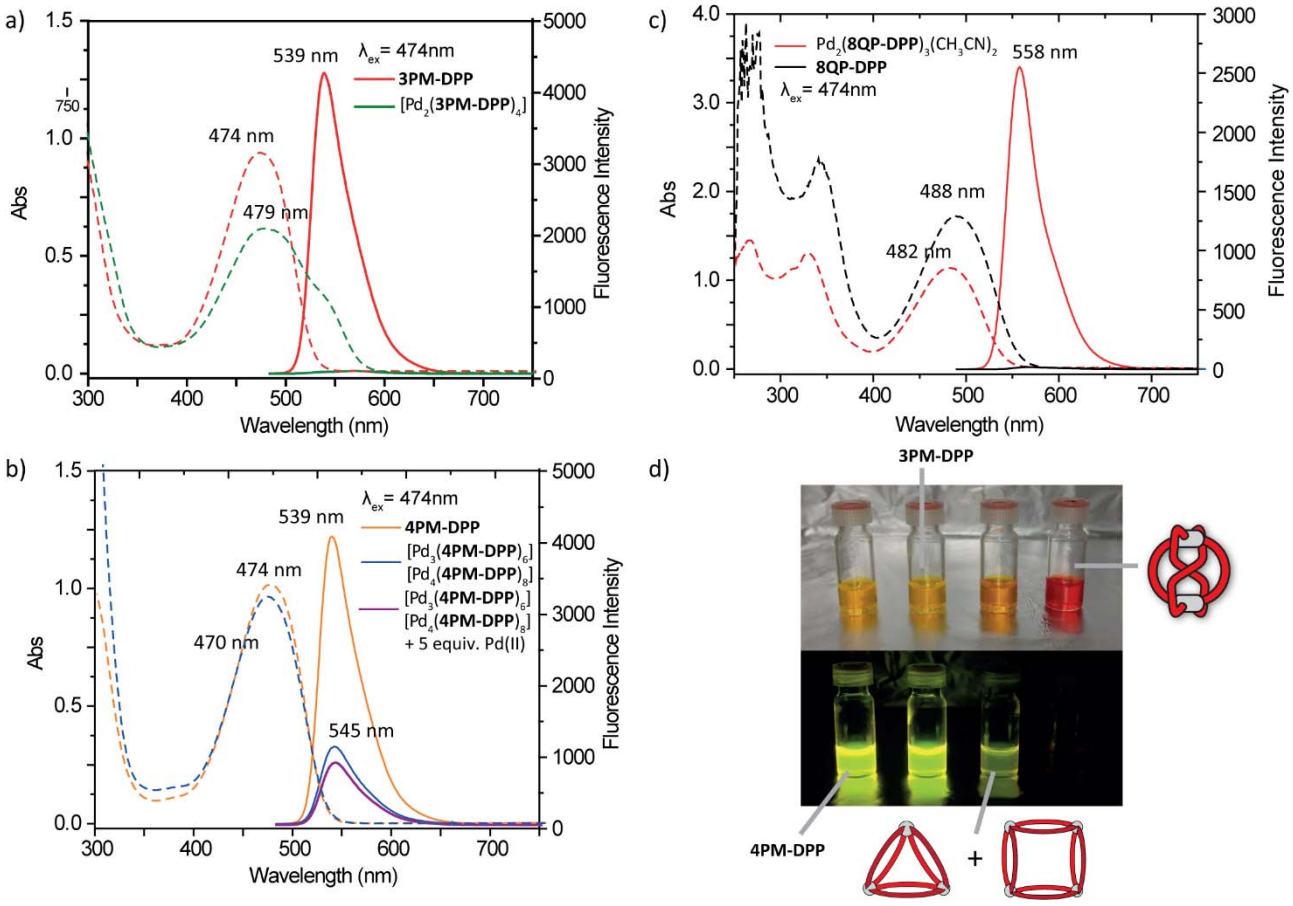

Figure 3.21: UV-Vis absorption (dashed lines) and emission (solid lines) of a) **3PM-DPP** (in red) and [Pd_2(**3PM-DPP**)$_4$] (in green), b) **4PM-DPP** (in orange) and [Pd_3(**4PM-DPP**)$_6$] + [Pd_4(**4PM-DPP**)$_8$] (in blue) and with 5 equiv. of Pd(II) (in violet), c) **8QP-DPP** (in red) and [Pd_2(**8QP-DPP**)$_3$(solvent)$_2$] (in black). All the samples have a ligand concentration of 0.31 mM in DMSO, the optical path of the cuvette used for the absorption measurement is 0.2 cm and, for all the emission measurement reported, the same λ_{ex} = 474 nm and the same bandwidth of 1 nm in excitation and 2.5 nm in emission have been used. d) Picture under ambient light (top) and UV lamp (λ_{ex}= 365 nm, bottom) of vials containing in the order **4PM-DPP, 3PM-DPP,** [Pd_3(**4PM-DPP**)$_6$] + [Pd_4(**4PM-DPP**)$_8$] and [Pd_2(**3PM-DPP**)$_4$].

The molar extinction coefficients, ε (L $mol^{-1}cm^{-1}$), in DMSO at the maximum of absorption for all six species have been calculated and the values are reported in the following table. Each ε refers to a single dye unit:

Table 3.2: Molar extinction coefficients ε in DMSO at the maximum of absorption for the **DPP**-based ligands and corresponding assemblies.

	3PM-DPP λ_{max} 474nm	**4PM-DPP** λ_{max} 474nm	**8QP-DPP** λ_{max} 482nm	[Pd_2(**3PM-DPP**)$_4$] λ_{max} 479nm	[Pd_3(**4PM-DPP**)$_6$] + [Pd_4(**4PM-DPP**)$_8$] λ_{max} 470nm	[Pd_2(**8QP-DPP**)$_3$(solvent)$_2$] λ_{max} 488nm
ε (L mol^{-1} cm^{-1})	15987.74	16129.03	18225.80	9677.42	14247.54	27419.35

3.4 Preliminary heteroleptic assemblies with ligand 8QP-DPP

Besides the photopysical properties of the homoleptic assemblies compared to the single components, the **DPP**-based structures are interesting to be studied for their donor/acceptor properties in combination with other known donor/acceptor moieties such as dimethyl fluorene,[29] carbazole,[30] fluorenone[31] and **DPP**s themselves.[32,33] The approach is to realize systems comprising more functionalities together in the same Pd-based structure by a non-statistical design. In other words, constructing *N*-donor ligands in such a way that by mixing two or more ligands, upon Pd(II) addition, one assembly product can selectively be obtained, rather than the statistical distribution of all possible combinations.[34]

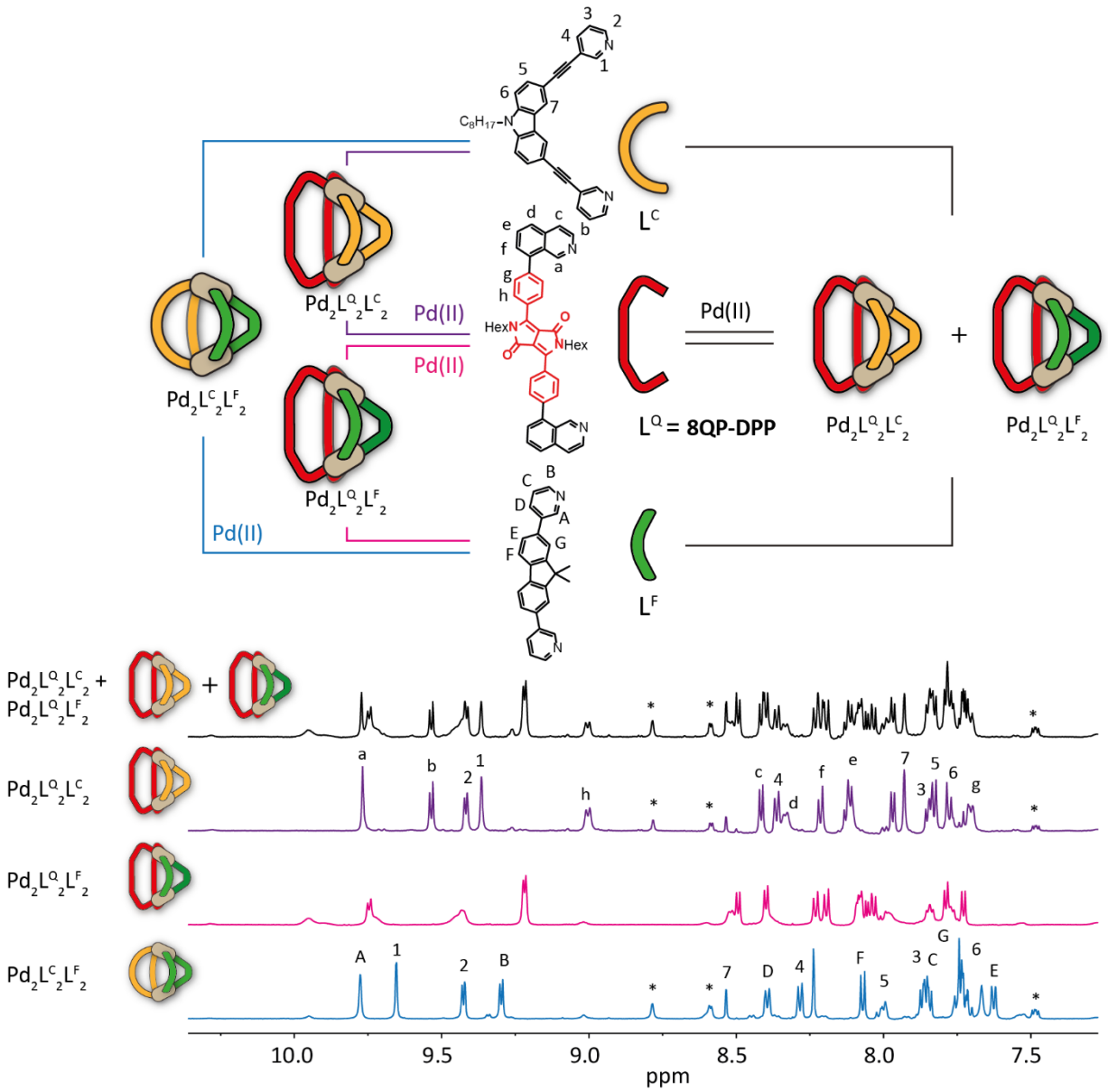

Figure 3.22: On the top, schematic illustration of the mixing experiments. L^Q is depicted in red, L^F in green and L^C in yellow. The resulting ^{1}H NMR spectra (DMSO-d_6 at 25°C) are reported, only the aromatic region for better understanding, on the bottom as indicated. The colors of the spectra match the colors of the lines in the scheme that join 2 or more ligands to form the respective heteroleptic cage(s). The * correspond to residual [$Pd_2L^C_4$] homoleptic cage.

It has already been reported in the literature that a mixture of two shape-complementary ligands, with carefully matched angular relationships, reacted with Pd(II), forms a single product. This reaction quantitatively produces a heteroleptic cage, as this structure is of higher thermodynamic stability than

the other possible structures.[24,25] More recently, exploiting the same approach, a heteroleptic cage was designed,[35] in which a carbazole-based bispyridine ligand (L^C) is combined with the shorter dimethyl fluorene-based bispyridine ligand (L^F) to yield a *cis*-$[Pd_2L^C_2L^F_2]$ cage (Figure 3.22 in blue). When ligand **8QP-DPP** (from this point on L^Q for brevity) is mixed in a 1:1 ratio with ligand L^F followed by the addition of 0.5 equiv. of Pd(II) salt, the corresponding ^{1}H NMR spectrum (Figure 3.22 in green) is rather broadened but it still allows to understand that neither of the homoleptic species form but rather a single new structure. The formation of a heteroleptic $[Pd_2L^Q_2L^F_2]$ cage is confirmed by ESI mass spectrometry which highlights the formation of the species with *m/z* values corresponding to $[Pd_2L^Q_2L^F_2+nBF_4]^{4-n+}$ with n=0-2. The broadened and preliminary spectrum does not allow for assignment at this stage. In order to overcome possible broadening due to dynamics of the structure, higher temperature NMR measurements will be recorded. Similarly, when ligand L^Q is mixed with ligand L^C in equimolar amounts, followed by the addition of 0.5 equiv. of Pd(II), the resulting ^{1}H NMR spectrum shows one set of signals for each ligand that does not correspond to the superimposition of the homoleptic assemblies (Figure 3.22 in yellow). The new species has been characterized as the heteroleptic cage $[Pd_2L^Q_2L^C_2]$ by ESI mass spectrometry in which the species with *m/z* values corresponding to $[Pd_2L^Q_2L^C_2+nBF_4]^{4-n+}$ with n=0-2 are measured. Both these cages will be studied for their optical properties and possible photoinduced processes involving the photoactive moieties, constituents of the cages. Interestingly, when all three ligands are mixed together in a ratio L^Q:L^F:L^C 2:1:1 followed by the addition of Pd(II), the resulting NMR and MS spectra represent the perfect superimposition of the ones deriving from the two heteroleptic cages $[Pd_2L^Q_2L^F_2]$ and $[Pd_2L^Q_2L^C_2]$ leaving no trace of the heteroleptic cage $[Pd_2L^C_2L^F_2]$.

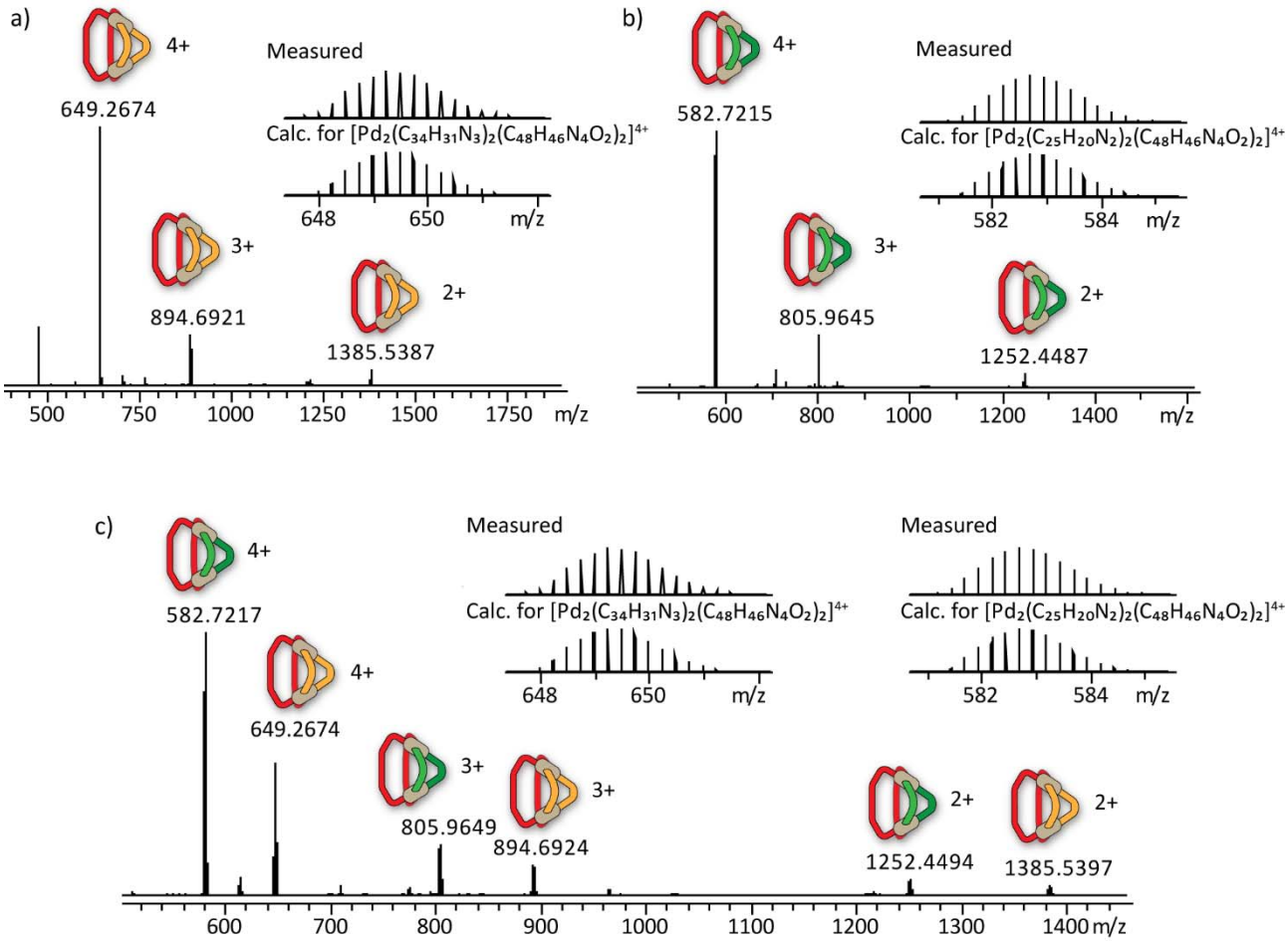

Figure 3.23: ESI-MS spectra of a) cage $[Pd_2L^Q_2L^C_2+nBF_4]^{4-n+}$ with n=0-2 with measured and simulated isotopic patterns of $[Pd_2L^Q_2L^C_2]^{4+}$; b) cage $[Pd_2L^Q_2L^F_2+nBF_4]^{4-n+}$ with n=0-2 with measured and simulated isotopic patterns of $[Pd_2L^Q_2L^F_2]^{4+}$; c) mixture of heteroleptic cages $[Pd_2L^Q_2L^C_2+nBF_4]^{4-n+}$ with n=0-2 and $[Pd_2L^Q_2L^F_2+nBF_4]^{4-n+}$ with n=0-2 with measured and simulated isotopic patterns of $[Pd_2L^Q_2L^C_2]^{4+}$ and $[Pd_2L^Q_2L^F_2]^{4+}$.

Inspired by the results, specifically by the absence of the heteroleptic cage $[Pd_2L^C{}_2L^F{}_2]$ when all three ligands are mixed together, a series of cage-to-cage transformations were performed (see experimental part for experimental details). Starting from the ligands, all three homoleptic species were formed and characterized by ^{1}H NMR spectroscopy and ESI-MS (Figure 3.24 and Figure 3.25). L^C was reported to form a $[Pd_2L^C{}_4]$ cage and L^F a mixture of $[Pd_3L^F{}_6]$ rings and $[Pd_4L^F{}_8]$ tetrahedrons. When the two solutions containing the homoleptic assemblies are combined and heated for 1 day at 70°C, they completely convert into the heteroleptic $[Pd_2L^C{}_2L^F{}_2]$ cage. When this solution is successively mixed in the correct ratio with the solution containing the homoleptic assembly derived from ligand L^Q, a successive conversion of the cages leads to the mixture of heteroleptic cages $[Pd_2L^Q{}_2L^F{}_2]$ and $[Pd_2L^Q{}_2L^C{}_2]$. The heteroleptic cage $[Pd_2L^C{}_2L^F{}_2]$ is "eaten up" by the homoleptic $[Pd_2(\mathbf{8QP\text{-}DPP})_3(solvent)_2]$ to form the thermodynamically more stable heteroleptic combinations. The unfavored coordination of ligand L^Q around the Pd(II) centers is probably what drives the system to these products.

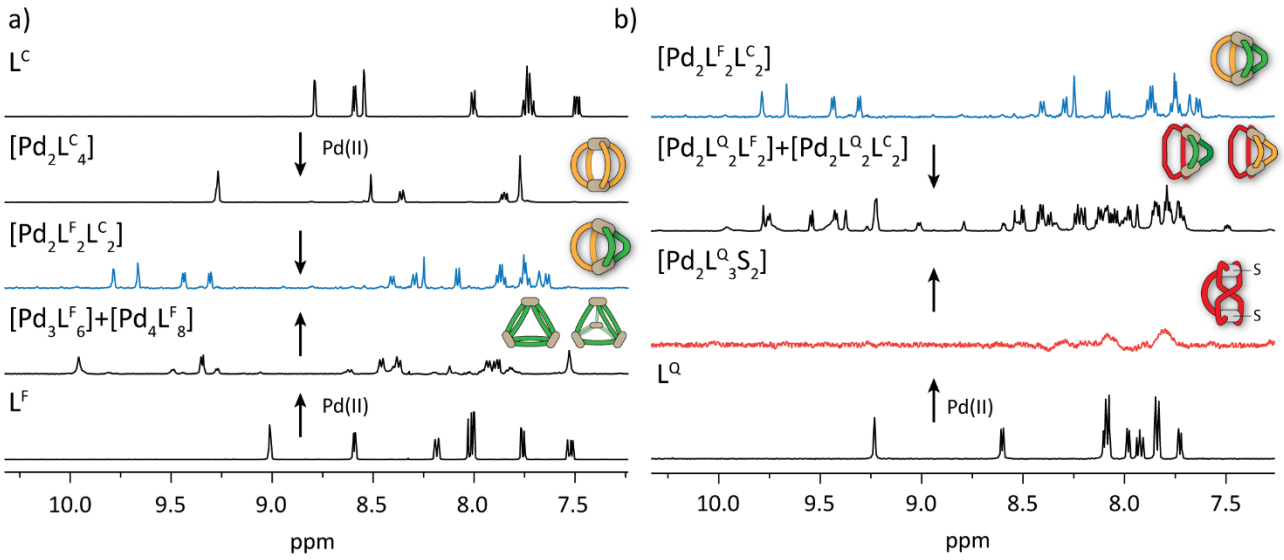

Figure 3.24: Stacked ^{1}H NMR spectra (DMSO-d_6 at 25°C) of a) assembly of L^C into $[Pd_2L^C{}_4]$ cage and L^F into $[Pd_3L^F{}_6]+[Pd_4L^F{}_8]$ and successive conversion into $[Pd_2L^C{}_2L^F{}_2]$; b) cage-to-cage transformation of $[Pd_2L^C{}_2L^F{}_2]$ and $[Pd_2(\mathbf{8QP\text{-}DPP})_3(solvent)_2]$ into cages $[Pd_2L^Q{}_2L^F{}_2]$ + $[Pd_2L^Q{}_2L^C{}_2]$.

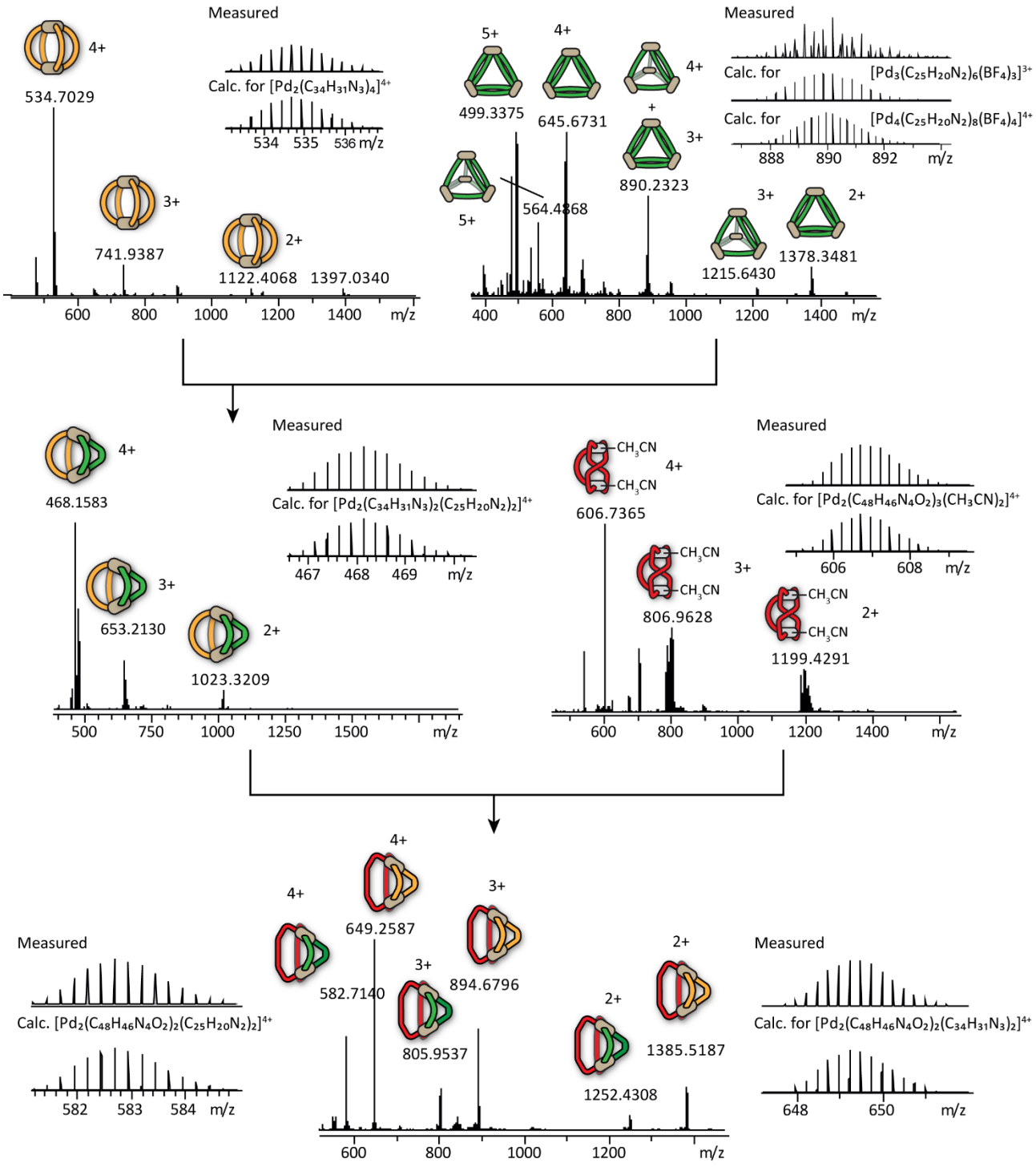

Figure 3.25: ESI-MS spectra (from the DMSO-d_6 solutions presented in Figure 3.24) of $[Pd_2L^C_4]$ cage and $[Pd_3L^F_6]$+$[Pd_4L^F_8]$ and successive conversion into $[Pd_2L^C_2L^F_2]$, cage-to-cage transformation of $[Pd_2L^C_2L^F_2]$ and $[Pd_2(\mathbf{8QP\text{-}DPP})_3(solvent)_2]$ into cages $[Pd_2L^Q_2L^F_2]$ + $[Pd_2L^Q_2L^C_2]$. a) $[Pd_2L^C_4+nBF_4]^{4-n+}$, n=0-2 with measured and simulated pattern for $[Pd_2L^C_4]^{4+}$. b) $[Pd_3L^F_6+nBF_4]^{6-n+}$, n=1-4 +$[Pd_4L^F_8+nBF_4]^{8-n+}$, n=3-5 with measured and simulated pattern for m/z at 890.2323 which corresponds to the superimposition of $[Pd_3L^F_6+3BF_4]^{3+}$+$[Pd_4L^F_8+4BF_4]^{4+}$. c) $[Pd_2L^C_2L^F_2+nBF_4]^{4-n+}$, n= 0-2 with measured and simulated pattern for $[Pd_2L^C_2L^F_2+nBF_4]^{4+}$. d) $[Pd_2(\mathbf{8QP\text{-}DPP})_3(CH_3CN)_2+nBF_4]^{4-n+}$, n= 0-2 with measured and simulated pattern for $[Pd_2(\mathbf{8QP\text{-}DPP})_3(CH_3CN)_2]^{4+}$. e) Mixture of heteroleptic cages $[Pd_2L^Q_2L^C_2+nBF_4]^{4-n+}$ with n=0-2 and $[Pd_2L^Q_2L^F_2+nBF_4]^{4-n+}$ with n=0-2 with measured and simulated isotopic patterns of $[Pd_2L^Q_2L^C_2]^{4+}$ and $[Pd_2L^Q_2L^F_2]^{4+}$.

3.5 Conclusion and outlook

In conclusion, four different bis-monodentate banana-shaped ligands based on the **DPP** structure were synthesized. Upon Pd(II) addition, different topologies originated from the different designs, a $[Pd_4L_8]$ ring, a $[P_3L_6]$ ring, a $[Pd_2L_3]$ "bowl" caused by steric hindrance of the isoquinoline moieties around the coordination center, with the most interesting being the never reported homoleptic, self-penetrated "Figure 8" topology $[Pd_2L_4]$. The assembly properties of the last structure were deeper analyzed in several different solvent conditions to understand whether it could form also the "canonical" $[Pd_2L_4]$ cage and guest molecules could enter the cavity (Figure 3.26 a). However, the π-stacking of the chromophores was shown to be energetically more favored. In future research study, we plan to investigate the guest-induced cage transformation with the guest depicted in Figure 3.26 b). The paracyclophane moiety should perfectly resemble the π-π distance between the stacked chromophores within the structure. Furthermore, the negative charges of the sulphonated groups would point directly at the Pd(II) ions and serve as electrostatic anchors.

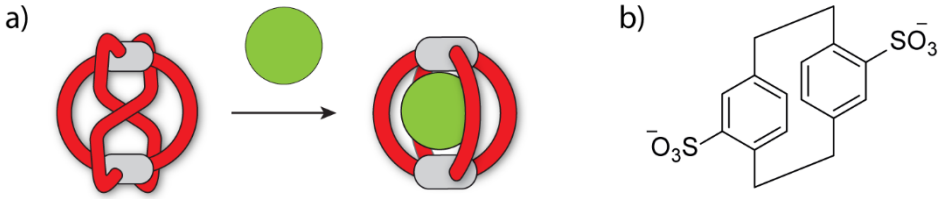

Figure 3.26: a) Schematic representation of the intended guest-induced cage transformation from Fig8-$[Pd_2L_4]$ to the host-guest complex with the "canonical" $[Pd_2L_4]$ cage. b) Proposed guest for the cage-induced transformation, a 4,16-disulfonated [2.2]paracyclophane.

Beside the photophysical properties of the homoleptic assemblies compared to the single components, we were interested in studying their donor/acceptor properties in combination with other known donor/acceptor moieties. For this purpose, the isoquinoline ligand was mixed with a dimethyl fluorene-based ligand and a carbazole-based one. The approach was to realize systems comprising both functionalities in the same Pd-based structure with a non-statistical design. Further exciting results were obtained when the three ligands were mixed together and successive cage-to-cage transformations, leading to the mixture of only two heteroleptic cages over all possible products. The optical properties of the heteroleptic assemblies will be investigated with time resolved spectroscopy in collaboration with experts of the field. The **DPP** moieties are vastly reported in the literature (see introduction of the chapter, section 3.1) for their energy/electron donor/acceptor behavior depending on further substituents or partner moieties. In this context, the new structures including two different photoactive moieties are promising candidates and combined with the newly-discovered cage-to-cage transformation could enable the tuning of optical properties with outside stimuli (for example by addition of a new ligand that would cause the transformation to happen).

3.6 Experimental part

3.6.1 General methods

NMR

NMR spectroscopic data was measured on the spectrometers Bruker AV 500 Avance NEO and AV 600 Avance III HD. For ^{1}H and ^{13}C NMR spectra, chemical shifts were calibrated to the solvent lock signal. Chemical shifts δ are given in ppm, coupling constants *J* in Hz. The following abbreviations are used to describe signal multiplicity for ^{1}H NMR spectra: s: singlet, d: doublet, t: triplet, dd: doublet of doublets; dt: doublet of triplets; m: multiplet, br: broad. All proton and carbon signals were assigned with the aid of 2D NMR spectra. All spectra were recorded in standard 5 mm NMR tubes at the indicated temperature.

Mass spectrometry
Mass spectrometry data were measured on Bruker ESI-timsTOF (electrospray ionization-trapped ion mobility-time of flight) and Bruker compact high-resolution LC mass spectrometers (positive/negative mode). For calibration of the TIMS and TOF devices, Agilent ESI-Low Concentration Tuning Mix was used.

UV-Vis
UV vis spectra were recorded on a DAD HP-8453 UV-Vis spectrometer. Cuvette path length 0.2 mm, wavelength: 250 nm – 800 nm, step size: 1 nm.

Fluorescence spectroscopy
Fluorescence spectra were recorded on a Jasco FP-8300 fluorimeter. Cuvette path length 0.2 mm in absorption and 10 mm in emission.

Experimental procedures
Where necessary, experiments were performed under nitrogen atmosphere using standard Schlenk techniques. Chemicals and standard solvents were purchased from Sigma Aldrich, Acros Organics, Carl Roth, TCI Europe, VWR, ABCR and used as received, if not mentioned differently. Dry solvents were purchased or purified and dried over absorbent-filled columns on a GS-Systems solvent purification system (SPS). Reactions were monitored with thin layer chromatography (TLC) using silica coated aluminium plates (Merck, silica 60, fluorescence indicator F254, thickness 0.25 mm). For column chromatography, silica (Merck, silica 60, 0.02–0.063 mesh ASTM) was used as the stationary phase.

3.6.2 Synthesis of the ligands

Ligand 3P-DPP

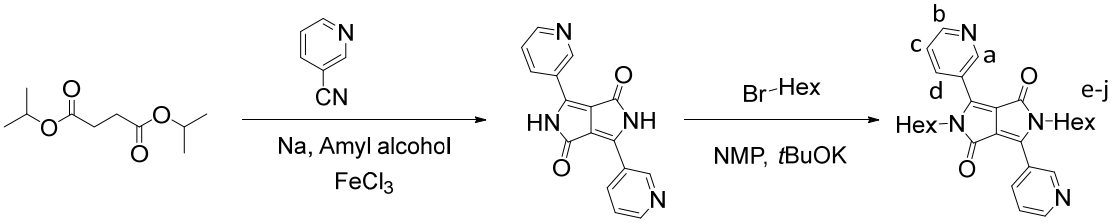

Figure 3.27: Synthesis of ligand **3P-DPP**.

Synthesis of $H_2$3P-DPP
Under argon atmosphere, sodium (1.0 g, 48 mmol), $FeCl_3$ (15 mg) and dry *tert*-amyl alcohol (25 mL) were heated to 90 °C until the sodium was dissolved. The mixture was cooled to 50 °C, 3-pyridinecarbonitrile (4.50 g, 43.1 mmol) was added and then the mixture was heated to 90 °C. Succinic acid diisopropyl ester (4.00 mL, 4.0 g, 19.6 mmol) was added dropwise. After standing for 16 h at 120 °C the reaction mixture is cooled down to 40°C and a mixture acetic acid : water : methanol 1 : 1 : 1 (10 mL) was added. The mixture was then heated to 120 °C. After standing for 1 h, the precipitate was filtered and washed with hot water and hot methanol repeatedly and dried.

Due to the very poor solubility of the obtained compound it was not possible to obtain characterization information or to further purify it; therefore, it was directly used for the next step.

Synthesis of the ligand 3P-DPP
$H_2$3P-DPP (0.725 g, 1.0 equiv., 1.63 mmol), potassium *tert*-butoxide (0.401 g, 2.2 equiv., 3.58 mmol) and *N*-methyl-2-pyrrolidone (NMP; 15 mL) were heated to 60 °C. 1-Bromohexane (1.37 mL, 6 equiv., 9.75 mmol) was slowly added and the mixture was stirred at 60 °C for 24 h. After cooling to room temperature, toluene (100 mL) was added into the reaction mixture and washed with water to remove

NMP. The organic solution was concentrated using a rotary evaporator. Crude product was purified by column chromatography on silica using dichloromethane as solvent to yield a red powder (420 mg, 0.92 mmol, 37%).

^{1}H NMR (500 MHz, Chloroform-*d*) δ 8.95 (d, J = 2.3 Hz, 1H, Ha), 8.74 (dd, J = 4.9, 1.6 Hz, 1H, Hb), 8.26 (dt, J = 8.0, 2.0 Hz, 1H, Hd), 7.50 (dd, J = 8.0, 4.8 Hz, 1H, Hc), 3.87 – 3.59 (m, 2H, He), 1.57 (p, J = 7.5 Hz, 2H, Hf), 1.36 – 1.08 (m, 6H, Hg-i), 0.81 (t, J = 6.7 Hz, 3H, Hj).

^{13}C NMR (126 MHz, Chloroform-*d*) δ 162.21 (C=O), 151.70 (Cb), 148.59 (Ca), 145.82 (N-**C**=C), 136.58 (Cd), 124.59 (C^{q}, Ca-**C**-Cd), 123.89 (Cc), 110.68 (N-C=**C**), 41.99 (Ce), 31.23 (Cg), 29.54(Cf), 26.38 (Ch), 22.48 (Ci), 13.98 (Cj).

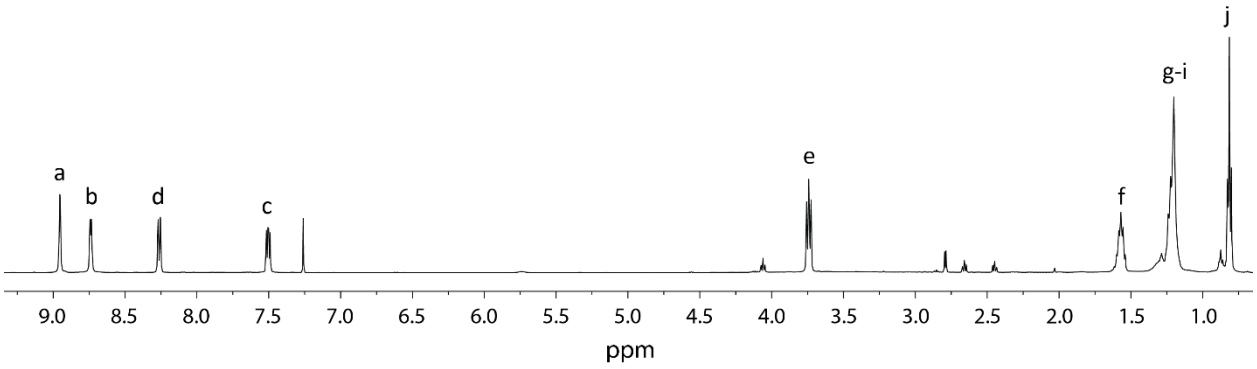

Figure 3.28: ^{1}H NMR spectrum (500 MHz, 298K, $CDCl_3$) of **3P-DPP**.

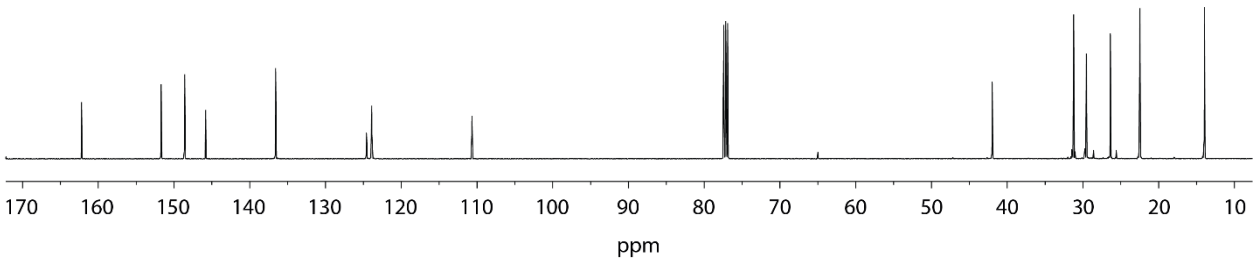

Figure 3.29: ^{13}C NMR spectrum (126 MHz, 298K, $CDCl_3$) of **3P-DPP**.

Ligand 4PM-DPP

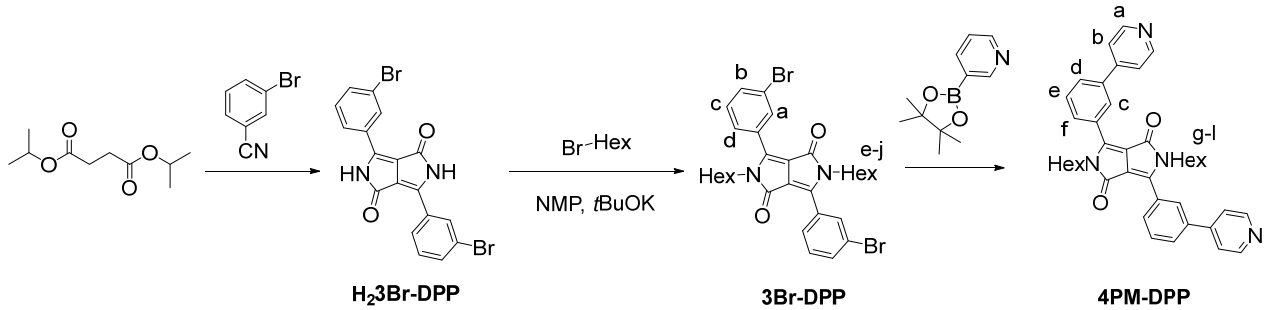

Figure 3.3.30: Synthesis of ligand **4PM-DPP**.

Synthesis of $H_2$3Br-DPP

Under argon atmosphere, sodium (1.0 g, 48 mmol), $FeCl_3$ (0.015 g) and dry *tert*-amyl alcohol (20 mL) were heated to 90 °C until the sodium was dissolved. The mixture was cooled to 50 °C, 4-bromobenzonitrile (3.92 g, 21.5 mmol) was added and then the mixture was heated to 90 °C. Succinic acid diisopropyl ester (1.98 g, 9.79 mmol) was added dropwise for 1 h. After standing for 16 h, a mixture acetic acid : water : methanol 1 : 1 : 1 (10 mL) was added. The mixture was then heated to 120 °C. After

standing for 1 h, the precipitate was filtered and washed with hot water and hot methanol repeatedly and dried. Due to the very poor solubility of the obtained compound it was not possible to obtain characterization information or to further purify it; therefore, it was directly used for the next step.

Synthesis of 3Br-DPP

$H_2$3Br-DPP (3.4 g, 1.0 equiv., 7.62 mmol), potassium *tert*-butoxide (1.88 g, 2.2 equiv., 16.77 mmol) and *N*-methyl-2-pyrrolidone (NMP; 30 mL) were heated to 60 °C. 1-bromohexane (6.42 mL, 6 equiv., 45.73 mmol) was slowly added and the mixture was stirred at 60 °C for 24 h. After cooling to room temperature, toluene (150 mL) was added into the reaction mixture and washed with water to remove NMP. The organic solution was concentrated using a rotary evaporator. Crude product was purified by column chromatography on silica using dichloromethane as solvent to yield **3Br-DPP** as orange-red polycrystalline powder (1.2 g, 1.87 mmol, 25%).

^{1}H NMR (500 MHz, Chloroform-*d*) δ 7.93 (t, J = 1.8 Hz, 1H, Ha), 7.77 (dt, J = 7.8, 1.3 Hz, 1H, Hb), 7.65 (dd, J = 7.3, 1.8 Hz, 1H, Hd), 7.41 (t, J = 7.9 Hz, 1H, Hc), 3.76 – 3.69 (m, 2H, He), 1.61 – 1.55 (m, 2H, Hf), 1.22 (qq, J = 8.9, 5.3, 3.6 Hz, 6H, Hg-i), 0.88 – 0.80 (m, 3H, Hj).

^{13}C NMR (126 MHz, Chloroform-*d*) δ 162.42 (**C**=O), 147.19 (N-C=C), 134.24 (Cd), 131.37 (Ca), 130.62 (Cc), 130.13 (C^q, C-Br), 127.53 (C^q, Ca-**C**-Cd), 123.09 (Cb), 110.34 (N-C=**C**), 42.07(Ce), 31.31 (Cf), 29.55 (Cg), 26.46 (Ch), 22.60 (Ci), 14.08 (Cj).

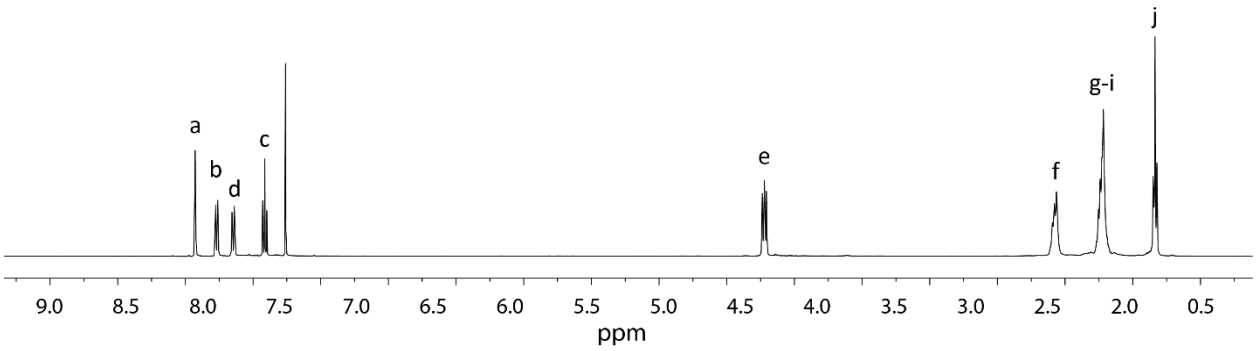

Figure 3.31: ^{1}H NMR spectrum (500 MHz, 298K, $CDCl_3$) of **3Br-DPP**.

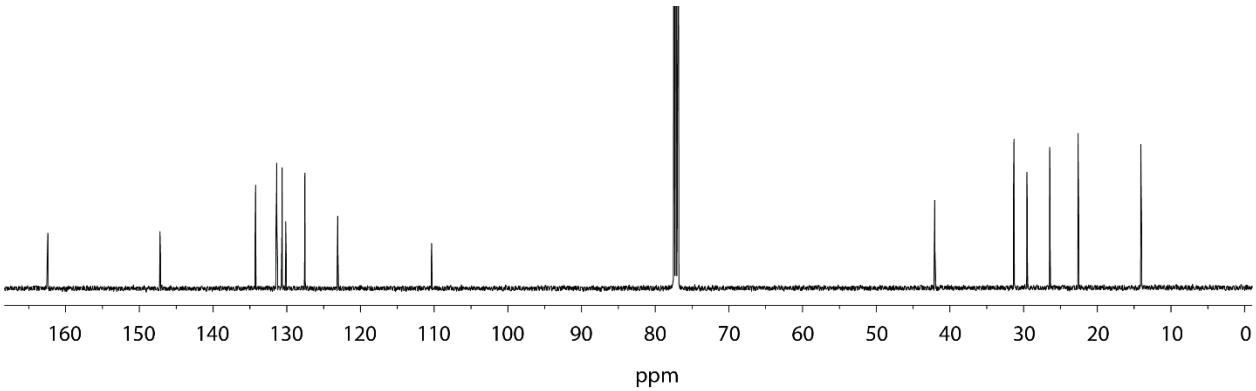

Figure 3.32: ^{13}C NMR spectrum (126 MHz, 298K, $CDCl_3$) of **3Br-DPP**.

Ligand 4PM-DPP

4-Pyridine-boronic acid 1,3-propanediol ester (200 mg, 1 mmol, 3.0 equiv.), **3Br-DPP** (200 mg, 0.325 mmol, 1.0 equiv.), and $K_3PO_4 \cdot H_2O$ (2.25 g, 9.77 mmol, 30 equiv.) were suspended in a mixture of 1,4-dioxan/H_2O (4:1, 10 mL). This mixture was degassed using the *Freeze-Pump-Thaw*-method. $Pd(PPh_3)_4$ (0.06 equiv.) was added and it was stirred for 24 h at 90 °C. After cooling down to room temperature, dichloromethane (100 mL) was added and the organic phase was washed with water (3 x 20 mL), dried over $MgSO_4$ and the solvent was removed under reduced pressure. The crude product

was purified by column chromatography on silica using dichloromethane as solvent to yield **4PM-DPP** as orange-red polycrystalline powder (105 mg, 0.172 mmol, 53%). If necessary, the **4PM-DPP** was further purified by recrystallization from DMSO.

^{1}H NMR (500 MHz, Chloroform-*d*) δ 8.73 (d, J = 5.1 Hz, 2H, Ha), 8.24 (d, J = 1.8 Hz, 1H, Hc), 7.80 (m, 2H, He, Hf), 7.66 (m, 3H, Hb, Hd), 3.98 – 3.70 (m, 2H, Hg), 1.64 (p, J = 7.6 Hz, 2H, Hh), 1.35 – 1.10 (m, 6H, Hi, Hj, Hk), 0.81 (t, J = 6.7 Hz, 3H, Hl).

^{13}C NMR (126 MHz, Chloroform-*d*) δ 162.78 (C=O), 150.35 (Ca), 148.17 (N-**C**=C), 147.77 (C^{q}, Cc-**C**-Cf), 139.12 (C^{q}, C-Cb), 129.87 (Cd), 129.75 (C^{q}, Cc-**C**-Cd), 129.22 and 128.62 (Ce and Cf), 128.24 (Cc), 121.96 (Cb), 110.39 (N-C=**C**), 42.21(Cg), 31.36(Ci), 29.67(Ch), 26.53(Cj), 22.60(Ck), 14.07(Cl).

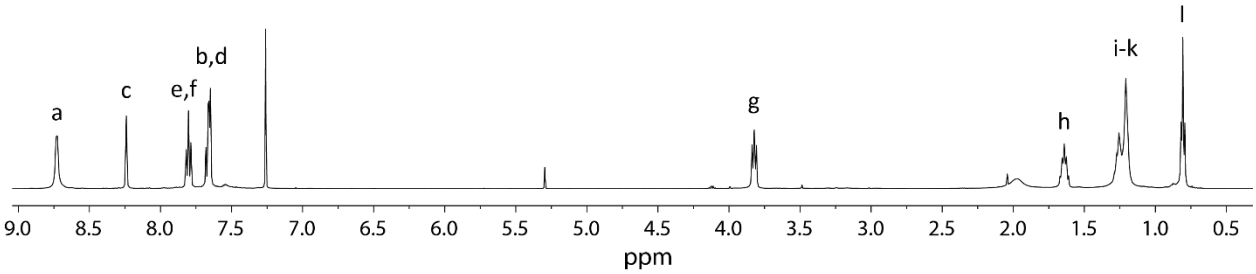

Figure 3.33: ^{1}H NMR stacked spectra (500 MHz, 298K, $CDCl_3$) of **4PM-DPP**.

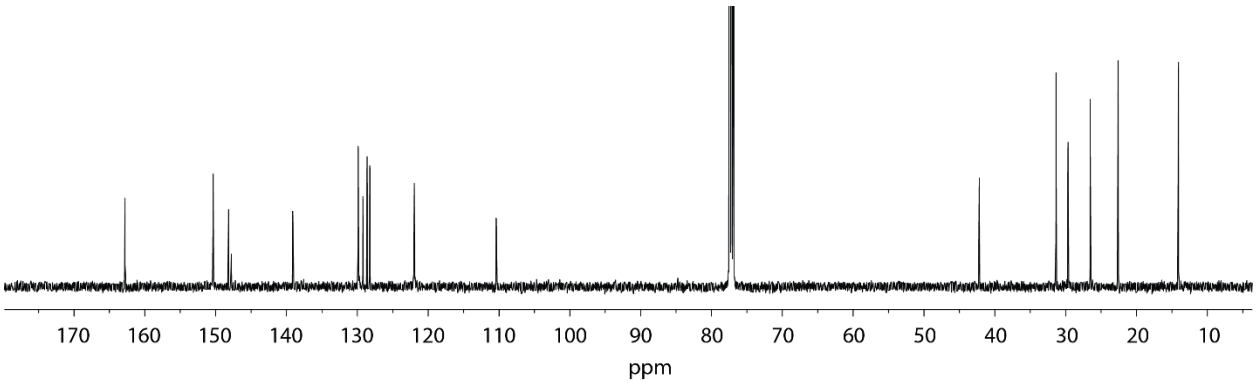

Figure 3.34: ^{13}C NMR spectrum (126 MHz, 298K, $CDCl_3$) of **4PM-DPP**.

Ligand 3PM-DPP

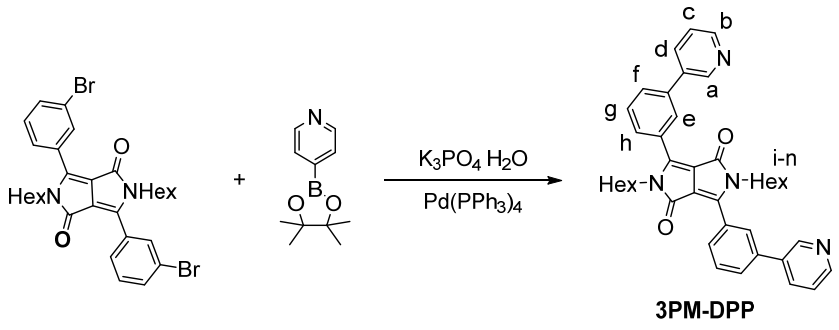

Figure 3.35: Synthesis of ligand **3PM-DPP**.

3-Pyridine-boronic acid 1,3-propanediol ester (200 mg, 1 mmol, 3.0 equiv.), **3Br-DPP** (200 mg, 0.325 mmol, 1.0 equiv.), and $K_3PO_4 \cdot H_2O$ (2.25 g, 9.77 mmol, 30 equiv.) were suspended in a mixture of 1,4-dioxan/H_2O (4:1, 10 mL). This mixture was degassed using the *Freeze-Pump-Thaw*-method. $Pd(PPh_3)_4$ (0.06 equiv.) was added and it was stirred for 24 h at 90 °C. After cooling down to room temperature, dichloromethane (100 mL) was added and the organic phase was washed with water (3 x 20 mL), dried over $MgSO_4$ and the solvent was removed under reduced pressure. The crude product

was purified by column chromatography on silica using dichloromethane as solvent to yield **3PM-DPP** as orange-red polycrystalline powder (90 mg, 0.147 mmol, 45%).

^{1}H NMR (600 MHz, 298 K, Dimethyl sulfoxide-d_6) δ 9.02 (d, J = 2.4 Hz, 1H, Ha), 8.64 (dd, J = 4.7, 1.6 Hz, 1H, Hd), 8.25 (d, J = 1.8 Hz, 1H, He), 8.19 (dt, J = 8.0, 2.0 Hz, 1H, Hb), 7.98 (dt, J = 7.8, 1.3 Hz, 1H, Hf), 7.86 (dt, J = 7.9, 1.3 Hz, 1H, Hh), 7.75 (t, J = 7.8 Hz, 1H, Hg), 7.56 (dd, J = 7.9, 4.7 Hz, 1H, Hc), 3.79 (t, J = 7.5 Hz, 2H, Hi), 1.48 (p, J = 7.3 Hz, 2H, Hj), 1.20 – 1.02 (m, 6H, Hk-m), 0.73 (t, J = 6.8 Hz, 3H, Hn).

^{13}C NMR (151 MHz, 298 K, Dimethyl sulfoxide-d_6) δ 161.62 (**C**=O), 149.04(**C**d), 147.81 (**C**a), 147.75 (N-**C**=C), 137.73 (Cf-**C**-Ce), 134.74 (Cd-**C**-Ca), 134.33 (**C**b), 129.87(**C**g), 129.76(**C**f), 128.50 (Ch-**C**-Ce), 127.76 (**C**h), 127.33 (**C**e), 124.03 (**C**c), 109.06 (N-C=**C**), 40.94 (Ci), 30.47 (Cl), 28.54 (Cj), 25.62 (Ck), 21.83 (Cm), 13.74 (Cn).

^{1}H NMR (500 MHz, 298 K, Chloroform-*d*) δ 8.94 (d, J = 2.3 Hz, 1H), 8.65 (dd, J = 4.9, 1.6 Hz, 1H), 8.14 (t, J = 1.8 Hz, 1H), 8.03 (ddd, J = 7.9, 2.4, 1.6 Hz, 1H), 7.84 – 7.71 (m, 2H), 7.65 (t, J = 7.8 Hz, 1H), 7.43 (ddd, J = 7.9, 4.8, 0.8 Hz, 1H), 3.93 – 3.71 (m, 2H), 1.78 – 1.56 (m, 2H), 1.35 – 1.09 (m, 6H), 0.91 – 0.72 (m, 3H).

^{1}H NMR (600 MHz, 298 K, Acetonitrile-d_3) δ 9.04 – 8.88 (m, 1H), 8.62 (dd, J = 4.8, 1.6 Hz, 1H), 8.21 (t, J = 1.9 Hz, 1H), 8.10 (ddd, J = 7.9, 2.4, 1.6 Hz, 1H), 7.93 – 7.79 (m, 2H), 7.70 (t, J = 7.8 Hz, 1H), 7.48 (ddd, J = 8.0, 4.8, 0.9 Hz, 1H), 3.90 – 3.72 (m, 2H), 1.54 (p, J = 7.4 Hz, 2H), 1.25 – 1.11 (m, 6H), 0.78 (t, J = 6.8 Hz, 3H).

^{13}C NMR (151 MHz, 298 K, Acetonitrile-d_3) δ 163.30, 150.11, 149.20, 149.01, 139.42, 136.37, 135.34, 130.72, 130.68, 130.06, 128.85, 128.81, 124.80, 110.89, 42.33, 31.87, 29.91, 26.93, 23.14, 14.20.

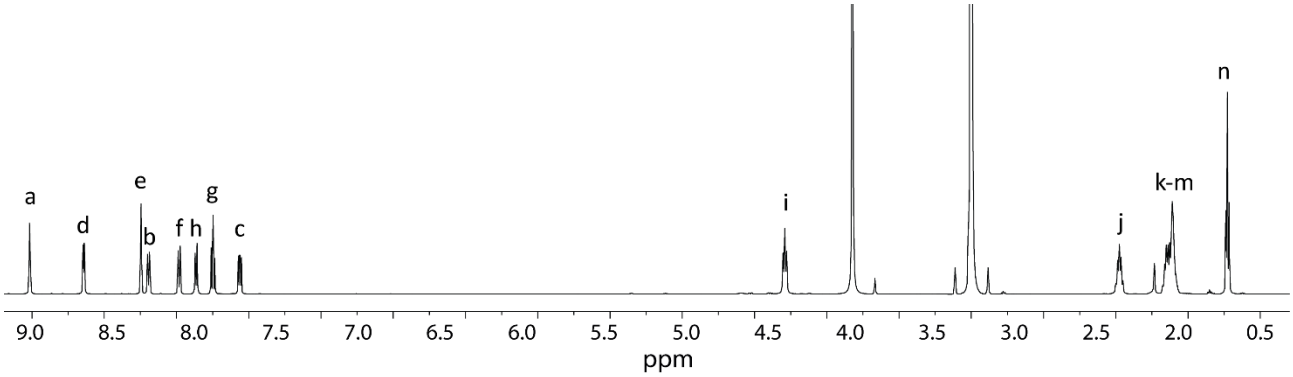

Figure 3.36: ^{1}H NMR spectrum (600 MHz, 298K, DMSO-d_6) of **3PM-DPP**.

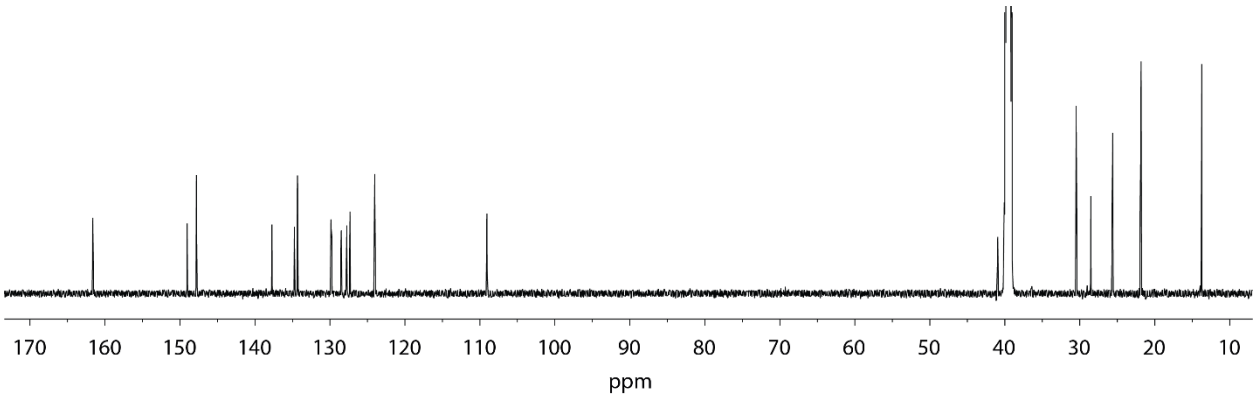

Figure 3.37: ^{13}C NMR spectrum (151 MHz, 298K, DMSO-d_6) of **3PM-DPP**.

Ligand 8QP-DPP (or L^Q)

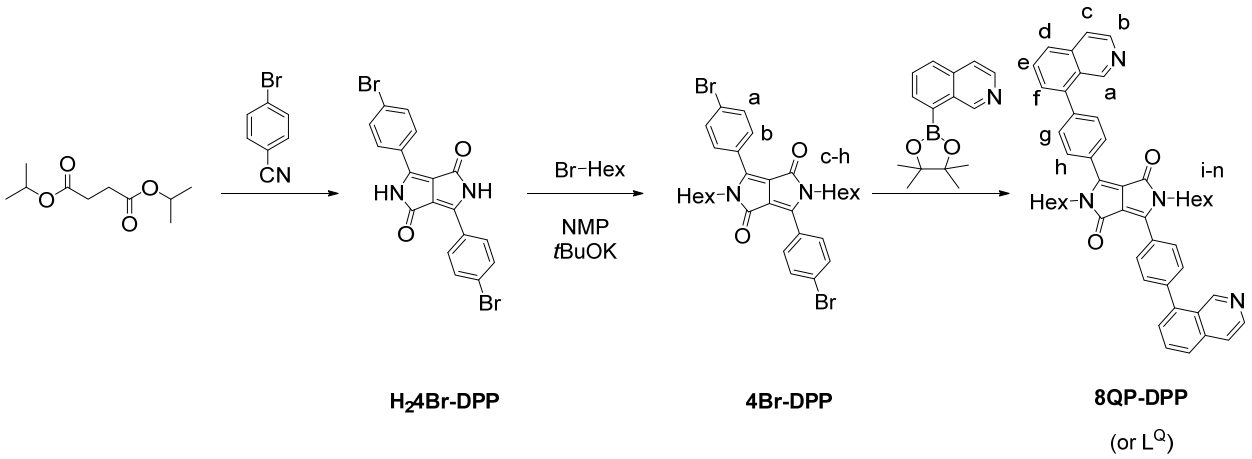

Figure 3.38: Synthesis of ligand **8QP-DPP**.

Synthesis of $H_2$4Br-DPP

Under argon atmosphere, sodium (1.104 g, 48 mmol), $FeCl_3$ (0.015 g) and dry *tert*-amyl alcohol (20 mL) were heated to 90 °C until the sodium was dissolved. The mixture was cooled to 50 °C, 4-bromobenzonitrile (3.92 g, 21,5 mmol) was added and then the mixture was heated to 90 °C. Succinic acid diisopropyl ester (1.98 g, 9.79 mmol) was added dropwise for 1 h. After standing for 16 h, a mixture acetic acid : water : methanol 1 : 1 : 1 (10 mL) was added. The mixture was then heated to 120 °C. After standing for 1 h, the precipitate was filtered and washed with hot water and hot methanol repeatedly and dried. Due to the very poor solubility of the obtained compound it was not possible to obtain characterization information or to further purify it; therefore, it was directly used for the next step.

Synthesis of 4Br-DPP

$H_2$4Br-DPP (1.5 g, 1.0 equiv., 3.36 mmol), potassium *tert*-butoxide (0.830 g, 2.2 equiv., 7.40 mmol) and *N*-methyl-2-pyrrolidone (NMP; 30 mL) were heated to 60 °C. 1- Bromohexane (2.83 mL, 6.0 equiv., 20.2 mmol) was slowly added and the mixture was stirred at 60 °C for 24 h. After cooling to room temperature, toluene (100 mL) was added into the reaction mixture and washed with water to remove NMP. The organic solution was concentrated using a rotary evaporator. Crude product was purified by column chromatography on silica using dichloromethane as solvent to yield **4Br-DPP** orange-red polycrystalline powder (0.400 g, 0.622 mmol, 19%).

^{1}H NMR (500 MHz, Chloroform-*d*) δ 7.73 – 7.58 (m, 4H, Ha, Hb), 3.79 – 3.66 (m, 2H, Hc), 1.67 – 1.48 (m, 2H, Hd), 1.28 – 1.15 (m, 6H, He-g), 0.83 (t, J = 6.8 Hz, 3H, Hh).

^{13}C NMR (126 MHz, Chloroform-*d*) δ 162.56 (C=O), 147.57 (N-**C**=C), 132.38 (Ca), 130.22 (Cb), 127.09 and 125.95 (C^q, C-Br and C^q, C-Cb), 110.07 (N-C=**C**), 42.02(Cc), 31.32(Ce), 29.52(Cd), 26.49(Cf), 22.58(Cg), 14.07(Ch).

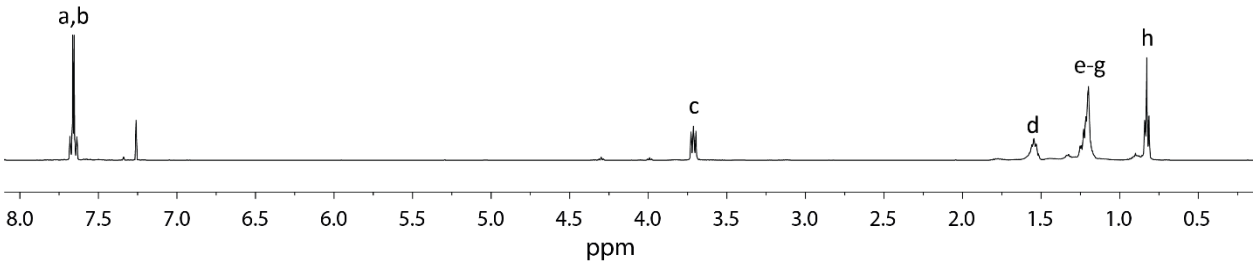

Figure 3.39: ^{1}H NMR spectrum (500 MHz, 298K, $CDCl_3$) of **4Br-DPP**.

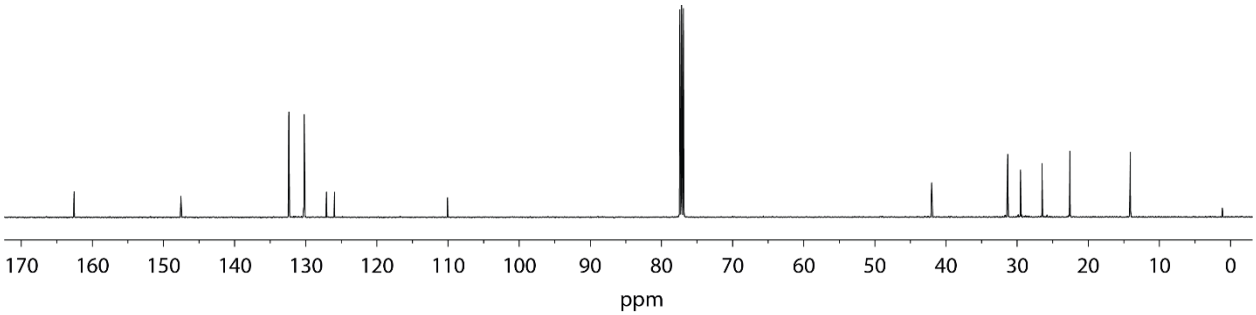

Figure 3.40: ^{13}C NMR spectrum (126 MHz, 298K, $CDCl_3$) of **4Br-DPP**.

Synthesis of 8QP-DPP (or L^Q)

8-Isoquinoline-boronic acid (110 mg, 4.23 mmol, 3.0 equiv.), **4Br-DPP** (130 mg, 0.212 mmol, 1.0 equiv.), and $K_3PO_4 \cdot H_2O$ (1.46 g, 6.35 mmol, 30 equiv.) were suspended in a mixture of 1,4-dioxan/H_2O (4:1, 10 mL). This mixture was degassed using the *Freeze-Pump-Thaw*-method. $Pd(PPh_3)_4$ (25 mg, 0.06 equiv., 0.021 mmol) was added and it was stirred for 24 h at 90 °C. After cooling down to room temperature, dichloromethane (100 mL) was added and the organic phase was washed with water (3 x 20 mL), dried over $MgSO_4$ and the solvent was removed under reduced pressure. The crude product was purified by column chromatography on silica using dichloromethane as solvent to yield **8QP-DPP** as orange-red polycrystalline powder (20 mg, 0.028 mmol, 13%).

^1H NMR (700 MHz, Chloroform-*d*) δ 9.38 (s, 1H, Ha), 8.60 (d, *J* = 5.7 Hz, 1H, Hb), 8.04 (d, *J* = 8.2 Hz, 2H, Hh), 7.89 (d, *J* = 8.3 Hz, 1H, Hd), 7.78 (dd, *J* = 8.1, 7.0 Hz, 1H, He), 7.74 (m, 3H, Hc, Hg), 7.60 (d, *J* = 6.5 Hz, 1H, Hf), 4.00 – 3.80 (m, 2H, Hi), 1.72 (p, *J* = 7.6 Hz, 2H, Hj), 1.42 – 1.19 (m, 6H, Hk, Hl, Hm), 0.85 (t, *J* = 6.9 Hz, 3H, Hn).

^{13}C NMR (176 MHz, Chloroform-*d*) δ 162.82(C=O), 150.83 (Ca), 148.08 (C-**C**=N), 143.23 (Cb), 141.64 (C^q, C-Ch), 139.87(C^q, C-Cg), 136.29 (C^q, Cc-**C**-Cd), 130.64 (Cg), 129.92 (Ce), 128.92 (Ch), 128.37 (Cf), 127.84 (C^q, C-Cf), 126.73 (Cd), 126.39 (C^q, C-Ca), 120.64 (Cc), 110.21(**C**-C=N), 42.22 (Ci), 31.26(Cl), 29.57(Cj), 26.46(Ck), 22.49(Cm), 13.98(Cn).

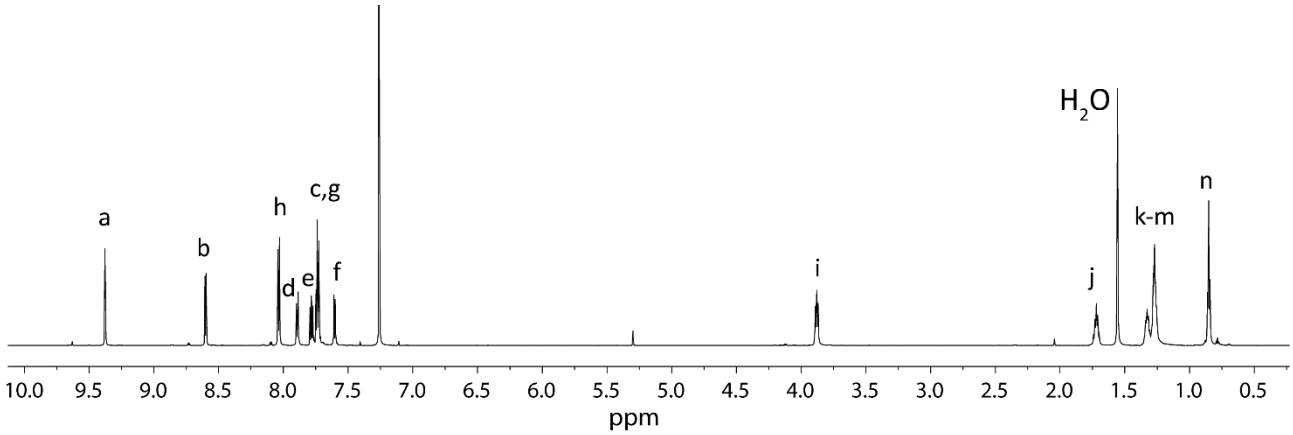

Figure 3.41: ^1H NMR spectrum (700 MHz, 298K, $CDCl_3$) of **8QP-DPP**.

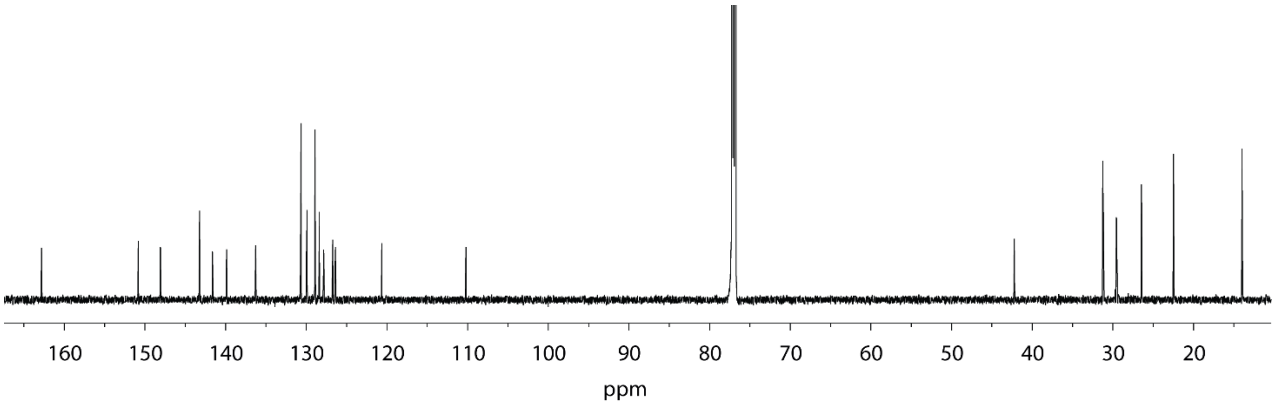

Figure 3.42: ^{13}C NMR spectrum (176 MHz, 298K, $CDCl_3$) of **8QP-DPP**.

3.6.3 Synthesis of the assemblies

All the assemblies were synthetized accordingly to the same general procedure. To 450 µL of a 3.11 mM solution of the ligands in the specified solvent, 50 µL of a 15 mM solution of $[Pd(CH_3CN)_4](BF_4)_2$ in the same solvent (unless otherwise stated) are added. The mixture was than heated to 70 °C for 30 min.

$[Pd_x(3P\text{-}DPP)_{2x}]$

A mixture of ligand **3PM-DPP** (450 µL of a 3.11 mM solution) and $[Pd(CH_3CN)_4](BF_4)_2$ (50 µL of a 15 mM solution in the same solvent) was heated at 70 °C for 30 min. The assembly process was attempted both in DMSO-d_6 and in CD_3CN. Due to the origination of difficult spectra originated it was not possible to assign and further characterize the product. In the discussion part of this chapter more information about the techniques tried are provided.

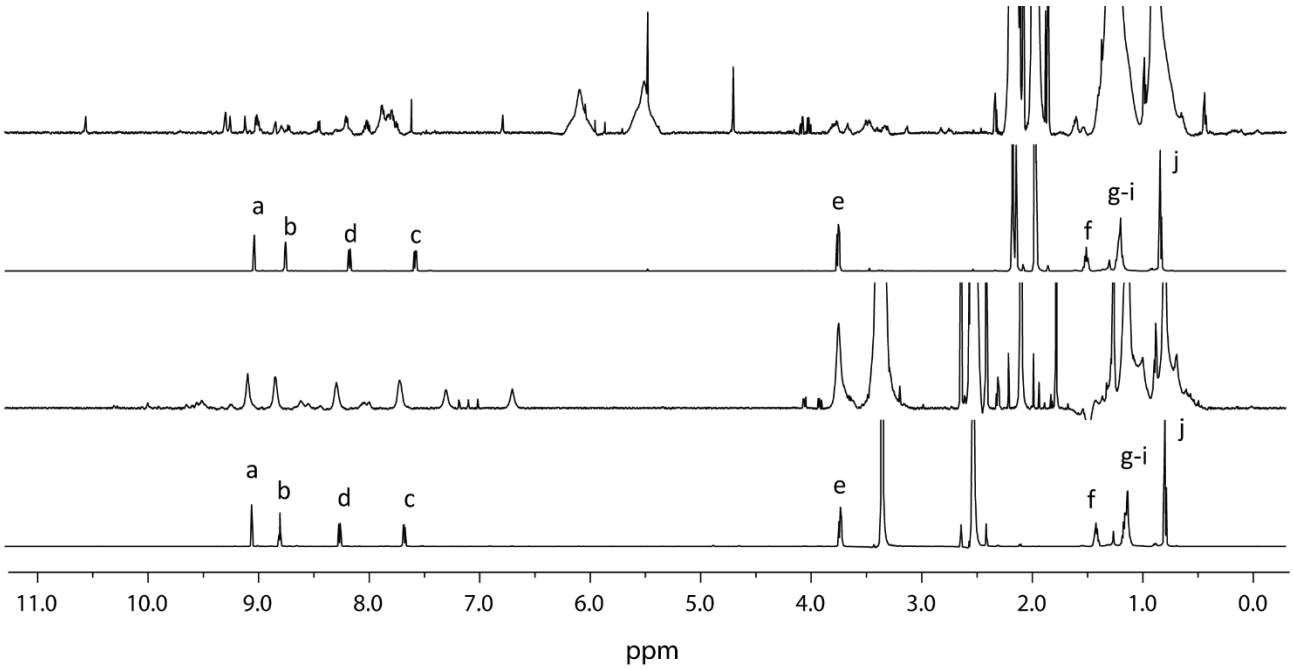

Figure 3.43: Stacked ^1H NMR spectra (500 MHz, 298K) of the ligand **3P-DPP** and upon 0.5 equiv. Pd(II) addition in DMSO-d_6 (first two spectra from the bottom) and CD_3CN (last two).

[Pd$_3$(4PM-DPP)$_6$](BF$_4$)$_6$ (+ [Pd$_4$(4PM-DPP)$_8$](BF$_4$)$_8$)

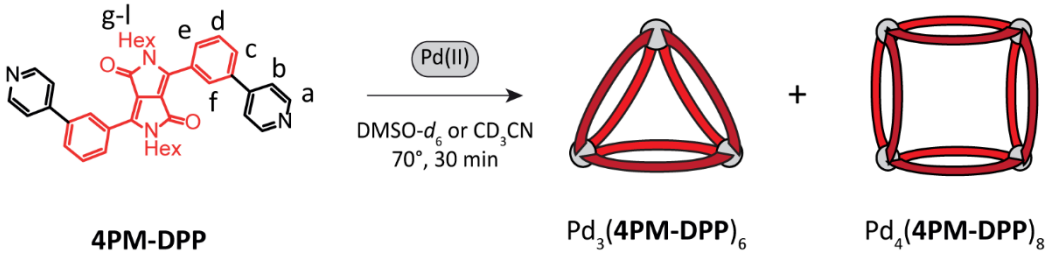

4PM-DPP Pd$_3$(**4PM-DPP**)$_6$ Pd$_4$(**4PM-DPP**)$_8$

Figure 3.44: Formation of the [Pd$_3$(**4PM-DPP**)$_6$] + [Pd$_4$(**4PM-DPP**)$_8$] rings upon addition of 0.5 equiv. Pd(II) cations to ligand **4PM-DPP**.

A mixture of ligand **4PM-DPP** (450 µL of a 3.11 mM solution in DMSO-d_6) and [Pd(CH$_3$CN)$_4$](BF$_4$)$_2$ (50 µL of a 15 mM solution in DMSO-d_6) was heated at 70 °C for 30 min to afford the solution mixture of [Pd$_3$(**4PM-DPP**)$_6$] and [Pd$_4$(**4PM-DPP**)$_8$] rings.

^{1}H NMR (500 MHz, Dimethyl sulfoxide-d_6) δ 9.60 – 9.40 (m), 8.35 – 8.09 (m), 8.06-8.01 (m), 7.99 – 7.86 (m), 7.85-7.75 (m), 4.03 – 3.49 (m), 1.21 (m), 1.10 – 0.67 (m), 0.83 – 0.28 (m).

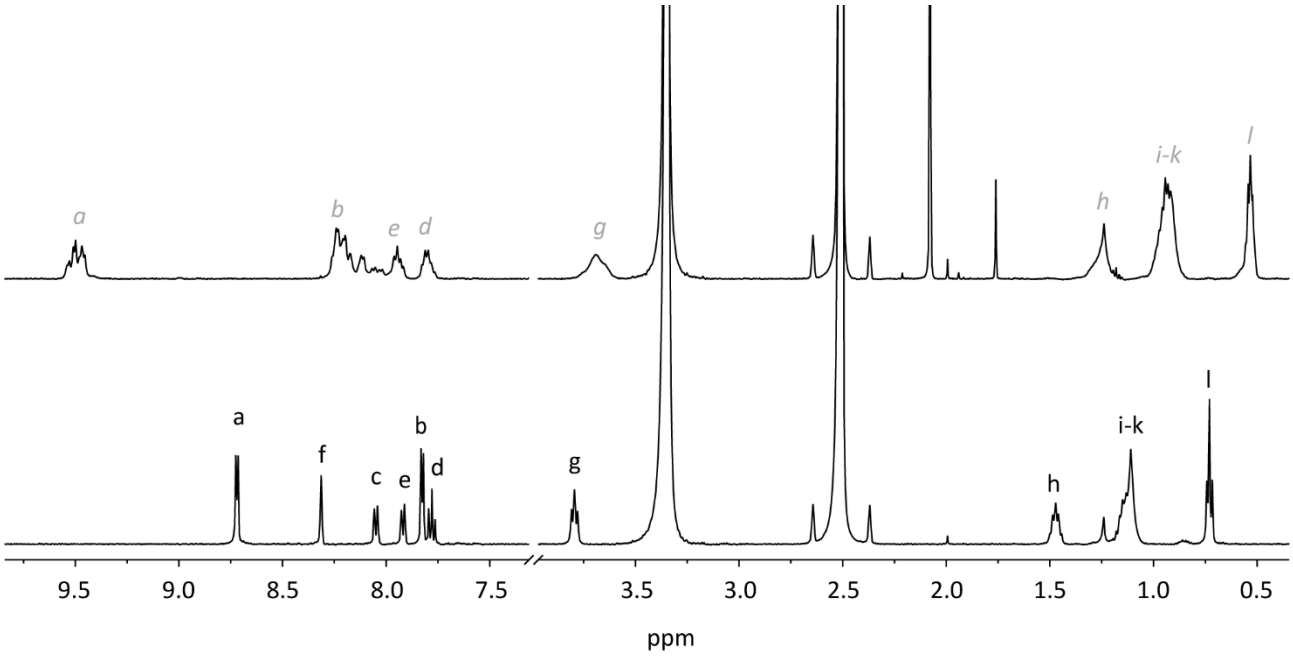

Figure 3.45: Stacked ^{1}H NMR spectra (500 MHz, 298K, DMSO-d_6) of the ligand **4PM-DPP** and upon addition of 0.5 equiv. Pd(II) to yield the mixture of [Pd$_3$(**4PM-DPP**)$_6$] and [Pd$_4$(**4PM-DPP**)$_8$].

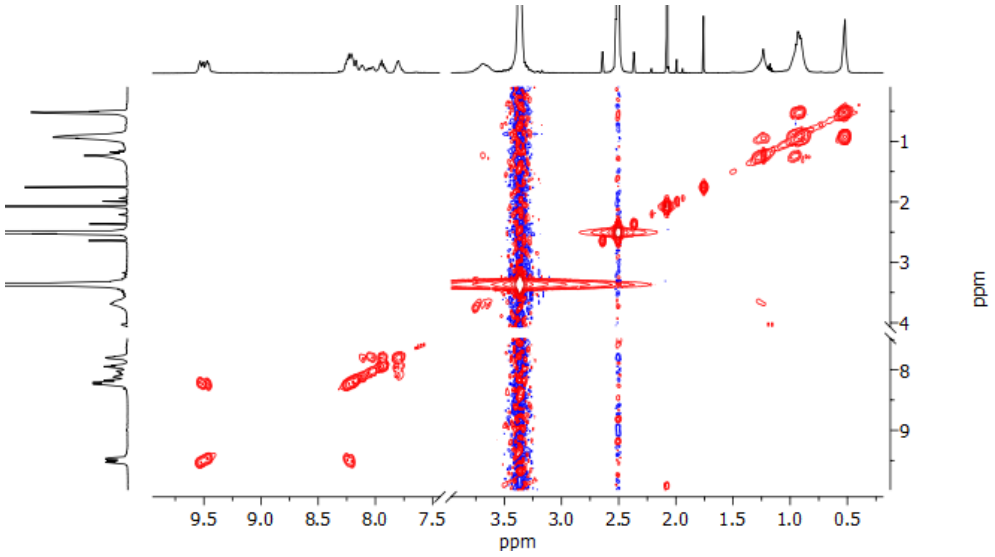

Figure 3.46: ^{1}H-^{1}H COSY NMR spectrum (500 MHz, 298K, DMSO-d_6) of the mixture of [Pd_3(**4PM-DPP**)$_6$] and [Pd_4(**4PM-DPP**)$_8$].

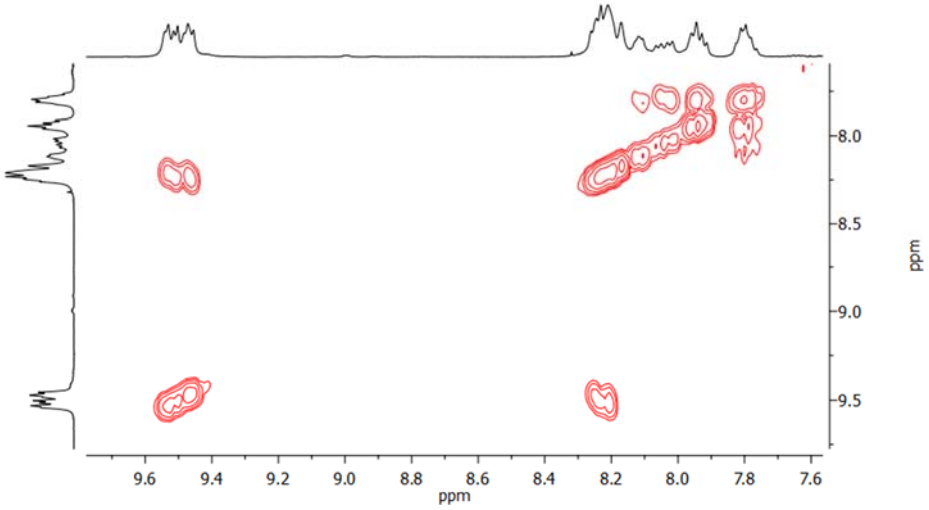

Figure 3.47: Enlargement of the aromatic area of ^{1}H-^{1}H COSY NMR spectrum (500 MHz, 298K, DMSO-d_6) of the mixture of [Pd_3(**4PM-DPP**)$_6$] and [Pd_4(**4PM-DPP**)$_8$].

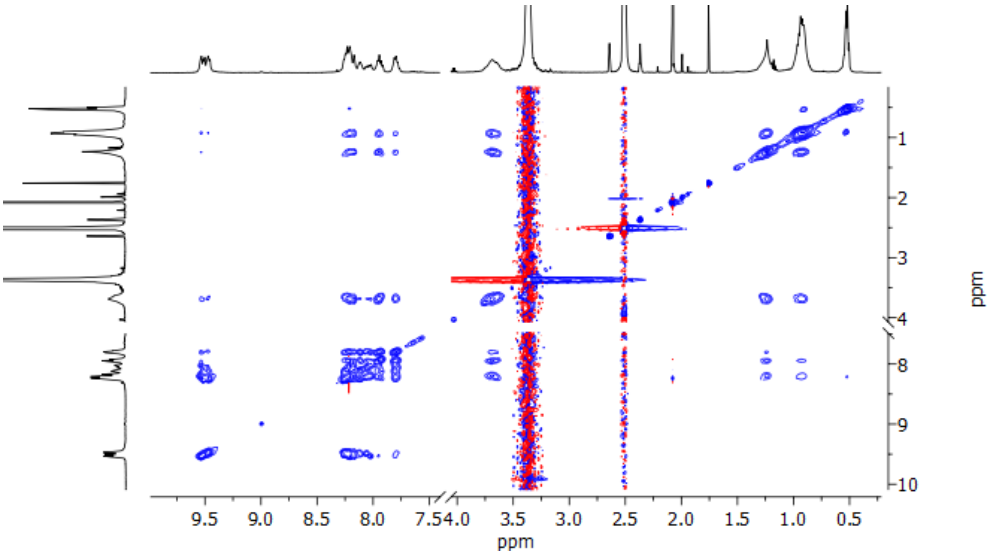

Figure 3.48: ^{1}H-^{1}H NOESY NMR spectrum (500 MHz, 298K, DMSO-d_6) of the mixture of [Pd_3(**4PM-DPP**)$_6$] and [Pd_4(**4PM-DPP**)$_8$].

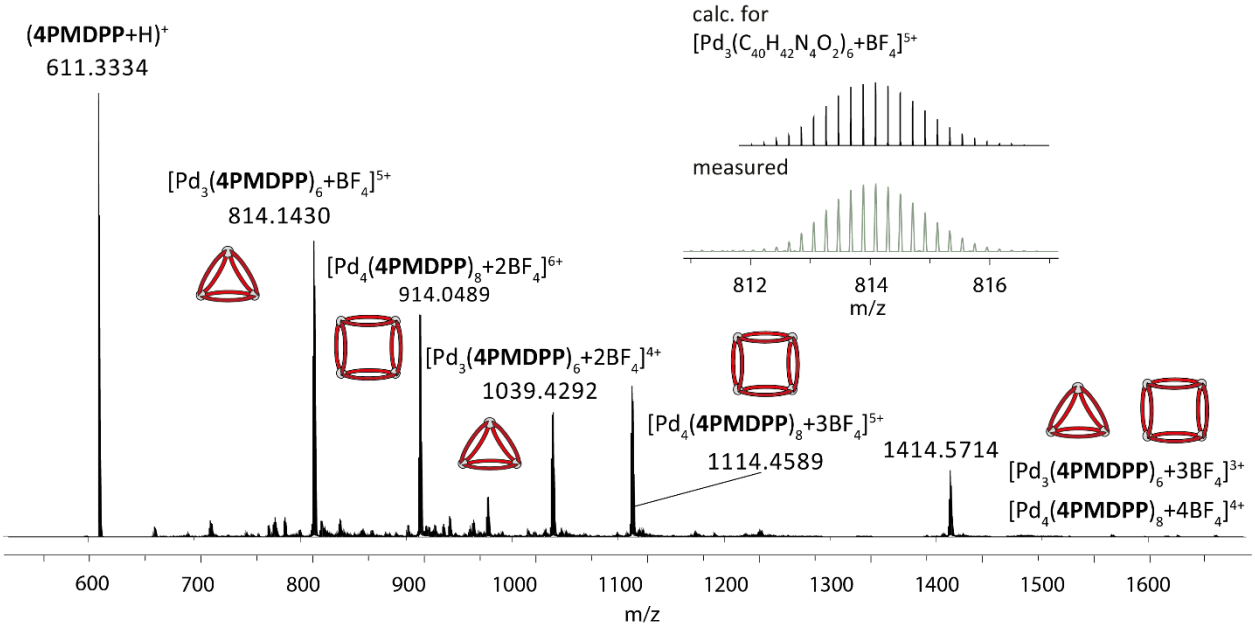

Figure 3.49: ESI-MS spectrum of [Pd_3(**4PM-DPP**)$_6$+nBF_4]$^{(6-n)+}$ with n=1-3 and [Pd_4(**4PM-DPP**)$_8$+nBF_4]$^{(8-n)+}$ with n=2-4. The observed and calculated isotopic patterns of [Pd_3(**4PM-DPP**)$_6$+BF_4]$^{5+}$ is shown in the inset.

Fig 8 **- [Pd_2(3PM-DPP)$_4$](BF_4)$_4$**

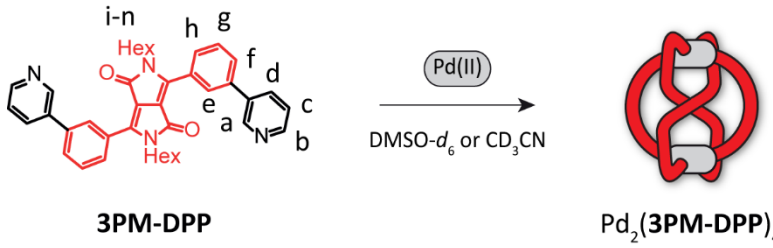

Figure 3.50: Formation of the cage *Fig8*-[Pd_2(**3PM-DPP**)$_4$] upon addition of 0.5 equiv. Pd(II) cations to ligand **3PM-DPP**.

A mixture of ligand **3PM-DPP** (450 µL of a 3.11 mM solution) and $[Pd(CH_3CN)_4](BF_4)_2$ (50 µL of a 15 mM solution in the same solvent) was heated at 70 °C for 30 min to afford a 0.7 mM solution of cage *Fig8*-$[Pd_2($**3PM-DPP**$)_4]$. The assembly was successfully tested in DMSO-d_6, CD_3CN, acetone-d_6, THF-d_8, MeNO2-d_3, DMF-d_7.

^{1}H NMR (600 MHz, Dimethyl sulfoxide-d_6) δ 10.64 (d, J = 2.0 Hz, 1H, Ha), 10.53 – 10.29 (m, 1H, Hb‘), 9.98 (s, 1H, He), 9.55 (d, J = 1.9 Hz, 1H, Ha‘), 8.96 (d, J = 5.5 Hz, 1H, Hb), 8.87 (d, J = 8.0 Hz, 1H, Hd), 8.68 (d, J = 8.1 Hz, 1H, Hd‘), 8.48 – 8.26 (m, 1H, Hf), 8.20 (dd, J = 8.1, 6.0 Hz, 1H, Hc‘), 7.97 (dd, J = 8.0, 5.5 Hz, 1H, Hc), 7.89 (d, J = 7.8 Hz, 1H, Hf‘), 7.85 – 7.72 (m, 2H, Hg, Hh‘), 7.65 (t, J = 7.7 Hz, 1H, Hg‘), 7.36 (s, 1H, He‘), 7.22 (d, J = 8.0 Hz, 1H, Hh), 2.90 (q, J = 11.0, 9.4 Hz, 1H), 2.78 – 2.58 (m, 1H), 2.42 – 2.23 (m, 2H), 0.84 (d, J = 16.8 Hz, 1H), 0.77 – 0.55 (m, 6H), 0.55 – 0.42 (m, 4H), 0.36 (q, J = 7.4, 5.8 Hz, 5H), 0.28 – 0.16 (m, 1H), 0.14 (t, J = 7.3 Hz, 3H), 0.10 – -0.15 (m, 2H).

^{1}H NMR (600 MHz, Acetonitrile-d_3) δ 10.66 (d, J = 2.1 Hz, 1H, Ha), 10.01 (d, J = 1.9 Hz, 1H, He), 9.98 (dd, J = 6.0, 1.3 Hz, 1H, Hb’), 9.61 (d, J = 2.0 Hz, 1H, Ha’), 8.73 (dd, J = 5.6, 1.2 Hz, 1H, Hb), 8.53 (dt, J = 8.1, 1.5 Hz, 1H, Hd), 8.38 (dt, J = 8.2, 1.6 Hz, 1H, Hd’), 8.03 (dd, J = 7.7, 1.9 Hz, 1H, Hf), 7.96 (dd, J = 8.1, 6.0 Hz, 1H, Hc’), 7.83 – 7.70 (m, 3H, Hf’, Hc, Hh’), 7.67 (t, J = 7.8 Hz, 1H, Hg), 7.58 (t, J = 7.7 Hz, 1H, Hg’), 7.40-7.36 (m, He’), 7.34 – 7.24 (m, 1H, Hh), 2.91 (ddd, J = 14.8, 12.6, 5.5 Hz, 1H), 2.66 (ddd, J = 14.4, 8.2, 6.0 Hz, 1H), 2.57 (ddd, J = 15.0, 8.5, 7.0 Hz, 1H), 2.39 (ddd, J = 14.8, 12.6, 4.3 Hz, 1H), 0.86 (qd, J = 8.4, 7.1, 4.2 Hz, 2H), 0.74 (dd, J = 10.9, 4.0 Hz, 2H), 0.70 – 0.57 (m, 6H), 0.53 (t, J = 7.4 Hz, 3H), 0.41 (dq, J = 13.0, 8.8, 7.7 Hz, 3H), 0.29 (q, J = 7.4, 6.7 Hz, 4H), 0.21 – -0.01 (m, 2H).

^{13}C NMR (151 MHz, Dimethyl sulfoxide-d_6) δ 171.42, 162.41 (**C**=O), 159.89(**C**=O), 151.67 (Cb), 150.69 (Cb’), 146.88 (Ca), 146.02 (Ca’), 139.49, 139.18 (Cd’), 138.21 (Cd), 137.12, 133.88, 133.33, 131.44, 130.81, 130.15, 129.03, 128.84, 127.96, 127.76, 127.67, 127.54, 125.20 (Ce’), 118.09, 109.87 (N-C=**C**), 108.31(N-C=**C**), 43.45, 29.99, 29.36, 27.23, 26.36, 25.33, 24.95, 21.62, 21.42, 13.54 (-CH3), 13.32(-CH3). Partial assignment form ^{1}H-^{13}C HSQC spectral analysis.

^{13}C NMR (151 MHz, Acetonitrile-d_3) δ 163.97, 161.49, 151.76, 151.45, 148.94, 148.40, 147.36, 141.31, 140.41, 139.15, 139.04, 135.29, 134.66, 132.75, 131.61, 131.55, 131.00, 130.38, 129.90, 129.62, 129.38, 129.20, 128.74, 127.15, 111.51, 110.12, 44.96, 40.23, 31.40, 31.04, 28.71, 27.99, 26.66, 26.23, 23.01, 22.82, 14.10, 13.97 (2 C overlapping).

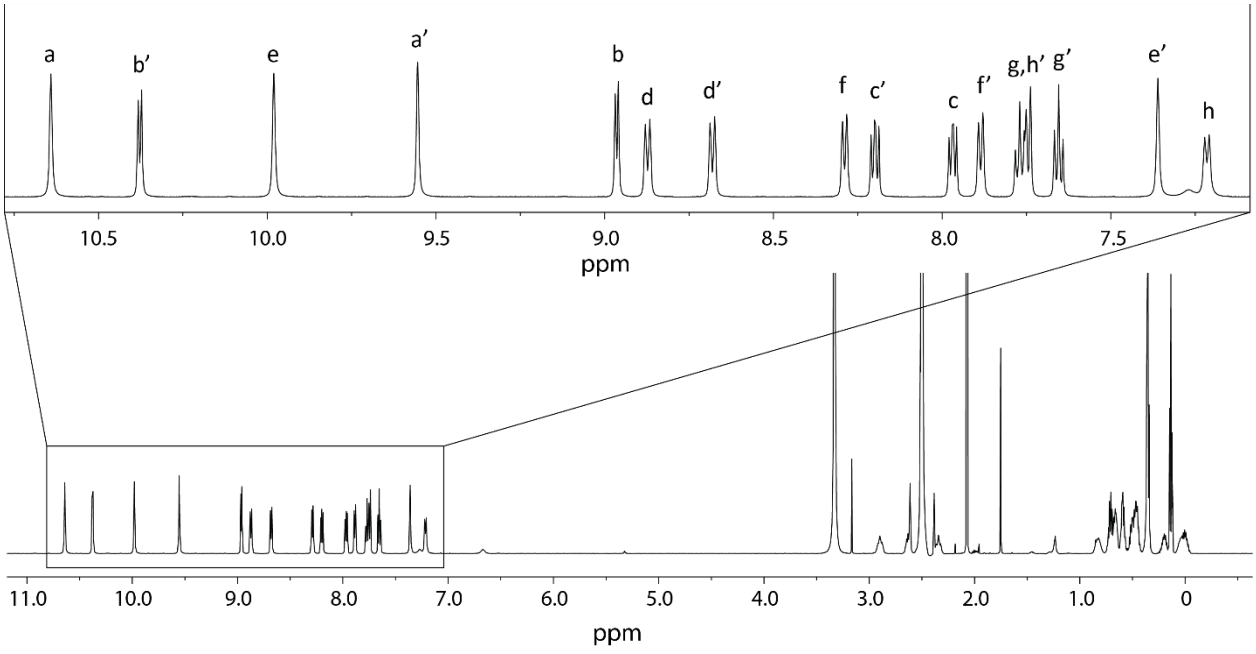

Figure 3.51: ^{1}H NMR spectrum (600 MHz, 298K, DMSO-d_6) of the cage $[Pd_2($**3PM-DPP**$)_4](BF_4)_2$.

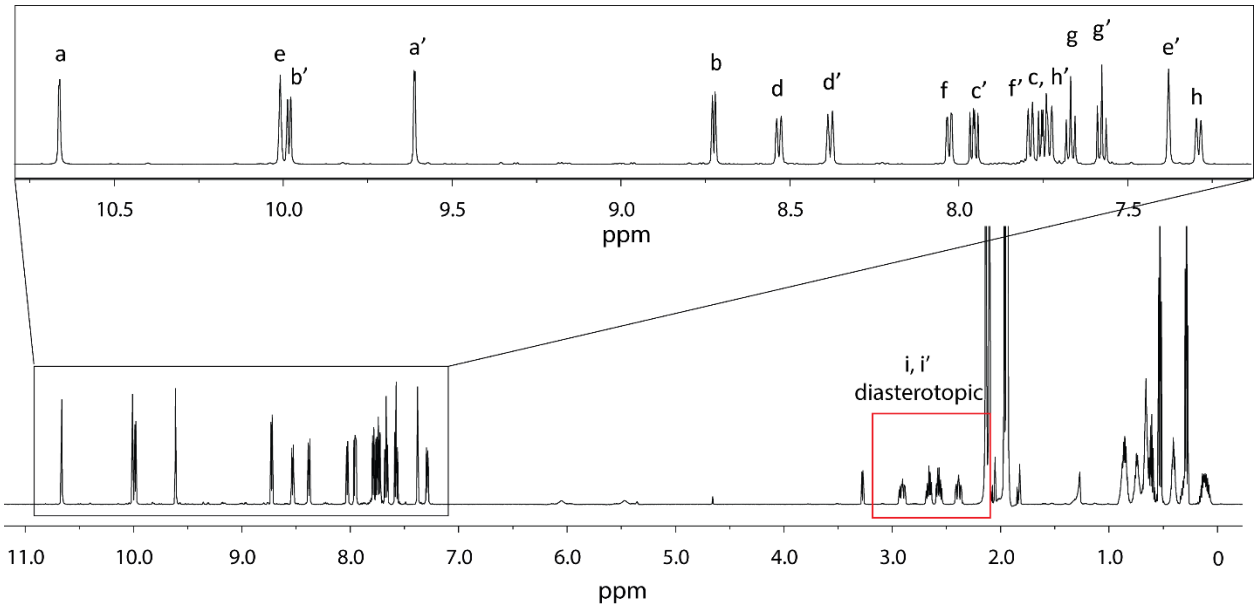

Figure 3.52: ^{1}H NMR spectrum (600 MHz, 298K, CD_3CN) of the cage $[Pd_2(\mathbf{3PM\text{-}DPP})_4](BF_4)_2$.

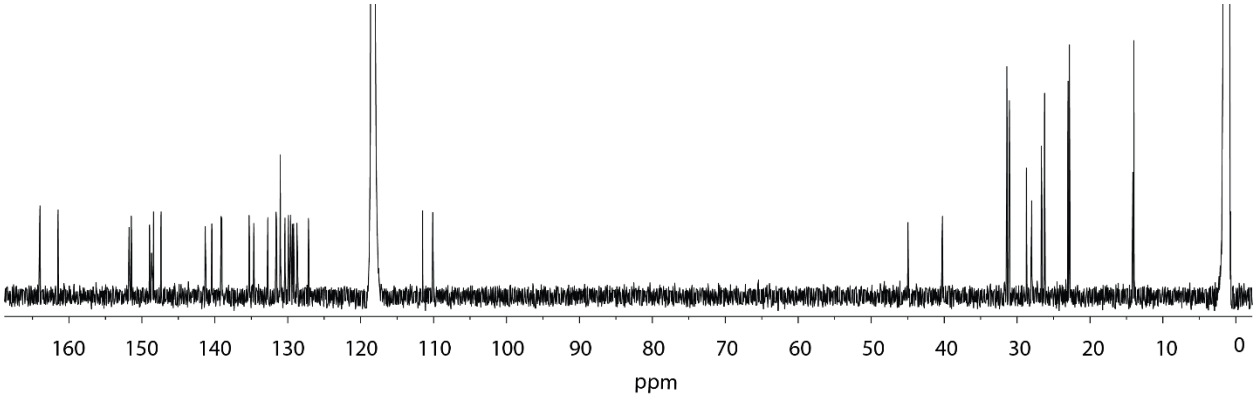

Figure 3.53: ^{13}C NMR spectrum (151 MHz, 298K, CD_3CN) of the cage $[Pd_2(\mathbf{3PM\text{-}DPP})_4](BF_4)_2$.

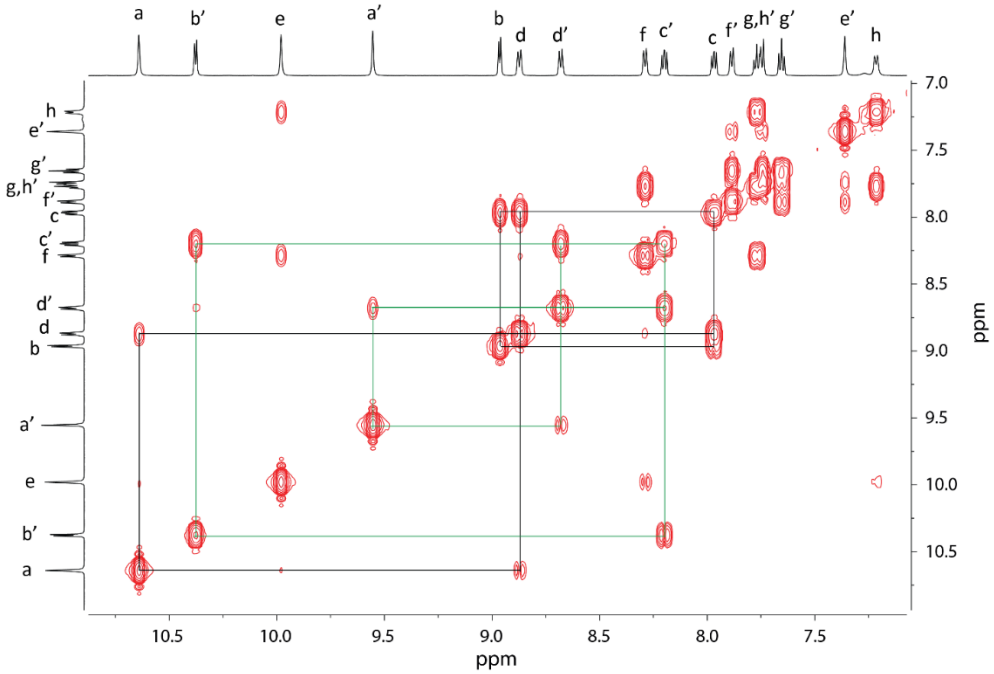

Figure 3.54: Enlargement of the aromatic area of ^{1}H-^{1}H COSY NMR spectrum (600 MHz, 298K, DMSO-d_6) of the cage $[Pd_2(\mathbf{3PM\text{-}DPP})_4](BF_4)_2$.

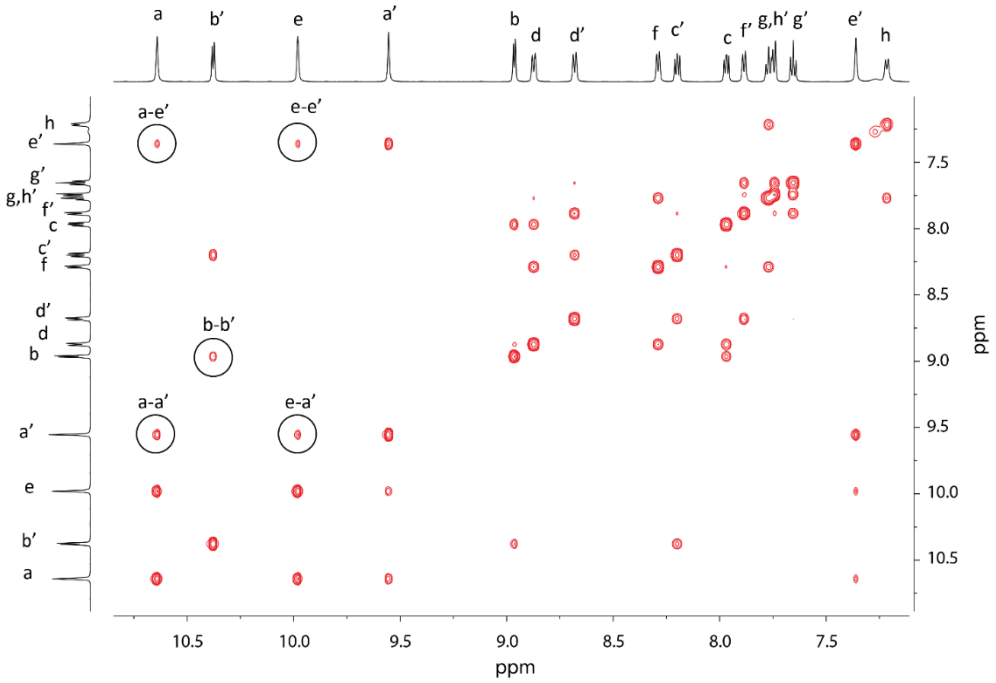

Figure 3.55: Enlargement of the aromatic area of ^{1}H-^{1}H NOESY NMR spectrum (600 MHz, 298K, DMSO-d_6) of the cage $[Pd_2(\mathbf{3PM\text{-}DPP})_4](BF_4)_2$.

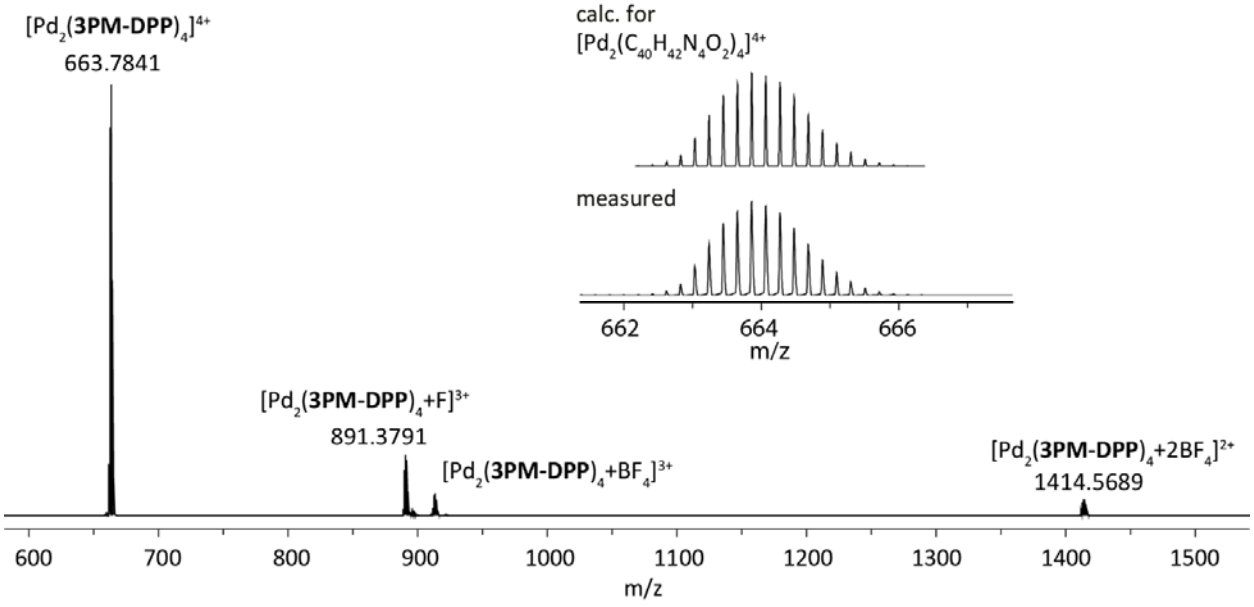

Figure 3.56: ESI-MS spectrum of $[Pd_2(\mathbf{3PM\text{-}DPP})_4{+}nBF_4]^{(4-n)+}$ with n=0-2. The observed and calculated isotopic patterns of $[Pd_2(\mathbf{3PM\text{-}DPP})_4]^{4+}$ are shown in the inset.

Host-guest chemistry

The host-guest chemistry experiments followed the same general procedure. To a 3.11 mM solution of ligand **3PM-DPP** in DMSO-d_6 21 µL of the guest (A-H and J-O) were added in form of a 15 mM DMSO solution. Successively 50 µL of a 15 mM solution of $[Pd(CH_3CN)_4](BF_4)_2$ were added and after 30 min ^{1}H NMR spectra were recorded. Guest I was added as a solid to the pre-formed *Fig8*-$[Pd_2(\mathbf{3PM\text{-}DPP})_4]$ cage and the heterogeneous solution was stirred for 1 day before recording the ^{1}H NMR spectrum. In Table 3.3 a summary of the results is reported.

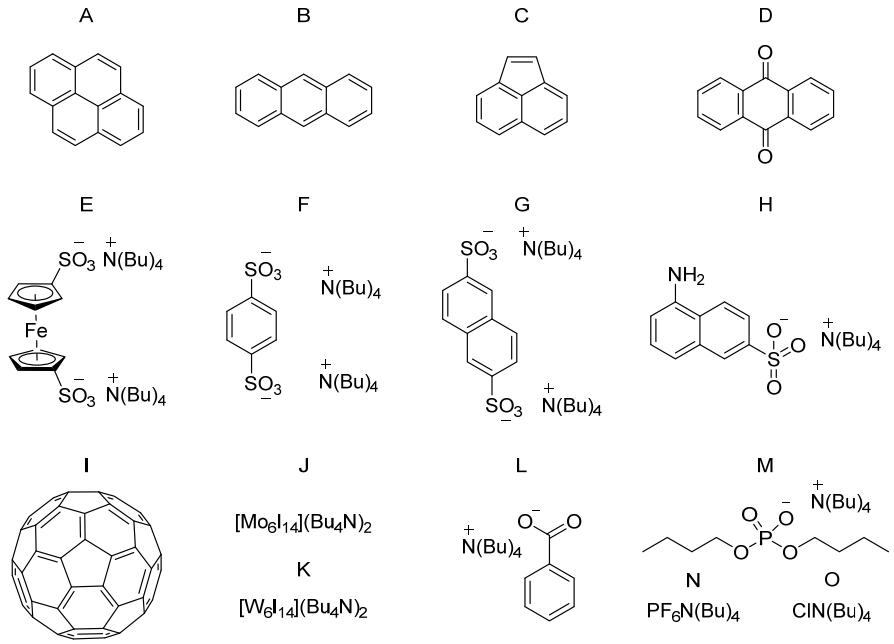

Figure 3.57: List of guests used for the (unsuccessful) transformation of *Fig8*-[Pd_2L_4] to the 'canonical' [Pd_2L_4].

Table 3.3: Summary of the attempted host-guest chemistry results. The letters correspond to the guests in Figure 3.49 and the experiments followed the general procedure.

A	No effect
B	No effect
C	No effect
D	No effect
E	No effect
F	Described in the chapter
G	No effect
H	No effect

I	No effect
J	precipitation
K	precipitation
L	Cage decomposition to free ligand
M	No effect
N	No effect
O	Cage decomposition to free ligand

[Pd_2(8QP-DPP)$_3$(CH_3CN)$_2$](BF_4)$_4$

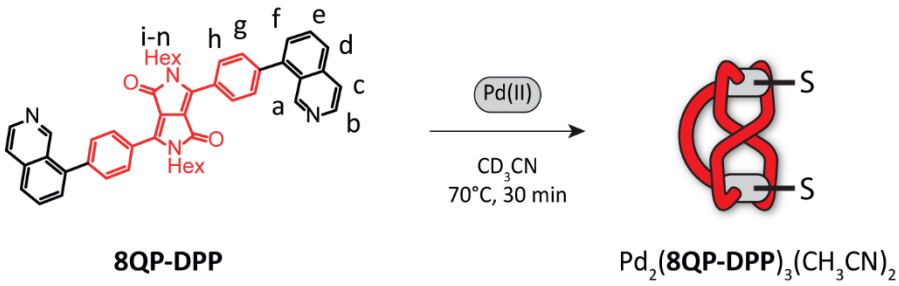

8QP-DPP Pd_2(**8QP-DPP**)$_3$(CH_3CN)$_2$

Figure 3.58: Formation of the assembly [Pd_2(**8QP-DPP**)$_3$(CH_3CN)$_2$] and depiction of possible topology. The S in the figure stands for a solvent molecule.

A mixture of ligand **8QP-DPP** (450 µL of a 3.11 mM solution in CD_3CN) and [$Pd(CH_3CN)_4$](BF_4)$_2$ (75 µL of a 15 mM solution in CD_3CN) was heated at 70 °C for 30 min to afford a 0.89 mM solution of cage *Fig8*-[Pd_2(**3PM-DPP**)$_4$]. The assembly was successful also in DMSO-d_6.

^{1}H NMR (600 MHz, Acetonitrile-d_3) δ 9.91 (s, 1H, Ha), 9.58 – 9.55 (m, 1H, Ha'), 9.38 – 9.32 (m, 2H, Ha'', Hb), 9.13 (d, *J* = 6.7 Hz, 1H, Hb'), 8.76 (d, *J* = 6.7 Hz, 1H, Hb''), 8.38 – 8.33 (m, 3H, Hc), 8.26 – 8.21 (m, 1H), 8.15 – 8.01 (m, 4H, Hc'), 8.03 – 7.91 (m, 5H, Hc''), 7.79 – 7.69 (m, 7H), 7.53 – 7.48 (m, 2H), 7.42 (s,

2H), 5.51 (s, 0H), 4.01 – 3.95 (m, 1H), 3.83 – 3.72 (m, 1H), 3.72 – 3.65 (m, 0H), 3.60 (ddd, *J* = 14.7, 9.6, 4.9 Hz, 0H), 3.48 (t, *J* = 4.2 Hz, 1H), 2.84 – 2.62 (m, 2H), 2.18 (s, 118H), 2.15 (s, 6H), 1.76 – 1.70 (m, 1H), 1.53 (t, *J* = 7.2 Hz, 1H), 1.45 (s, 10H), 1.40 (d, *J* = 6.8 Hz, 1H), 1.34 (dt, *J* = 7.2, 2.9 Hz, 3H), 1.21 – 1.15 (m, 2H), 1.14 – 1.06 (m, 2H), 0.99 – 0.92 (m, 7H), 0.91 – 0.85 (m, 4H), 0.82 – 0.76 (m, 1H), 0.69 (t, *J* = 7.3 Hz, 3H). Partial assignment form ^{1}H-^{1}H COSY spectral analysis.

^{13}C NMR (151 MHz, Acetonitrile-d_3) δ 162.94, 162.83, 162.81, 154.53, 154.40, 153.95, 149.08, 148.77, 148.39, 147.85, 143.76, 142.46, 142.24, 141.21, 141.18, 140.72, 140.52, 140.31, 139.95, 137.80, 137.61, 137.42, 134.53, 134.45, 132.56, 132.14, 131.72, 131.48, 131.25, 131.08, 130.99, 130.78, 130.37, 130.24, 128.97, 128.83, 128.67, 127.91, 127.67, 127.47, 126.00, 125.39, 111.17, 110.89, 109.89, 43.79, 43.42, 43.31, 31.85, 31.79, 31.58, 31.31, 30.97, 30.86, 29.90, 29.20, 28.97, 27.14, 27.03, 26.73, 26.53, 22.99, 22.93, 22.85, 22.70, 22.64, 14.01, 13.87, 13.78, 13.73.

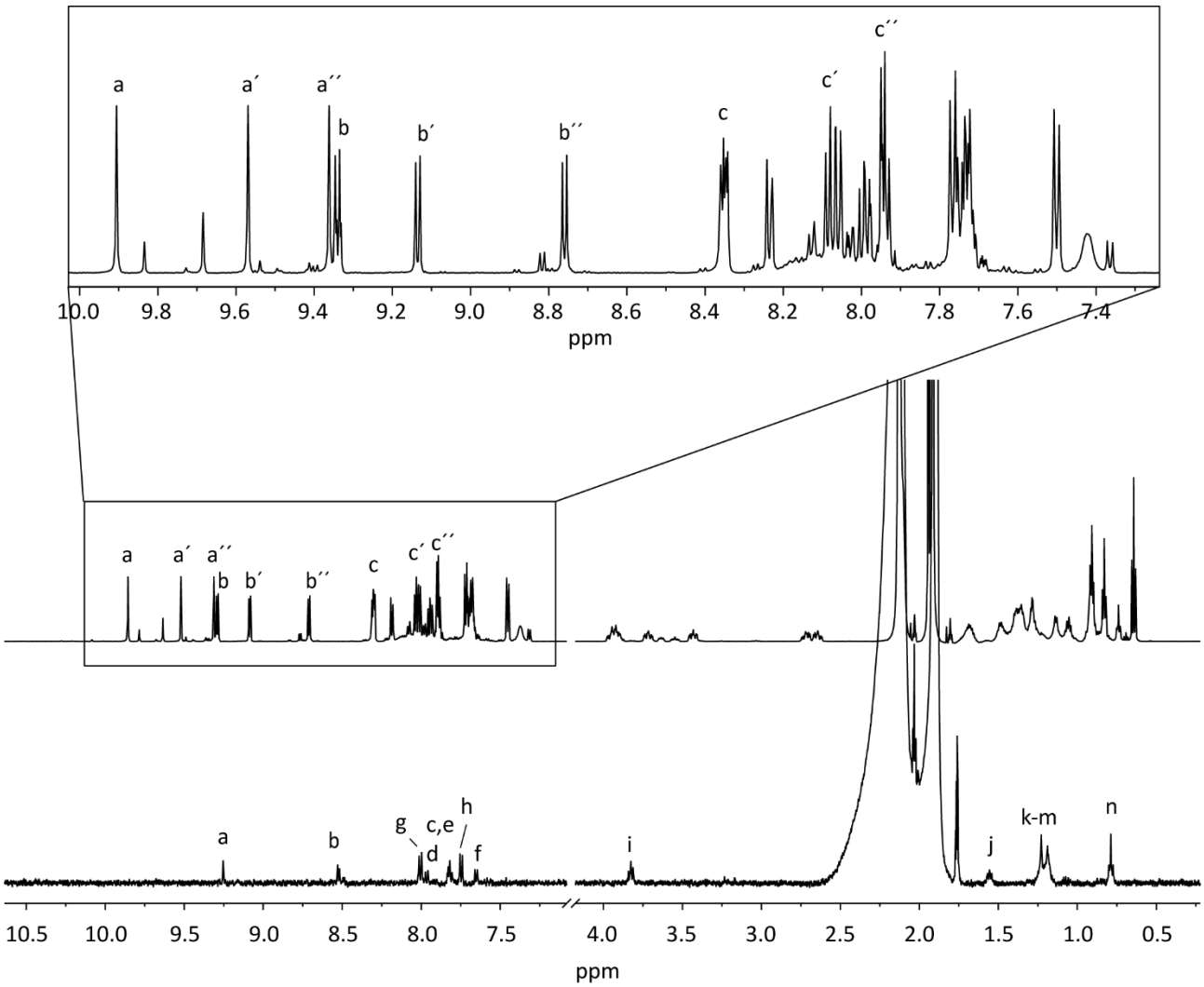

Figure 3.59: Stacked ^{1}H NMR spectra (600 MHz, 298K, CD_3CN) of the ligand **8QP-DPP** and upon 0.5 equiv. Pd(II) addition to form the assembly [Pd_2(**8QP-DPP**)$_3$(CH_3CN)$_2$].

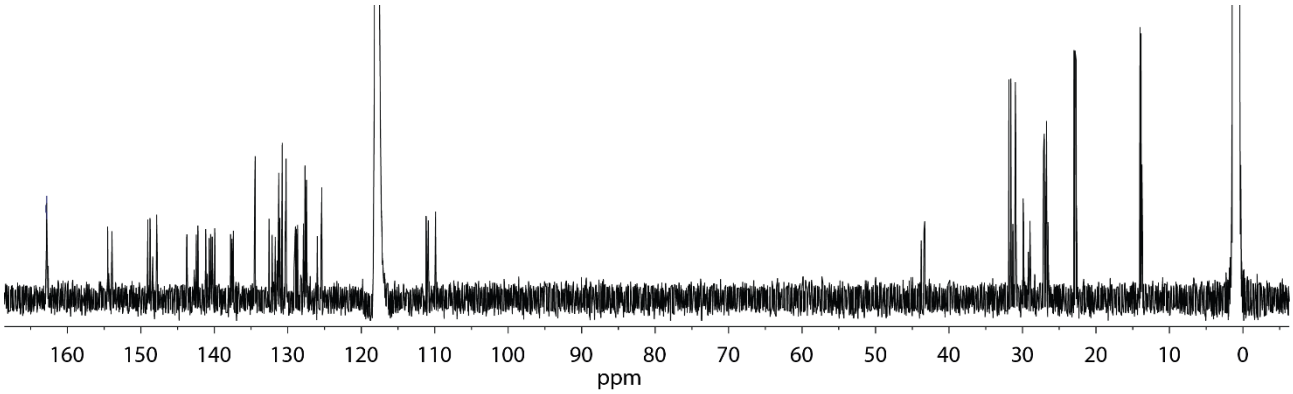

Figure 3.60: ^{13}C NMR spectrum (151 MHz, 298K, CD_3CN) of the assembly $[Pd_2(\mathbf{8QP\text{-}DPP})_3(CH_3CN)_2]$.

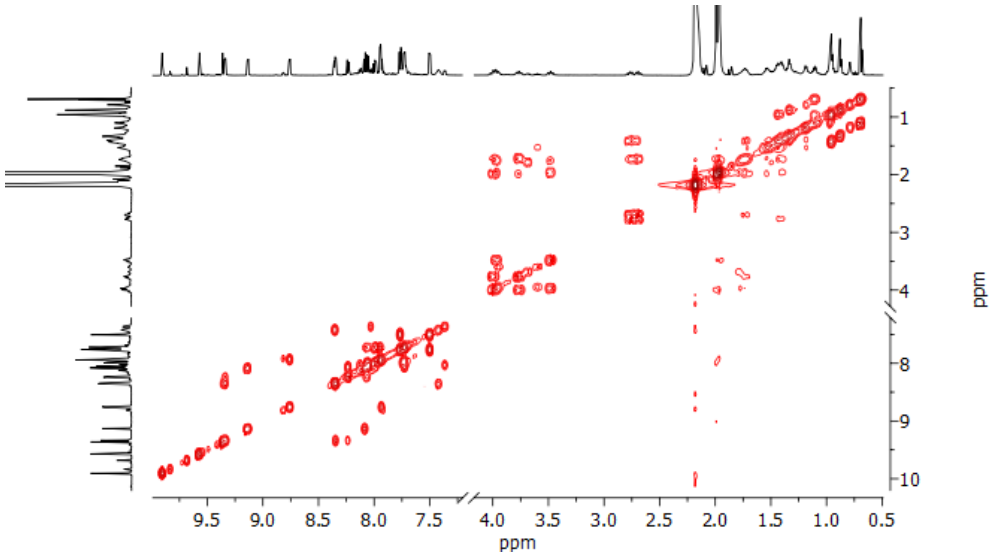

Figure 3.61: ^{1}H-^{1}H COSY NMR spectrum (600 MHz, 298K, DMSO-d_6) of the assembly $[Pd_2(\mathbf{8QP\text{-}DPP})_3(CH_3CN)_2]$.

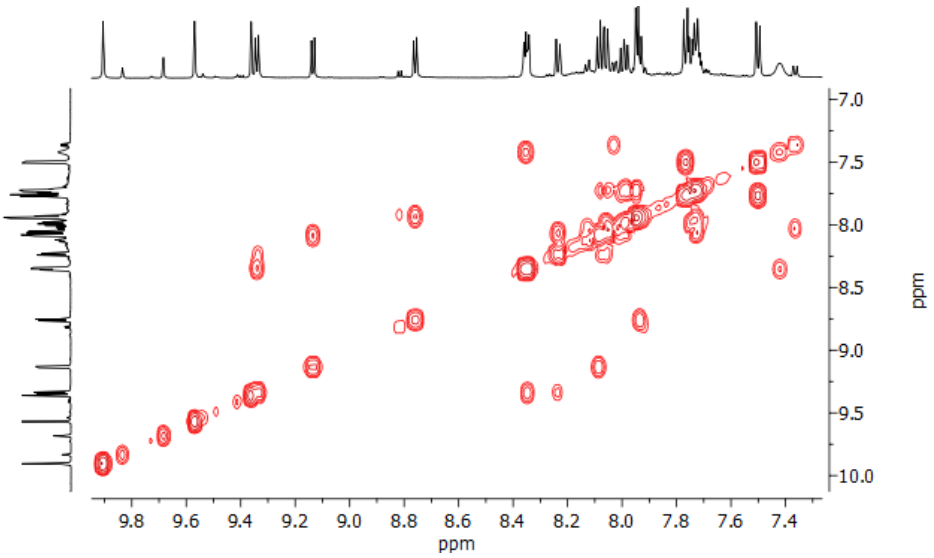

Figure 3.62: Enlargement of the aromatic area of ^{1}H-^{1}H COSY NMR spectrum (600 MHz, 298K, DMSO-d_6) of the assembly $[Pd_2(\mathbf{8QP\text{-}DPP})_3(CH_3CN)_2]$.

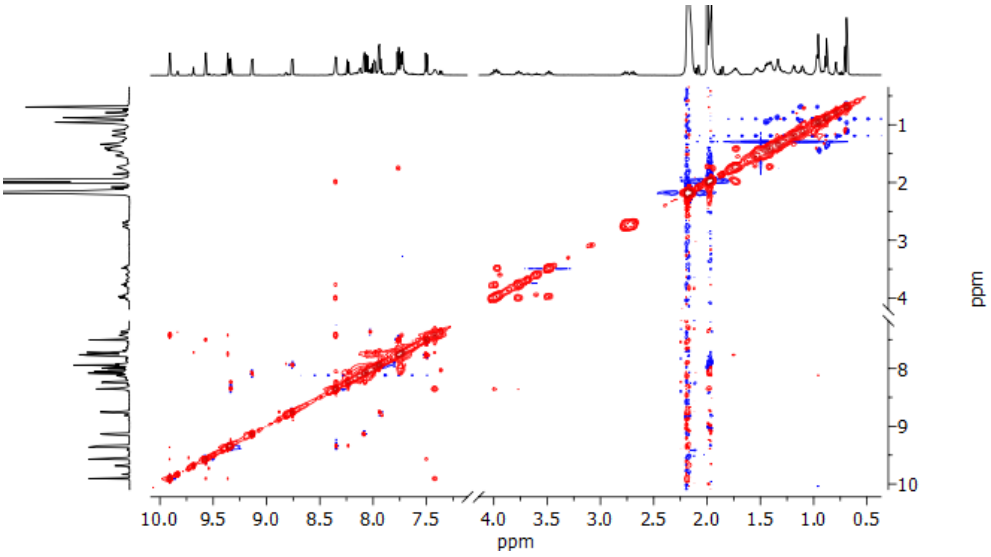

Figure 3.63: ^{1}H-^{1}H NOESY NMR spectrum (600 MHz, 298K, DMSO-d_6) of the assembly [Pd_2(**8QP-DPP**)$_3$(CH_3CN)$_2$].

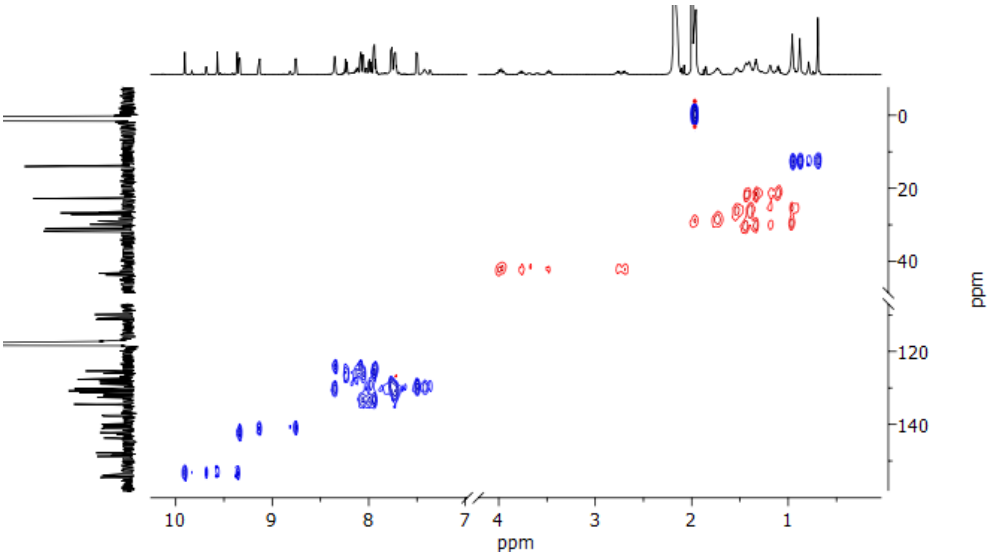

Figure 3.64: ^{1}H-^{13}C HSQC NMR spectrum (600 MHz, 298K, DMSO-d_6) of the assembly [Pd_2(**8QP-DPP**)$_3$(CH_3CN)$_2$].

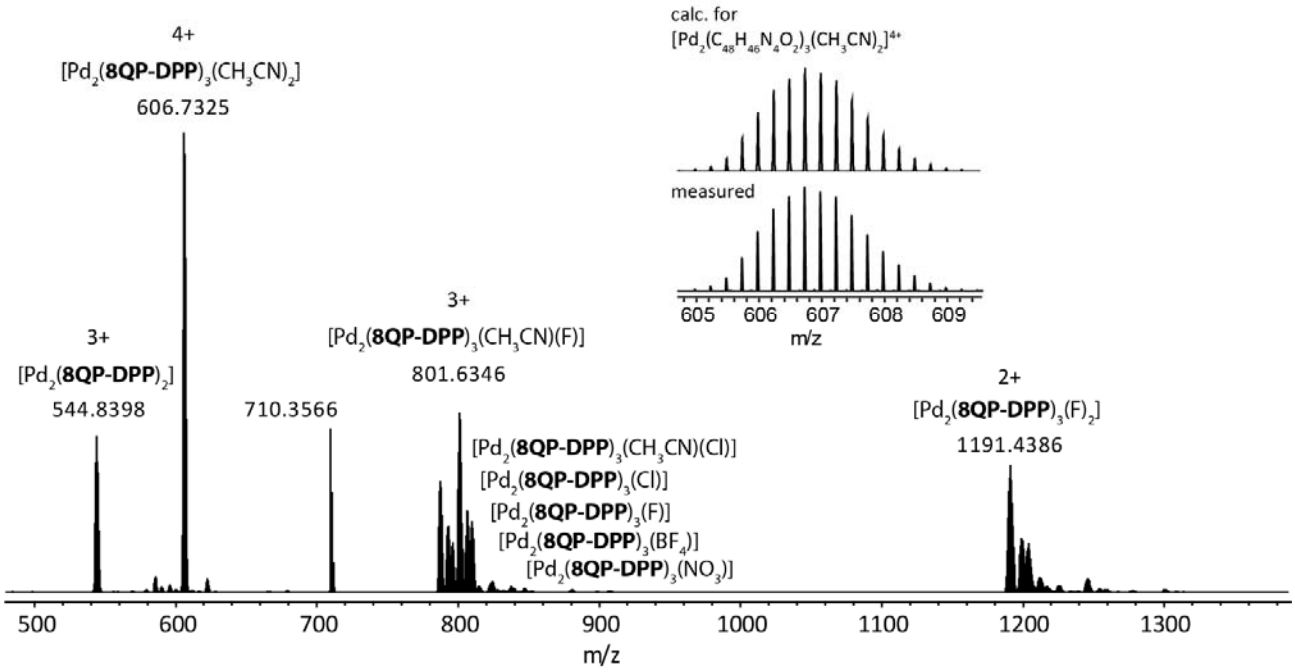

Figure 3.65: ESI-MS spectrum of $[Pd_2(\mathbf{8QP\text{-}DPP})_3(CH_3CN)_2{+}nBF_4]^{4-n+}$ with measured and simulated pattern for $[Pd_2(\mathbf{8QP\text{-}DPP})_3(CH_3CN)_2]^{4+}$ shown in the inset. Species in which the solvent molecules are exchanged for various anions are assigned in the spectrum.

$[Pd_2L^Q{}_2L^C{}_2](BF_4)_4$

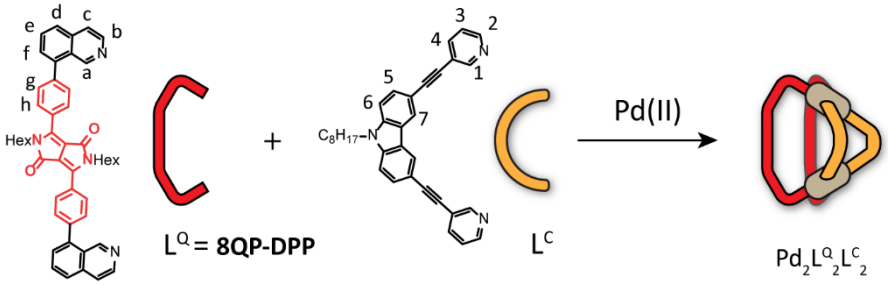

Figure 3.66: Formation of the assembly $[Pd_2L^Q{}_2L^C{}_2](BF_4)_4$.

A mixture of ligand L^Q (250 µL of a 2.8 mM solution in DMSO-d_6) and ligand L^C (250 µL of a 2.8 mM solution in DMSO-d_6) and $[Pd(CH_3CN)_4](BF_4)_2$ (50 µL of a 15 mM solution in DMSO-d_6) was heated at 70 °C overnight to afford a 0.63 mM solution of cage $[Pd_2L^Q{}_2L^C{}_2](BF_4)_4$.

^{1}H NMR (600 MHz, Dimethyl sulfoxide-d_6) δ 9.98 (s, 1H, Ha), 9.75 (d, J = 6.6 Hz, 1H, Hb), 9.65 – 9.61 (m, 1H, H2), 9.60 – 9.56 (m, 1H, H1), 9.22 (d, J = 7.8 Hz broad, Hh), 8.63 (d, J = 6.7 Hz, 1H, Hc), 8.56 (dd, J = 18.0, 8.0 Hz, 2H, H4, Hd), 8.43 (d, J = 8.1 Hz, 1H, Hf), 8.36 – 8.31 (m, 1H, He), 8.18 (d, J = 6.8 Hz, 1H), 8.14 (m, 1H, H7), 8.09 – 8.02 (m, 2H, H3, H5), 7.99 (d, J = 8.9 Hz, 1H, H6), 7.93 (dd, J = 10.9, 8.4 Hz, broad, Hg), 4.64 (d, J = 34.8 Hz, 2H), 4.48 (s, 1H), 4.35 (d, J = 14.6 Hz, 1H), 1.87 (s, 2H), 1.65 – 1.15 (m, 9H), 1.19 – 0.68 (m, 6H), 0.51 – 0.36 (m, 2H), 0.27 (dt, J = 15.2, 5.5 Hz, 2H), 0.19 – -0.05 (m, 5H).

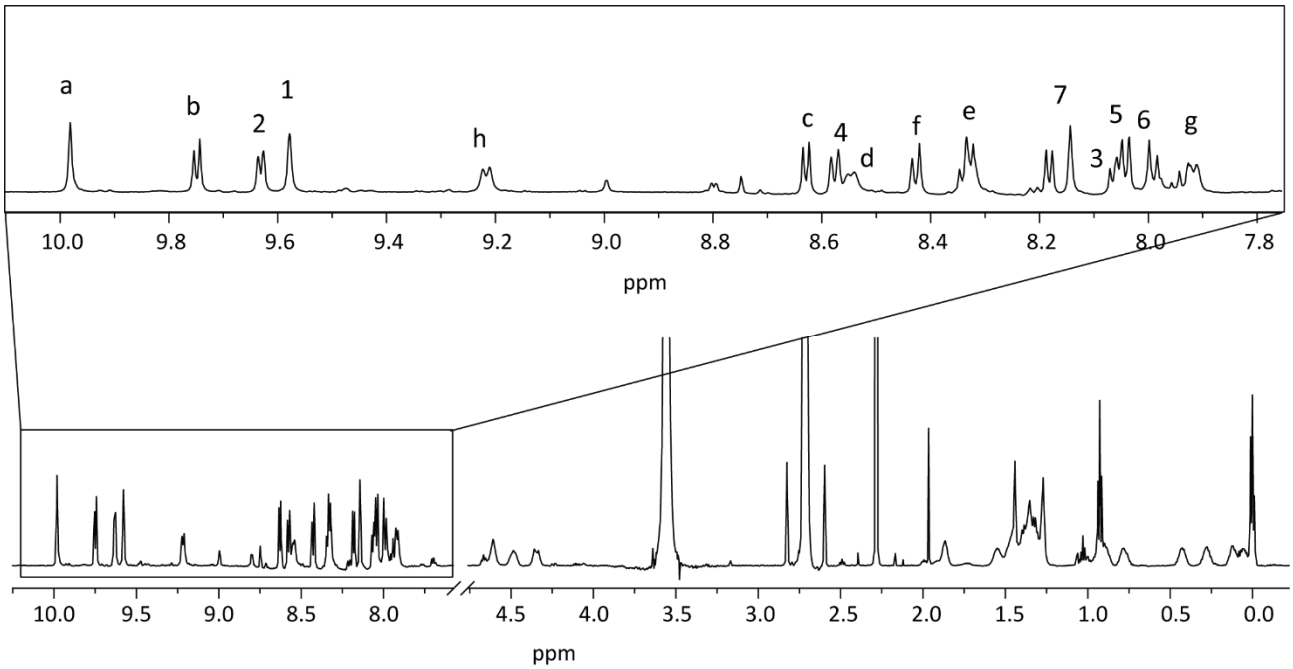

Figure 3.67: ^{1}H NMR spectrum (600 MHz, 298K, DMSO-d_6) of the cage $[Pd_2L^{Q}{}_2L^{C}{}_2](BF_4)_4$.

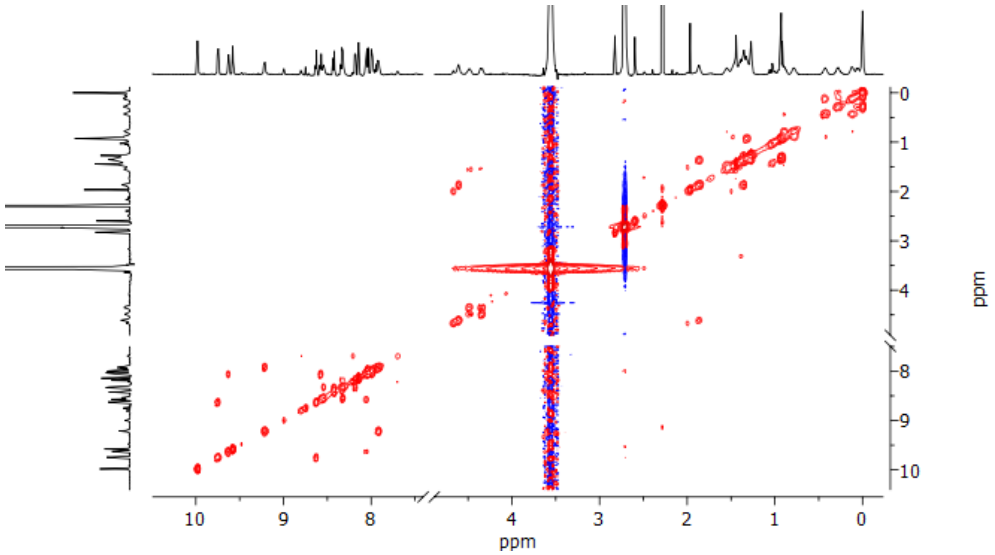

Figure 3.68: ^{1}H-^{1}H COSY NMR spectrum (600 MHz, 298K, DMSO-d_6) of the cage $[Pd_2L^{Q}{}_2L^{C}{}_2](BF_4)_4$.

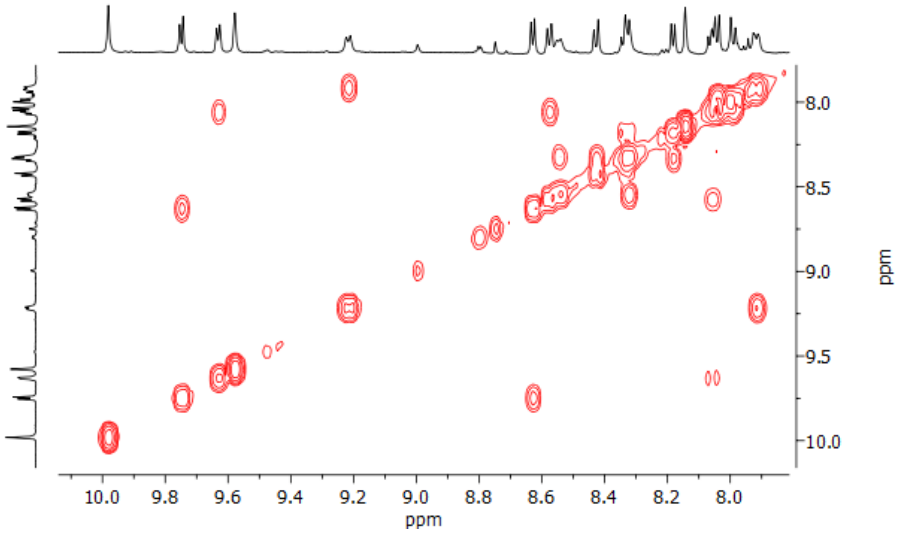

Figure 3.69: Enlargement on the aromatic area of ^{1}H-^{1}H COSY NMR spectrum (600 MHz, 298K, DMSO-d_6) of the cage $[Pd_2L^Q{}_2L^C{}_2](BF_4)_4$.

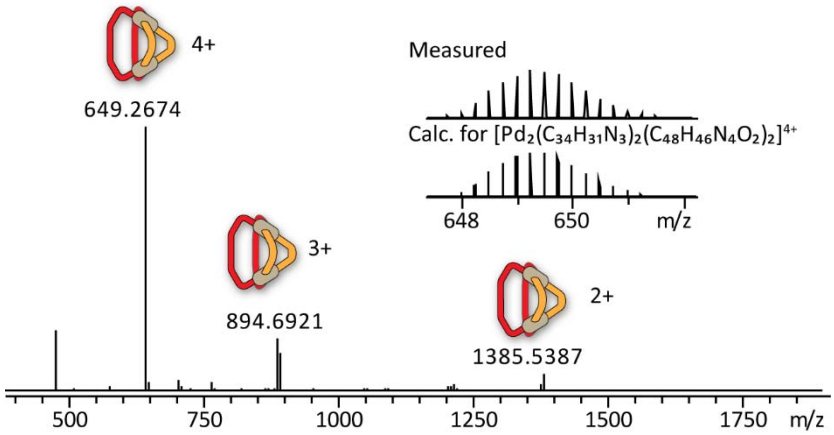

Figure 3.70: : ESI-MS spectrum of cage $[Pd_2L^Q{}_2L^C{}_2+nBF_4]^{4-n+}$ with n=0-2 with measured and simulated isotopic patterns of $[Pd_2L^Q{}_2L^C{}_2]^{4+}$.

$[Pd_2L^Q{}_2L^F{}_2](BF_4)_4$

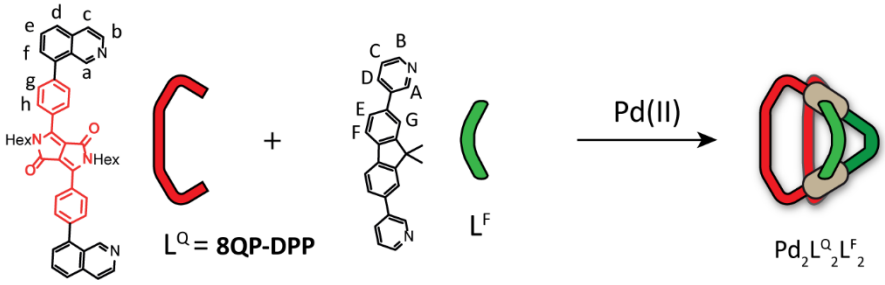

Figure 3.71: Formation of the assembly $[Pd_2L^Q{}_2L^F{}_2](BF_4)_4$.

A mixture of ligand L^Q (250 µL of a 2.8 mM solution in DMSO-d_6) and ligand L^F (250 µL of a 2.8 mM solution in DMSO-d_6) and $[Pd(CH_3CN)_4](BF_4)_2$ (50 µL of a 15 mM solution in DMSO-d_6) was heated at 70 °C overnight to afford a 0.63 mM solution of cage $[Pd_2L^Q{}_2L^F{}_2](BF_4)_4$.

^{1}H NMR (600 MHz, Dimethyl sulfoxide-d_6) δ 9.96 (s, broad), 9.75 (d, J = 6.5 Hz), 9.44 (s, broad), 9.23 (d, J = 5.6 Hz,), 8.51 (dd, J = 15.3, 7.0 Hz), 8.41 (d, J = 6.6 Hz), 8.22 (dd, J = 21.8, 8.3 Hz), 8.14 – 7.92 (m), 7.79 (ddd, J = 35.5, 29.3, 6.7 Hz), 4.04 (dd, J = 11.1, 4.3 Hz), 2.20 (d, J = 11.3 Hz), 1.98 (d, J = 23.6 Hz), 1.71 – 1.56 (m), 1.52 – 1.34 (m), 1.16 (d, J = 28.6 Hz), 1.06 – 0.78 (m), 0.63 (t, J = 7.0 Hz).

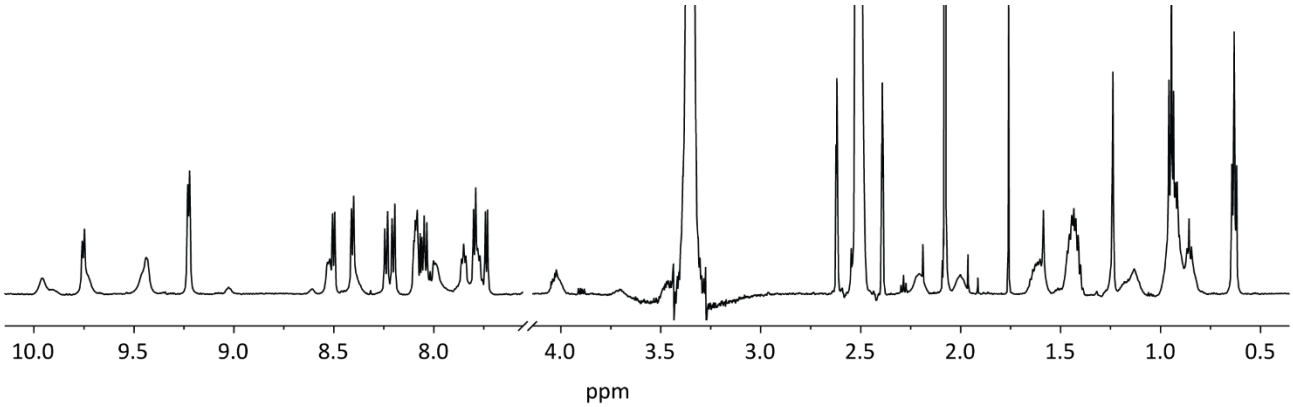

Figure 3.72: ^{1}H NMR spectrum (600 MHz, 298K, DMSO-d_6) of the cage $[Pd_2L^{Q}{}_2L^{F}{}_2](BF_4)_4$.

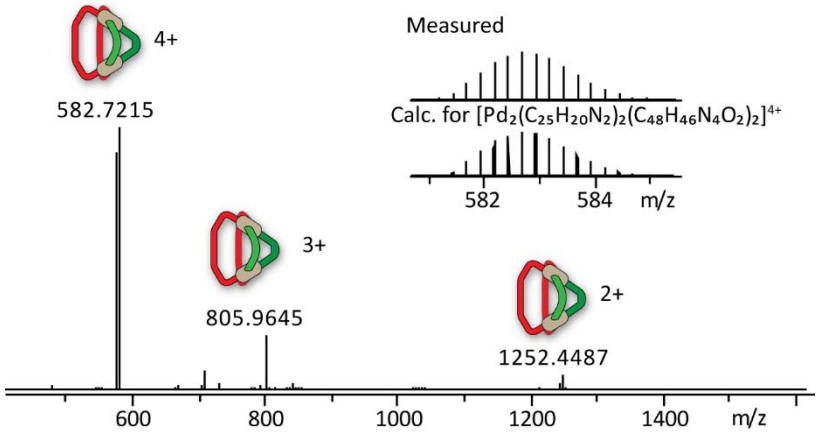

Figure 3.73: ESI-MS spectrum of cage $[Pd_2L^{Q}{}_2L^{F}{}_2+nBF_4]^{4-n+}$ with n=0-2 with measured and simulated isotopic patterns of $[Pd_2L^{Q}{}_2L^{F}{}_2]^{4+}$.

Self-sorted mixture of $[Pd_2L^{Q}{}_2L^{F}{}_2](BF_4)_4$ and $[Pd_2L^{Q}{}_2L^{F}{}_2](BF_4)_4$

A mixture of ligand L^{Q} (250 µL of a 2.8 mM solution in DMSO-d_6), L^{C} (125 µL of a 2.8 mM solution in DMSO-d_6) and ligand L^{F} (125 µL of a 2.8 mM solution in DMSO-d_6) and $[Pd(CH_3CN)_4](BF_4)_2$ (50 µL of a 15 mM solution in DMSO-d_6) was heated at 70 °C overnight to afford the mixture of $[Pd_2L^{Q}{}_2L^{F}{}_2](BF_4)_4$ and $[Pd_2L^{Q}{}_2L^{F}{}_2](BF_4)_4$.

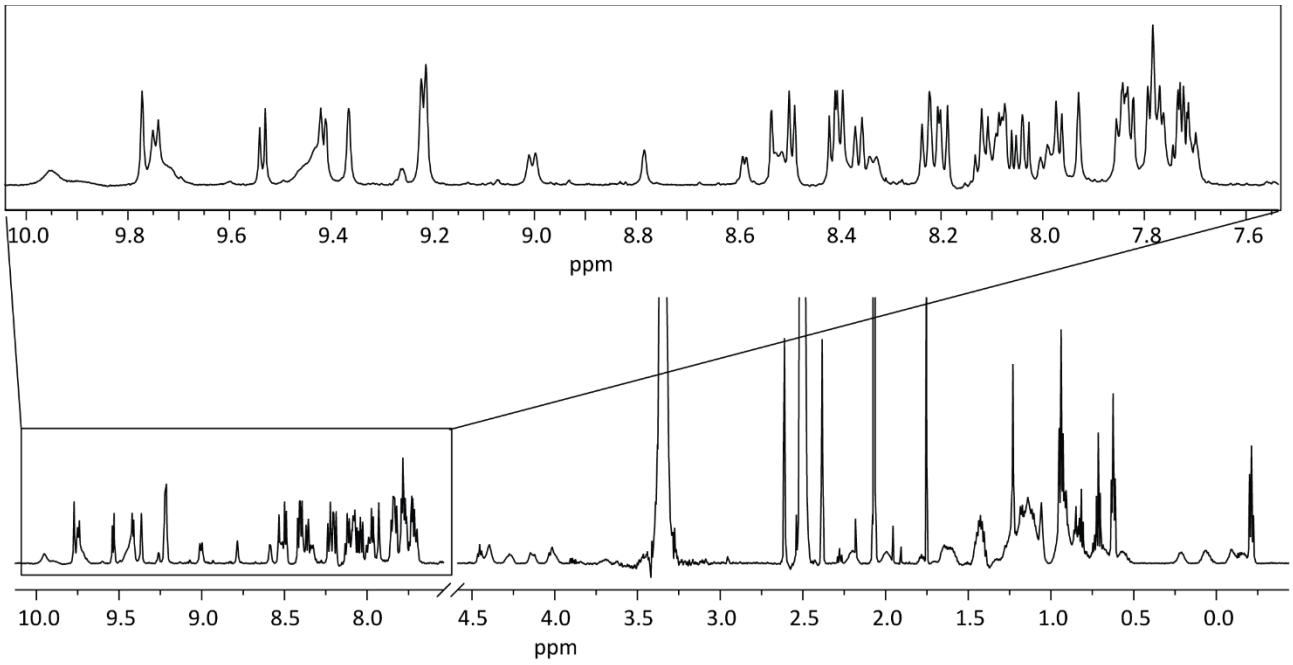

Figure 3.74: ^{1}H NMR spectrum (600 MHz, 298K, DMSO-d_6) of the mixture of $[Pd_2L^Q{}_2L^F{}_2](BF_4)_4$ and $[Pd_2L^Q{}_2L^F{}_2](BF_4)_4$.

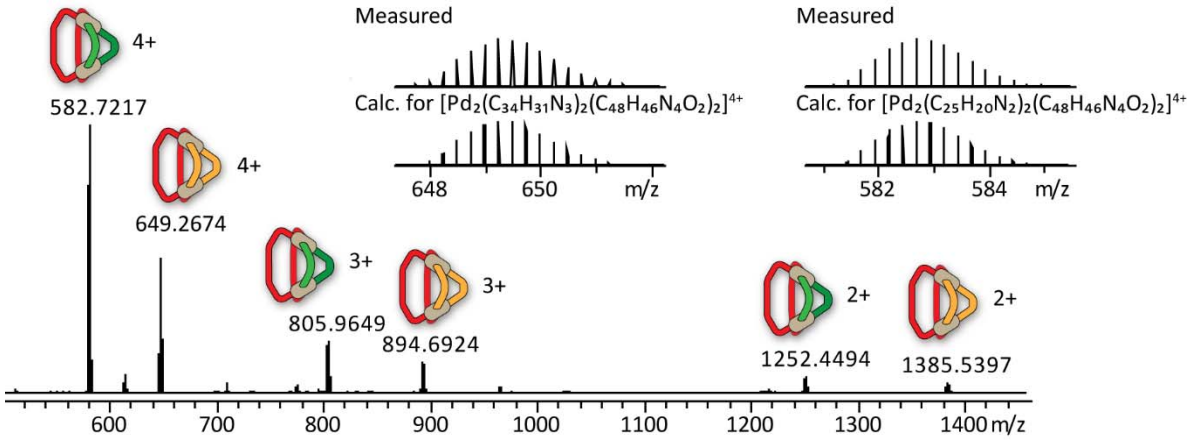

Figure 3.75: ESI-MS spectrum of the mixture of heteroleptic cages $[Pd_2L^Q{}_2L^C{}_2+nBF_4]^{4-n+}$ with n=0-2 and $[Pd_2L^Q{}_2L^F{}_2+nBF_4]^{4-n+}$ with n=0-2 with measured and simulated isotopic patterns of $[Pd_2L^Q{}_2L^C{}_2]^{4+}$ and $[Pd_2L^Q{}_2L^F{}_2]^{4+}$.

Cage-to-cage transformation

The cage-to-cage transformation was carried out in DMSO-d_6. Homoleptic assemblies $[Pd_2L^C{}_4](BF_4)_4$ and $[Pd_3L^F{}_6](BF_4)_6$ + $[Pd_4L^F{}_8](BF_4)_8$ were obtained from ligands L^C and L^Q, respectively, by addition of 0.5 equiv. Pd(II) as previously reported.[35] The mixture solution of cage $[Pd_2L^C{}_4](BF_4)_4$ (250 µL, concentration of L^C 2.8 mM) and $[Pd_3L^F{}_6](BF_4)_6$ + $[Pd_4L^F{}_8](BF_4)_8$ (250 µL, concentration of L^F 2.8 mM) was heated at 70 °C overnight to afford heteroleptic cage $[Pd_2L^C{}_2L^F{}_2](BF_4)_4$. The homoleptic assembly $[Pd_2(\mathbf{8QP\text{-}DPP})_3(CH_3CN)_2]$ was formed with an excess of ligand **8QP-DPP** to guaranty an overall concentration of 2.8 mM of the ligand in solution: a mixture of ligand **8QP-DPP** (450 µL of a 3.11 mM) and $[Pd(CH_3CN)_4](BF_4)_2$ (50 µL of a 15 mM solution in CD_3CN) was heated at 70 °C for 30 min. The mixture solution of cage $[Pd_2L^C{}_2L^F{}_2](BF_4)_4$ (250 µL, concentration of L^C 1.4 mM and L^F 1.4 mM) and $[Pd_2(\mathbf{8QP\text{-}DPP})_3(CH_3CN)_2]$ (250 µL, concentration of L^F 2.8 mM) was heated at 70 °C overnight to afford the heteroleptic cages $[Pd_2L^Q{}_2L^C{}_2](BF_4)_4$ and $[Pd_2L^Q{}_2L^F{}_2](BF_4)_4$ mixture.

3.6.4 Crystallographic information

The X-ray diffraction analysis was performed with the help of Dr. Julian Holstein and Ass.-Prof. Dr. Shinnosuke Horiuchi. Two different supramolecular assemblies [Pd_3(**4PM-DPP**)$_6$] and *Fig8*-[Pd_2(**3PM-DPP**)$_4$] and one ligand **3PM-DPP** were studied using single-crystal X-ray crystallography. Ligand **3PM-DPP** could be studied on in-house diffractometer using microfocussed MoK_α radiation. In contrast, crystals of supramolecular assemblies were extremely sensitive to loss of organic solvent. Due to very thin plate or needle-shaped crystals, the analysis was further hampered by the limited scattering power of the samples not allowing to reach the desired (sub-)atomic resolution using our a modern microfocussed X-ray in-house MoK_α source. Gaining detailed structural insight thus required cryogenic crystal handling and highly brilliant synchrotron radiation. Hence, diffraction data of most of supramolecular assemblies was collected during three beamtime shifts at macromolecular synchrotron beamline P11, PETRA III, DESY.[36] Counterion and solvent flexibility required carefully adapted macromolecular refinement protocols employing geometrical restraint dictionaries, similarity restraints and restraints for anisotropic displacement parameters (ADPs).

Structure ID	**3PM-DPP**	[Pd_3(**4PM-DPP**)$_6$]	*Fig8*-[Pd_2(**3PM-DPP**)$_4$]
Empirical formula	$C_{40}H_{42}N_4O_2$	$C_{240}H_{252}B_2F_8N_{24}O_{12}Pd_3$	$C_{160}H_{168}B_3F_{12}N_{16}O_8Pd_2$
Formula weight	610.77	4157.46	2916.32
Temperature [K]	100(2)	80(2)	80(2)
Crystal system	monoclinic	triclinic	triclinic
Space group (number)	$C2/c$ (15)	$P\overline{1}$ (2)	$P\overline{1}$ (2)
a [Å]	30.5195(6)	18.590(4)	19.108(4)
b [Å]	6.26290(10)	24.413(5)	20.566(4)
c [Å]	16.8093(4)	34.288(7)	20.919(4)
α [Å]	90	73.77(3)	89.12(3)
β [Å]	100.7230(10)	82.35(3)	69.94(3)
γ [Å]	90	84.15(3)	83.03(3)
Volume [Å^3]	3156.83(11)	14774(6)	7662(3)
Z	4	2	2
ρ_{calc} [g/cm^3]	1.285	0.935	1.264
μ [mm^{-1}]	0.080	0.213	0.282
F(000)	1304	4352	3038
Crystal size [mm^3]	0.500x0.500x0.500	0.500×0.200×0.010	0.500×0.200×0.010
Crystal color	red	red	red
Crystal shape	block	plate	plate
Radiation	MoK_α (λ=0.71073 Å)	synchrotron (λ=0.6888 Å)	synchrotron (λ=0.6888 Å)
2Θ range [°]	4.93 to 53.48 (0.79 Å)	1.21 to 34.24 (1.17 Å)	1.93 to 37.55 (1.07 Å)
Index ranges	-38 ≤ h ≤ 38 -7 ≤ k ≤ 7 -21 ≤ l ≤ 21	-15 ≤ h ≤ 15 -20 ≤ k ≤ 20 -29 ≤ l ≤ 29	-17 ≤ h ≤ 17 -19 ≤ k ≤ 19 -19 ≤ l ≤ 19
Reflections collected	50790	64206	42556
Independent reflections	3346 R_{int} = 0.1164 R_{sigma} = 0.0452	18536 R_{int} = 0.0437 R_{sigma} = 0.0407	12452 R_{int} = 0.0595 R_{sigma} = 0.0600
Completeness to θ = 25.242°	100.0 %	96.0 %	95.0 %
Data / Restraints / Parameters	3346/0/209	18536/5628/2803	12452/4579/2102
Goodness-of-fit on F^2	1.131	1.740	1.582
Final *R* indexes [$I \geq 2\sigma(I)$]	R_1 = 0.0427 wR_2 = 0.1113	R_1 = 0.1417 wR_2 = 0.3922	R_1 = 0.1304 wR_2 = 0.3654
Final *R* indexes [all data]	R_1 = 0.0614 wR_2 = 0.1331	R_1 = 0.1704 wR_2 = 0.4169	R_1 = 0.1669 wR_2 = 0.4037
Largest peak/hole [eÅ^3]	0.27/-0.41	1.41/-1.00	0.87/-0.61

Crystal structure of 3PM-DPP

Red blocks crystals of **3PM-DPP** were grown by cooling down a solution of **3PM-DPP** in acetonitrile from 70 °C to room temperature. A single crystal in mother liquor was mounted onto a 0.5 mm nylon loop using NVH oil. Single crystal X-ray diffraction data was collected on a Bruker D8 venture equipped with an Incoatec microfocus source (Iμs 2.0) using Mokα radiation on a four axis κ-goniometer, equipped with an Oxford Cryostream 800 and a Photon 100 detector. Data integration was done with SAINT. Data scaling and absorption correction were performed with SADABS. The space group was determined using XPREP.[37] The structure was solved by intrinsic phasing/direct methods using SHELXT[38] and refined with SHELXL[39] for full-matrix least-squares routines on F^2 and ShelXle[40] as a graphical user interface.

Crystal structure of [Pd_3(4PM-DPP)$_6$]

Colorless, needle shaped crystals of [Pd_3(**4PM-DPP**)$_6$] were grown by slow vapor diffusion of ethyl acetate in the DMSO solution of [Pd_3(**4PM-DPP**)$_6$] at room temperature. A single crystal in mother liquor was pipetted onto a glass slide containing NVH oil. To avoid collapse of the crystal lattice, the crystal was quickly mounted onto a 0.2 mm nylon loop and immediately flash cooled in liquid nitrogen. Crystals were stored at cryogenic temperature in dry shippers, in which they were safely transported to macromolecular beamline P11 at Petra III[34], DESY, Germany. A wavelength of λ = 0.6888 Å was chosen using a liquid N_2 cooled double crystal monochromator. Single crystal X-ray diffraction data was collected at 80(2) K on a single axis goniometer, equipped with an Oxford Cryostream 800 a Pilatus 6M. Data integration and reduction were undertaken using XDS.[41] The structure was solved by intrinsic phasing/direct methods using SHELXT[38] and refined with SHELXL[39] using 22 cpu cores for full-matrix least-squares routines on F^2 and ShelXle[40] as a graphical user interface and the DSR program plugin was employed for modeling.[42] Stereochemical restraints for the **4PM-DPP** ligands were generated by the GRADE program using the GRADE Web Server (http://grade.globalphasing.org) and applied in the refinement. A GRADE dictionary for SHELXL contains target values and standard deviations for 1,2-distances (DFIX) and 1,3-distances (DANG), as well as restraints for planar groups (FLAT). All displacements for non-hydrogen atoms were refined anisotropically. The refinement of ADP's for carbon, nitrogen and oxygen atoms was enabled by a combination of similarity restraints (SIMU) and rigid bond restraints (RIGU).[43] The contribution of the electron density from disordered counterions and solvent molecules, which could not be modeled with discrete atomic positions were handled using the SQUEEZE[44] routine in PLATON.[45] The solvent mask file (.fab) computed by PLATON were included in the SHELXL refinement via the ABIN instruction leaving the measured intensities untouched.

Crystal structure of [Pd_2(3PM-DPP)$_4$]

Colorless, needle shaped crystals of [Pd_2(**3PM-DPP**)$_4$] were grown by slow vapor diffusion of ethyl acetate in the DMSO solution of [Pd_2(**3PM-DPP**)$_4$] at room temperature. A single crystal in mother liquor was pipetted onto a glass slide containing NVH oil. To avoid collapse of the crystal lattice, the crystal was quickly mounted onto a 0.2 mm nylon loop and immediately flash cooled in liquid nitrogen. Crystals were stored at cryogenic temperature in dry shippers, in which they were safely transported to macromolecular beamline P11 at Petra III[36], DESY, Germany. A wavelength of λ = 0.6888 Å was chosen using a liquid N_2 cooled double crystal monochromator. Single crystal X-ray diffraction data was collected at 80(2) K on a single axis goniometer, equipped with an Oxford Cryostream 800 a Pilatus 6M. Data integration and reduction were undertaken using XDS.[41] The structure was solved by intrinsic phasing/direct methods using SHELXT[38] and refined with SHELXL[39] using 22 cpu cores for full-matrix least-squares routines on F^2 and ShelXle[40] as a graphical user interface and the DSR program plugin was employed for modeling.[42] Stereochemical restraints for the **3PM-DPP** ligands were generated by the GRADE program using the GRADE Web Server (http://grade.globalphasing.org) and applied in the refinement. A GRADE dictionary for SHELXL contains target values and standard deviations for 1,2-distances (DFIX) and 1,3-distances (DANG), as well as restraints for planar groups (FLAT). All displacements for non-hydrogen atoms were refined anisotropically. The refinement of ADP's for carbon, nitrogen and oxygen atoms was enabled by a combination of similarity restraints (SIMU) and

rigid bond restraints (RIGU).[43] The contribution of the electron density from disordered counterions and solvent molecules, which could not be modeled with discrete atomic positions were handled using the SQUEEZE[43] routine in PLATON.[45] The solvent mask file (.fab) computed by PLATON were included in the SHELXL refinement via the ABIN instruction leaving the measured intensities untouched.

3.7 References

[1] M. Kaur, D. H. Choi, *Chem. Soc. Rev.* **2015**, *44*, 58–77.
[2] M. Grzybowski, D. T. Gryko, *Adv. Opt. Mater* **2015**, *3*, 280–320.
[3] D. G. Farnum, G. Mehta, G. G. I. Moore, F. P. Siegal, *Tetrahedron Lett.* **1974**, *15*, 2549–2552.
[4] A. Tang, C. Zhan, J. Yao, E. Zhou, *Adv. Mater.* **2017**, *29*, 1600013.
[5] G. Zhang, K. Liu, Y. Li, M. Yang, *Polym Int* **2009**, *58*, 665–673.
[6] Y.-Z. Wu, Y.-C. Zhang, J.-J. Chen, L.-J. Fan, *Chinese J. Polym. Sci* **2019**, *37*, 1092–1098.
[7] A. Ruiz-Carretero, N. R. Á. Rovelo, S. Militzer, P. J. Mésini, *J. Mater. Chem. A* **2019**, *7*, 23451–23475.
[8] S. Qu, H. Tian, *Chem. Commun.* **2012**, *48*, 3039.
[9] E. D. Głowacki, H. Coskun, M. A. Blood-Forsythe, U. Monkowius, L. Leonat, M. Grzybowski, D. Gryko, M. S. White, A. Aspuru-Guzik, N. S. Sariciftci, *Org. Electron.* **2014**, *15*, 3521–3528.
[10] H. Ftouni, F. Bolze, H. de Rocquigny, J.-F. Nicoud, *Bioconjug. Chem.* **2013**, *24*, 942–950.
[11] Q. Liu, S. E. Bottle, P. Sonar, *Adv. Mater.* **2019**, *32*, 1903882.
[12] W. Li, L. Wang, H. Tang, D. Cao, *Dyes Pigm.* **2019**, *162*, 934–950.
[13] Z. Liu, G. Zhang, D. Zhang, *Acc. Chem. Res.* **2018**, *51*, 1422–1432.
[14] V. A. S. Almodôvar, A. C. Tomé, *J. Porphyr. Phthalocyanines* **2020**, *24*, 43–66.
[15] O. Vakuliuk, A. Purc, G. Clermont, M. Blanchard-Desce, D. T. Gryko, *ChemPhotoChem* **2017**, *1*, 243–252.
[16] W. M. Bloch, J. J. Holstein, B. Dittrich, W. Hiller, G. H. Clever, *Angew. Chem. Int. Ed.* **2018**, *57*, 5534–5538.
[17] R. Zhu, J. Lübben, B. Dittrich, G. H. Clever, *Angew. Chem. Int. Ed.* **2015**, *54*, 2796–2800.
[18] T. R. Schulte, M. Krick, C. I. Asche, S. Freye, G. H. Clever, *RSC Adv.* **2014**, *4*, 29724–29728.
[19] M. Frank, M. D. Johnstone, G. H. Clever, *Chem. Eur. J.* **2016**, *22*, 14104–14125.
[20] M. Han, Y. Luo, B. Damaschke, L. Gómez, X. Ribas, A. Jose, P. Peretzki, M. Seibt, G. H. Clever, *Angew. Chem. Int. Ed.* **2015**, *55*, 445–449.
[21] D. K. Chand, K. Biradha, M. Kawano, S. Sakamoto, K. Yamaguchi, M. Fujita, *Chem. Asian J.* **2006**, *1*, 82–90.
[22] D. M. Engelhard, S. Freye, K. Grohe, M. John, G. H. Clever, *Angew. Chem. Int. Ed.* **2012**, *51*, 4747–4750.
[23] S. Löffler, J. Lübben, L. Krause, D. Stalke, B. Dittrich, G. H. Clever, *J. Am. Chem. Soc.* **2015**, *137*, 1060–1063.
[24] W. M. Bloch, Y. Abe, J. J. Holstein, C. M. Wandtke, B. Dittrich, G. H. Clever, *J. Am. Chem. Soc.* **2016**, *138*, 13750–13755.
[25] W. M. Bloch, J. J. Holstein, W. Hiller, G. H. Clever, *Angew. Chem. Int. Ed.* **2017**, *56*, 8285–8289.
[26] B. Chen, J. J. Holstein, S. Horiuchi, W. G. Hiller, G. H. Clever, *J. Am. Chem. Soc.* **2019**, 2019, *141*, 8907–8913
[27] R. Li, PhD Thesis, TU Dortmund **2018**.
[28] Z. Chen, A. Lohr, C. R. Saha-Möller, F. Würthner, *Chem. Soc. Rev.* **2008**, *38*, 564–584.
[29] S. Yao, H.-Y. Ahn, X. Wang, J. Fu, E. W. V. Stryland, D. J. Hagan, K. D. Belfield, *J. Org. Chem.* **2010**, *75*, 3965–3974.
[30] P. Ledwon, *Org. Electron.* **2019**, *75*, 105422.
[31] F. Lincker, B. Heinrich, R. D. Bettignies, P. Rannou, J. Pécaut, B. Grévin, A. Pron, B. Donnio, R. Demadrille, *J. Mater. Chem.* **2011**, *21*, 5238–5247.
[32] M. Chandrasekharam, M. A. Reddy, K. Ganesh, G. D. Sharma, S. P. Singh, J. L. Rao, *Org. Electron.* **2014**, *15*, 2116–2125.
[33] F. Trilling, O. Sachnik, U. Scherf, *Polym. Chem.* **2019**, *10*, 627–632.
[34] W. M. Bloch, G. H. Clever, *Chem. Commun.* **2017**, *53*, 8506–8516.
[35] B. Zhang, PhD Thesis, TU Dortmund **2019**.
[36] A. Burkhardt, T. Pakendorf, B. Reime, J. Meyer, P. Fischer, N. Stübe, S. Panneerselvam, O. Lorbeer, K. Stachnik, M. Warmer, P. Rödig, D. Göries, A. Meents, *Eur. Phys. J. Plus* **2016**, *131*, 56.
[37] Bruker-Nonius, APEX, SAINT, SADABS and XPREP, Bruker AXS Inc., Madison (USA), **2013**.
[38] G. Sheldrick, *Acta Crystallogr. Sect. A* **2015**, *71*, 3-8.
[39] G. Sheldrick, *Acta Crystallogr. Sect. C* **2015**, *71*, 3-8.
[40] C. B. Hubschle, G. M. Sheldrick, B. Dittrich, *J. Appl. Crystallogr.* **2011**, *44*, 1281-1284.
[41] W. Kabsch, *Acta Crystallogr. Sect. D* **2010**, *66*, 125-132.
[42] D. Kratzert, J. J. Holstein, I. Krossing, *J. Appl. Crystallogr.* **2015**, *48*, 933-938.
[43] A. Thorn, B. Dittrich, G. M. Sheldrick, *Acta Crystallogr. Sect. A* **2012**, *68*, 448-451.
[44] A. Spek, *Acta Crystallogr. Sect. C* **2015**, *71*, 9-18.
[45] A. Spek, *Acta Crystallogr. Sect. D* **2009**, *65*, 148-155.

4. Coal-tar dyes-based coordination cages

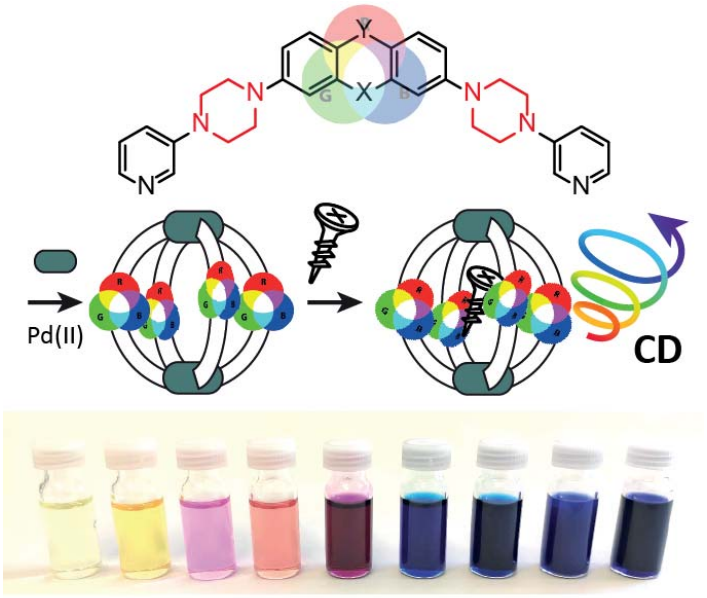

4.1 Introduction

The so-called "coal-tar dyes" (such as di- or triarylmethanes, xanthenes and phenothiazine derivatives) belong to the first block-buster products of the emerging chemical industry in the 19th century (see chapter 1, Introduction). Until today, they are produced in megaton scale and find widespread application as redox and pH indicators,[1] photosensitizers,[2] dye-based lasers,[3] for tissue staining[4] and imaging purposes,[5] aside from their industrial application for coloring fabrics, polymers, paper, hair, food and other materials. In the context of self-assembled systems, however, they turn out to be underrepresented as integral structural elements and have been merely used as additives, e.g. as photosensitizers for $^1O_2$ generation to initiate cascade reactions.[6] Non-covalently encapsulated in metal-organic hosts, such dyes were employed for proton reduction in combination with cobalt nodes in the architecture for catalytic hydrogen generation.[7]

This chapter deals with the implementation of coal-tar dyes (Michler's ketone **MK**, crystal violet **CV**, methylene blue **MB**, rhodamine B **RB**, which will be shortly presented in the next section) into supramolecular self-assembled architectures. It is shown how the implementation of piperazine linkers between dye-based backbones and coordinating donors allows to retain the typical chromophore characteristics (Figure 4.1). Furthermore, as aliphatic linkers, piperazines electronically decouple backbones and donors and at the same time do not interfere with coordination of the donors to the metal centers, despite their ethylene diamine-like substructure. Two choices of donor groups (3-pyridyl **P** and 8-isoquinolinyl **Q**) were examined, giving rise to eight (plus one derivative) ligands that were all found to form intensely colored Pd(II)-mediated cages. Moreover, it is shown how chiral anionic guests interacting with the cages translate their configurational information onto the assemblies.

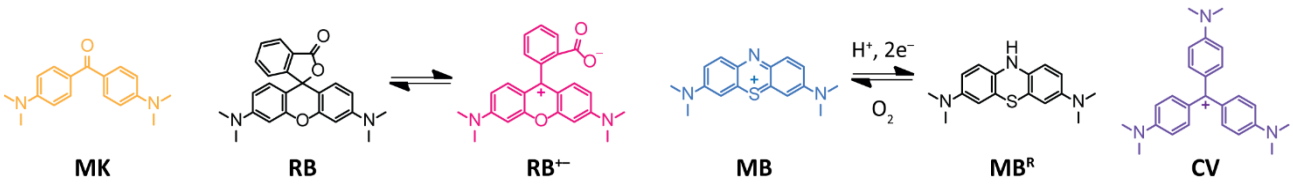

Figure 4.1: Dyes chosen for the presented study. Michler's ketone **MK**, rhodamine B dye **RB** as equilibrium of rhodamine in protic solvents between the lactone and the zwitterion **RB**$^{+-}$, methylene blue **MB** in its blue oxidized and neutral colorless reduced (**MB**^{R}) forms, and crystal violet **CV**.

4.1.1 Michler´s Ketone (MK)

Michler's ketone **MK** is an electron-rich derivative of benzophenone which was named after the German chemist Wilhelm Michler.[8] It servers as intermediate for the production of multiple dyes and pigments for paper, textiles, and leather.[9] Condensation with various aniline derivatives gives dyes called methyl violet, such as crystal violet. It is commonly used as an additive as a sensitizer for photoreactions, for example it can efficient abstract hydrogen from cyclohexane, provided that the concentration of the acceptor is sufficiently high to quench the photoreaction of Michler's ketone with itself.[10]

4.1.2 Rhodamine B (RB)

Due to their luminescent properties, rhodamines — amino derivatives of the heterocycle xanthene — are widely used in science and technology. For example, they are employed as fluorescent labels for imaging purposes,[11] solar energy collectors,[12] as active media for tunable lasers,[3] and as highly sensitive and selective on–off sensors for Pb^{2+}, Hg^{2+}, Fe^{3+}, and other ions.[13]

Rhodamines, containing a carboxyphenyl fragment (e.g., rhodamine B **RB**), exhibit an equilibrium which depends on temperature, pH, solvent, and concentration. In protic solvents **RB** exists as a mixture of a colorless lactone and a highly fluorescent colored zwitterion (**RB**$^{+-}$ in Figure 4.1) that is readily soluble in water and gives a bluish-red coloration.[14] The position of the equilibrium has been shown to depend on both the hydrogen-bonding ability and polarizability of the solvent. As temperature increases the equilibrium shifts toward the less polar lactone.

4.1.3 Methylene Blue (MB)

Dimethylaminophenothiazin-5-ium chloride, better known as methylene blue **MB** is a heterocyclic aromatic member of the thiazine dyes. For decades, this compound has been used as a redox indicator,[9] a photosensitizer,[10] a dye for cellular staining procedures,[15] an antiseptic and a drug candidate against Alzheimer's disease.[16]

In the oxidized state, the color of **MB** is blue since the phenothiazinium molecule absorbs visible light strongly in the region of 600-700 nm (λ_{max}=670 nm). In its reduced leuco form (**MB^{R}** in Figure 4.1) it is colorless and does not absorb light in the visible region. Oxidized **MB** and **MB^{R}** together form a reversible redox couple. The redox indicator properties of this couple have been used extensively in the quantitative analysis of a large number of reducing agents, such as glucose and ascorbic acid.[17] When exposed to light, **MB** becomes photosensitized; it absorbs energy and is then able to transfer the energy to molecular oxygen creating singlet oxygen ($^1O_2$). This has been exploited to make organic peroxides by a Hetero-Diels-Alder reaction which is spin-forbidden with normal atmospheric $^3O_2$.[18] In the field of medicine, it has been utilized as photosensitizer in cancer treatment thanks to the produced singlet oxygen being a highly active and short-lived cytotoxic species.[19]

4.1.4 Crystal Violet (CV)

Crystal Violet **CV** is a well-known triarylmethane dye famous for its use as a histological stain, particularly in Gram staining for classifying bacteria.[20] It has antibacterial, antifungal, anthelmintic, antiangiogenic and antitumor proprieties.[21] Despite those properties, when conducting DNA gel electrophoresis, it can be used as a nontoxic stain. Interestingly, it shows a very high binding affinity for DNA and can be used to specifically target G-quadruplex structures over duplex structures.[22] Crystal violet has also been reported to be a selective fluorescent "switch-on" probe for i-motif DNA. This interaction has been exploited for developing a label-free DNA-based "OR" logic gate for potassium and protons.[23]

4.2 Design

In Figure 4.2 the design concept of the project is depicted. Taking advantage of the coordination geometry of palladium(II) complexes, highly directional and with opportune ligand-exchange kinetics and diamagnetism, the flat C_{2v}-symmetric structure of chromophores embedded in bis-monodentate ligand is incorporated in three-dimensional supramolecular architectures namely "*3D chromophores*". Depending on the design of the ligand, and especially by engineering the donor group that coordinates to the metal cation, multiple structural products can be designed.[24] The small $[Pd_2L_4]$ assemblies are of interest of this chapter. They represent one of the simplest, and at the same time most important, self-assembled architectures. Thanks to their inherent guest recognition features, suitably functionalized members of this compound class show the potential to mimic natural binding pockets found in regulatory proteins and enzymes. They promise therefore to be employed in a wide variety of applications for the transport of molecular cargo and catalysis. $[Pd_2L_4]$ structures can still be differentiated in multiple arrangements of the four ligands around the Pd-Pd axis. Recently our group reported a mechanically-interlocked $[Pd_2L_4]$ motif based on the dimerization of two peptide-based lemniscates. In the structure each ligand chelates the same Pd(II) cation and is interlocked with a ligand that chelate the other Pd(II) center.[25] In the previous chapter, an example of $[Pd_2L_4]$ assembly was shown in which two couples of ligands where occupying positions not equivalent to each other: one set of ligands are bridging the Pd cations from outside the cage cavity in a banana shape conformation, while the other set of ligands are in a '*S*' conformation and cross in the middle of the cage cavity (crystal structure in Figure 3.14). This chapter focuses on other structural arrangements of the ligands in the $[Pd_2L_4]$ topology because, however interesting for multiple aspects the *Fig8*-$[Pd_2L_4]$ structure might be, it does not allow access to the cavity of the structure.

As covered in the Introduction, section 1.2.2, N donor-based ligands characterized by angles between the bonding vectors (defined by the direction of the lone pair to the N atom) which are approximatively 0°, tend to form [Pd_2L_4] structures with D_{4h} point group. All the ligands are equivalent to each other, there is a C_4 axis going through both Pd centers, four C_2 axes and a mirror plane perpendicular to the main C_4 axis. On the other hand, ligands characterized by inward pointing donor groups, forming angles between the bonding vectors smaller than 0°, if defined by a large enough distance between the donor groups, are also capable of coordinating to two different Pd(II) centers forming a [Pd_2L_4] structure. The resulting structure is characterized by a strong helical twist of the ligands around the Pd-Pd coordination axis caused by the propeller disposition of the donor groups to overcome steric hindrance. The supramolecular cage is characterized by a C_4 axis that goes along the two Pd centers and four C_2 axes perpendicular to the main one. The lack of the mirror plane symmetry operation attributes a D_4 symmetry point group to the structure. In other words, the resulting structure is defined by helical chirality and results in the two enantiomeric configurations (*M*), and (*P*)-[Pd_2L_4].

The chemical structures designed for the two different ligands are **DYE-P**, where the central general dye backbone is connected to two pyridines (**P**) with the nitrogen in meta position, to simulate as close as possible a 0° angle within the bonding vectors, and **DYE-Q**, where the **Q** stands for 8yl-isoquinoline, to form inward pointing ligands. The ligand names are composed of backbone and donor label (e.g. **MB-P** is the **m**ethylene **b**lue-based bis-**p**yridine ligand while **MB-Q** is the **m**ethylene **b**lue-based bis-iso**q**uinolin ligand).

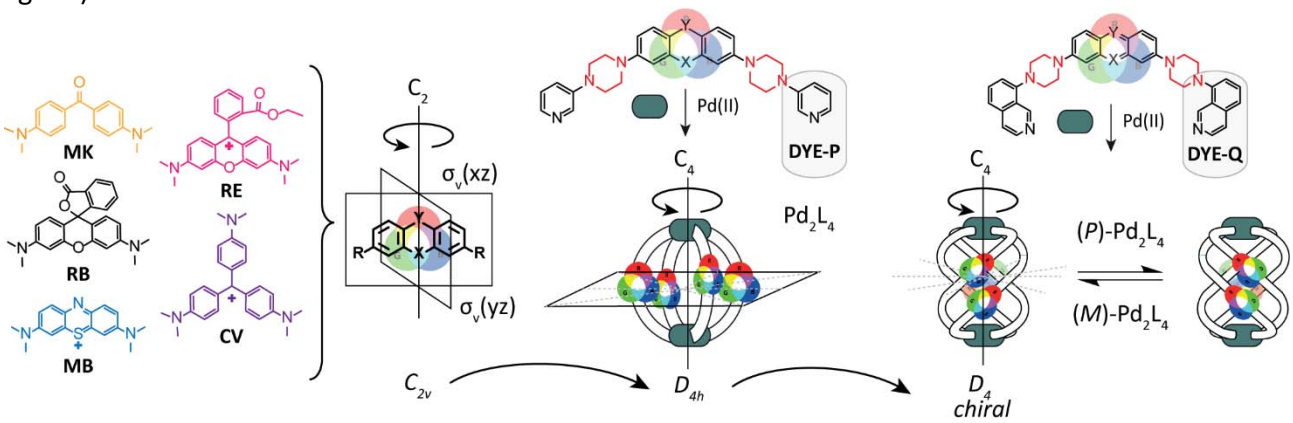

Figure 4.2: Design and concept for the dye-based cages. The dyes' chemical structures are shown on the left and own a C_{2v} symmetry. Their implementation in the **DYE-P** design leads, upon Pd(II) addition, to *3D chromophores* with D_{4h} symmetry. While their implementation in the **DYE-Q** design results in dynamic structures with helical chirality and D_4 symmetry.

However, geometrical considerations are not the only ones that need to be taken into account. In fact, when designing the ligands, the priority is to keep the main electronic structure of the parental dye so that their integration into the three-dimensional structural arrangements, enriches them with the specific interaction that the chromophores have with the visible part of the electromagnetic spectrum. When examining the general structure of the herein studied dyes (Figure 4.2), it becomes apparent that the attachment of typical linkers such as alkynes or arenes is not feasible. In particular, removing the auxochromic dialkyl amines would not be tolerated, as they are fundamental parts of the delocalized π-system, giving rise to intense color in the visible region. For this project, a new design was conceived in which the connection to the donor groups occurs through a piperazine linker (Figure 4.3). The resulting ligands are much more flexible than the usual ones, since the piperazine moieties are aliphatic bridges characterized by multiple possible conformations (*chair-boat-chair* interconversion equilibrium).[26] Piperazine moieties are known to coordinate metal cations and in the boat conformations to chelate them.[27] It will be shown in the following sections, how the piperazine linkers and ligand flexibility did not hamper the assemblies´ formation and provided substantial beneficial properties in the applicability of the systems for chiral recognition of small and larger anionic molecules.

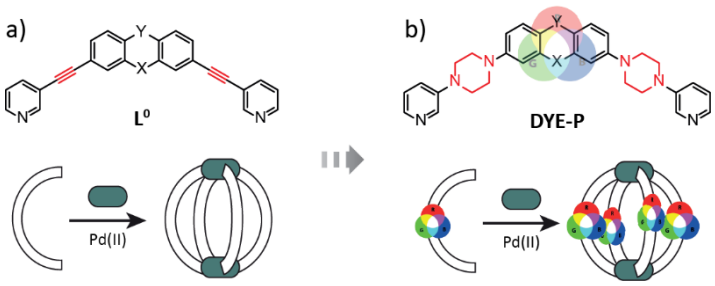

Figure 4.3: a) Generic ligand **L⁰** resulting from the connection of the backbone to the pyridine donor groups with an alkyne bond. The electronic properties of the dye are not translated to the cage because main electron donor groups are missing. b) Piperazine-based design that connects the ligand backbone to the pyridine donor groups employing a piperazine moiety (**DYE-P**). The resulting assembly upon Pd(II) addition still possess the chromophore properties.

4.3 Synthesis of DYE-P ligands and cages

4.3.1 Pyridine ligands synthesis (DYE-P)

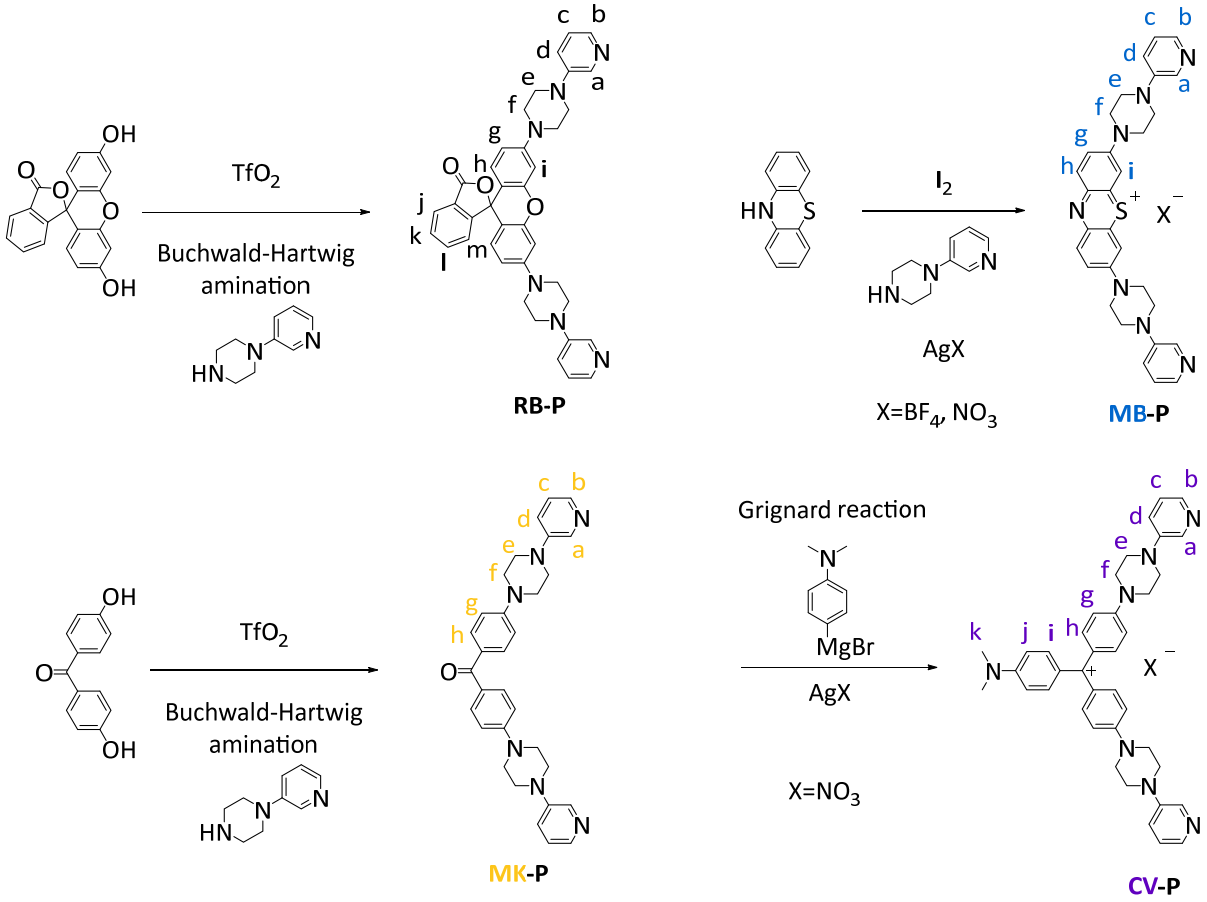

Figure 4.4: Synthetic routes for ligands **RB-P**, **MB-P**, **MK-P** and **CV-P**.

Ligand **RB-P** and corresponding cage were first synthesized by Dr. Marina Frank during her PhD studies. While Dr. Bin Chen initiated the synthesis of ligand **MB-P** obtaining the compound **MB-P**I. The synthesis of ligand **RB-P** with only two synthetic steps straightforward and comprises a Buchwald-Hartwig amination of literature-described tosylated fluorescein with commercially available 3-piperazyl-pyridine. Following the same synthetic pattern starting from 4,4'-dihydroxybenzophenone, ligand **MK-P** has been obtained (Figure 4.4). Ligand **CV-P** was obtained installing the **CV** electronic structure on ligand **MK-P** through a Grignard reaction of 4-MgBr-*N,N*-dimethylaniline (Figure 4.4). The synthesis of ligand **MB-P** followed a procedure already reported[28] for differently substituted **MB** derivatives and comprises the oxidation of phenotiazine with I_2 followed by the attachment of the two 3-piperazyl-pyridine arms.

Both **CV-P** and **MB-P** carry one positive charge and, as a final step of the synthesis, the halogen counter anions have been exchanged for non-coordinating anions such as BF_4^- or NO_3^- by an anion metathesis reaction with addition of the correspondent silver salt, followed by precipitation of insoluble silver halogen salts. When necessary for the discussion, explicit counterions will be attached to the ligand code (for example **MB-P**BF_4).

The ligands (**DYE-P, DYE-Q**) have been characterized with one and two-dimensional NMR spectroscopy and ESI mass spectrometry (ESI-MS). The full procedures and characterization information are reported in the experimental part of this chapter (section 4.7). The ligands' absorption properties have been studied and reported in section 4.4 together with the corresponding assemblies. ^{1}H DOSY measurements are reported in the section 4.4.2 together with the diffusion coefficient and hydrodynamic radius for the assemblies [Pd_2(**DYE-P**)$_4$] and [Pd_2(**DYE-Q**)$_4$] for better comparison.

In order to verify that the electronic properties of the parental dyes have been maintained within the new ligand design, ligands **RB-P** and **MB-P** properties were studied with absorption and fluorescence spectroscopy.

Ligand RB-P

Rhodamine B is characterized by solvent dependent equilibrium between the zwitterion, optically active and the neutral, colorless lactone forms. Ligand **RB-P** maintains this property. When an acetonitrile solution of **RB-P** is subjected to increasing amounts of acid, in this case aqueous HCl, the lactone ring opens upon protonation of the carboxylic acid, causing the appearance of a strong absorption band at 551 nm (Figure 4.5) and some other bands of weaker intensity at 352 nm, 267 nm and 226 nm, while bands at 243 nm and 298 nm decrease in intensity. Upon irradiation with an excitation wavelength of 352 nm, the emission spectrum of **RB-P** shows an increasing emission band at 579 nm, typical for the rhodamine B dye.[15] With the addition of a base like NEt_3, the protonation is reversible, the lactone equilibrium shifts back to the closed form and the absorption band at 551 nm and the emission band at 579 nm, disappear.

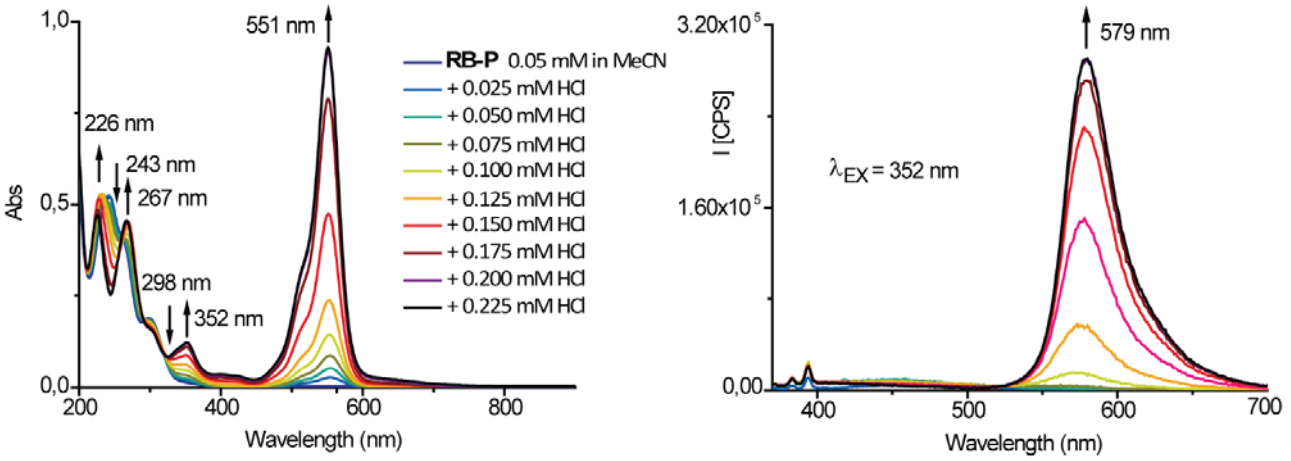

Figure 4.5: Absorption and fluorescence spectra of titration of HCl in the acetonitrile solution of ligand **RB-P**. The opening of the lactone ring is monitored by the increase of intensity in the band at 551 nm in absorption and at 579 nm in emission.

Ligand MB-P

A typical famous experiment to attract young students to chemistry is the so called "Blue Bottle Experiment", a color-changing redox chemical reaction. In this experiment, a water solution of methylene blue, sodium hydroxide and glucose is prepared in a closed bottle containing air. In these conditions the methylene blue is reduced by the sugar to the leuco form and the solution appears colorless. By shaking the bottle, a part of the oxygen present in the bottle oxydizes back the dye to its

colored form and the solution turns blue. By keeping the bottle standing, the oxygen in solution gets consumed while the **MB** is reduced again to the neutral form. This cycle can be repeated many times. The same experiment with ligand **MB-P**NO_3, which is soluble in water, could be performed and monitored with absorption spectroscopy (Figure 4.6).

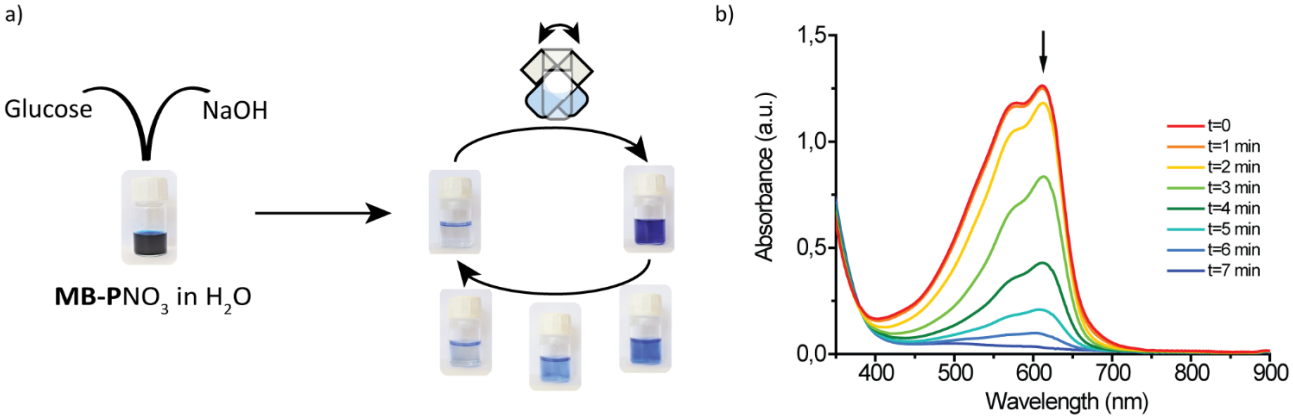

Figure 4.6: a) Pictures of the steps of the "Blue Bottle" experiment with ligand **MB-P**NO_3. Starting from an aqueous solution of the ligand, glucose and NaOH are added. The final solution appears colorless, upon shaking of the vial the solution turns blue and left untouched for some minutes it turns again colorless. b) After the vial has been shaken the blue solution results in a strong absorption band with maximum at 640 nm. Next, one spectrum every minute has been recorded to monitor the disappearance of the band.

Ligand **MB-P**BF_4 crystallizes in very thin needles that are suitable for synchrotron X-ray diffraction techniques. From the obtained structure reported in Figure 4.7 c), the chair conformation of the piperazine linkers can be noted. Excitingly, in collaboration with Dr. Grüne (University of Vienna), the same structure was determined with a resolution of 0.9 Å from a crystal of the size of 1 x 2 μm^2 employing electron diffraction.[28] This result is the proof-of-principle that shows one great advantage of electron crystallography over structure determination with single-crystal X-ray diffraction, as the latter requires to sufficiently large crystals.

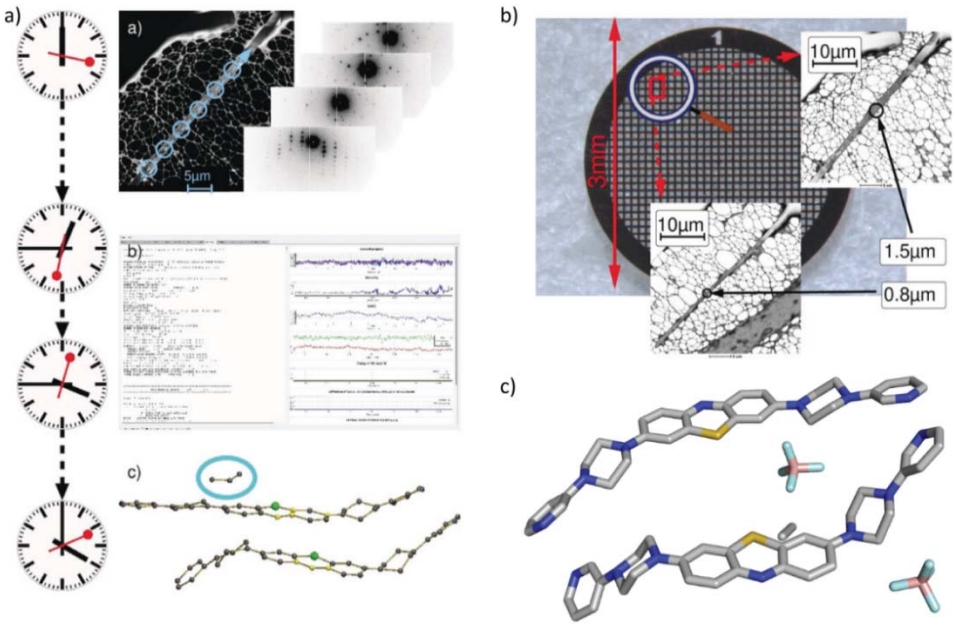

Figure 4.7: a) Structure determination of **MB-P**BF_4 with electrons, comparable with modern X-ray instruments. b) STEM micrographs of the **MB-P**BF_4 needle (contrast inverted for better visibility), lying on the TEM grid. Data were collected in segments along the needle. c) Synchrotron X-ray obtained structure.[28]

4.3.2 Assembly and properties of [Pd_2(DYE-P)$_4$] cages

The quantitative formation of cages [Pd_2(**DYE-P**)$_4$] was achieved by mixing the ligands in a 2 : 1 ratio with the palladium(II) salts [$Pd(CH_3CN)_4$](BF_4)$_2$ or $Pd(NO_3)_2 \cdot 2H_2O$ (the counterion of the palladium salt was chosen to match the ligand counterion) in DMSO-d_6 at 70 °C for 15 min. In full accordance with our previously reported Pd(II) cages based on banana shaped ligands,[29,30] coordination of ligands to the palladium(II) cations was indicated by the downfield shift of the pyridine ^{1}H NMR signals (in particular H_a and H_b in Figure 4.8) with the shift being larger the closer the correspondent proton is located to the metal center. In Figure 4.8, the stacked ^{1}H NMR spectra of the ligands and corresponding Pd-assemblies are reported. A single set of signals could be observed for the assemblies, indicating that the self-assembled species are highly symmetrical, and the ligands occupy equivalent positions in the respective structure. Compared to the signals of the single components, the signals of the assemblies are all slightly more broadened. Such effect could be ascribed to aggregation effects (usually observed together with a decrease of the signals intensity), dynamics of the assemblies (for example involving the piperazine linker conformational equilibrium) or exchange of solvent molecules or counterions in the cage cavities. A further explanation concerning cage [Pd_2(**RB-P**)$_4$] regards the possible mutual orientation of the spirolactone group within the cage structure. From all the possible combinations of the ligands in the two possible orientations, four isomers can originate (Figure 4.12). Supporting this explanation, in the crystal structure of such assembly, the functional group has been found disordered in two possible orientation (see Figure 4.12).

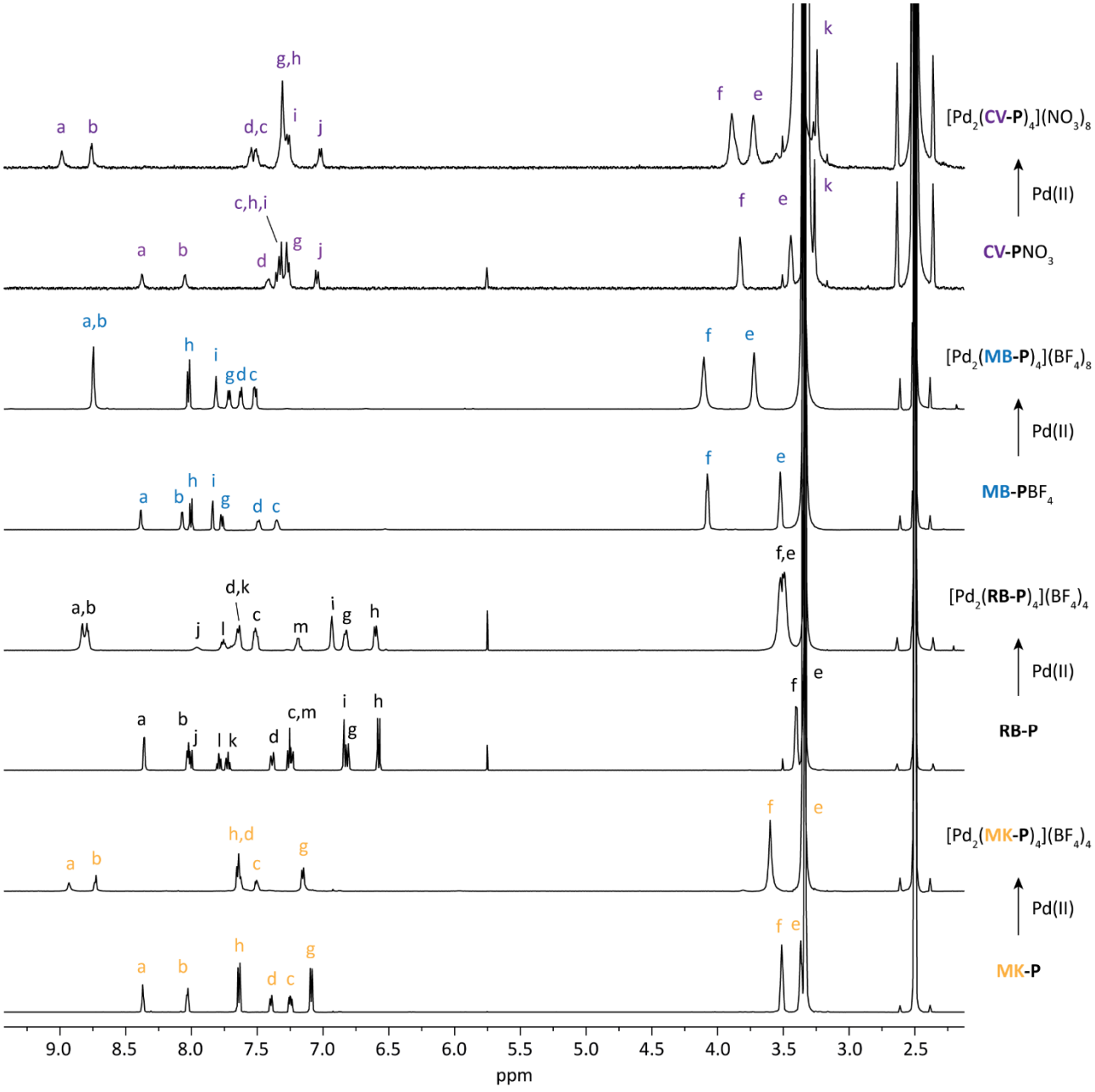

Figure 4.8: Stacked ^{1}H NMR spectra of **DYE-P** ligands and upon addition of 0.5 equiv. Pd(II) salts in DMSO-d_6 at 298 K. Every spectrum corresponds to the species written on the right. The signal assignment refers to Figure 4.4.

Interestingly, besides in DMSO (Figure 4.124), the cage $[Pd_2(\mathbf{MB\text{-}P})_4](NO_3)_8$ could be assembled also in water. In Figure 4.9, the stacked ^{1}H NMR of ligand **MB-P**NO_3 and corresponding cage upon addition of 0.5 equiv. $Pd(NO_3)_2{\cdot}2H_2O$ in D_2O are shown. The typical downfield shift of the signals due to coordination to the metal cation could be observed, however not as pronounced as in DMSO-d_6. Hydrophobic interactions have extensively been exploited as driving force to encapsulate neutral molecules in water-soluble cages, capsules or any kind of supramolecular architecture with a hydrophobic cavity.[31–35] Attempts to encapsulate neutral aromatic compounds in cage $[Pd_2(\mathbf{MB\text{-}P})_4](NO_3)_8$ exploiting the same effect were, however, unsuccessful. The character of the cage cavity is probably not particular hydrophobic considering the overall +8 charge for a small $[Pd_2L_4]$ topology.

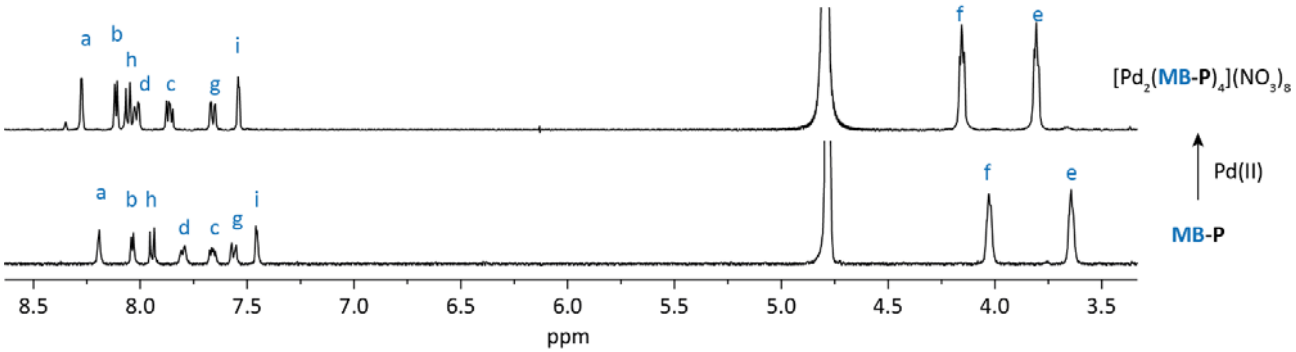

Figure 4.9: Stacked ^{1}H NMR spectra (D_2O, 298K) of ligand **MB-P**NO_3 and corresponding cage upon addition of 0.5 equiv. Pd(II).

Further evidence that the desired topologies formed was given by ESI-mass spectrometry measurements. In Figure 4.10, the measured spectra are reported for all the assemblies with the peaks corresponding to a) $[Pd_2(\mathbf{MK\text{-}P})_4+nBF_4]^{(4-n)+}$ with n = 1,2, b) $[Pd_2(\mathbf{RB\text{-}P})_4+nBF_4]^{(4-n)+}$ with n = 1,2, c) $[Pd_2(\mathbf{MB\text{-}P})_4+nBF_4]^{(8-n)+}$ with n = 1-5 and d) $[Pd_2(\mathbf{CV\text{-}P})_4+nNO_3]^{(8-n)+}$ with n = 2-5.

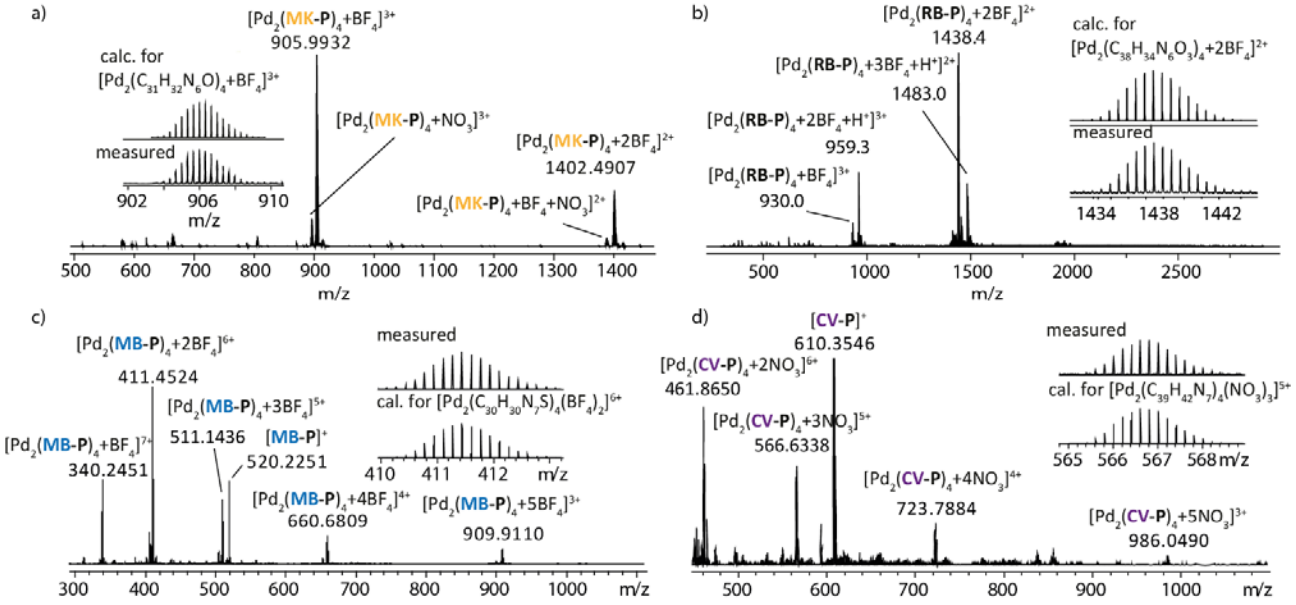

Figure 4.10: ESI-MS spectrum of a) $[Pd_2(\mathbf{MK\text{-}P})_4+nBF_4]^{(4-n)+}$ with n=1,2. The observed and calculated isotopic patterns of $[Pd_2(\mathbf{MK\text{-}P})_4+BF_4]^{3+}$ are shown in the inset; b) $[Pd_2(\mathbf{RB\text{-}P})_4+nBF_4]^{(4-n)+}$ with n=1,2. The observed and calculated isotopic pattern of $[Pd_2(\mathbf{RB\text{-}P})_4+2BF_4]^{2+}$ is shown in the inset; c) $[Pd_2(\mathbf{MB\text{-}P})4+nBF_4]^{(8-n)+}$ with n=1-5. The observed and calculated isotopic pattern of $[Pd_2(\mathbf{MB\text{-}P})_4+2BF_4]^{6+}$ are shown in the inset; d) ESI-MS spectrum of $[Pd_2(\mathbf{CV\text{-}P})_4+nNO_3]^{(8-n)+}$ with n=2-5. The observed and calculated isotopic pattern of $[Pd_2(\mathbf{CV\text{-}P})_4+3NO_3]^{5+}$ are shown in the inset.

Slow diffusion of ethyl acetate in the DMSO solution of $[Pd_2(\mathbf{RB\text{-}P})_4]$, toluene in the DMSO solution of $[Pd_2(\mathbf{MK\text{-}P})_4]$ and of methyl *tert*-butyl ether in the DMF solution of $[Pd_2(\mathbf{CV\text{-}P})_4]$ afforded single crystals suitable for X-ray diffraction. In Figure 4.11, the three crystal structures together with the DFT (B3LYP/def2-SV(P)) calculated structure for cage $[Pd_2(\mathbf{MB\text{-}P})_4]$ are shown.

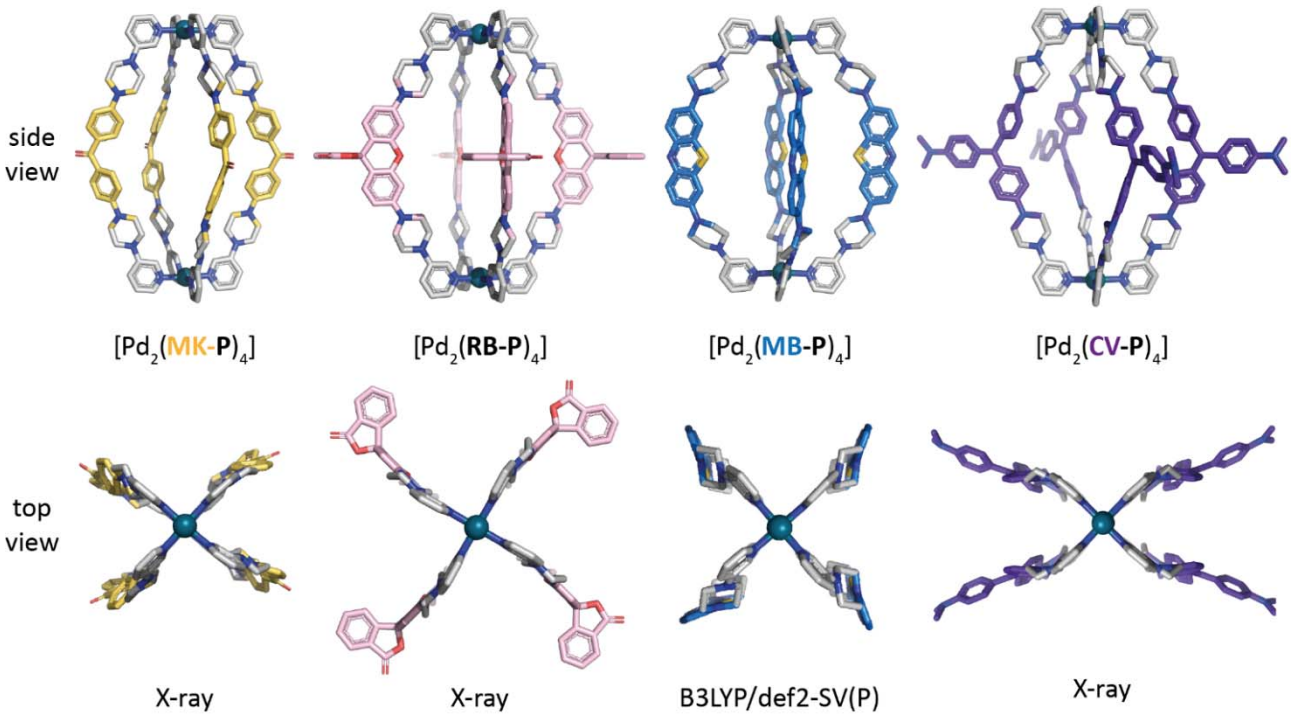

Figure 4.11: Side and top view of the X-ray crystal structures for $[Pd_2(\mathbf{MK\text{-}P})_4]$, $[Pd_2(\mathbf{RB\text{-}P})_4]$ and $[Pd_2(\mathbf{CV\text{-}P})_4]$ and the DFT (B3LYP/def2-SV(P)) calculated structure for $[Pd_2(\mathbf{MB\text{-}P})_4]$ as indicated in the Figure. Counterions and solvent molecules have been omitted for clarity.

As already mentioned above, the structure of $[Pd_2(\mathbf{RB\text{-}P})_4]$ reveals two possible orientations for the spirolactone group in each ligand, giving rise to four possible isomers (Figure 4.12) which is consistent with the broadened ^{1}H NMR spectrum observed for this cage.

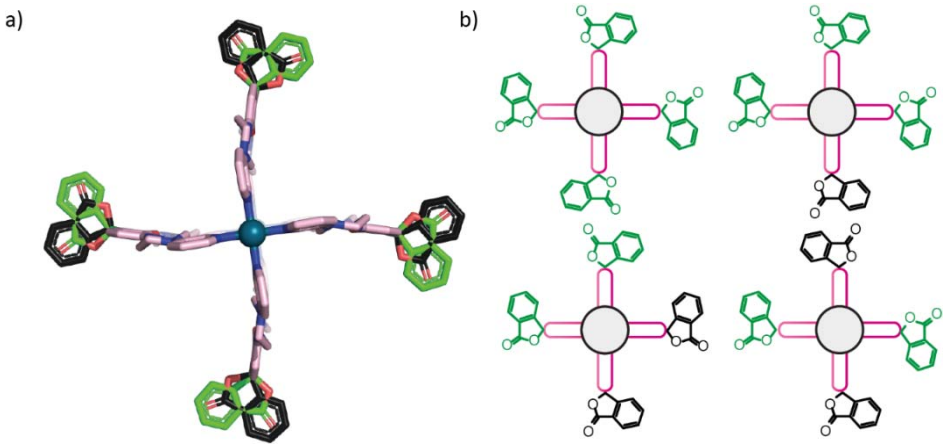

Figure 4.12: a) Top view of the crystal structure of $Pd_2(\mathbf{RB\text{-}P})_4]$ with the two disordered position of the spirolactone group visible in black and green. b) Schematic top view on the four different conformers that can originate from the mutual disposition of the lactone functional group in the ligand **RB-P**.

For the highest-resolution structure obtained (0.80 Å, see section 4.8.4), $[Pd_2(\mathbf{MK\text{-}P})_4]$, disorder was found around the piperazine linkers of the molecule, indicating the high flexibility of the structure and supporting the dynamic nature of the linker, which is characterized by the conformational interconversion equilibrium.

4.3.3 Electronic properties of the parental dyes

Interested in understanding whether the electronic properties of the parental dyes were maintained also in the supramolecular architectures, some experiments were performed with cages $[Pd_2(\mathbf{MB\text{-}P})_4](BF_4)_8$ and $[Pd_2(\mathbf{RB\text{-}P})_4](BF_4)_4$.

The methylene blue dye functionality is embedded in cage $[Pd_2(\mathbf{MB\text{-}P})_4](BF_4)_8$, which, as explained in the introduction of this chapter, can be reduced to its neutral and colorless leuco form $\mathbf{MB^R}$. In the cage assembly, the most straightforward technique to assess different charge states of the assembly upon reduction of the ligands' backbones, relies on mass spectrometry. Indeed, treating the cage sample in DMSO with zinc powder, afforded a high resolution mass spectrum in which the statistical distribution of oxidized (**MB-P**) and reduced ($\mathbf{MB^R\text{-}P}$) ligands were contained in the $[Pd_2L_4]$ assembly, described by the formula $\{[Pd_2(\mathbf{MB\text{-}P})_x(\mathbf{MB^R\text{-}P})_{4-x}](BF_4)_{4+x-z}\}^{z+}$(x=1..3; z=2-4). The HR-ESI mass spectrum is reported in Figure 4.13 together with the isotopic pattern simulation of the species observed with charge 2+ - 4+.

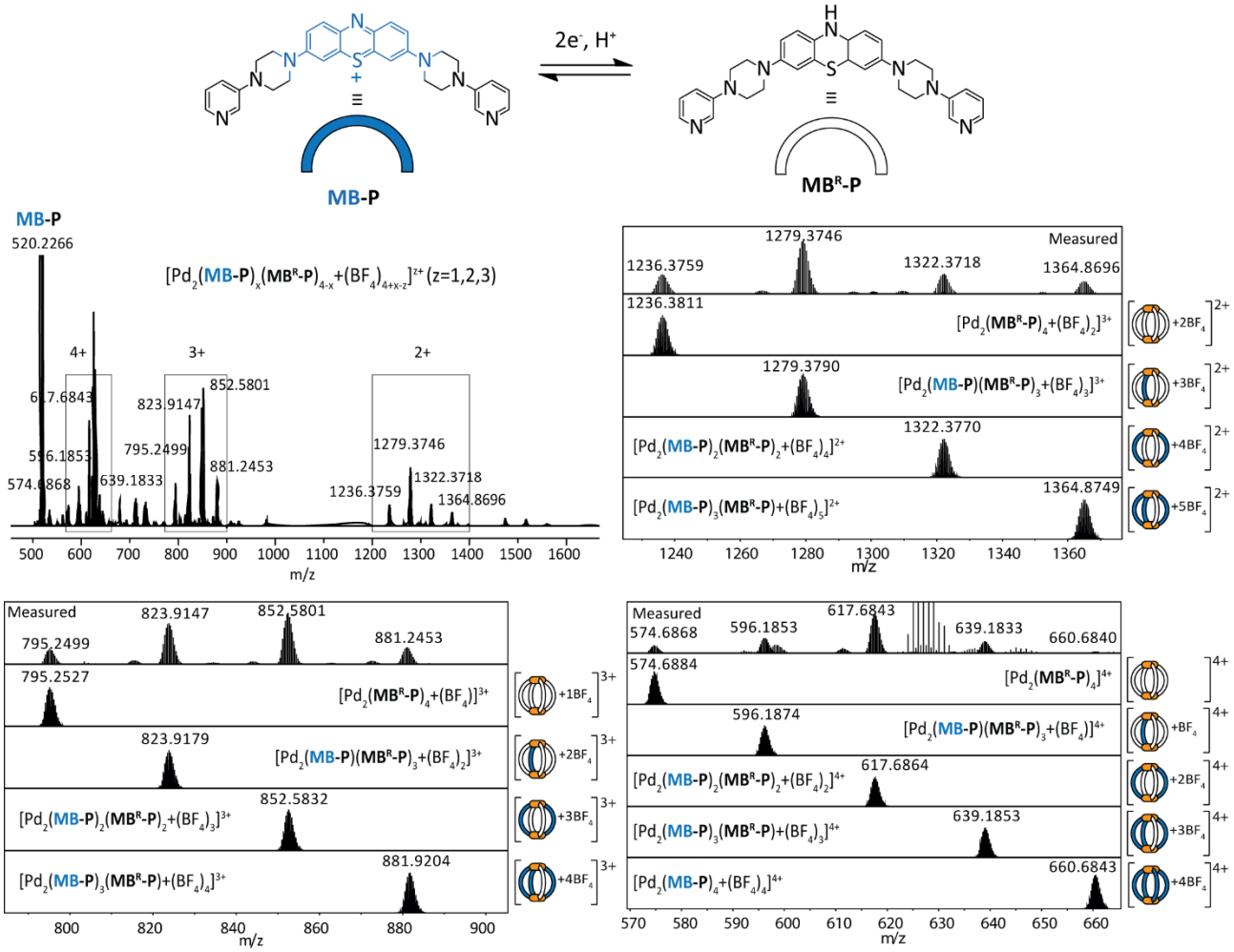

Figure 4.13: ESI-MS spectrum of $\{[Pd_2(\mathbf{MB\text{-}P})_x(\mathbf{MB^R\text{-}P})_{4-x}](BF_4)_{4+x-z}\}^{z+}$ with x=0-3 and z=2-4, obtained by treating the 0.7 mM DMSO solution of $[Pd_2(\mathbf{MB\text{-}P})_4](BF_4)_8$ with Zn powder, diluting with degassed acetonitrile, and directly injected into the mass spectrometer. Top left, full spectrum with assignment of the peak at 520.2266 to ligand **MB-P**. Top right, zoom in the spectral area 1230-1380 m/z where the 2+ peaks are present and their isotopic patter simulation with formula and assignment are shown in the Figure. Bottom left, zoom in the spectral area 785-910 m/z where the 3+ peaks are present and their isotopic patter simulation with formula and assignment are shown in the Figure. Bottom right, zoom in the spectral area 570-670 m/z where the 4+ peaks are present and their isotopic patter simulation with formula and assignment are shown in the Figure.

On the other hand, when a colorless DMSO (Reichardt solvent polarity $E_T^N = 0.44$)[36] solution of $[Pd_2(\mathbf{RB\text{-}P})_4]$ was exposed to increasing amounts of more polar solvent like acetonitrile ($E_T^N = 0.46$), methanol

(E_T^N = 0.76) or water (E_T^N = 1.00), the typical intense pink color of the optical active zwitterionic form of the dye was observed (**RB**$^{+-}$). In Figure 4.14, pictures of the vials containing [Pd_2(**RB-P**)$_4$] in DMSO/polar solvent mixtures in different ratios are shown. Even by eye, the change in the solution coloration can be nicely appreciated. ^{1}H NMR spectra served as controls to assess cage stability under such solvent polarity (see experimental part, Figure 4.113). Furthermore, in some solvent mixtures (e.g. 9:1 water:DMSO), it could be observed that, while the ligand is not soluble and forms a pink flakes precipitate, the Pd-assembly represents dark pink homogeneous solutions (Figure 4.14 c).

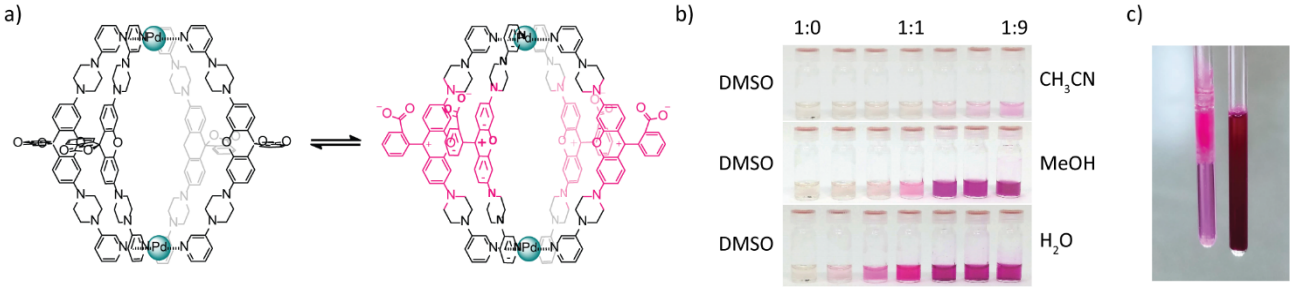

Figure 4.14: a) Schematic representation of the lactone equilibrium of the Rhodamine B ligand embedded in the cage assembly. b) Pictures of vials containing [Pd_2(**RB-P**)$_4$] and increasing amounts of the polar solvent CH_3CN, MeOH and H_2O. The pink coloration arising corresponds to the open zwitterionic form of the dye. c) Picture of two NMR tubes containing ligand **RB-P** and cage [Pd_2(**RB-P**)$_4$] in the DMSO:D_2O 1:9 ratio. The ligand is not soluble in this condition whereas the cage represents a homogeneous solution.

Unfortunately, quantification of the fraction of opened chromophores was hampered by strong signal broadening of the NMR spectra of DMSO/polar solvents mixtures.

4.3.4 Cage [Pd_2(RE-P)$_4$](EtSO$_4$)$_4$(BF$_4$)$_4$

Ligand **RB-P** was converted into ligand **RE-P** in which the colored open form is secured by esterification of the carboxylic moiety. The corresponding cage [Pd_2(**RE-P**)$_4$] could then be formed and unambiguously characterized as described for the other systems. In Figure 4.15, the synthetic route, ESI-MS spectrum, and the stacked ^{1}H NMR spectra of ligand **RE-P** and corresponding cage are reported.

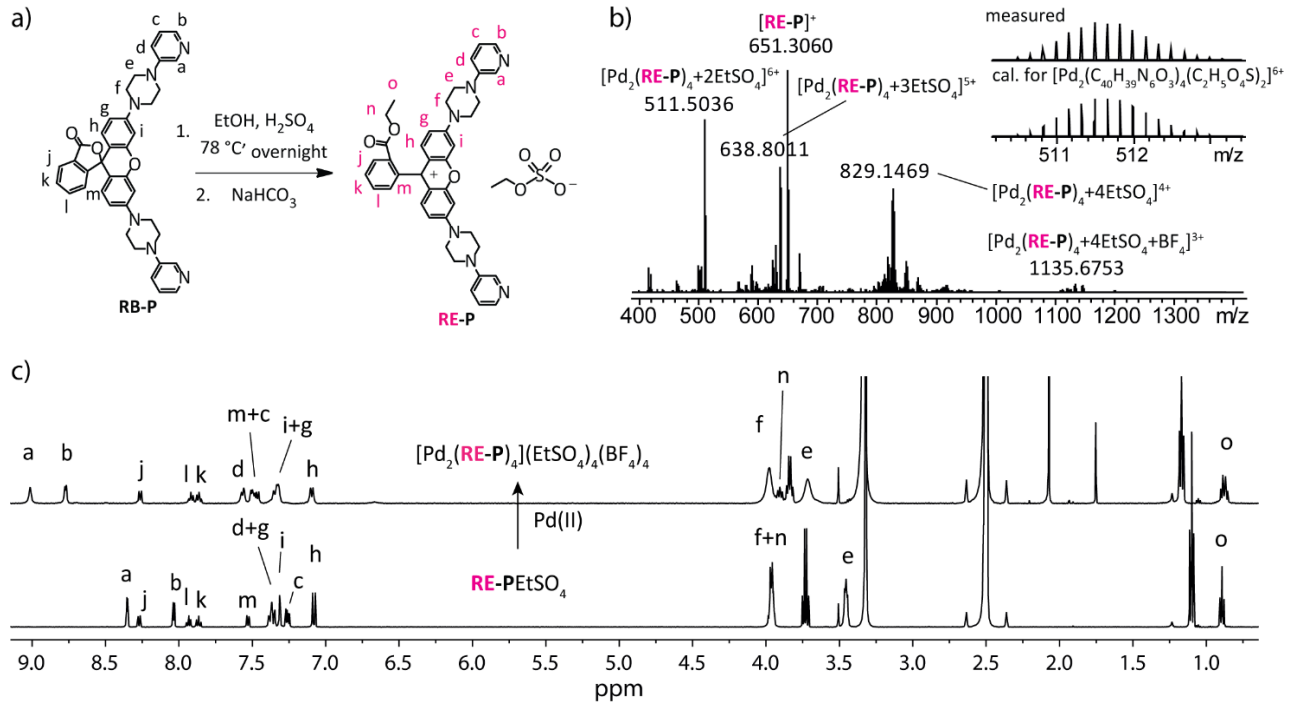

Figure 4.15: a) Synthesis of ligand **RE-P** from **RB-P**, b) ESI-MS spectrum of [Pd_2(**RE-P**)$_4$+n$EtSO_4$+mBF_4]$^{(8-n-m)+}$ with n=2-4, m=0,1. The observed and calculated isotopic patterns of [Pd_2(**RE-P**)$_4$+2$EtSO_4$]$^{6+}$ are shown in the inset. c) Stacked ^{1}H spectra NMR of ligand **RE-P** and corresponding cage.

4.4 Synthesis of DYE-Q ligands and cages

4.4.1 Isoquinoline ligands synthesis (DYE-Q)

To furthermore increase the structural complexity of the systems and confer a helical twist to the [Pd_2L_4] cages, isoquinoline coordinating groups were introduced instead of the pyridine ones (Figure 4.4). Ligands **MK-Q**, **RB-Q**, **MB-Q**, **CV-Q** were synthesized according to the previous described procedure for **DYE-P** ligands (section 4.3.1) employing 8-(piperazin-1-yl)isoquinoline (Figure 4.16). The newly synthetized compound was obtained from a Buchwald-Hartwig amination of 8-bromoisoquinoline with piperazine.

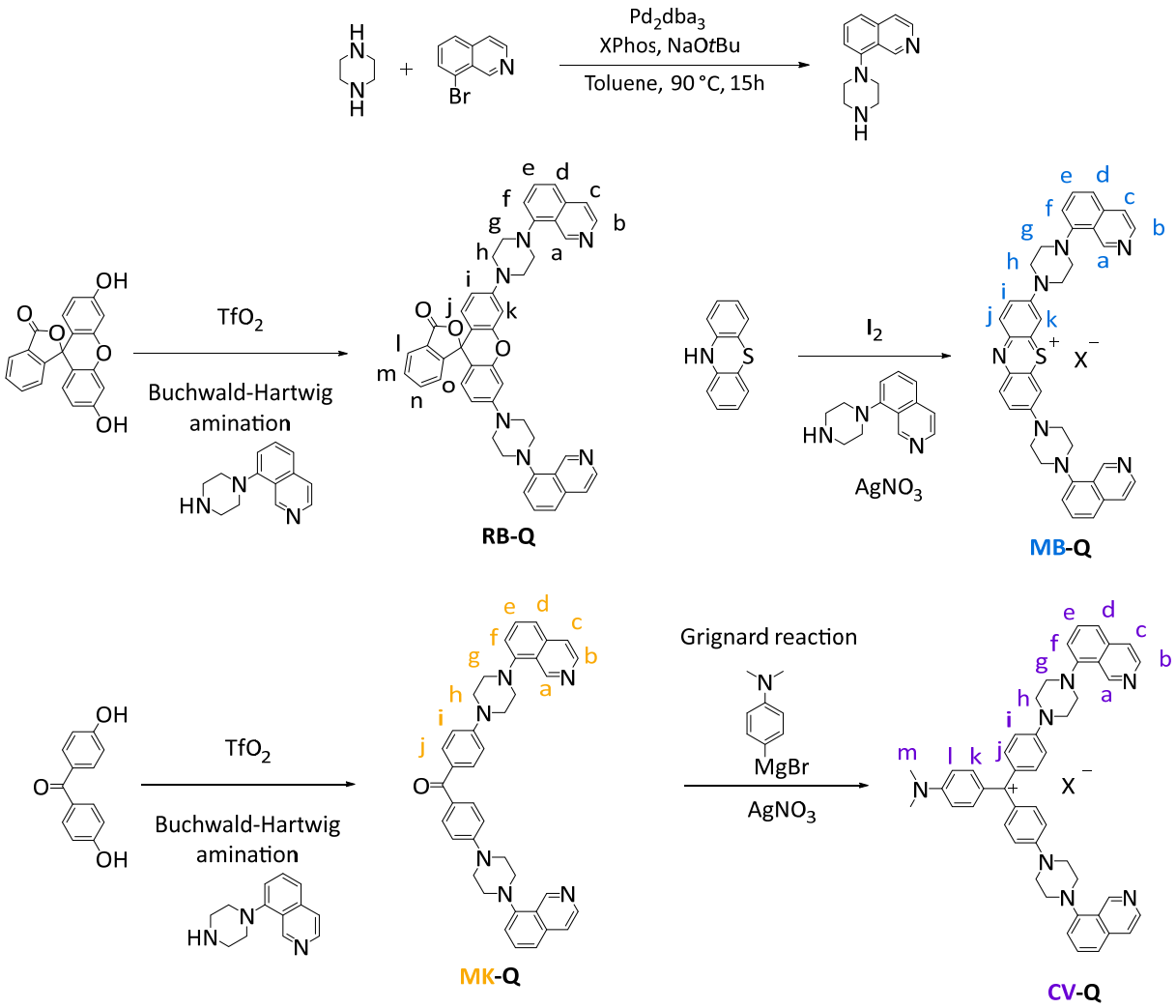

Figure 4.16: Synthetic routes for ligands **RB-Q**, **MB-Q**, **MK-Q** and **CV-Q.**

4.4.2 Assembly and properties of [Pd_2(DYE-Q)$_4$] cages

Corresponding [Pd_2L_4] cages were assembled as previously described for the pyridine derivatives but differ from the latter by their characteristic dynamic behavior. As already observed by the Clever group,[37] coordination cages deriving from ligands possessing two inward-pointing isoquinolin-8-yl donors adopt a helical structure as the ligands twist around the Pd_2-axis, resulting in a *M*- or *P*-configured chiral conformation. The formation of the desired species was confirmed *in primis* by ESI-MS spectrometry (Figure 4.18), since ^{1}H NMR spectra were, in some cases, of difficult interpretation. Further experimental support was obtained with ^{1}H DOSY measurements (section 4.5.2). In Figure 4.17, the stacked ^{1}H NMR spectra of the ligands and assemblies are depicted. It can be noted how, upon palladium addition, the signals get generally more broadened, an indication for highly dynamic systems. In order

to give a more exhaustive description of the studied supramolecular architectures, in the next sections each assembly will be covered separately.

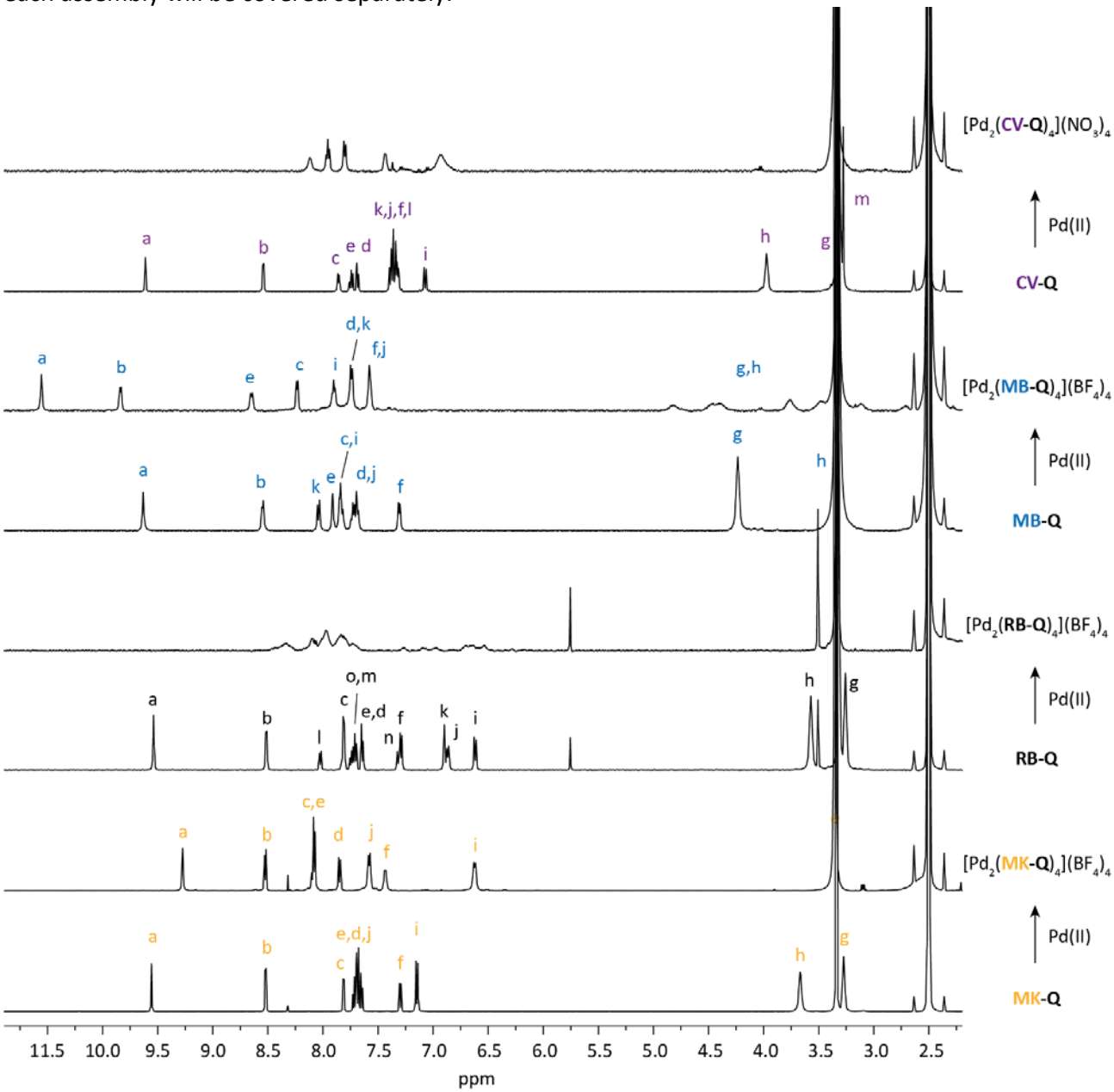

Figure 4.17: Stacked ^{1}H NMR spectra of **DYE-Q** ligands and upon addition of 0.5 equiv. Pd(II) salts in DMSO-d_6 at 298 K. Every spectrum corresponds to the species written on the right. The assignment refers to Figure 4.16.

In Figure 4.18, the measured spectra for the [Pd_2(**DYE-Q**)$_4$] assemblies with the peaks corresponding to a) [Pd_2(**MK-Q**)$_4$+nBF_4]$^{(4-n)+}$ with n=1-2, b) [Pd_2(**RB-Q**)$_4$+nBF_4]$^{(4-n)+}$ with n=1-2, c) [Pd_2(**MB-Q**)4+nBF_4]$^{(8-n)+}$ with n=2-5 and d) [Pd_2(**CV-Q**)$_4$+nNO_3]$^{(8-n)+}$ with n=3-6 are reported. In Figure 4.19 the DFT (B3LYP/def2-SV(P)) calculated structures for the helical twisted supramolecular assemblies are reported (only one enantiomer per cage).

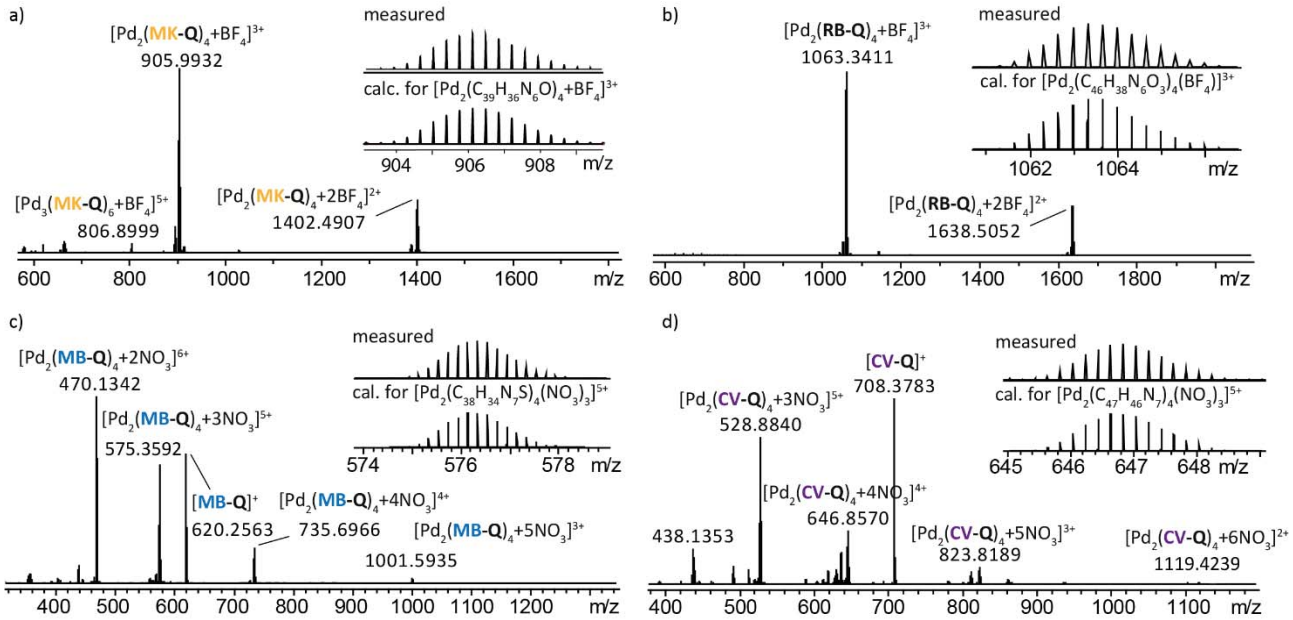

Figure 4.18: ESI-MS spectra of $[Pd_2(\mathbf{DYE\text{-}Q})_4]$ assemblies. a) $[Pd_2(\mathbf{MK\text{-}Q})_4+nBF_4]^{(4-n)+}$ with n=1,2. The observed and calculated isotopic patterns of $[Pd_2(\mathbf{MK\text{-}Q})_4+BF_4]^{3+}$ are shown in the inset; b) $[Pd_2(\mathbf{RB\text{-}Q})_4+nBF_4]^{(4-n)+}$ with n=1,2. The observed and calculated isotopic patterns of $[Pd_2(\mathbf{RB\text{-}Q})_4+BF_4]^{3+}$ are shown in the inset; c) $[Pd_2(\mathbf{MB\text{-}Q})4+nNO_3]^{(8-n)+}$ with n=2-5. The observed and calculated isotopic patterns of $[Pd_2(\mathbf{MB\text{-}Q})_43BF_4]^{5+}$ are shown in the inset; d) ESI-MS spectrum of $[Pd_2(\mathbf{CV\text{-}Q})_4+nNO_3]^{(8-n)+}$ with n=3-6. The observed and calculated isotopic patterns of $[Pd_2(\mathbf{CV\text{-}Q})_4+3NO_3]^{5+}$ are shown in the inset.

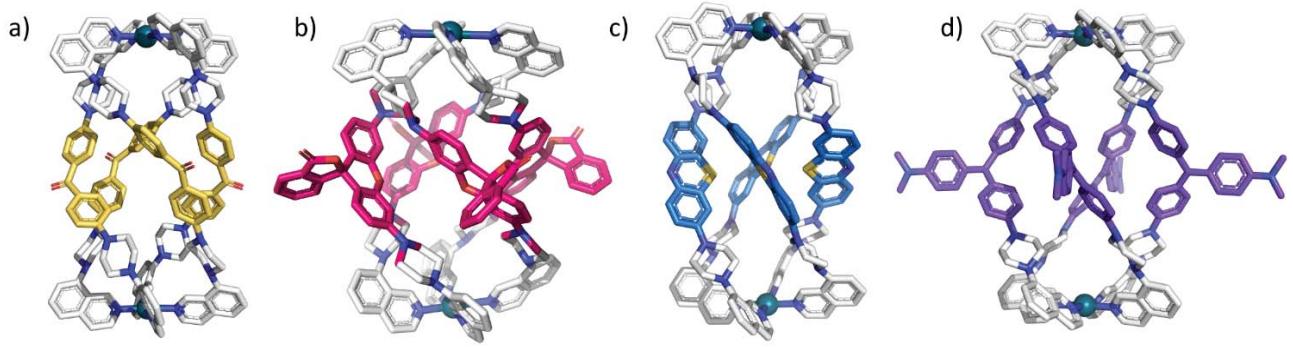

Figure 4.19: DFT calculated models (B3LYP/def2-SV(P)) for $[Pd_2(\mathbf{DYE\text{-}Q})_4]$ cages a) $[Pd_2(\mathbf{MK\text{-}Q})_4]$, b) $[Pd_2(\mathbf{RB\text{-}Q})_4]$, c) $[Pd_2(\mathbf{MB\text{-}Q})_4]$ and d) $[Pd_2(\mathbf{CV\text{-}Q})_4]$.

Cage $[Pd_2(\mathbf{MB\text{-}Q})_4]$

When ligand **MB-Q** is mixed in a 2:1 ratio with $Pd(NO_3)_2{\cdot}2H_2O$, the cage $[Pd_2(\mathbf{MB\text{-}Q})_4]$ forms both in DMSO and in water (where the ligand **MB-Q** is not soluble). In Figure 4.20, the ^{1}H NMR spectra in DMSO-d_6 of the cage are depicted at various temperatures. At r.t. the signals assigned to the -CH_2- protons of the piperazine moieties split into eight broad signals, resulting from slow dynamics of the piperazine chair conformers and their diastereotopic nature within the chiral environment in the helically twisted overall structures. At 75 °C the signals coalesce into two broad signals, as expected for a situation where both the piperazine ring-flip as well as the overall cage twist are fast on the NMR time scale. These dynamics were assumed to be dependent on the solvent. Indeed, the ^{1}H NMR spectrum of $[Pd_2(\mathbf{MB\text{-}Q})_4]$ in D_2O at r.t. shows only two signals (Figure 4.21), indicating faster exchange dynamics in the aqueous medium.

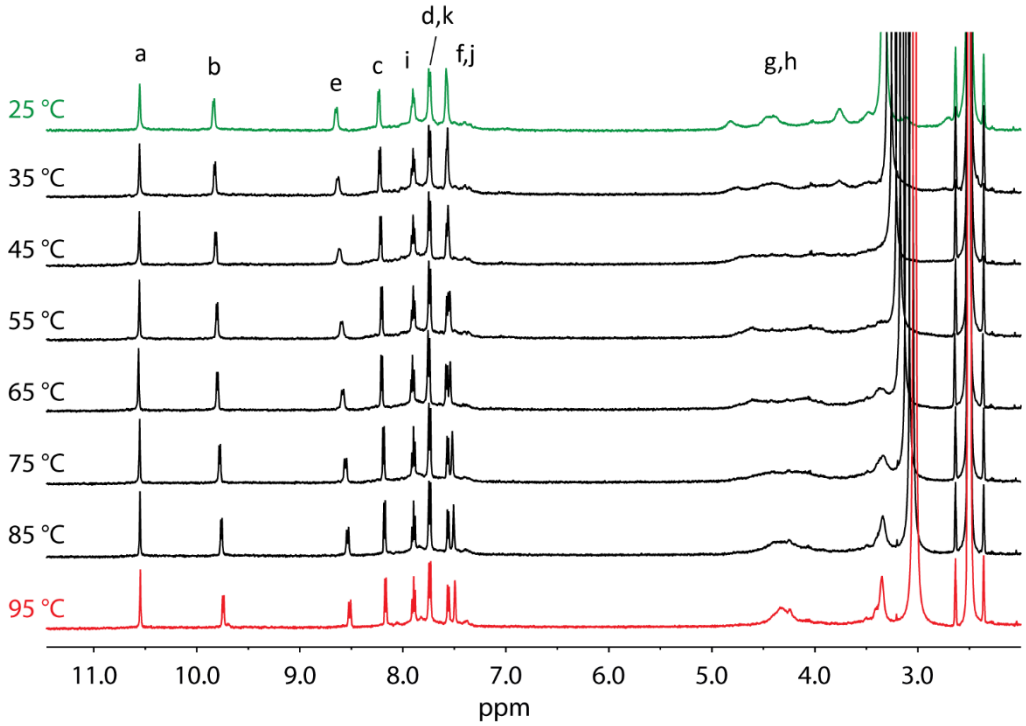

Figure 4.20: Stacked ^{1}H NMR spectra (500 MHz, DMSO-d_6) of cage [Pd_2(**MB-Q**)$_4$] at different temperatures indicated in the Figure. The assignment of the signals refers to Figure 4.16. The region around 5-3 ppm shows the coalescence of the signals assigned to protons H^g and H^h into 2 signals upon rising of the temperature.

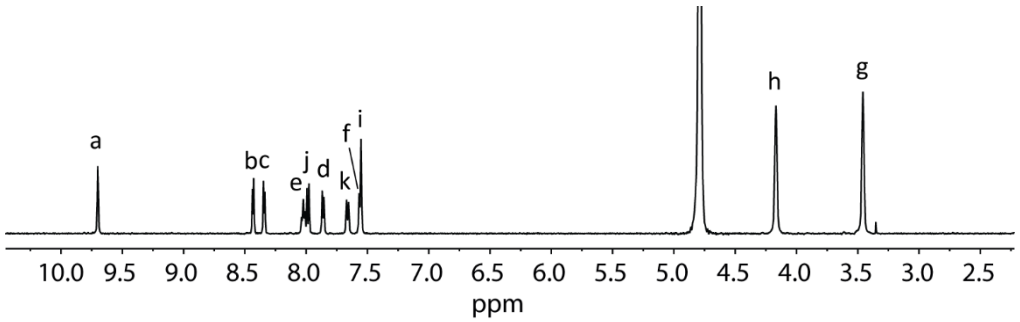

Figure 4.21: ^{1}H NMR spectrum (600 MHz, 298K, D_2O) of the cage [Pd_2(**MB-Q**)$_4$]. The assignment of the signals refers to Figure 4.16.

Cage [Pd_2(MK-Q)$_4$]

Similar to [Pd_2(**MB-Q**)$_4$], [Pd_2(**MK-Q**)$_4$] assembles in DMSO from ligand **MK-Q** and [$Pd(CH_3CN)_4$](BF_4)$_2$. In contrast to [Pd_2(**MB-Q**)$_4$], the signals assigned to proton H^a and H^b, the closest to the coordinating nitrogen atom, instead of being subjected to a downfield shift upon coordination to the Pd(II), they shift in the opposite direction (Figure 4.17, first two stacked spectra, yellow assignment). Such effect is rarely observed, since the usual shift is downfield, however, the coordination of the nitrogen atom to the metal cation is not the only effect that causes the shift, also the steric hindrance around the coordination center and the forced propeller disposition of the donor groups might influence the chemical and magnetic environment around the involved protons. The high dynamicity of the assembly is evidenced by the disappearance of the piperazine signals (H^g and H^h) from the spectrum at r.t. Upon rising of the temperature, one single, broadened signal appears around 2.7 ppm (Figure 4.22).

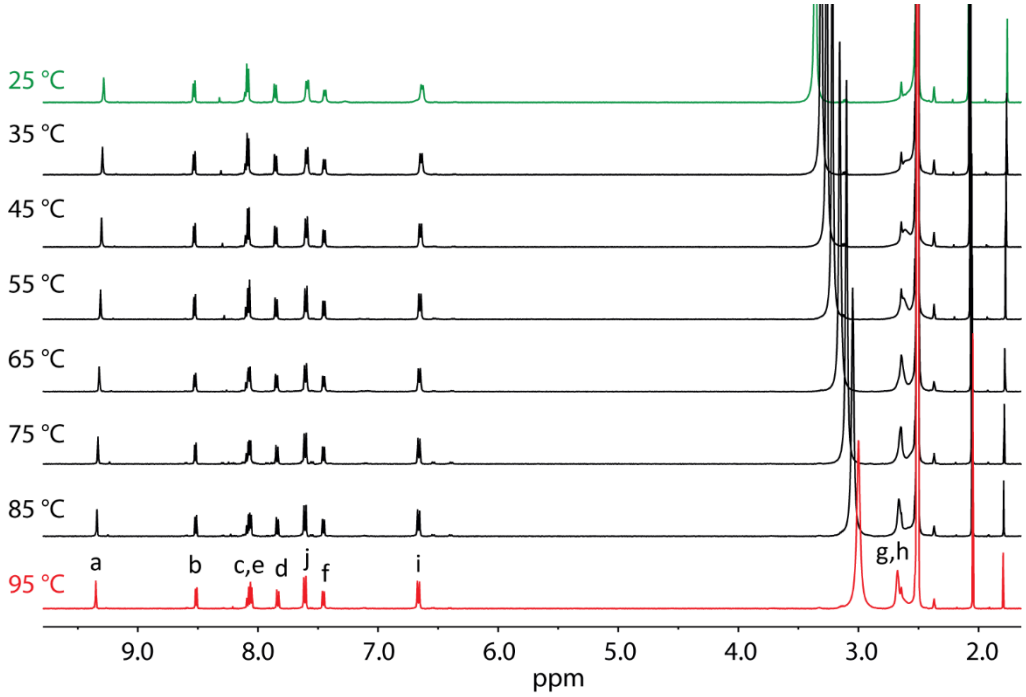

Figure 4.22: Stacked ^{1}H NMR spectra (500 MHz, DMSO-d_6) of cage [Pd_2(**MK-Q**)$_4$] at different temperatures indicated in the Figure. The assignment of the signals refers to Figure 4.16. The region around 3-2 ppm shows appearance of signals assigned to protons H^g and H^h into one signal upon rising of the temperature.

By slow vapor diffusion of toluene into the DMSO solution of [Pd_2(**MK-Q**)$_4$], small yellow crystals suitable for synchrotron X-ray diffraction were obtained. While ESI-MS clearly supports the dinuclear [Pd_2(**MK-Q**)$_4$] stoichiometry in solution (Figure 4.18 a), the obtained solid-state structure surprisingly revealed the formation of a three-membered ring [Pd_3(**MK-Q**)$_6$] (Figure 4.23). The conformational flexibility of the **MK** backbone facilitates the structural rearrangement in the course of the crystallization process. From the structure, it is possible to appreciate the nice propeller disposition of the isoquinoline donor groups around the metal centers and the overall twisted ligand conformation.

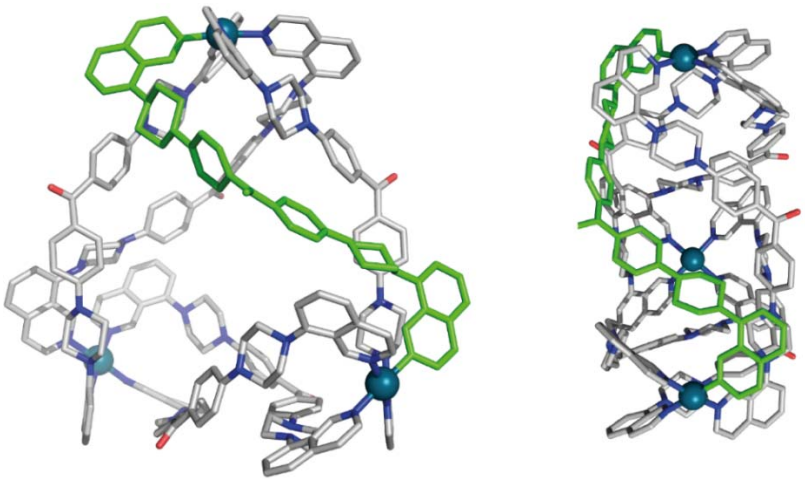

Figure 4.23: Two views of the X-ray crystal structure of one of the found enantiomers for [Pd_3(**MK-Q**)$_6$]. One ligand has been colored green for better comprehension of the structure. Counterions and solvent molecules have been omitted for clarity.

In solution, ^{1}H DOSY spectroscopy reveals one prevalent species with hydrodynamic values inline with the other [Pd_2(**DYE-Q**)$_4$] cages (Table 4.1), and a second species (Figure 4.24 a), in very low concentration,

with a integral ratio of 100:4, and only visible if the spectral intensity is increased (Figure 4.24 b; red) with larger hydrodynamic radius.

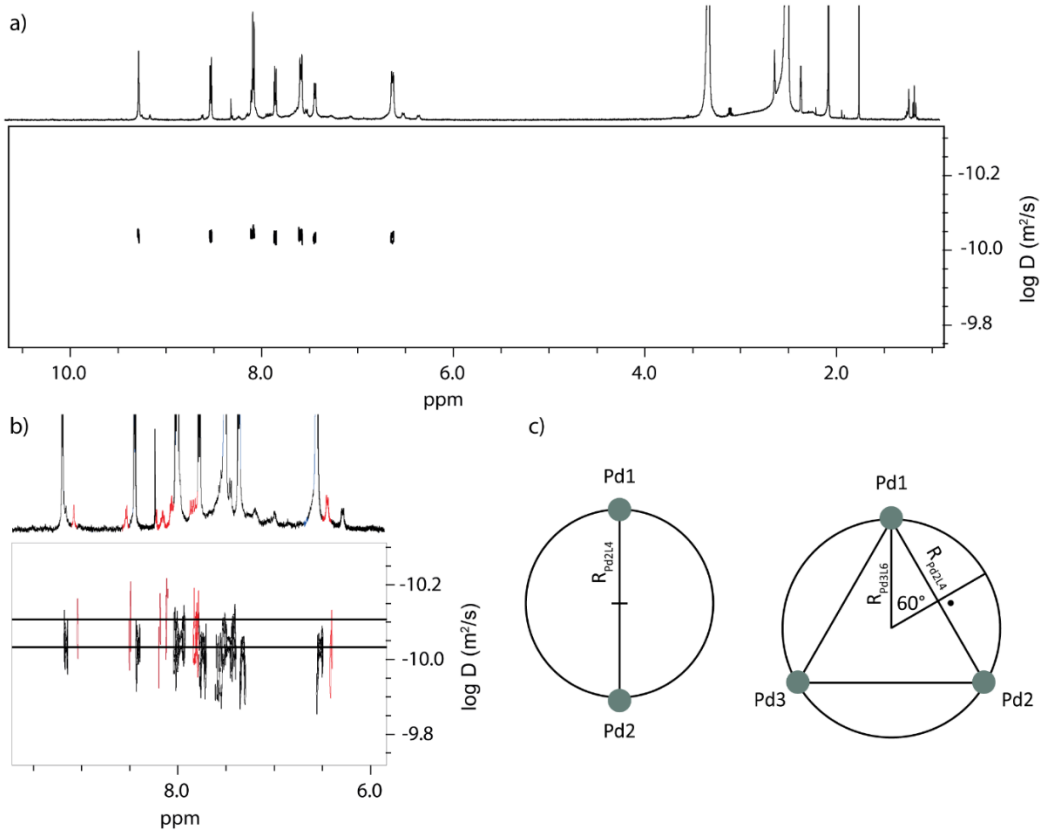

Figure 4.24: a) ^{1}H DOSY spectrum (500 MHz, 298K, DMSO-d_6) of $[Pd_2(\mathbf{MK\text{-}Q})_4](BF_4)_4$. Diffusion coefficient: 9.399×10^{-11} m^2s^{-1}, log D=−10.003. Hydrodynamic radius=11.68 Å. b) Enlargement of ^{1}H DOSY spectrum (500 MHz, 298K, DMSO-d_6) of $[Pd_2(\mathbf{MK\text{-}Q})_4](BF_4)_4$. A second species with higher diffusion coefficient can be observed: 8.039×10^{-11} m^2s^{-1}, log D=-10.095. Hydrodynamic radius=13.65 Å. Such hydrodynamic radius matches with expected hydrodynamic radius for $[Pd_3(\mathbf{MK\text{-}Q})_6](BF_4)_6$. c) Geometrical estimation of the hydrodynamic radius for $[Pd_3(\mathbf{MK\text{-}Q})_6](BF_4)_6$ and comparison with the measured one with ^{1}H DOSY spectroscopy. In the 2D simplification, the Pd-Pd distances in the cage $[Pd_2L_4]$ and in the ring P_3L_6 are assumed to be equal.

The second larger assembly was assumed to be the $[Pd_3L_6]$ ring. In order to support this hypothesis, the expected increase in hydrodynamic radius from a $[Pd_2L_4]$ cage to a $[Pd_3L_6]$ ring was calculated. In a 2D geometrical simplification where the Pd-Pd distances in the two assemblies are the same (Figure 4.24 c), the two hydrodynamic radii are associated by the equivalence in the formula:

$$R_{Pd_3L_6} \simeq \frac{2}{\sqrt{3}} R_{Pd_2L_4}$$

Table 4.1: Hydrodynamic radii calculated from the diffusion coefficient deriving from DOSY experiments and the calculated hydrodynamic radius calculated using the formula here above described.

	DOSY	Calc.
$R_{Pd_2L_4}$	11.63 Å	11.63 Å (input)
$R_{Pd_3L_6}$	13.65 Å	13.43 Å (result)

In Table 4.1, the hydrodynamic radii extrapolated from DOSY measurement of the two species, the smaller one attributed to $[Pd_2L_4]$ with 11.63 Å and the larger one assigned to $[Pd_3L_6]$ with 13.65 Å, and the expected hydrodynamic radius for $[Pd_3L_6]$ deriving from the calculation of 13.43 Å, are reported. In

view of the small deviation for the measured and calculated values for $[Pd_3L_6]$, it can be concluded that ligand **MK-Q** mainly assembles in $[Pd_2L_4]$ topology in solution, however with a small percentage of formation of the $[Pd_3L_6]$ topology which is the preferred one in the solid state in the particular crystallization conditions with a DMSO/toluene mixture.

Cage $[Pd_2(RB\text{-}Q)_4]$

Cage $[Pd_2(\mathbf{RB\text{-}Q})_4]$ can be assembled from ligand **RB-Q** and $[Pd(CH_3CN)_4](BF_4)_2$ both in CD_3CN and DMSO-d_6. The ^1H NMR spectrum of cage $[Pd_2(\mathbf{RB\text{-}Q})_4]$ at r.t. is very broadened and different temperatures have the effect of sharpening the signals but leading to complicated splitting effects (Figure 4.25 a). Since its ESI-MS analysis indicated the exclusive formation of $[Pd_2(\mathbf{RB\text{-}Q})_4]$, the convoluted NMR behavior is assigned to the isomery of the spirolactons (as discussed for $[Pd_2(\mathbf{RB\text{-}P})_4]$), in combination with dynamic interconversion between two chiral conformers (Figure 4.26 b).

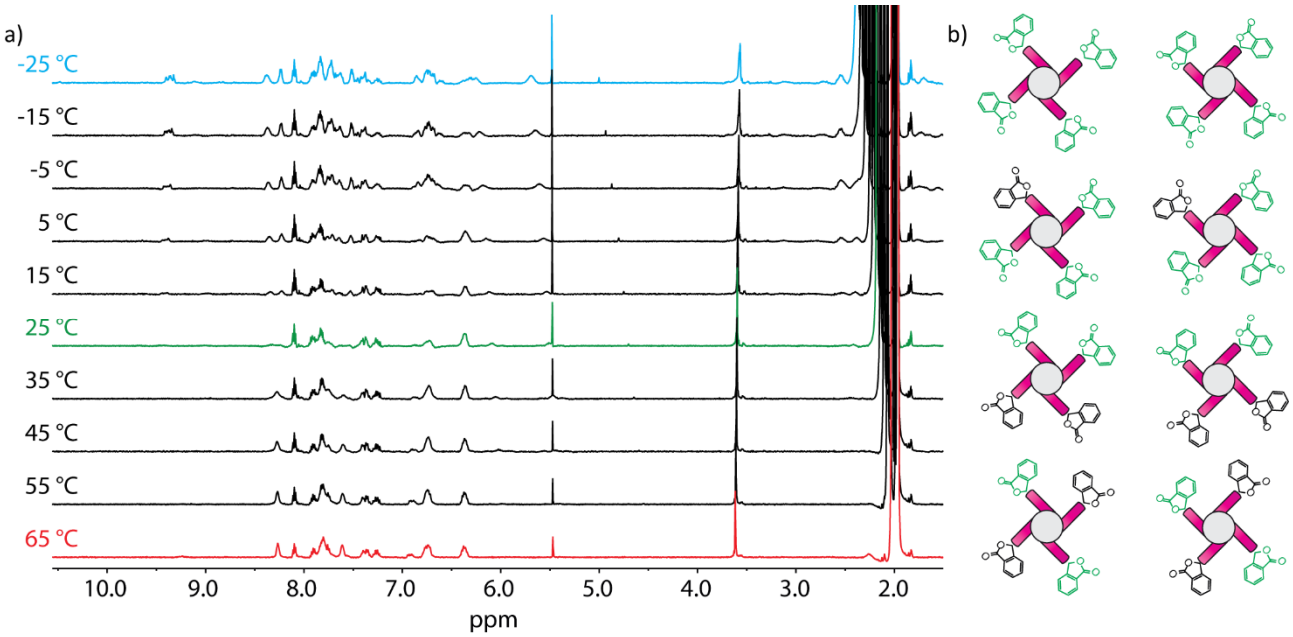

Figure 4.25: a) Stacked ^1H NMR spectra (500 MHz, CD_3CN) of cage $[Pd_2(\mathbf{RB\text{-}Q})_4]$ at different temperatures indicated in the Figure. In green r.t., in blue the lowest temperature and in red the highest temperature. Both signals at higher and lower temperature are sharper than at r.t. with the lower one showing also signals at high ppm values. However, the complicated spectrum did not allow assignment of the signals. b) Schematic top view on the four different conformers for $[Pd_2(\mathbf{RB\text{-}Q})_4]$ that can originate from the mutual disposition of the lactone functional group in the ligand **RB-Q** in combination with the direction of the helical twist.

Cage $[Pd_2(CV\text{-}Q)_4]$

Cage $[Pd_2(\mathbf{CV\text{-}Q})_4]$ can be assembled both in CD_3CN and DMSO-d_6. In Figure 4.26 the stacked ^1H NMR spectra of ligand **CV-Q** (in black) and after addition of the Pd(II) salt (in green) are depicted for both solvents. While the ^1H NMR spectrum in CD_3CN is well resolved and full assignment with the signals being subjected to the typical downfield shift is possible, the DMSO-d_6 spectrum is broadened and multiple signals are missing. Also this assembly is characterized by solvent dependent dynamics as confirmed by variable temperature NMR experiments (Figure 4.27). In DMSO-d_6 the signals sharpen with the rising of the temperature until full-assignable spectra are measured from 75°C and higher. In CD_3CN, increasing the temperature from r.t. causes coalescence of the signals assigned to the piperazine signals around 3 ppm, while decreasing the temperature has the effect of broadening the signals with a situation at -25°C being similar to the r.t. spectrum in DMSO-d_6 (blue line in b) and green line in a).

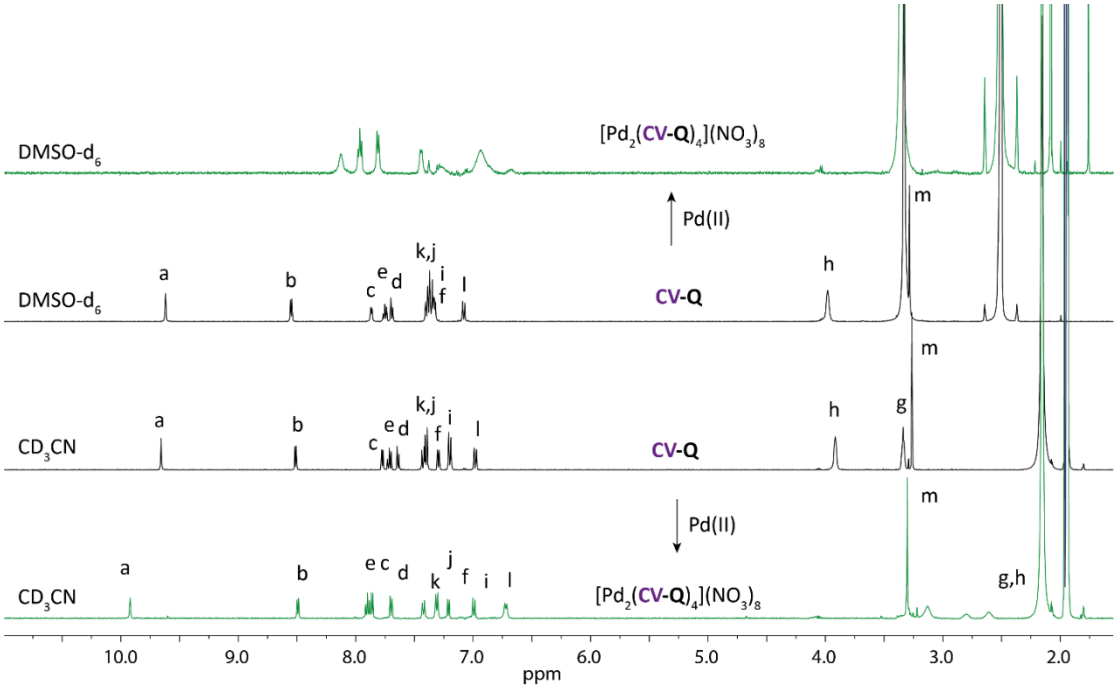

Figure 4.26: Stacked ^{1}H NMR spectra (500 MHz, 298K) of ligand **CV-Q** (in the middle in black) in CD_3CN and DMSO-d_6 and the correspondent cage $[Pd_2(\mathbf{CV\text{-}Q})_4](NO_3)_8$ (in green) upon addition of 0.5 equiv. of Pd(II) salt in DMSO-d_6 on the top and CD_3CN on the bottom, as indicated in the figure. The assignment of the signals refers to Figure 4.16.

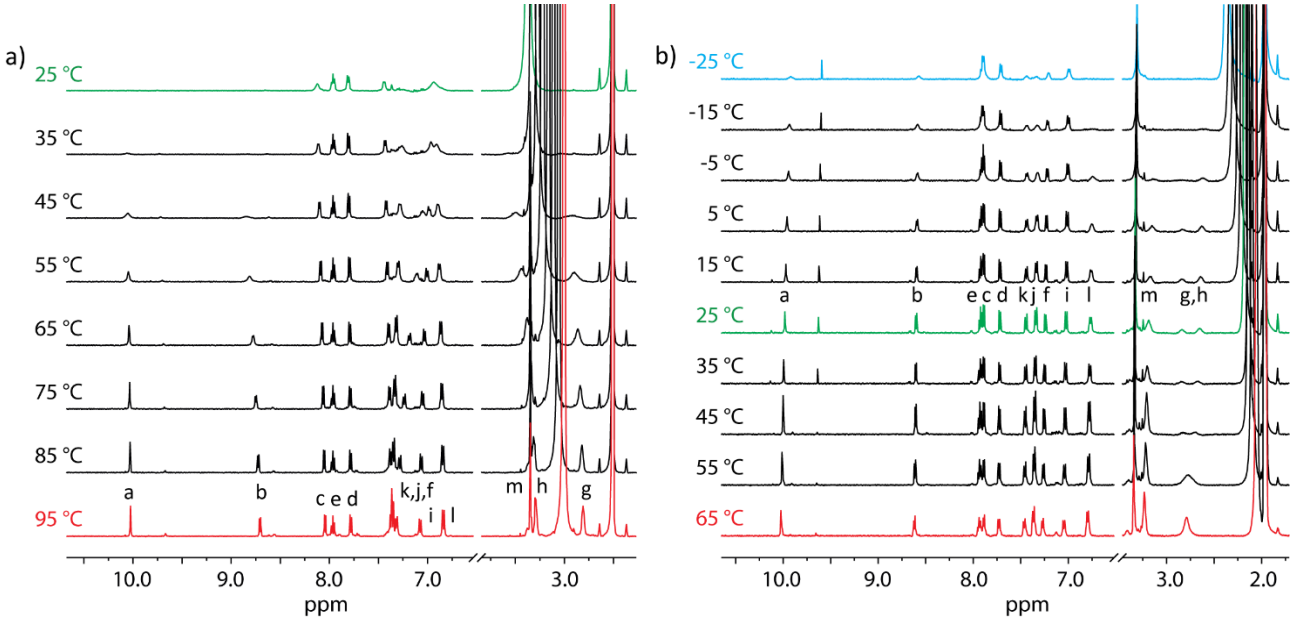

Figure 4.27: Stacked ^{1}H NMR (500 MHz) spectra of cage $[Pd_2(\mathbf{CV\text{-}Q})_4]$ at the different temperature indicated in the Figure. In green r.t., in blue the lowest temperature and in red the highest temperature. The assignment of the signals refers to Figure 4.16. a) In DMSO-d_6, the signals become sharper with the rising of the temperature until full assignable spectra are measured from 75°C and higher. b) In CD_3CN, increasing the temperature from r.t. causes coalescence of the piperazine signals around 3 ppm, while decreasing the temperature has the effect of broadening the signals with a situation at -25°C being similar to the r.t. spectrum in DMSO-d_6 (blue line in b) and green line in a). The signal at 9.6 ppm in b) that is not assigned to the cage, is attributed to decomposition caused by the measurements at high temperature.

4.5 Properties of the assemblies and building blocks

4.5.1 UV-Vis absorption properties

The optical properties of the new colored ligands and corresponding cages have been studied and characterized. In Figure 4.28, the absorption spectra are reported. The **DYE-P/Q** ligands' absorption maxima closely match the ones reported in the literature for the parental dyes (**MB**,[38] **RB**,[15] **MK**[39] and **CV**[40]). The absorption maximum of the ligand **RE-P** at 551 nm matches the absorption maxima of the protonated ligand **RB-P** (see Figure 4.5). Upon palladium addition, the absorption spectra blue-shift by about 10-30 nm with the shoulder band at higher energies becoming more pronounced.

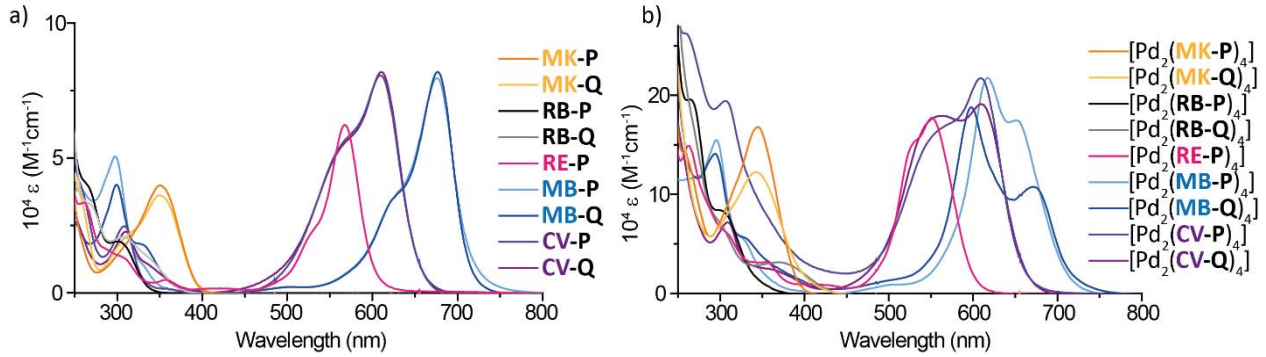

Figure 4.28: Absorption spectra in DMSO of a) the ligands **MK-P** (yellow), **MK-Q** (orange), **RB-P** (black) **RB-Q** (grey), **RE-P** (pink) **MB-P** (light blue), **MB-Q** (dark blue), **CV-P** (light violet), **CV-Q** (dark violet) and b) corresponding cages (with the same color scheme).

4.5.2 ^{1}H-DOSY spectroscopy

To gather additional information over the size of the assemblies, diffusion-ordered spectroscopy (DOSY) experiments were performed on the colored **DYE-P** and **DYE-Q** ligands and corresponding cages. In recent years, DOSY has become a widespread analytical tool for the solution characterization of supramolecular systems. This unique technique allows to virtually separate species present in solution based on their diffusion coefficient (*D*), which is directly correlated to the hydrodynamic radius (r_H), i.e. to the dimension and shape of the diffusing species.[41] Accurate *D* were extrapolated from the T_1 relaxation module analysis from the fitting with the Stejskal-Tanner-Equation[42] of the experimental signal decay (for more details see the experimental part of this chapter, section 4.8.1). In Table 4.1, the values of the self-diffusion coefficients and corresponding hydrodynamic radius, calculated for each assembly and the single molecular building units, are summarized. The Stokes-Einstein equation[43,44] was used to calculate the values of the hydrodynamic radii from the experimental diffusion coefficients determined with DOSY experiments.

$$D = \frac{k_B T}{f^\circ} = \frac{k_B T}{6\pi\eta r_{sph}}$$

where: k_B is the Boltzmann constant, T is the absolute temperature, f° is the friction coefficient in the spherical approximation and $f^\circ = 6\pi\eta r_{sph}$, η being the fluid viscosity, dependent from solvent and temperature. This formula applies to hard spheres that moves in a continuum fluid and does not consider any interaction with the solvent or other specific ones such as ion-pair interaction.[41] For objects that deviate from the ideal sphere, a correction in the friction coefficient that includes the shape factor of the investigated object must be applied. For an ellipsoidal object, it includes a shape factor containing the ratio between semi major (a) and semi minor (b) axes[45] as described by the formula:

$$f = f^\circ \left(\frac{P^{-\frac{1}{3}}(P^2-1)^{1/2}}{\ln[P + (P^2-1)^{1/2}]} \right) \qquad P = \frac{a}{b}$$

Table 4.2: Experimental diffusion coefficient values *D* determined from ^{1}H-DOSY experiments. Hydrodynamic radii r_H calculated from Stokes-Einstein equation. Conditions: [a] (500 MHz, 298K, DMSO-d_6), [b] (500 MHz, 298K, CD_3CN).

	D (m^2s^{-1})	Log *D*	r_H (Å)		*D* (m^2s^{-1})	Log *D*	r_H (Å)
MK-P [a]	1.902×10^{-10}	−9.721	5.77	$[Pd_2(\mathbf{MK\text{-}P})_4]$[a]	8.559×10^{-11}	−10.068	12.83
RB-P [a]	1.667×10^{-10}	−9.778	6.59	$[Pd_2(\mathbf{RB\text{-}P})_4]$[a]	8.642×10^{-11}	−10.063	12.71
MB-P [a]	1.625×10^{-10}	−9.789	6.75	$[Pd_2(\mathbf{MB\text{-}P})_4]$[a]	8.253×10^{-11}	−10.083	13.30
CV-P [a]	1.599×10^{-10}	−9.797	6.87	$[Pd_2(\mathbf{CV\text{-}P})_4]$[a]	7.990×10^{-11}	−10.098	13.74
RE-P [a]	1.558×10^{-10}	−9.808	7.05	$[Pd_2(\mathbf{RE\text{-}P})_4]$[a]	8.231×10^{-11}	−10.085	13.54
MK-Q [a]	1.705×10^{-10}	−9.768	6.44	$[Pd_2(\mathbf{MK\text{-}Q})_4]$[a]	9.399×10^{-11}	−10.003	11.68
RB-Q [b]	9.206×10^{-10}	−9.036	7.11	$[Pd_2(\mathbf{RB\text{-}Q})_4]$[a]	-	-	-
MB-Q [a]	1.500×10^{-10}	−9.824	7.32	$[Pd_2(\mathbf{MB\text{-}Q})_4]$[a]	10.928×10^{-11}	−9.967	10.05
CV-Q [b]	8.771×10^{-10}	−9.057	7.44	$[Pd_2(\mathbf{CV\text{-}Q})_4]$[b]	5.293×10^{-10}	−9.276	12.36

From the comparison of the values reported in Table 4.2, the designed structural features of the cages can be extrapolated. While ligands **DYE-Q** are larger than **DYE-P** in terms of their larger donor group, $[Pd_2(\mathbf{DYE\text{-}Q})_4]$ cages are characterized by slightly smaller hydrodynamic radii as compared to their **DYE-P** siblings. This observation is in line with the X-ray/DFT structure results, showing a more globular shape with larger cavity for the $[Pd_2(\mathbf{DYE\text{-}P})_4]$ cages and helically twisted structures with smaller and less accessible cavities for the $[Pd_2(\mathbf{DYE\text{-}Q})_4]$ cages. An example is reported in Figure 4.29 for the DFT (B3LYP/def2-SV(P)) calculated structural models of $[Pd_2(\mathbf{MB\text{-}P})_4]$ and $[Pd_2(\mathbf{MB\text{-}Q})_4]$. While the pyridine-based ligand coordinates the metal cations almost perfectly perpendicularly to the plane that cuts in half the Pd-Pd axis with a small extent of propeller disposition of the pyridines around the coordination center, the isoquinoline-based ones are highly twisted. Moreover, the structures are visualized in the space filling mode and the different extent of accessible cavity can be noted. The $[Pd_2(\mathbf{DYE\text{-}P})_4]$ cage offers a larger available space for small molecule to bind inside the cavity.

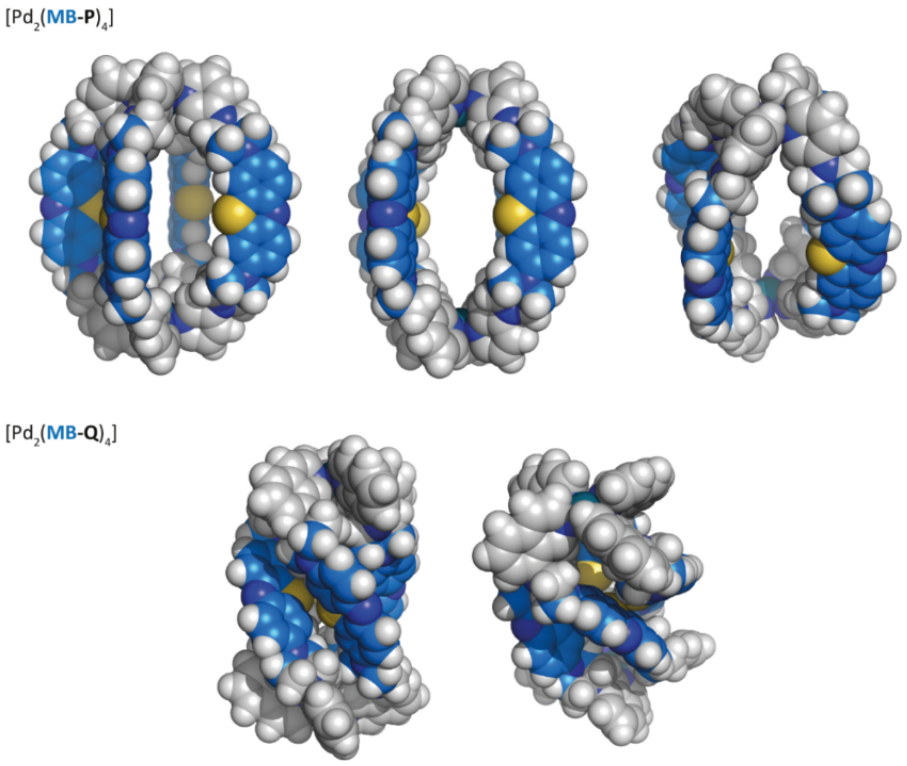

Figure 4.29: Space filling representation of calculated DFT (B3LYP/def2-SV(P)) models of $[Pd_2(\mathbf{MB\text{-}P})_4]$ and $[Pd_2(\mathbf{MB\text{-}Q})_4]$.

4.6 Host-Guest Chemistry with anionic small molecules

4.6.1 Interaction with guest (*R*)-camphor sulfonate (CSA)

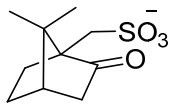

(*R*)-**CSA**

Figure 4.30: Chemical structure of guest (*R*)-camphor sulfonate (**CSA**).

Owing to the cages' helical structure and strong absorption in the visible spectrum, their application in the chiral recognition of small molecules has been investigated. Encapsulation of (*R*)-camphor sulfonate (**CSA**) in cages [Pd_2(**RB-P**)$_4$] and [Pd_2(**RE-P**)$_4$] in DMSO could be verified by ^{1}H NMR spectroscopy (Figure 4.31 and experimental part section 4.9 Figure 4.173) and ESI-MS spectrometry (Figure 4.33). In Figure 4.31, the ^{1}H NMR spectra of cage [Pd_2(**RB-P**)$_4$] in the presence of 1.0 equiv. and 2.0 equiv. (*R*)-**CSA** are reported. It can be noted how the largest shift is observed for proton H^a, which points inside the cage cavity, while, for example, proton H^b, which points outside the cage cavity, is not subjected to any shift. Hence, it can be concluded that the guest binds inside the cage cavity. However neither of these host-guest complexes showed a CD signature in the region 250-800 nm, which would be indicative of a guest-to-host chirality transfer. As similar observations were made for all other seven cages (Figure 4.32), even if the host-guest complexes could be detected with ESI mass spectrometry, it was assumed that the rather small, singly charged (*R*)-**CSA** molecule was not able to induce preferred population of one diastereomeric host-guest complex over the other. While (*R*)-**CSA** indeed showed strong guest-to-host chirality transfer in another chromophore-based [Pd_2L_4] cage as reported.[46]

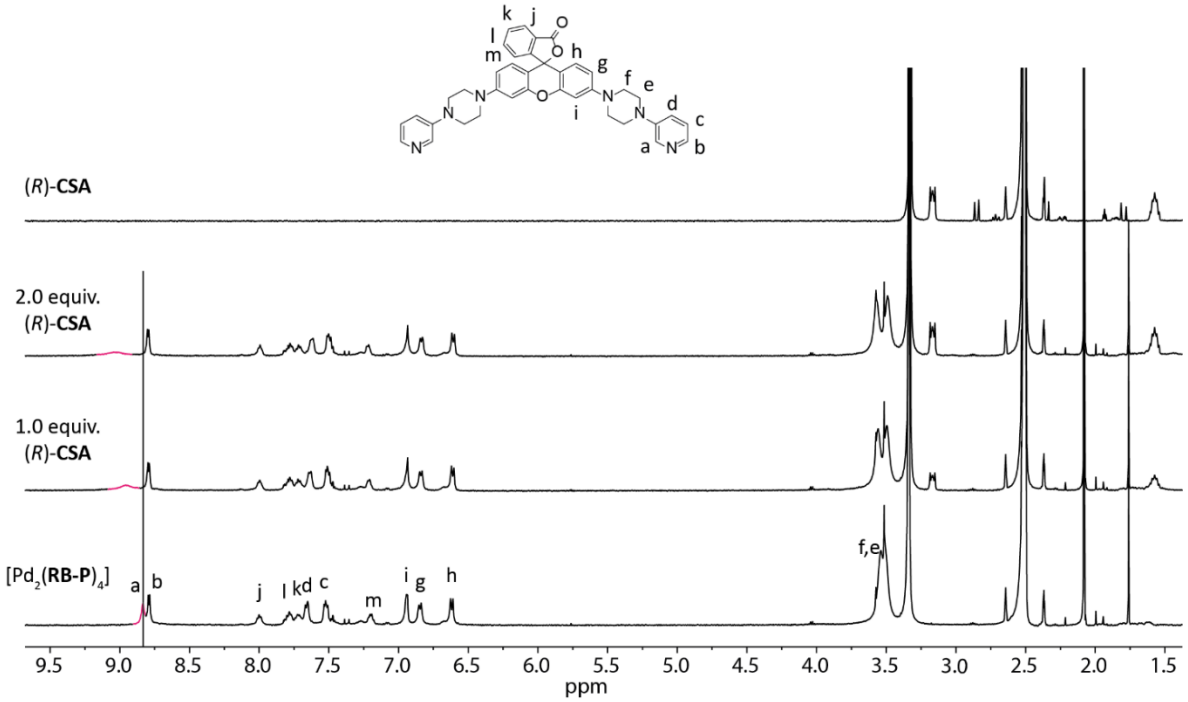

Figure 4.31: Stacked ^{1}H NMR spectra at 25 °C in DMSO-d_6 of cage [Pd_2(**RB-P**)$_4$], with 1.0 and 2.0 equiv. of guest (*R*)-**CSA**.

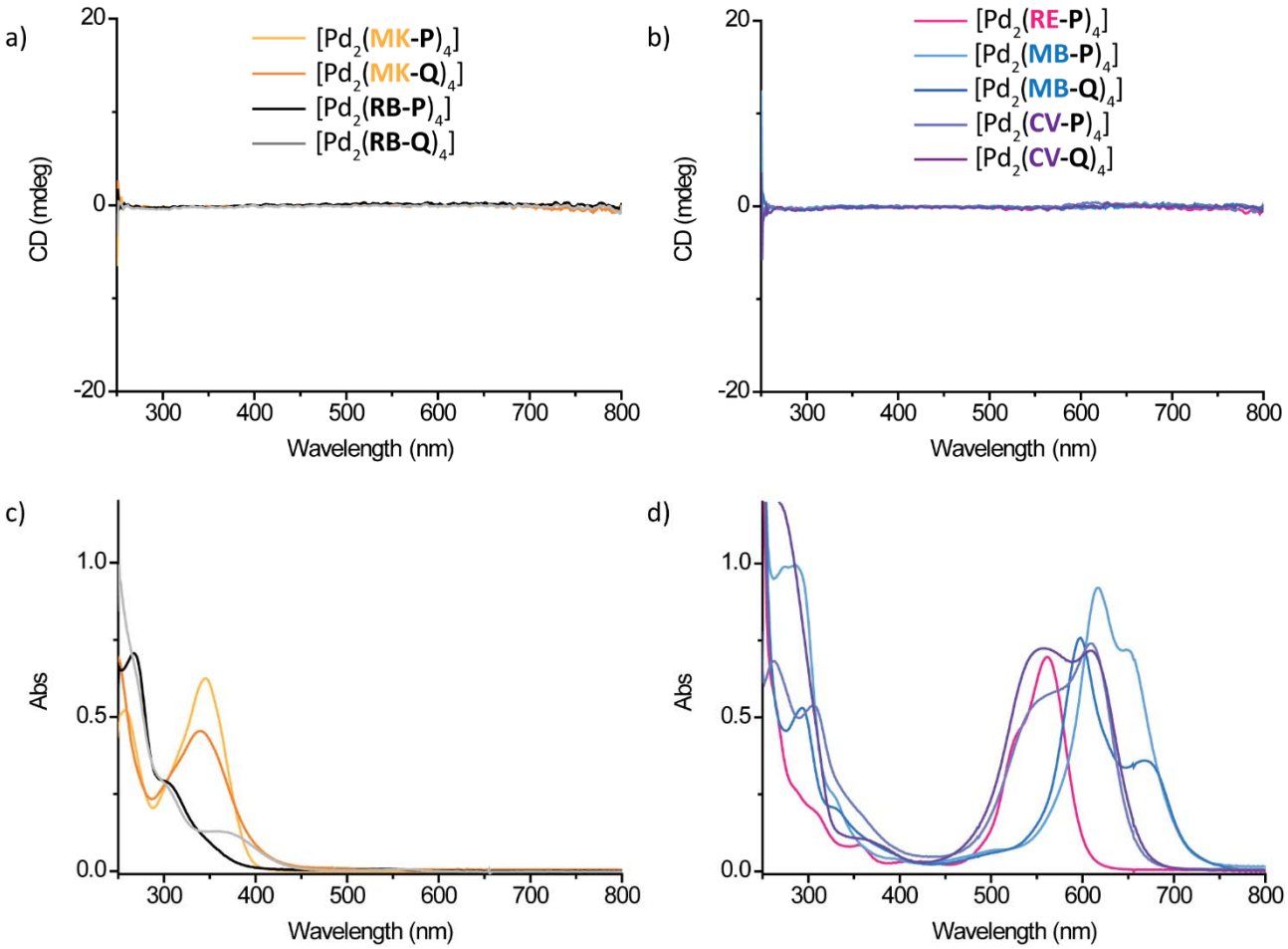

Figure 4.32: 1:1 solution (18.75 µM) in DMSO at 25 °C of the dye-based cages and guest (*R*)-**CSA**. a) CD and c) UV-Vis absorption spectra of the cages that show absorption below 400 nm: $[Pd_2(\mathbf{MK\text{-}P})_4]$, $[Pd_2(\mathbf{MK\text{-}Q})_4]$, $[Pd_2(\mathbf{RB\text{-}P})_4]$ and $[Pd_2(\mathbf{RB\text{-}Q})_4]$. b) CD and d) UV-Vis absorption spectra of the cages that absorb also at higher wavelengths: $[Pd_2(\mathbf{RE\text{-}P})_4]$, $[Pd_2(\mathbf{MB\text{-}P})_4]$, $[Pd_2(\mathbf{MB\text{-}Q})_4]$, $[Pd_2(\mathbf{CV\text{-}P})_4]$ and $[Pd_2(\mathbf{CV\text{-}Q})_4]$.

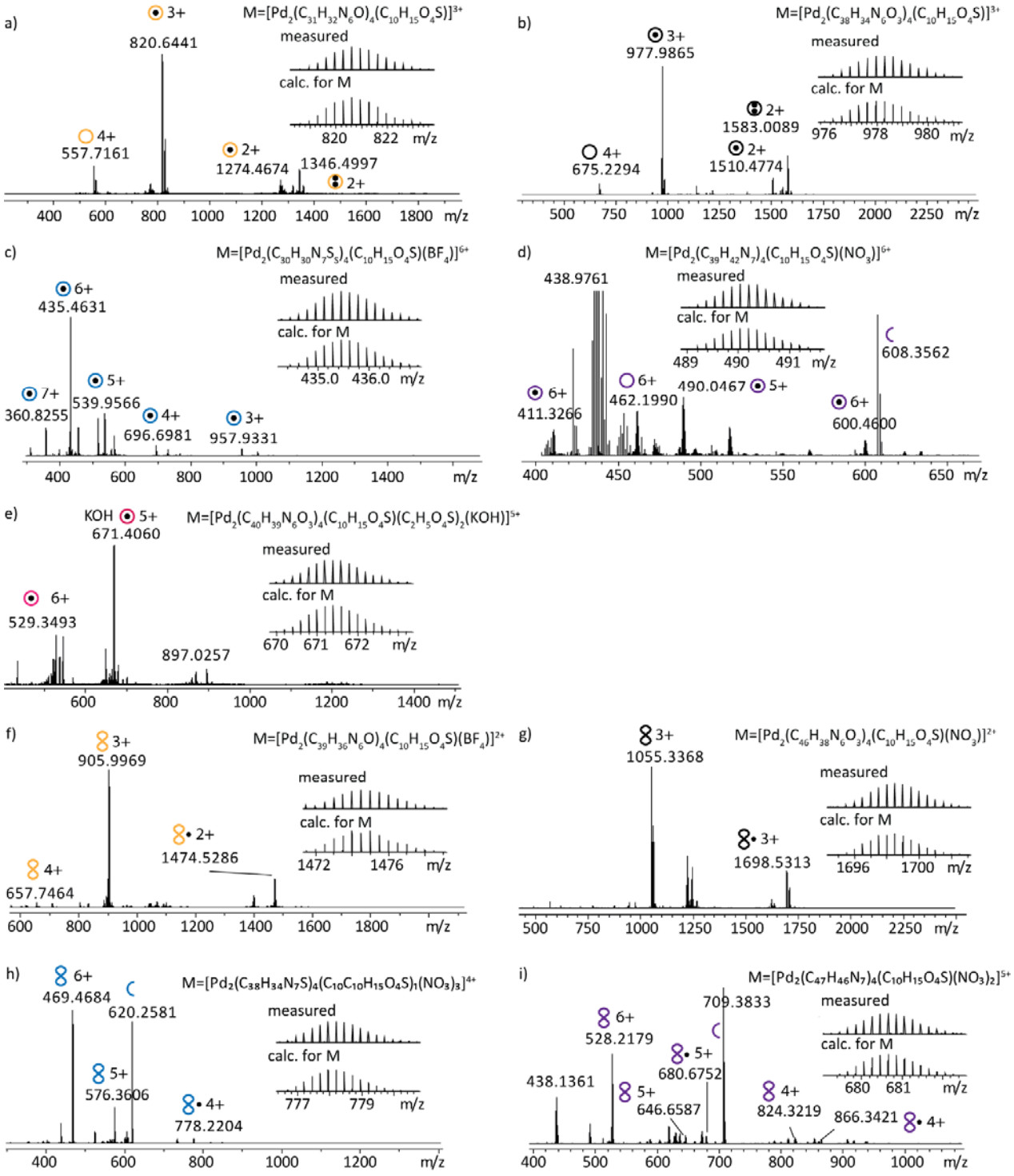

Figure 4.33: ESI-MS spectra of the nine colored cages (as colored circles or helices) presented in this chapter with the small anionic guest (*R*)-**CSA** (as small black dot). a) [(*R*)-**CSA**@Pd_2(**MK-P**)$_4$+nBF_4]$^{3-n+}$, n=0,1 with measured and calculated isotopic pattern of [(*R*)-**CSA**@Pd_2(**MK-P**)$_4$]$^{3+}$; b) [(*R*)-**CSA**@Pd_2(**RB-P**)$_4$+nBF_4]$^{3-n+}$, n=0,1 with measured and calculated isotopic pattern of [(*R*)-**CSA**@Pd_2(**RB-P**)$_4$]$^{3+}$; c) [(*R*)-**CSA**@Pd_2(**MB-P**)$_4$+nBF_4]$^{7-n+}$, n=0-4 with measured and calculated isotopic pattern of [(*R*)-**CSA**@Pd_2(**MB-P**)$_4$+BF_4]$^{6+}$; d) [(*R*)-**CSA**@Pd_2(**CV-P**)$_4$+nNO_3]$^{7-n+}$, n=1-3 with measured and calculated isotopic pattern of [(*R*)-**CSA**@Pd_2(**CV-P**)$_4$+NO_3]$^{6+}$; e) [(*R*)-**CSA**@Pd_2(**RE-P**)$_4$]+n$EtSO_4$]$^{7-n+}$, n=1,2 (and one KOH adduct) with measured and calculated isotopic pattern of [(*R*)-**CSA**@Pd_2(**RE-P**)$_4$($C_2H_5O_4S$)$_2$(KOH)]$^{5+}$; f) [(*R*)-**CSA**+Pd_2(**MK-Q**)$_4$]+nBF_4]$^{3-n+}$, n=1 with measured and calculated isotopic pattern of [(*R*)-**CSA**+Pd_2(**MK-Q**)$_4$+BF_4]$^{2+}$; g) [(*R*)-**CSA**+Pd_2(**RB-Q**)$_4$+nNO_3]$^{3-n+}$, n=1 with measured and calculated isotopic pattern of [(*R*)-**CSA**+Pd_2(**RB-Q**)$_4$+NO_3]$^{2+}$; h) [(*R*)-**CSA**+Pd_2(**MB-Q**)$_4$+nNO_3]$^{3-n+}$, n=3 with measured and calculated isotopic pattern of [(*R*)-**CSA**+Pd_2(**MB-Q**)$_4$+3NO_3]$^{4+}$; i) [(*R*)-**CSA**+Pd_2(**CV-Q**)$_4$ nNO_3]$^{3-n+}$, n=2,3 with measured and calculated isotopic pattern of [(*R*)-**CSA**+Pd_2(**CV-Q**)$_4$+2NO_3]$^{5+}$.

4.6.2 Interaction with guest (*R*)-1,1'-binaphthyl-2,2'-disulfonate (BINSO$_3$)

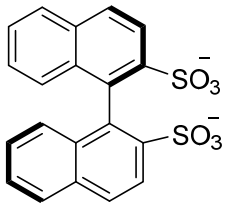

(*R*)-**BINSO$_3$**

Figure 4.34: Chemical structure of guest (*R*)-1,1'-binaphthyl-2,2'-disulfonate (**BINSO$_3$**).

Since guest (*R*)-**CSA** was found to be too small to induce the arrangement of colored cages in a chiral conformation, the larger, doubly negatively charged guest (*R*)-1,1'-binaphthyl-2,2'-disulfonate (**BINSO$_3$**) was tested. Equimolar solutions of each of the 9 colored cages together with (*R*)-**BINSO$_3$** were prepared in DMSO and the CD and UV-Vis absorption spectra of the visible-light absorbing host-guest complexes are reported in Figure 4.35. In spectral regions where the cages absorb, induced CD signals originate from the interaction between guest and host leading to a transfer of chiral information onto the chromophore arrangement. Induction of chirality seems to be strong for cages [Pd$_2$(**RE-P**)$_4$], [Pd$_2$(**CV-Q**)$_4$], [Pd$_2$(**MB-P**)$_4$] and [Pd$_2$(**MB-Q**)$_4$]. Smaller, but still significant, are the signatures corresponding to cages [Pd$_2$(**CV-P**)$_4$] and [Pd$_2$(**MK-P**)$_4$] and [Pd$_2$(**RB-P**)$_4$]. While for cages [Pd$_2$(**MK-Q**)$_4$] and [Pd$_2$(**RB-Q**)$_4$], inconclusive results are obtained as the guest signal covers possible indicative induced CD (ICD) bands.

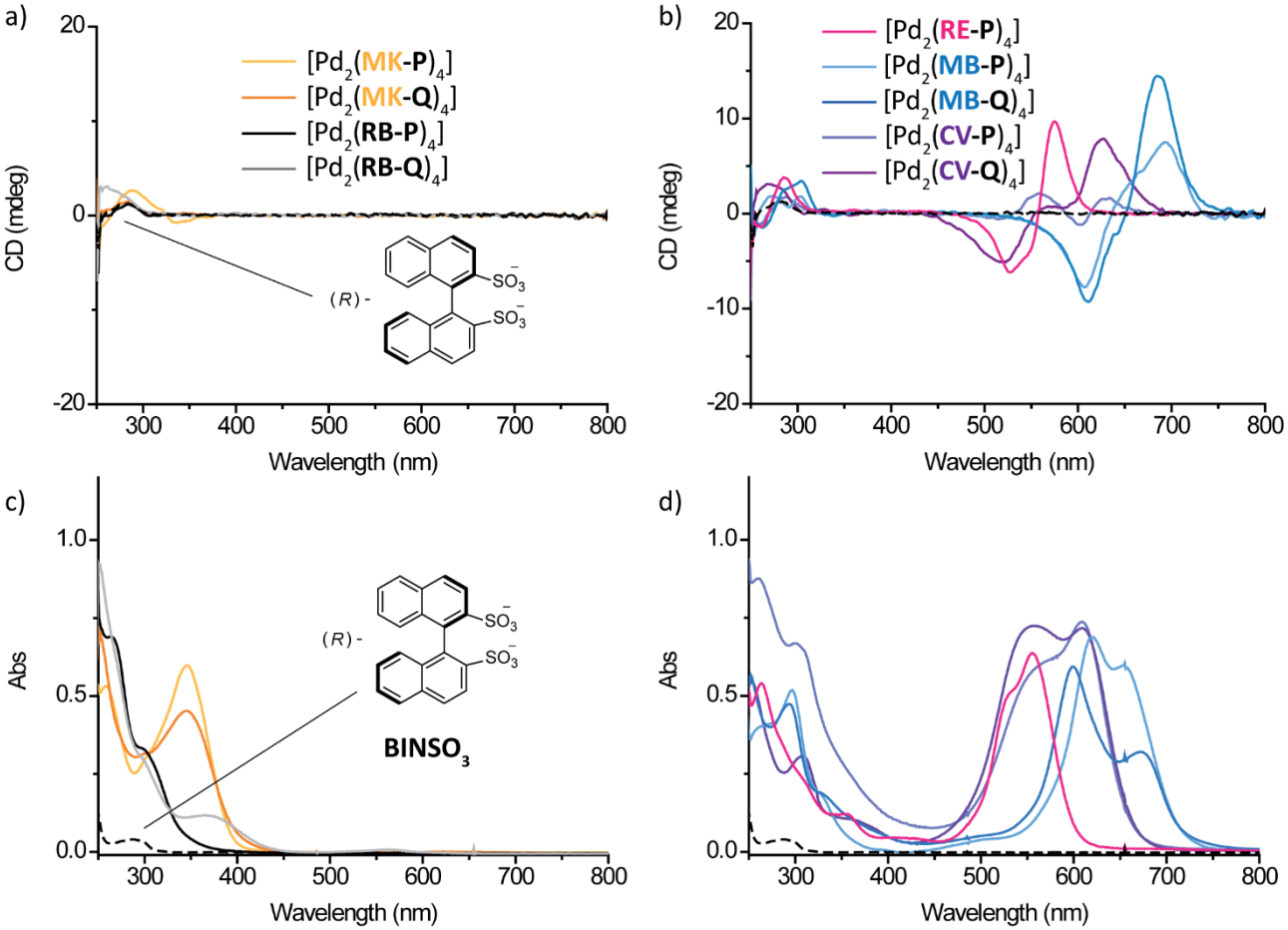

Figure 4.35: 1:1 solution (18.75 µM) in DMSO at 25 °C of the dye-based cages and guest (*R*)-**BINSO$_3$**. a) CD and c) UV-Vis absorption spectra of the cages that show absorption below 400 nm: [Pd$_2$(**MK-P**)$_4$], [Pd$_2$(**MK-Q**)$_4$], [Pd$_2$(**RB-P**)$_4$] and [Pd$_2$(**RB-Q**)$_4$]. b) CD and d) UV-Vis absorption spectra of the cages that absorb also at higher wavelengths: [Pd$_2$(**RE-P**)$_4$], [Pd$_2$(**MB-P**)$_4$], [Pd$_2$(**MB-Q**)$_4$], [Pd$_2$(**CV-P**)$_4$] and [Pd$_2$(**CV-Q**)$_4$].

The host guest complexes formed with [Pd_2(**DYE-P**)$_4$] cages are easily measurable with mass spectrometry (Figure 4.36 a-e). While for cages [Pd_2(**DYE-Q**)$_4$] the corresponding peak is either not found (Figure 4.36 f and g) or is small and in the presence of multiple peaks of the free host (Figure 4.36 h a-i).

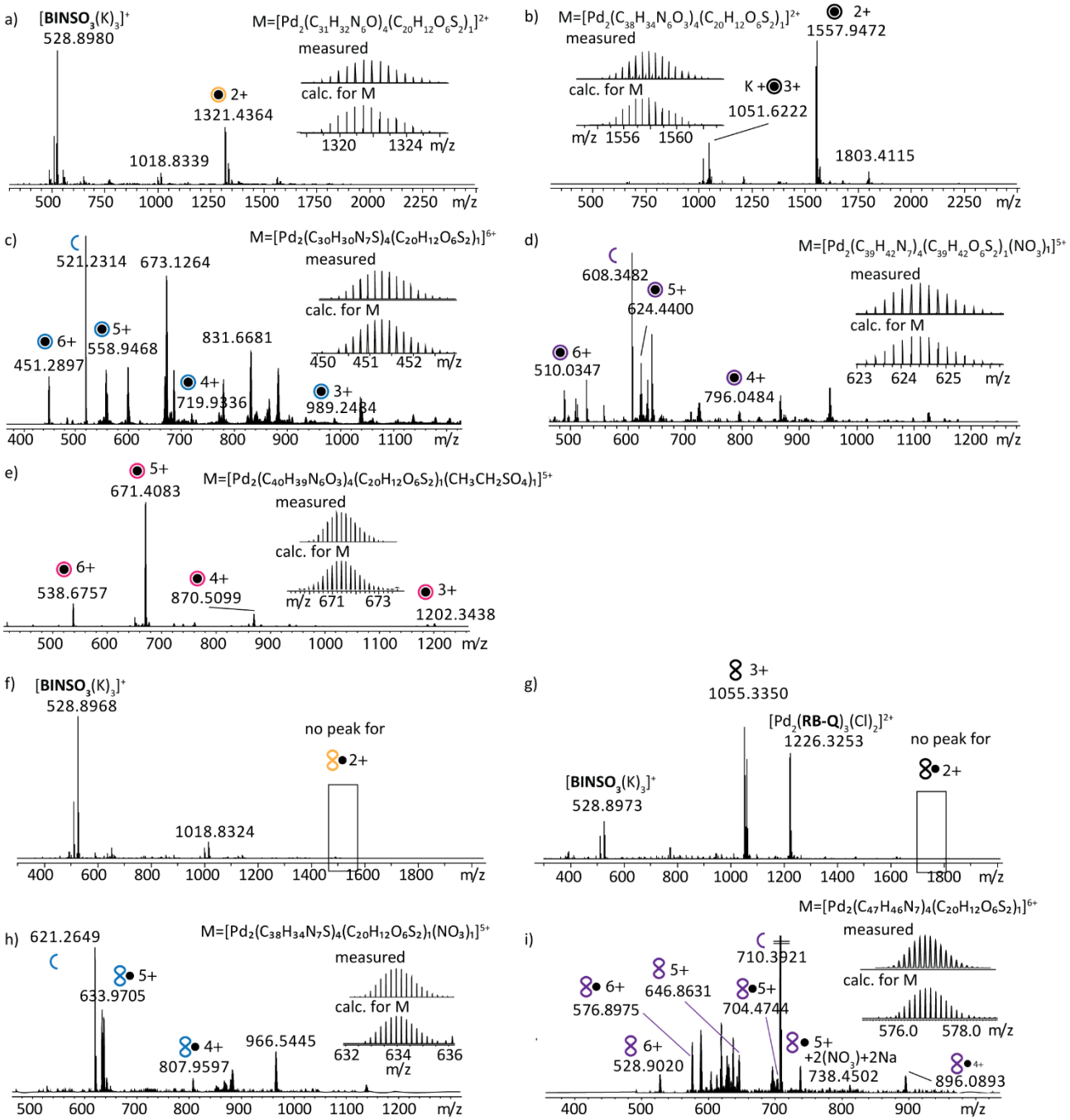

Figure 4.36: ESI-MS spectra of the nine colored cages (as colored circles or helices) presented in this chapter with the small anionic guest (*R*)-**BINSO$_3$** (as small black dot). a) [(*R*)-**BINSO$_3$**@Pd_2(**MK-P**)$_4$+nBF_4]$^{2-n+}$, n=0 with measure and calculated isotopic pattern of [(*R*)-**BINSO$_3$**@Pd_2(**MK-P**)$_4$]$^{2+}$; b) [(*R*)-**BINSO$_3$**@Pd_2(**RB-P**)$_4$+nBF_4]$^{2-n+}$, n=0 (and one K^+ adduct) with isotopic pattern simulation of [(*R*)-**BINSO$_3$**@**BINSO$_3$**@Pd_2(**RB-P**)$_4$]$^{2+}$; c) [(*R*)-**BINSO$_3$**@Pd_2(**MB-P**)$_4$+nBF_4]$^{6-n+}$, n=0-3 with isotopic pattern simulation of [(*R*)-**BINSO$_3$**@Pd_2(**MB-P**)$_4$]$^{6+}$; d) [(*R*)-**BINSO$_3$**@Pd_2(**CV-P**)$_4$+nNO_3]$^{6-n+}$, n=0-2 with isotopic pattern simulation of [(*R*)-**BINSO$_3$**@Pd_2(**CV-P**)$_4$(NO_3)]$^{5+}$; e) [(*R*)-**BINSO$_3$**@Pd_2(**RE-P**)$_4$+n$EtSO_4$]$^{6-n\ +}$, n=0-3 with isotopic pattern simulation of [(*R*)-**BINSO$_3$**@Pd_2(**RE-P**)$_4$($C_2H_5O_4S$)]$^{5+}$; f) cage [Pd_2(**MK-Q**)$_4$] and guest (*R*)-**BINSO$_3$**, no signals for the host-guest complex nor the empty cage are found; g) cage [Pd_2(**RB-Q**)$_4$] and guest (*R*)-**BINSO$_3$**, no signals for the host-guest complex are found but a signal relative to the empty [Pd_2(**RB-Q**)$_4$]; h) [(*R*)-**BINSO$_3$**+Pd_2(**MB-Q**)$_4$+nNO_3]$^{6-n+}$, n=1,2 with isotopic pattern simulation of [**BINSO$_3$**+Pd_2(**MB-Q**)$_4$(NO_3)]$^{5+}$; i) [(*R*)-**BINSO$_3$**+Pd_2(**CV-Q**)$_4$+nNO_3]$^{6-n+}$, n=0-2 with isotopic pattern simulation of [(*R*)-**BINSO$_3$**+Pd_2(**CV-Q**)$_4$]$^{6+}$.

Controls experiments were made to verify that the measured effects cannot be ascribable to the decomposition components of the cages. In Figure 4.37 the CD, and UV-Vis absorption spectra of equimolar solutions of (*R*)-**BINSO$_3$** and ligands **RE-P**, **MB-P**, **MB-Q**, **CV-P** and **CV-Q** are depicted. Since no ICD signal could be measured, the ligands either do not interact with (*R*)-**BINSO$_3$** or if interacting, they are not subjected to chiral rearrangement.

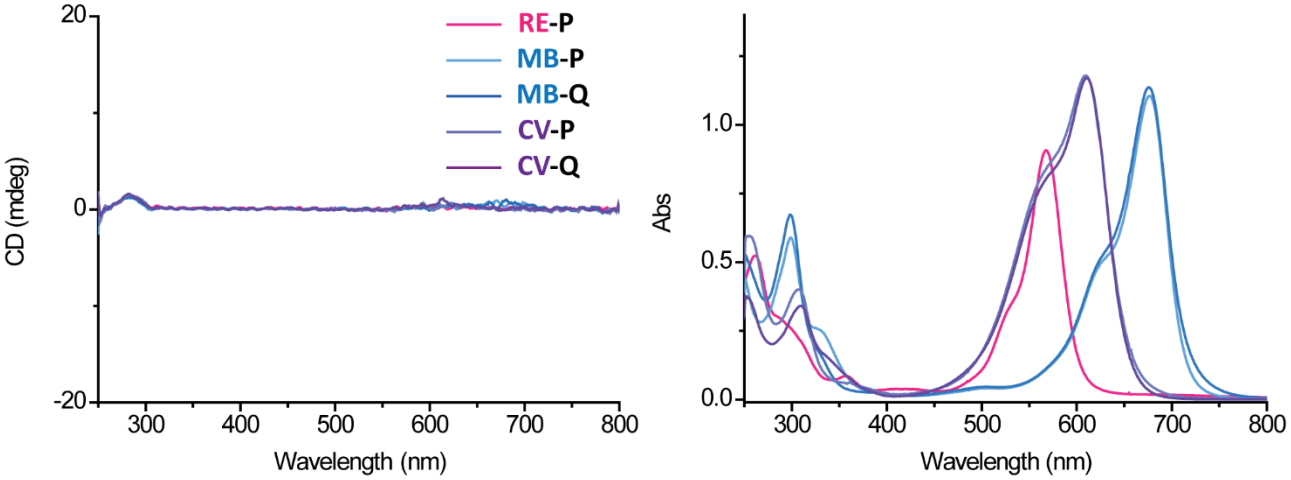

Figure 4.37: a) CD and b) UV-Vis absorption spectra of 1:1 solutions (18.75 µM) in DMSO at 25 °C of the dye-based ligands **RE-P**, **MB-P**, **MB-Q**, **CV-P**, **CV-Q** and the guest (*R*)-**BINSO$_3$**.

The chiral induction on the cages [Pd_2(**MB-P**)$_4$] and [Pd_2(**RE-P**)$_4$] was deeper investigated with the method of continuous variation. 11 solutions were prepared where the sum of the concentrations of the cage and the guest (*R*)-**BINSO$_3$** was kept constant and equal to 35.7 µM and the relative molar ratio was continuously increased between 0.0 and 1.0, with 0.1 steps, for the guest and continuously decreased for the cage.

$$[\text{cage}] + (R)\text{-}[\textbf{BINSO}_3] = 35.7\ \mu M$$

Starting with cage [Pd_2(**MB-P**)$_4$], in the situations in which only the cage or only the guest are present, a CD signal in the region 550-750 nm is not expected as the guest does not show a CD band in this region and the cage is not chiral. Measuring the other solutions containing both binding partners, a signal which increases the closer it gets to the ideal stoichiometric ratio could be measured. By plotting the CD intensity of the signal at 684 nm over the molar ratio of the cage (X_{CAGE}), a bell-shaped curve with the maximum around X_{CAGE} of 0.6 was obtained. The possible explanations for such value are the following: either a coexistence of [Pd_2(**MBP**)$_4$]:(*R*)-**BINSO$_3$** 1:1 and 2:1 are observed or, more reasonable, at this dilution the real concentration of the cage is smaller than the assumed one as it is partially disassembled (because the cage is always in equilibrium with the basic components) and, therefore, the overall bell-shaped curve, which would actually indicate a clean 1:1 stoichiometry, is shifted to the right.

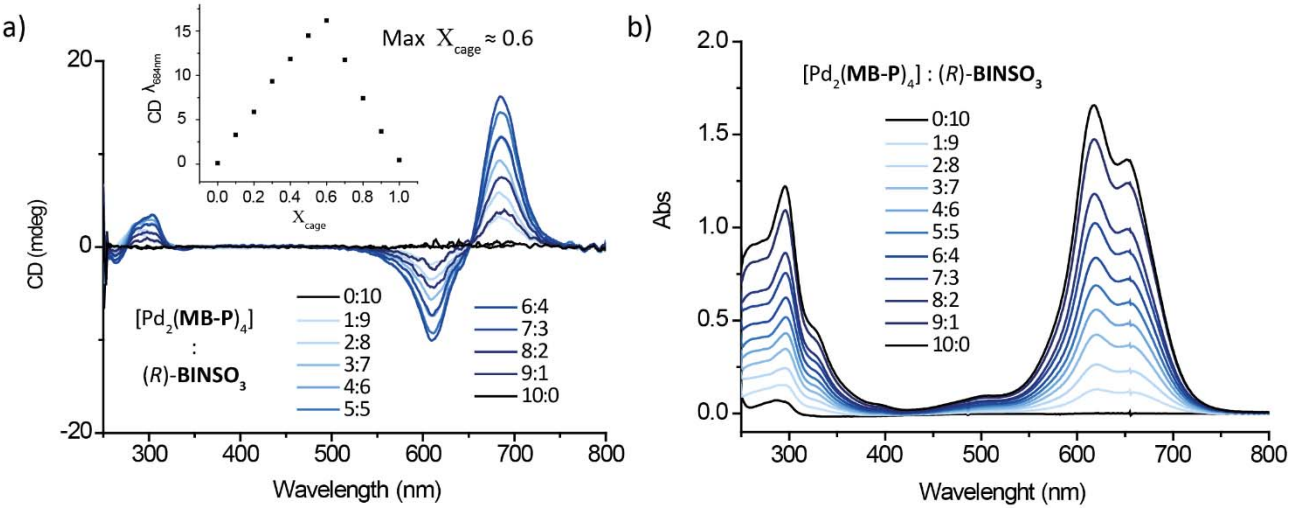

Figure 4.38: Method of continuous variation for cage $[Pd_2(\mathbf{MB\text{-}P})_4]$ and (R)-$\mathbf{BINSO_3}$ in DMSO at 25 °C. Total concentration kept constant at 37.5 µM. a) CD spectra with Job Plot inset with CD intensity at 684 nm and b) UV-Vis spectra.

Similar to the experiment with $[Pd_2(\mathbf{MB\text{-}P})_4]$, the experiment was performed with cage $[Pd_2(\mathbf{RE\text{-}P})_4]$ and the CD intensity of the signal at 574 nm over X_{CAGE} was plotted. A bell-shaped curve centred at X_{CAGE} of 0.7 was observed. The even more pronounced shift of the bell-shaped curve from the value of 0.5 might be indicative of a higher tendency of the cage to disassemble at this concentration or a higher tendency of two cages to bind one guest molecule. However, the mass spectra of both cages $[Pd_2(\mathbf{MB\text{-}P})_4]$ and $[Pd_2(\mathbf{RE\text{-}P})_4]$ in combination with (R)-$\mathbf{BINSO_3}$ clearly shows 1:1 stoichiometry complexes (Figure 4.36 c and e). Therefore, the hypothesis is that the cages partially disassemble at the used dilutions and that the real X_{CAGE} is lower than one calculated from the expected concentration, is even more reasonable.

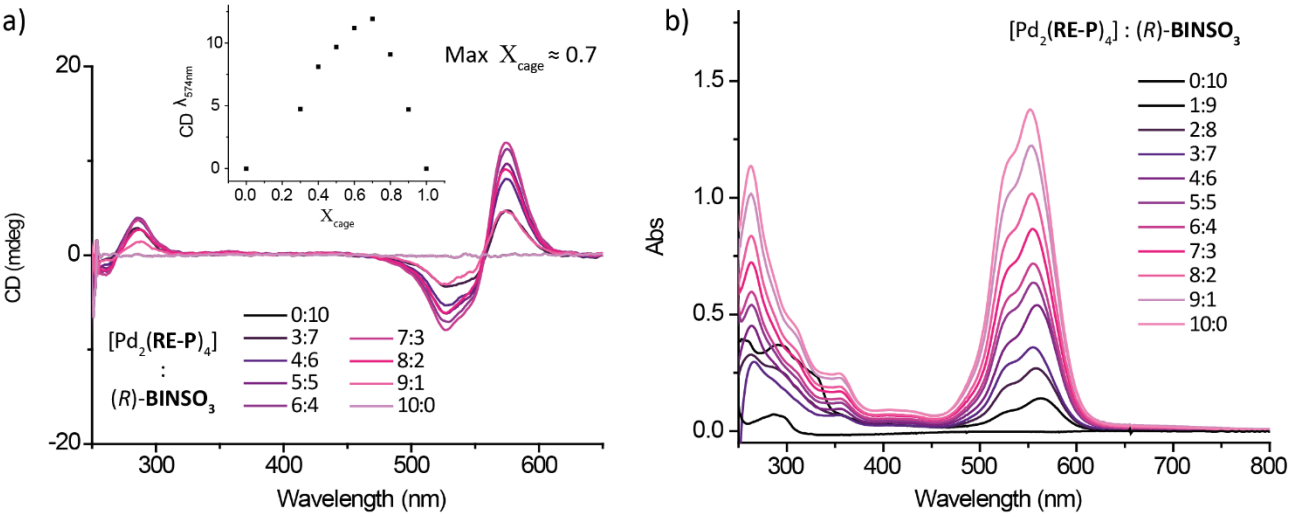

Figure 4.39: Method of continuous variation for cage $[Pd_2(\mathbf{RE\text{-}P})_4]$ and (R)-$\mathbf{BINSO_3}$ in DMSO at 25 °C. Total concentration kept constant and at 18.75 µM. a) CD spectra with Job Plot inset with CD intensity at 574 nm and b) UV-Vis spectra.

The interaction of cage $[Pd_2(\mathbf{MB\text{-}P})_4]$ with (R)-$\mathbf{BISNO_3}$ has also been investigated with titrations followed by ^{1}H NMR spectroscopy. At r.t., the cage signals broaden and slightly shift, indicating an interaction with the guest but with exchange rates comparable to the NMR time scale (section 4.9 Figure 4.174). In order to escape the coalescence temperature, the same titration was performed also at 65 °C (Figure 4.40). Also in this case, line broadening could be observed, but only the signals assigned to the protons H^a and H^i, which point inside the cage cavity, gradually disappeared upon stepwise addition of the guest. Hence,

it could be concluded that the guest binds inside the cage cavity. Such data does not allow to obtain a binding constant for the complex.

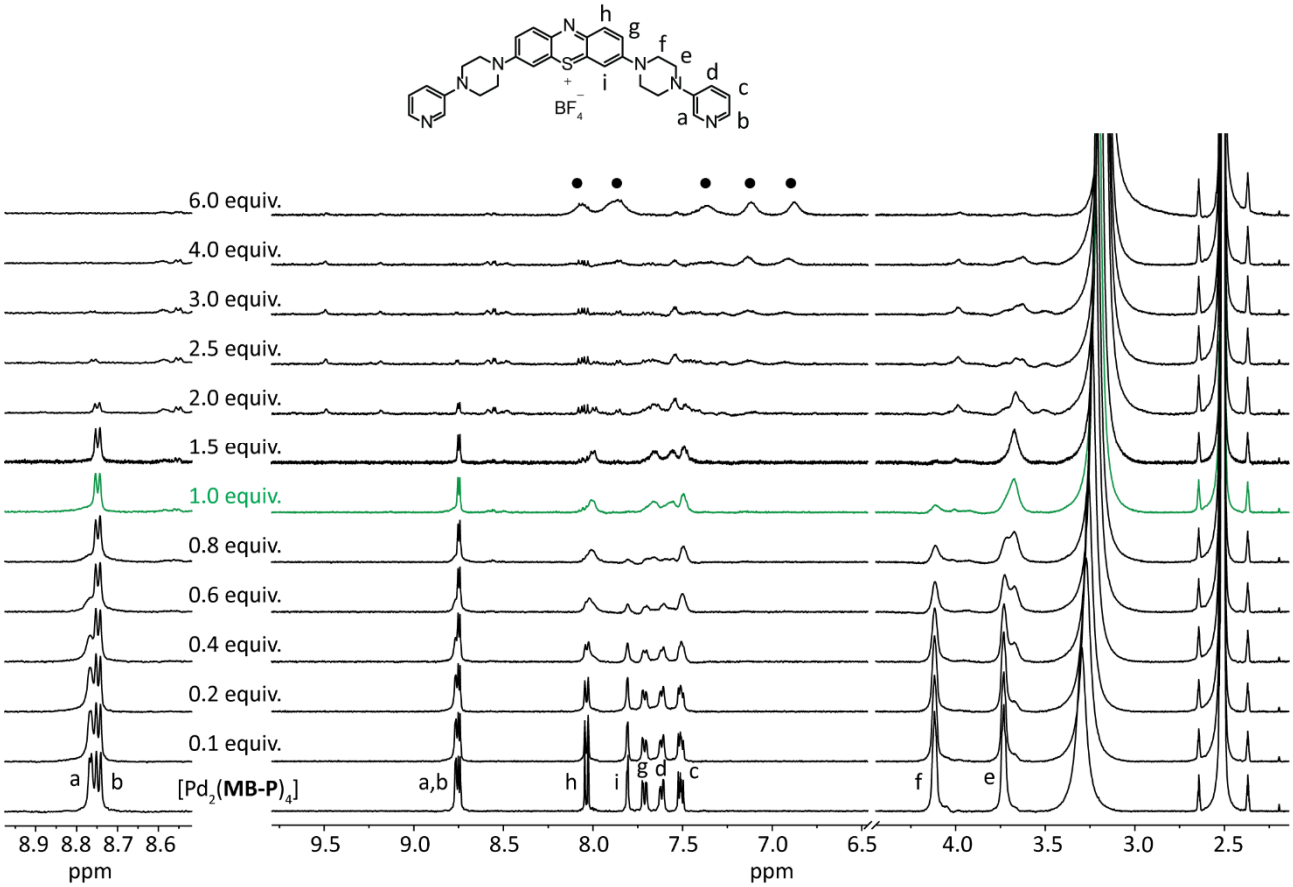

Figure 4.40: ^{1}H NMR titration at 65 °C of guest (*R*)-**BINSO$_3$** to cage [Pd$_2$(**MB-P**)$_4$]. The green line corresponds to the addition of 1.0 equiv. of the guest. On the left, enlargement of the region 9.0-8.4 ppm, on the right the full spectrum. At 6.0 equiv. the signals corresponding to the free guest are clearly visible and indicated with black dots.

On the contrary, when guest (*R*)-**BINSO$_3$** is titrated into a solution of cage [Pd$_2$(**MB-Q**)$_4$], no shift is observed but only the decrease of all cage signals with the appearance of the free guest signals. Such effect is usually ascribed to aggregation effects and would suggest that guest (*R*)-**BINSO$_3$** is binding outside the cavity of [Pd$_2$(**MB-Q**)$_4$] (Figure 4.41).

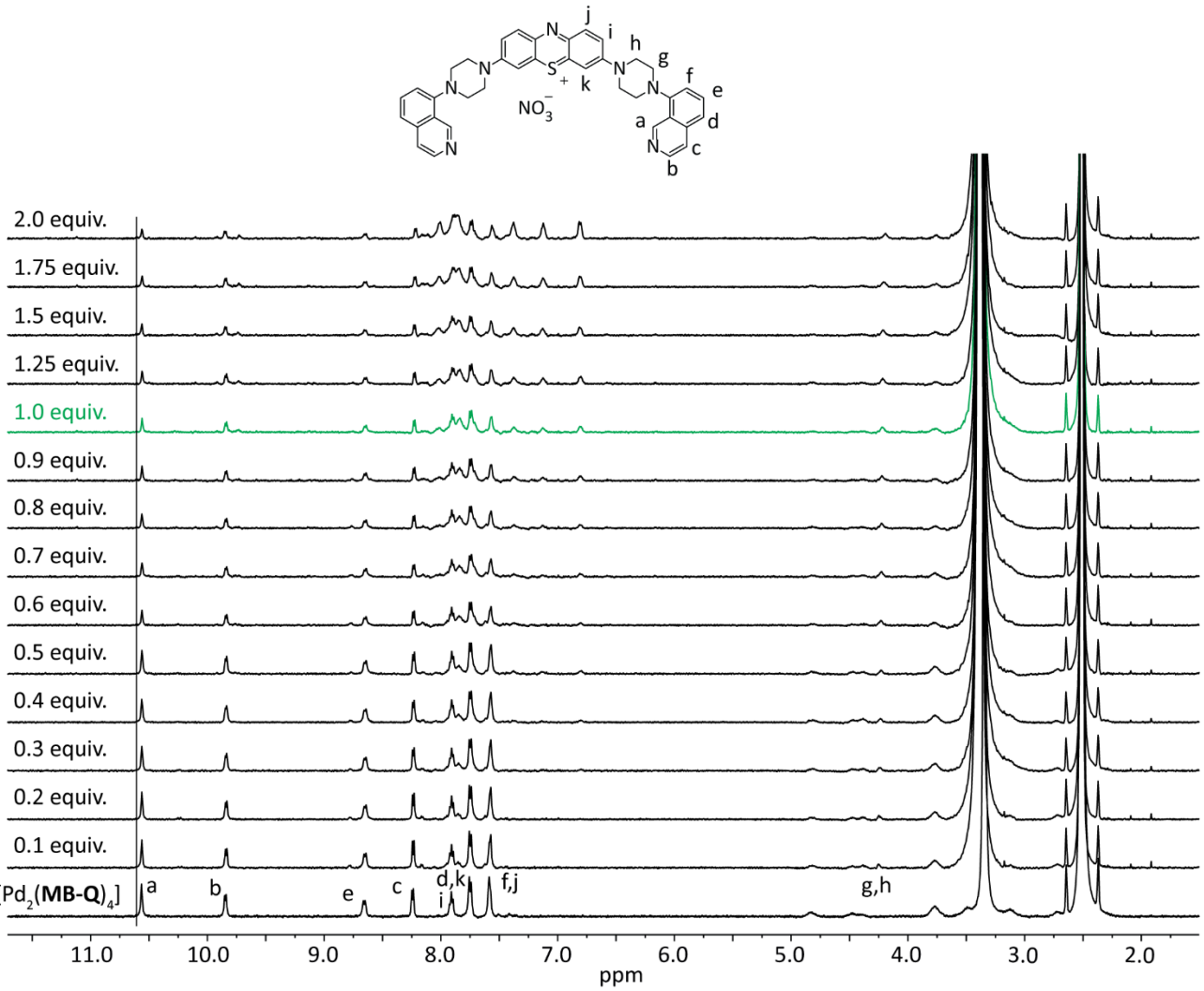

Figure 4.41: ^{1}H NMR titration at 25 °C of guest (*R*)-**BINSO$_3$** in cage [Pd$_2$(**MB-Q**)$_4$]. The green line corresponds to 1.0 equiv. of the guest. The signals that slowly increase around 7-8 ppm correspond to the free guest.

When (*R*)-**BINSO$_3$** is present in a kinetically-trapped narcissistic 1:1 mixture of [Pd$_2$(**RE-P**)$_4$] and [Pd$_2$(**MB-Q**)$_4$], prepared by mixing the two pre-formed cages together (for ^{1}H NMR of the cages mixture see section 4.9 Figure 4.175), it has a stronger preference to interact with the pink globular cage [Pd$_2$(**RE-P**)$_4$] rather than the blue helical one [Pd$_2$(**MB-Q**)$_4$]. A titration experiment could be followed by CD spectroscopy (Figure 4.42).

While the band at 574 nm assigned to [Pd$_2$(**RE-P**)$_4$] increases until 1 equiv. of guest is added, the band at 693 nm assigned to [Pd$_2$(**MB-Q**)$_4$], increases only when more than 1 equiv. is added (Figure 4.42 c). Such behavior is ascribed to the propensity of guest (*R*)-**BINSO$_3$** to bind inside the cage cavity of pyridine based cages [Pd$_2$(**DYE-P**)$_4$] (as demonstrated by ^{1}H NMR titration with cage [Pd$_2$(**MB-P**)$_4$]) while for isoquinoline based cages [Pd$_2$(**DYE-Q**)$_4$] it is rather outside binding. NMR titration experiments of (*R*)-**BINSO$_3$** in the [Pd$_2$(**MB-Q**)$_4$] solution were indicative for an anion-induced aggregation of the cationic assemblies. Moreover, while ESI-MS spectra of (*R*)-**BINSO$_3$** with cages [Pd$_2$(**DYE-P**)$_4$] show only peaks for the host-guest complexes, for cages [Pd$_2$(**DYE-Q**)$_4$], the expected peak is either not found at all or is rather small and accompanied by multiple peaks of the free host (Figure 4.36). Trapped ion mobility mass spectrometry (TIMS) experiments support the proposed outside binding mode. In Figure 4.43 the collisional cross sections obtained from high resolution trapped ion mobility spectrometry of the free cages compared to the corresponding host-guest complex in the same charge states are depicted. While the host-guest complex with cage [Pd$_2$(**RE-P**)$_4$] shows a smaller CCS value compared to the free cage,

indicating that the guest is inside the cage cavity, the host-guest complex with cage [Pd_2(**MB-Q**)$_4$] shows a larger CCS value compared to the empty cage. The experiments carried support the outside binding of the guest molecule.

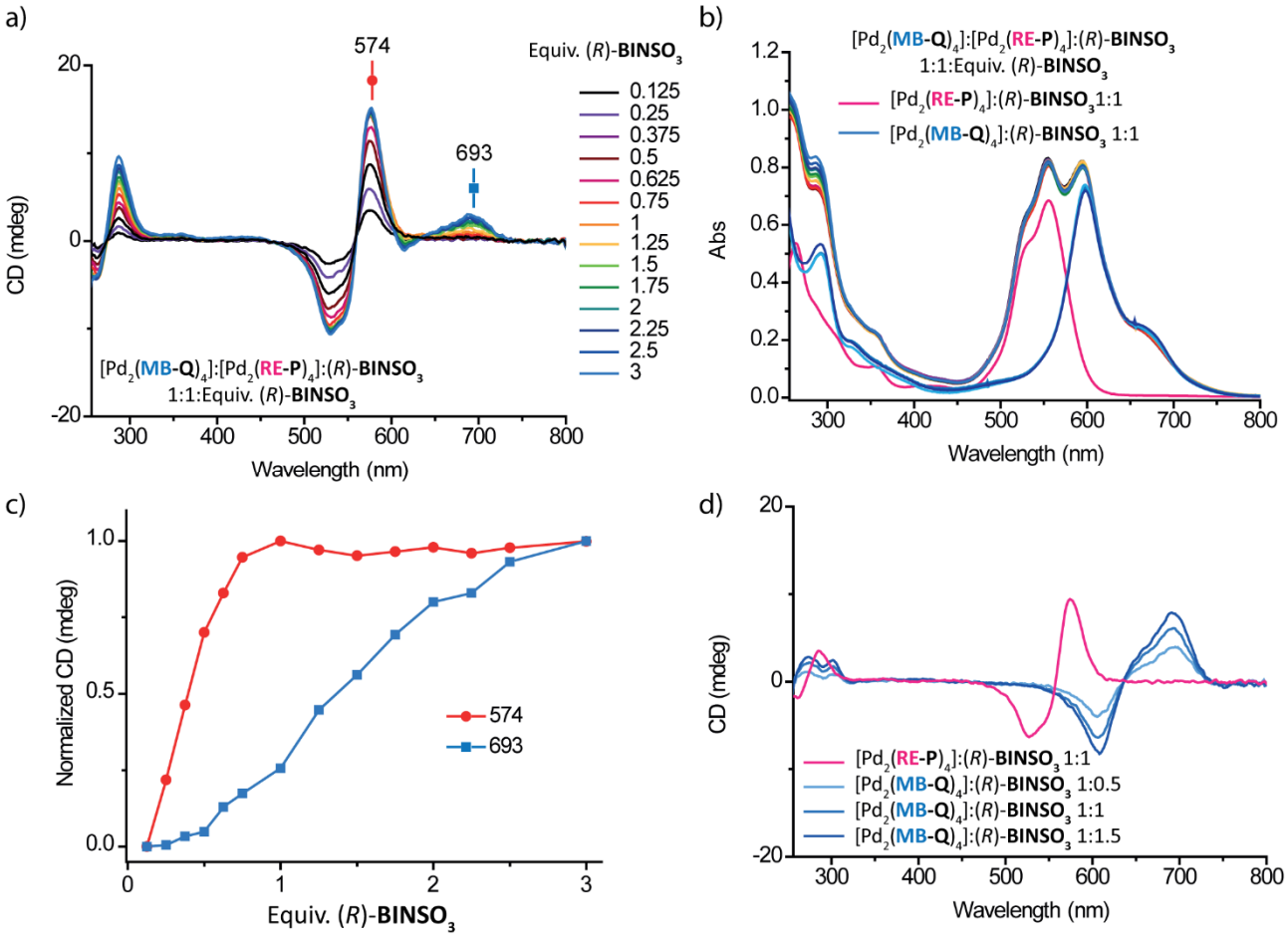

Figure 4.42: a) CD and b) UV-Vis absorption spectra of equimolar 18.75 µM DMSO solution of cages [Pd_2(**MB-Q**)$_4$] and [Pd_2(**RE-P**)$_4$] and guest (*R*)-**BINSO$_3$** in a 1:1:Equiv. (*R*)-**BINSO$_3$** (indicated in the Figure), c) normalized CD intensities at 574 nm (selective for [Pd_2(**RE-P**)$_4$]) and 574 nm (selective for [Pd_2(**MB-Q**)$_4$]) d) CD spectra of DMSO 18.75 µM solutions of [Pd_2(**RE-P**)$_4$] and guest (*R*)-**BINSO$_3$** in a 1:1 ratio in pink, [Pd_2(**MB-Q**)$_4$] and guest (*R*)-**BINSO$_3$** in 1:0.5, 1:1 and 1:1.5 ratios in different shades of blue.

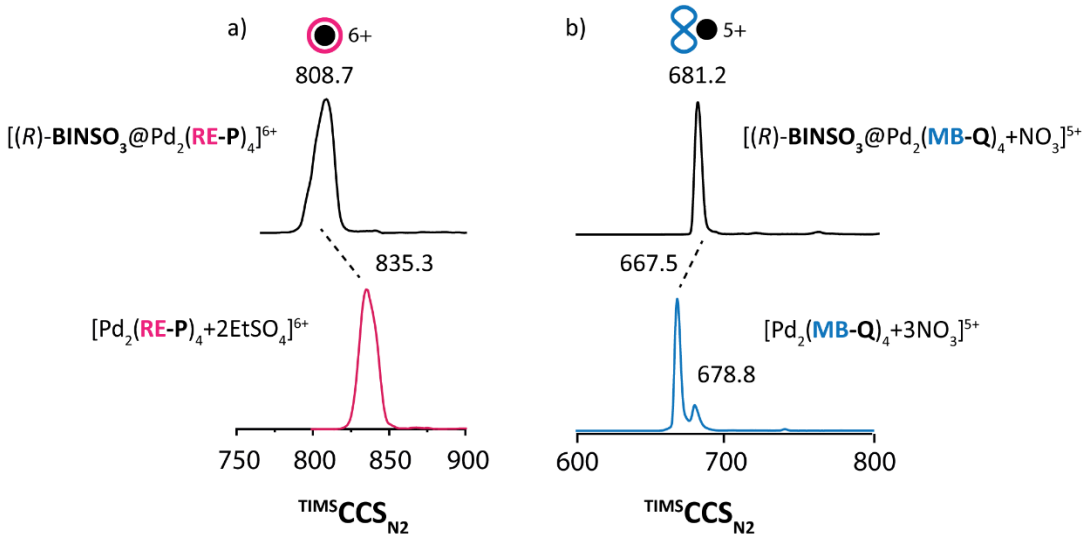

Figure 4.43: Collisional cross sections obtained from high-resolution trapped ion mobility spectrometry of a) $[Pd_2(\textbf{RE-P})_4+2(EtSO_4)]^{6+}$ and $[(R)\text{-}\textbf{BINSO}_3@Pd_2(\textbf{RE-P})_4]^{6+}$; b) $[Pd_2(\textbf{MB-Q})_4+3NO_3]^{5+}$ and $[(R)\text{-}\textbf{BINSO}_3@Pd_2(\textbf{MB-Q})_4+NO_3]^{5+}$. While the host-guest complex (in black) with cage $[Pd_2(\textbf{RE-P})_4]$ is showing a smaller CCS value compared to the free cage (in pink), indication that the guest is inside the cage cavity, the host-guest complex (in black) with cage $[Pd_2(\textbf{MB-Q})_4]$ shows a larger CCS value compared to the empty cage (in blue).

Mixing ligands **MB-Q** and **RE-P** followed by Pd(II) addition leads to the statistical mixture of all the possible combination of the ligands in the cage structure $[Pd_2(\textbf{MB-Q})_x(\textbf{RE-P})_{4-x}]$ with (x=0-4) (for ^{1}H NMR spectrum see section 4.9 Figure 4.175). In combination with guest (*R*)-**BINSO$_3$**, the statistical mixture leads to the CD and UV-Vis absorption spectra reported in Figure 4.44 in black, indicating the interaction of the guest with all the cages present in solution.

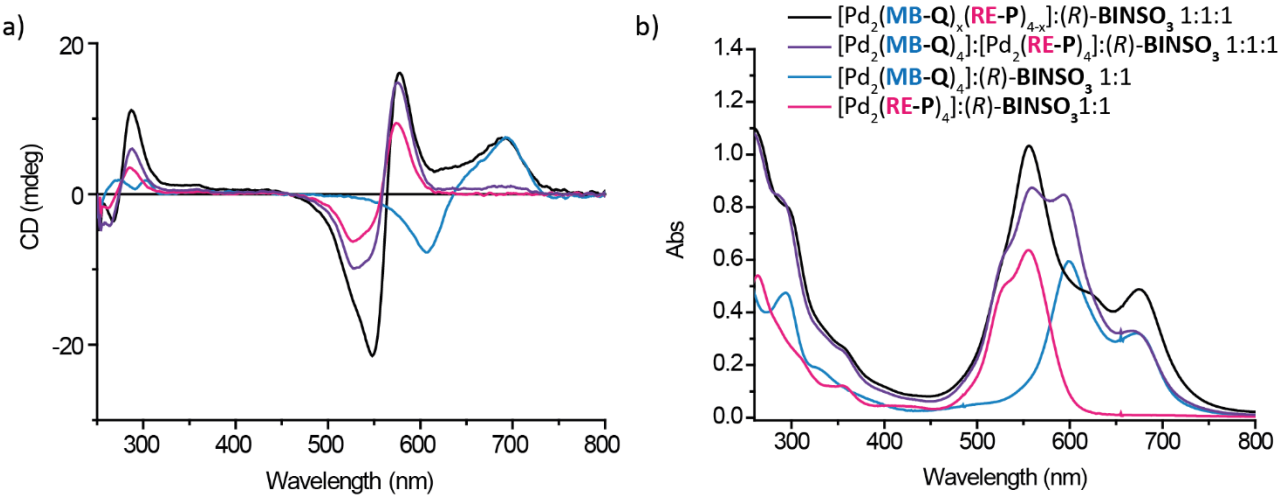

Figure 4.44: CD spectra (on the left) and UV-Vis absorption spectra (on the right) of DMSO solution at 25 °C of the statistical mixture $[Pd_2(\textbf{MB-Q})_x(\textbf{RE-P})_{4-x}]$ with x=1-4 and guest (*R*)-**BINSO$_3$** in a 1:1:1 ratio (where 1 corresponds to 18.75 µM of each cage in the narcissistic self-sorting situation) in black, cages $[Pd_2(\textbf{MB-Q})_4]$ and $[Pd_2(\textbf{RE-P})_4]$ and guest (*R*)-**BINSO$_3$** in a 1:1:1 ratio in violet, cage $[Pd_2(\textbf{MB-Q})_4]$ and guest (*R*)-**BINSO$_3$** in a 1:1 ratio in blue and cage $[Pd_2(\textbf{RE-P})_4]$ and guest (*R*)-**BINSO$_3$** in a 1:1 ratio in pink.

4.6.3 Biologically relevant chiral phosphates

The applicability of the colored cages in the recognition of small chiral anionic molecules, together with their maximum of absorption in a region where typical small biologically relevant molecules do not absorb, sparked the interest in applying the newly designed host in the recognition of essential-for-life chiral phosphates. The first selection included four different molecules to screen structural and chemical

diversity: guanosine monophosphate (**GMP**), guanosine diphosphate (**GDP**), (D)-glucose phosphate (**glucPO$_4$**) and (D)-fructose phosphate (**fructPO$_4$**).

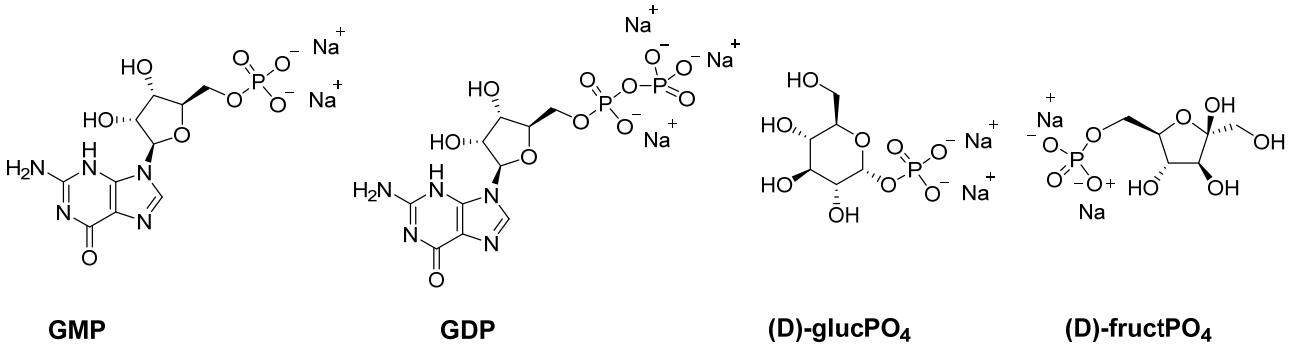

Figure 4.45: Chemical structure of chiral guanosine monophosphate (**GMP**), guanosine diphosphate (**GDP**), (D)-glucose phosphate (**glucPO$_4$**) and (D)-fructose phosphate (**fructPO$_4$**).

Equimolar solutions of the dye-based cages [Pd$_2$(**RE-P**)$_4$], [Pd$_2$(**CV-P**)$_4$], [Pd$_2$(**MB-P**)$_4$], [Pd$_2$(**CV-Q**)$_4$] and [Pd$_2$(**MB-Q**)$_4$] and the four guests were prepared by mixing the stock solution of the cages in DMSO with a concentration of 0.7 mM and the stock solution of the phosphates as sodium salts in water with a concentration of 15 mM. The final solution in DMSO (with 1 µL of water for each 800 µL of solution) had a concentration of 18.75 µM both in cage and in phosphate. CD measurements highlighted how the cage [Pd$_2$(**RE-P**)$_4$] has the highest propensity to read the chiral information of the phosphates rearranging in a chiral conformation to give very high ellipticities (Figure 4.46 in pink). Cage [Pd$_2$(**MB-P**)$_4$] shows small CD bands with positive cotton effect in interaction with the phosphates (Figure 4.46 in blue). On the contrary, cages [Pd$_2$(**CV-P**)$_4$], [Pd$_2$(**CV-Q**)$_4$] and [Pd$_2$(**MB-Q**)$_4$] are not subjected to preferential population of a chiral conformation and measurable CD signals were not observed (section 4.9 Figure 4.176). Control experiments with **RE-P** ligand and **gluPO$_4$** confirmed that the chiral recognition effect is based on the structural three-dimensional arrangement of the chromophores since the free ligand shows no ICD. Probably, the distinct selectivity among the colored cages is caused by their inherent different structural features. Cages [Pd$_2$(**CV-Q**)$_4$] and [Pd$_2$(**MB-Q**)$_4$] are helically twisted and lack of a big cavity available for interactions with small anionic molecules. Moreover, the steric hindrance that causes the isoquinoline groups to adopt a propeller disposition, might block possible conformations of the cages that would better accommodate the guests. Cages [Pd$_2$(**RE-P**)$_4$], [Pd$_2$(**MB-P**)$_4$] and [Pd$_2$(**CV-P**)$_4$], have a globular shape and are highly flexible. Within each other, they differ in the extent of delocalized positive charge on the ligands and by chemical substitutions. The external substitution that characterize **RE-P** might be the source of interaction that better fits the chiral recognition of the examined substrates.

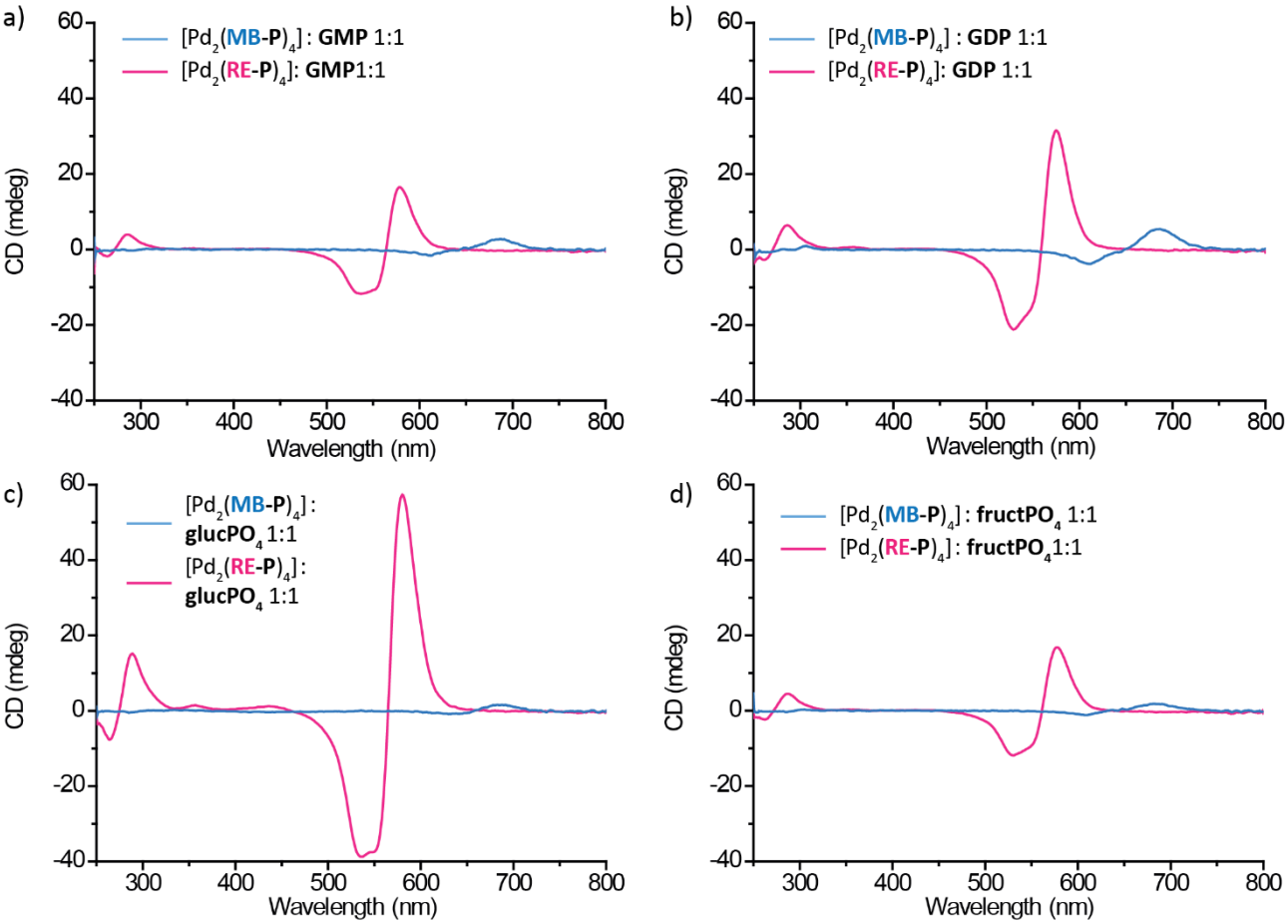

Figure 4.46: CD spectra of 1:1 solutions of cage [Pd_2(**MB-P**)$_4$] in blue or cage [Pd_2(**RE-P**)$_4$]in pink with guests a) **GMP**, b) **GDP** , c) **glucPO$_4$**, d) and **fructPO$_4$**. All measurements were performed in DMSO at 25°C and the concentrations of both binding partners kept equal and constant to 18.75 µM.

Upon addition of 1 equiv. of guests **GDP** and **gluPO$_4$** to cages [Pd_2(**MB-P**)$_4$] and [Pd_2(**RE-P**)$_4$], in the resulting ^{1}H NMR spectra, it can be observed, *in primis*, that the supramolecular architectures are stable in presence of the sugars and nucleobase phosphates. Indeed, from Figure 4.47, it can be noted that upon addition of the small chiral molecules, signals of the free ligand do not appear. At the same time, for cage [Pd_2(**MB-P**)$_4$] a small shift of most of the protons, H^b, H^i, H^g, H^d and H^c, can be noted, indicating a rather unspecific binding that involves the whole cage structure (external and internal surfaces). Besides the shift of the signals, slightly more pronounced for signal H^a with **gluPO$_4$**, in the ^{1}H NMR spectra with cage [Pd_2(**RE-P**)$_4$], also a new set of signals (* in the Figure) appears. Two-dimensional and DOSY NMR could elucidate whether they correspond to the encapsulated/bounded phosphate molecule, or to cage signals of the complex in slow exchange or even a completely new species that forms from the decomposition of [Pd_2(**RE-P**)$_4$]. ESI-MS measurements of the complexes were not successful in providing this information as the assemblies-relative peaks could not be found. The binding, involving also the external surface of the cage, might be weaker than with the previously discussed guests ((*R*)-**CSA** and (*R*)-**BINSO$_3$**) and usual mass measurement conditions break the interactions. Cryo-based techniques could be tested in this context.

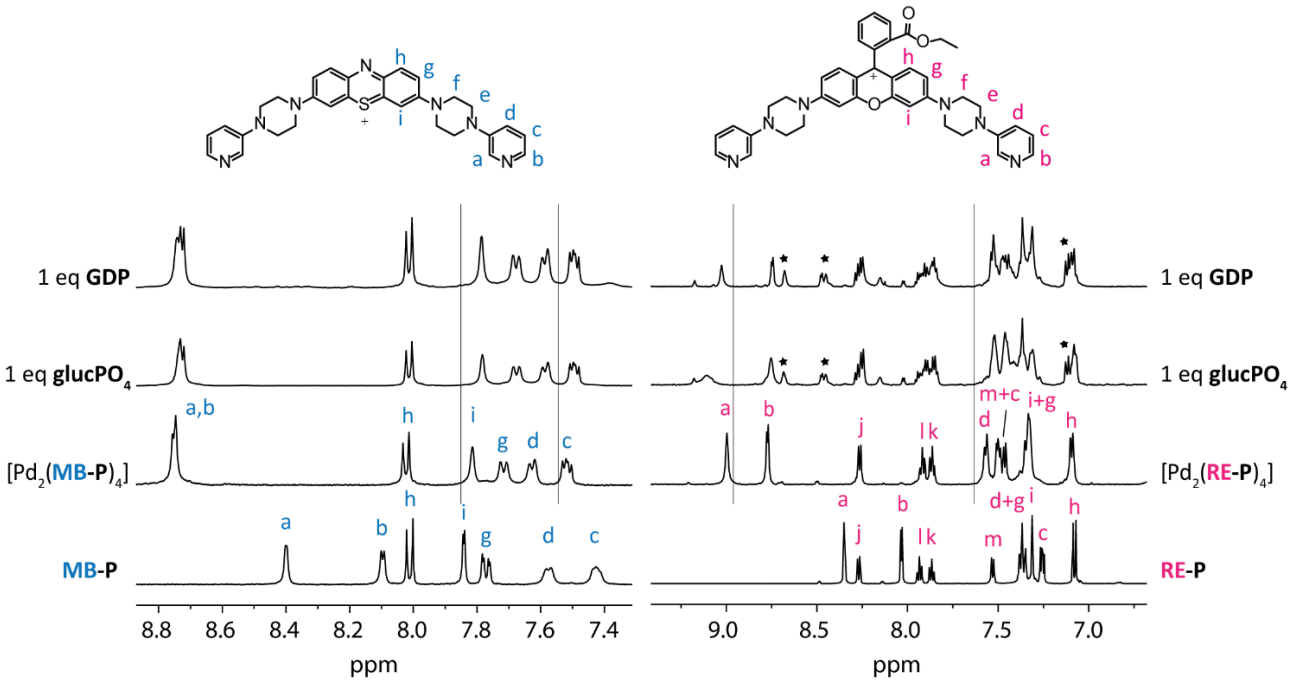

Figure 4.47: Stacked ^{1}H NMR spectra at 25 °C in DMSO-d_6 of (on the left) **MB-P** ligand, cage [Pd_2(**MB-P**)$_4$], cage [Pd_2(**MB-P**)$_4$] with addition of 1.0 equiv. of **glucPO$_4$** and cage [Pd_2(**MB-P**)$_4$] with addition of 1.0 equiv. of **GDP**, (on the right) **REP** ligand, cage [Pd_2(**RE-P**)$_4$], cage [Pd_2(**RE-P**)$_4$] with addition of 1.0 equiv. of glucPO4 and cage [Pd_2(**RE-P**)$_4$] with addition of 1.0 equiv. of GDP.

4.7 Conclusion and outlook

The synthesis of nine new [Pd_2L_4] cages based on the new design of bridging coal-tar dye functionalities to two N-donor groups, pyridine and isoquinoline, with piperazine linkers has been reported. The new ligand family results in two different structural arrangements of the four ligands around the Pd_2-axis, a lantern shaped and a helical twisted one. The cages are shown to maintain the electronic structure of the parental dyes and strongly absorb in the visible spectrum of light. The structural and optical features of the new cages have been exploited in diagnostics of chiral recognition events of small molecules. Promising results are also presented in the application of the newly designed supramolecular structures in the recognition of chiral biologically relevant phosphate molecules. Future research studies will focus on deepening the interaction study of such molecules and understanding which parts of the supramolecular architecture (ligand backbones, cage cavity, coordination centers) are involved in the binding and chiral induction. Moreover, the selection of binding partners is sought to be expanded, and many more relevant chiral anionic molecules, as well as biological molecules and polymers (see chapter 5 for discussion of this topic), can be screened. Other than bringing advantage in the recognition of small molecules, the new functional supramolecular assemblies promise to serve valuable roles also in the field of photoredox catalysis. The photosensitizing ability of the dyes embedded in the hollow structures could be exploited for the light-driven catalytic transformation of small molecules with different/enhanced regio-selectivity than compared to bulk conditions. Moreover, in view of the ability of the structure to undergo chiral-rearrangement, a dual approach could be postulated in which the role as chiral information carrier is combined with the photosensitizing feature, leading to enantioselective, light-driven photocatalytic reactions inside the cavity, dynamically controlled by outside binding chiral mediators.

4.8 Experimental part

4.8.1 General methods

NMR

NMR spectroscopic data was measured on the spectrometers Bruker AV 500 Avance NEO and AV 600 Avance III HD. For ^{1}H and ^{13}C NMR spectra, chemical shifts were calibrated to the solvent lock signal. Chemical shifts δ are given in ppm, coupling constants *J* in Hz. The following abbreviations are used to describe signal multiplicity for ^{1}H NMR spectra: s: singlet, d: doublet, t: triplet, dd: doublet of doublets; dt: doublet of triplets; m: multiplet, br: broad. All proton and carbon signals were assigned with the aid of 2D NMR spectra. All spectra were recorded in standard 5 mm NMR tubes at the indicated temperature. ^{1}H DOSY NMR spectra were recorded with a dstebpgp3s pulse sequence[47,48] with diffusion delays D20 of 0.06-0.10 s and gradient powers P30 of 800 to 2000 µs for each species optimized. Diffusion coefficients were extrapolated with the T1 relaxation module analysis from the fitting with the Stejskal-Tanner-Equation[42] of the decay of each signal´s integration. In Figure 4.48 one example is reported. The hydrodynamic radius was calculated with the Stokes-Einstein equation[43,44] for all ligands and corresponding assemblies.

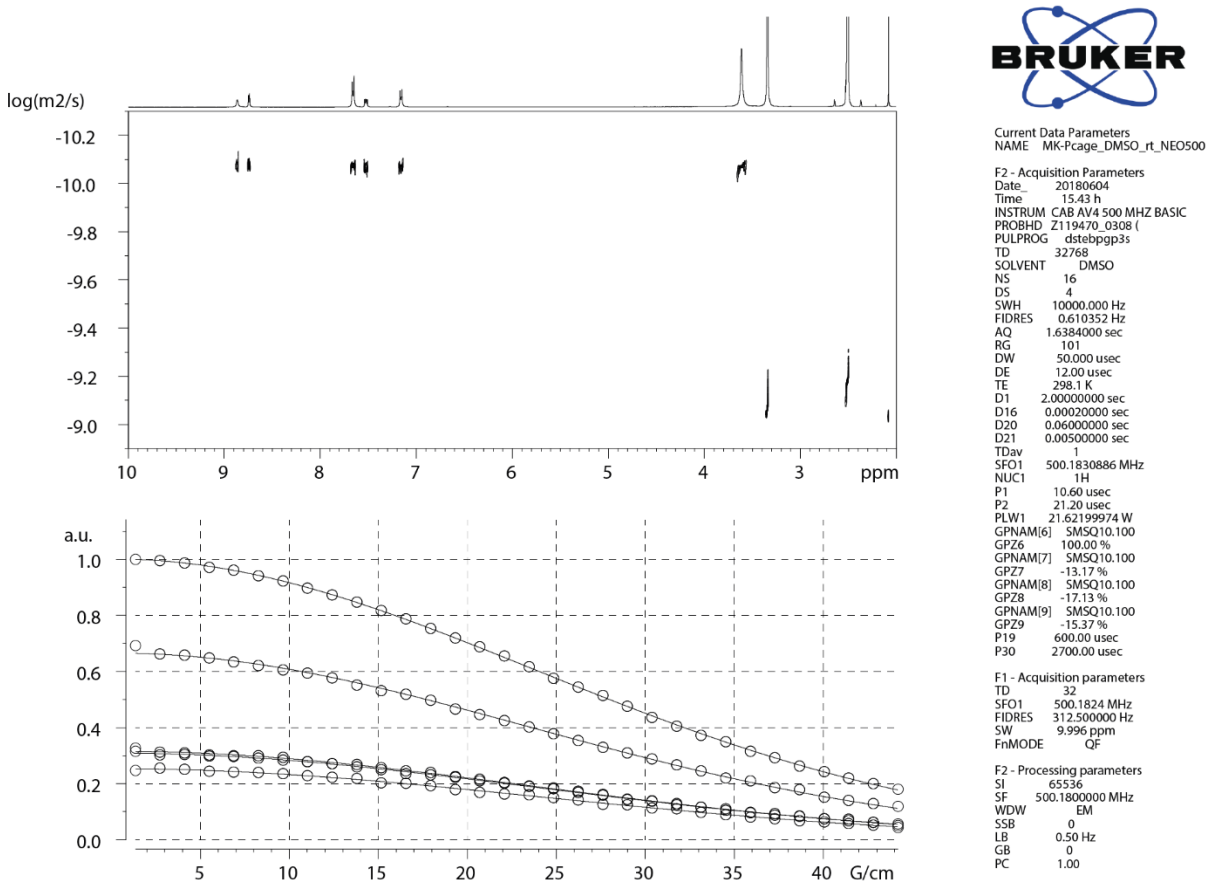

Figure 4.48: ^{1}H DOSY spectrum (500 MHz, 298K, DMSO-d_6) of $[Pd_2(\mathbf{MK\text{-}P})_4](BF_4)_4$ (0.7 mM), T1 analysis and acquisition parameters.

Mass spectrometry

Mass spectrometry data were measured on Bruker ESI-timsTOF (electrospray ionization-trapped ion mobility-time of flight) and Bruker compact high-resolution LC mass spectrometers (positive/negative mode). For calibration of the TIMS and TOF devices, Agilent ESI-Low Concentration Tuning Mix was used.

UV-Vis

UV vis spectra were recorded on a DAD HP-8453 UV-Vis spectrometer. Cuvette path length 0.2 mm, wavelength: 250 nm – 800 nm, step size: 1 nm.

CD

Circular dichroism spectra were recorded in DMSO with an Applied Photophysics Chirascan qCD Spectrometer with a temperature-controlled cuvette holder from the prepared NMR solutions with the proper dilution. The spectra were background-corrected and smoothed with a window size of 5. Cuvette path length 0.2 mm, wavelength: 250 nm – 800 nm, step size: 1 nm, band width: 0.5 nm.

Ion Mobility measurements

Ion mobility measurements were performed by Dr. Ananya Baksi on a Bruker timsTOF instrument combining a trapped ion mobility (TIMS) with a time-of-flight (TOF) mass spectrometer in one instrument. In contrast to the conventional drift tube method to determine mobility data, where ions are carried by an electric field through a stationary drift gas, the TIMS method is based on an electric field ramp to hold ions in place against a carrier gas pushing them in the direction of the analyzer. Consequently, larger sized ions that experience more carrier gas impacts leave the TIMS units first and smaller ions elute later. This method offers a much higher mobility resolution despite a smaller device size.

Briefly, in trapped ion mobility spectrometry (TIMS) the ions are held by an electric field gradient (EFG) while exposed to a constant N_2 flow. The source of the flow is a pressure difference (Δp) between the entrance and the exit of the TIMS-tunnel. Lowering the EFG results in the elution of the analyte according to its inverse mobility ($1/K_0$). Depending on the difference between start-EFG and end-EFG (ΔEFG) as well as the duration of this reduction (ramp time = t_r), rather high ion mobility resolutions can be achieved. Resolutions of 200 and higher was targeted in all the experiments using custom mode of measurement. In front of the trapping part of the TIMS-tunnel, a second ramp accumulates the ions for a given period of time (accumulation time = t_a) in order to enhance the overall duty cycle. Since TIMS doesn't operate on first principles, a calibration is necessary. For calibration, Agilent Tune-Mix™ was used as purchased and the reported drift tube $^{DT}CCS_{N2}$ values published by Stow et al.[49] have been used. TIMS determines (calibrated) inverse mobilities which were converted to the tabulated $^{TIMS}CCS_{N2}$ values following Mason-Schamion equation

$$CCS = \left(\frac{3}{16N}\right)\left(\frac{2\pi}{kT}\right)^{0.5}\frac{q}{\sqrt{\mu}}\frac{1}{K_0}$$

where, q is the charge of the ion, N the number density of the collision gas, μ is the reduced mass of the ion and the N_2 collision gas, k the Boltzmann's constant, T the temperature in Kelvin. Both the analyte solution and the calibrants have been electrosprayed in cationic mode with the same experimental conditions. Therefore, the first part of the equation is constant for every ions measured in the same condition. The constant was found by calculating the reduced mobility of the calibrant ions and plotting them against their reported CCS. The plot was fitted using linear fit with fixed intercept at 0. The slope is the constant for the specific experiment. The $1/K_0$ found from the experiment was then multiplied as per the equation. Optimized parameters: After the generation of ions by electrospray ionisation (ESI, analyte concentration: 0.1 mg/mL solvent: Acetonitrile, capillary voltage: 2000V, end plate offset voltage: 150V, nebulizer gas pressure: 0.3 bar, dry gas flow rate: 3.0 l/min, dry temperature: 75 °C) the desired ions were orthogonally deflected into the TIMS cell consisting of an entrance funnel, the TIMS analyser (carrier gas: N_2, temperature: 305 K, entrance pressure: 2.72 mbar, exit pressure: 0.96 mbar, Δp = 1.77 mbar, t_r = 450 ms, t_a = 5 ms, a stepwise reduction of the electric field strength leads to a release of ion packages separated by their mobility. After a subsequent focussing, the separated ions are transferred to the TOF-analyser.

Experimental procedures

Where necessary, experiments were performed under nitrogen atmosphere using standard Schlenk techniques. Chemicals and standard solvents were purchased from Sigma Aldrich, Acros Organics, Carl

Roth, TCI Europe, VWR, ABCR and used as received, if not mentioned differently. Dry solvents were purchased or purified and dried over absorbent-filled columns on a GS-Systems solvent purification system (SPS). Reactions were monitored with thin layer chromatography (TLC) using silica coated aluminium plates (Merck, silica 60, fluorescence indicator F254, thickness 0.25 mm). For column chromatography, silica (Merck, silica 60, 0.02–0.063 mesh ASTM) was used as the stationary phase.

4.8.2 Synthesis of the ligands

Synthesis of MK-P

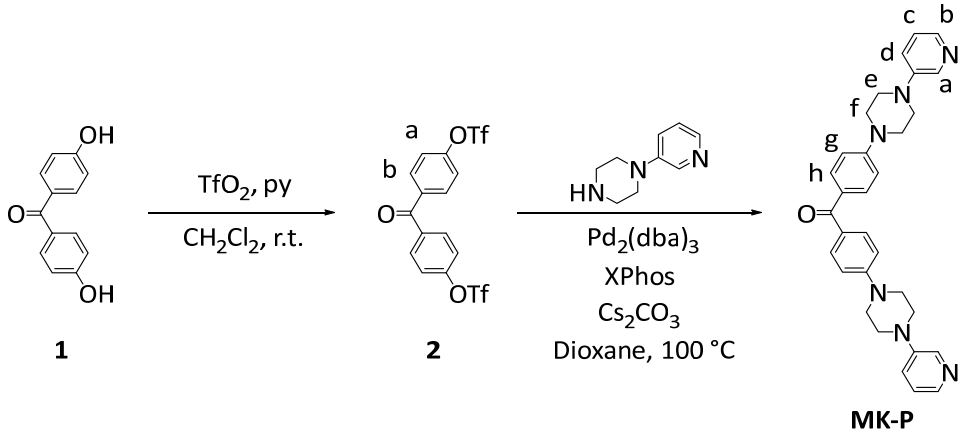

Figure 4.49: Synthesis of **MK-P**.

4,4-Di(trifluoromethanesulfonyl)benzophenone (2)

The synthesis of 4,4-Di(trifluoromethanesulfonyl)benzophenone was carried out according to a procedure described by Plietzsch and co-workers [50].

To a solution of 4,4-dihydroxybenzophenone (2.00 g, 9.34 mmol, 1 equiv.) in dry pyridine (25 mL), trifluoromethanesulfonic anhydride (3.4 mL, 5.79 g, 20.5 mmol, 2.2 equiv.) was added dropwise at 0 °C under N_2 atmosphere. The reaction mixture was stirred for 14 h and was allowed to warm to r.t.. The reaction was quenched with water (40 mL). The aqueous reaction mixture was extracted with CH_2Cl_2 (3 × 40 mL). The combined organic layers were washed with 10% HCl (40 mL) and 1M NaOH solution (40 mL), dried over $MgSO_4$ and the solvent was removed under reduced pressure. The crude product was purified by column chromatography (0-10 % EtOAc/*n*-Hexane solvent gradient). The product was isolated as white solid (3.96 g, 8.28 mmol, 88.7 %).

^{1}H NMR (500 MHz, 298 K, Chloroform-*d*) δ 7.91 (d, *J* = 8.8 MHz 4H, Hb), 7.43 (d, *J* = 8.8 MHz 4H, Ha).

^{13}C NMR (126 MHz, 298 K, Chloroform-*d*) δ 192.99 (C=O), 152.44 (C^q, **C**-Ca), 136.80 (C^q, **C**-Cb), 132.29 (Cb), 121.88 (Ca), 118.73 (**C**F_3, $J_{C\text{-}F}$=321.17 Hz).

HR ESI-MS: measured for $(C_{15}H_8F_6O_7S_2H)^+$: 478.9696

Calculated: 478.9688

Synthesis of MK-P

Compound **2** (100 mg, 210 µmol, 1.0 equiv.) was added together with $Pd_2(dba)_3$ (19.0 mg, 20.9 µmol, 0.1 equiv.), XPhos (30.0 mg, 62.7 µmol, 0.3 equiv.), Cs_2CO_3 (190 mg, 585 µmol, 2.8 equiv.) and 1- (Pyridin-3-yl)piperazine (75.1 mg, 459.9 µmol, 2.2 equiv.) in dioxane into a schlenk tube und the mixture was degassed via the *pump- and freeze-method*. The mixture was heated to 100 °C for 18 h. The solvent was evaporated and the reaction mixture was purified by column chromatography (0-5 % CH_2Cl_2/MeOH solvent gradient). The product was isolated as a yellow solid (87 mg, 172.4 µmol, 82.5 %).

^{1}H NMR (600 MHz, 298 K, Chloroform-*d*) δ 8.31 (s, 1H, Ha), 8.10 (s, 1H, Hb), 7.75 – 7.70 (m, 2H, Hh), 7.20 – 7.12 (m, 2H, Hc, Hd), 6.93 – 6.87 (m, 2H, Hg), 3.49 – 3.45 (m, 4H, Hf), 3.35 – 3.31 (m, 4H, He).

^{13}C NMR (151 MHz, 298 K, Chloroform-*d*) δ 194.08 (C=O), 153.41 (C^{q}, Cg-**C**), 146.85(C^{q}, Cd-**C**-Ca), 141.37 (Cb), 138.92 (Ca), 132.22 (Ch), 129.15 (Ch-**C**), 123.77 (Cd), 122.87 (Cc), 114.00 (Cg), 48.59 (Ce), 47.77 (Cf).

HR ESI-MS: measured for ($C_{31}H_{32}N_6OH^+$): 505.2710

calculated: 505.2706

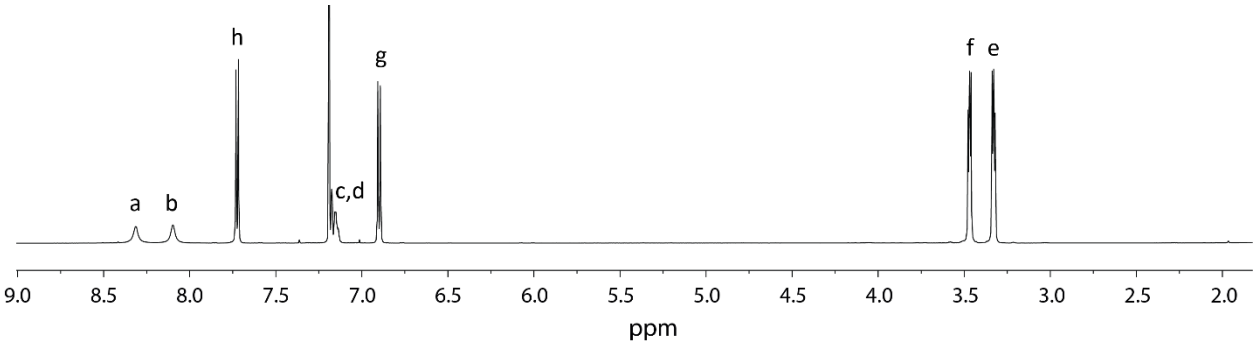

Figure 4.50: ^{1}H NMR spectrum (600 MHz, 298K, $CDCl_3$) of the ligand **MK-P**.

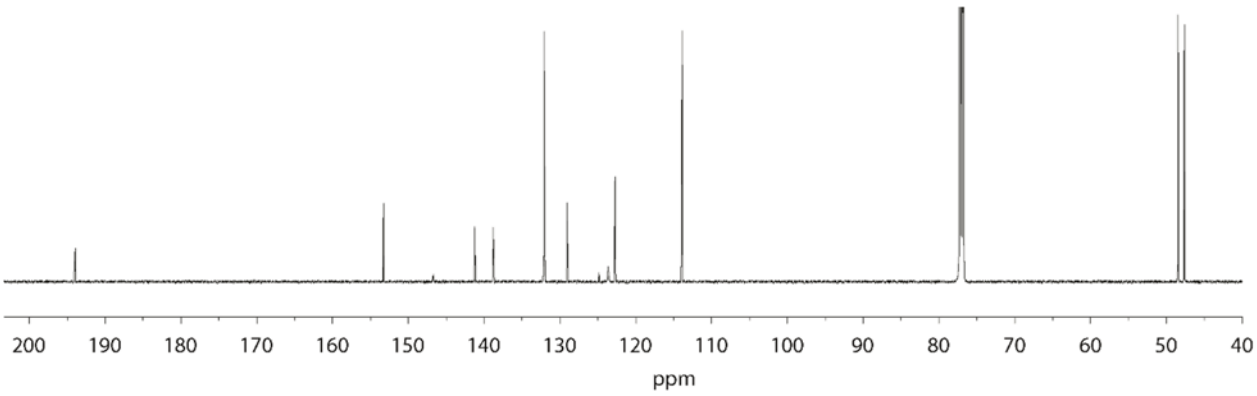

Figure 4.51: ^{13}C NMR spectrum (151 MHz, 298K, $CDCl_3$) of the ligand **MK-P**.

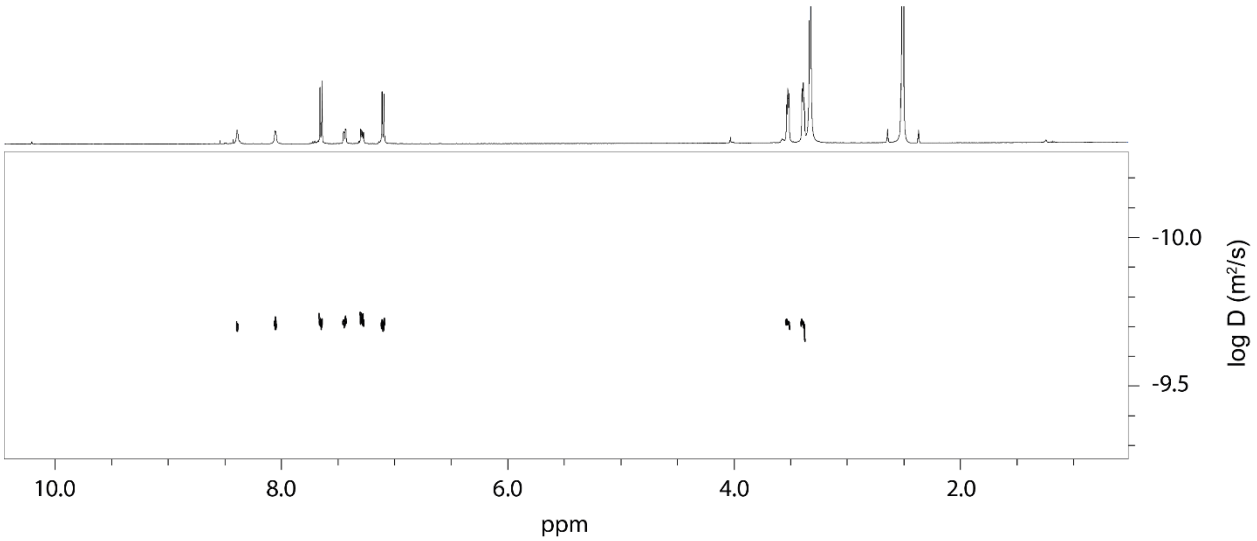

Figure 4.52: ^{1}H DOSY spectrum (500 MHz, 298K, DMSO-d_6) of **MK-P** (2.8 mM). Diffusion coefficient: 1.902×10^{-10} m^2s^{-1}, log D=-9.721. Hydrodynamic radius= 5.77 Å.

Synthesis of RB-P

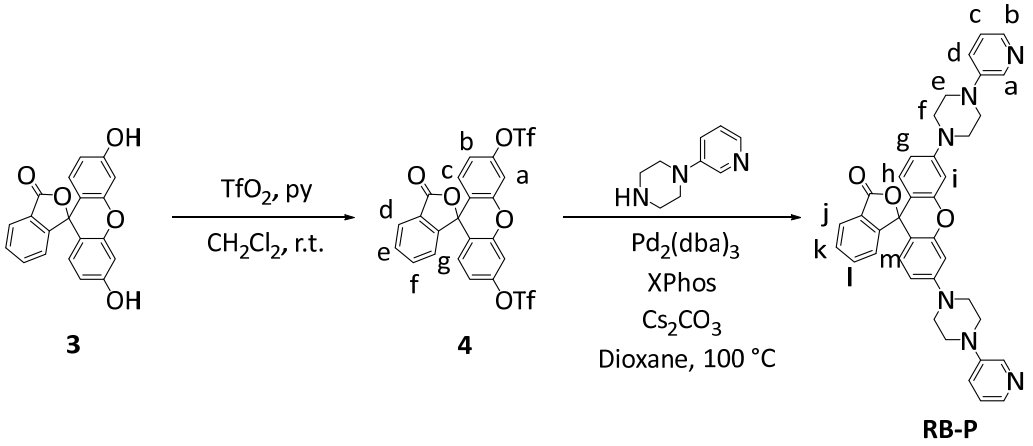

Figure 4.53: Synthesis of **RB-P**.

Synthesis of 3-Oxo-3H-spiro[isobenzofuran-1,9'-xanthene]-3',6'-diyl bis(trifluoromethanesulfonate) (4)

The synthesis of 4,4-Di(trifluoromethanesulfonyl)benzophenone was carried out according to a procedure described by Grimm and co-workers.[51]

Fluorescein (2.50 g, 7.52 mmol, 1.0 equiv.) was dissolved in 30 mL of CH_2Cl_2 and the solution was degassed via the *pump- and freeze-method*. The solution was cooled to 0 °C with an ice bath. Pyridine (4.76 g, 4.87 mL, 60.2 mmol, 8.0 equiv.) and trifluoromethanesulfonic anhydride (8.49 g, 5.06 mL, 30.1 mmol, 4.0 equiv.) were added. The ice bath was removed and the reaction mixture was stirred for 21 h at r.t.. The reaction mixture was mixed with water (30 mL) and the product was extracted with CH_2Cl_2 (2 x 30 mL). The organic extracts were collected, washed with NaCl (each 30 mL) and dried over $MgSO_4$. The solvent was removed and the crude product was purified by column chromatography (0-30 % EtOAc/*n*-Hexane solvent gradient). The product was isolated as yellow solid (3.73 g, 6.26 mmol, 83 %).

^{1}H NMR (300 MHz, 298 K, Chloroform-*d*) δ = 8.11 – 8.04 (m, 1H, Hd), 7.78 – 7.65 (m, 2H, He, Hf), 7.30 (d, *J* = 2.4 Hz, 2H, Ha), 7.22 – 7.15 (m, 1H, Hg), 7.03 (dd, *J* = 8.8 Hz, 2.4 Hz, 2H, Hb), 6.96 (d, *J* = 8.8 Hz, 2H, Hc).

^{13}C NMR (75 MHz, 298 K, Chloroform-*d*) *δ* 168.57(**C**=O), 152.32 (C^q, **C**-Cd) 151.48 (C^q, **C**-Ca), 150.38 (C^q, **C**-Cc), 135.94 (Ce), 130.83 (Cf), 130.11 (Cc), 125.87 (Cd), 125.78 (C^q, **C**-Cg), 123.89 (Cg), 119.51 (C^q, Ca-**C**-Cb), 118.71 (**C**F_3, $J_{C\text{-}F}$=119.52 Hz), 117.52(Cb), 110.84 (Ca), 80.22(spiro C^q).

HR ESI-MS: measured for ($C_{22}H_{10}F_6O_9S_2H^+$): 596.9742

calculated: 596.9743

Synthesis of RB-P

Compound **4** (280 mg, 470 µmol, 1.0 equiv.) was added together with $Pd_2(dba)_3$ (86 mg, 94 µmol, 0.2 equiv.), XPhos (67 mg, 141 µmol, 0.3 equiv.), Cs_2CO_3 (429 mg, 1.31 mmol, 2.8 equiv.) and 1-(pyridin-3-yl)piperazine (168.6 mg, 1.03 mmol, 2.2 equiv.) in dioxane into a schlenk tube und the mixture was degassed via *the pump- and freeze-method*. The mixture was heated to 100 °C for 18 h. The solvent was evaporated and the reaction mixture was purified by column chromatography (0-10 % MeOH /CH_2Cl_2). The product was isolated as a light pink solid (230 mg, 369 µmol, 78.7 %).

^{1}H NMR (600 MHz, 298 K, Acetonitrile–d_3) δ 8.34 (d, *J* = 3.0 Hz, 2H, Ha), 8.05 (dd, *J* = 4.6, 1.1 Hz, 2H, Hb), 7.98 (dt, *J* = 7.7, 1.0 Hz, 1H, Hm), 7.74 (td, *J* = 7.5, 1.2 Hz, 1H, Hk), 7.68 (td, *J* = 7.5, 1.0 Hz, 1H, Hl), 7.32 (ddd, *J* = 8.6, 3.1, 1.4 Hz, 2H, Hd), 7.24 – 7.15 (m, 3H, Hc, Hj), 6.80 (d, *J* = 2.5 Hz, 2H, Hi), 6.74 (dd, *J* = 8.9, 2.5 Hz, 2H, Hg), 6.66 (d, *J* = 8.9 Hz, 2H, Hh), 3.45-3.39 (m, 8H, Hf), 3.39-3-34 (m, 8H, He).

^{13}C NMR (151 MHz, 298 K, Acetonitrile–d_3) δ 169.79 (C=O), 153.60 (C^q, Cg-**C**-Ci), 153.54 (C^q, **C**-Cm), 153.07 (C^q, Cg-**C**-Ci), 147.52(C^q, Ca-**C**-Cd), 141.09 (Cb), 139.04 (Ca), 135.79 (Cl), 130.37 (Ck), 129.26 (Ch), 127.48 (C^q, **C**-Cj), 125.16 (Cj), 124.41 (Cm), 124.08 (Cc), 122.91 (Cd), 112.49 (Cg), 109.88 (C^q, C-Ch), 102.21 (Ci), 84.15 (spiro C^q), 48.55 (Ce), 48.24 (Cf).

HR ESI-MS: measured for ($C_{38}H_{34}N_6O_3H^+$): 623.2762

calculated: 623.2765

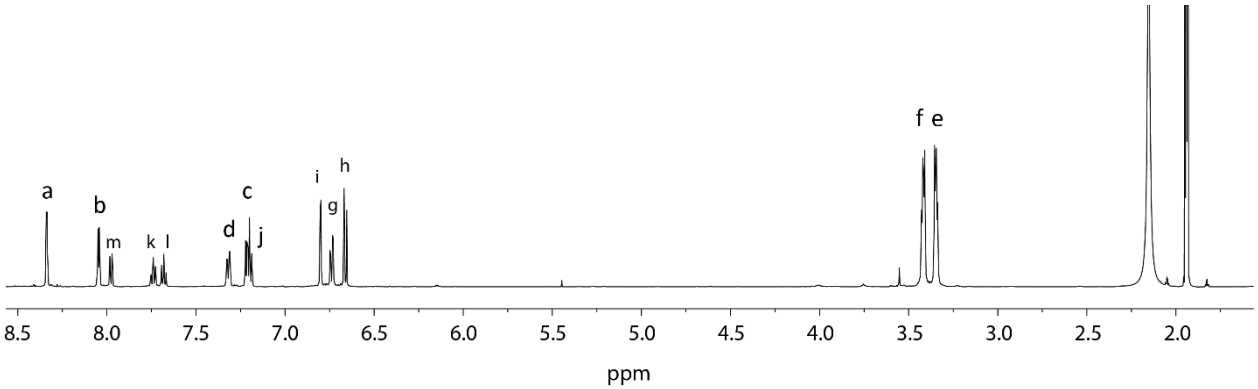

Figure 4.54: ^{1}H NMR spectrum (600 MHz, 298K, CD_3CN) of the ligand **RB-P**.

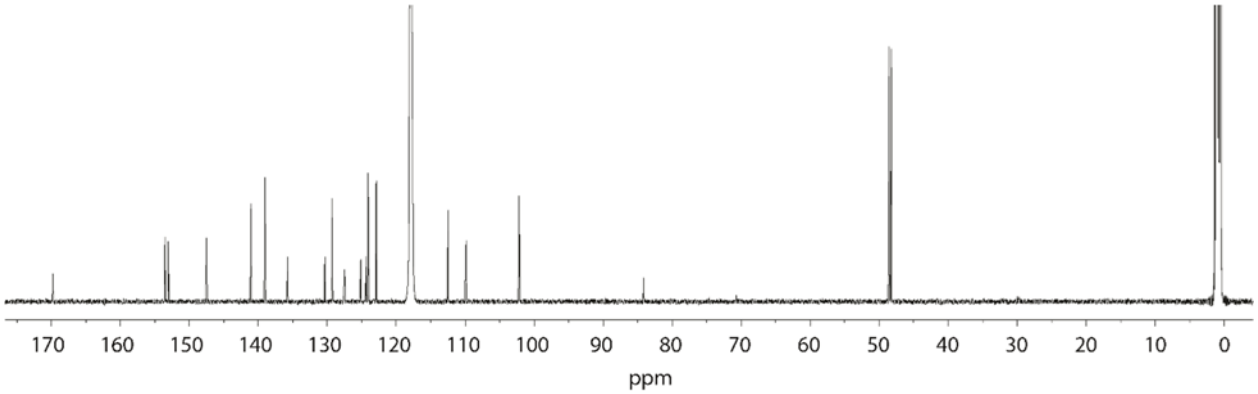

Figure 4.55: ^{13}C NMR spectrum (151 MHz, 298K, CD_3CN) of the ligand **RB-P**.

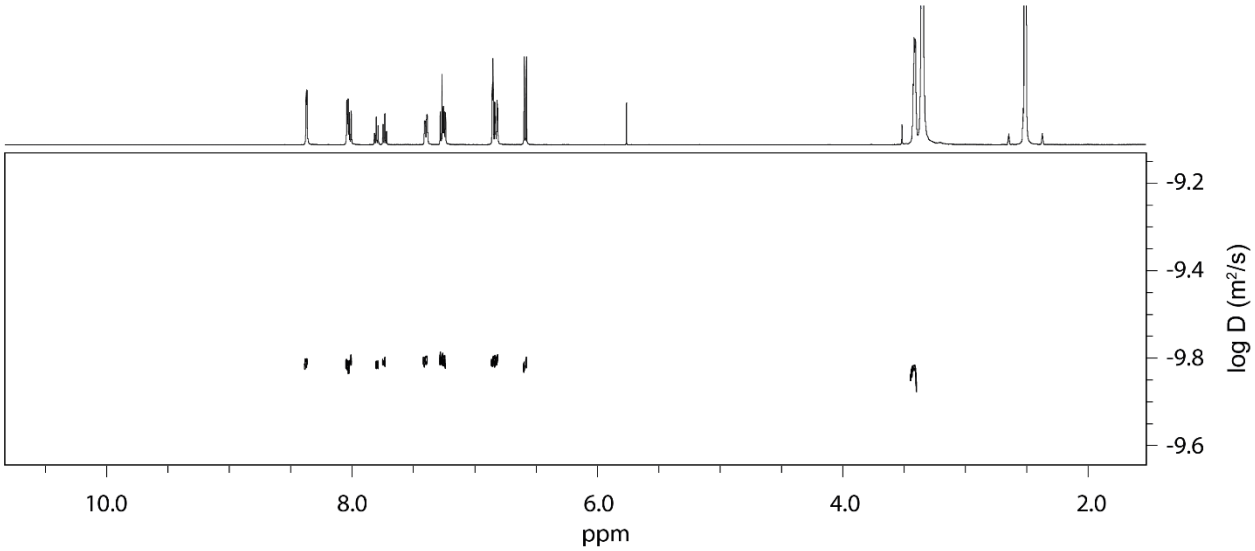

Figure 4.56: ^{1}H DOSY spectrum (500 MHz, 298K, DMSO-d_6) of **RB-P** (2.8 mM). Diffusion coefficient: 1.667×10^{-10} m^2s^{-1}, log D=-9.778. Hydrodynamic radius= 6.59 Å.

Synthesis of MB-PBF_4 and MB-PNO_3

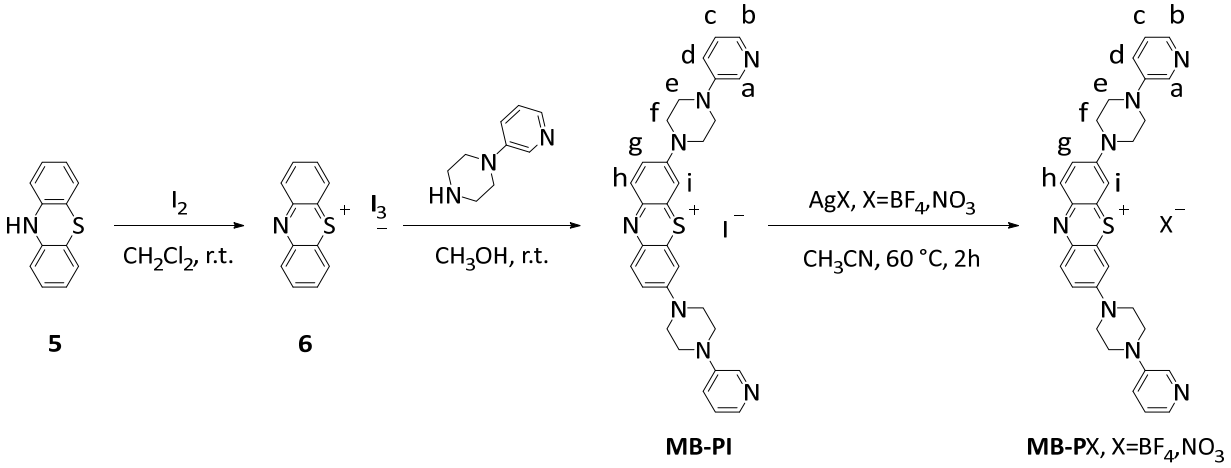

Figure 4.57: Synthesis of ligands **MB-P**BF_4 and **MB-P**NO_3.

Oxidation of 10H-phenothiazine (6)

10H-Phenothiazine (2 g, 10 mmol) was dissolved in 50 mL of CH_2Cl_2 at r.t.. A solution of iodine (8 g, 30 mmol) in CH_2Cl_2 (150 mL) was added, and the whole mixture stirred for 10 h at r.t.. The resulting purple-black solid was filtered and washed free of iodine by using large amounts of CH_2Cl_2. Yield: 5.00 g. The compound was directly used in the next step.

Synthesis of MB-PI

To a solution of the above-mentioned black powder **6** (1 mmol, 0.706 g, 1 equiv.) in methanol (15 mL) a methanol (15 mL) solution of 1–(3–pyridinyl)piperazine (1.63 g, 10 mmol, 10 equiv.) was added drop-wise. The reaction was carried out under stirring at r.t.. When the reaction was complete (15 h, TLC control), the solution was evaporated to dryness under vacuum and purified by flash column chromatography (Rf=0.4, CH_2Cl_2 : MeOH 95 : 5). After collection and evaporation, the compound was purified by reprecipitation using CH_3OH/EtOAc and the desired product was obtained as a dark blue powder (180 mg).

^{1}H NMR (500 MHz, 298 K, Acetonitrile–d_3) δ 8.31 (d, *J* = 2.5 Hz, 2H, Ha), 8.07 (d, *J* = 3.4 Hz,2H, Hb), 8.00 (d, *J*=9.6 Hz, 2H, Hh), 7.57 (dd, *J*=9.8, 2.5 Hz, 2H, Hg), 7.46 (d, *J*=2.4 Hz, 2H, Hi), 7.36 (d, *J*=7.6 Hz, 2H, Hd), 7.29 (dd, *J*=8.3, 4.6 Hz, 2H, Hc), 3.96–4.02 (m, 8H, Hf), 3.57–3.43 (m, 8H, He).

^{13}C NMR (126 MHz, 298 K, Acetonitrile–d_3) δ 146.65 (C^q, Ca-**C**-Cd), 140.44 (Cb), 139.28 (Ch), 137.65 (C^q, **C**-Ch), 137.08 (Ca), 135.82 (C^q, **C**-Ci), 124.38 (Cc), 122.81 (Cd), 119.87 (Cg), 107.39 (Ci), 47.65 (Ce,Cf). C^q, Ci-**C**-Cg not found.

HR ESI-MS: measured for ($C_{30}H_{30}N_7S^+$): 520.2254

calculated: 520.2278

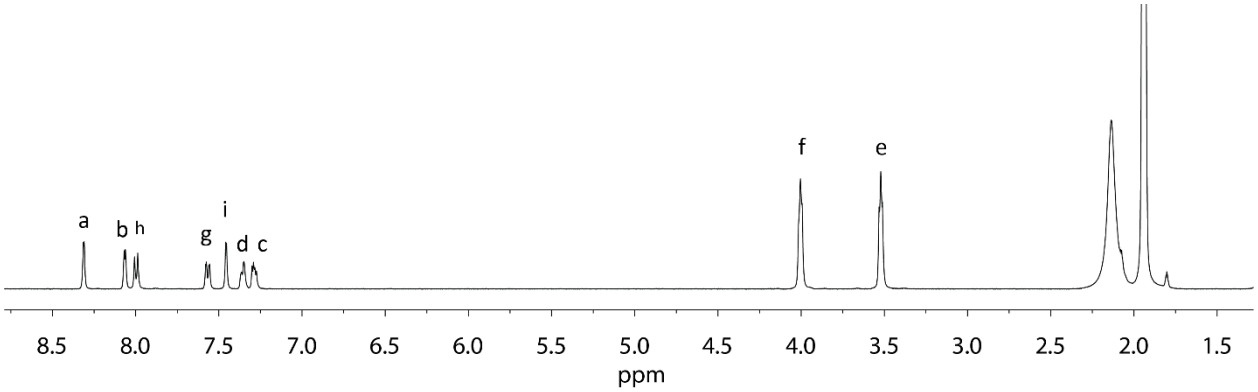

Figure 4.58: ^{1}H NMR spectrum (500 MHz, 298K, CD_3CN) of **MB-P**I.

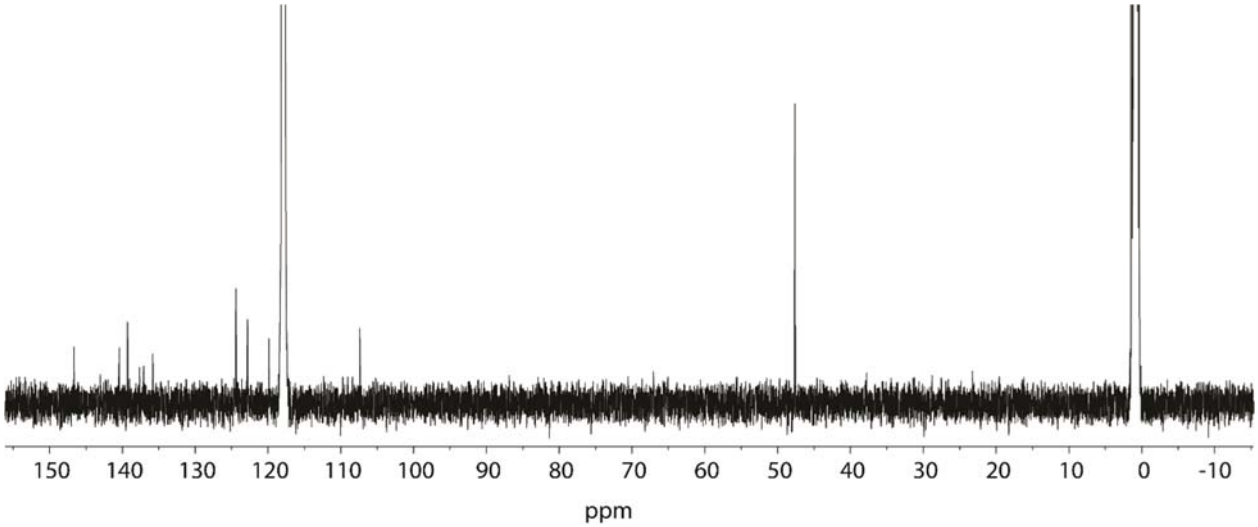

Figure 4.59: ^{13}C NMR spectrum (126 MHz, 298K, CD_3CN) of **MB-P**I.

Synthesis of MB-PBF_4 and MB-PNO_3.

To an acetonitrile (10 mL) solution of **MB-P**I (64.76 mg, 0.1 mmol, 1 equiv.) was added the silver salt of the desired counterion ($AgBF_4$ or $AgNO_3$) (0.11 mmol, 1.1 equiv.). The reaction was carried out under stirring at 60 °C for 2 h. After cooling down to r.t., the resulting solution was filtered and washed by using acetonitrile to get the filtrate. The solvent was evaporated to obtain the product in a quantitative yield.

MB-PBF_4

^{1}H NMR (600 MHz, 298 K, Acetonitrile–d_3) δ 8.29 (d, *J* = 2.8 Hz, 1H, Ha), 8.06 (dd, *J* = 4.6,1.1 Hz, 1H, Hb), 8.00 (d, *J* = 9.6 Hz, 1H, Hh), 7.56 (dd, *J* = 9.7, 2.8 Hz, 1H, Hg), 7.44 (d, *J* = 2.8 Hz, 1H, Hi),7.43–7.38 (m, 1H, Hd), 7.33 (dd, *J* = 8.5, 4.7 Hz, 1H, Hc), 4.04–3.96 (m, 4H, Hf), 3.58–3.49 (m, 4H, He).

^{13}C NMR (151 MHz, 298 K, Acetonitrile–d_3) δ 154.53 (C^q, Ci-**C**-Cg), 147.19 (C^q, Ce-**C**-Cd), 139.66 (Cb), 139.62 (Ch), 137.44 (C^q, **C**-Ch), 136.70 (Ca), 136.18 (C^q, **C**-Ci), 125.14 (Cc), 123.91 (Cd), 120.21 (Cg), 107.70 (Ci), 47.89 (Ce), 47.74 (Cf).

HR ESI-MS: measured for ($C_{30}H_{30}N_7S^+$): 520.2256

calculated: 520.2278

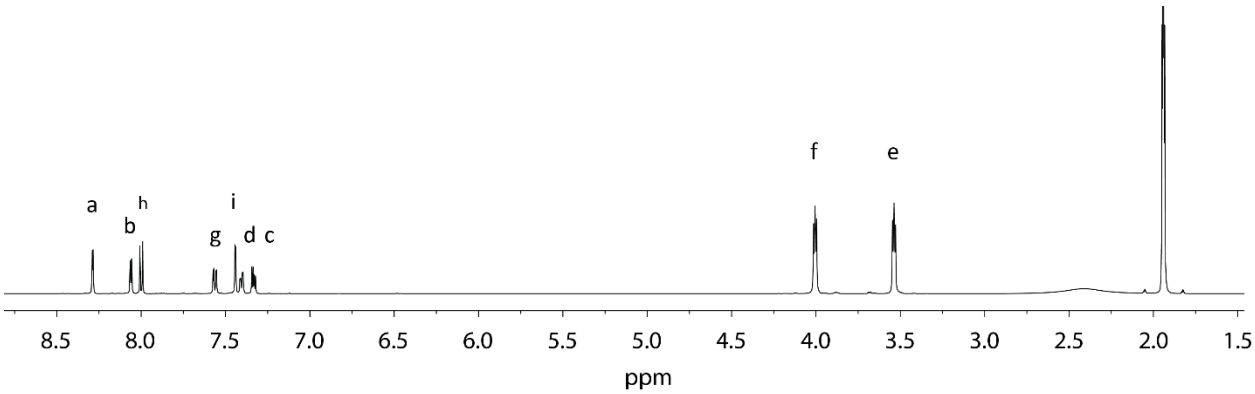

Figure 4.60: ^{1}H NMR spectrum (600 MHz, 298K, CD_3CN) of the ligand **MB-P**BF_4.

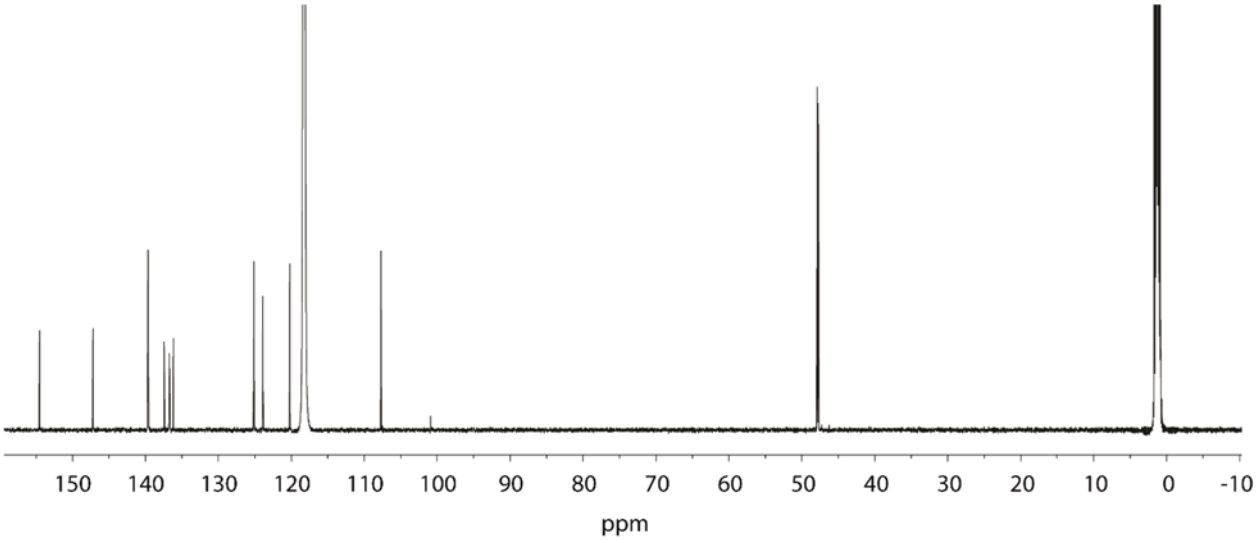

Figure 4.61: ^{13}C NMR spectrum (151 MHz, 298K, CD_3CN) of the ligand **MB-P**BF_4.

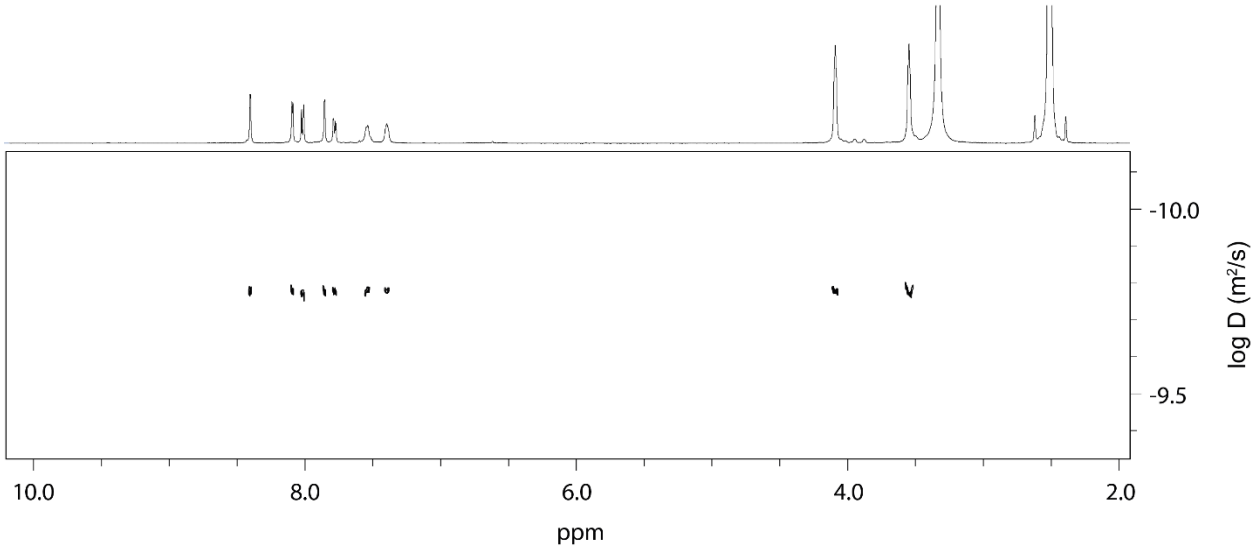

Figure 4.62: ^{1}H DOSY spectrum (500 MHz, 298K, DMSO-d_6) of **MB-P**BF_4 (2.8 mM). Diffusion coefficient: 1.625×10^{-10} m^2s^{-1}, log D=-9.789. Hydrodynamic radius= 6.75 Å.

MB-PNO_3

^{1}H NMR (600 MHz, 298 K, Methanol-d_4) δ 8.33 (s, 1H, Ha), 8.10 – 8.05 (m, 2H, Hb, Hc), 7.72 (dd, *J* = 9.7, 2.8 Hz, 1H, Hg), 7.63 - 7.67 (m, 2H, Hd, Hi), 7.50 (dd, *J* = 8.9, 4.9 Hz, 1H, Hc), 4.12 (t, *J* = 5.4 Hz, 4H, Hf), 3.63 (t, *J* = 5.4 Hz, 4H, He).

^{13}C NMR (151 MHz, 298 K, Methanol-d_4) δ 155.16 (C^q, Cg-**C**-Ci), 148.40 (C^q, Ca-**C**-Cd), 140.05 (Ch), 137.93 (Cb), 136.75 (2 overlapping C^q, Ch-**C** and Ci-**C**), 135.06 (Ca) 126.31 (Cd), 125.85 (Cc), 120.49 (Cg), 107.90 (Ci), 48.10 (Ce), 48.02 (Cf).

HR ESI-MS: measured for ($C_{30}H_{30}N_7S^+$): 520.2338

calculated: 520.2278

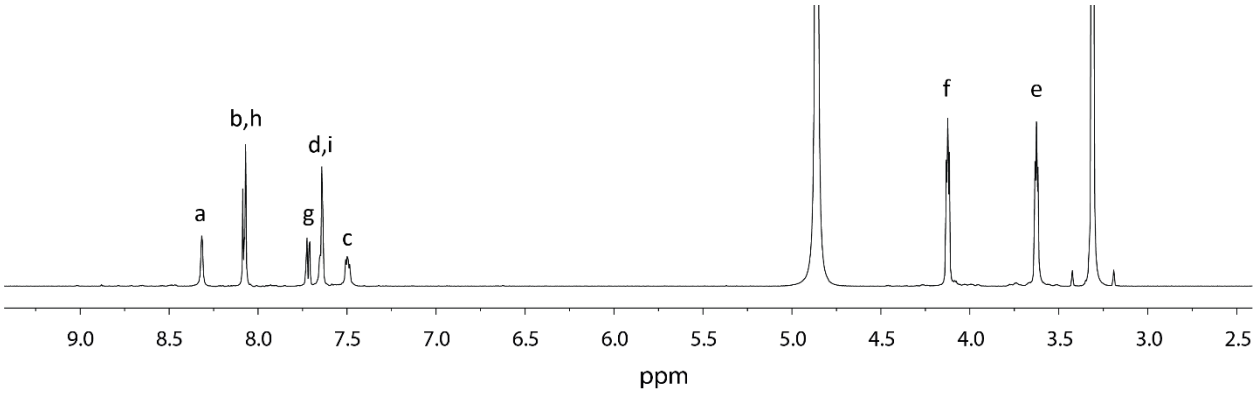

Figure 4.63: ^{1}H NMR spectrum (600 MHz, 298K, MeOD) of the ligand **MB-P**NO_3.

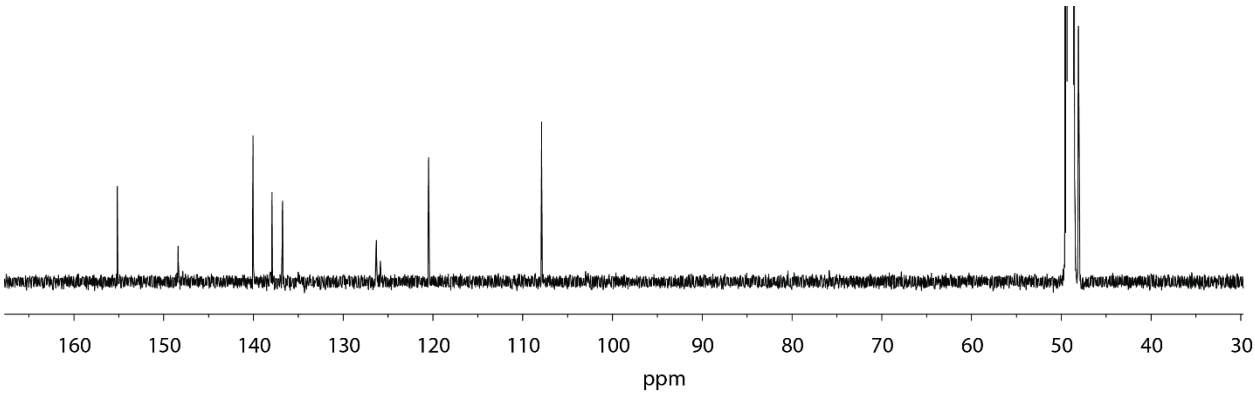

Figure 4.64: ^{13}C NMR spectrum (151 MHz, 298K, MeOD) of the ligand **MB-P**NO_3.

Synthesis of CV-P

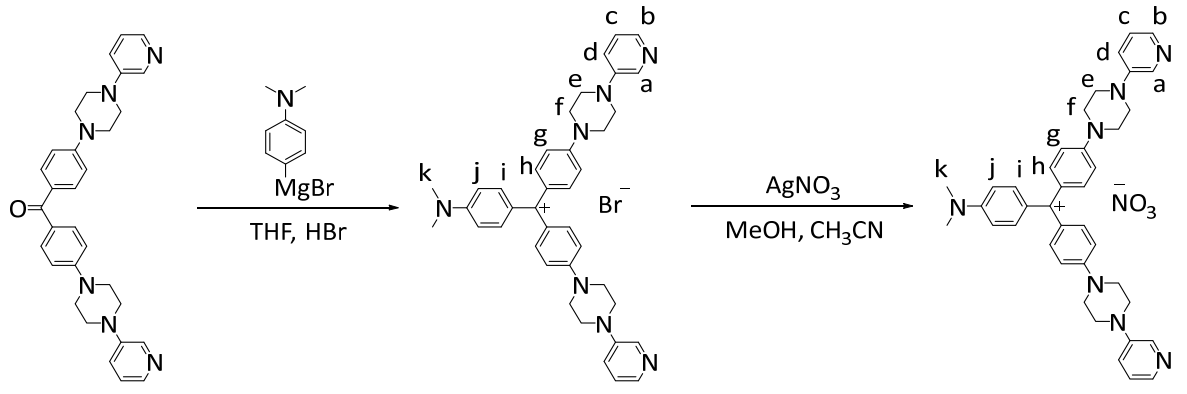

MK-P **CV-P**Br **CV-P**

Figure 4.65: Synthesis of ligand **CV-P**.

Synthesis of CV-PBr

To a round bottom flask already equipped with stir bar, Mg (160 mg, 1.3 equiv., 6.60 mmol) was added and heated under vacuum to remove any trace of water. 4-Bromo-N,N-dimethylaniline (1 g, 1 equiv., 5 mmol) was added and the whole system is evacuated for some minutes. To the solids 10 mL of dry THF were added together with a small iodine crystal. The flask was gently warmed to reflux for 90 minutes. During this time the solution changes from dark to dingy gray. An ice bath was then used to cool down to r.t. the flask.

In a dry round bottom flask **MK-P** (113 mg, 1 equiv., 223 µmol) was added together with 4 mL of dry THF. To the yellow suspension, 1.5 mL of the grey suspension above described are added and the system was put under reflux for 5 minutes and again cooled down to r.t. with an ice bath. Slowly 4 mL of HBr (10% W/W) are added to obtain the final product. The color of the solution changes from bright yellow to deep violet/blue. The solution was than neutralized with a saturated solution of $NaHCO_3$ and as soon as pH 7 was reached the desired product precipitates as blue flakes. All the volatiles are removed and the product purified by column chromatography (0-10 % MeOH /CH_2Cl_2). The product was isolated as a dark violet solid (90 mg, 130 µmol, 58%).

^{1}H NMR (500 MHz, 298 K, Methanol-d_4) δ 8.30 (d, J = 3.0 Hz, 1H, Ha), 8.02 (d, J = 4.7 Hz, 1H, Hb), 7.50 (dd, J = 8.5, 2.7 Hz, 1H, Hd), 7.43 (m, 3H, Hi, Hh), 7.35 (dd, J = 8.5, 4.6 Hz, 1H, Hc), 7.23 (d, J = 8.9 Hz, 2H, Hg), 7.04 (d, J = 9.1 Hz, 1H, Hj), 3.87 (t, J = 5.2 Hz, 4H, Hf), 3.66 (s, 3H, Hk), 3.49 (t, J = 5.1 Hz, 4H, He).

^{13}C NMR (151 MHz, 298 K, Methanol-d_4) δ 179.79 (C+), 158.14 (C^q, **C**-Cj), 156.91 (C^q, **C**-Cg), 148.50 (C^q, Ca-**C**-Cd), 141.63 (Ci), 140.81 (Ch), 140.79(Cb), 138.15 (Ca), 129.36(C^q, **C**-Ch), 128.22(C^q, **C**-Ci), 125.44 (Cc), 124.47 (Cd), 114.65 (Cg), 114.12 (Cj), 71.57 (Ck), 47.58 (Ce), 47.57 (Cf).

HR ESI-MS: measured for ($C_{39}H_{42}N_7^+$): 608.3498

calculated: 608.3496

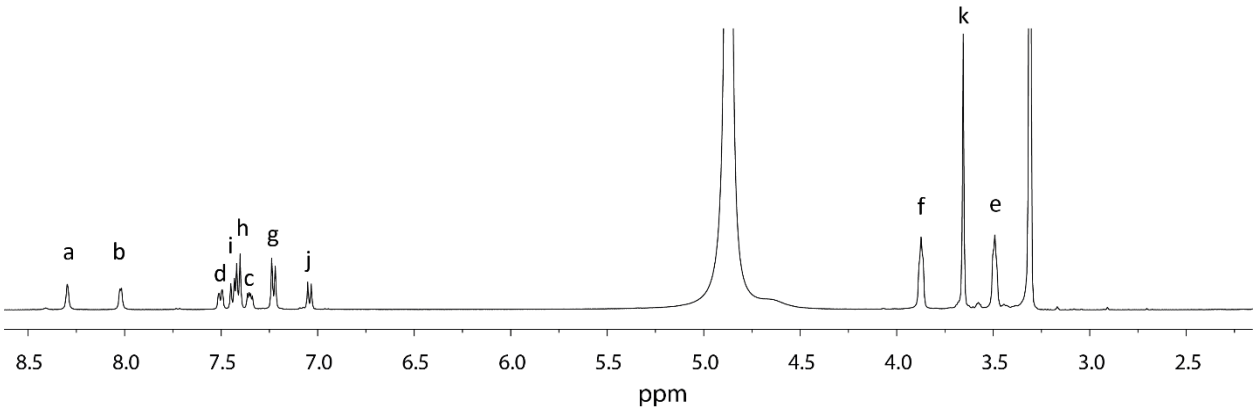

Figure 4.66: ^{1}H NMR (500 MHz, 298K, MeOD) spectrum of **CV-P** Br.

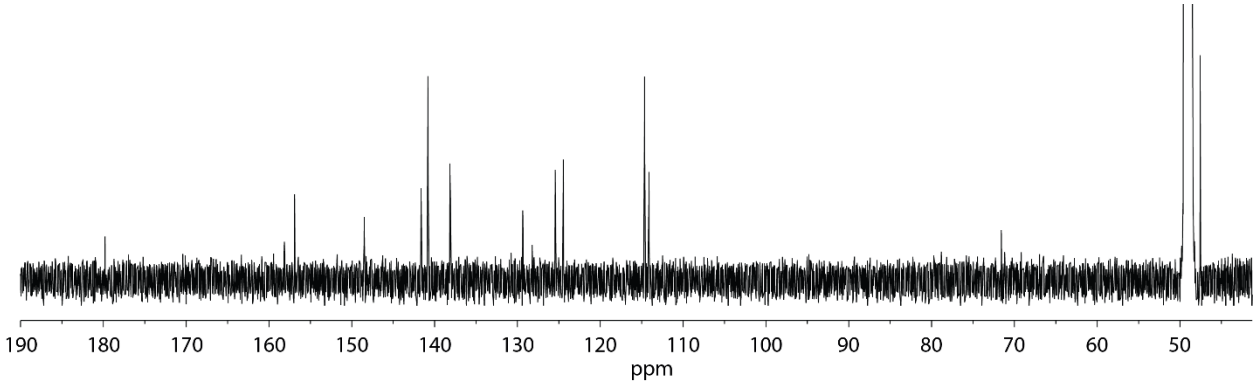

Figure 4.67: ^{13}C NMR (151 MHz, 298K, MeOD) spectrum of **CV-P** Br.

Synthesis of CV-P

To a methanol (15 mL) solution of **CV-P**Br (40 mg, 1 equiv., 58 µmol) was added $AgNO_3$ (11 mg, 1.1 equiv., 64 µmol). The reaction was carried out under stirring at 60 °C for 1 h. After cooling down to r.t., the resulting solution was filtered and washed by using methanol to get the filtrate. The solvent was then evaporated to obtain the product (quantitative).

^{1}H NMR (500 MHz, 298 K, Dimethyl sulfoxide-d_6) δ 8.38 (s, 1H, Ha), 8.05 (s, 1H, Hb), 7.42 (s, 1H, Hd), 7.39 – 7.21 (m, 5H, Hc, Hh, Hi), 7.05 (d, *J* = 9.0 Hz, 1H, Hj), 3.83 (t, *J* = 5.2 Hz, 4H, Hf), 3.45 (d, *J* = 5.3 Hz, 4H, He), 3.26 (s, 3H, Hk).

^{1}H NMR (600 MHz, Methanol-d_4) δ 8.30 (s, 1H, Ha), 8.03 (d, *J* = 4.2 Hz, 1H, Hb), 7.53 – 7.40 (m, 4H, Hd, Hi, Hh), 7.34 (dd, *J* = 8.5, 4.6 Hz, 1H, Hc), 7.23 (d, *J* = 9.3 Hz, 2H, Hg), 7.05 (d, *J* = 9.3 Hz, 1H, Hj), 3.93 – 3.77 (m, 4H, Hf), 3.54 – 3.45 (m, 4H, He).

^{13}C NMR (151 MHz, Methanol-d_4) δ 179.78 (C+), 158.13 (C^q, **C**-Cj), 156.90 (C^q, **C**-Cg), 148.49(C^q, Ca-**C**-Cd), 141.62 (Cb), 140.80 (Ch), 140.76 (Ci), 138.13 (Ca), 129.35(C^q, **C**-Cg), 128.21 (C^q, **C**-Ci), 125.44 (Cc), 124.47 (Cd), 114.65 (Cg), 114.11 (Cj), 71.54, 66.91,(Ce under MeOD signal) 47.57 (Cf), 40.72 (Ck).

HR ESI-MS: measured for ($C_{39}H_{42}N_7^+$): 608.3500

calculated: 608.3496

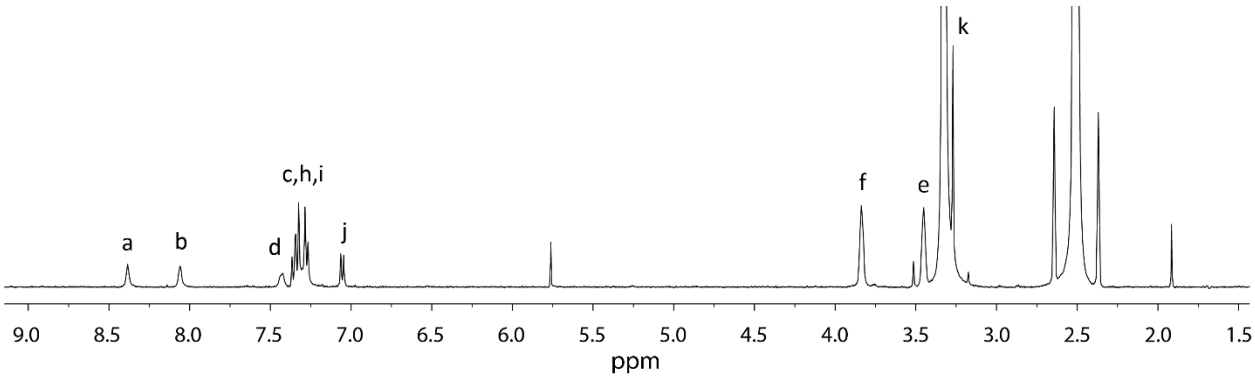

Figure 4.68: ^{1}H NMR (500 MHz, 298K, DMSO-d_6) spectrum of **CV-P**.

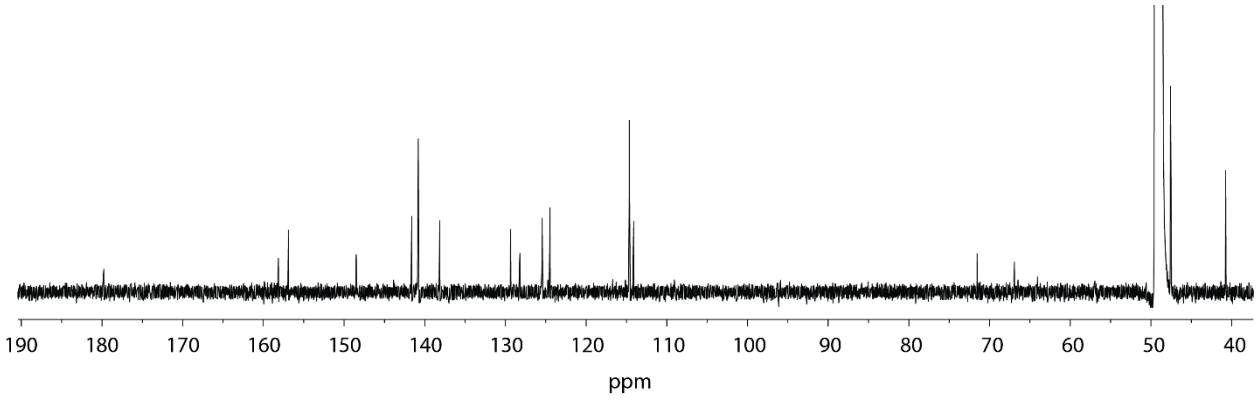

Figure 4.69: ^{13}C NMR (151 MHz, 298K, MeOD) spectrum of **CV-P**.

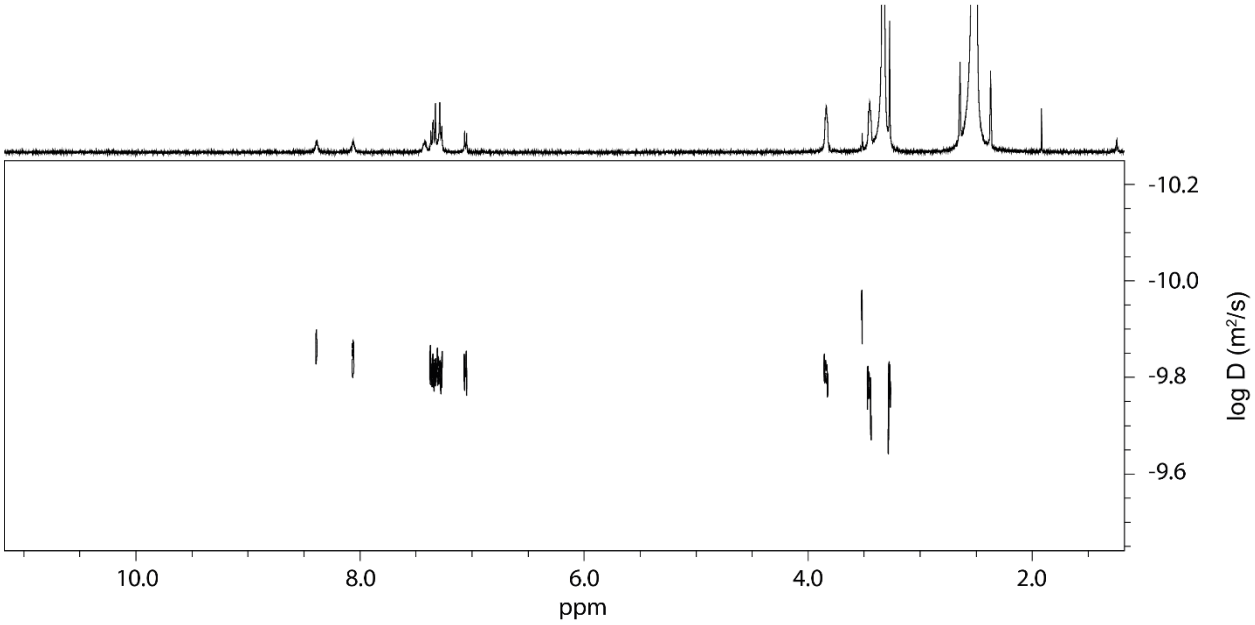

Figure 4.70: ^{1}H DOSY spectrum (500 MHz, 298K, DMSO-d_6) of **CV-P** (2.8 mM). Diffusion coefficient: $1.599\times10\times10^{-10}$ m^2s^{-1}, log D=-9.797. Hydrodynamic radius= 6.87 Å.

Synthesis of RE-P

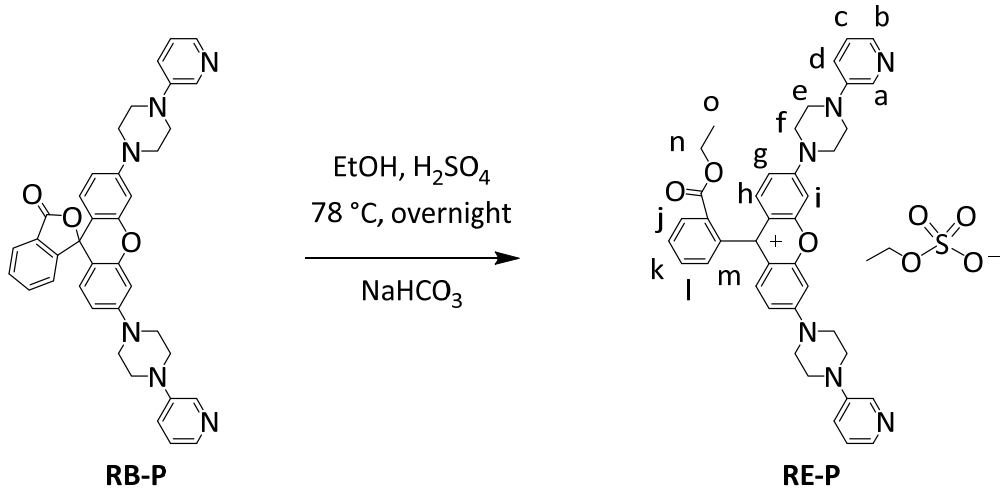

Figure 4.71: Synthesis of ligand **RE-P**.

Ligand **RB-P** (200 mg, 321 mmol) was dissolved in ethanol (5 mL, 321 mmol). Concentrated sulfuric acid (300 µL) was added, and the mixture was heated at 78°C for 16 h. The mixture was than cool down to r.t. and neutralized with a saturated solution of $NaHCO_3$. The solvents were removed in vacuo and the dark viscous solid was purified with column chromatography on silica gel (CH_2Cl_2/MeOH: 95/5) to give ligand **RE-P** (120 mg, 0.184 mmol, 48%). The ligand was further purified with reprecipitation from EtOH/EtO_2.

^{1}H NMR (500 MHz, Dimethyl sulfoxide-d_6) δ 8.35 (d, *J* = 3.0 Hz, 2H, Ha), 8.27 (dd, *J* = 7.9, 1.4 Hz, 1H, Hj), 8.04 (dd, *J* = 4.5, 1.3 Hz, 2H, Hb), 7.93 (td, *J* = 7.5, 1.4 Hz, 1H, Hl), 7.87 (td, *J* = 7.7, 1.4 Hz, 1H, Hk), 7.53 (dd, *J* = 7.6, 1.3 Hz, 1H, Hm), 7.42 – 7.33 (m, 4H, Hd, Hg), 7.31 (d, *J* = 2.4 Hz, 2H, Hi), 7.26 (dd, *J* = 8.5, 4.5 Hz, 2H, Hc), 7.08 (d, *J* = 9.5 Hz, 2H, Hh), 3.96 (m, 10H, Hf, Hn), 3.73 (q, *J* = 7.1 Hz, 2H, -CH_2 counterion), 3.45 (t, *J* = 5.3 Hz, 8H, He), 1.10 (t, *J* = 7.1 Hz, 3H, -CH_3 counterion), 0.89 (t, *J* = 7.1 Hz, 3H, Ho).

^{13}C NMR (151 MHz, Dimethyl sulfoxide-d_6) δ 164.69 (0-**C**=0), 158.63 (C^q, **C**-Cm), 157.45 (C^q, **C**-Ci), 156.48 (C^q, **C**-Ch), 145.84 (C^q, Ca-**C**-Cd), 139.93 (Cb), 137.41 (Ca), 133.20 (C-Cj), 132.89 (Cl), 131.01 (Ch), 130.89 (C+), 130.65 (Cj), 130.35 (Ck), 129.70 (Cm), 123.61 (Cc), 121.62 (Cd), 115.31 (Cg), 113.83 (C^q, **C**-Cg), 97.16 (Ci), 61.16(-**C**H$_2$ counterion), 61.11 (Cn), 46.81 (Cf), 46.36 (Ce), 15.14 (-**C**H$_3$ counterion), 13.45 (Co).

HR ESI-MS: measured for ($C_{40}H_{39}N_6O_3^+$): 651.3060

calculated: 651.3078

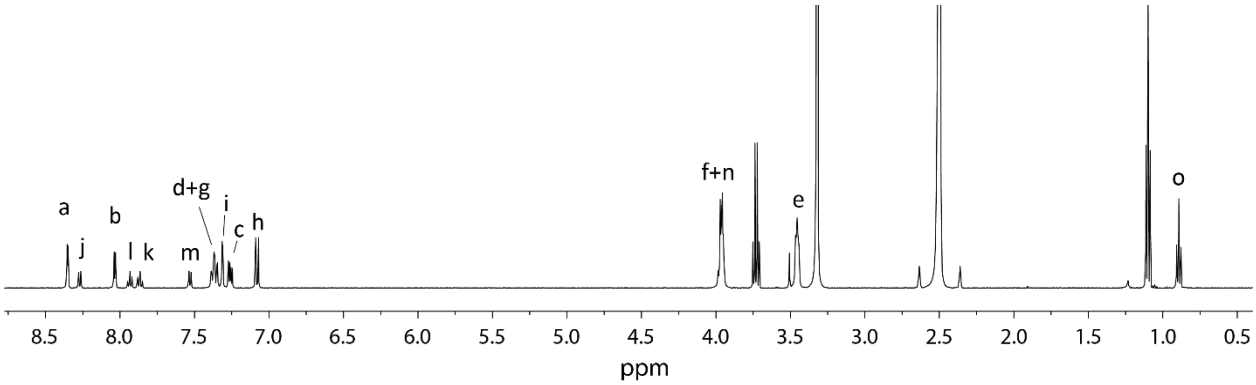

Figure 4.72: ^{1}H NMR (500 MHz, 298K, DMSO-d_6) spectrum of **RE-P**.

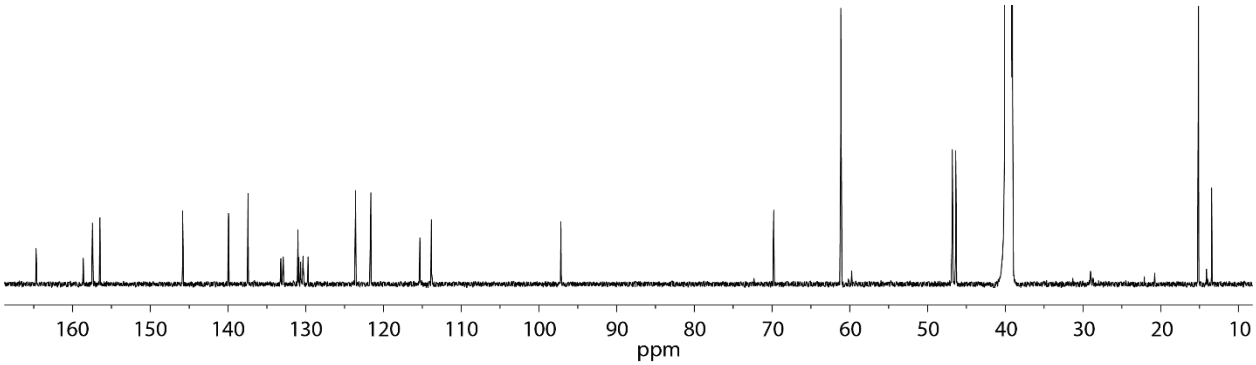

Figure 4.73: ^{13}C NMR spectrum (151 MHz, 298K, DMSO-d_6) of **RE-P**.

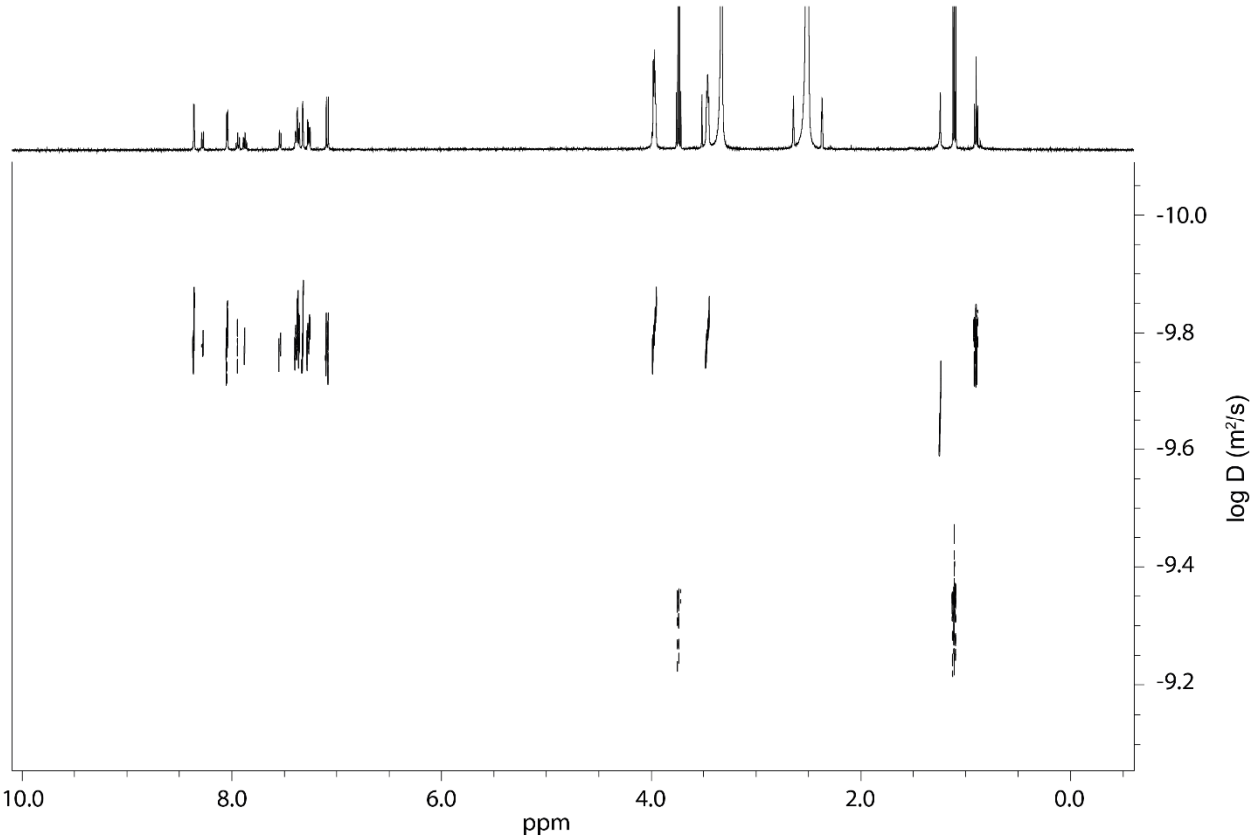

Figure 4.74: ^{1}H DOSY spectrum (500 MHz, 298K, DMSO-d_6) of **RE-P** (2.8 mM). Diffusion coefficient: 1.558×10-$^{-10}$ m^2s^{-1}, log D=-9. 808. Hydrodynamic radius= 7.05 Å.

Synthesis of 8-(piperazin-1-yl)isoquinoline (7)

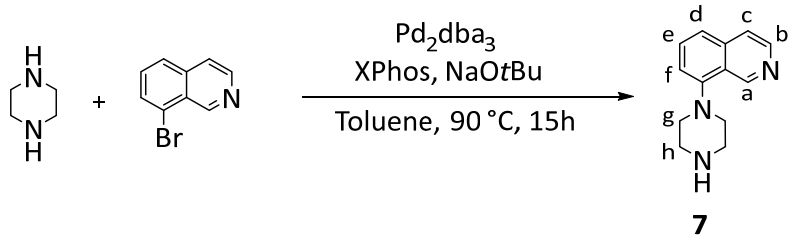

Figure 4.75: Synthesis of the linker 8-(piperazin-1-yl)isoquinoline (7)

8-Bromoisoquinoline (500 mg, 2.4 mmol, 1.0 equiv.) was dissolved in toluene (10mL). To the solution was added piperazine (516 mg, 6.0 mmol, 2.5 equiv.), Pd_2dba_3 (110 mg, 0.12 mmol, 0.05 equiv.), XPhos (172 mg, 0.36 mmol, 0.15 equiv.), and sodium *t*-butoxide (324 mg, 3.36 mmol, 1.4 equiv.). The mixture was degassed with the *freeze and pump method* and then heated to 90°C for about 12 hours. The reaction was allowed to cool to r.t., diluted with diethyl ether and filtered through celite. The filtrate was concentrated, and the dark residue was chromatographed on silica gel (CH_2Cl_2/MeOH/EtOAc : 70/20/10) to give about 450 mg of 8-(piperazin-1-yl)isoquinoline (88%).

^{1}H NMR (500 MHz, 298 K, Chloroform-*d*) δ 9.52 (s, 1H, Ha), 8.43 (d, *J* = 5.6 Hz, 1H, Hb), 7.58 – 7.48 (m, 2H, Hc, He), 7.41 (d, *J* = 8.2 Hz, 1H, Hd), 7.06 (dd, *J*=7.5, 0.6 Hz, 1H, Hf), 3.11 (s, 8H).

^{13}C NMR (126 MHz, 298 K, Chloroform-*d*) δ 151.06 (C^q, **C**-Cc), 149.13 (Ca), 143.00 (Cb), 137.41 (C^q, **C**-Ca), 130.72 (Ce), 123.64 (C^q, **C**-Cf), 121.44 (Cd), 120.69 (Cc), 115.58 (Cf), 54.56 (Cg), 46.32 (Ch).

HR ESI-MS: measured for ($C_{13}H_{15}N_3H^+$): 214.1330

calculated: 214.1339

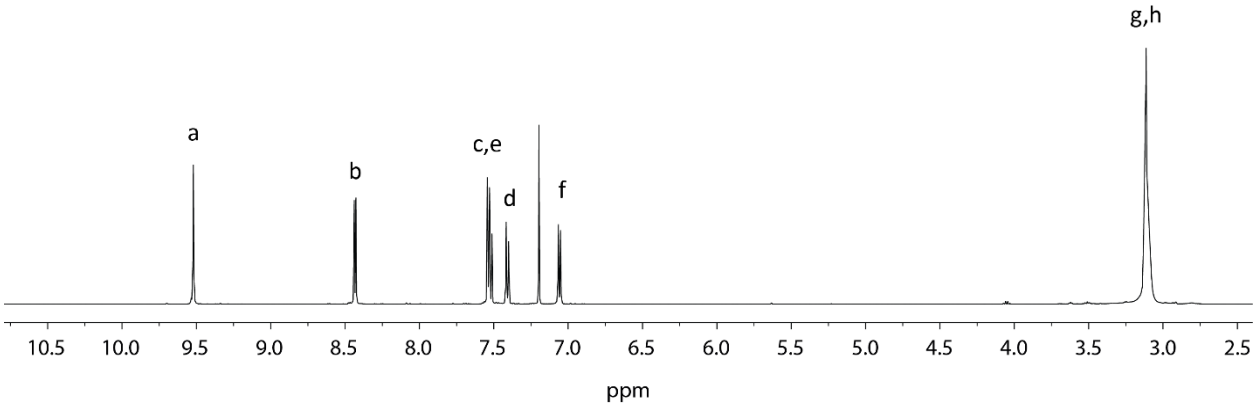

Figure 4.76: ^{1}H NMR spectrum (600 MHz, 298K, $CDCl_3$) of 8-(piperazin-1-yl)isoquinoline.

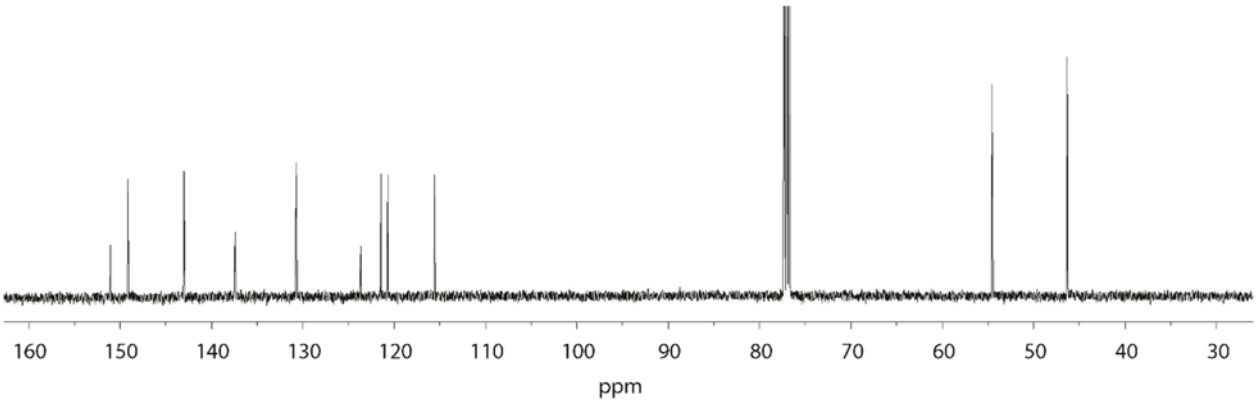

Figure 4.77: ^{13}C NMR spectrum (151 MHz, 298K, $CDCl_3$) of 8-(piperazin-1-yl)isoquinoline.

Synthesis of MK-Q

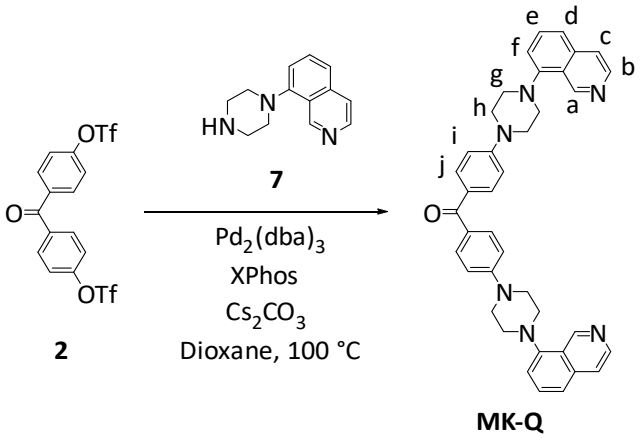

Figure 4.78: Synthesis of ligand **MK-Q**.

Compound **2** (500 mg, 1.52 mmol, 1.0 equiv.) was added together with $Pd_2(dba)_3$ (278 mg, 0.3 mmol, 0.2 equiv.), XPhos (217 mg, 0.45 mmol, 0.3 equiv.), Cs_2CO_3 (1.39 g, 4.25 mmol, 2.8 equiv.) and **7** (712.5 mg, 3.34 mmol, 2.2 equiv.) in dioxane into a schlenk tube und the mixture was degassed via the *freeze and pump-method*. The mixture was heated to 100 °C for 18 h. The solvent was evaporated and the reaction mixture was purified by column chromatography (0-5 % CH_2Cl_2/MeOH). The product was isolated as a yellow solid (625 mg, 1.03 mmol, 68 %).

^{1}H NMR (500 MHz, 298 K, Dimethyl sulfoxide-d_6) δ 9.56 (s, 1H, Ha), 8.52 (d, *J* = 5.6 Hz, 1H, Hb), 7.81 (dd, *J* = 5.6, 1.0 Hz, 1H, Hc), 7.77 – 7.55 (m, 4H, He, Hd, Hj), 7.30 (dd, *J* = 7.6, 1.1 Hz, 1H, Hf), 7.15 (d, *J* = 9.0 Hz, 2H, Hi), 3.75 – 3.59 (t, *J* = 5.0 Hz, 4H, Hh), 3.27 (t, *J* = 5.0 Hz, 4H, Hg).

^{13}C NMR (176 MHz, 298 K, Dimethyl sulfoxide-d_6) δ 192.41 (C=O), 153.24 (C^q, **C**-Cj), 149.77 (C^q, **C**-Cc), 148.32 (Ca), 142.96 (Cb), 136.85 (C^q, **C**-Ca), 131.49 (Cj), 130.95 (Ce), 127.49 (C^q, **C**-Ci), 122.78 (C^q, **C**-Cf), 121.57 (Cd), 120.66 (Cc), 115.95 (Cf), 113.45 (Ci), 52.78 (Cg), 47.17 (Ch).

HR ESI-MS: measured for ($C_{39}H_{36}N_6OH^+$): 605.3021

calculated: 605.3023

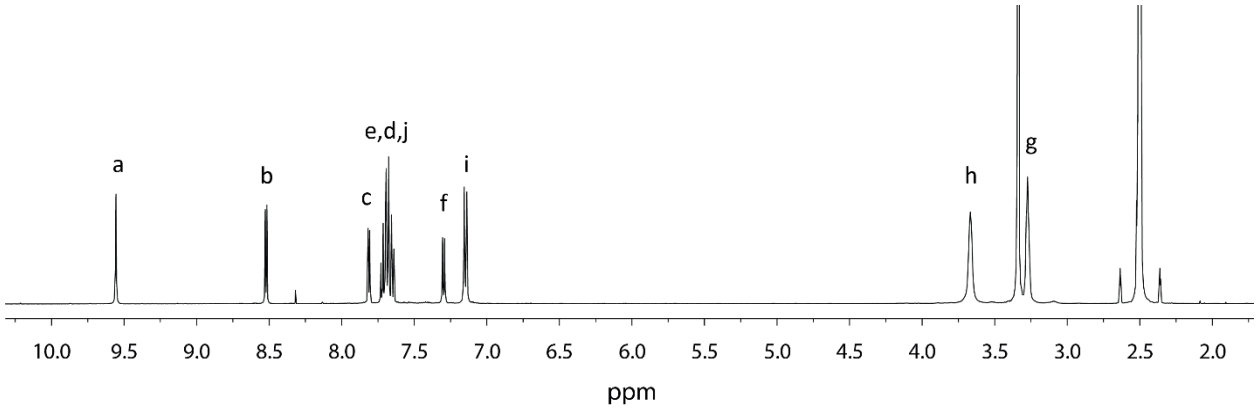

Figure 4.79: ^{1}H NMR spectrum (600 MHz, 298K, DMSO-d_6) of the ligand **MK-Q**.

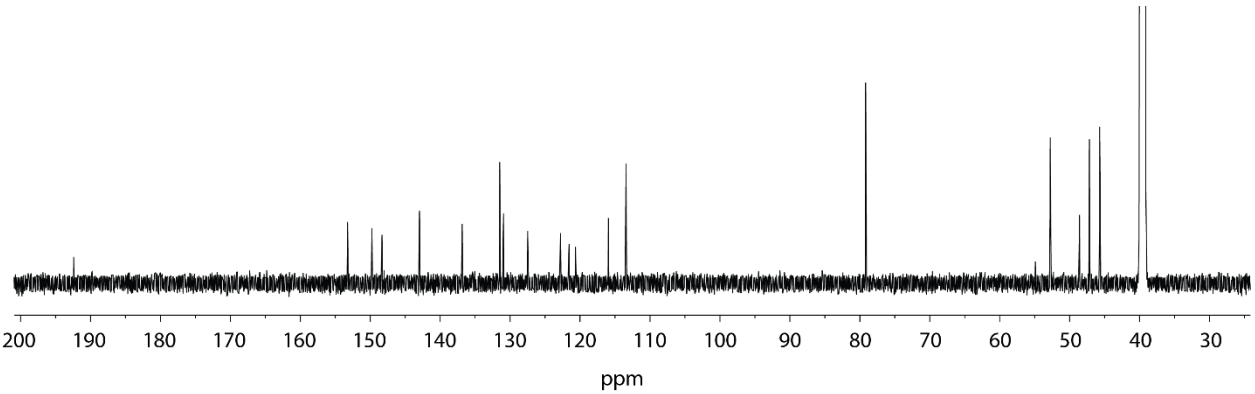

Figure 4.80: ^{13}C NMR spectrum (176 MHz, 298K, DMSO-d_6) of the ligand **MK-Q**.

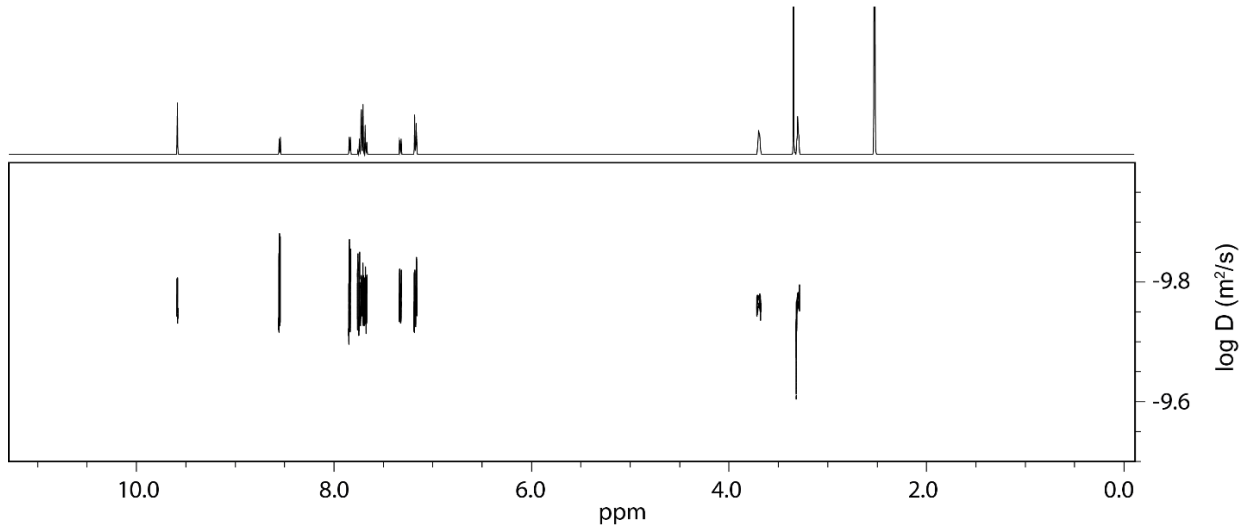

Figure 4.81: ^{1}H DOSY spectrum (500 MHz, 298K, DMSO-d_6) of **MK-Q** (2.8 mM). Diffusion coefficient: 1.705×10^{-10} m^{2}s^{-1}, log D=-9. 768. Hydrodynamic radius= 6.44 Å.

Synthesis of RB-Q

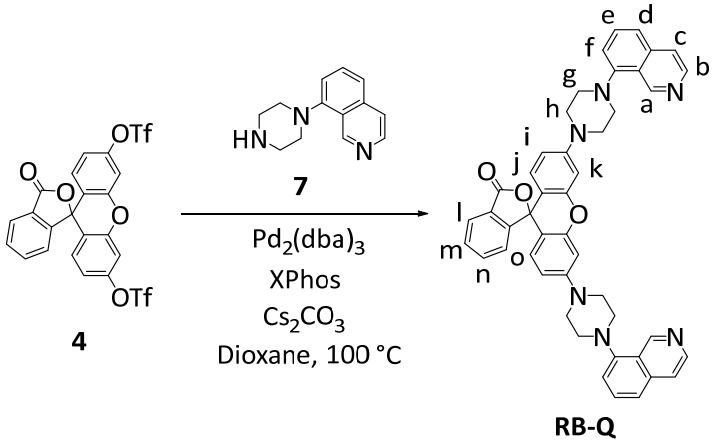

Figure 4.82: Synthesis of ligand **RB-Q**.

Compound **4** (280 mg, 470 µmol, 1.0 equiv.) was added together with $Pd_2(dba)_3$ (86 mg, 94 µmol, 0.2 equiv.), XPhos (67.0 mg, 141 µmol, 0.3 equiv.), Cs_2CO_3 (430 mg, 1.3 mmol, 2.8 equiv.) and **7** (220 mg, 1.0 mmol, 2.2 equiv.) in dioxane into a schlenk tube und the mixture was degassed via the pump- and freeze-method. The mixture was heated to 100 °C for 18 h. The solvent was evaporated and the reaction mixture was purified by column chromatography (0-10 % MeOH /CH_2Cl_2). The product was isolated as a pink solid (185 mg, 256 µmol, 54.5 %).

^{1}H NMR (500 MHz, 298 K, Acetonitrile-d_3) δ 9.59 (s, 2H, Ha), 8.49 (d, *J* = 5.7 Hz, 2H, Hb), 7.99 (d, *J* = 7.6 Hz, 1H, Hl), 7.76 (t, *J* = 7.5 Hz, 1H, Ho), 7.73 – 7.62 (m, 3H, Hc, Hm), 7.58 (m, 4H, He, Hd), 7.25 (m, 3H, Hf, Hn), 6.86 (d, *J* = 2.4 Hz, 2H, Hk), 6.79 (dd, *J* = 9.1, 2.4 Hz, 2H, Hj), 6.70 (d, *J* = 8.8 Hz, 2H, Hi), 3.53-3.56 (m, 8H, Hh), 3.39 – 3.21 (m, 8H, Hg).

^{13}C NMR (126 MHz, 298 K, Acetonitrile-d_3) δ 182.01 (from HMBC, C=O), 153.55, 151.27 (from HMBC), 149.65 (Ca), 144.10 (Cb), 131.81, 136.10 (from HSQC, Co), 131.40 (from HSQC, Cm), 129.70 (Ci), 125.37 (from HSQC, Cl), 124.43 (Cn), 122.69 (Ce and Cd, two signals overlaying), 121.56 (Cc), 116.79 (from HSQC, Cf), 112.67 (from HSQC, Cj), 110.31, 102.63 (Ck), 53.99 (Cg), 49.23 (Ch). 3 C^{q} are not distinguishable from the noise.

HR ESI-MS: measured for ($C_{46}H_{38}N_6O_3H^+$): 723.3079

calculated: 723.3078

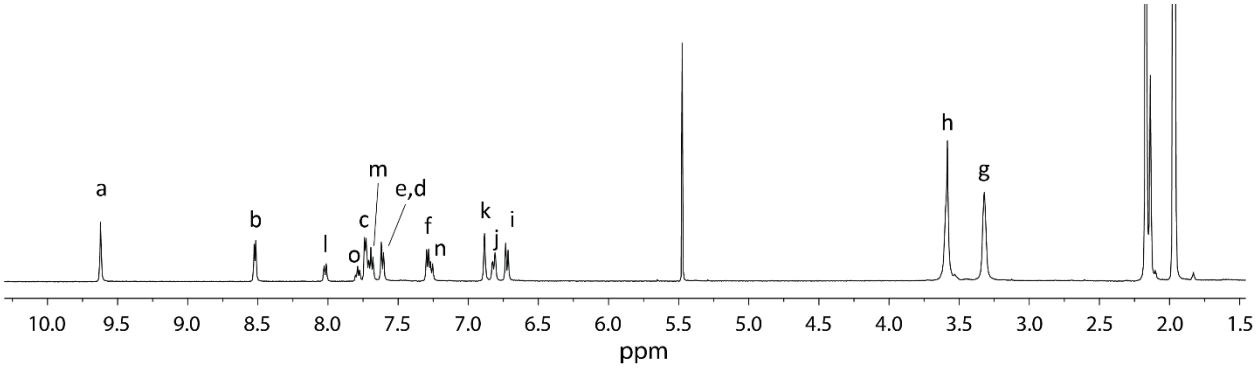

Figure 4.83: ^{1}H NMR spectrum (500 MHz, 298K, CD_3CN) of the ligand **RB-Q**.

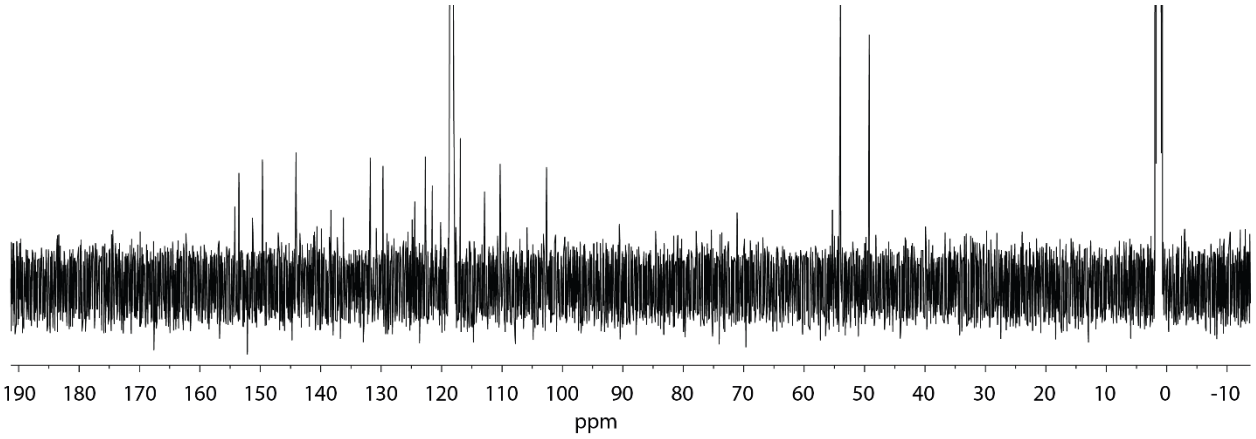

Figure 4.84: ^{13}C NMR spectrum (126 MHz, 298K, CD_3CN) of the ligand **RB-Q**.

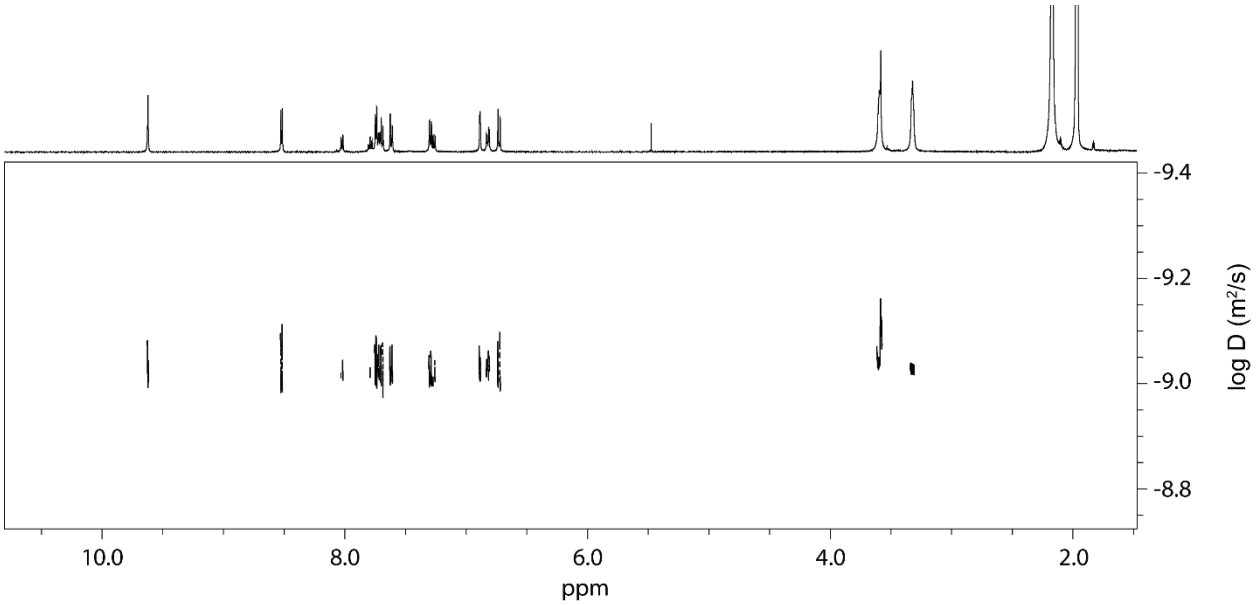

Figure 4.85: ^{1}H DOSY spectrum (500 MHz, 298K, CD_3CN) of **RB-Q** (2.8 mM). Diffusion coefficient: 9.206×10^{-10} m^2s^{-1}, log D=-9.036. Hydrodynamic radius= 7.11 Å.

Synthesis of MB-Q

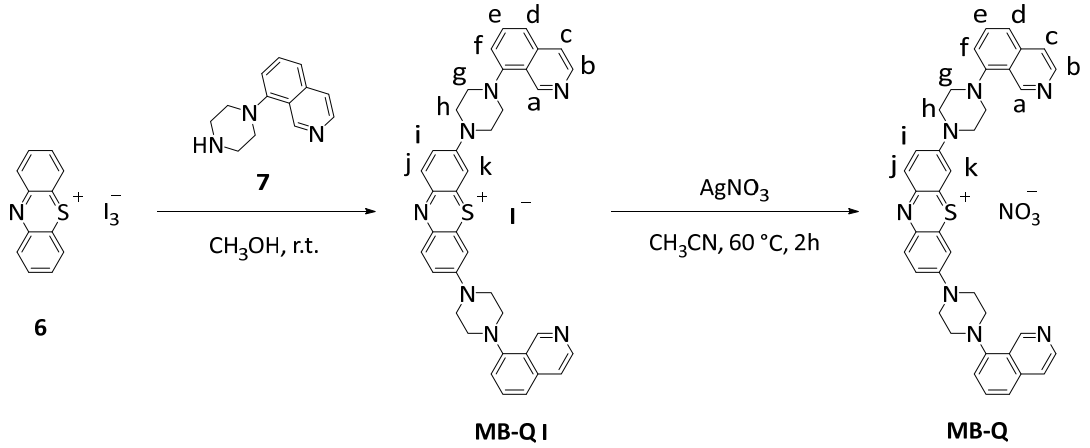

Figure 4.86: Synthesis of ligand **MB-Q**.

Synthesis of the ligand MB-QI

To a solution of the oxidized 10H-phenotiazine (300 mg, 1.0 equiv.) in methanol (15 mL) was added dropwise the methanol (15 mL) solution of 8-(piperazin-1-yl)isoquinoline (885 mg, 8.0 equiv.). The reaction was carried out under stirring at r.t. for 15 h. When the reaction was complete, the solution was evaporated to dryness under vacuum and purified by flash column chromatography (R_f=0.5, CH_2Cl_2/MeOH=95/5). After collection and evaporation, the compound was recrystallized by using CH_3OH/EtOAc as a blue powder.

^{1}H NMR (600 MHz, 298 K, Acetonitrile-d_3) δ 9.69 (s, 1H, Ha), 8.56 (d, *J* = 5.6 Hz, 1H, Hb), 8.05 (d, *J* = 9.6 Hz, 1H, Hj), 7.77 (d, *J* = 5.7 Hz, 1H, Hc), 7.71 (t, *J* = 7.8 Hz, 1H, He), 7.69 – 7.64 (m, 2H, Hd, Hi), 7.55 (d, *J* = 2.8 Hz, 1H, Hk), 7.30 (dd, *J* = 7.4, 1.1 Hz, 1H, Hf), 4.16 (t, *J* = 4.9 Hz, 4H, Hh), 3.40 (t, *J* = 5.0 Hz, 4H, Hg).

^{13}C NMR (151 MHz, 298 K, Acetonitrile-d_3) δ 154.73 (C^q, **C**-Cj), 150.26 (C^q, **C**-Cf), 149.48 (Ca), 144.12 (Cb), 139.68 (Cj), 138.27 (C^q, Ck-**C**-Ci), 137.53 (C^q, Cc-**C**-Cd), 136.26 (C^q, **C**-Ck), 131.72 (Ce), 124.36 (C^q, **C**-Ca), 123.30 (Ci), 121.57 (Cc), 120.41 (Cd), 117.45 (Cf), 107.98 (Ck), 53.69 (Cg), 49.00 (Ch).

HR ESI-MS: measured for ($C_{38}H_{34}N_7S^+$): 620.2594

calculated: 620.2634

Synthesis of the ligand MB-Q

To an acetonitrile (15 mL) solution of **MB-Q**I (40 mg, 1 equiv.) was added $AgNO_3$ (12 mg, 1.3 equiv.). The reaction was carried out under stirring at 60 °C for 1 h. After cooling down to r.t., the resulting solution was filtered and washed by using acetonitrile to get the filtrate. The solvent was then evaporated to obtain the product.

^{1}H NMR (600 MHz, 298 K, Acetonitrile-d_3) δ 9.69 (s, 1H, Ha), 8.56 (d, *J* = 5.6 Hz, 1H, Hb), 8.05 (d, *J* = 9.6 Hz, 1H, Hj), 7.77 (d, *J* = 5.7 Hz, 1H, Hc), 7.71 (t, *J* = 7.8 Hz, 1H, He), 7.69 – 7.64 (m, 2H, Hd, Hi), 7.55 (d, *J* = 2.8 Hz, 1H, Hk), 7.30 (dd, *J* = 7.4, 1.1 Hz, 1H, Hf), 4.16 (t, *J* = 4.9 Hz, 4H, Hh), 3.40 (t, *J* = 5.0 Hz, 4H, Hg).

^{13}C NMR (151 MHz, 298 K, Acetonitrile-d_3) δ 154.38 (C^q, **C**-Cj), 149.91 (C^q, **C**-Cf), 149.12 (Ca), 143.76 (Cb), 139.33 (Cj), 137.92 (C^q, Ck-**C**-Ci), 137.19 (C^q, Cc-**C**-Cd), 135.92 (C^q, **C**-Ck), 131.37 (Ce), 124.01 (C^q, **C**-Ca), 122.95 (Ci), 121.22 (Cc), 120.06 (Cd), 117.10 (Cf), 107.61 (Ck), 53.32 (Cg), 48.63 (Ch).

HR ESI-MS: measured for ($C_{38}H_{34}N_7S^+$): 620.2591

calculated: 620.2634

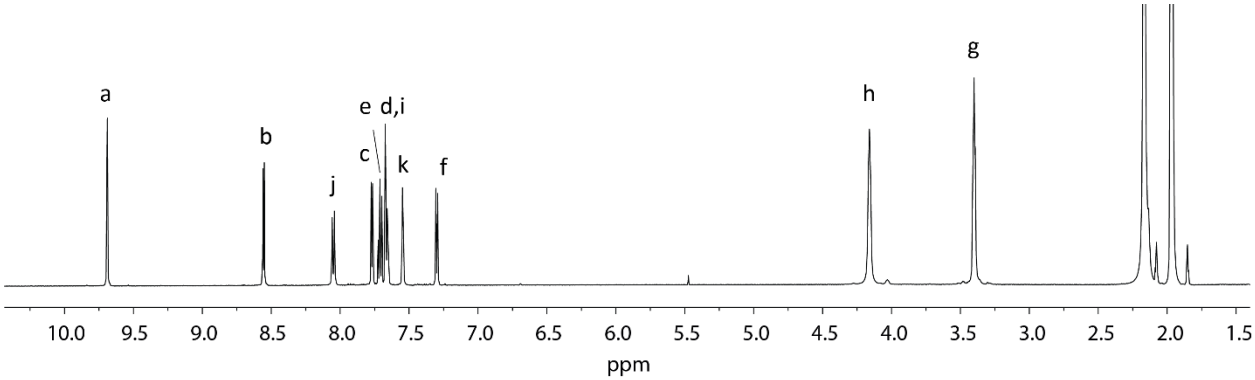

Figure 4.87: ^{1}H NMR spectrum (600 MHz, 298K, CD_3CN) of the ligand **MB-Q**.

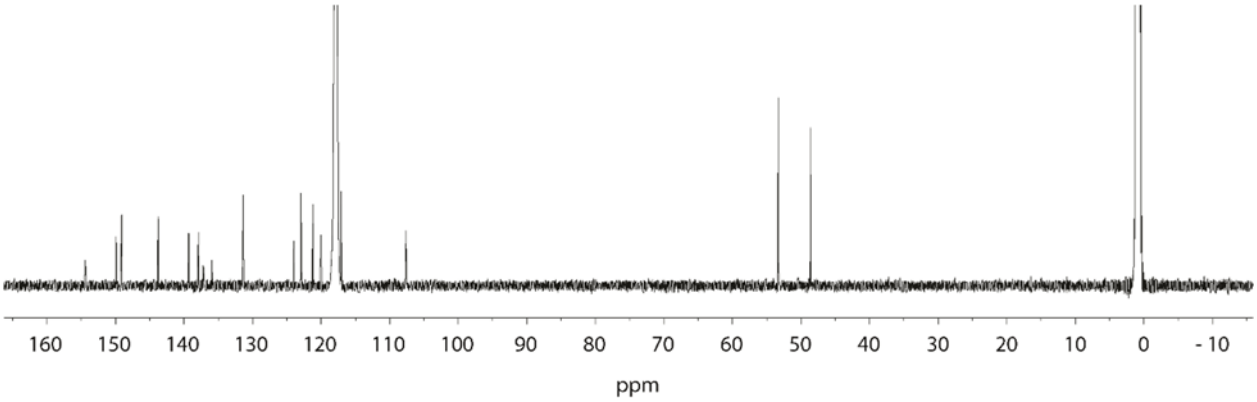

Figure 4.88: ^{13}C NMR spectrum (151 MHz, 298K, CD_3CN) of the ligand **MB-Q**.

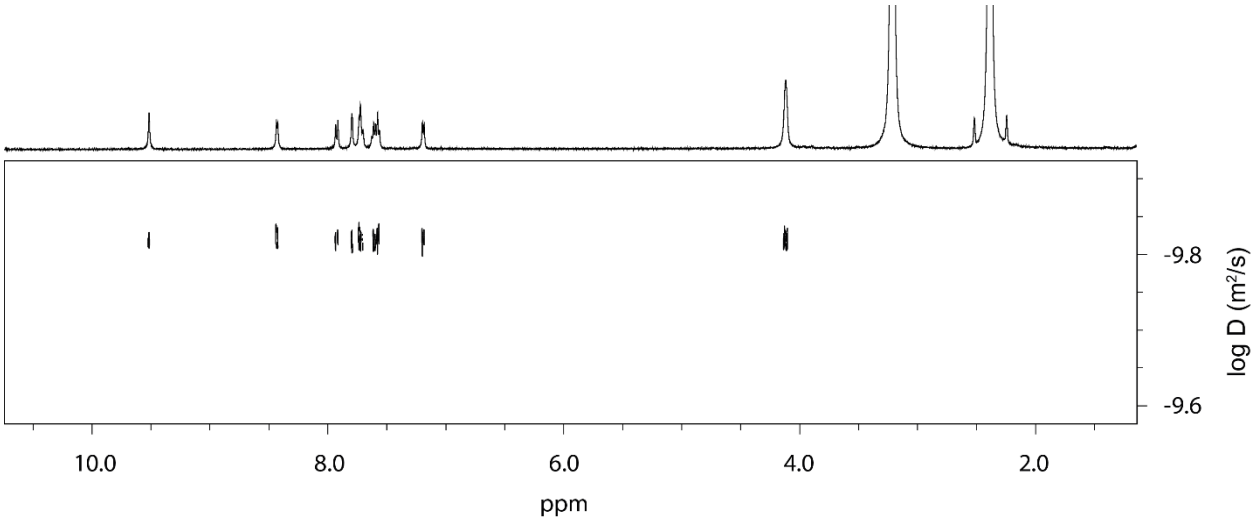

Figure 4.89: ^{1}H DOSY spectrum (500 MHz, 298K, DMSO-d_6) of **MB-Q** (2.8 mM). Diffusion coefficient: 1.500×10^{-10} m^2s^{-1}, log D=−9. 824. Hydrodynamic radius= 7.32 Å.

Synthesis of CV-Q

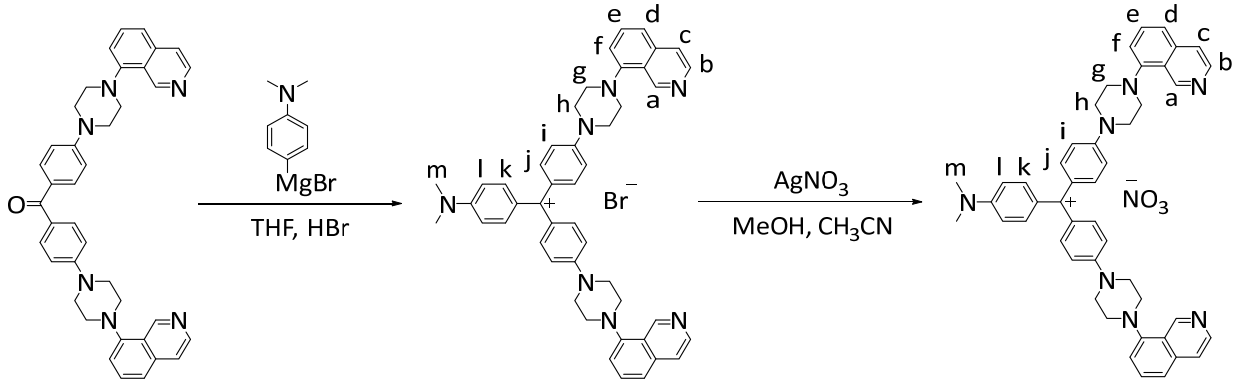

BPQ **CV-Q Br** **CV-Q**

Figure 4.90: Synthesis of ligand **CV-Q**.

Synthesis of CV-QBr

To a round bottom flask already equipped with stir bar, Mg (160 mg, 1.3 equiv., 6.60 mmol) was added and heated under vacuum to remove any trace of water. 4-Bromo-*N*,*N*-dimethylaniline (1.0 g, 5 mmol) was then added and the whole system was evacuated for some minutes. To the solids 10 mL of dry THF are added together with a small iodine crystal. The flask was gently warmed to reflux for 90 minutes. During this time the solution changes from dark to dingy gray. An ice bath was then used to cool down to r.t. the flask.

In a dry round bottom flask **MK-Q** (300 mg, 490 µmol) was added together with 8 mL of dry THF. To the yellow suspension, 3 mL of the grey suspension above described are added and the system was put under reflux for 5 minutes and then again cooled down to r.t. with an ice bath. Slowly 8 mL of HBr 10% are added to obtain the final product. The color of the solution changes from bright yellow to deep violet/blue. The solution was than neutralized with a saturated solution of $NaHCO_3$ and as soon as pH 7 was reached the desired product precipitates as blue flakes. All the volatiles are removed, and the product purified by column chromatography (0-10 % MeOH /CH_2Cl_2). The product was isolated as a dark violet solid (213 mg, 270 µmol, 55%).

^{1}H NMR (600 MHz, 298 K, Acetonitrile-d_3) δ 9.65 (d, *J* = 0.9 Hz, 1H, Ha), 8.52 (d, *J* = 5.7 Hz, 1H, Hb), 7.75 (dd, *J* = 5.7, 1.0 Hz, 1H, Hc), 7.70 (dd, *J* = 8.2, 7.5 Hz, 1H, He), 7.63 (d, *J* = 8.2 Hz, 1H, Hd), 7.46 – 7.38 (m, 3H, Hk, Hj), 7.29 (dd, *J* = 7.5, 1.1 Hz, 1H, Hf), 7.23 – 7.16 (m, 2H, Hi), 6.98 (d, *J* = 9.3 Hz, 1H, Hl), 3.92 (t, *J* = 4.8 Hz, 4H, Hh), 3.34 (t, *J* = 5.1 Hz, 4H, Hg), 3.26 (s, 3H, Hm).

^{13}C NMR (151 MHz, 298 K, Acetonitrile-d_3) δ 178.77 (C+), 157.22 (C^q, **C**-Ck), 156.33 (C^q, **C**-Cj), 150.53 (C^q, **C**-Cc), 148.96 (Ca), 143.35 (Cb), 141.04 (Ck), 140.14 (Cj), 138.02 (C^q, **C**-Ca), 131.58 (Ce), 128.59 (C^q, **C**-Ci), 127.33 (C^q, **C**-Cl), 124.00 (C^q, **C**-Cf), 122.63 (Cd), 121.35 (Cc), 117.27 (Cf), 114.09 (Ci), 113.49 (Cl), 53.38 (Cg), 47.58 (Ch), 40.64 (Cm).

HR ESI-MS: measured for ($C_{47}H_{46}N_7^+$): 708.3854

calculated: 708.3809

Synthesis of CV-Q

To a methanol (15 mL) solution of **CV-Q**Br (60 mg, 76 µmol, 1 equiv.) was added $AgNO_3$ (14 mg, 84 µmol, 1.1 equiv.). The reaction was carried out under stirring at 60 °C for 1 h. After cooling down to r.t., the resulting solution was filtered and washed by using methanol to get the filtrate. The solvent was then evaporated to obtain the product.

^{1}H NMR (500 MHz, 298 K, Acetonitrile-d_3) δ 9.66 (s, 1H, Ha), 8.51 (d, *J* = 5.8 Hz, 1H, Hb), 7.77 (d, *J* = 5.7 Hz, 1H, Hc), 7.71 (t, *J* = 7.9 Hz, 1H, He), 7.64 (d, *J* = 8.2 Hz, 1H, Hd), 7.41 (m, 3H, Hk, Hj), 7.30 (dd, *J* = 7.5, 1.0 Hz, 1H, Hf), 7.20 (d, *J* = 9.2 Hz, 2H, Hi), 6.98 (d, *J* = 9.4 Hz, 1H, Hl), 3.92 (t, *J* = 5.0 Hz, 4H, Hh), 3.34 (t, *J* = 5.0 Hz, 4H, Hg), 3.26 (s, 3H, Hm).

^{13}C NMR (151 MHz, 298 K, Acetonitrile-d_3) δ 178.74 (C+), 157.23 (C^q, **C**-Ck), 156.31 (C^q, **C**-Cj), 150.66 (C^q, **C**-Cc), 149.08 (Ca), 143.04 (Cb), 141.04 (Ck), 140.14 (Cj), 138.16 (C^q, **C**-Ca), 131.98 (Ce), 128.59 (C^q, **C**-Ci), 127.33 (C^q, **C**-Cl), 124.02 (C^q, **C**-Cf), 122.63 (Cd), 121.66 (Cc), 117.93 (Cf), 114.10 (Ci), 113.51 (Cl), 53.40 (Cg), 47.57 (Ch), 40.65 (Cm).

HR ESI-MS: measured for ($C_{47}H_{46}N_7^+$): 708.3783

calculated: 708.3809

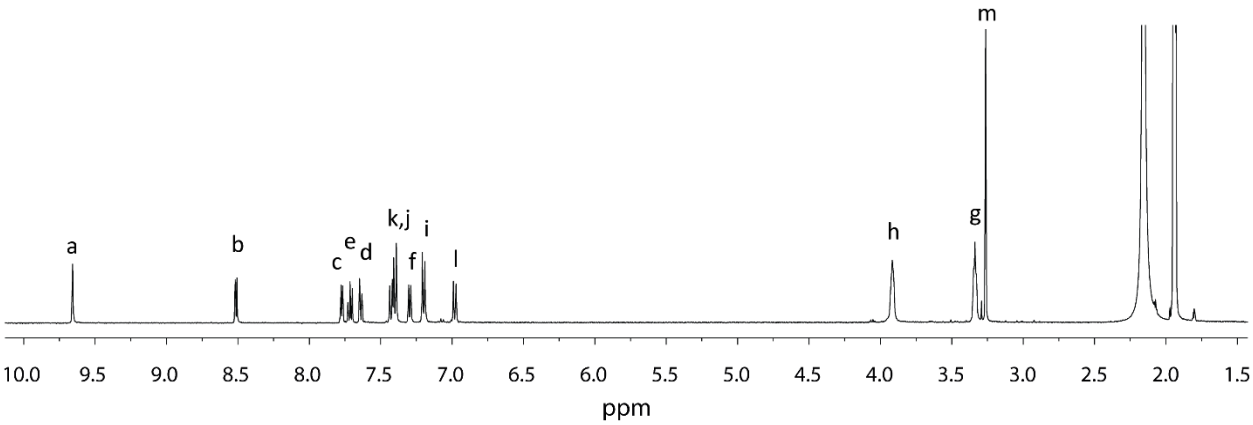

Figure 4.91: ^{1}H NMR spectrum (600 MHz, 298K, CD_3CN) of the ligand **CV-Q**.

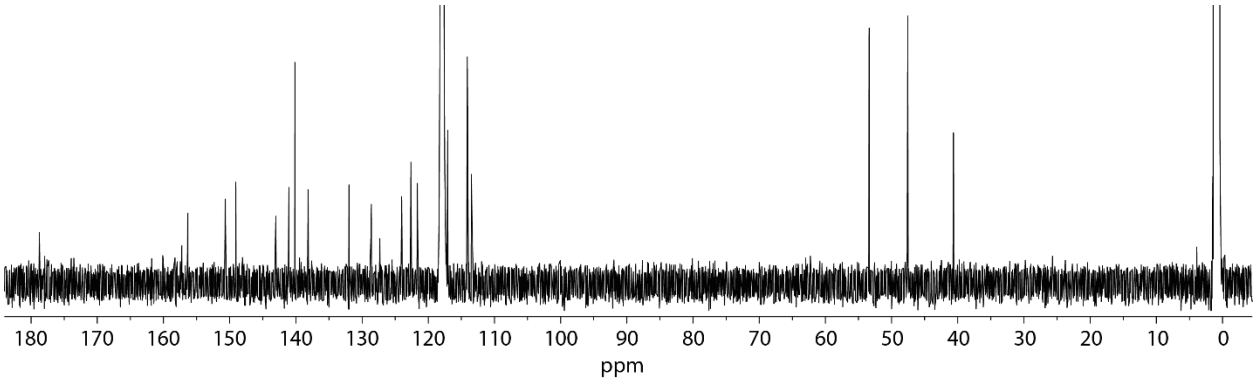

Figure 4.92: ^{13}C NMR spectrum (151 MHz, 298K, CD_3CN) of the ligand **CV-Q**.

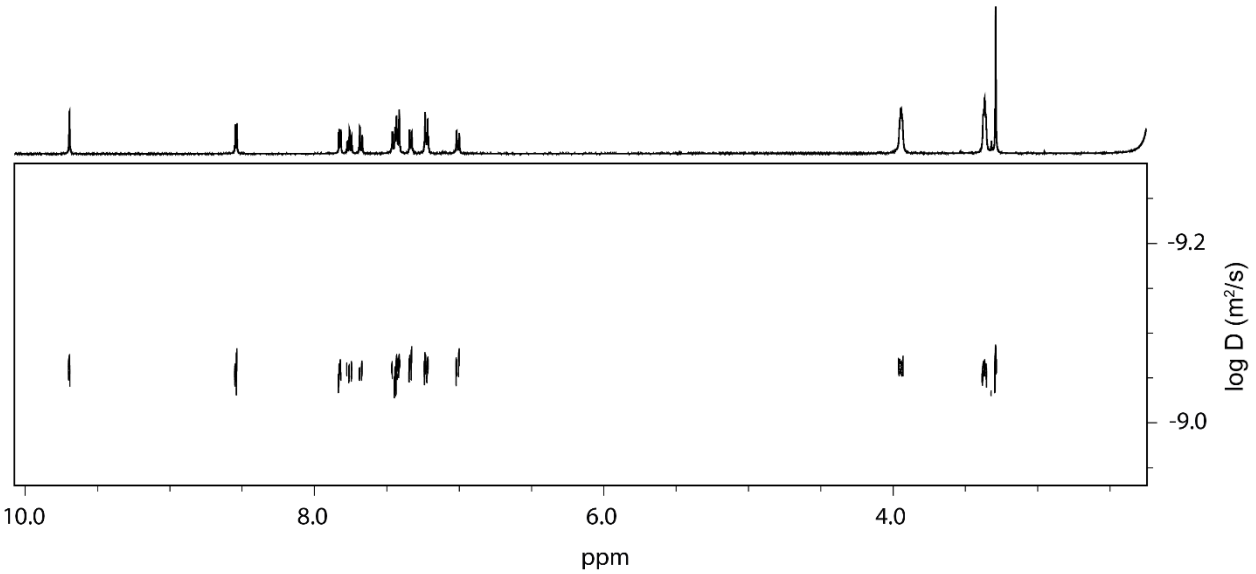

Figure 4.93: ^{1}H DOSY spectrum (500 MHz, 298K, CD_3CN) of **CV-Q** (2.8 mM). Diffusion coefficient: 8.771×10^{-10} m^2s^{-1}, log D=−9.057. Hydrodynamic radius= 7.44 Å.

4.8.3 Assembly of the cages

All the $[Pd_2L_4]$ coordination cages were synthetized accordingly to the same general procedure. To 450 µL of a 3.11 mM solution of the ligands in the specified solvent, 50 µL of a 15 mM solution of the Pd(II) salts in the same solvent (unless otherwise stated) are added. The mixture was than heated to 70 °C for 2 hours.

$[Pd_2(MK\text{-}P)_4](BF_4)_4$

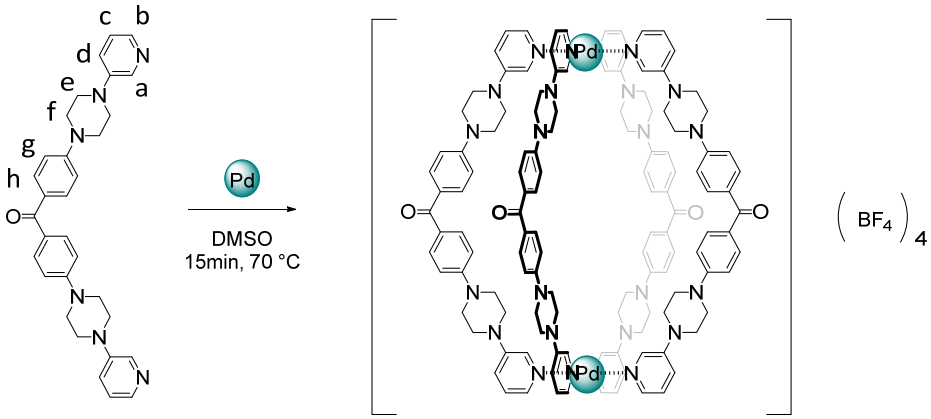

MK-P $[Pd_2(\mathbf{MK\text{-}P})_4](BF_4)_4$

Figure 4.94: Self-Assembly of cage $[Pd_2(\mathbf{MK\text{-}P})_4](BF_4)_4$.

A mixture of ligand **MK-P** (450 µL of a 3.11 mM solution in DMSO-d_6) and $[Pd(CH_3CN)_4](BF_4)_2$ (50 µL of a 15 mM solution in DMSO-d_6) was heated at 70 °C for 15 min to afford a 0.7 mM solution of $[Pd_2(\mathbf{MK\text{-}P})_4](BF_4)_4$.

^{1}H NMR (600 MHz, 298 K, Dimethyl sulfoxide-d_6) δ 8.92 (s, 1H, Ha), 8.72 (d, J = 5.3 Hz, 1H, Hb), 7.67-7.60 (m, 3H, Hd, Hh), 7.51 (dd, J=8.4, 5.3 Hz, 1H, Hc), 7.14 (d, J = 8.4 Hz, 2H, Hg), 3.58 (s, 8H, Hf, He).

^{13}C NMR (151 MHz, 298 K, Dimethyl sulfoxide-d_6) δ 192.40 (C=O), 153.47 (C^q, **C**-Cg), 148.07 (C^q, Cd-**C**-Ca), 140.00 (Cb), 136.27 (Ca), 132.03 (Ch), 127.86 (C^q, Ch-**C**), 126.99 (Cd), 124.70 (Cc), 113.87 (Cg), 46.48 (Ce), 46.19 (Cf).

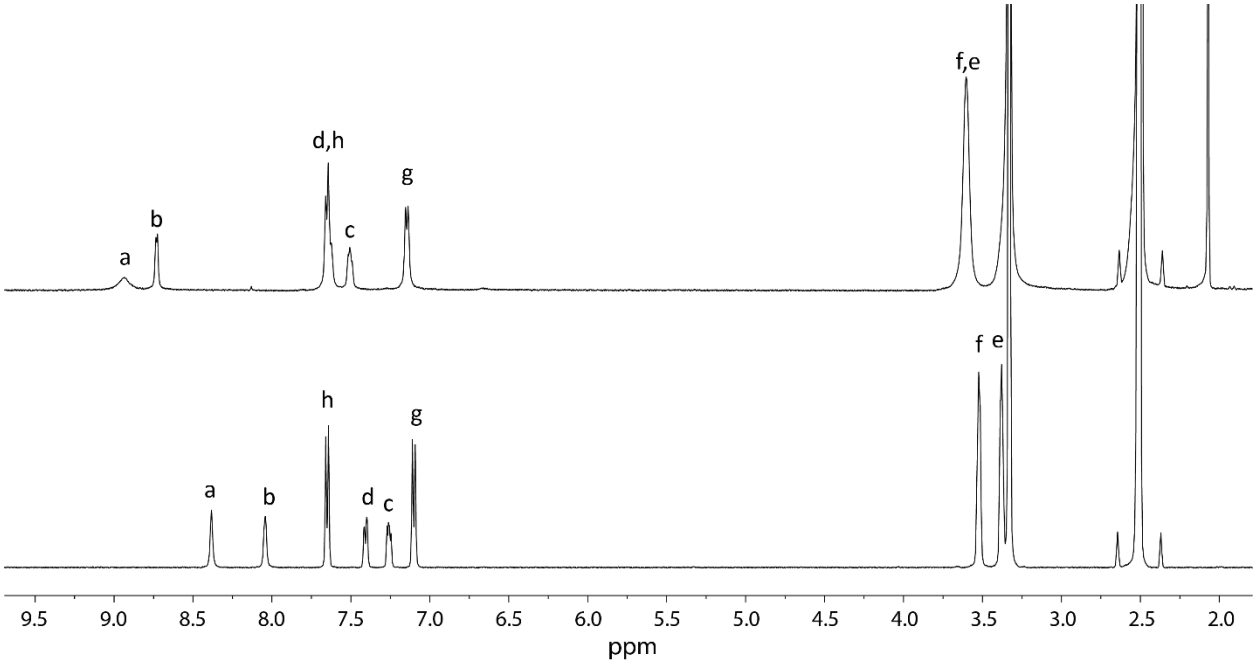

Figure 4.95: ^{1}H NMR stacked spectra (600 MHz, 298K, DMSO-d_6) of ligand **MK-P** (bottom) and the correspondent cage $[Pd_2(\mathbf{MK\text{-}P})_4](BF_4)_4$ (top) upon addition of 0.5 Equiv. of Pd(II) salt.

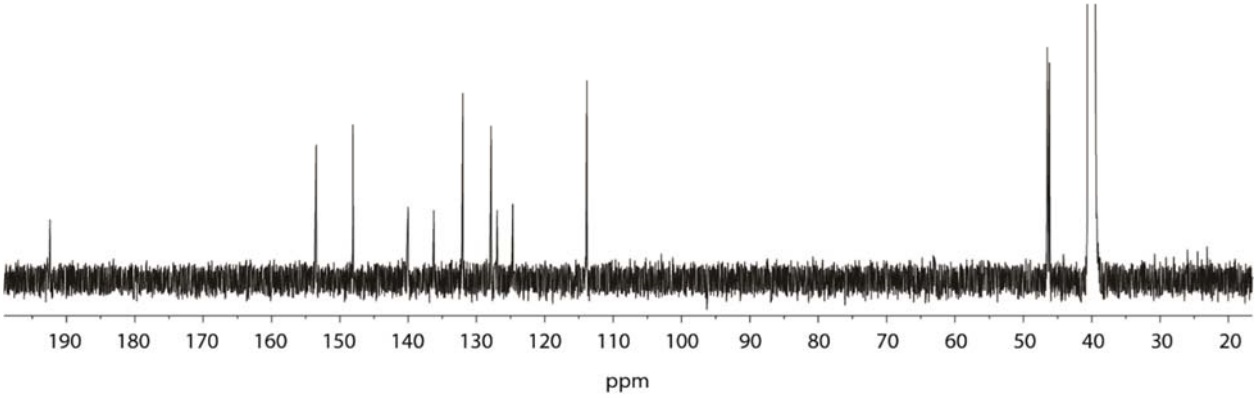

Figure 4.96: ^{13}C NMR spectrum (151 MHz, 298K, DMSO-d_6) of the cage $[Pd_2(\mathbf{MK\text{-}P})_4](BF_4)_4$.

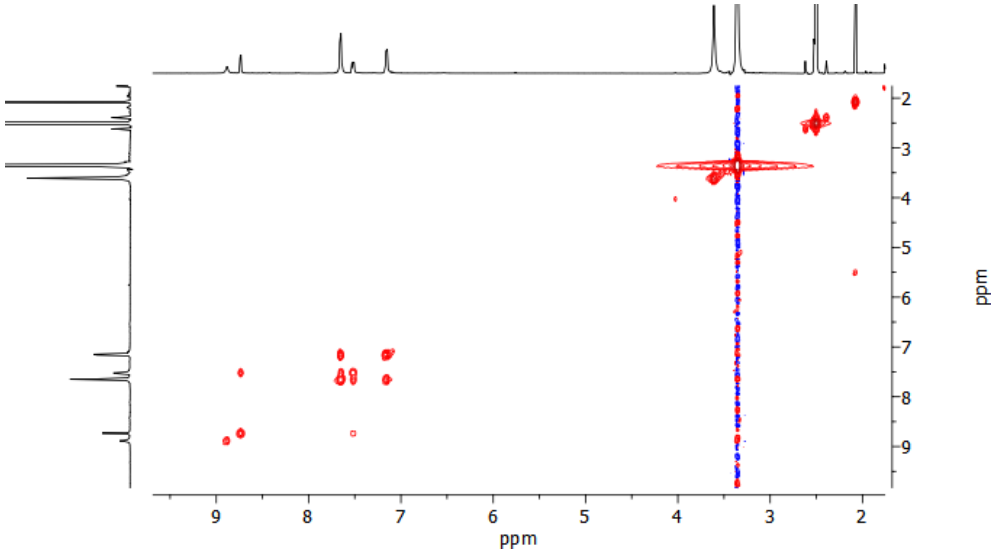

Figure 4.97: ^{1}H –^{1}H COSY spectrum (600 MHz, 298K, DMSO-d_6) of cage $[Pd_2(\mathbf{MK\text{-}P})_4](BF_4)_4$.

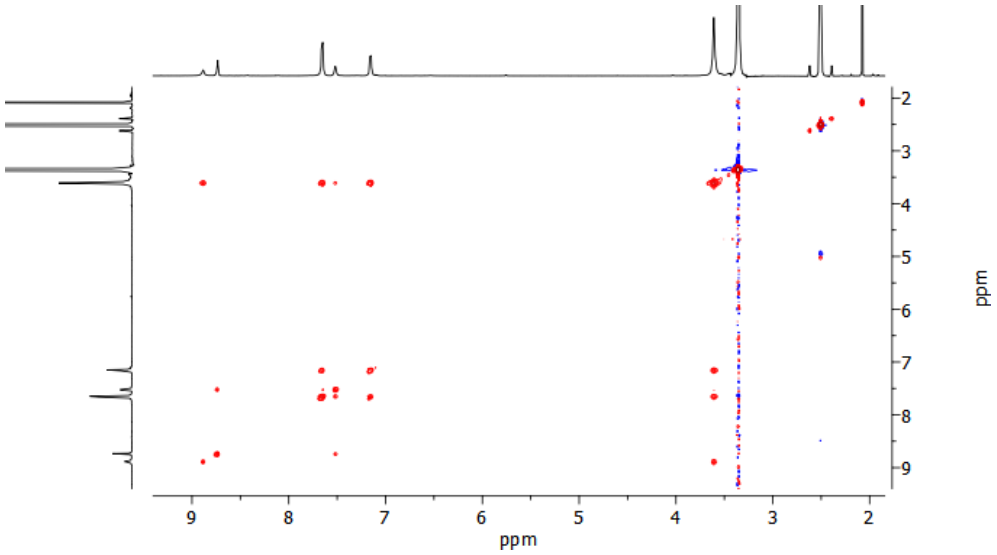

Figure 4.98: ^{1}H–^{1}H NOESY spectrum (600 MHz, 298K, DMSO-d_6) of cage $[Pd_2(\mathbf{MK\text{-}P})_4](BF_4)_4$.

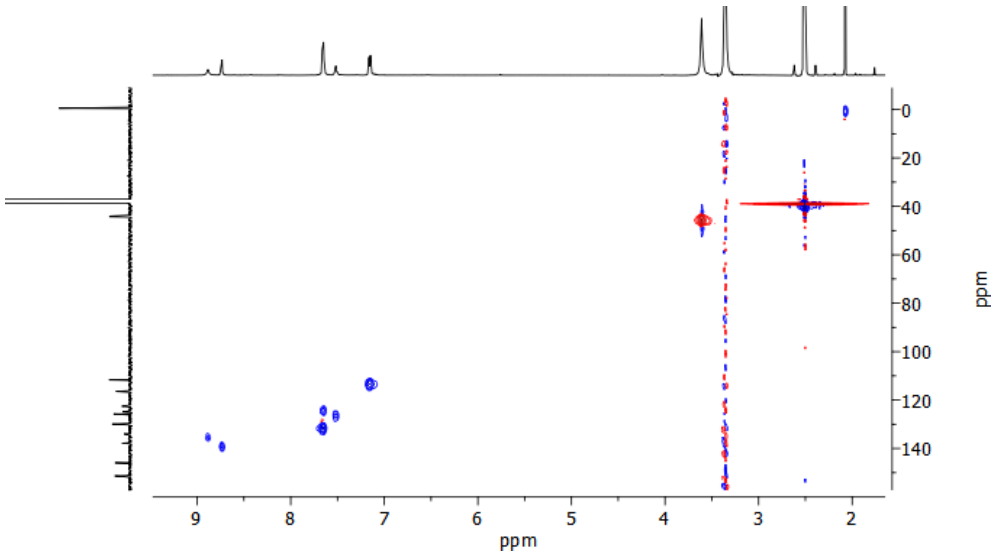

Figure 4.99: ^{1}H–^{13}C HSQC spectrum (600 MHz, 298K, DMSO-d_6) of cage $[Pd_2(\mathbf{MK\text{-}P})_4](BF_4)_4$.

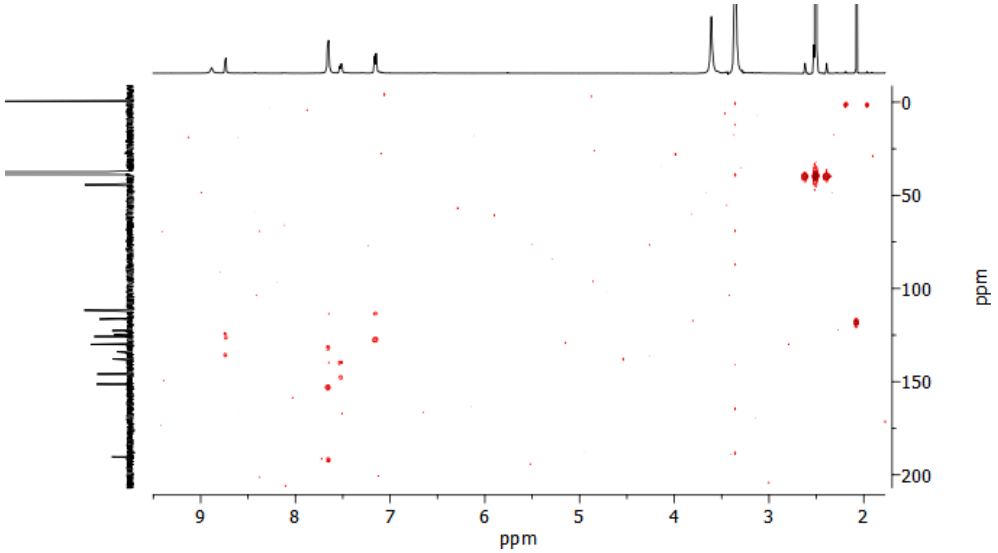

Figure 4.100: ^{1}H–^{13}C HMBC spectrum (600 MHz, 298K, DMSO-d_6) of cage $[Pd_2(\mathbf{MK\text{-}P})_4](BF_4)_4$.

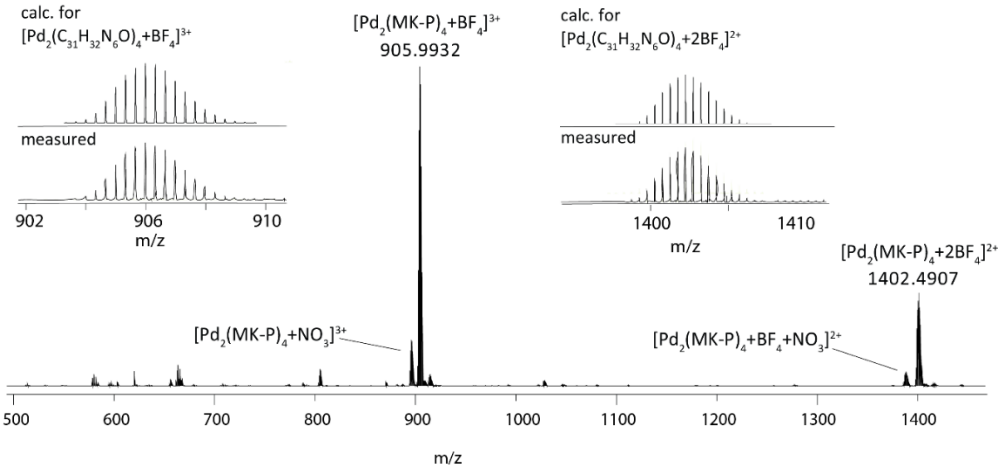

Figure 4.101: ESI-MS spectrum of $[Pd_2(\mathbf{MK\text{-}P})_4]+nBF_4]^{(4-n)+}$ with n=0-2. The observed and calculated isotopic patterns of $[Pd_2(\mathbf{MK\text{-}P})_4]+BF4]^{3+}$ and $[Pd_2(\mathbf{MK\text{-}P})_4]+2BF_4]^{2+}$ are shown in the inset.

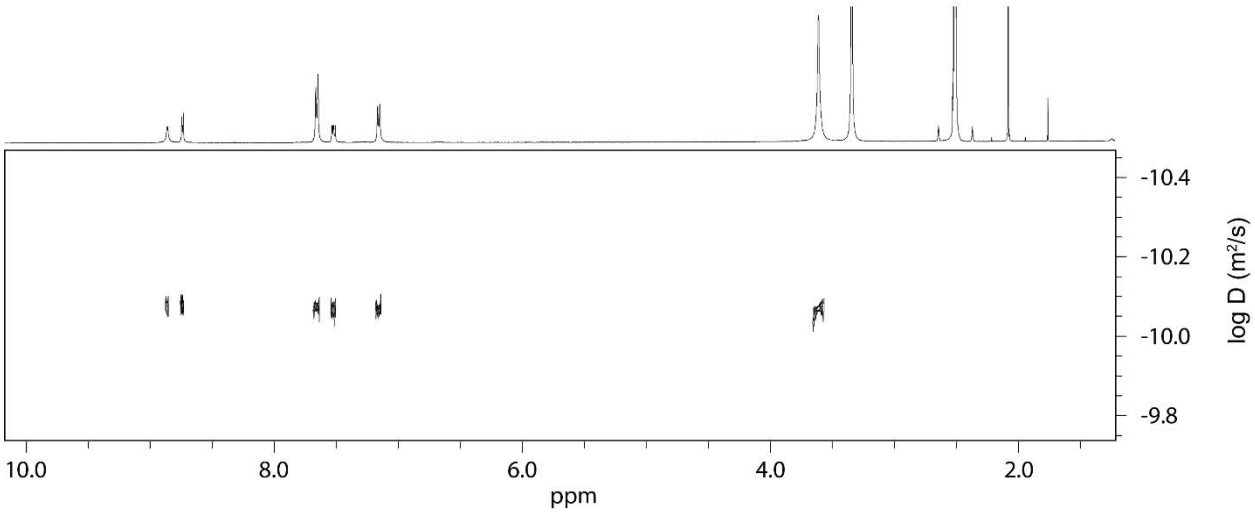

Figure 4.102: ^{1}H DOSY spectrum (500 MHz, 298K, DMSO-d_6) of $[Pd_2(\mathbf{MK\text{-}P})_4](BF_4)_4$ (0.7 mM). Diffusion coefficient: 8.559×10^{-11} m^2s^{-1}, log D=-10.068. Hydrodynamic radius= 12.83 Å.

$[Pd_2(RB\text{-}P)_4](BF_4)_4$

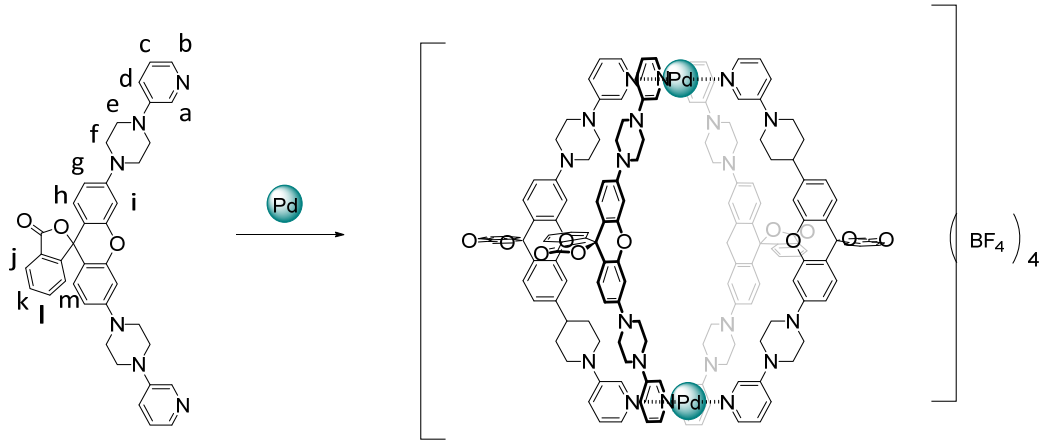

RB-P $[Pd_2(\mathbf{RB\text{-}P})_4](BF_4)_4$

Figure 4.103: Self-Assembly of cage $[Pd_2(\mathbf{RB\text{-}P})_4](BF_4)_4$.

A mixture of ligand **RB-P** (450 µL of a 3.11 mM solution in DMSO-d_6) and $[Pd(CH_3CN)_4](BF_4)_2$ (50 µL of a 15 mM solution in DMSO-d_6) was heated at 70 °C for 15 min to afford a 0.7 mM solution of $[Pd_2(\mathbf{RB\text{-}P})_4](BF_4)_4$

^{1}H NMR (500 MHz, 298 K, Dimethyl sulfoxide-d_6) δ 8.91 – 8.72 (m, 4H, Ha, Hb), 7.96 (s, 1H, Hj), 7.76 (t, *J* = 6.9 Hz, 1H, Hl), 7.64 (d, *J* = 9.2 Hz, 3H, Hd, Hk), 7.51 (dd, *J* = 8.7, 5.2 Hz, 2H, Hc), 7.24 – 7.13 (m, 1H, Hm), 6.93 (s, 2H, Hi), 6.83 (d, *J* = 9.2 Hz, 2H, Hg), 6.60 (d, *J* = 8.7 Hz, 2H, Hh), 3.79 – 3.43 (m, 16H, Hf, He).

^{13}C NMR (151 MHz, 298 K, Dimethyl sulfoxide-d_6) δ 171.43 (C=O), 168.80 (C^q), 152.24 (C^q), 151.92 (C^q, C-Cm), 147.69 (C^q, Ca-**C**-Cd), 139.84 (Cb), 135.90 (Ca), 135.60 (Cl), 130.11 (Ck), 128.76 (Ch), 126.55 (Cc), 126.10 (C^q), 124.66 (Cd and Cj overlapping from HSQC), 123.82 (Cm), 118.10 (acetronitrile), 111.86 (Cg), 108.85 (C^q, Cg-C-Ci), 101.14 (Ci), 83.01 (C^q, spiroC), 46.63 (Ce), 45.84 (Cf).

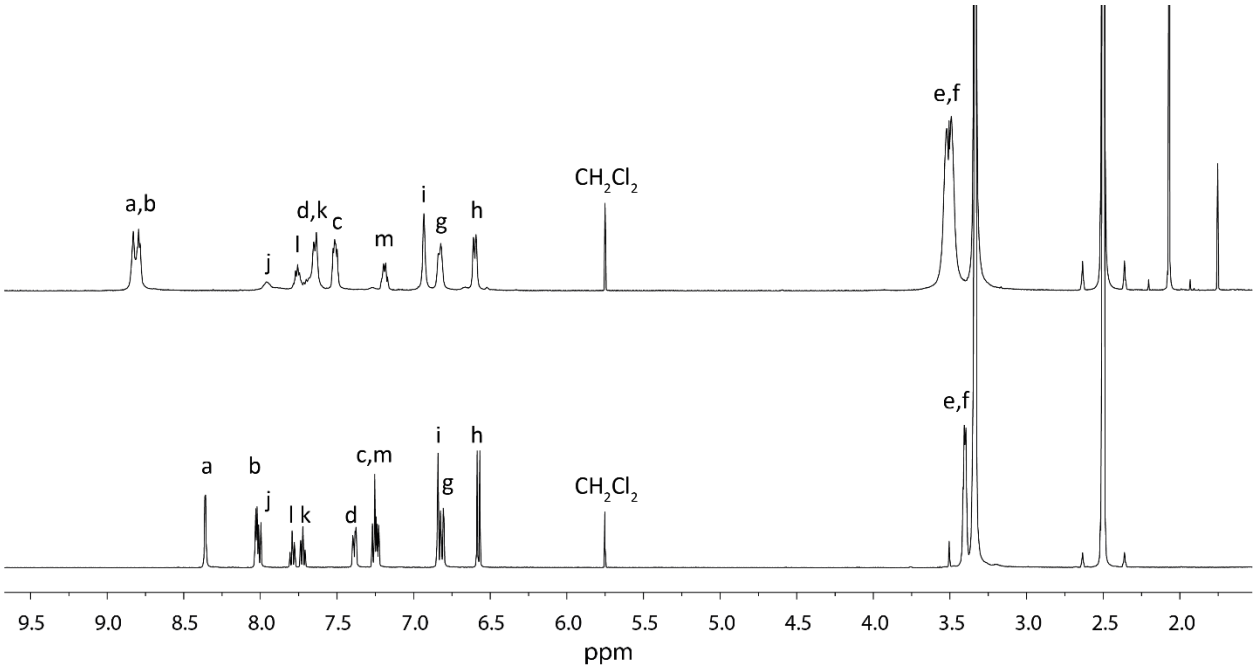

Figure 4.104: ^{1}H NMR stacked spectra (600 MHz, 298K, DMSO-d_6) of ligand **RB-P** (bottom) and the correspondent cage $[Pd_2(\mathbf{RB\text{-}P})_4](BF_4)_4$ (top) upon addition of 0.5 Equiv. of Pd(II) salt.

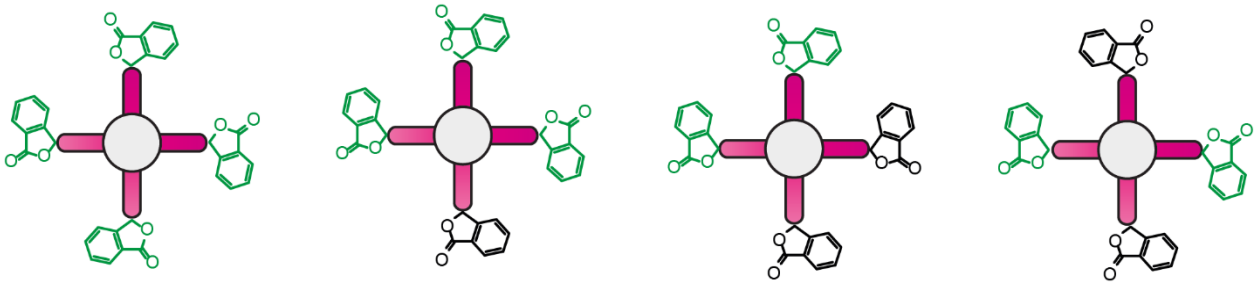

Figure 4.105: Schematic top view on the four different conformers for [[Pd_2(**RB-P**)$_4$](BF_4)$_4$ that can originate from the mutual disposition of the lactone functional group in the ligand **RB-P**.

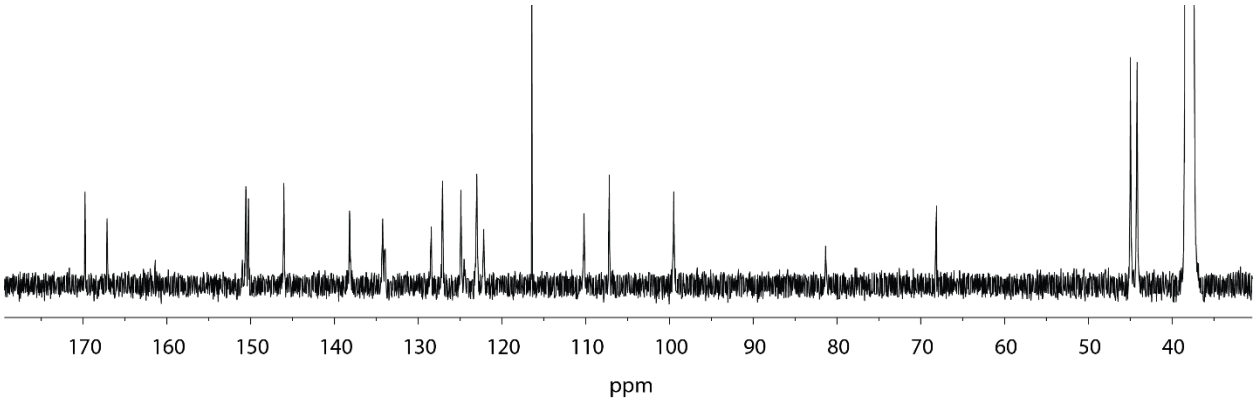

Figure 4.106: ^{13}C NMR spectrum (151 MHz, 298K, DMSO-d_6) of the cage [Pd_2(**RB-P**)$_4$](BF_4)$_4$.

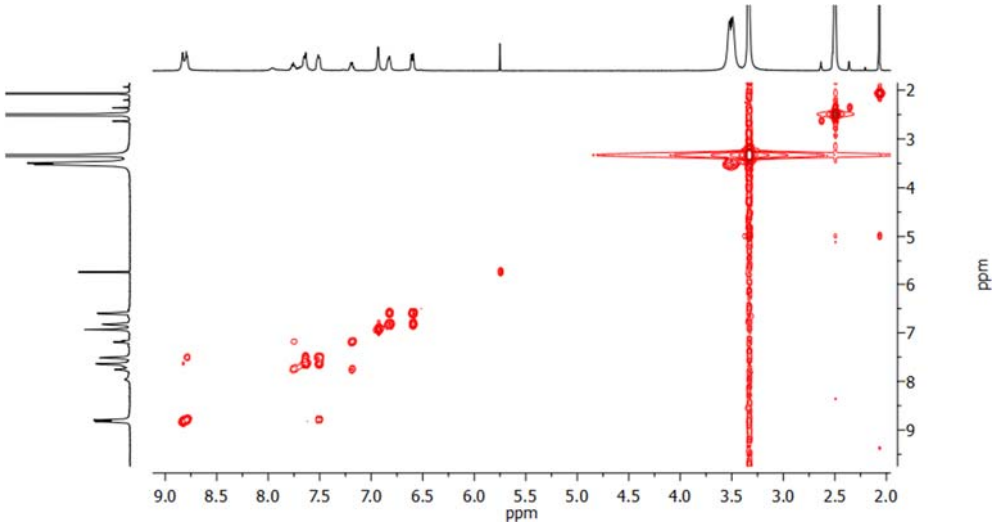

Figure 4.107: ^{1}H–^{1}H COSY spectrum (600 MHz, 298K, DMSO-d_6) of cage [Pd_2(**RB-P**)$_4$](BF_4)$_4$.

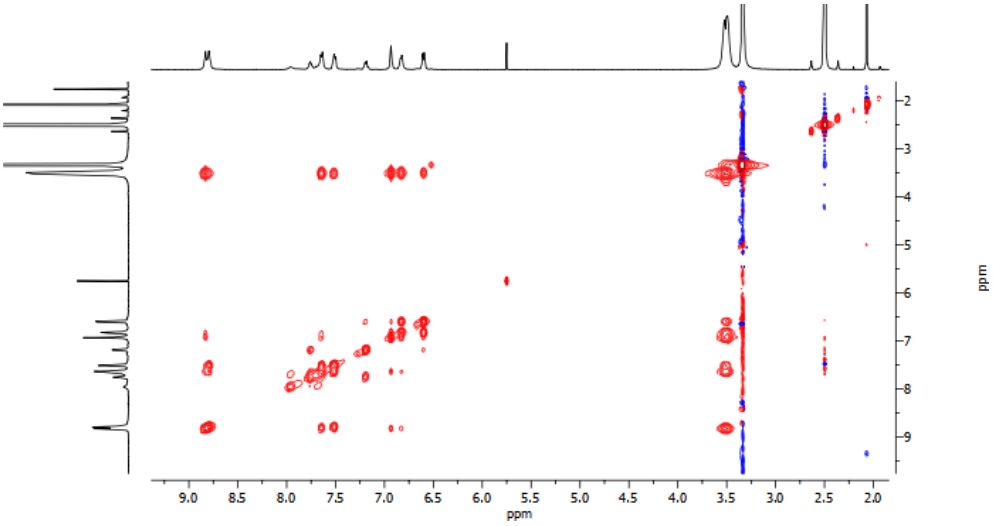

Figure 4.108: ^{1}H–^{1}H NOESY spectrum (600 MHz, 298K, DMSO-d_6) of cage $[Pd_2(\mathbf{RB\text{-}P})_4](BF_4)_4$.

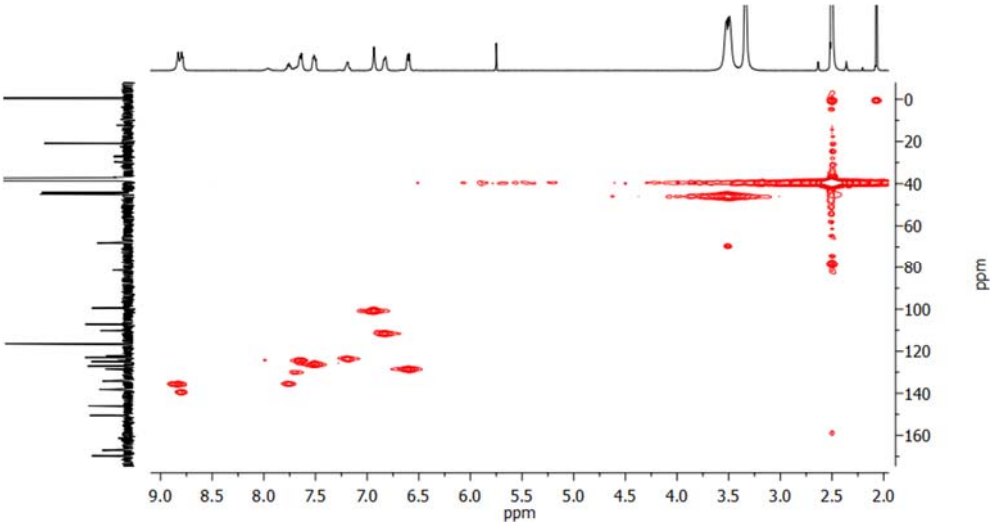

Figure 4.109: ^{1}H–^{13}C HSQC spectrum (600 MHz, 298K, DMSO-d_6) of cage $[Pd_2(\mathbf{RB\text{-}P})_4](BF_4)_4$.

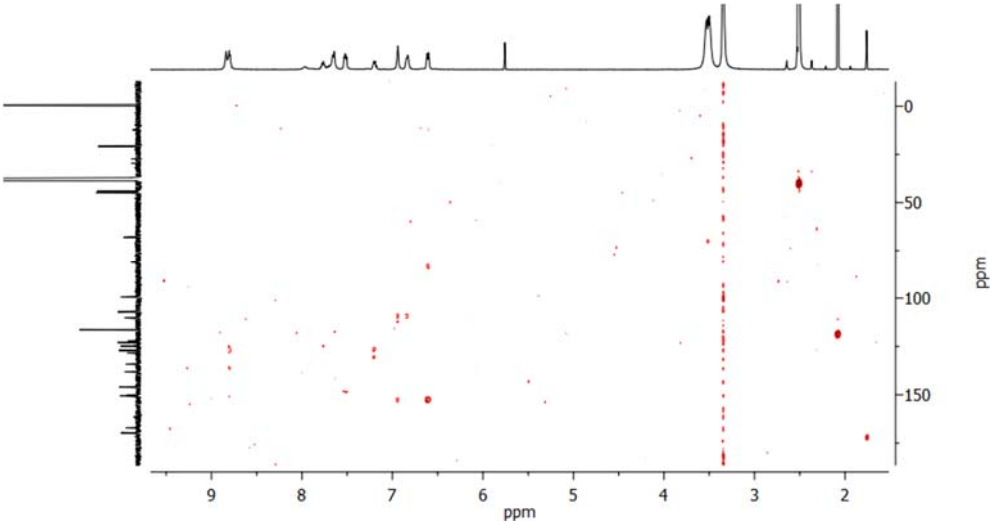

Figure 4.110: ^{1}H–^{13}C HMBC spectrum (600 MHz, 298K, DMSO-d_6) of cage $[Pd_2(\mathbf{RB\text{-}P})_4](BF_4)_4$.

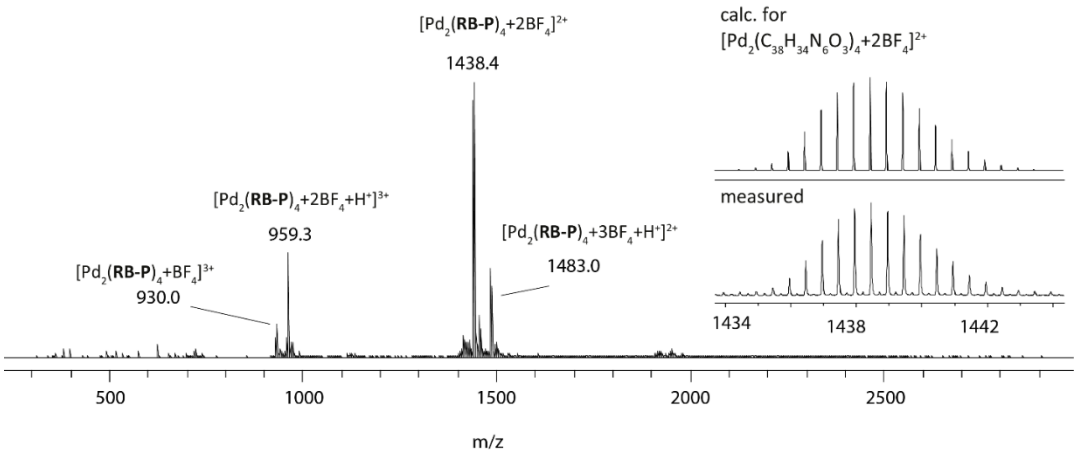

Figure 4.111: ESI-MS spectrum of $[Pd_2(\mathbf{RB\text{-}P})_4]+nBF_4]^{(4-n)+}$ with n=0-2. The observed and calculated isotopic pattern of $[Pd_2(\mathbf{RB\text{-}P})_4]+2BF_4]^{2+}$ is shown in the inset.

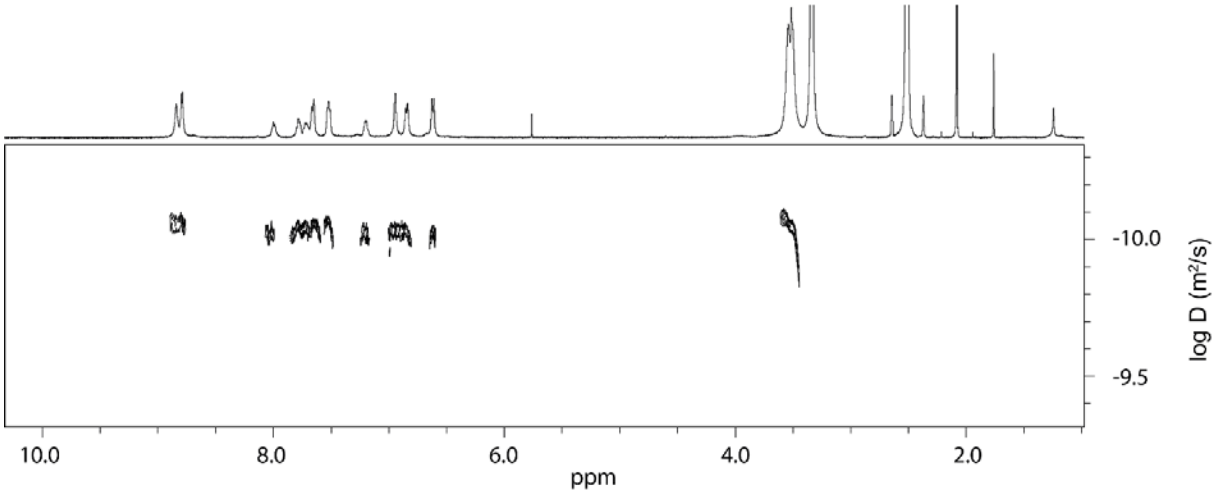

Figure 4.112: ^{1}H DOSY spectrum (500 MHz, 298K, DMSO-d_6) of $[Pd_2(\mathbf{RB\text{-}P})_4](BF_4)_4$ (0.7 mM). Diffusion coefficient: 8.642×10^{-11} m^2s^{-1}, log D=-10.063. Hydrodynamic radius= 12.71 Å.

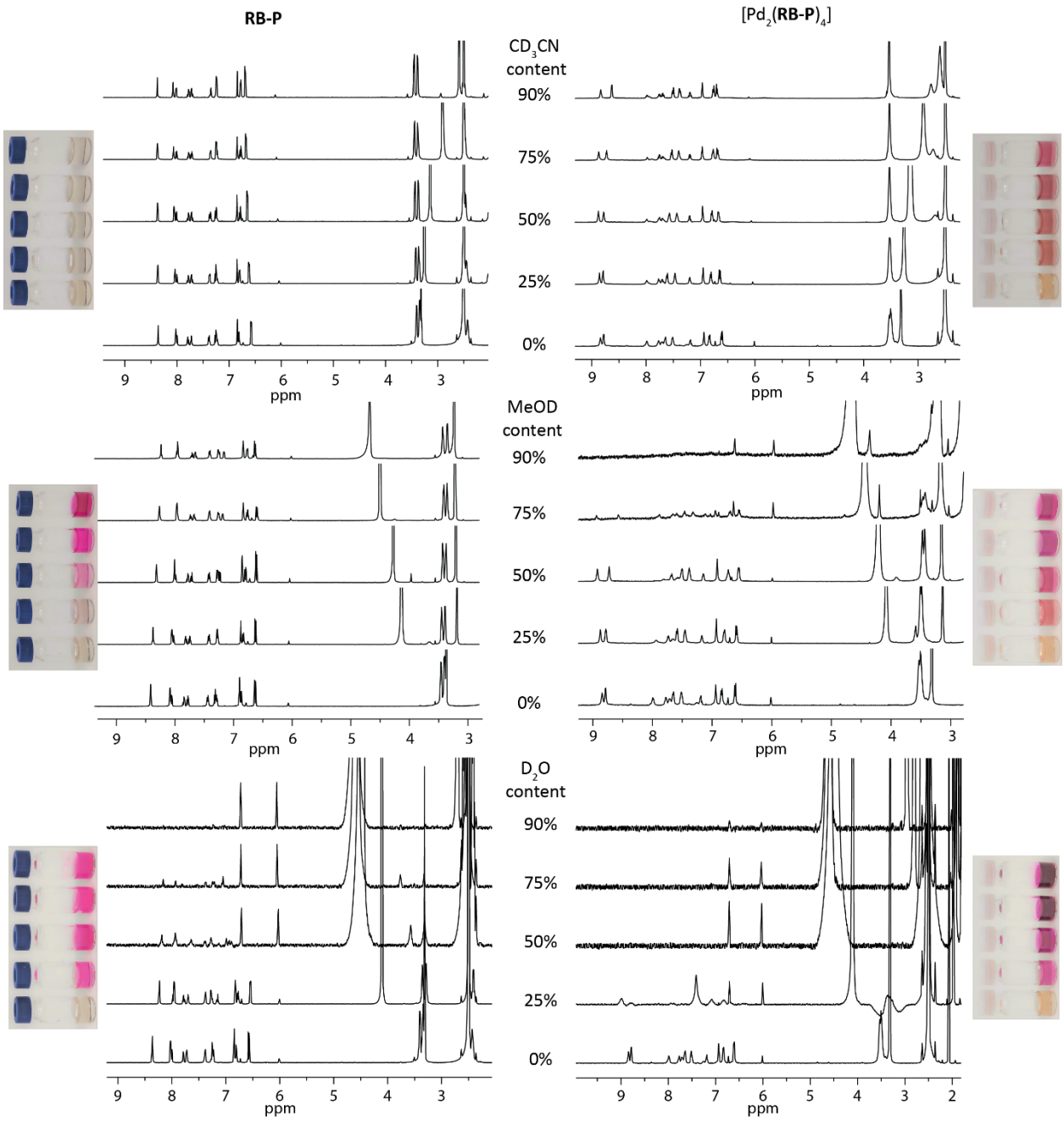

Figure 4.113: Stacked ^{1}H NMR spectra and pictures of DMSO-d_6 and CD_3CN, MeOD or D_2O different contents of **RB-P** on the left and $[Pd_2(\mathbf{RB\text{-}P})_4](BF_4)_4$ on the right. The specific contents are indicated in the Figure.

$[Pd_2(MB\text{-}P)_4](BF_4)_8$ and $[Pd_2(MB\text{-}P)_4](NO_3)_8$

$[Pd_2(MB\text{-}P)_4](BF_4)_8$

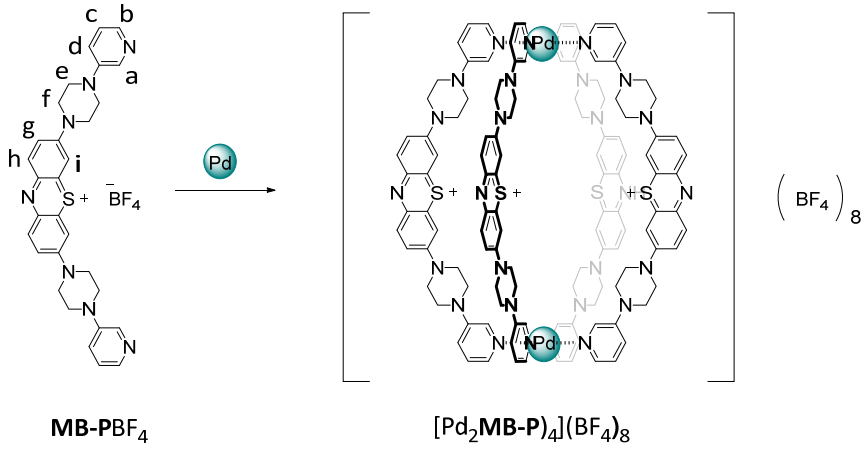

MB-PBF_4 $[Pd_2$**MB-P**$)_4](BF_4)_8$

Figure 4.114: Self-Assembly of cage $[Pd_2($**MB-P**$)_4](BF_4)_8$.

A mixture of ligand **MB-P**BF_4 (450 µL of a 3.11 mM solution in DMSO-d_6) and $[Pd(CH_3CN)_4](BF_4)_2$ (50 µL of a 15 mM solution in DMSO-d_6) was heated at 70 °C for 15 min to afford a 0.7 mM solution of $[Pd_2($**MB-P**$)_4](BF_4)_8$.

^{1}H NMR (600 MHz, 298 K, Dimethyl sulfoxide-d_6) δ 8.76 (m, 2H, Ha, Hb), 8.03 (d, J = 9.5 Hz, 1H, Hh), 7.82 (d, J = 2.5 Hz, 1H, Hi), 7.72 (dd, J = 9.5, 2.5 Hz, 1H, Hg), 7.69 – 7.59 (m, 1H, Hd), 7.53 (dd, J = 8.6, 5.4 Hz, 1H, Hc), 4.11 (m, 4H, Hf), 3.73 (m, 4H, He).

^{13}C NMR (151 MHz, 298 K, Dimethyl sulfoxide-d_6) δ 153.13 (C^q, **C**-Ch), 146.73(C^q, **C**-Ci), 139.27 (Cb), 138.25 (Ch), 135.83 (C^q, Cg-**C**-Ci), 134.75 (Ca-**C**-Cd), 134.31 (Ca), 126.40 (Cc), 123.75 (Cd), 119.38 (Cg), 106.95 (Ci), 46.00 (Ce), 44.60 (Cf).

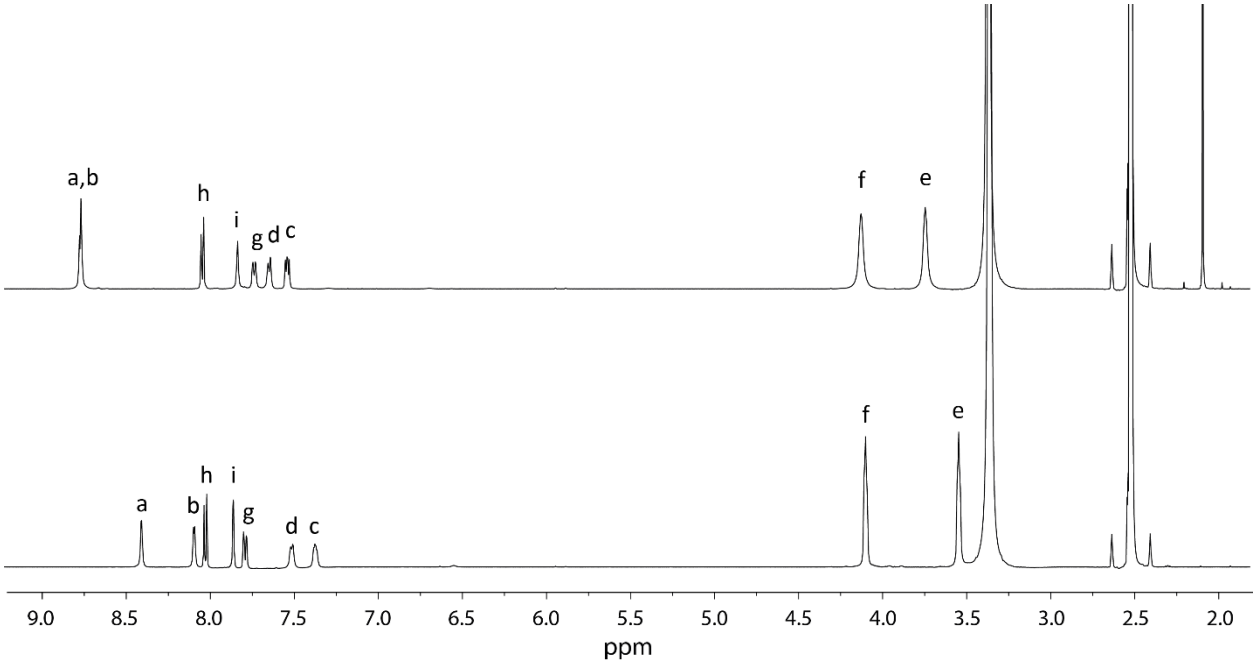

Figure 4.115: ^{1}H NMR stacked spectra (600 MHz, 298K, DMSO-d_6) of ligand **MB-P**BF_4 (bottom) and the correspondent cage $[Pd_2($**MB-P**$)_4](BF_4)_8$ (top) upon addition of 0.5 Equiv. of Pd(II) salt.

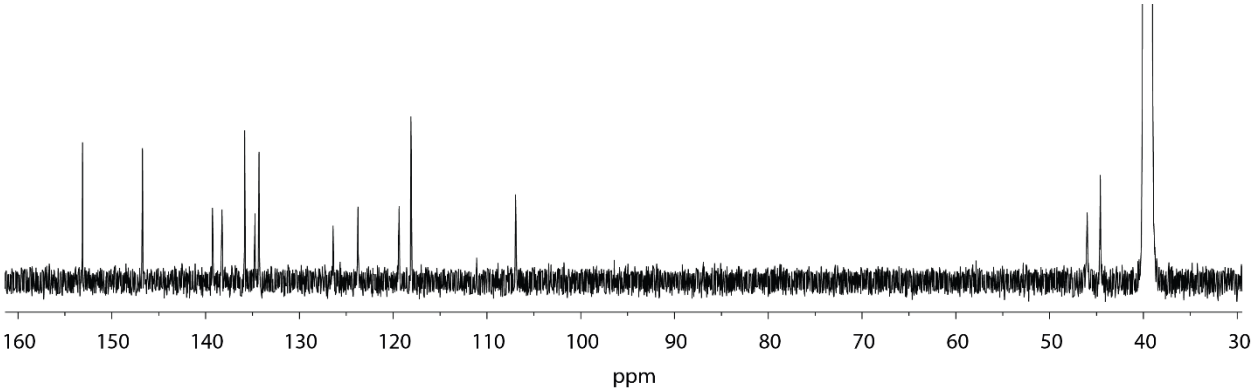

Figure 4.116: ^{13}C NMR spectrum (151 MHz, 298K, DMSO-d_6) of the cage $[Pd_2(\mathbf{MB\text{-}P})_4](BF_4)_8$.

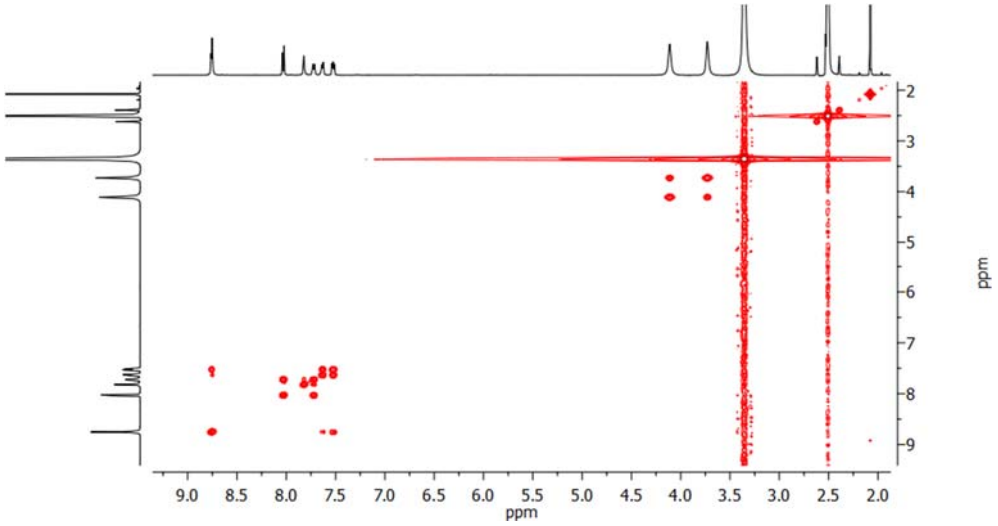

Figure 4.117: ^{1}H–^{1}H COSY spectrum (600 MHz, 298K, DMSO-d_6) of cage $[Pd_2(\mathbf{MB\text{-}P})_4](BF_4)_8$.

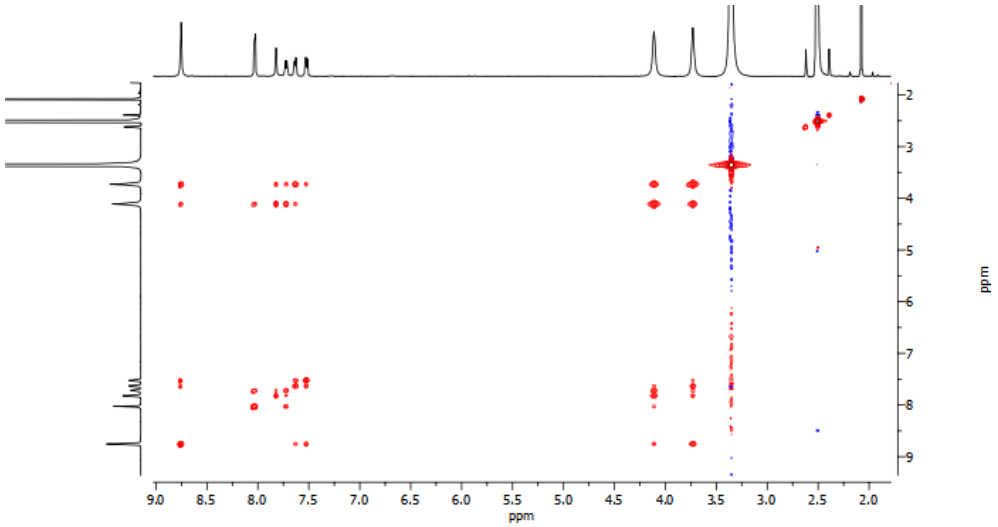

Figure 4.118: ^{1}H–^{1}H NOESY spectrum (600 MHz, 298K, DMSO-d_6) of cage $[Pd_2(\mathbf{MB\text{-}P})_4](BF_4)_8$.

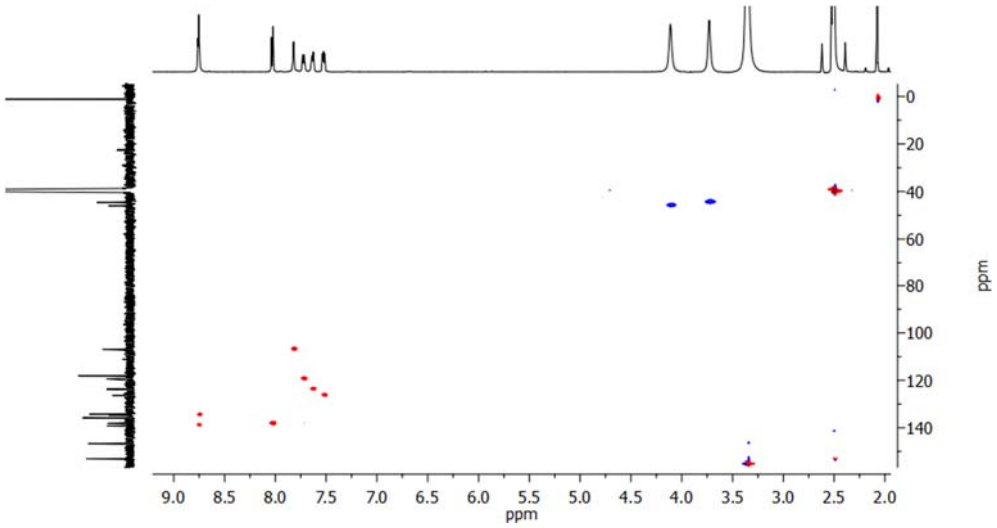

Figure 4.119: $^{1}H–^{13}C$ HSQC spectrum (600 MHz, 298K, DMSO-d_6) of cage $[Pd_2(\mathbf{MB\text{-}P})_4](BF_4)_8$.

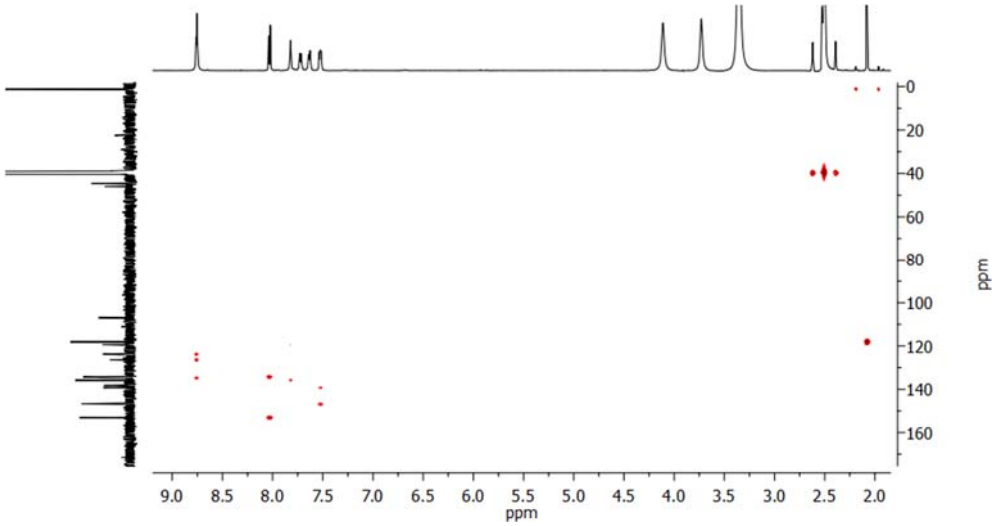

Figure 4.120: $^{1}H–^{13}C$ HMBC spectrum (600 MHz, 298K, DMSO-d_6) of cage $[Pd_2(\mathbf{MB\text{-}P})_4](BF_4)_8$.

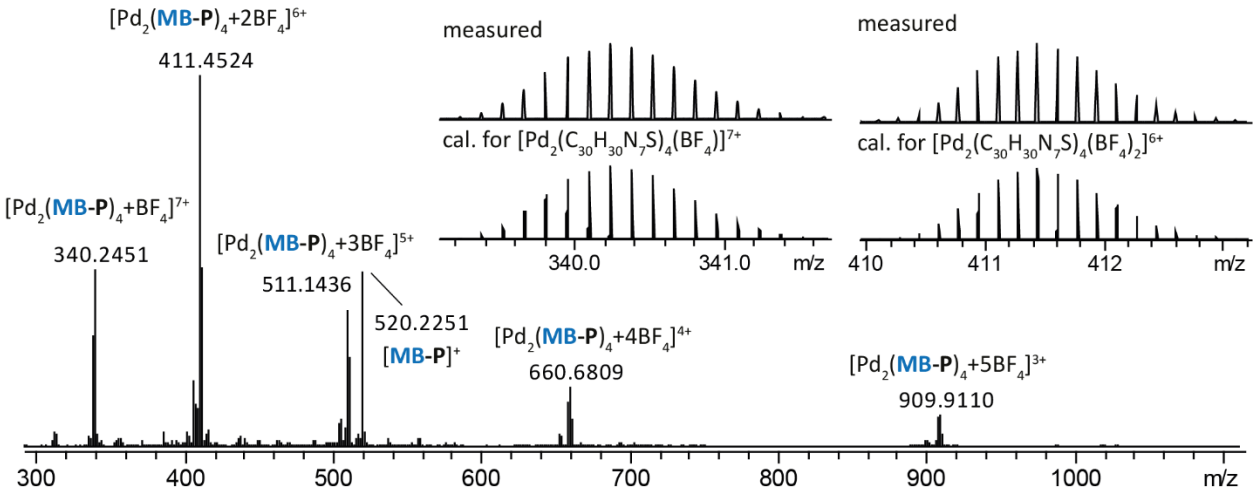

Figure 4.121: ESI-MS spectrum of $[Pd_2(\mathbf{MB\text{-}P})_4]+nBF_4]^{(8-n)+}$ with n=1-5. The observed and calculated isotopic pattern of $[Pd_2(\mathbf{MB\text{-}P})_4]+BF_4]^{7+}$ and $[Pd_2(\mathbf{MB\text{-}P})_4]+2BF_4]^{6+}$ are shown in the inset.

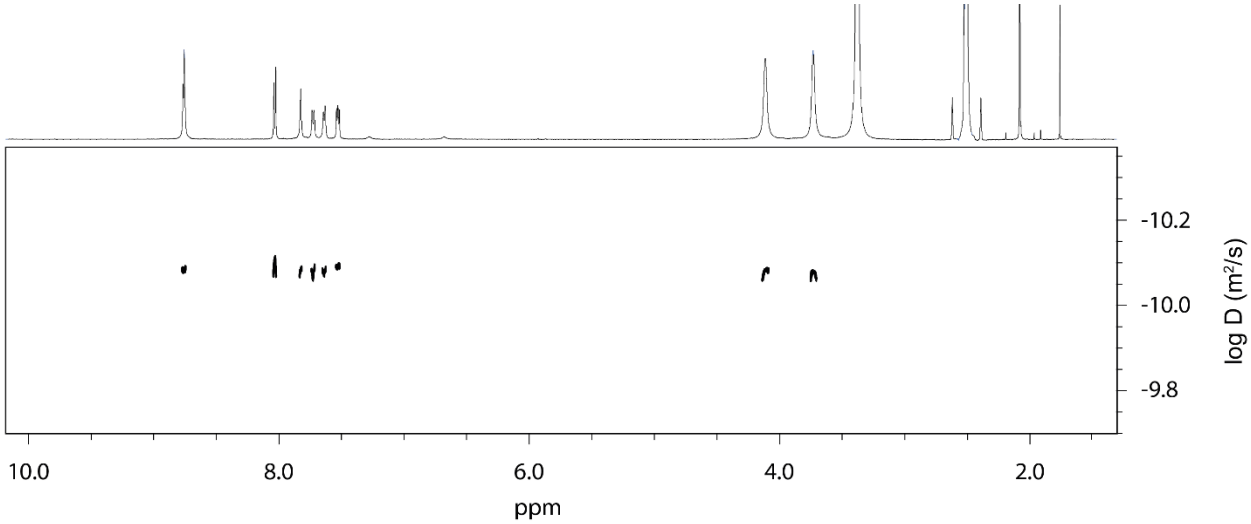

Figure 4.122: ^{1}H DOSY spectrum (500 MHz, 298K, DMSO-d_6) of $[Pd_2(\mathbf{MB\text{-}P})_4](BF_4)_8$ (0.7 mM). Diffusion coefficient: 8.253×10^{-11} m^2s^{-1}, log D=-10.083. Hydrodynamic radius= 13.304 Å.

$[Pd_2(MB\text{-}P)_4](NO_3)_8$

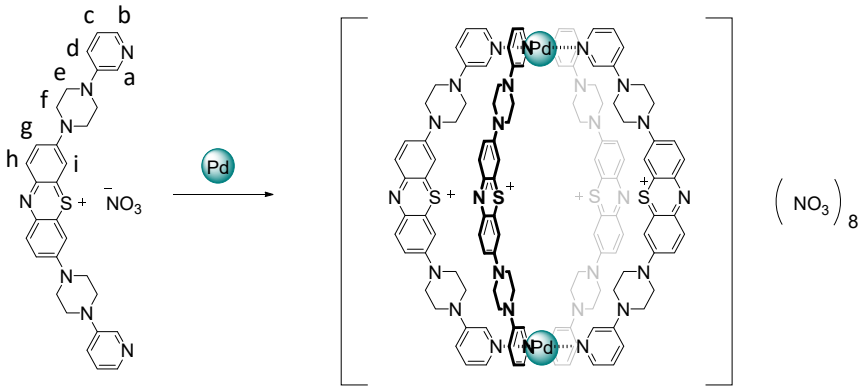

MB-PNO_3 $[Pd_2(\mathbf{MB\text{-}P})_4](NO_3)_8$

Figure 4.123: Self-Assembly of cage $[Pd_2(\mathbf{MB\text{-}P})_4](NO_3)_8$.

A mixture of ligand **MB-P**NO_3 (450 µL of a 3.11 mM solution in DMSO-d_6) and $Pd(NO_3)_2$ (50 µL of a 15 mM solution in DMSO-d_6) was heated at 70 °C for 15 min to afford a 0.7 mM solution of $[Pd_2(\mathbf{MB\text{-}P})_4](NO_3)_8$.

^{1}H NMR (600 MHz, 298 K, Dimethyl sulfoxide-d_6) δ 8.95 (s, 1H, Ha), 8.73 (d, J = 5.5 Hz, 1H, Hb), 8.09 – 7.97 (m, 2H, Hh, Hi), 7.71 (d, J = 9.5 Hz, 1H, Hg), 7.62 (d, J = 8.8 Hz, 1H, Hd), 7.50 (dd, J = 8.6, 5.5 Hz, 1H, Hc), 4.20-4.06 (m, 4H, Hf), 3.85 – 3.63 (m, 4H, He).

^{13}C NMR (151 MHz, 298 K, Dimethyl sulfoxide-d_6) δ 153.10 (C^q, **C**-Ch), 146.77 (C^q, **C**-Ci), 139.32 (Cb), 138.20 (Ch), 135.85 (C^q, Cg-**C**-Ci), 135.20 (C^q, Ca-**C**-Cd), 134.42 (Ca), 126.37 (Cc), 123.72 (Cd), 119.32 (Cg), 107.34 (Ci), 46.17 (Ce), 44.88 (Cf).

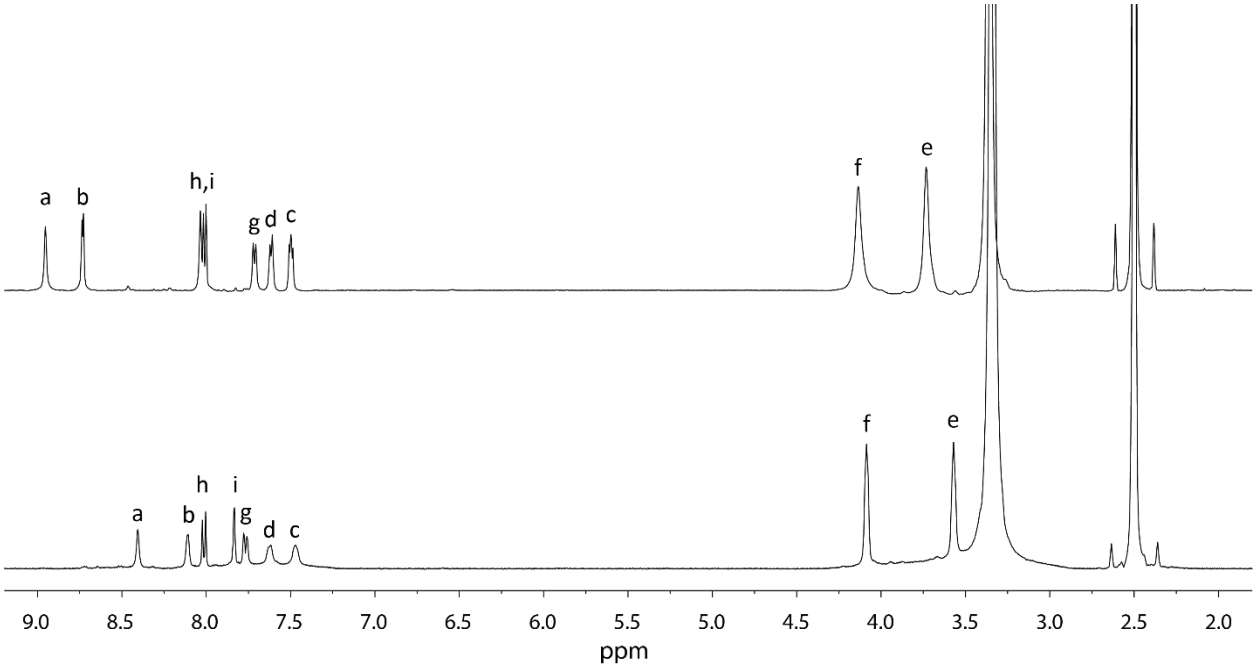

Figure 4.124: ^{1}H NMR stacked spectra (600 MHz, 298K, DMSO-d_6) of ligand **MB-P**NO_3 (bottom) and the correspondent cage $[Pd_2(\mathbf{MB\text{-}P})_4](NO_3)_8$ (top) upon addition of 0.5 Equiv. of Pd(II) salt.

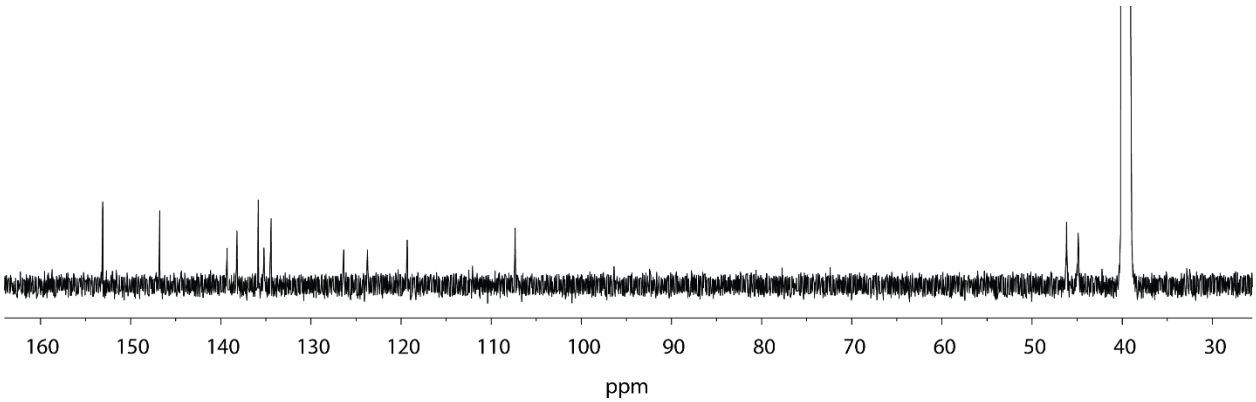

Figure 4.125: ^{13}C NMR spectrum (151 MHz, 298K, DMSO-d_6) of the cage $[Pd_2(\mathbf{MB\text{-}P})_4](NO_3)_8$.

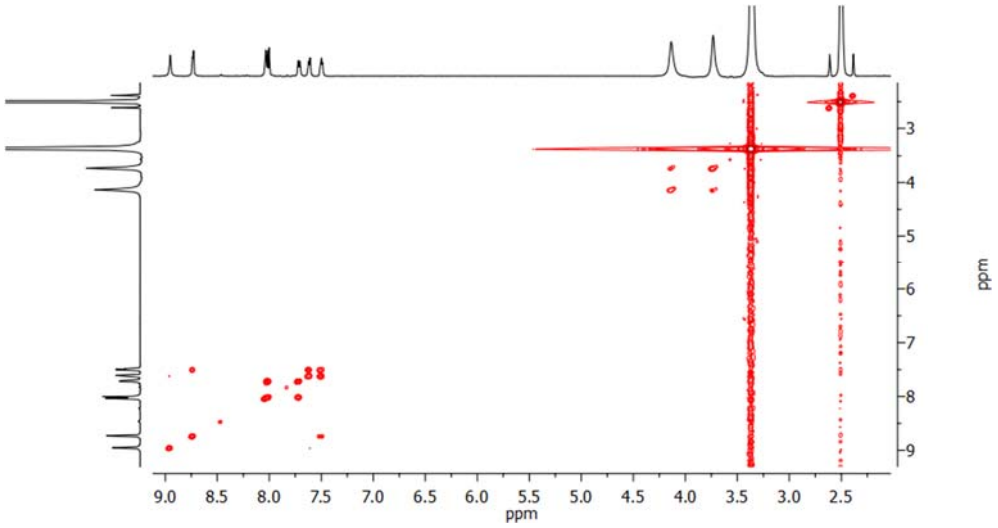

Figure 4.126: ^{1}H–^{1}H COSY spectrum (600 MHz, 298K, DMSO-d_6) of cage $[Pd_2(\mathbf{MB\text{-}P})_4](NO_3)_8$.

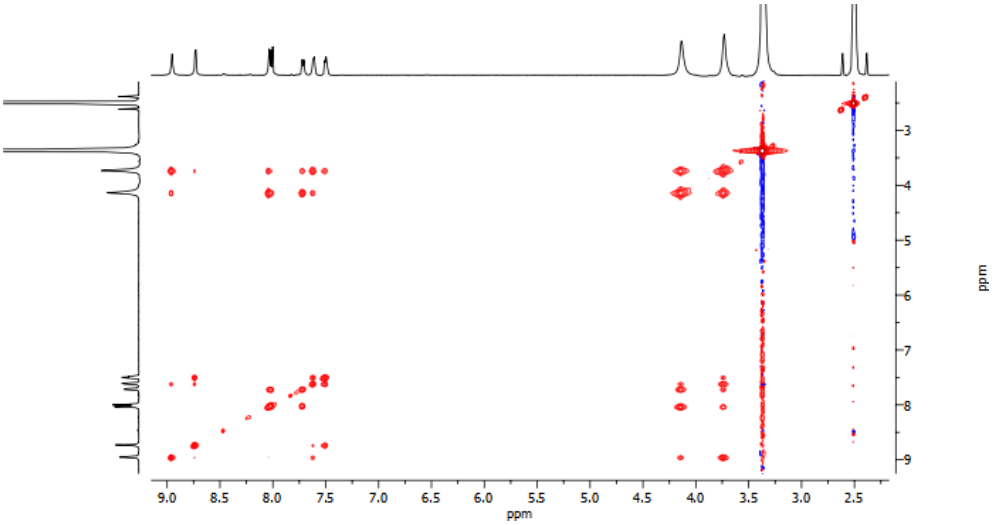

Figure 4.127: ^{1}H –^{1}H NOESY spectrum (600 MHz, 298K, DMSO-d_6) of cage [Pd_2(**MB-P**)$_4$](NO_3)$_8$.

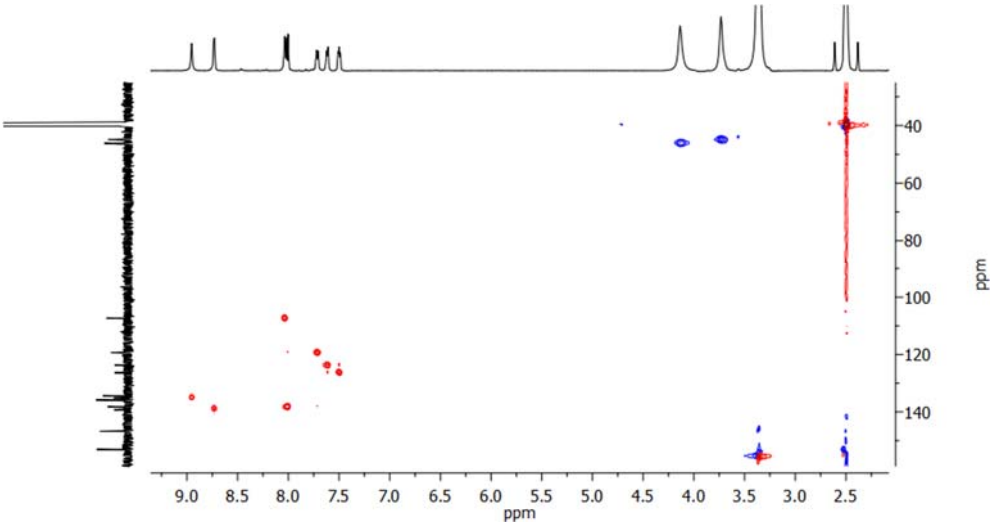

Figure 4.128: ^{1}H–^{13}C HSQC spectrum (600 MHz, 298K, DMSO-d_6) of cage [Pd_2(**MB-P**)$_4$](NO_3)$_8$.

A mixture of ligand **MB-P** in D_2O (450 µL of a 3.11 mM solution) and $Pd(NO_3)_2$ (50 µL of a 15 mM solution in DMSO-d_6) was heated at 70 °C for 15 min to afford a 0.7 mM solution of [Pd_2(**MB-P**)$_4$](NO_3)$_8$.

^{1}H NMR (500 MHz, Deuterium Oxide) δ 8.30 – 8.25 (m, 1H, Ha), 8.11 (d, J = 5.4 Hz, 1H, Hb), 8.04 (d, *J* = 9.7 Hz, 1H, Hh), 7.99 (d, *J* = 8.4 Hz, 1H, Hd), 7.84 (dd, *J* = 8.9, 5.4 Hz, 1H, Hc), 7.65 (d, *J* = 9.8 Hz, 1H, Hg), 7.53 (s, 1H, Hi), 4.17 – 4.10 (m, 2H), 3.83 – 3.72 (m, 4H).

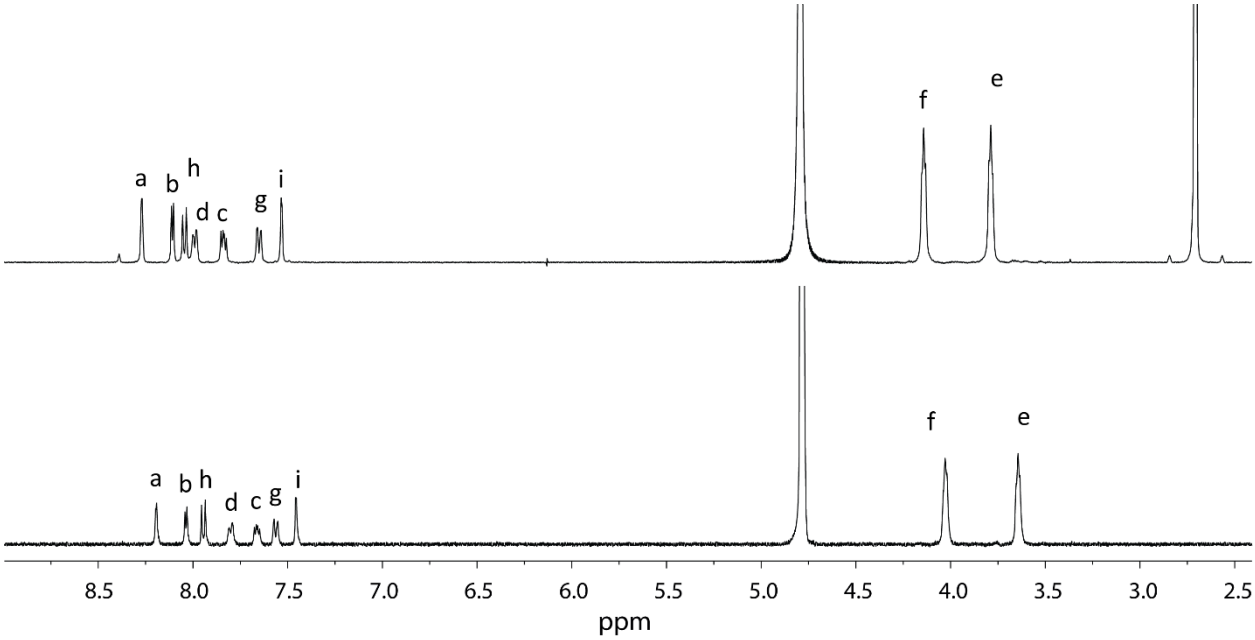

Figure 4.129: ^{1}H NMR stacked spectra (500 MHz, 298K, D_2O) of ligand **MB-P**NO_3 (bottom) and the correspondent cage $[Pd_2(\mathbf{MB\text{-}P})_4](NO_3)_8$ (top) upon addition of 0.5 Equiv. of Pd(II) salt.

$[Pd_2(CV\text{-}P)_4](NO_3)_8$

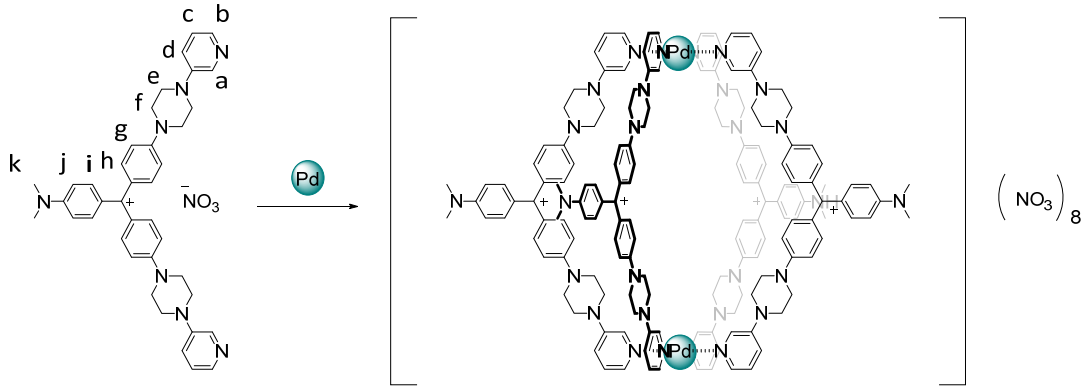

CV-P $[Pd_2(\mathbf{CV\text{-}P})_4](NO_3)_8$

Figure 4.130: Self-Assembly of cage $[Pd_2(\mathbf{CV\text{-}P})_4](NO_3)_8$.

A mixture of ligand **CV-P** (450 µL of a 3.11 mM solution in DMSO-d_6) and $Pd(NO_3)_2$ (50 µL of a 15 mM solution in DMSO-d_6) was heated at 70 °C for 15 min to afford a 0.7 mM solution of $[Pd_2(\mathbf{CV\text{-}P})_4](NO_3)_8$.

^{1}H NMR (500 MHz, 298 K, Dimethyl sulfoxide-d_6) δ 8.92 (s, 1H, Ha), 8.70 (d, J = 4.9 Hz, 1H, Hb), 7.47 (dd, J = 20.9, 7.9 Hz, 2H, Hd, Hc), 7.22 (m, 5H, Hg, Hh, Hi), 6.96 (d, J = 9.2 Hz, 1H, Hj), 3.98 – 3.72 (m, 4H, Hf), 3.72 – 3.55 (m, 4H, He), 3.18 (s, 3H, Hk).

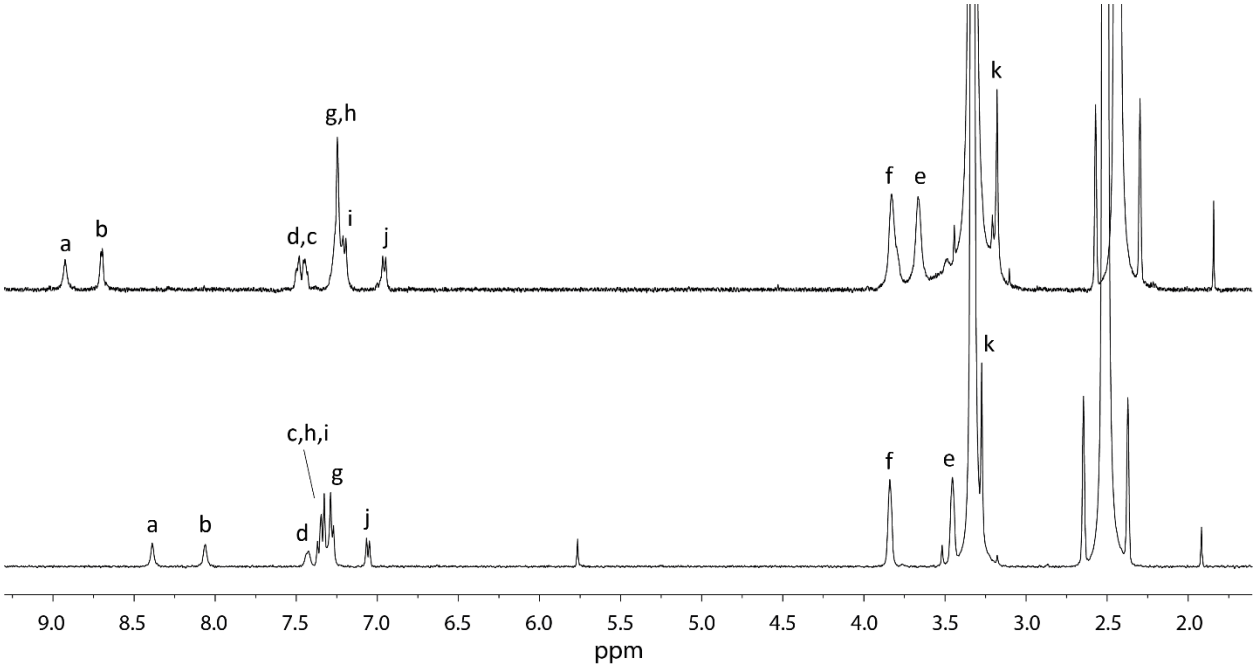

Figure 4.131: ^{1}H NMR stacked spectra (600 MHz, 298K, DMSO-d_6) of ligand **CV-P** (bottom) and the correspondent cage $[Pd_2(\mathbf{CV\text{-}P})_4](NO_3)_8$ (top) upon addition of 0.5 Equiv. of Pd(II) salt.

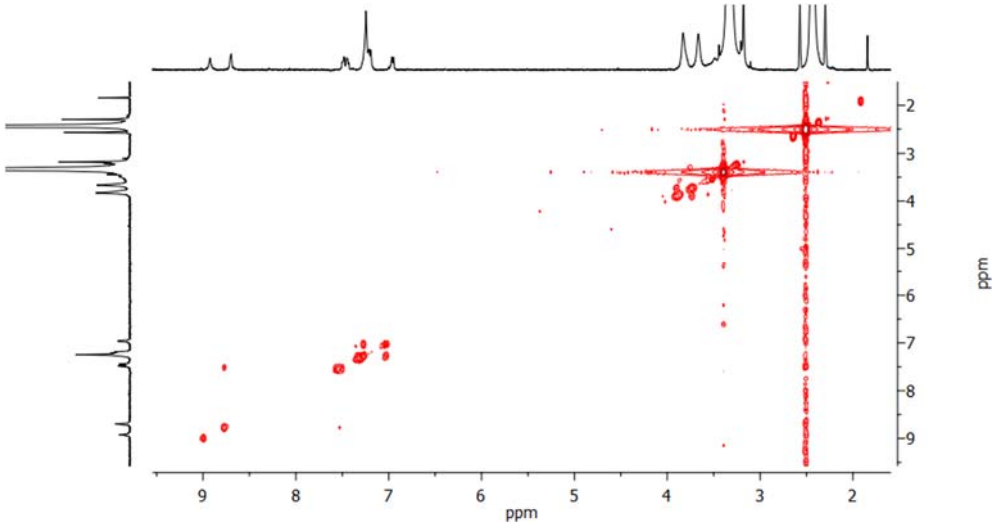

Figure 4.132: ^{1}H–^{1}H COSY spectrum (600 MHz, 298K, DMSO-d_6) of cage $[Pd_2(\mathbf{CV\text{-}P})_4](NO_3)_8$.

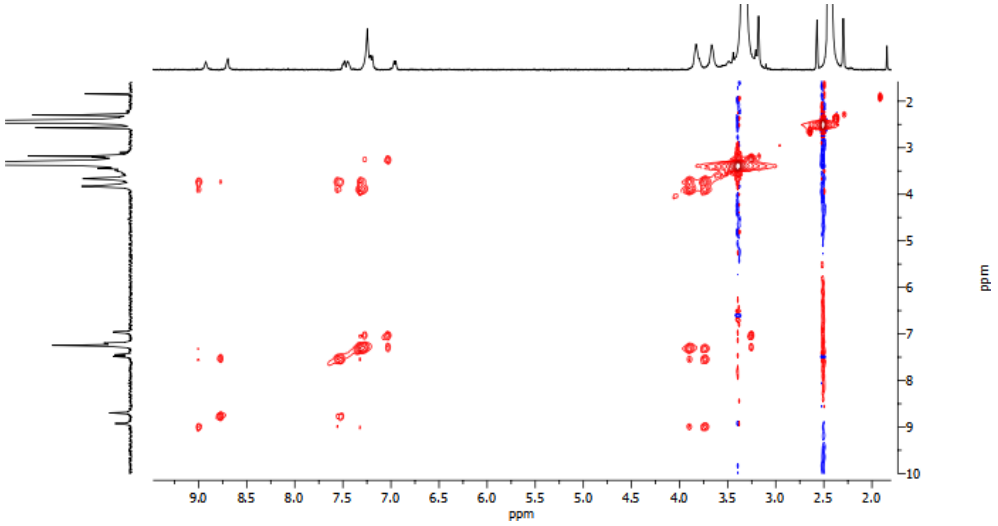

Figure 4.133: ^{1}H–^{1}H NOESY spectrum (600 MHz, 298K, DMSO-d_6) of cage $[Pd_2(\mathbf{CV\text{-}P})_4](NO_3)_8$.

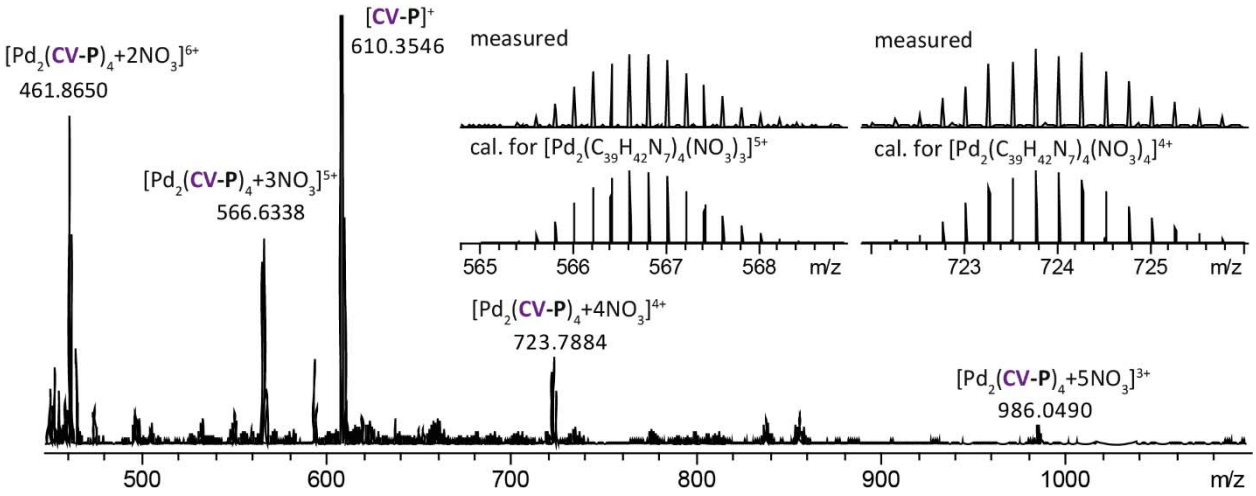

Figure 4.134: ESI-MS spectrum of $[Pd_2(\mathbf{CV\text{-}P})_4{+}nNO_3]^{(8-n)+}$ with n=2-5. The observed and calculated isotopic pattern of $[Pd_2(\mathbf{CV\text{-}P})_4{+}3NO_3]^{5+}$ and $[Pd_2(\mathbf{CV\text{-}P})_4{+}4NO_3]^{4+}$ are shown in the inset.

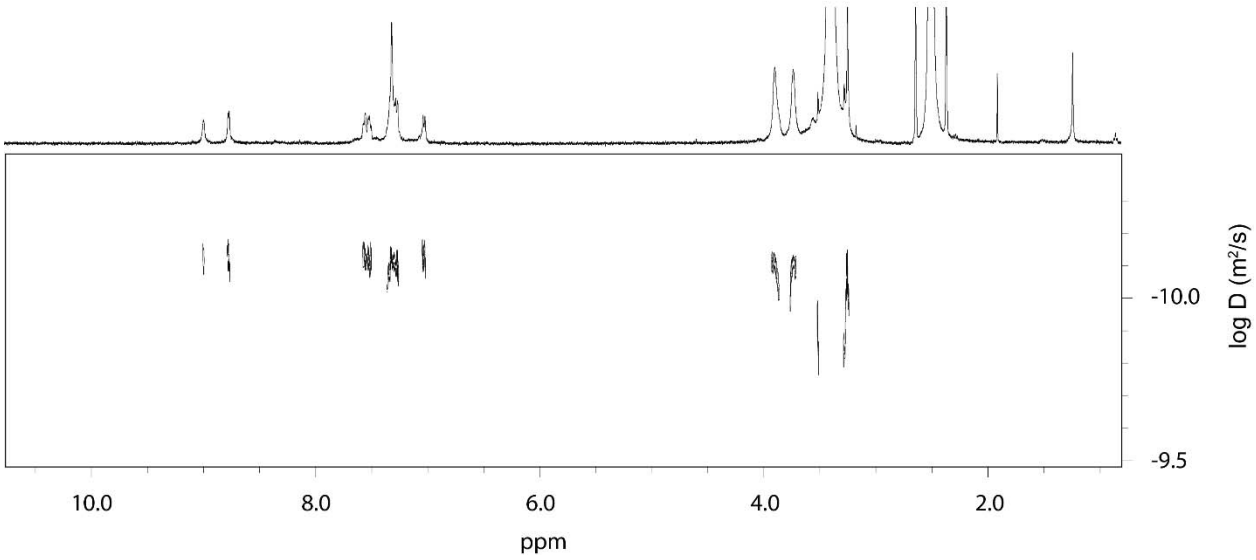

Figure 4.135: ^{1}H DOSY spectrum (500 MHz, 298K, DMSO-d_6) of $[Pd_2(\mathbf{CV\text{-}P})_4](NO_3)_8$ (0.7 mM). Diffusion coefficient: 7.990×10^{-11} m^2s^{-1}, log D=-10.098. Hydrodynamic radius= 13.74 Å.

[Pd_2(RE-P)$_4$]($EtSO_4$)$_4$(BF_4)$_4$

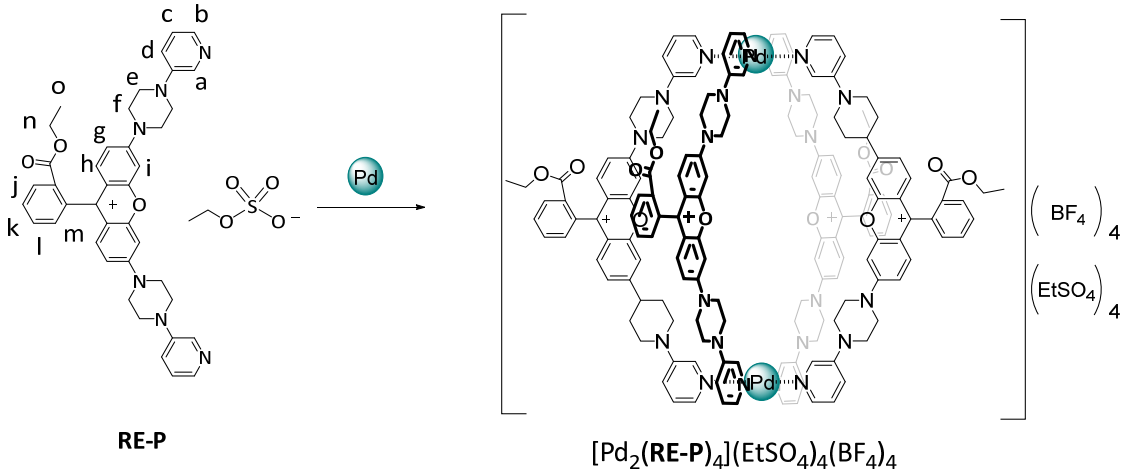

Figure 4.136: Self-Assembly of cage [Pd_2(**RE-P**)$_4$]($EtSO_4$)$_4$(BF_4)$_4$.

A mixture of ligand **RE-P** (450 µL of a 3.11 mM solution in DMSO-d_6) and [Pd(CH_3CN)$_4$](BF_4)$_2$ (50 µL of a 15 mM solution in DMSO-d_6) was heated at 70 °C for 15 min to afford a 0.7 mM solution of [Pd_2(**RE-P**)$_4$]($EtSO_4$)$_4$(BF_4)$_4$.

^{1}H NMR (600 MHz, Dimethyl sulfoxide-d_6) δ 9.00 (s, 1H), 8.77 (d, *J* = 5.5 Hz, 1H), 8.26 (d, *J* = 7.8 Hz, 1H), 7.92 (t, *J* = 7.6 Hz, 0H), 7.86 (t, *J* = 7.4 Hz, 1H), 7.57 (d, *J* = 8.9 Hz, 1H), 7.53 – 7.42 (m, 1H), 7.34 (t, *J* = 8.3 Hz, 2H), 7.15 – 7.05 (m, 1H), 3.98 (s, 6H), 3.94 – 3.87 (m, 1H), 3.81 (q, *J* = 7.1 Hz, 4H), 3.71 (s, 3H), 1.15 (t, *J* = 7.1 Hz, 5H), 0.96 – 0.81 (m, 2H).

^{13}C NMR (151 MHz, Dimethyl sulfoxide-d_6) δ 164.57(C^q), 157.46 (C^q), 156.62 (C^q), 146.77 (C^q), 146.77 (C^q), 139.20 (Cb), 135.46 (Ca), 133.24 (Cl), 132.82 (Ch), 131.02 (Cj and Ck), 129.57 (Cm), 126.42 (Cc), 123.43 (Cd), 118.08 (acetonitrile?), 115.38 (Cg), 113.92 (C^q), 96.97 (Ci), 61.28 (-**C**H_2 counterion), 61.04 (Cn), 45.80 (Cf), 44.76 (Ce), 15.21(-**C**H_3 counterion), 13.51 (Co).

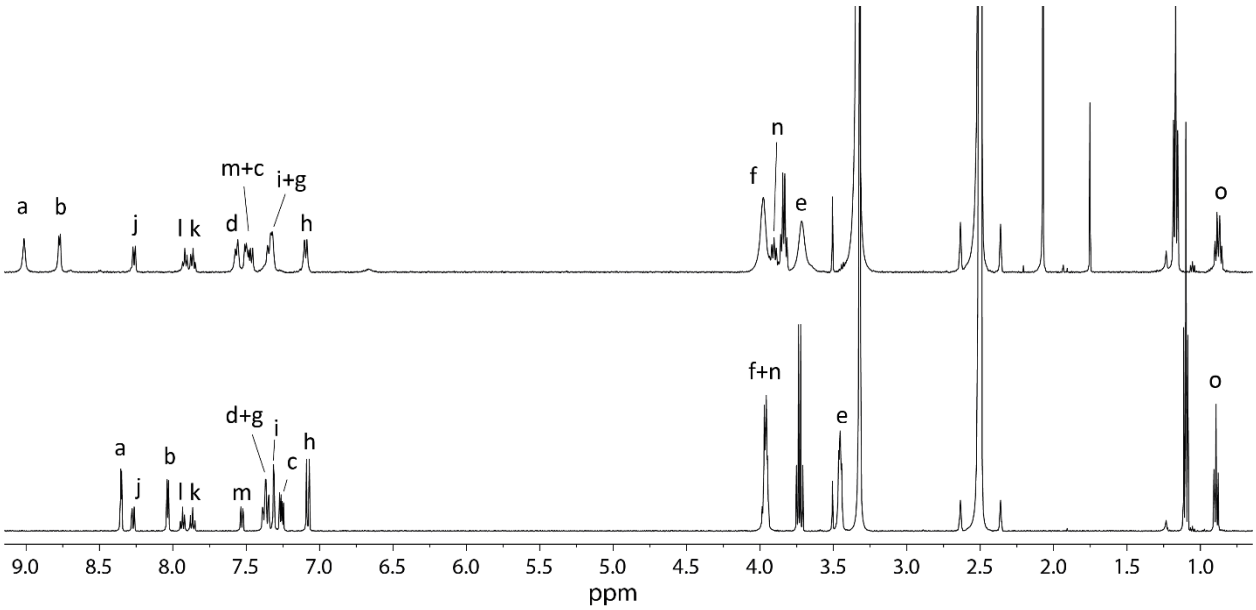

Figure 4.137: ^{1}H NMR stacked spectra (600 MHz, 298K, DMSO-d_6) of ligand **RE-P** (bottom) and the correspondent cage [Pd_2(**RE-P**)$_4$]($EtSO_4$)$_4$(BF_4)$_4$ (top) upon addition of 0.5 Equiv. of Pd(II) salt.

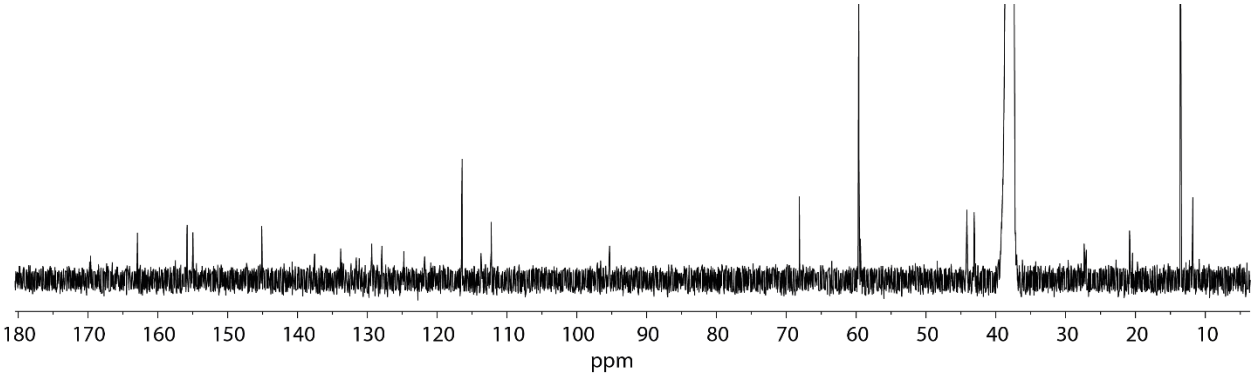

Figure 4.138: ^{13}C NMR spectrum (151 MHz, 298K, DMSO-d_6) of the cage $[Pd_2(\mathbf{RE\text{-}P})_4](EtSO_4)_4(BF_4)_4$.

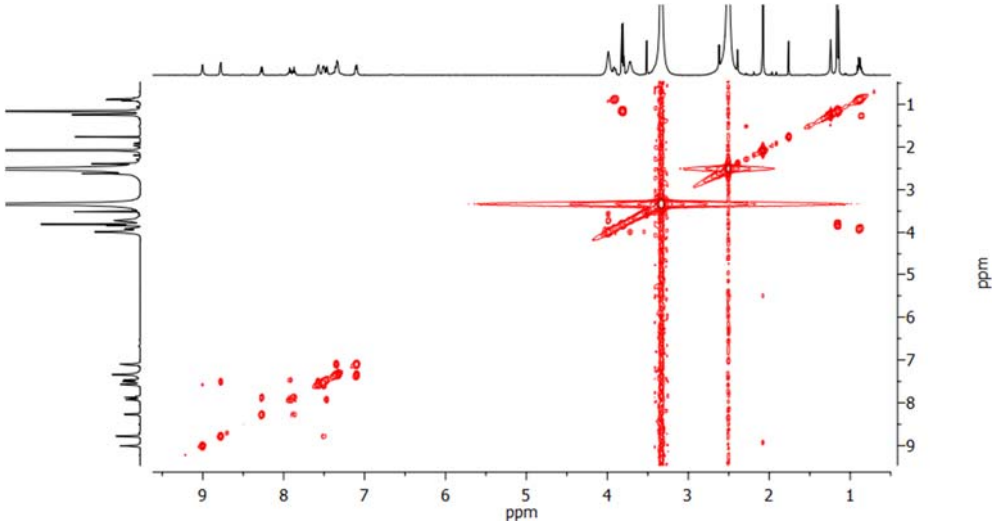

Figure 4.139: ^{1}H–^{1}H COSY spectrum (600 MHz, 298K, DMSO-d_6) of cage $[Pd_2(\mathbf{RE\text{-}P})_4](EtSO_4)_4(BF_4)_4$.

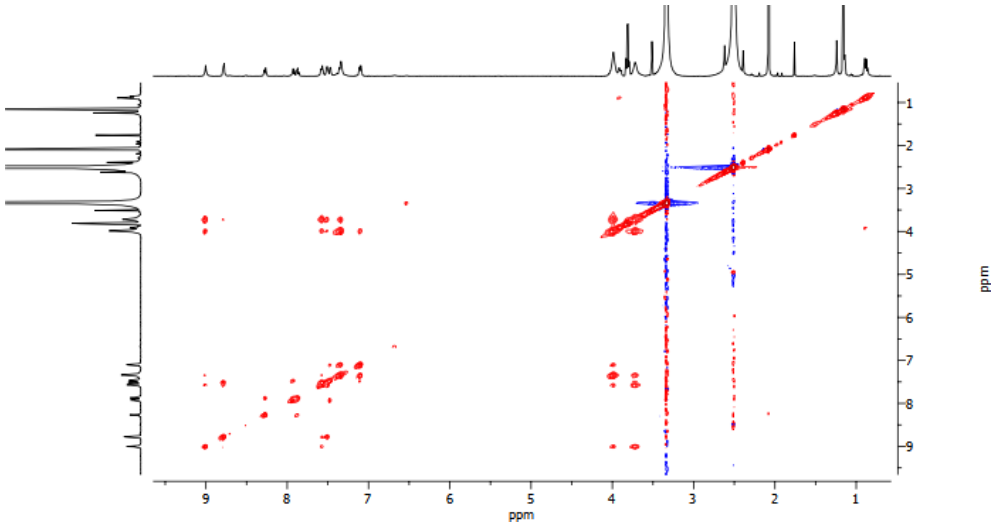

Figure 4.140: ^{1}H–^{1}H NOESY spectrum (600 MHz, 298K, DMSO-d_6) of cage $[Pd_2(\mathbf{RE\text{-}P})_4](EtSO_4)_4(BF_4)_4$.

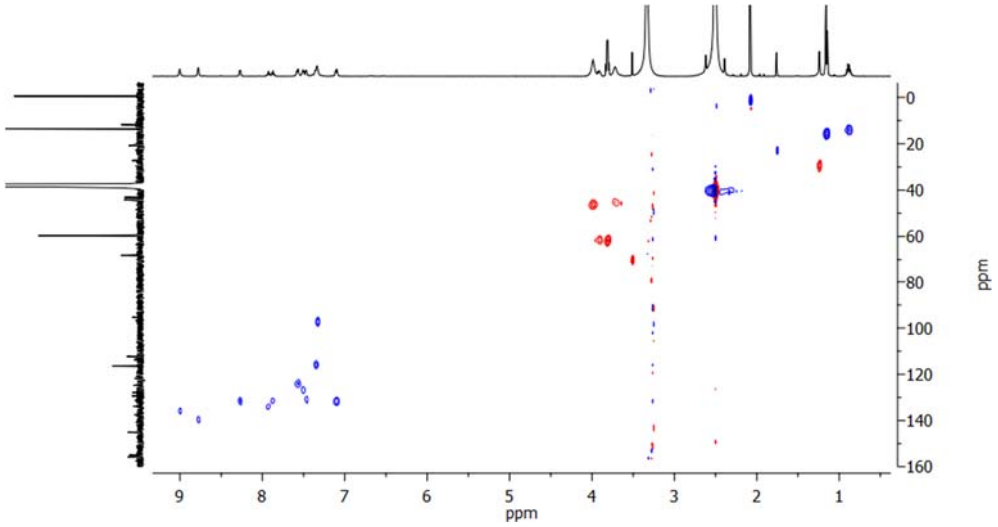

Figure 4.141: $^{1}H–^{13}C$ HSQC spectrum (600 MHz, 298K, DMSO-d_6) of cage $[Pd_2(\mathbf{RE\text{-}P})_4](EtSO_4)_4(BF_4)_4$.

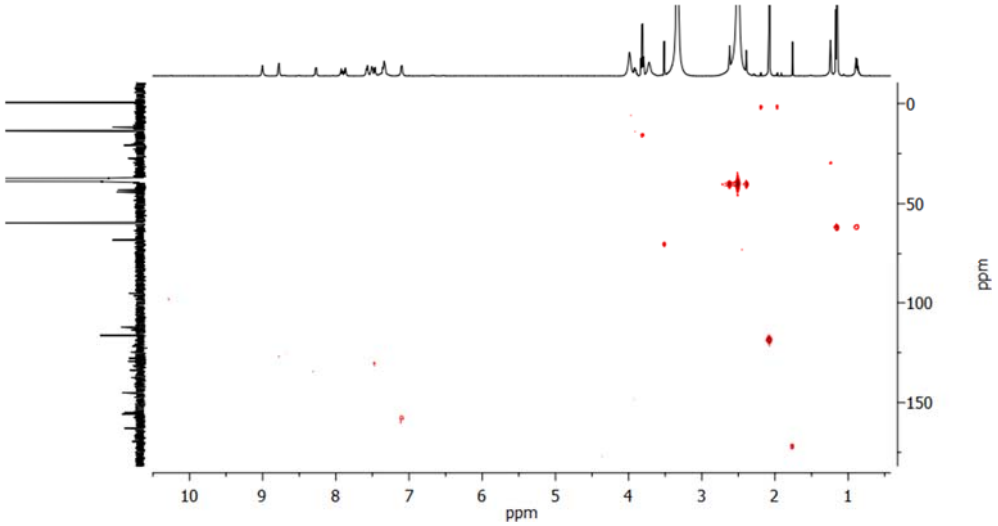

Figure 4.142: $^{1}H–^{13}C$ HMBC spectrum (600 MHz, 298K, DMSO-d_6) of cage $[Pd_2(\mathbf{RE\text{-}P})_4](EtSO_4)_4(BF_4)_4$.

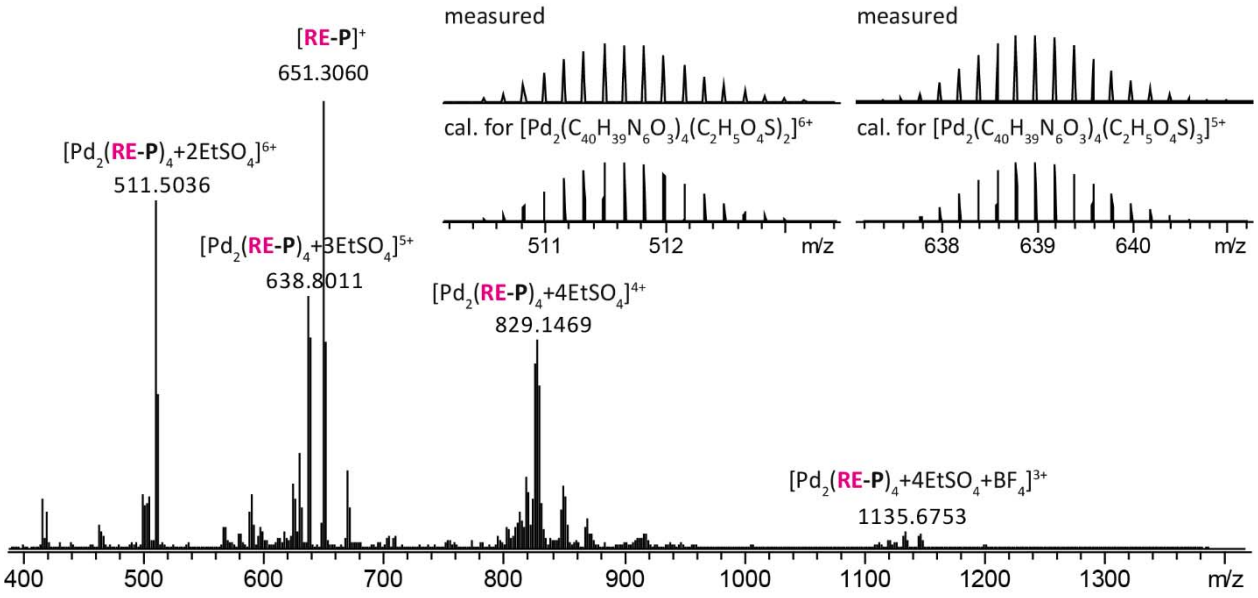

Figure 4.143: ESI-MS spectrum of $[Pd_2(\mathbf{RE\text{-}P})_4]+nEtSO_4+mBF_4]^{(8-n)+}$ with n=2-4 and m=0,1. The observed and calculated isotopic pattern of $[Pd_2(\mathbf{RE\text{-}P})_4]+2EtSO_4]^{6+}$ and $[Pd_2(\mathbf{RE\text{-}P})_4]+3EtSO_4]^{5+}$ are shown in the inset.

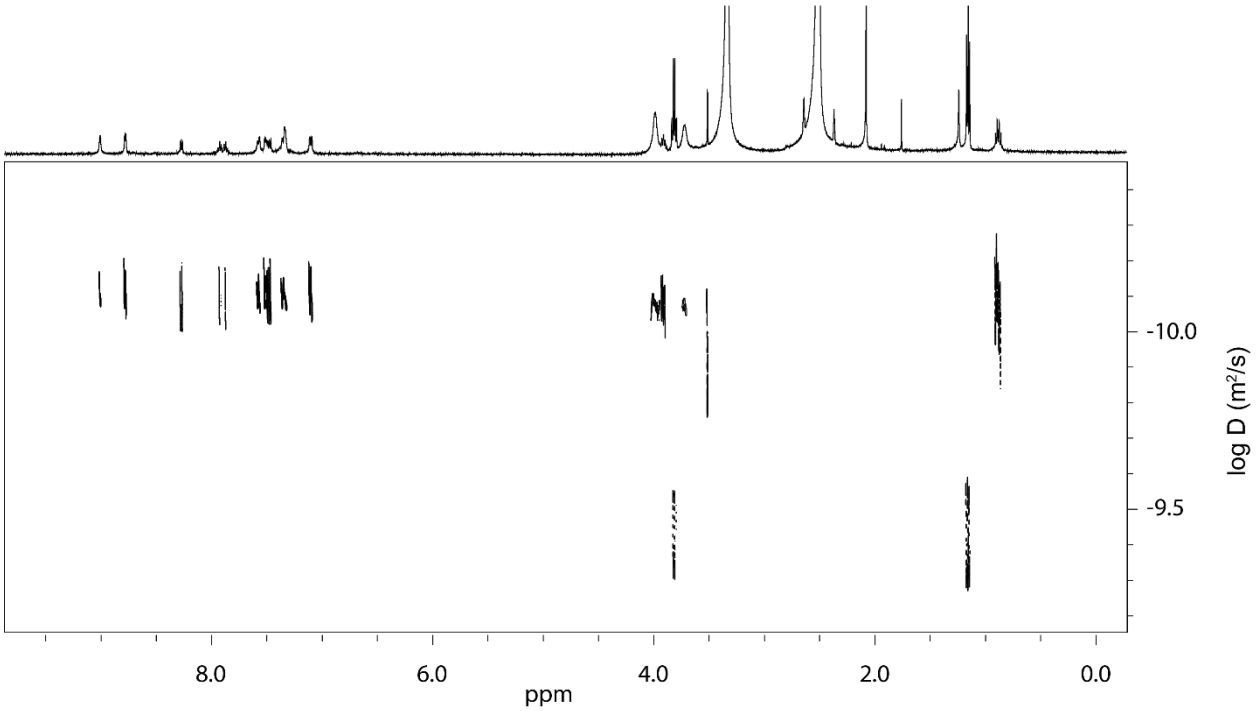

Figure 4.144: ^{1}H DOSY spectrum (500 MHz, 298K, DMSO-d_6) of $[Pd_2(\mathbf{RE\text{-}P})_4](EtSO_4)_4(BF_4)_4$ (0.7 mM). Diffusion coefficient: 8.232×10^{-11} m^2s^{-1}, log D=-10.085. Hydrodynamic radius=13.54 Å.

$[Pd_2(MK\text{-}Q)_4](BF_4)_4$

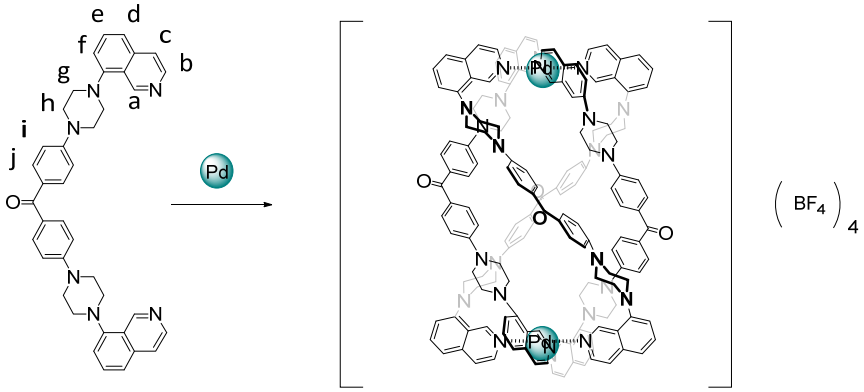

MK-Q $[Pd_2(\mathbf{MK\text{-}Q})_4](BF_4)_4$

Figure 4.145: Self-Assembly of cage $[Pd_2(\mathbf{MK\text{-}Q})_4](BF_4)_4$.

A mixture of ligand **MK-Q** (450 µL of a 3.11 mM solution in DMSO-d_6) and $[Pd(CH_3CN)_4](BF_4)_2$ (50 µL of a 15 mM solution in DMSO-d_6) was heated at 70 °C for 15 min to afford a 0.7 mM solution of $[Pd_2(\mathbf{MK\text{-}Q})_4](BF_4)_4$.

^{1}H NMR (500 MHz, 298 K, Dimethyl sulfoxide-d_6) δ 9.27 (s, 1H, Ha), 8.52 (d, *J* = 6.5 Hz, 1H, Hb), 8.12 – 8.05 (m, 2H, Hc, He), 7.85 (d, *J* = 8.3 Hz, 1H, Hd), 7.58 (d, *J* = 8.4 Hz, 2H, Hj), 7.43 (d, *J* = 7.7 Hz, 1H, Hf), 6.62 (d, *J* = 8.4 Hz, 2H, Hi). He and Hf broad.

^{13}C NMR (176 MHz, 298 K, Dimethyl sulfoxide-d_6) δ 171.40 (C=O), 153.56 (Ca), 151.12 (C^q, **C**-Ci), 149.61 (C^q, Cd-**C**-Cc), 143.20 (Cb), 137.30 (C^q, **C**-Ca), 135.26 (Ce), 130.87 (Cj), 129.08 (C^q, **C**-Ci), 124.72 (Cc), 123.25 (C^q, C-Cf), 121.94 (Cd), 119.17 (Cf), 118.05 (*CH_3CN*), 114.74 (Ci), 45.77 (Ch, Cg).

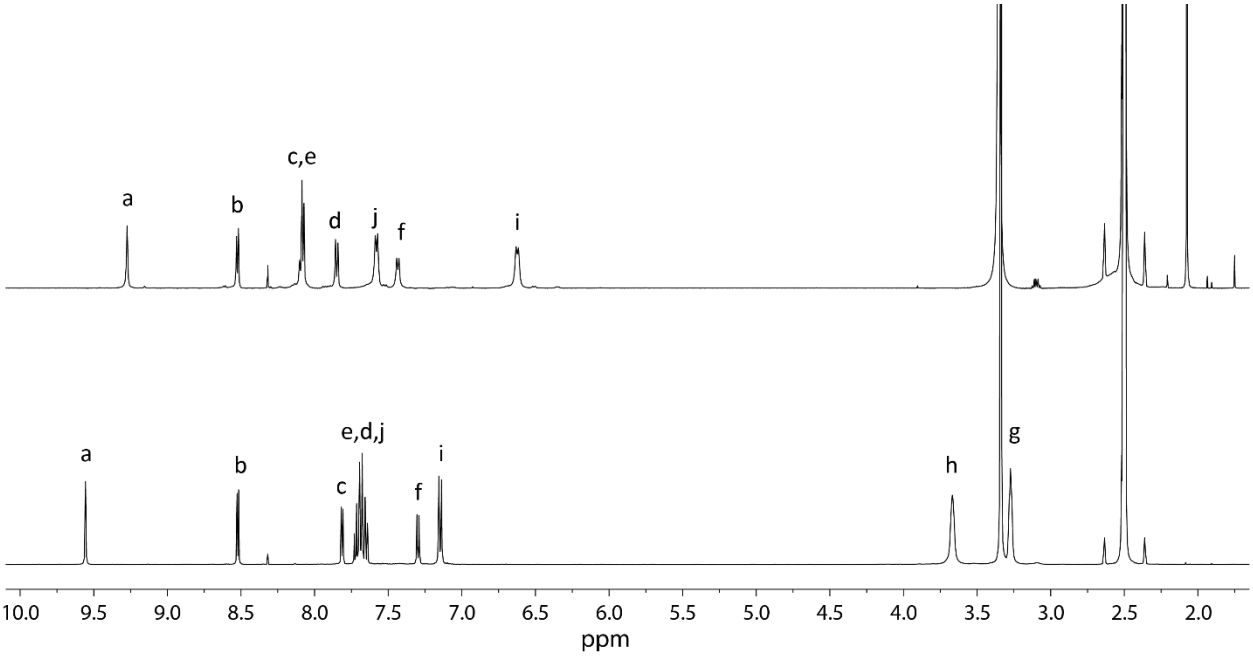

Figure 4.146: ^{1}H NMR stacked spectra (600 MHz, 298K, DMSO-d_6) of ligand **MK-Q** (bottom) and the correspondent cage $[Pd_2(\mathbf{MK\text{-}Q})_4](BF_4)_4$ (top) upon addition of 0.5 Equiv. of Pd(II) salt.

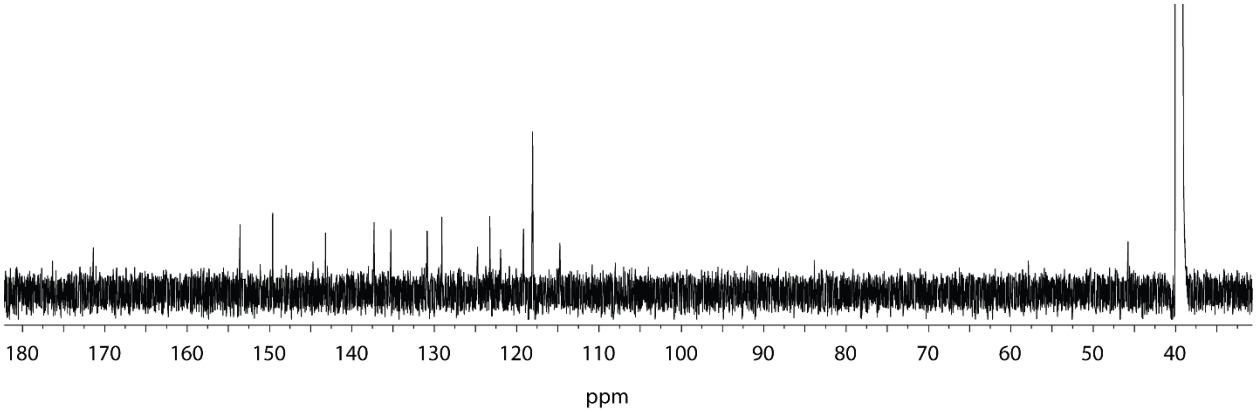

Figure 4.147: ^{13}C NMR spectrum (176 MHz, 298K, DMSO-d_6) of the cage $[Pd_2(\mathbf{MK\text{-}Q})_4](BF_4)_4$.

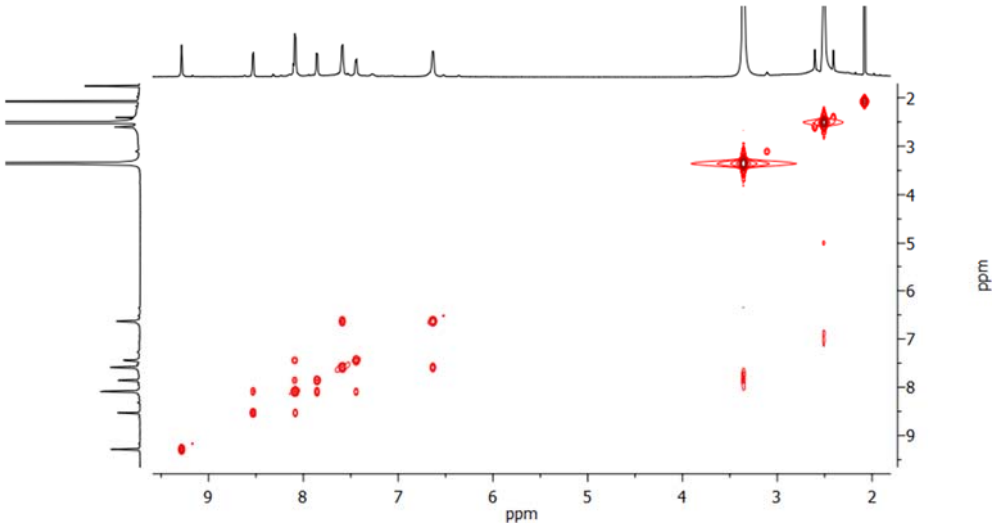

Figure 4.148: ^{1}H–^{1}H COSY spectrum (600 MHz, 298K, DMSO-d_6) of cage $[Pd_2(\mathbf{MK\text{-}Q})_4](BF_4)_4$.

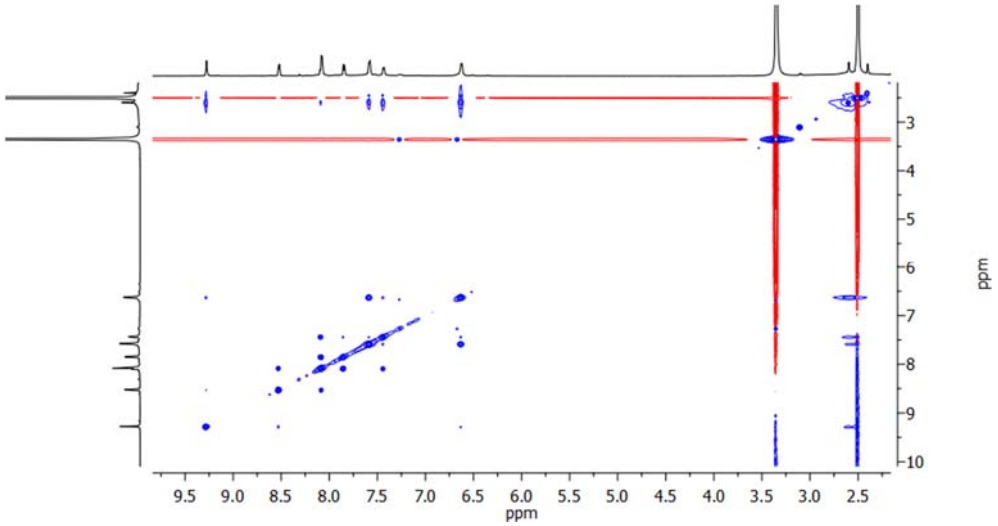

Figure 4.149: ^{1}H–^{1}H NOESY spectrum (600 MHz, 298K, DMSO-d_6) of cage $[Pd_2(\mathbf{MK\text{-}Q})_4](BF_4)_4$.

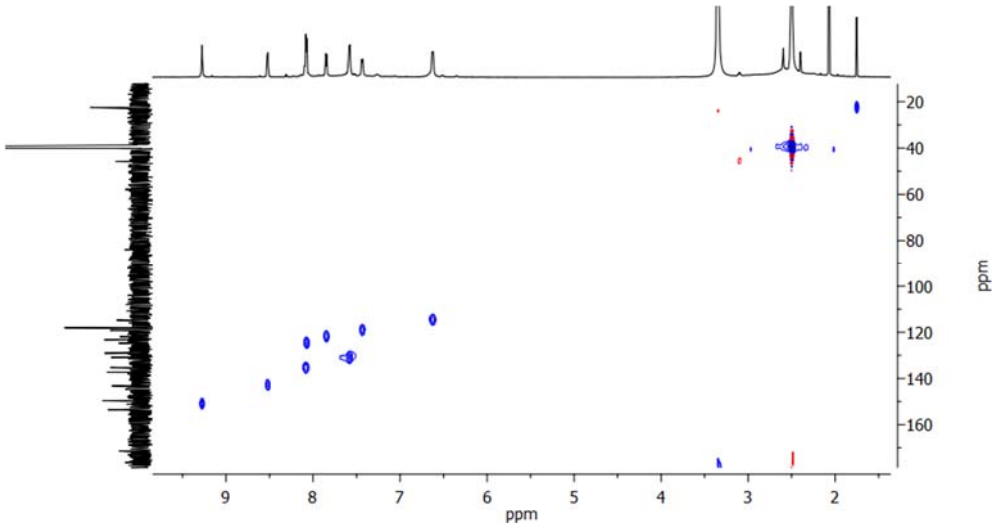

Figure 4.150: ^{1}H–^{13}C HSQC spectrum (600 MHz, 298K, DMSO-d_6) of cage $[Pd_2(\mathbf{MK\text{-}Q})_4](BF_4)_4$.

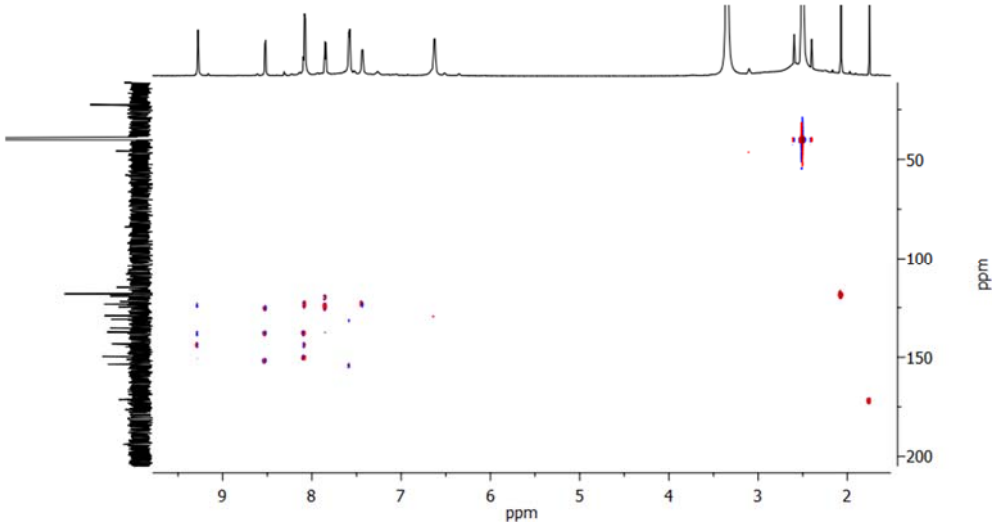

Figure 4.151: ^{1}H –^{13}C HMBC spectrum (600 MHz, 298K, DMSO-d_6) of cage $[Pd_2(\mathbf{MK\text{-}Q})_4](BF_4)_4$.

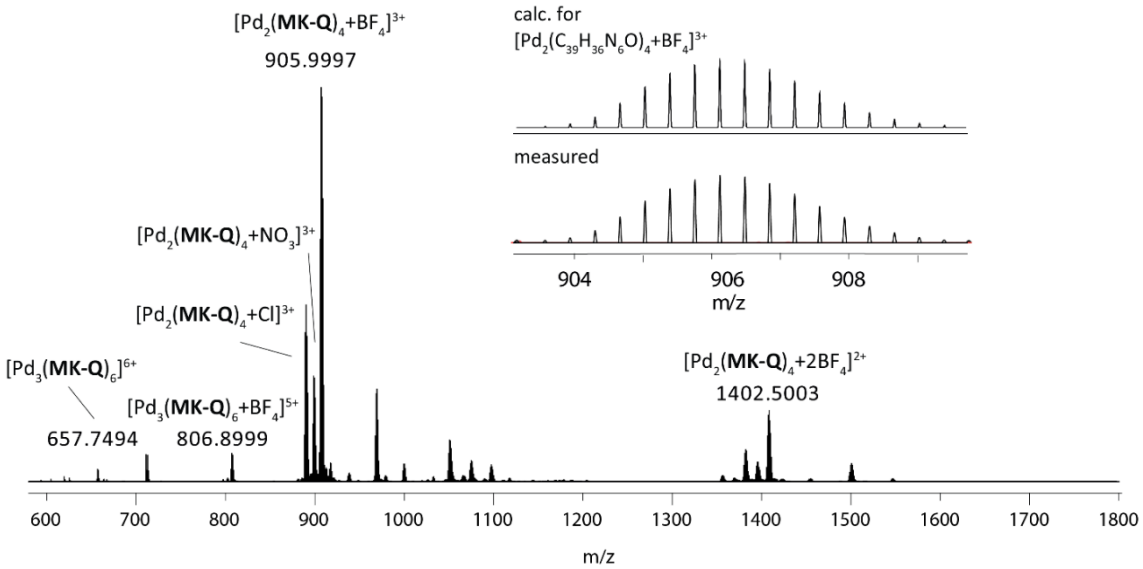

Figure 4.152: ESI-MS spectrum $[Pd_2(\mathbf{MK\text{-}Q})_4]+nBF_4]^{(4-n)+}$ with n=0-2. The observed and calculated isotopic pattern of $[Pd_2(\mathbf{MK\text{-}Q})_4+BF_4]^{3+}$ is shown in the inset.

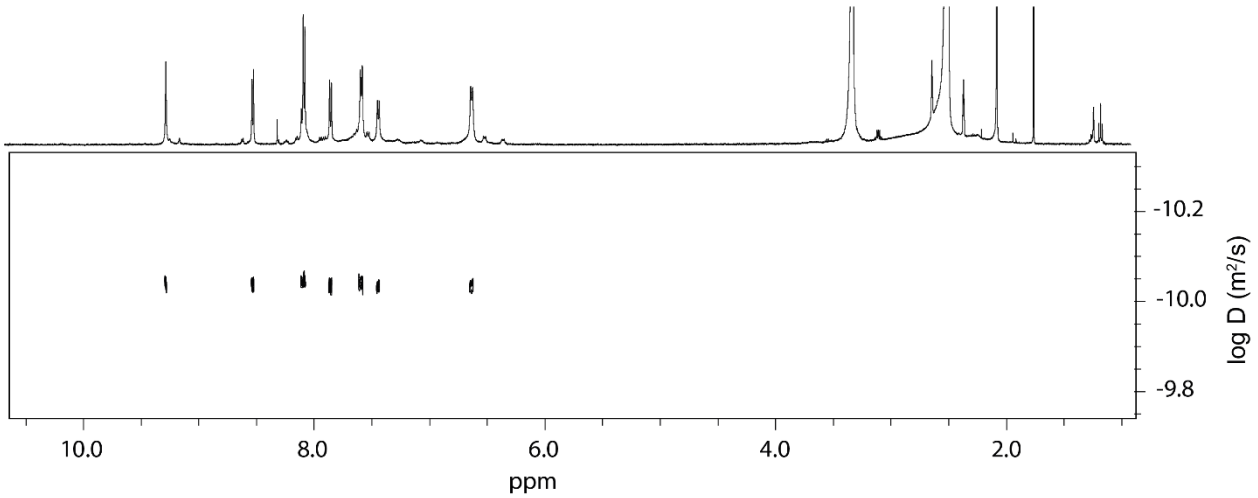

Figure 4.153: ^{1}H DOSY spectrum (500 MHz, 298K, DMSO-d_6) of $[Pd_2(\mathbf{MK\text{-}Q})_4](BF_4)_4$ (0.7 mM). Diffusion coefficient: 9.399×10^{-11} m^2s^{-1}, log D=-10.003. Hydrodynamic radius=11.68 Å.

$[Pd_2(RB\text{-}Q)_4](BF_4)_4$

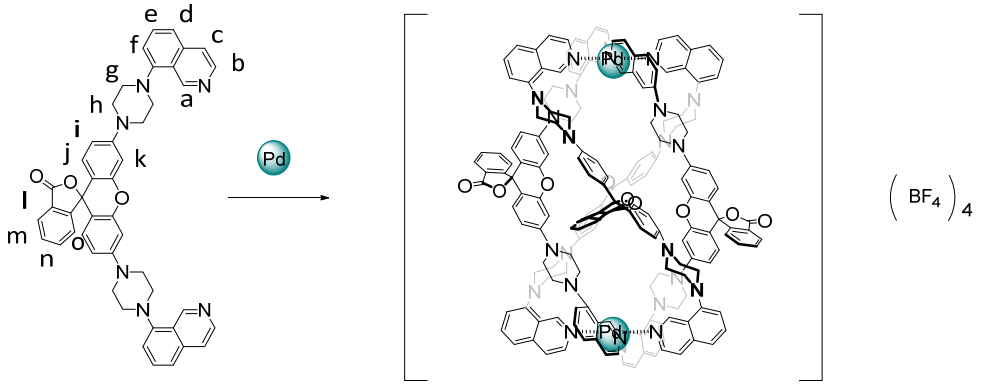

RB-Q $[Pd_2(\mathbf{RB\text{-}Q})_4](BF_4)_4$

Figure 4.154: Self-Assembly of cage $[Pd_2(\mathbf{RB\text{-}Q})_4](BF_4)_4$.

A mixture of ligand **RB-Q** (450 µL of a 3.11 mM solution in CD_3CN) and $[Pd(CH_3CN)_4](BF_4)_2$ (50 µL of a 15 mM solution in CD_3CN) was heated at 70 °C for 15 min to afford a 0.7 mM solution of $[Pd_2(\mathbf{RB\text{-}Q})_4](BF_4)_4$.

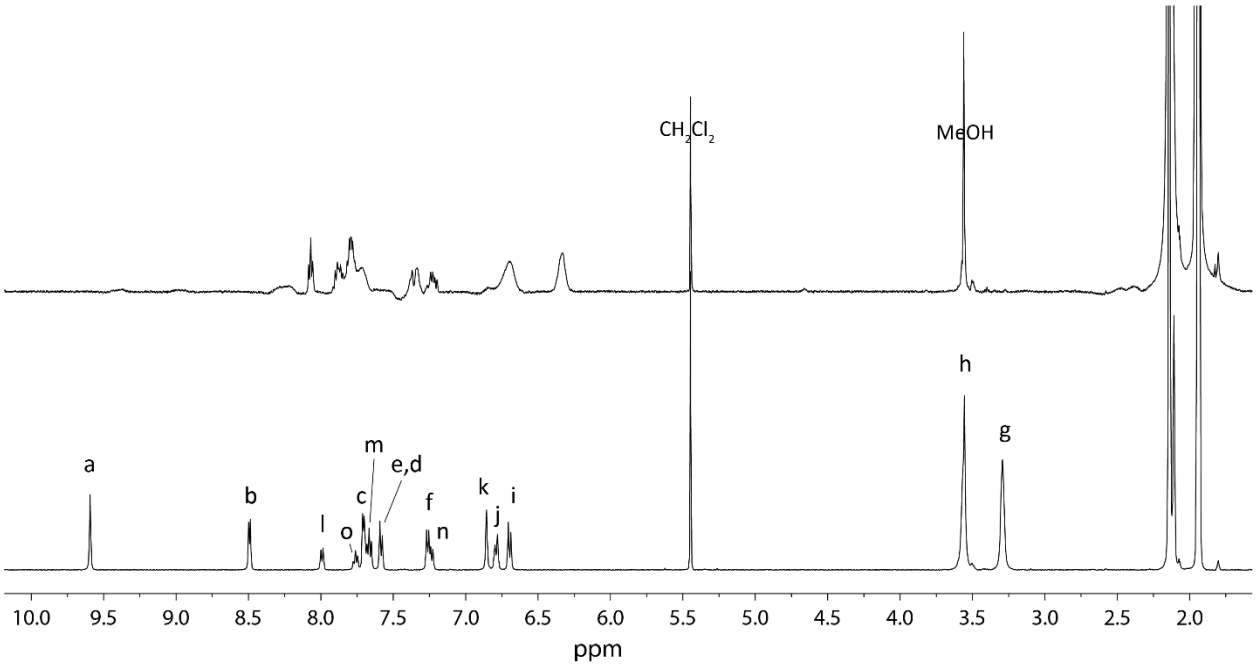

Figure 4.155: ^{1}H NMR stacked spectra (600 MHz, 298K, CD_3CN) of ligand **RB-Q** (bottom) and the correspondent cage $[Pd_2(\mathbf{RB\text{-}Q})_4](BF_4)_4$ (top) upon addition of 0.5 Equiv. of Pd(II) salt.

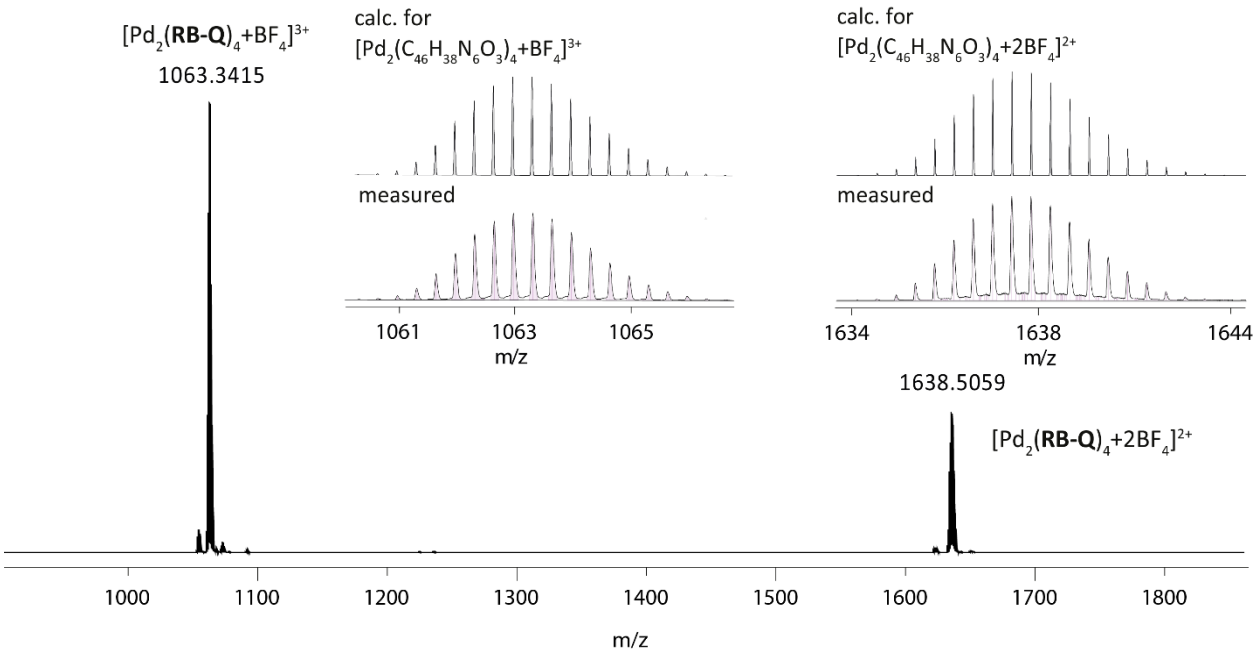

Figure 4.156: ESI-MS spectrum of $[Pd_2(\mathbf{RB\text{-}Q})_4+nBF_4]^{(4-n)+}$ with n=0-2. The observed and calculated isotopic patterns of $[Pd_2(\mathbf{RB\text{-}Q})_4+BF_4]^{3+}$ and $[Pd_2(\mathbf{RB\text{-}Q})_4+2BF_4]^{2+}$ are shown in the inset.

$[Pd_2(MB\text{-}Q)_4](NO_3)_8$

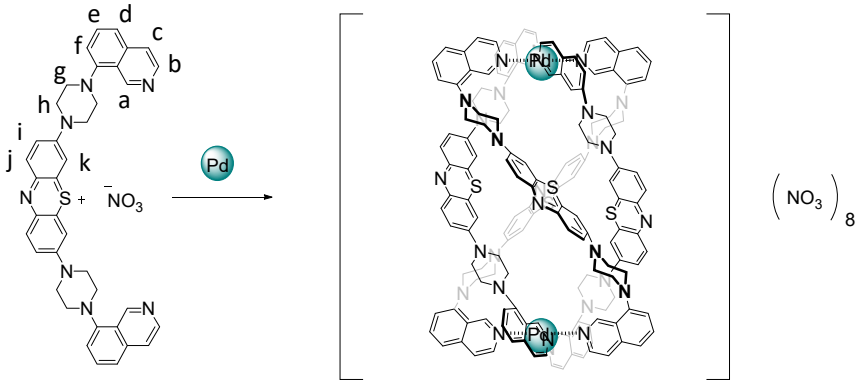

MB-Q $[Pd_2(\mathbf{MB\text{-}Q})_4](NO_3)_8$

Figure 4.157: Self-Assembly of cage $[Pd_2(\mathbf{MB\text{-}Q})_4](NO_3)_8$.

A mixture of ligand **MB-Q** (450 µL of a 3.11 mM solution in DMSO-d_6) and $Pd(NO_3)_2$ (50 µL of a 15 mM solution in DMSO-d_6) was heated at 70 °C for 15 min to afford a 0.7 mM solution of $[Pd_2(\mathbf{MB\text{-}Q})_4](NO_3)_8$.

^{1}H NMR (500 MHz, 298 K, Dimethyl sulfoxide-d_6) δ 10.56 (s, 1H, Ha), 9.84 (d, J = 6.8 Hz, 1H, Hb), 8.65 (d, J = 8.0 Hz, 1H, He), 8.23 (d, J = 6.6 Hz, 1H, Hc), 7.90 (t, J = 7.8 Hz, 1H, Hi), 7.74 (d, J = 8.3 Hz, 2H, Hd, Hk), 7.57 (d, J = 6.6 Hz, 2H, Hf, Hj), 4.82 (s, 1H), 4.43 (s, 1H), 3.76 (s, 1H), 3.12(s, 1H), 2.73(s, 1H) (one signal overlapping with the solvent).

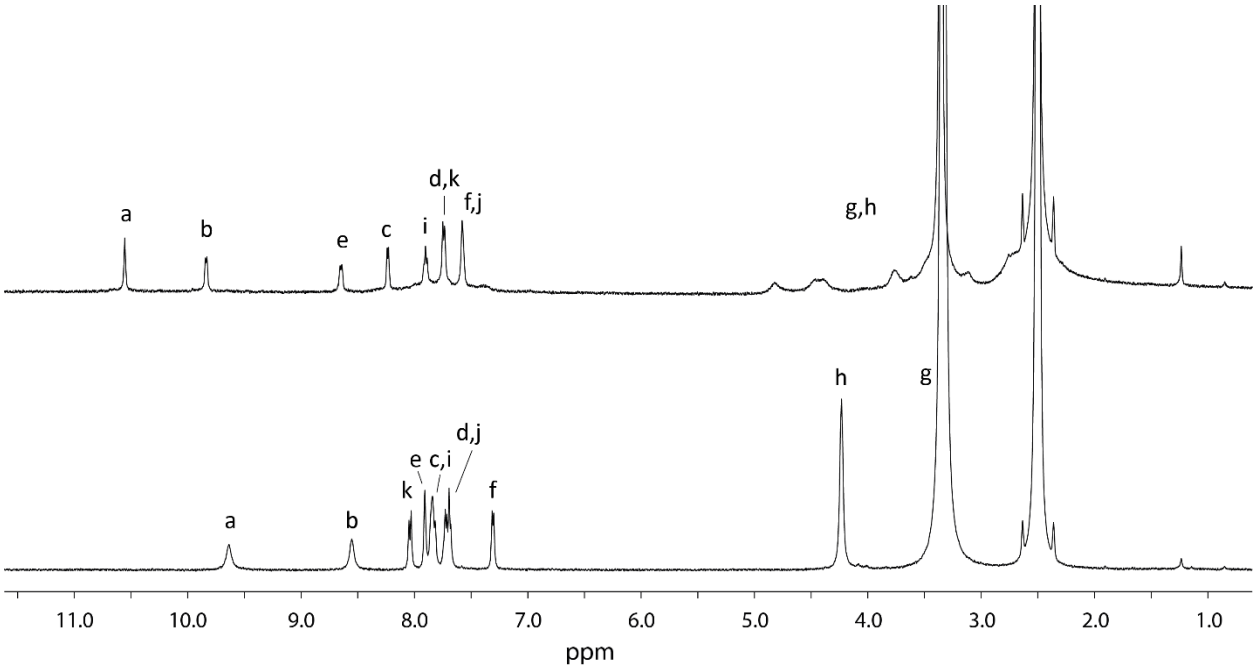

Figure 4.158: ^{1}H NMR stacked spectra (600 MHz, 298K, DMSO-d_6) of ligand **MB-Q** (bottom) and the correspondent cage $[Pd_2(\mathbf{MB\text{-}Q})_4](NO_3)_8$ (top) upon addition of 0.5 Equiv. of Pd(II) salt.

A mixture of ligand **MB-Q** suspended in D_2O (450 µL of a 3.11 mM solution) and $Pd(NO_3)_2$ (50 µL of a 15 mM solution in D_2O) was heated at 70 °C for 15 min to afford a 0.7 mM solution of $[Pd_2(\mathbf{MB\text{-}Q})_4](NO_3)_8$.

^{1}H NMR (600 MHz, 298 K, Deuterium Oxide) δ 9.70 (s, 1H, Ha), 8.43 (d, J = 6.9 Hz, 1H, Hb), 8.34 (d, J = 6.6 Hz, 1H, Hc), 8.02 (t, J = 8.0 Hz, 1H, He), 7.98 (d, J = 9.5 Hz, 1H, Hj), 7.86 (d, J = 8.3 Hz, 1H, Hd), 7.66 (d, J = 9.7 Hz, 1H, Hk), 7.56 (d, J = 8.8 Hz, 2H, Hf, Hi), 4.17 (t, J = 5.0 Hz, 4H, Hh), 3.46 (t, J = 5.0 Hz, 4H, Hg).

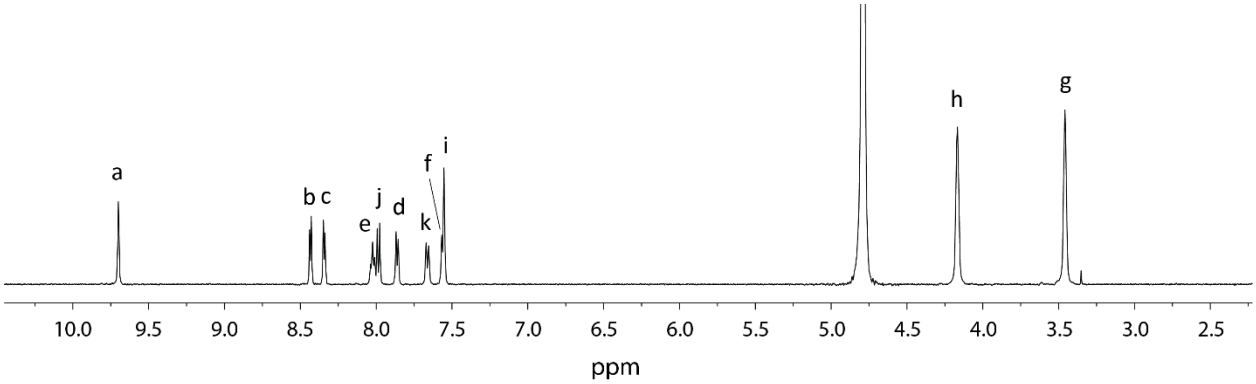

Figure 4.159: ^{1}H NMR spectrum (600 MHz, 298K, D_2O) of the cage $[Pd_2(\mathbf{MB\text{-}Q})_4](NO_3)_8$.

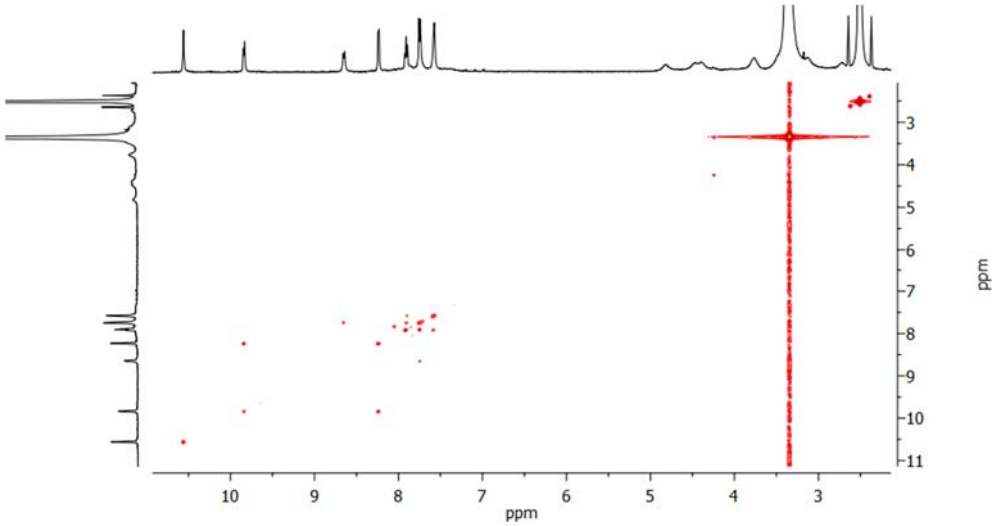

Figure 4.160: ^{1}H–^{1}H COSY spectrum (600 MHz, 298K, DMSO-d_6) of cage $[Pd_2(\mathbf{MB\text{-}Q})_4](NO_3)_8$.

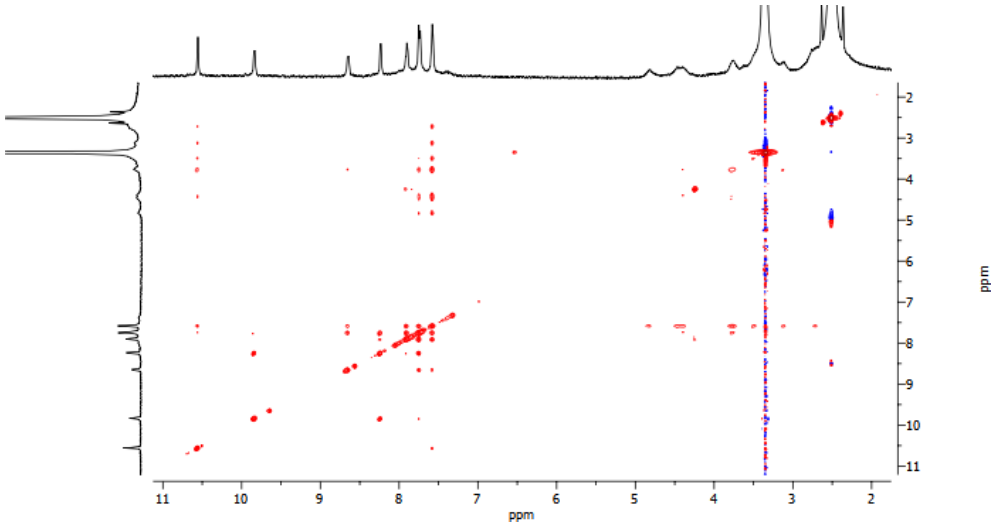

Figure 4.161: ^{1}H–^{1}H NOESY spectrum (600 MHz, 298K, DMSO-d_6) of cage $[Pd_2(\mathbf{MB\text{-}Q})_4](NO_3)_8$.

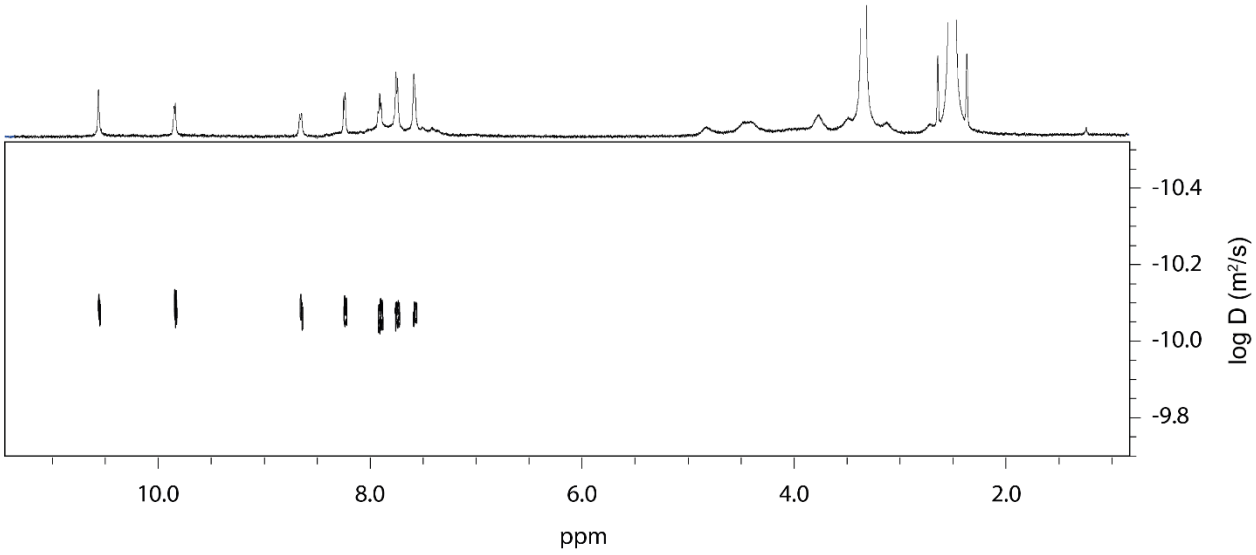

Figure 4.162: ^{1}H DOSY spectrum (500 MHz, 298K, DMSO-d_6) of $[Pd_2(\mathbf{MB\text{-}Q})_4](NO_3)_8$ (0.7 mM). Diffusion coefficient: 10.928×10^{-11} m^2s^{-1}, log D=-9.967. Hydrodynamic radius= 10.05 Å.

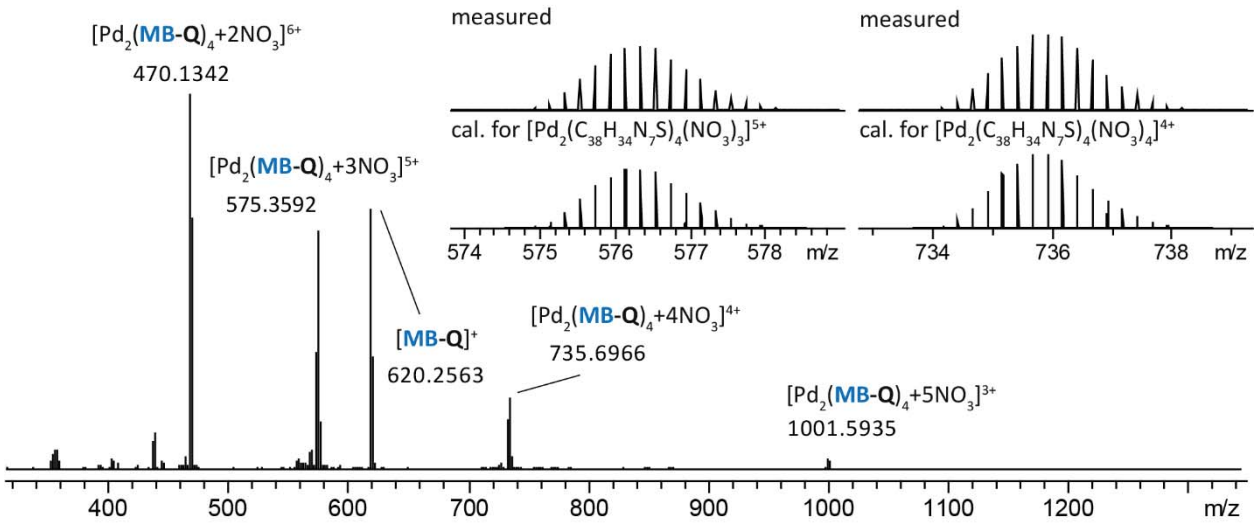

Figure 4.163: ESI-MS spectrum of $[Pd_2(\mathbf{MB\text{-}Q})_4]+nNO_3]^{(8-n)+}$ with n=2-5. The observed and calculated isotopic pattern o of $[Pd_2(\mathbf{MB\text{-}Q})_4+3NO_3]^{5+}$ and $[Pd_2(\mathbf{MB\text{-}Q})_4+4NO_3]^{4+}$ are shown in the inset.

[Pd$_2$(CV-Q)$_4$](NO$_3$)$_8$

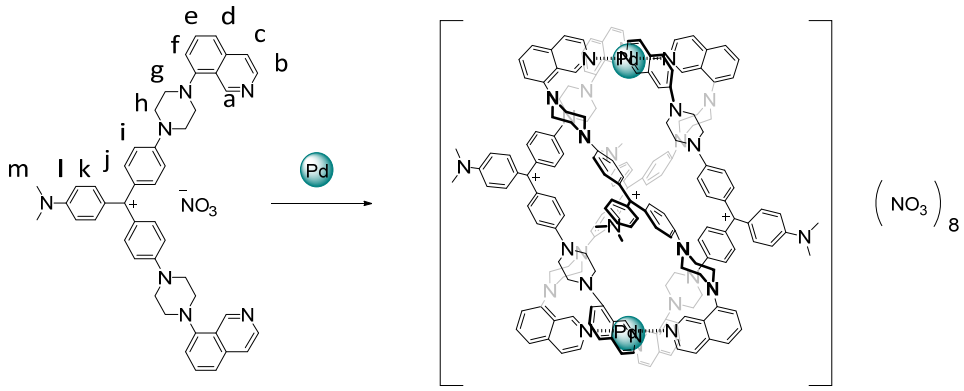

CV-Q [Pd$_2$(**CV-Q**)$_4$](NO$_3$)$_8$

Figure 4.164: Self-Assembly of cage [Pd$_2$(**CV-Q**)$_4$](NO$_3$)$_8$.

A mixture of ligand **CV-Q** (450 µL of a 3.11 mM solution in CD_3CN) and $Pd(NO_3)_2$ (50 µL of a 15 mM solution in CD_3CN) was heated at 70 °C for 15 min to afford a 0.7 mM solution of [Pd$_2$(**CV-Q**)$_4$](NO$_3$)$_8$.

^{1}H NMR (500 MHz, 298 K, Acetonitrile-d_3) δ 9.92 (s, 1H, Ha), 8.49 (d, *J* = 6.6 Hz, 1H, Hb), 7.95 – 7.82 (m, 2H, He, Hc), 7.70 (d, *J* = 8.2 Hz, 1H, Hd), 7.42 (d, *J* = 9.2 Hz, 1H, Hk), 7.31 (d, *J* = 8.8 Hz, 2H, Hj), 7.21 (d, *J* = 7.6 Hz, 1H, Hf), 6.99 (d, *J* = 9.4 Hz, 1H, Hl), 6.72 (d, *J* = 8.8 Hz, 2H, Hi), 3.13 (s, 3H, Hm), 2.80 (s, 2H), 2.61 (s, 2H).

^{13}C NMR (151 MHz, 298 K, Acetonitrile-d_3) δ 178.39 (C+), 157.70 (C^q, **C**-Ck), 156.36 (C^q, **C**-Cj), 153.90 (Ca), 151.21 (C^q, **C**-Cc), 143.57 (Cb), 141.54 (Ck), 139.62 (Cj), 138.45(C^q, **C**-Ca), 135.44 (Ce), 128.83 (C^q, **C**-Ci), 127.29 (C^q, **C**-Cl), 125.00 (Cc), 124.83 (C^q, **C**-Cf), 122.26 (Cd), 118.98 (Cf) 114.18 (Ci), 113.98 (Cj), 46.58 (Cg, Ch), 40.88 (Cm).

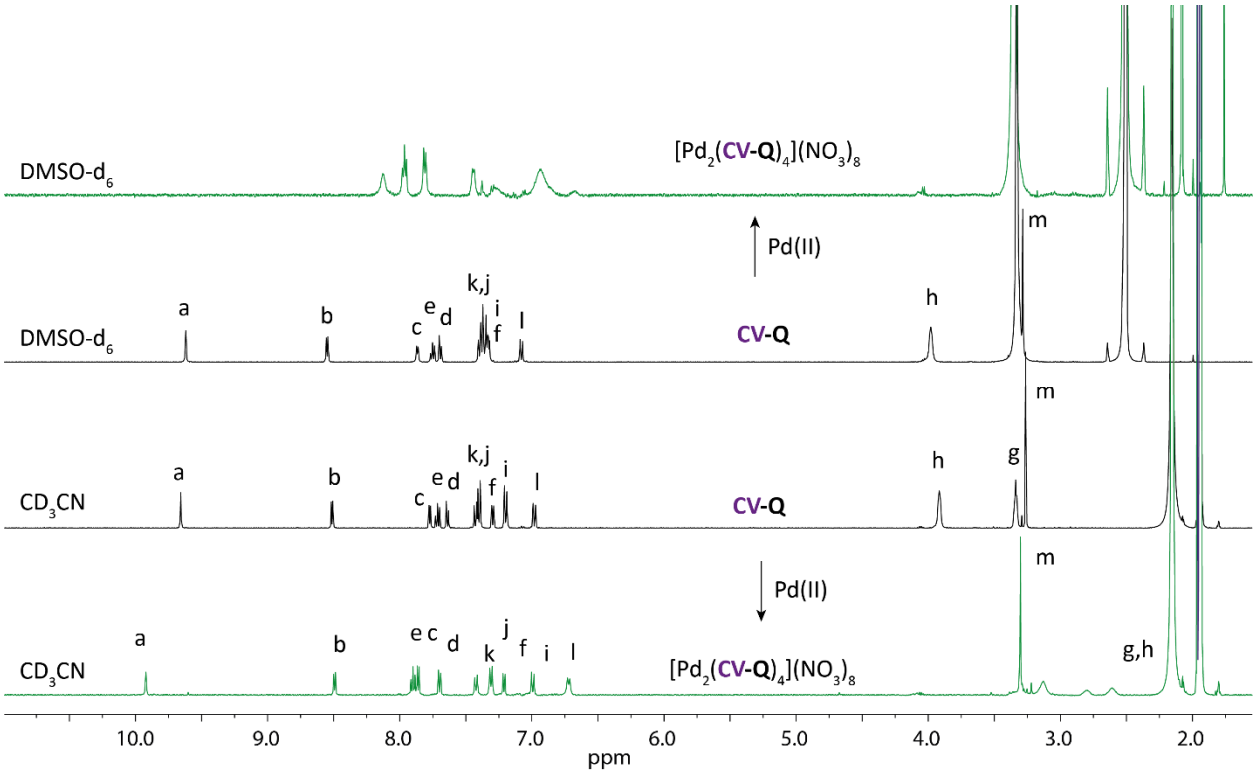

Figure 4.165: ^{1}H NMR stacked spectra (600 MHz, 298K) of ligand **CV-Q** (in the middle in black) in CD_3CN and DMSO-d_6 and the correspondent cage [Pd$_2$(**CV-Q**)$_4$](NO$_3$)$_8$ (in green) upon addition of 0.5 Equiv. of Pd(II) salt in DMSO-d_6 on the top and CD_3CN on the bottom.

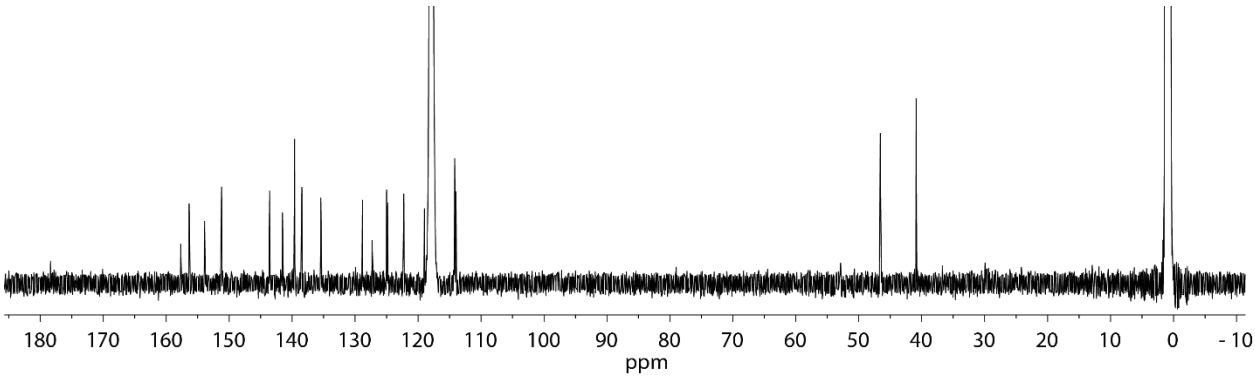

Figure 4.166: ^{13}C NMR spectrum (151 MHz, 298K, CD_3CN) of the cage $[Pd_2(\mathbf{CV\text{-}Q})_4](NO_3)_8$.

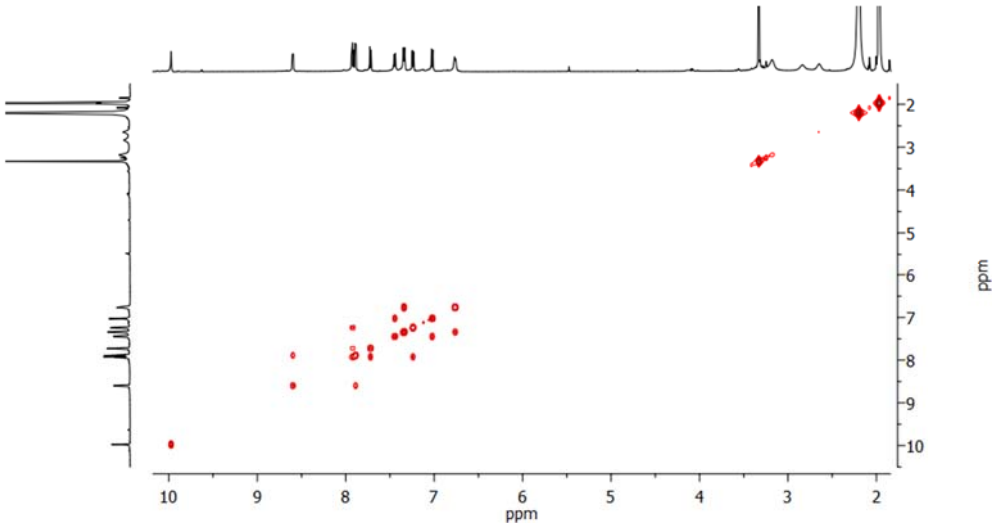

Figure 4.167: $^{1}H–^{1}H$ COSY spectrum (600 MHz, 298K, CD_3CN) of cage $[Pd_2(\mathbf{CV\text{-}Q})_4](NO_3)_8$.

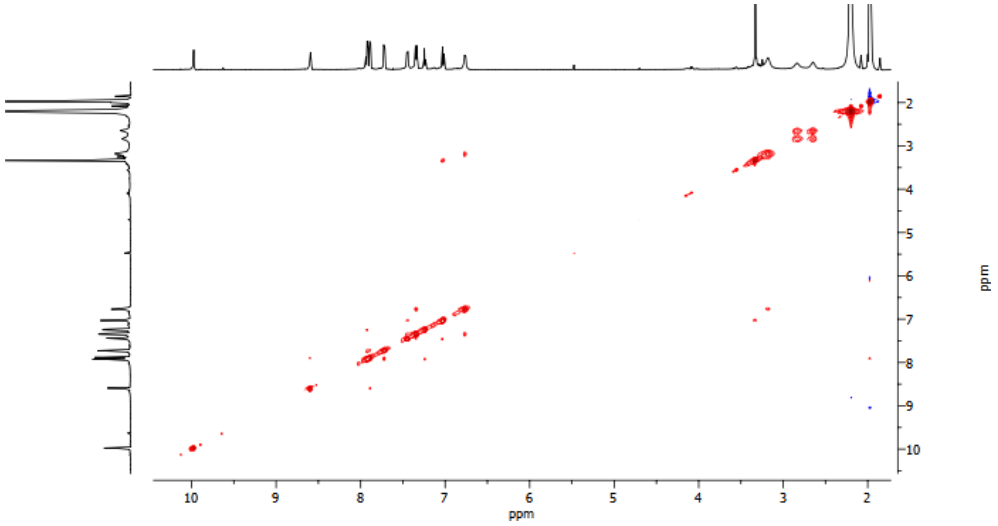

Figure 4.168: $^{1}H–^{1}H$ NOESY spectrum (600 MHz, 298K, CD_3CN) of cage $[Pd_2(\mathbf{CV\text{-}Q})_4](NO_3)_8$.

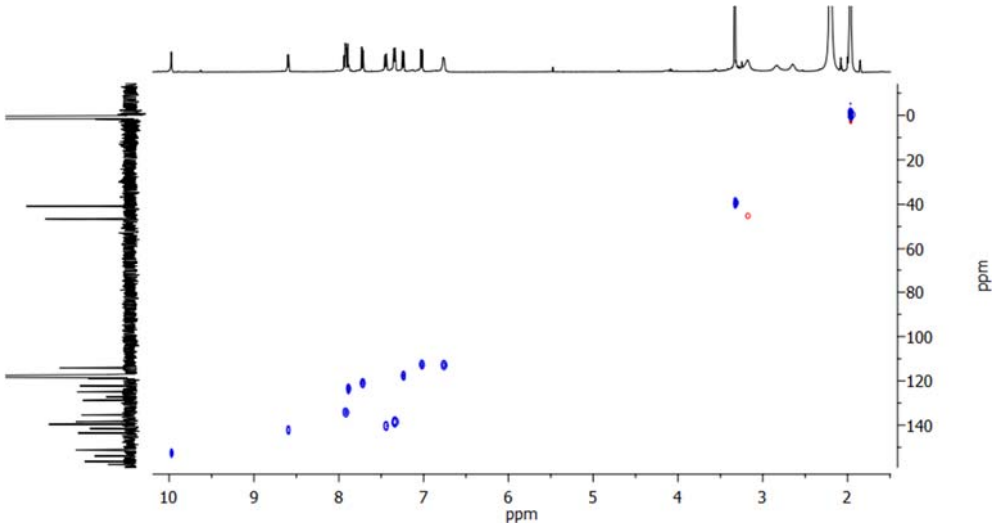

Figure 4.169: $^{1}H–^{13}C$ HSQC spectrum (600 MHz, 298K, CD_3CN) of cage $[Pd_2(\mathbf{CV\text{-}Q})_4](NO_3)_8$.

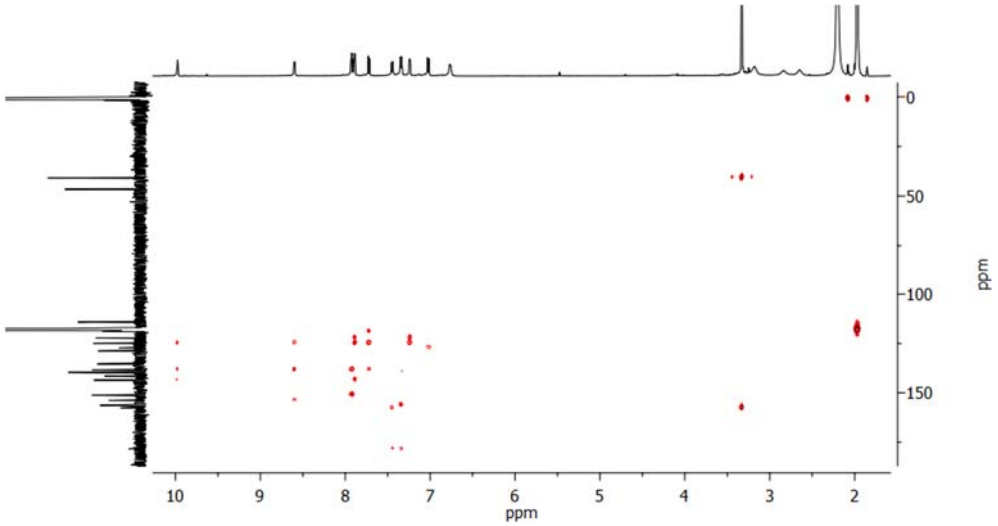

Figure 4.170: $^{1}H–^{13}C$ HMBC spectrum (600 MHz, 298K, CD_3CN) of cage $[Pd_2(\mathbf{CV\text{-}Q})_4](NO_3)_8$.

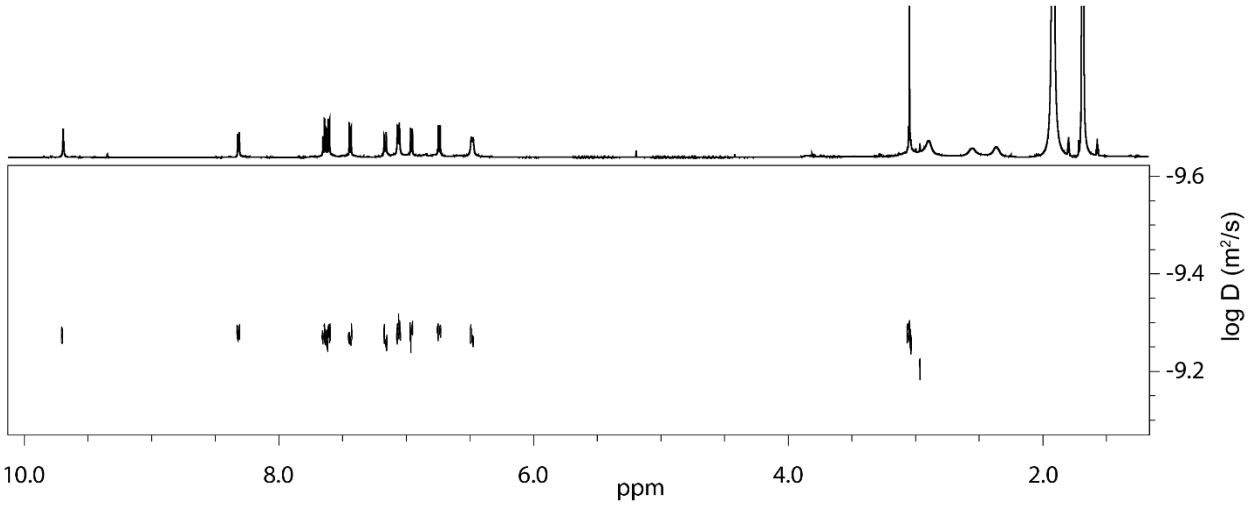

Figure 4.171: ^{1}H DOSY spectrum (500 MHz, 298K, CD_3CN) of $[Pd_2(\mathbf{CV\text{-}Q})_4](NO_3)_8$ (0.7 mM). Diffusion coefficient: 5.293×10^{-10} m^2s^{-1}, log D=-9.276. Hydrodynamic radius= 12.36 Å.

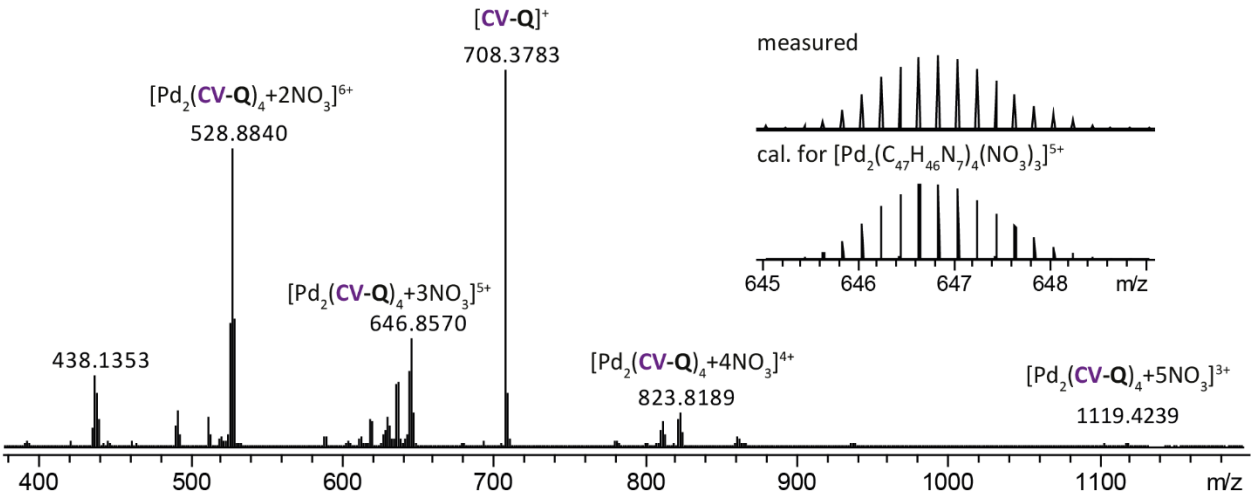

Figure 4.172: ESI-MS spectrum of $[Pd_2(\mathbf{CV\text{-}Q})_4{+}nNO_3]^{(8-n)+}$ with n=3-6. The observed and calculated isotopic pattern of $[Pd_2(\mathbf{CV\text{-}Q})_4{+}3NO_3]^{5+}$ are shown in the inset.

4.8.4 Crystallographic information

The X-ray diffraction analysis was performed with the help of Dr. Julian Holstein. Four different supramolecular assemblies $[Pd_2(\mathbf{MK\text{-}P})_4]$, $[Pd_2(\mathbf{RB\text{-}P})_4]$, $[Pd_2(\mathbf{CV\text{-}P})_4]$ and $[Pd_3(\mathbf{MK\text{-}Q})_6]$ were studied using single-crystal X-ray crystallography. Cage $[Pd_2(\mathbf{MK\text{-}P})_4]$ could be studied on in-house diffractometer using microfocussed CuK_α radiation. In contrast, crystals of supramolecular assemblies were extremely sensitive to loss of organic solvent. Due to very thin plate or needle-shaped crystals, the analysis was further hampered by the limited scattering power of the samples not allowing to reach the desired (sub-)atomic resolution using our a modern microfocussed X-ray in-house CuK_α source. Gaining detailed structural insight thus required cryogenic crystal handling and highly brilliant synchrotron radiation. Hence, diffraction data of most of supramolecular assemblies was collected during three beamtime shifts at macromolecular synchrotron beamline P11, PETRA III, DESY.[52] Counterion and solvent flexibility required carefully adapted macromolecular refinement protocols employing geometrical restraint dictionaries, similarity restraints and restraints for anisotropic displacement parameters (ADPs).

Structure ID	$[Pd_2(\mathbf{MK\text{-}P})_4]$	$[Pd_2(\mathbf{RB\text{-}P})_4]$	$[Pd_2(\mathbf{CV\text{-}P})_4]$	$[Pd_3(\mathbf{MK\text{-}Q})_6]$
CCDC number	**2035822**	**2035823**	**2035824**	**2035825**
Empirical formula	$C_{128}H_{140}B_4F_{16}N_{24}O_6Pd_2S_2$	$C_{152}H_{136}N_{24}O_{12}Pd_2$	$C_{156}H_{168}N_{31}O_9Pd_2$	$C_{240}H_{234}B_2F_8N_{36}O_9Pd_3S_3$
Formula weight	2734.79	2703.64	2834.00	4355.62
Temperature [K]	100(2)	80(2)	80(2)	80(2)
Crystal system	triclinic	tetragonal	monoclinic	triclinic
Space group (number)	$P\bar{1}$ (2)	$I4/\mathrm{m}$ (87)	$P2_1/\mathrm{m}$ (11)	$P\bar{1}$ (2)
a [Å]	15.1314(5)	23.200(3)	25.502(5)	20.140(4)
b [Å]	16.6317(5)	23.200(3)	21.570(4)	24.726(5)
c [Å]	17.0412(4)	27.606(6)	26.148(5)	32.071(6)
α [Å]	94.829(2)	90	90	104.73(3)
β [Å]	100.421(2)	90	113.39(3)	101.04(3)
γ [Å]	92.016(2)	90	90	105.04(3)
Volume [Å^3]	4197.3(2)	14859(5)	13201(5)	14339(6)
Z	1	2	2	2
ρ_{calc} [g/cm^3]	1.082	0.604	0.713	1.009
μ [mm^{-1}]	2.527	0.140	0.463	0.241

F(000)	1412	2808	2970	4532
Crystal size [mm^3]	0.120×0.100×0.020	0.170×0.050×0.040	0.050×0.020×0.010	0.090×0.020×0.010
Crystal colour	yellow	colorless	violet	yellow
Crystal shape	plate	needle	plate	needle
Radiation	CuK_α (λ=1.54178 Å)	synchrotron (λ=0.6888 Å)	synchrotron (λ=1.0332 Å)	synchrotron (λ=0.6888 Å)
2Θ range [°]	5.30 to 148.99 (0.80 Å)	2.22 to 38.29 (1.05 Å)	2.47 to 50.78 (1.20 Å)	1.32 to 42.98 (0.94 Å)
Index ranges	-18 ≤ h ≤ 18 -20 ≤ k ≤ 20 -21 ≤ l ≤ 20	-22 ≤ h ≤ 22 -22 ≤ k ≤ 22 -25 ≤ l ≤ 25	-21 ≤ h ≤ 21 -17 ≤ k ≤ 17 -21 ≤ l ≤ 21	-21 ≤ h ≤ 21 -26 ≤ k ≤ 26 -34 ≤ l ≤ 34
Reflections collected	121896	43623	47588	118447
Independent reflections	17076 R_{int} = 0.1085 R_{sigma} = 0.0589	3402 R_{int} = 0.0758 R_{sigma} = 0.0371	7661 R_{int} = 0.0615 R_{sigma} = 0.0404	34065 R_{int} = 0.0574 R_{sigma} = 0.0528
Completeness to θ = 67.679°	99.8 %	97.9 %	93.1 %	94.2 %
Data / Restraints / Parameters	17076/2346/1021	3402/965/287	7661/1726/889	34065/5456/2746
Goodness-of-fit on F^2	1.036	2.020	1.769	1.300
Final *R* indexes [I≥2σ(I)]	R_1 = 0.0970 wR_2 = 0.2692	R_1 = 0.1618 wR_2 = 0.4435	R_1 = 0.1372 wR_2 = 0.4081	R_1 = 0.1026 wR_2 = 0.3201
Final *R* indexes [all data]	R_1 = 0.1261 wR_2 = 0.2972	R_1 = 0.1806 wR_2 = 0.4654	R_1 = 0.1626 wR_2 = 0.4335	R_1 = 0.1326 wR_2 = 0.3445
Largest peak/hole [eÅ^3]	1.47/-1.38	1.83/-0.65	0.78/-0.58	1.43/-0.89

Crystal structure of [Pd_2(MK-P)$_4$]

Yellow plate crystals of [Pd_2(**MK-P**)$_4$] were grown by slow vapor diffusion of toluene in the DMSO solution of [Pd_2(**MK-P**)$_4$] at r.t.. A single crystal in mother liquor was mounted onto a 0.1 mm nylon loop using NVH oil. Single crystal X-ray diffraction data was collected on a Bruker D8 venture equipped with an Incoatec microfocus source (Iμs 2.0) using Cukα radiation on a four axis κ-goniometer, equipped with an Oxford Cryostream 800 and a Photon 100 detector. Data integration was done with SAINT. Data scaling and absorption correction were performed with SADABS. The space group was determined using XPREP.[61] The structure was solved by intrinsic phasing/direct methods using SHELXT[53] and refined with SHELXL[54] for full-matrix least-squares routines on F^2 and ShelXle[55] as a graphical user interface.

Three of the four piperazine rings in the two ligands of the asymmetric unit as well as the co-crystallized DMSO solvent molecule were disordered and modelled with two discrete positions refining their occupancy factor using a free variable and ensuring sensible geometry by employing stereochemical restraints.

Stereochemical restraints for the **MK-P** ligands were generated by the GRADE program using the GRADE Web Server (http://grade.globalphasing.org) and applied in the refinement. A GRADE dictionary for SHELXL contains target values and standard deviations for 1,2-distances (DFIX) and 1,3-distances (DANG), as well as restraints for planar groups (FLAT). All displacements for non-hydrogen atoms were refined anisotropically. The refinement of ADP's for carbon, nitrogen and oxygen atoms was enabled by a combination of similarity restraints (SIMU) and rigid bond restraints (RIGU).[58] The contribution of the electron density from disordered counterions and solvent molecules, which could not be modeled with discrete atomic positions were handled using the SQUEEZE[59] routine in PLATON.[60] The solvent mask

file (.fab) computed by PLATON were included in the SHELXL refinement via the ABIN instruction leaving the measured intensities untouched.

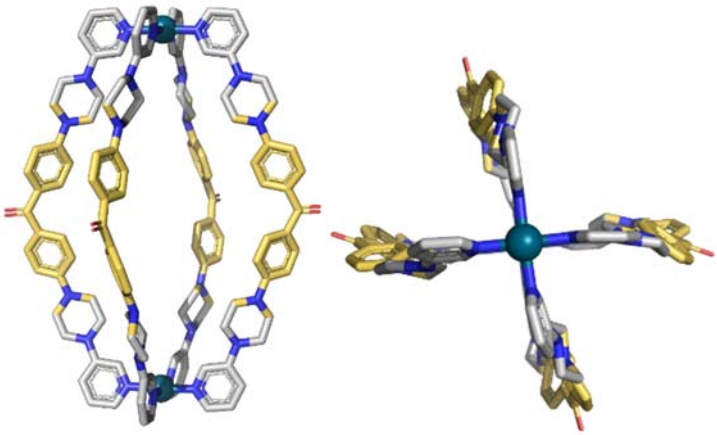

Figure 4.173: Two views of the X-ray crystal structure of [Pd_2(**MK-P**)$_4$]. Counterions and solvent molecules have been omitted for clarity.

Crystal structure of [Pd_2(RB-P)$_4$]

Colorless, needle shaped crystals of [Pd_2(**RB-P**)$_4$] were grown by slow vapor diffusion of ethyl acetate in the DMSO solution of [Pd_2(**RB-P**)$_4$] at r.t.. A single crystal of [Pd_2(**RB-P**)$_4$] in mother liquor was pipetted onto a glass slide containing NVH oil. To avoid collapse of the crystal lattice, the crystal was quickly mounted onto a 0.06 mm nylon loop and immediately flash cooled in liquid nitrogen. Crystals were stored at cryogenic temperature in dry shippers, in which they were safely transported to macromolecular beamline P11 at Petra III[1], DESY, Germany. A wavelength of λ = 0.6888 Å was chosen using a liquid N_2 cooled double crystal monochromator. Single crystal X-ray diffraction data was collected at 80(2) K on a single axis goniometer, equipped with an Oxford Cryostream 800 a Pilatus 6M. 1800 diffraction images were collected in a 360° ϕ sweep at a detector distance of 190 mm, 100% filter transmission, 0.2° step width and 0.1 seconds exposure time per image. Data integration and reduction were undertaken using XDS.[56] The structure was solved by intrinsic phasing/direct methods using SHELXT[53] and refined with SHELXL[54] using 22 cpu cores for full-matrix least-squares routines on F^2 and ShelXle[55] as a graphical user interface and the DSR program plugin was employed for modeling.[57]

High space group symmetry was broken by disorder of the rhodamine backbone part located in the mirror plane. It was modelled with two discrete positions refining their occupancy factor using a free variable. Disorder and extremely poor crystal quality required stereochemical restraints to be employed for ensuring a sensible geometry of the organic part of the structure.

Stereochemical restraints for the **RB-P** ligands were generated by the GRADE program using the GRADE Web Server (http://grade.globalphasing.org) and applied in the refinement. A GRADE dictionary for SHELXL contains target values and standard deviations for 1,2-distances (DFIX) and 1,3-distances (DANG), as well as restraints for planar groups (FLAT). All displacements for non-hydrogen atoms were refined anisotropically. The refinement of ADP's for carbon, nitrogen and oxygen atoms was enabled by a combination of similarity restraints (SIMU) and rigid bond restraints (RIGU).[58] The contribution of the electron density from disordered counterions and solvent molecules, which could not be modeled with discrete atomic positions were handled using the SQUEEZE[59] routine in PLATON.[60] The solvent mask file (.fab) computed by PLATON were included in the SHELXL refinement via the ABIN instruction leaving the measured intensities untouched.

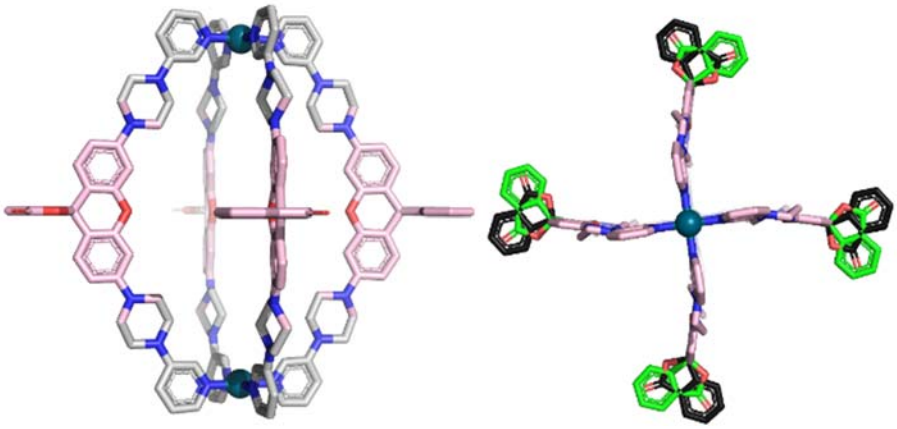

Figure 4.174: Two views of the X-ray crystal structure of [Pd_2(**RB-P**)$_4$]. Counterions and solvent molecules have been omitted for clarity.

Crystal structure of [Pd_2(CV-P)$_4$]

Violet plate crystals of [Pd_2(**CV-P**)$_4$] were grown by slow vapor diffusion of methyl tert-butyl ether in the dimethylformamide solution of [Pd_2(**CV-P**)$_4$] at r.t.. A single crystal of [Pd_2(**CV-P**)$_4$] in mother liquor was pipetted onto a glass slide containing NVH oil. To avoid collapse of the crystal lattice, the crystal was quickly mounted onto a 0.3 mm nylon loop and immediately flash cooled in liquid nitrogen. Crystals were stored at cryogenic temperature in dry shippers, in which they were safely transported to macromolecular beamline P11 at Petra III[1], DESY, Germany. A wavelength of λ = 1.0332Å was chosen using a liquid N_2 cooled double crystal monochromator. Single crystal X-ray diffraction data was collected at 80(2) K on a single axis goniometer, equipped with an Oxford Cryostream 800 a Pilatus 6M. 3600 diffraction images were collected in a 360° ϕ sweep at a detector distance of 200 mm, 13.4% filter transmission, 0.1° step width and 0.1 seconds exposure time per image. Data integration and reduction were undertaken using XDS.[56] The structure was solved by intrinsic phasing/direct methods using SHELXT[53] and refined with SHELXL[54] using 22 cpu cores for full-matrix least-squares routines on F^2 and ShelXle[55] as a graphical user interface and the DSR program plugin was employed for modeling.[57]

All three nitrate counterions were disordered over special position (mirror plane) and occupancy factor were therefore fixed to 50%. Poor crystal quality and low experimental resolution of 1.2 Å required stereochemical restraints to be employed for ensuring a sensible geometry of the organic part of the structure.

Stereochemical restraints for the **CV-P** ligands were generated by the GRADE program using the GRADE Web Server (http://grade.globalphasing.org) and applied in the refinement. A GRADE dictionary for SHELXL contains target values and standard deviations for 1,2-distances (DFIX) and 1,3-distances (DANG), as well as restraints for planar groups (FLAT). All displacements for non-hydrogen atoms were refined anisotropically. The refinement of ADP's for carbon, nitrogen and oxygen atoms was enabled by a combination of similarity restraints (SIMU) and rigid bond restraints (RIGU).[58] The contribution of the electron density from disordered counterions and solvent molecules, which could not be modeled with discrete atomic positions were handled using the SQUEEZE[59] routine in PLATON.[60] The solvent mask file (.fab) computed by PLATON were included in the SHELXL refinement via the ABIN instruction leaving the measured intensities untouched.

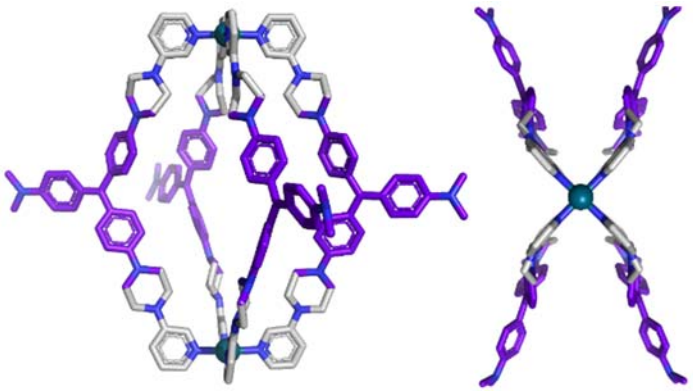

Figure 4.175: Two views of the X-ray crystal structure of $[Pd_2(\mathbf{CV\text{-}P})_4]$. Counterions and solvent molecules have been omitted for clarity.

Crystal structure of $[Pd_3(MK\text{-}Q)_6]$

Yellow, needle shaped crystals of $[Pd_3(\mathbf{MK\text{-}Q})_6]$ were grown by slow vapor diffusion of toluene in the DMSO solution of $[Pd_2(\mathbf{MK\text{-}Q})_4]$ at r.t.. A single crystal of $[Pd_3(\mathbf{MK\text{-}Q})_6]$ in mother liquor was pipetted onto a glass slide containing NVH oil. To avoid collapse of the crystal lattice, the crystal was quickly mounted onto a 0.06 mm nylon loop and immediately flash cooled in liquid nitrogen. Crystals were stored at cryogenic temperature in dry shippers, in which they were safely transported to macromolecular beamline P11 at Petra III[1], DESY, Germany. A wavelength of λ = 0.6888 Å was chosen using a liquid N_2 cooled double crystal monochromator. Single crystal X-ray diffraction data was collected at 80(2) K on a single axis goniometer, equipped with an Oxford Cryostream 800 a Pilatus 6M. 3600 diffraction images 36were collected in a 360° ϕ sweep at a detector distance of 154.1 mm, 75.5% filter transmission, 0.1° step width and 0.1 seconds exposure time per image. Data integration and reduction were undertaken using XDS.[56] The structure was solved by intrinsic phasing/direct methods using SHELXT[53] and refined with SHELXL[54] using 22 cpu cores for full-matrix least-squares routines on F^2 and ShelXle[55] as a graphical user interface and the DSR program plugin was employed for modeling.[57]

Poor crystal quality and high flexibility required stereochemical restraints to be employed for ensuring a sensible geometry of the organic part of the structure.

Stereochemical restraints for the **MK-Q** ligands were generated by the GRADE program using the GRADE Web Server (http://grade.globalphasing.org) and applied in the refinement. A GRADE dictionary for SHELXL contains target values and standard deviations for 1,2-distances (DFIX) and 1,3-distances (DANG), as well as restraints for planar groups (FLAT). All displacements for non-hydrogen atoms were refined anisotropically. The refinement of ADP's for carbon, nitrogen and oxygen atoms was enabled by a combination of similarity restraints (SIMU) and rigid bond restraints (RIGU).[58] The contribution of the electron density from disordered counterions and solvent molecules, which could not be modeled with discrete atomic positions were handled using the SQUEEZE[59] routine in PLATON.[60] The solvent mask file (.fab) computed by PLATON were included in the SHELXL refinement via the ABIN instruction leaving the measured intensities untouched.

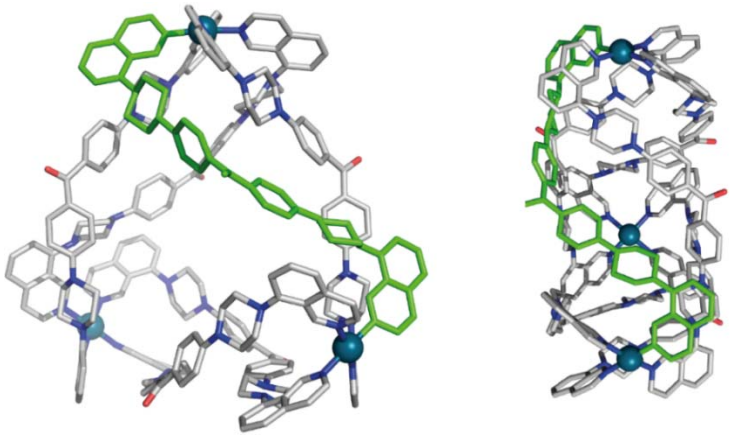

Figure 4.176: Two views of the X-ray crystal structure of one of the found enantiomers for [Pd_3(**MK-Q**)$_6$]. One ligand has been colored green for better comprehension of the structure. Counterions and solvent molecules have been omitted for clarity.

4.9 Appendix

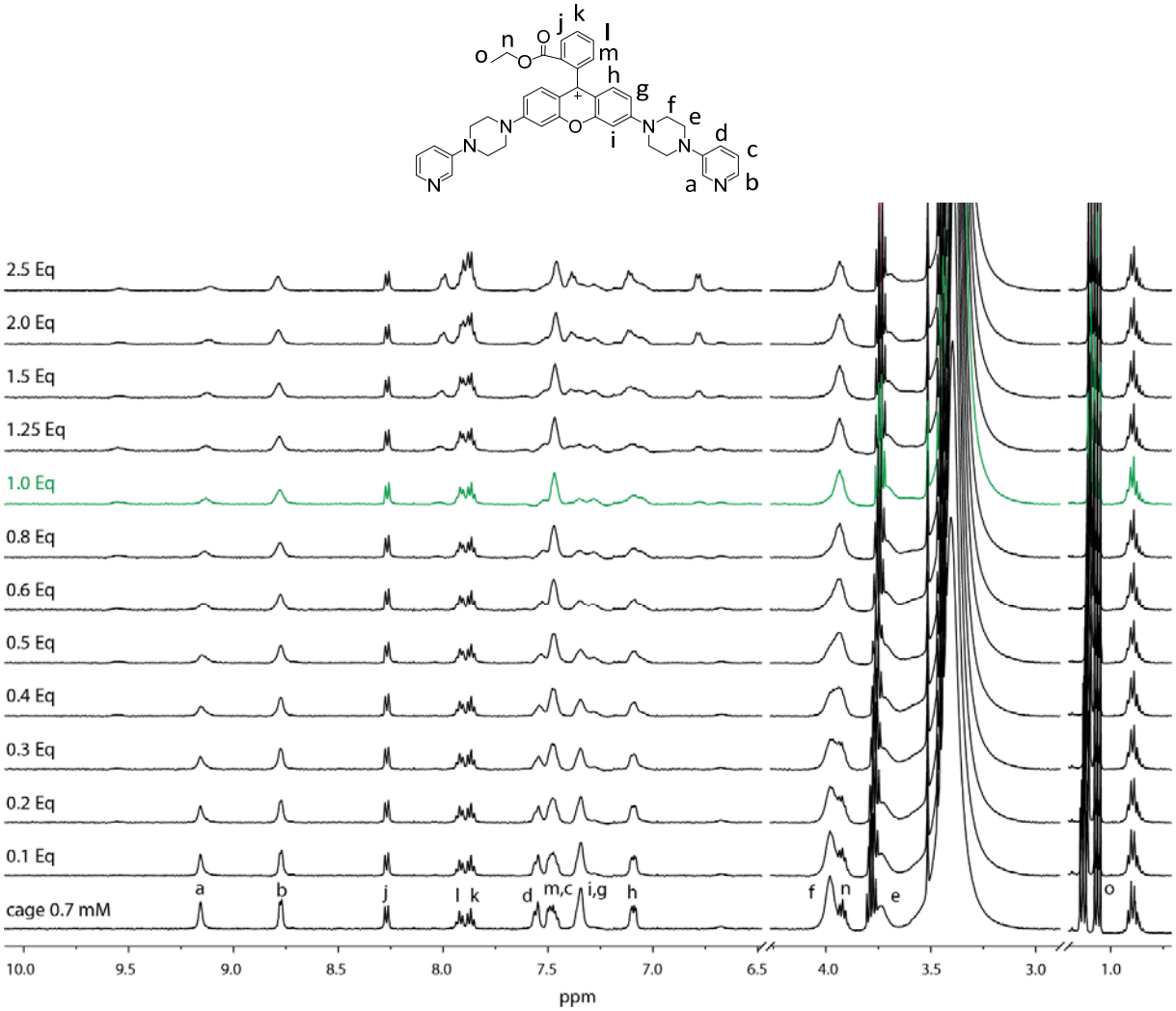

Figure 4.177: ^{1}H NMR titration at 25 °C of guest (*R*)-**BINSO$_3$** in cage [Pd_2(**RE-P**)$_4$]. The green line corresponds to 1 equiv. of the guest.

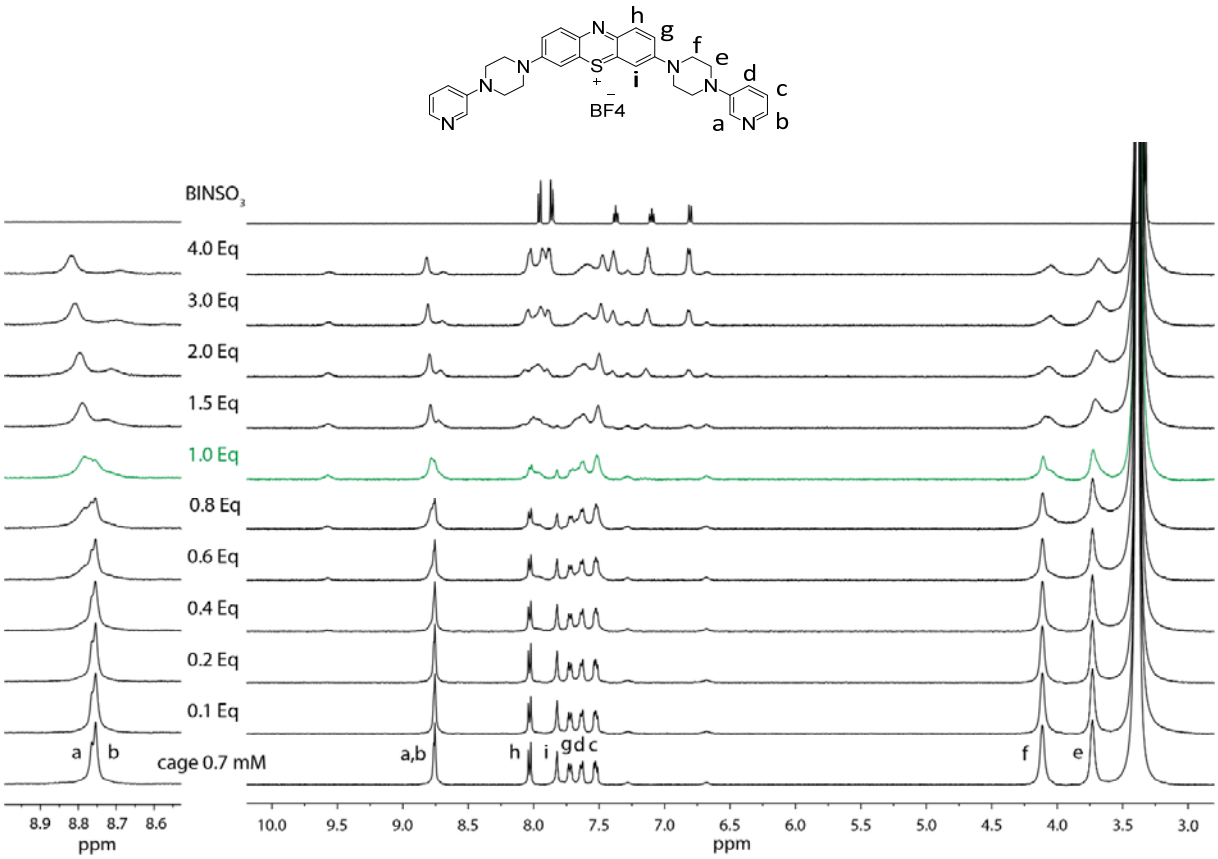

Figure 4.178: ^{1}H NMR titration at 25 °C of guest (*R*)-**BINSO$_3$** in cage [Pd$_2$(**MB-P**)$_4$]. The green line corresponds to 1 equiv. of the guest. On the left enlargement of the region 9.0-8.4 ppm, on the right the full spectrum.

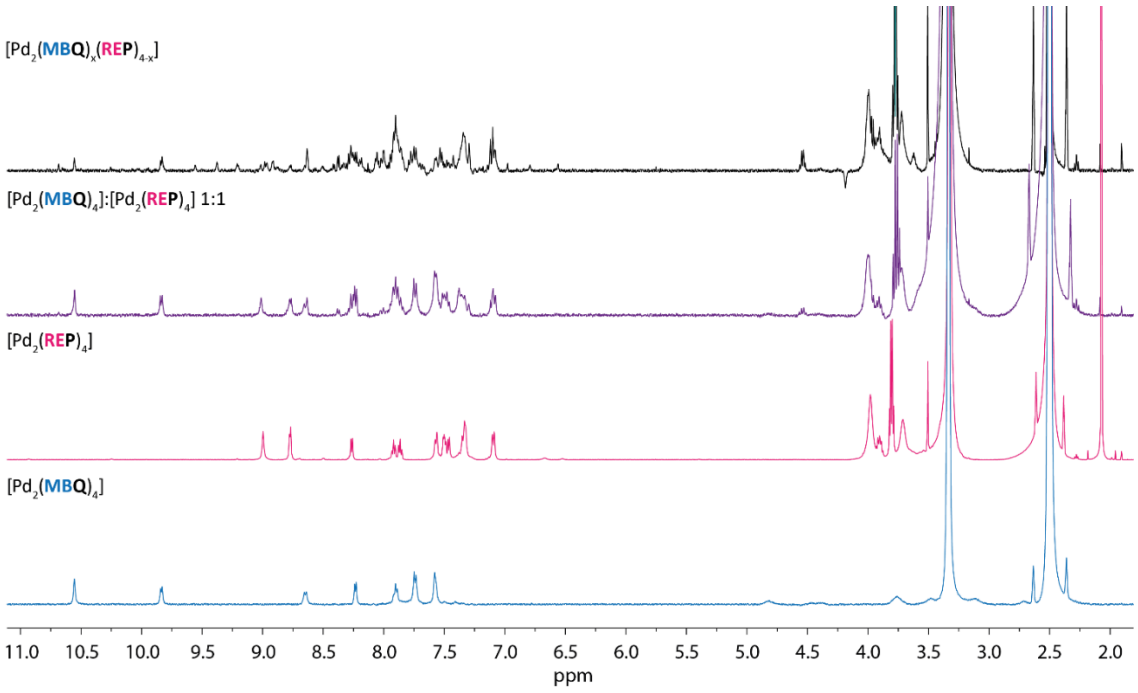

Figure 4.179: stacked ^{1}H NMR spectra at 25 °C in DMSO-d_6 from the bottom cage [Pd$_2$(**MB-Q**)$_4$] in blue, [Pd$_2$(**RE-P**)$_4$] in pink, kinetically-trapped cages [Pd$_2$(**MB-Q**)$_4$] and [Pd$_2$(**RE-P**)$_4$] in violet, statistical mixture [Pd$_2$(**MB-Q**)$_x$(**RE-P**)$_{4-x}$] with x=1-4 in black.

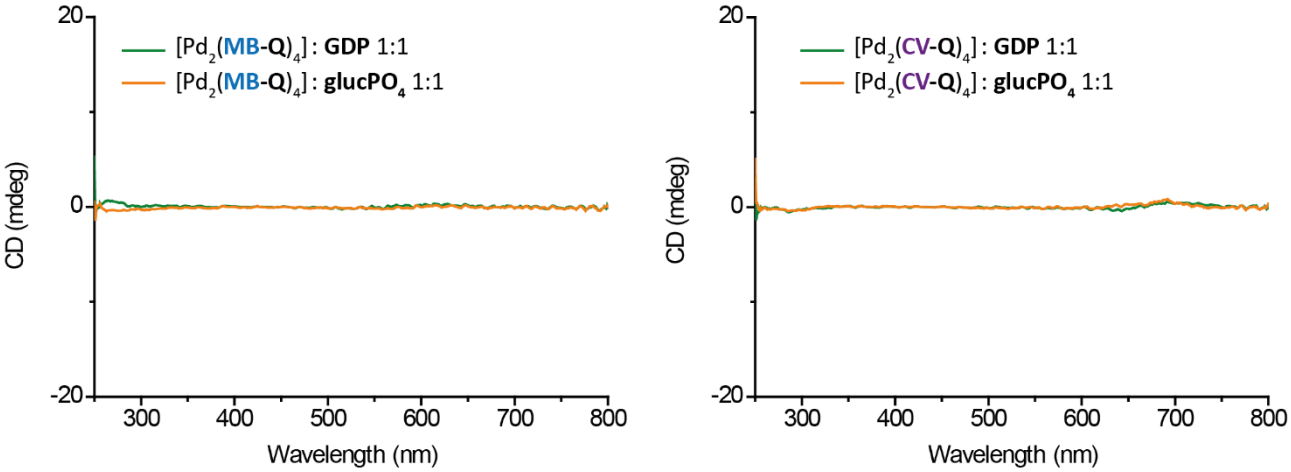

Figure 4.180: CD spectra of 1:1 solutions of (on the left) cage $[Pd_2(\mathbf{MB\text{-}Q})_4]$ with **GDP** in green and **glucPO$_4$** in orange and of (on the right) cage $[Pd_2(\mathbf{CV\text{-}Q})_4]$ with **GDP** in green and **glucPO$_4$** in orange.

4.10 References

[1] T. Gessner, U. Mayer, **2012**, *Ullmann's Encyclopedia of Industrial Chemistry*, Triarylmethane and Diarylmethane Dyes, *37*.

[2] N. A. Romero, D. A. Nicewicz, *Chem. Rev.* **2016**, *116*, 10075–10166.

[3] R. Coico, *Curr Protoc Microbiol.* **2006**, *00*, A.3C.1-A.3C.2.

[4] S. Wang, B. Li, F. Zhang, *ACS Cent. Sci.* **2020**, *6*, 1302–1316.

[5] A. G. Salles, S. Zarra, R. M. Turner, J. R. Nitschke, *J. Am. Chem. Soc.* **2013**, *135*, 19143–19146.

[6] L. Zhao, J. Wei, J. Zhang, C. He, C. Duan, *Angew. Chem. Int. Ed.* **2017**, *56*, 15284–15288.

[7] H. Wang, L. Li, X. Li, C. He, *Isr. J. Chem.* **2018**, *59*, 273–279.

[8] Z. Heinrich, *Color Chemistry*, Wiley-VCH, **2003**.

[9] N. A. Romero, D. A. Nicewicz, *Chem. Rev.* **2016**, *116*, 10075–10166.

[10] P. Suppan, *J. Chem. Soc. Faraday Trans.*, **1975**,*71*, 539-547.

[11] P. J. Macdonald, S. Gayda, R. A. Haack, Q. Ruan, R. J. Himmelsbach, S. Y. Tetin *Anal. Chem.* **2018**, *90*, 15, 9165–9173.

[12] F. J. Duarte, L. W. Hillman, Eds., *Dye Laser Principles: With Applications*, Academic Press, **1990.**

[13] J. Du, J. Fan, X. Peng, P. Sun, J. Wang, H. Li, S. Sun, *Org. Lett.* **2010**, *12*, 476–479.

[14] D. A. Hinckley, P. G. Seybold, *J. Chem. Educ.* **1987**, *64*, 362.

[15] X. Hu, V. Laguerre, D. Packert, A. Nakasone, L. Moscinski, *Int. J. Cell Biol.* **2015**, *2015*, 1–4.

[16] P. R. Ginimuge, S. D. Jyothi, *J. Anaesthesiol., Clin. Pharmacol.* **2010**, *26*, 517–20.

[17] S. Mowry, P. J. Ogren, *J Chem Educ* **1999**, *76*, 970.

[18] M. C. DeRosa, R. J. Crutchley, *Coord. Chem. Rev.* **2002**, *233*, 351–371.

[19] J. P. Tardivo, A. D. Giglio, C. S. de Oliveira, D. S. Gabrielli, H. C. Junqueira, D. B. Tada, D. Severino, R. de F. Turchiello, M. S. Baptista, *Photodiagn Photodyn.* **2005**, *2*, 175–191.

[20] J. A. Kiernan, *Color. Technol.* **2006**, *122*, 1–21.

[21] A. M. Maley, J. L. Arbiser, *Exp. Dermatol.* **2013**, *22*, 775–780.

[22] D.-M. Kong, Y.-E. Ma, J. Wu, H.-X. Shen, *Chem. Eur. J.* **2009**, *15*, 901-909.

[23] D.-L. Ma, M. H.-T. Kwan, D. S.-H. Chan, P. Lee, H. Yang, V. P.-Y. Ma, L.-P. Bai, Z.-H. Jiang, C.-H. Leung, *Analyst* **2011**, *136*, 2692.

[24] S. Saha, I. Regeni, G. H. Clever, *Coord. Chem. Rev.* **2018**, *374*, 1–14.

[25] T. R. Schulte, J. J. Holstein, L. Schneider, A. Adam, G. Haberhauer, G. H. Clever, *Angew. Chem. Int. Ed.* **2020**, accepted, DOI: 10.1002/anie.202010995

[26] H. S. Sahoo, D. K. Chand, *Dalton Trans.* **2010**, *39*, 7223–7225.

[27] C. Cretu, R. Tudose, L. Cseh, W. Linert, E. Halevas, A. Hatzidimitriou, O. Costisor, A. Salifoglou, *Polyhedron* **2015**, *85*, 48–59.

[28] T. Gruene, J. T. C. Wennmacher, C. Zaubitzer, J. J. Holstein, J. Heidler, A. Fecteau-Lefebvre, S. D. Carlo, E. Müller, K. N. Goldie, I. Regeni, T. Li, G. Santiso-Quinones, G. Steinfeld, S. Handschin, E. van Genderen, J. A. van Bokhoven, G. H. Clever, R. Pantelic, *Angew. Chem. Int. Ed.* **2018**, *57*, 16313–16317.

[29] T. R. Schulte, M. Krick, C. I. Asche, S. Freye, G. H. Clever, *RSC Adv.* **2014**, *4*, 29724–29728.

[30] M. Han, D. M. Engelhard, G. H. Clever, *Chem. Soc. Rev.* **2014**, *43*, 1848–1860.

[31] T. Murase, S. Sato, M. Fujita, *Angew. Chem. Int. Ed.* **2007**, *46*, 5133–5136.

[32] S. Hiraoka, Y. Kubota, M. Fujita, *Chem. Commun.* **2000**, 1509–1510.

[33] T. Murase, S. Horiuchi, M. Fujita, *J. Am. Chem. Soc.* 2010, *132*, 2866–2867.
[34] M. Yoshizawa, J. K. Klosterman, M. Fujita, *Angew. Chem. Int. Ed.* 2009, *48*, 3418–3438.
[35] V. Maurizot, M. Yoshizawa, M. Kawano, M. Fujita, *Dalton Trans.* 2006, *23*, 2750–2756.
[36] A. R. Katritzky, D. C. Fara, H. Yang, K. Tämm, T. Tamm, M. Karelson, *Chem. Rev.* 2004, *104*, 175–198.
[37] W. M. Bloch, Y. Abe, J. J. Holstein, C. M. Wandtke, B. Dittrich, G. H. Clever, *J. Am. Chem. Soc.* 2016, *138*, 13750–13755.
[38] G. A. Shahinyan, A. Yu. Amirbekyan, S. A. Markarian, *Spectrochim. Acta A Mol. Biomol. Spectrosc.* 2019, *217*, 170–175.
[39] S. Spange, M. El-Sayed, H. Müller, G. Rheinwald, H. Lang, W. Poppitz, *Eur. J. Org. Chem.* 2002, *2002*, 4159–4168.
[40] M. Wielgus, M. Samoć, W. Bartkowiak, *J. Mol. Liq.* 2016, *222*, 125–132.
[41] A. Macchioni, G. Ciancaleoni, C. Zuccaccia, D. Zuccaccia, *Chem. Soc. Rev.* 2007, *37*, 479–489.
[42] E. O. Stejskal, J. E. Tanner, *J. Chem. Phys.* 1965, *42*, 288–292.
[43] A. Macchioni, G. Ciancaleoni, C. Zuccaccia, D. Zuccaccia, *Chem. Soc. Rev.* 2007, *37*, 479–489.
[44] L. Avram, Y. Cohen, *Chem. Soc. Rev.* 2014, *44*, 586–602.
[45] L. Allouche, A. Marquis, J.-M. Lehn, *Chem. Eur. J.* 2006, *12*, 7520–7525.
[46] R.-J. Li, J. J. Holstein, W. G. Hiller, J. Andréasson, G. H. Clever, *J. Am. Chem. Soc.* 2019, *141*, 2097–2103.
[47] A. Jerschow, N. Müller, *J. Magn. Reson.* 1996, *123*, 222–225.
[48] A. Jerschow, N. Müller, *J. Magn. Reson.* 1998, *132*, 13–18.
[49] *Anal. Chem.* 2017,*89*, 9048-9055.
[50] O. Plietzsch, A. Schade, A. Hafner, J. Huuskonen, K. Rissanen, M. Nieger, T. Muller, S. Bräse, *Eur. J. Org. Chem.* 2012, *2013*, 283–299.
[51] J. B. Grimm, L. D. Lavis, *Org. Lett.* 2011, *13*, 6354–7.
[52] A. Burkhardt, T. Pakendorf, B. Reime, J. Meyer, P. Fischer, N. Stübe, S. Panneerselvam, O. Lorbeer, K. Stachnik, M. Warmer, P. Rödig, D. Göries, A. Meents, *Eur. Phys. J. Plus* 2016, *131*, 56.
[53] G. Sheldrick, *Acta Crystallogr. Sect. A* 2015, *71*, 3-8.
[54] G. Sheldrick, *Acta Crystallogr. Sect. C* 2015, *71*, 3-8.
[55] C. B. Hubschle, G. M. Sheldrick, B. Dittrich, *J. Appl. Crystallogr.* 2011, *44*, 1281-1284.
[56] W. Kabsch, *Acta Crystallogr. Sect. D* 2010, *66*, 125-132
[57] D. Kratzert, J. J. Holstein, I. Krossing, *J. Appl. Crystallogr.* 2015, *48*, 933-938.
[58] A. Thorn, B. Dittrich, G. M. Sheldrick, *Acta Crystallogr. Sect. A* 2012, *68*, 448-451.
[59] A. Spek, *Acta Crystallogr. Sect. C* 2015, *71*, 9-18.
[60] A. Spek, *Acta Crystallogr. Sect. D* 2009, *65*, 148-155.
[61] Bruker-Nonius, APEX, SAINT, SADABS and XPREP, Bruker AXS Inc., Madison (USA), 2013.

5. Methylene blue-based metallo helicates for supramolecular DNA recognition

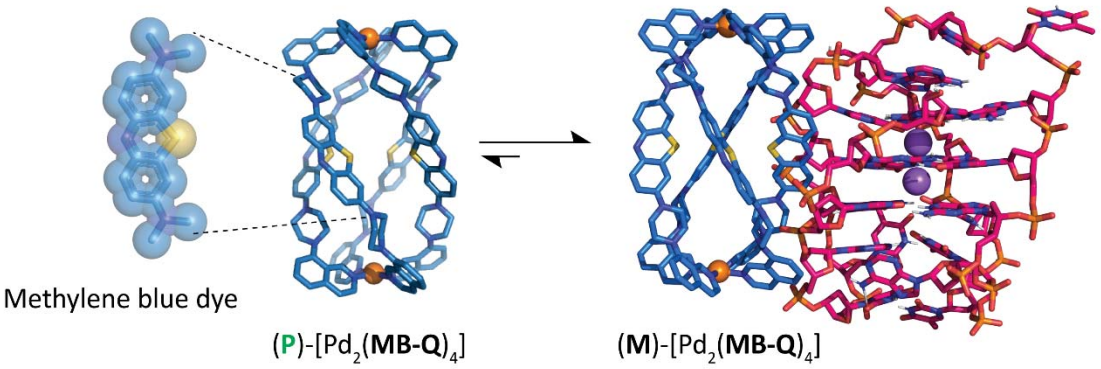

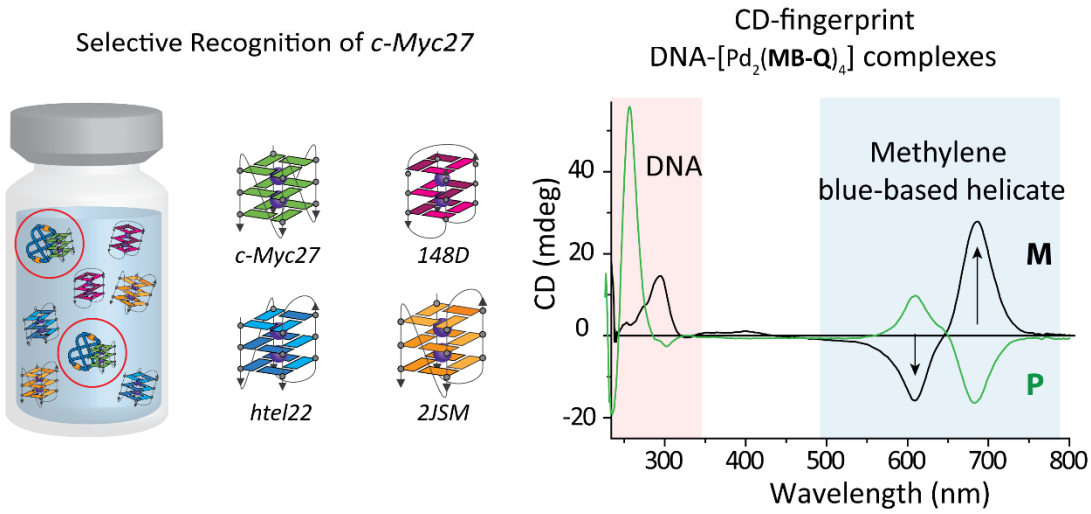

5.1 Introduction

5.1.1 DNA secondary structures

Alongside proteins, lipids and complex carbohydrates, nucleic acids are one the four major types of macromolecules that are essential for all known forms of life. DNA carries the genetic instruction for the development, functioning, growth and reproduction of all known organisms and many viruses. DNA strands are known as linear polynucleotides as they are composed of simple monomeric unites called nucleotides (Figure 5.1). Each nucleotide is composed of one of four nitrogen-containing nucleobases, a sugar called deoxyribose and a phosphate group. The four nitrogen-containing nucleobases can be divided into two groups, the purine bases with adenine [A] and guanine [G], and the pyrimidine bases with cytosine [C] and thymine [T] and are connected to the 1' carbon atom of the sugar *via* N-glycosidic bond. The nucleotides are joined to one another in a chain by covalent bonds (known as the phosphor-diester linkage) between the sugar of one nucleotide and the phosphate of the next, resulting in an alternating sugar-phosphate backbone. In the most commonly known secondary structure, the double helix, two strands are bound together, according to the Watson-Crick base pairing rules (A with T and G with C) with hydrogen bonds.[1]

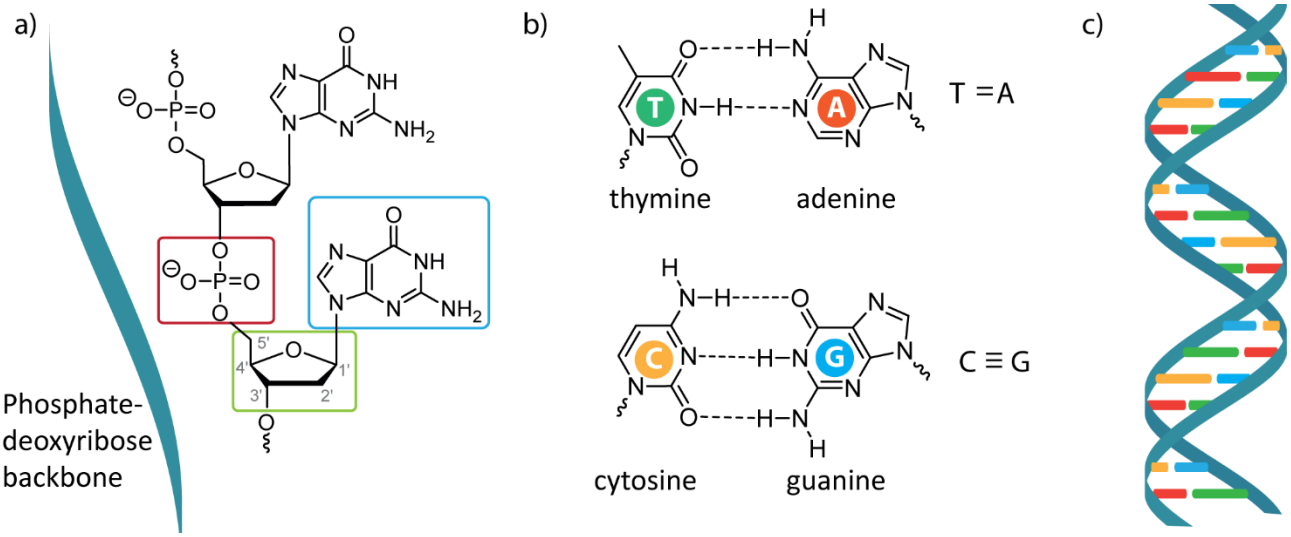

Figure 5.1: a) Polynucleotides' basic structure. A single nucleotide is composed of a base (blue box, here guanine), a deoxyribose (green box) and a phosphate (red box) and are connected to the other nucleotides through a phosphate-deoxyribose bond to form the phosphate-deoxyribose backbone. b) Canonical pyrimidine nucleobases, thymine (green) and cytosine (yellow) and purine nucleobases, adenine (red) and guanine (blue). c) Schematic illustration of double helical DNA, the colors match to the corresponding bases in order to satisfy the Watson-Crick base pairing rules.

However, in the last decades, it has been found that multiple different secondary structures can originate other than the canonical double helix (or B-DNA). A-DNA, a right-handed and more compact helical structure, can be formed under dehydrating conditions, typical conditions to induce crystallization, while left-handed Z-DNA has been observed at high salt concentrations in sequences alternating purine-pyrimidine bases. When involved in biological processes like transcription or replication, DNA unwinds in single strands that can refold in different secondary structures such as hairpins, three- and four-way junctions (3 and 4WJ) or Holliday junctions, triple-stranded DNA and quadruple-stranded DNA with G-quadruplexes and i-motifs.[2]

For the purpose of this thesis, particular focus will be set on the class of G-quadruplexes (G4s). Such structures originate from guanine-rich sequences where four guanines are bonded together through Hoogsteen hydrogen bonds to form a planar G-tetrad. To form the G4, two or more G-tetrads π-π stack on top of each other and are stabilized by cations that compensate the partial negative charge of the carbonyl oxygen atoms, pointing inside the G-tetrad, with stabilizing preference for monovalent cations

in the order K^+>Na^+>>Li^+. G4s are characterized by a high structural diversity, depending on how many strands come together to form the G-tetrad stack (molecularity), they can be unimolecular, when a single strand self-aggregates into the structure, or intermolecular, composed of two (bimolecular), three or four strands (tetramolecular). They can adopt a wide diversity of topologies arising from different combinations of strand direction, as well as number of G-tetrad and loop length and composition. Circular Dichroism (CD) spectroscopy can provide a great extent of insights in the G4 structures and topologies, since differences in the above mentioned structural elements (and shown in Figure 5.2 b)-d), lead to unique CD spectral signatures.[3,4] For particular G4 topologies, qualitative rules-of-thumb have evolved to associate them with CD spectral feature: parallel topologies show a maximum at ca. 260 nm and a minimum at ca. 240 nm, antiparallel topologies show a maximum at 290 nm and a minimum at 260 nm, and hybrid topologies show two maxima at 290 nm and 260 nm and a minimum at 240 nm. When more topologies are present at the same time, the CD signature is very similar to the hybrid one. Exceptions of this rules have been noted, but they are generally accepted for the characterization of potential G4 forming sequences.[5]

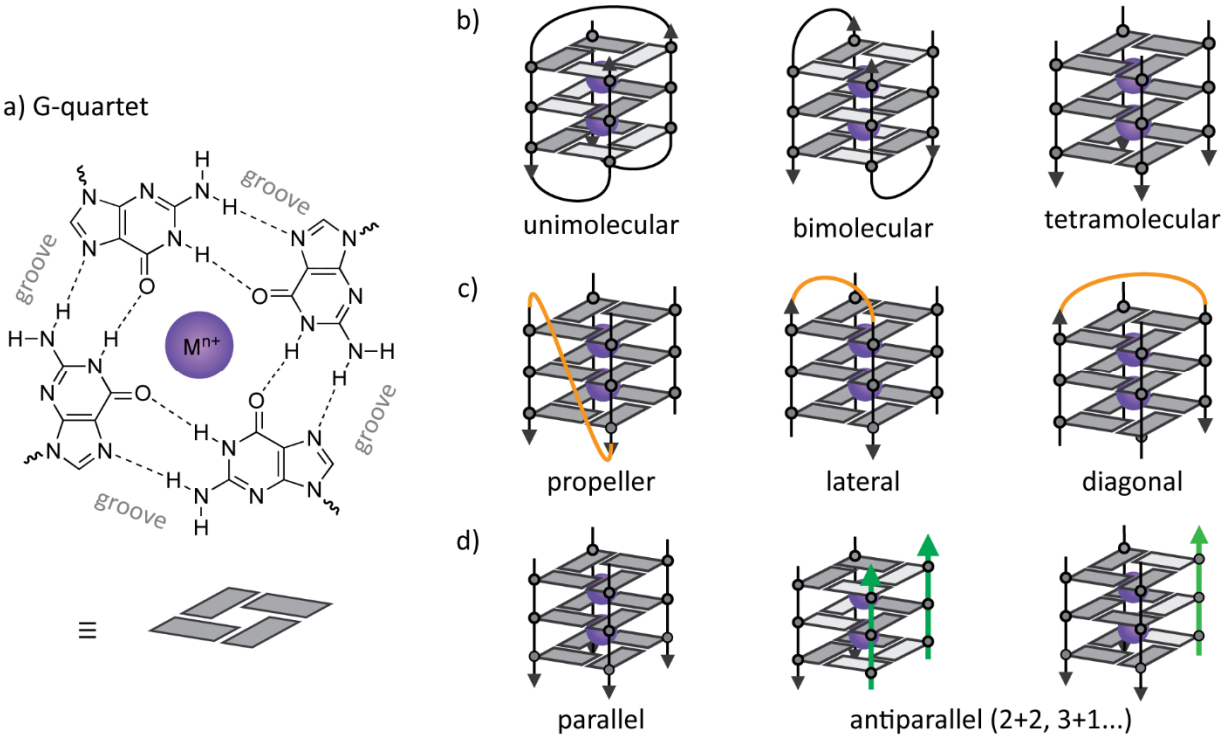

Figure 5.2: a) Schematic illustration of a G-tetrad formed from four guanine residues with explicit hydrogen bonds. The generic M^{n+} cation serves the purpose of compensating the partial negative charge of the carbonyl groups that point inside the tetrad. On the right, some examples of the high structural diversity of G4s are shown. b) G4s formed by a single strand are unimolecular, by two strands are bimolecular and by four strands are tetramolecular; c) the orientation of the loops can be for example propeller-like to the G4 tetrads stack, lateral (or edgewise) when it connects two adjacent guanines or diagonal when they are opposite to each other; d) strand orientation can be parallel or antiparallel.

In the last decades, G4s gained more and more attention as evidences pointed out their extremely important regulation role in multiple biological processes and are currently at the center of many anticancer and gene-regulation strategies.[6–8] Guanine-rich single-stranded DNA is found at the end of telomers, that are DNA sequences that comprise a large number of simple tandem repeats at the end of eukaryotic chromosomes, which protect against degradation and genomic instability. Telomerase plays a major part in maintaining cell immortalization by catalyzing telomer extension by synthetizing TTA GGG telomeric DNA repeats, and it is overexpressed in the majority of human cancers, therefore, stimulating interest in inhibiting its activity as anticancer strategy. The 3' ends of human telomeric DNA has been found to fold into G-quadruplex structures, which render the ends inaccessible to telomerase template recognition and hence telomerase repeat addition.[9] Several examples of small molecules that

further induce and stabilize G4 formation in this region have been reported.[10,11] Guanine-rich sequences are furthermore studied for their important regulatory roles in RNA transcription and translation, as well as their function in promoter regions of (onco-)genes, with the G-quadruplex-forming region in the MYC promoter being one of the most studied examples. Overexpression of the c-MYC oncogene is linked with cellular proliferation and inhibition of differentiation, leading to its association with a wide range of human cancers. The nuclease hypersensitivity element III (NHE III_1) of the c-MYC promoter controls 80-90% of the c-MYC transcription and consists on a 27-base pair sequence (*c-Myc27* in this study).[12–14] The function of the G-quadruplex is to act as down-regulator of gene transcription. This function is possibly achieved by acting as a steric block to transcription initiation, either directly or as a ligand to which a protein can bind and block transcription.[15]

In Figure 5.3, two G4-forming sequences found in the biological relevant regions of telomers and the promoter region of c-MYC are presented. *htel22* represents a 22 nucleotides-long sequence that contains 4 TTA GGG repeats (first two nucleotides truncated) and is known to form different G4 structures depending on the conditions. Folding in the presence of Na^+ electrolytes in solution forms an intramolecular G4 with antiparallel topology where the adopted N-glycosidic bond conformations of the guanosines around each tetrad are *syn-syn-anti-anti* with edgewise-diagonal-edgewise loops (pink schematic structure in Figure 5.3, the *syn* or *anti* dispositions of the guanines are indicated by different shades). By contrast, the crystal structure of the same sequence in the presence of K^+ ions revealed a completely different intramolecular G4, where all strands are parallel, guanines are *anti* oriented and loops adopt propeller orientation.[16] In K^+ electrolyte solutions however, a further different topology was discovered, an intramolecular G-quadruplex with a (3+1) core topology, or otherwise named hybrid 3-type topology (blue schematic structure in Figure 5.3).[17] *c-Myc27*, a 27 nucleotide-long sequence, contains six G-tracs of unequal length, which unsurprisingly form a complex mixture of parallel topology G4 structures in different electrolyte solutions.[13,14,18–20] This particular sequence will be explored in more details in section 5.3.1 of this chapter.

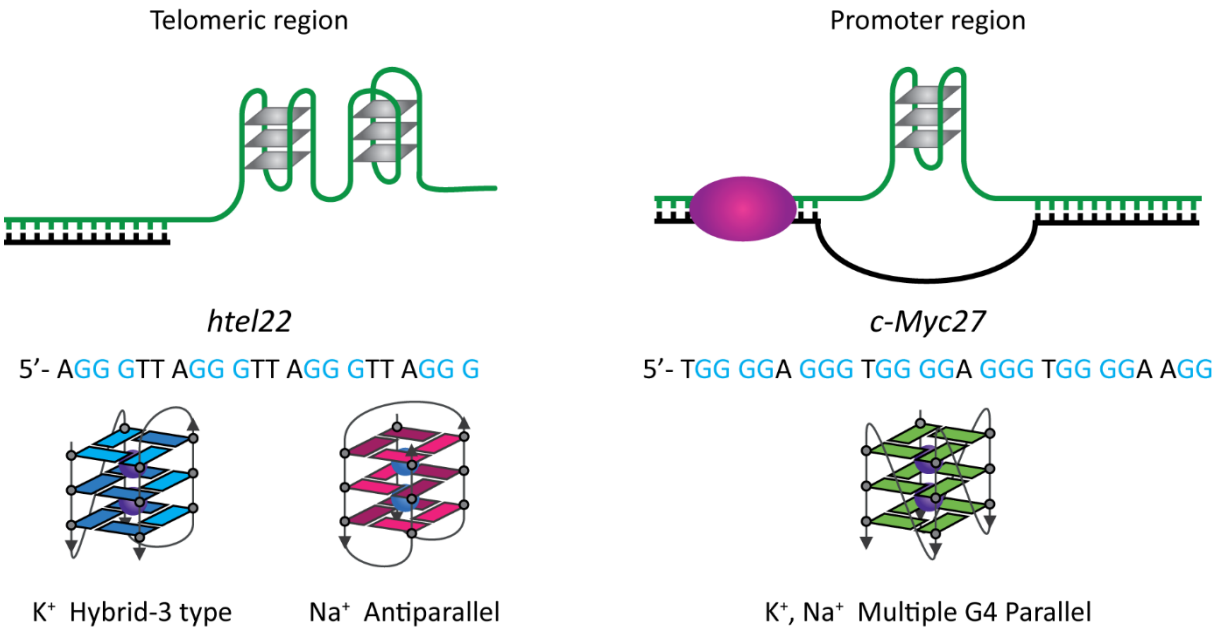

Figure 5.3: Two examples of biologically relevant G4s in the region of telomers (as a TTA GGG repeat) and as part of the promoter region of c-MYC. Sequence *htel22* in K^+ containing solution folds into a hybrid 3-type topology and in Na^+ ion solutions in antiparallel topology. Sequence *c-Myc27* can fold into multiple G4s, prevalently of parallel topology. The *syn* and *anti* conformation of the guanines are expressed by different shades.

5.1.2 Metallo helicates for supramolecular DNA recognition

One of the most thrilling aspects of supramolecular chemistry is the possibility of exploiting weak and reversible recognition processes to better understand the cycle of life. Non-covalent DNA recognition is of primary importance for controlling gene expression and it is a very attractive field where supramolecular interactions dominate. Supramolecular chemistry allows to design much larger structures than traditional covalent synthetic chemistry with little effort and allows to create structures that more closely mimic dimension and shape of protein-protein or protein-DNA recognition motifs. Recognition with small molecules through intercalation and minor groove binding of DNA has been extensively reported,[21] when rarely it has been possible to create agents that are entirely synthetic and bind in the major groove.

One of the first examples that opened the field of supramolecular DNA recognition with metallo-agents formed by self-assembly of organic ligands with metal cations was reported by the group of Nobel-laureate Jean-Marie Lehn in 1995. They synthetized polycationic Cu(I)-based double-helices of different length and the interaction with polyanionic long double-stranded DNA was characterized with UV-Vis spectroscopy methods. They found the helicates not only to bind the DNA in multiple ways, but also to mediate single strand photocleavage of DNA (Figure 5.4). The nature of the binding strength was addressed to the electrostatic interaction with a contribution of hydrophobic effects in light of the hydrophobic surface and size which is compatible with the major groove of the B form of DNA.[22]

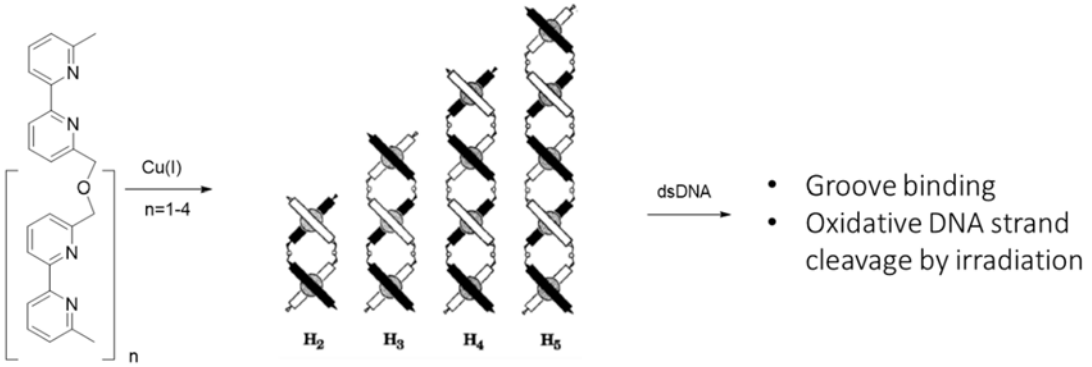

Figure 5.4: Lehn and coworkers' helicates of different length. Upon double strand addition, groove binding and subsequent oxidative DNA strand cleavage upon irradiation could be observed.[22]

In the context of DNA recognition by metallo-supramolecular agents, Mike Hannon and coworkers, brought their extensive contributions. They designed a tetracationic supramolecular helicate $[Fe_2L_3]^{4+}$, which is formed from three organic bis-pyridylimine strands wrapped around two Fe^{2+} ions, whose dimensions are similar to those of the α-helical DNA recognition unit of zinc finger proteins (Figure 5.5 a)). The metallo-supramolecular cylinder was shown to target the major groove of DNA with a binding constant larger than 10^7 M^{-1} and to induce DNA bending and intramolecular coiling.[23] Later, they were able to crystalize the same cylinder with a palindromic hexanucleotide and they observed that, among all the possible structures that satisfy the Watson-Crick base pairing, the cylinder chose to reside in the heart of a 3-way junction (Figure 5.5 b)).[24] The driving force, besides the electrostatic attraction, is a very strong π-π interaction between the aromatic surface of the cylinder and the DNA bases. Gel-electrophoresis studies revealed the strong stabilization effect of the metallo-helicates, with the righ-handed *M* enantiomer showing the highest effect, not only in the solid state with palindromic sequences, but also in solution with various kinds of 3WJ, establishing a new powerful binding mode.[25]

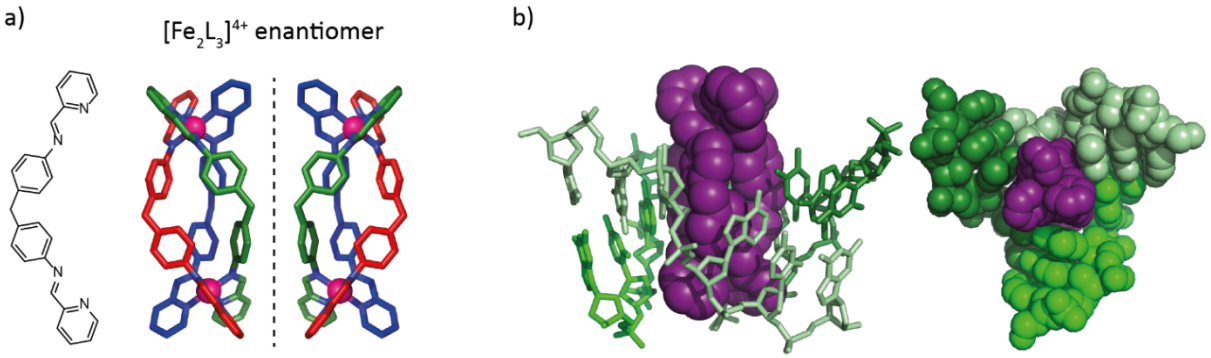

Figure 5.5: Hannon and coworkers' design of the Fe(II) helicate in the two chiral configurations. b) Side view and top view of the crystal structure of the helicate in the middle of a 3WJ.[24]

Since biological applications require a higher degree of stability of the binding agents in order to ascribe the measured results to the binding agents itself and not his decomposition components, the same group reported a similar cylinder based on Ru(II) for which they excitingly saw an anticancer activity which is only 2-5 times less active than observed for cisplatin. A remarkable result considering that the binding mode for the two anti-cancer drugs is completely different.[26] With the introduction of two ligand modifications, one on the backbone and one close to the coordinating group, the study on DNA interactions with biochemical and molecular biology methods was deepened. However, it was found that while the original helix can unwind DNA, with again the *M* enantiomer showing stronger responses than the *P* and preferential binding to alternating purine-pyrimidine sequences, the newly synthetized bulky helices showed no unwinding and no specificity.[27] Other than DNA, Hannon's research group put their interest in characterizing in detail the binding of the designed anticancer di-iron(II) supramolecular cylinder to RNA three-way junctions at atomic resolution in the solid state, in solution, and to establish the competition with a respective DNA 3WJ. Both nucleic acid 3WJs were similarly stabilized by the cylinder. This is surprising because of their inherent structural differences and the dynamic nature of the recognition of 3WJs by metal-based drugs.[28] Furthermore, it could be observed that the helicates condense plasmid DNA with a much higher potency than conventional DNA-condensing agents.[29]

The same metallo-helicate based both on Fe(II) and Ni(II) has then been studied by the group of X. Qu with different DNA secondary structures and it has been observed to selectively stabilize the class of G-quadruplex DNA and to show specific preference for the sequence of the human telomeric G4 sequence.[30] Furthermore, the *P* enantiomer of the helicate was able to convert the G4 topology from antiparallel to hybrid structure in Na^+ electrolyte solutions, implying chiral preference (Figure 5.6). The treatment on tumor cells with such helicates found that the chiral metallo-supramolecular complex, Ni-P, but not Ni-M, can induce an acute cell growth arrest and apoptosis in cancer cells rather than normal cells under the same experimental condition.[31] The interaction of the helicates with left-handed G4 DNA showed the opposite behavior: the *M* enantiomer owns the stabilization effect.[32] These findings have been merged and deeper analyzed in a following study. The interaction with natural D-human telomeric G4 and L-human telomeric G4 and 10 different metallo-helicates in their stable chiral conformations was investigated and the expected mirror-image dependence became apparent where D-DNA is stabilized by Δ-helicates and L-DNA is stabilized by Λ-helicates. [33]

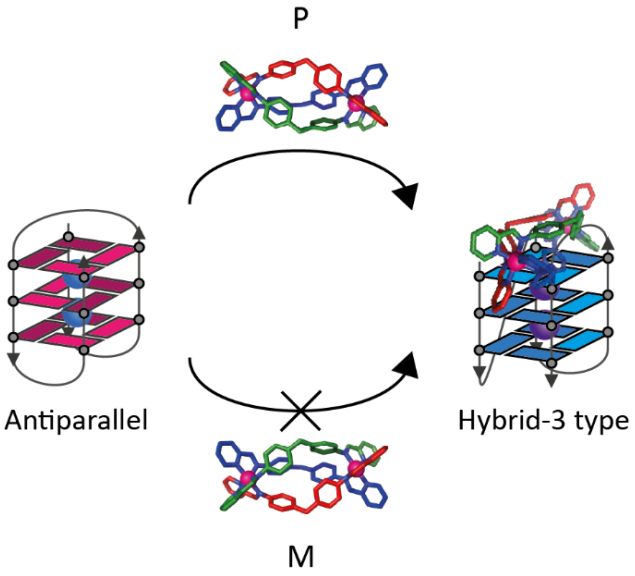

Figure 5.6: Binding of the metallo-helicate on the G4 *htel22*. The *P* enantiomer of the helicate selectively stabilizes the G4 and is able to convert its topology from antiparallel to hybrid in Na^+ electrolyte solutions. On the contrary, the *M* enantiomer showed no activity. [30]

In 2012, the group of Peter Scott reported a new design of helicates with flexible backbones (flexicates) obtained through sub-component self-assembly of a chiral amine with a bis-pyridincarboxyaldehyde in the presence of Fe(II) ions as an enantiopure compound (when the (*R*)-precursor amine was used, only the Δ-*R*-[Fe_2L_3] was obtained, and to obtain the Λ, the (*S*) was used) (Figure 5.7). [34] The flexicate exhibits specific interaction with DNA as well as promising antimicrobial activity. Furthermore, the same metallo-helix was found to have activity against cisplatin-resistant cancer cells supported with a DNA-interaction study and comparison with the more rigid helicates.[35] In 2014, a higher complexity design was reported, with asymmetric ligands and, despite no enantiopure formation of helicates could be observed from enantiopure starting materials, it led to a new class of metallo-helicates with high and selective activity against cancer cells,[36–38] and with the ability of killing – at low doses – a range of bacterial pathogens, including clinically problematic species such as members of the ESKAPE panel of microbes.[39]

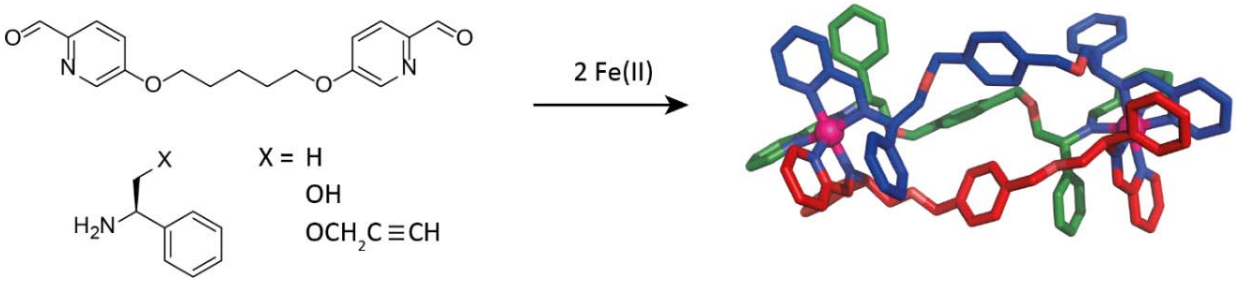

Figure 5.7: Sub-component self-assembly in the presence of Fe(II) ions of a flexicate as an enantiopure compound. The structure on the right is a crystal structure.

In 2017, in collaboration with the group of X. Li, they studied the interaction of their flexible metallohelicates with G-Quaduplex DNA.[40] They could observe that the enantiopure metallohelix, available from a diastereoselective synthesis with no need for resolution, can enantioselectively stabilize human telomeric hybrid G-quadruplex and strongly inhibit telomerase activity with an IC_{50} value of 600 nM. In contrast, no such a preference was observed for the mirror image complex. More intriguingly, neither of the two enantiomers binds specifically to human telomeric antiparallel G-quadruplex.

Further examples of supramolecular self-assembled architectures that interact with DNA, include a $Fe(II)_4L_4$ tetrahedron that selectively detect mismatched DNA base pairs,[41] and cationic metallo-grids that strongly bind double-stranded DNA.[42]

The state-of-the-art literature presented highlights the advancement that metal-mediated self-assembly chemistry of helicate structures brought to the field of supramolecular DNA recognition. Some common features on the different DNA binders developed can be named starting from their helical nature, accurately resembling the helical nature of DNA structures, their polycationic charge state which leads to attractive electrostatic interactions with the polyanionic oligonucleotides and their size being comparable to natural DNA binders. Most of the structures are triple helicates based on Fe(II), Ni(II) or Ru(II). The helicity of the assemblies derives from the two possible chiral conformation of the octahedral metal complexes, Δ or Λ, and the consequent twisted conformation of the ligands that coordinate to two metal centers. The fixed chirality of the complexes allows to separate the enantiomers and compare their different effects on DNA.

In this chapter, a new design for a metallo-helicate that binds DNA and is capable of special selectivity for the G-quadruplex structure formed in the promoter region of c-MYC, will be shown. Such structure differs substantially to the examples already reported in the literature since it is a quadruple helicate based on Pd(II), the chirality arises from the twist of the ligands around the metal cation because equipped with inward pointing donor groups and the resulting enantiomers of the assembly can easily interconvert within each other at room temperature, allowing the DNA to choose and populate the preferred one.

5.2 Results and discussion

In the previous chapter, the design of a new metallo-supramolecular assembly with dynamic helical structure, [Pd_2(**MB-Q**)$_4$], based on two square-planar Pd(II) cations coordinating four bis-isoquinoline ligands with a backbone based on the well-known methylene blue dye (**MB**) has been shown. The cage structure exists as a racemic mixture of two helical conformers of different handedness (**M** and **P**), rapidly interconverting in solution at room temperature (Figure 5.8). The assembly is soluble in water (see chapter 4, Figure 4.21 for ^{1}H NMR spectrum of the assembly), it strongly absorbs in a region of the visible spectrum of light, between 610 and 680 nm, where no typical biological molecules absorb (exceptions include e.g. protein cofactors like variously substituted porphyrins) and the backbone is based on the methylene blue dye which is well-known to interact with DNA.[43–56] Interestingly, derivates of **MB** were found to stabilize G4s with high selectivity for the c-MYC G4.[55]

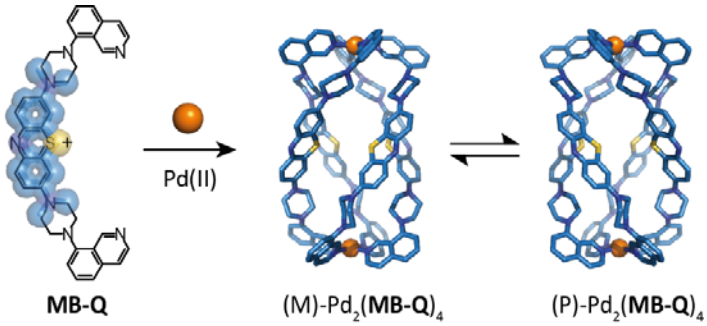

Figure 5.8: Representation of the assembly of the new helicate designed for DNA binding. Ligand **MB-Q**, based on the structure of the methylene blue dye, coordinates palladium cations to form the cage [Pd_2(**MB-Q**)$_4$], which can be of two handiness **M** or **P** in rapid exchange equilibrium.

When the highly cationic cage is allowed to interact with anionic DNA in buffered aqueous solution, preferential binding of one of the two cage enantiomers is observed, shifting the conformer equilibrium to one side (Figure 5.9). This results in a strong chiroptical answer in the visible part of the circular

dichroism (CD) spectrum of the DNA-cage mixture. This effect was employed for the CD fingerprint analysis and specific recognition of different DNA G4 topologies. Results show that the methylene blue-based metallo-helicate is able to selectively recognize with a distinguishable chiral recognition process the sequence *c-Myc27,* and related mutated or truncated sequences, found in the promotor region of the MYC proto-oncogene, even from mixtures of different G4s combined in the same sample.

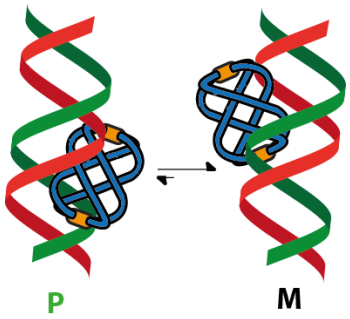

Figure 5.9: Schematic illustration of the interaction of helicate [Pd_2(**MB-Q**)$_4$] with a generic double-stranded DNA. The interaction is stronger with enantiomer **M** of the helicate and therefore the interconversion equilibrium shifts to its side.

5.2.1 Interaction with dsDNA (15bp DNA)

As already discussed in Chapter 4 (see for structural and synthetic insights), combination of bis-monodentate pyridine ligands **MB-Q**, **MB-P**, **CV-Q** and **RE-P** in a 2:1 ratio with Pd(II) cations (with BF_4^- or NO_3^- as counterion to match the ligands' ones), leads to the formation of visible light-absorbing Pd_2L_4 cages which are characterized by either a more globular shape (**MB-P** and **RE-P**) or a helical one which exists as a racemic mixture of interconverting enantiomers (**MB-Q** and **CV-Q**). The interaction of cages [Pd_2(**MB-Q**)$_4$], [Pd_2(**MB-P**)$_4$], [Pd_2(**CV-Q**)$_4$] and [Pd_2(**RE-P**)$_4$] with a short double-stranded DNA 15mer (5'- TGC AAG CTT GGC ACT), **15bp ds DNA**, was investigated. Each cage was mixed in a 1:1 ratio with the DNA in 9:1 water:DMSO buffered solution (10 mM sodium cacodylate, NaCaCo, pH 7.2) with 5 mM $Mg(ClO_4)_2$ and the UV-Vis absorption and CD spectra of the resulting solutions were measured. In absence of DNA, cages [Pd_2(**MB-P**)$_4$] (with BF_4^- counterions), [Pd_2(**CV-Q**)$_4$] and [Pd_2(**RE-P**)$_4$] are not soluble in the given conditions, and therefore the corresponding absorption spectra do not afford meaningful information. However, when the cages are mixed with the double-stranded DNA, they show the characteristic signature of the assemblies in the visible range, supporting that the cages interact with the DNA with the effect of bringing the metallo-assemblies in solution. On the other hand, cage [Pd_2(**MB-Q**)$_4$] is soluble in this conditions with the absorption spectrum showing the typical signature of the methylene blue functionality slightly blue shifted due to coordination of the isoquinoline groups to the Pd(II) cations. Upon addition of **15bp dsDNA,** an increase of the absorption intensity can be observed. Also in this case, the positive interaction between the polycation and polyanion species, increases the effective concentration (=concentration of cages not involved in aggregation phenomena) of the metallo-species in solution (see the insets in Figure 5.11). Similar effects were already noticed when a different cage, a double-interpenetrated multicavity cage featuring five consecutive pockets ([$5Cl@Pd_6L^1_8$]$^{7+}$ in Figure 5.10), was let to interact with short **15bp dsDNA** and long Calf-thymus DNA. There, the 7+ charged cage was obtained combining two approaches, the construction of a multidentate ligand that assembles into a two-cavity host and its dimerization via mechanical bond. It was found to aggregate in monolayered discs of 32 components and with a 14.2 nm diameter. Interestingly, it was observed that the cages' UV signature significantly rises in intensity after addition of equimolar amounts of DNA. Thus, the DNA breaks up colloidal cage aggregates, hence increasing the effective cage concentration in aqueous solution.[57]

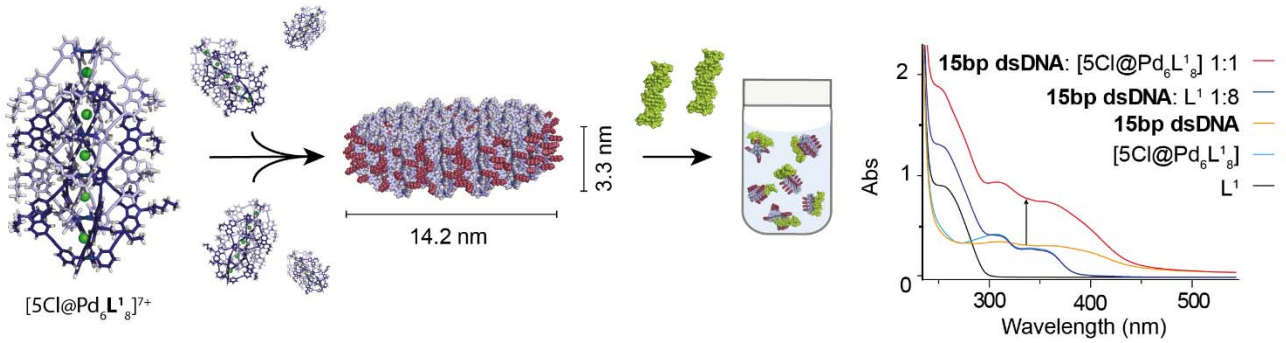

Figure 5.10: Cage [5Cl@$Pd_6L^1_8$] aggregates in 32-membered monolayered discs of the indicated dimensions. Interaction with double-stranded DNA (green in the Figure) breaks up the aggregates and brings the cages in solution as indicated by the rise in absorption intensities of the cage solutions in the presence of DNA. All measurements were performed in 10 mM sodium cacodylate buffer at pH 7.2 in a mixture of water:DMSO 9:1 in the presence of 5 mM $NaClO_4$. The concentration of **15bp dsDNA** and cage [5Cl@$Pd_6L^1_8$] were kept for all the measurement at 3 µM, while for ligand L^1 a concentration of 12 µM was kept.

Circular dichroism spectra of solutions composed exclusively of cages [Pd_2(**MB-Q**)$_4$], [Pd_2(**MB-P**)$_4$], [Pd_2(**CV-Q**)$_4$] and [Pd_2(**RE-P**)$_4$] naturally do not show any band, as they are characterized either by no chiral globular shapes or, even if helically twisted and therefore owing axial chirality, they are found as racemic mixtures equally populating the electronic transitions promoted by absorption of right- and left-handed circular polarized light. After mixing them with **15bp ds DNA** in a 1:1 ratio, signals with positive Cotton effects in spectral regions coinciding with the absorption of the 3D chromophores could be observed (Figure 5.11 a). Since the largest effect was observed for cage [Pd_2(**MB-Q**)$_4$], in the further course of the Chapter, we will only concentrate on this system.

Equimolar mixtures of [Pd_2(**MB-Q**)$_4$] and **15bp DNA** result in an induced CD (ICD) signal with positive Cotton effect with a maximum at 686 nm and a minimum at 609 nm, a spectral region coinciding with the absorption of the methylene blue chromophore. In Figure 5.11 b), all the control experiments are reported and confirm that this signal originates exclusively when the cages are assembled and is not caused by the interaction of the free ligand **MB-Q** with the DNA (there will be other examples in the following part where also the ligands undertake chiral conformations as a result of chiral induction from some G-Quadruplex structures). Next, the dependence of the relative concentration of the **15bp dsDNA** and cage [Pd_2(**MB-Q**)$_4$] on the extent of chiral induction was explored, making use of the method of continuous variation. Assuming that the effective concentration of the DNA-cage complex is directly proportional to the observed CD band intensity, the CD peak intensity at 686 nm was plotted against the molar fraction of the DNA (X_{DNA}) and a parabola-shaped curve centered at X_{DNA} = 0.5 was obtained, typical for a 1:1 stoichiometry.

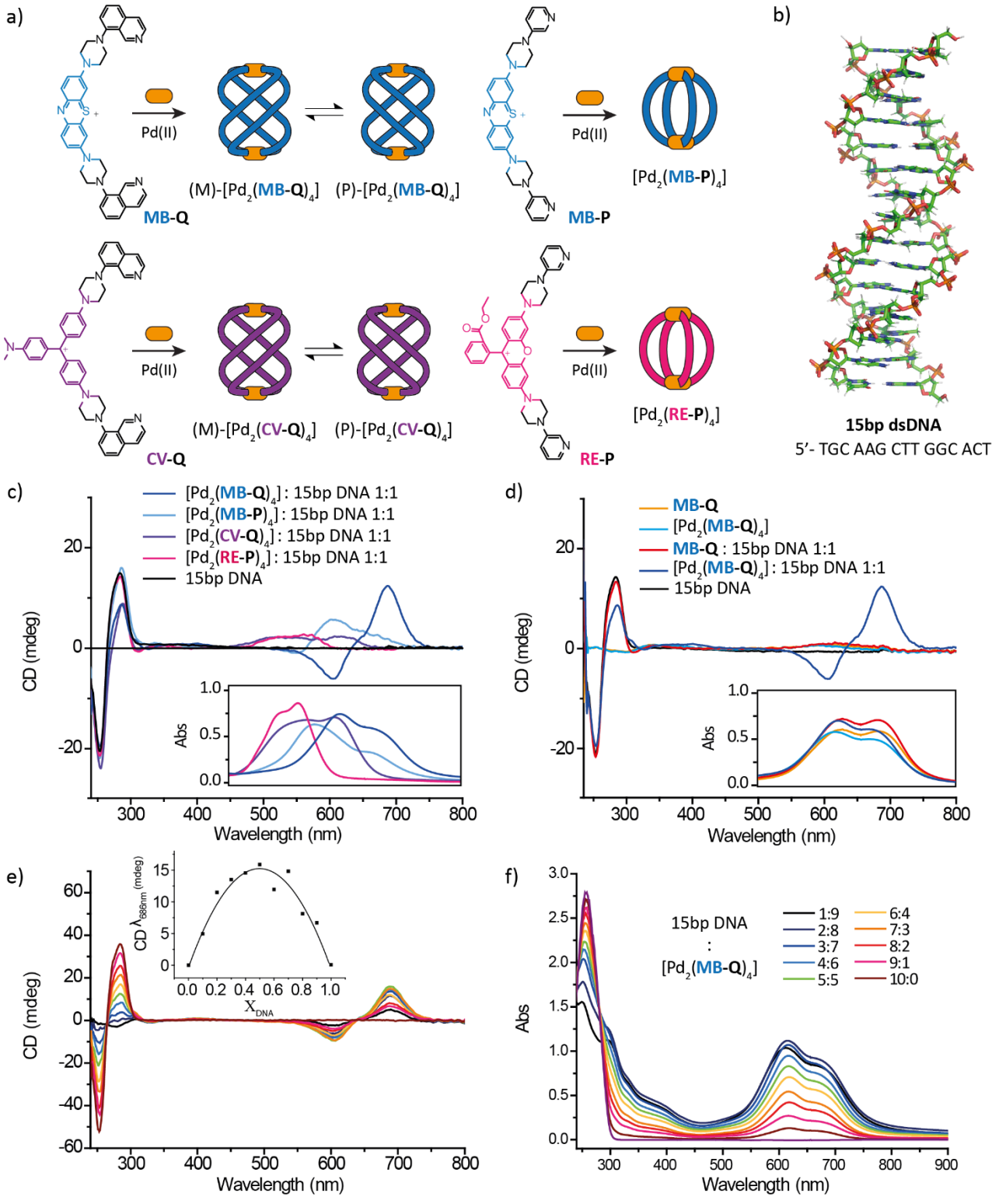

Figure 5.11: a) Cage formation from ligands **MB-Q**, **MB-P**, **CV-Q** and **RE-P**. b) Structure and sequence of **15bp dsDNA**. c) CD spectra with absorption spectra insets of 6 µM **15bp dsDNA** (black line) and: 6 µM [Pd_2(**MB-Q**)$_4$] (blue line); 6 µM [Pd_2(**MB-P**)$_4$] (light blue line); 6 µM [Pd_2(**CV-Q**)$_4$] (violet line); 6 µM [Pd_2(**RE-P**)$_4$] (pink line). d) CD spectra with absorption spectra insets of: 6 µM **15bp dsDNA** (black line); 24 µM ligand **MB-Q** (orange line); 6 µM [Pd_2(**MB-Q**)$_4$] (light blue line); 6 µM **15bp dsDNA** and 24 µM ligand **MB-Q** (red line); 6 µM **15bp dsDNA** and 6 µM [Pd_2(**MB-Q**)$_4$] (blue line). e) CD spectra with Job Plot inset with CD intensity at 686 nm and f) UV-Vis absorption spectra of method of continuous variation for cage [Pd_2(**MB-Q**)$_4$] and **15bp dsDNA**. The sum of cage and DNA concentration is kept constant and equal to 12 µM. All the measurements were performed in 9:1 H_2O:DMSO solutions at 25 °C with 10 mM NaCaCo buffer (pH 7.2), 5 mM $Mg(ClO_4)_2$.

Since the **M** and **P** enantiomers of [Pd_2(**MB-Q**)$_4$] are in a fast interconversion equilibrium, they cannot be separated and singularly studied. Therefore, direct assignment of the enantiomer that shows the greater binding preference with the DNA was not possible. For this reason, ECD calculations were performed on a DFT level using different functional/basis set combinations, allowing us to attribute the isomer with the positive Cotton effect to the (M)-[Pd_2(**MB-Q**)$_4$] cage isomer (see Experimental Part section 5.5.3). Other methods to obtain such information would rely on solid-state structure solution of the cage co-crystallized with a second compound of known absolute chirality and that is known to shift the enantiomer equilibrium to one side, measurable with CD. The same concept would also apply to the covalent attachment a chiral auxiliary to the structure.

The interaction of [Pd_2(**MB-Q**)$_4$] with single-stranded DNA (9:1 water:DMSO in 10 mM NaCaCo, pH 7.2, and 5mM $Mg(ClO_4)_2$), more precisely the two complementary strands that fold into **15bp dsDNA** (15bp ssDNA A and B), results in CD spectra (Figure 5.12 a) with a small ICD signal with a positive Cotton effect. The different extent of chiral induction might reflect the different degree of helicity adopted by double-stranded DNA compared to single-stranded DNA.

Shorter double-stranded DNA composed of 5 (**5bp dsDNA**), 7 (**7bp dsDNA**) and 10 base pairs (**10bp dsDNA**), in the same condition as previously described, interact with [Pd_2(**MB-Q**)$_4$], transferring their chiral information, measurable with CD spectroscopy. The originated signal has the same signature as with **15bp dsDNA**, however of lower intensity. It must be noted that the measurements are all recorded at 25°C, a temperature in which the short double-stranded DNA is in equilibrium with the unfolded single strands, especially for the shortest **5bp dsDNA**.

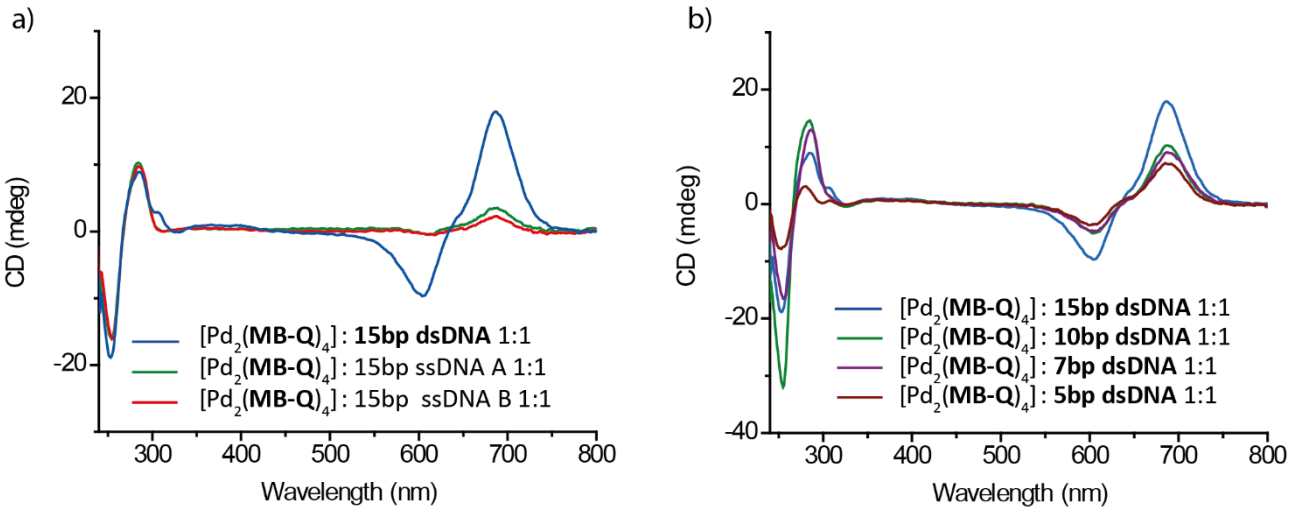

Figure 5.12: All the measurements were performed in 9:1 H_2O:DMSO solutions at 25 °C with 10 mM LiCaCo buffer (pH 7.2), 5 mM $Mg(ClO_4)_2$, DNA and cage concentration kept constant and equal to 6 µM. DNA: a) **15bp ds DNA** (blue line), 15bp ssDNA A single-stranded DNA (green line, 5'- TGC AAG CTT GGC ACT) and 15bp ssDNA B single-stranded DNA (red line, 3'-AGT GCC AAG CTT GCA); b) **15bp dsDNA** (blue line), **10bp dsDNA** (green line, 5'-TGC AAG CTT G), **7bp dsDNA** (violet line, 5'-TGC AAG C) and **5bp dsDNA** (brown line, 5'-TGC AA).

5.2.2 Interaction with G4s

Similar observations were made when [Pd_2(**MB-Q**)$_4$] was mixed in a 1:1 ratio with unimolecular G-quadruplex *htel22* (5'- AGG GTT AGG GTT AGG GTT AGG G) in lithium cacodylate (LiCaCo) buffer (pH 7.2) with 10 mM $KClO_4$, conditions in which this DNA sequence is known to adopt a hybrid-3 type topology. Virtually the same CD signature previously obtained with **15bp dsDNA** with a maximum at 686 nm and a minimum at 609 nm, indicating population of the (M)-[Pd_2(**MB-Q**)$_4$] enantiomer, was measured (Figure 5.13 b), suggesting a similar homochiral helical packing. Most interestingly, when the same conditions were applied to a different G-quadruplex, namely c-*Myc27* (5'- TGG GAG GGT GGG GAG GGT GGG GAAG G), known to form different parallel topologies, preference for the other enantiomer, (P)-Pd_2(**MB-Q**)$_4$, was detected. Nucleotides of htel22 and c-Myc27 own the same point chirality and their secondary structures exhibit the same helical chirality (right-handed). Consequently, different structural recognition processes must be involved in the interaction of the G4s with the cage to favorite opposite enantiomer. To explore the concentration dependence of the interaction between the G4s and the cage, the method of continuous variation with both sequences *htel22* and *cymc27* was performed under the same conditions as previously described. Assuming that the effective concentration of the preferred G4-cage complex (or the difference in concentration of the complexes formed with the two enantiomers of the cage) is directly proportional to the observed CD band intensity, the CD peak intensity at 686 nm was plotted against the molar fraction of the DNA (X_{DNA}). For *htel22*, a parabola-shaped curve centered at X_{DNA} = 0.5 was obtained, typical for a 1:1 stoichiometry (Figure 5.13 c). When the same experiment was performed with *c-Myc27*, a much more complicated curve shape resulted, indicating that at least two equilibria coexist in the system. As shown in Figure 5.13 d), at high X_{DNA} the CD signal gets more and more intense, while at low X_{DNA} the signal gradually loses intensity, indicating that the interconversion equilibrium shifts from the **P** enantiomer to the **M**. At X_{DNA} around 0.275 no CD signal is observed (CD=0 mdeg) indicating an equimolar concentration of **P** and **M** enantiomers. At lower X_{DNA} values, the **M** enantiomer becomes more pronounced.

Another intriguing effect was observed when Na^+ instead of K^+ was used as electrolyte in the solution. In the case of *htel22*, it was described that different electrolytes stabilize different topologies.[17] The DNA CD signature between 200-300 nm clearly shows a hybrid-3 topology with K^+ and an antiparallel with Na^+ as cation. Nevertheless, both samples show the same cage-related CD signature, however with different relative intensities, suggesting a stronger preference/higher binding constant for the (M-[Pd_2(**MB-Q**)$_4$] enantiomer in case of the hybrid-3 type topology (see Experimental Part Figure 5.22). In the case of *c-Myc27*, however, although only minor CD-spectral changes (besides an intensity modulation) are observed in the DNA region, different electrolyte solutions clearly favor the enrichment of different enantiomers of the cage (Figure 5.13 d). It is known that *c-Myc27* is a polymorphic sequence and can form multiple G4 structures. In the section 5.3.1 of this chapter a deeper investigation on such sequence will be presented.

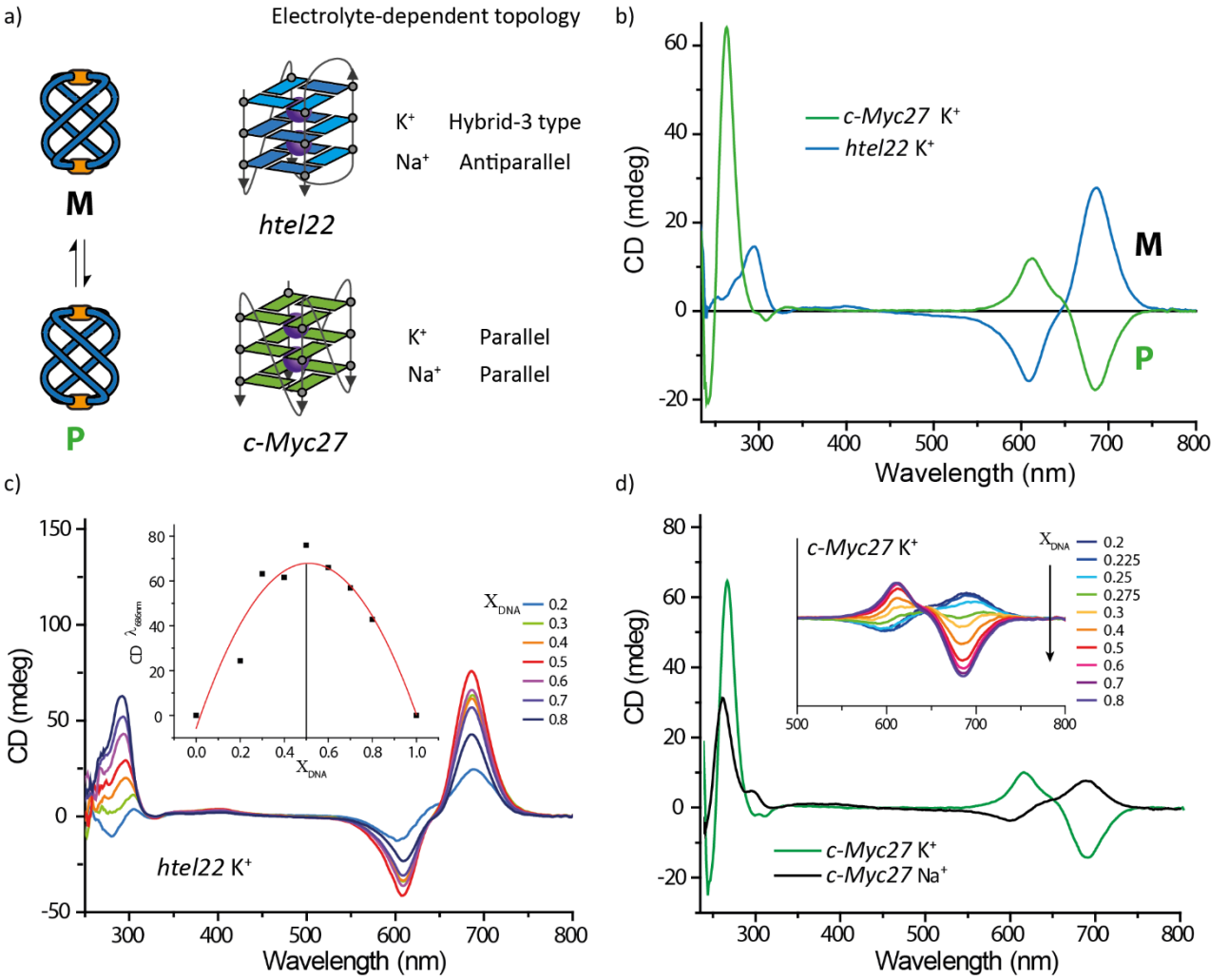

Figure 5.13: a) Schematic representation of *c-Myc27* and *htel22* with the corresponding topologies in different electrolytes conditions indicated. CD spectra of 9:1 H_2O:DMSO solutions with 10 mM LiCaCo buffer (pH 7.2) and specified electrolyte. b) 6 µM [Pd_2(**MB-Q**)$_4$] with 6 µM *htel22* (blue line) and *c-Myc27* (green line) in 10 mM $KClO_4$. c) Continuous concentration variation and Job plot of [Pd_2(**MB-Q**)$_4$] and *htel22*. The sum of the two concentration is constant and equal to 24 µM in 10 mM $KClO_4$. d) 6 µM [Pd_2(**MB-Q**)$_4$] with 6 µM *c-Myc27* in 10 mM $KClO_4$ (black line) and 10 mM $NaClO_4$ (green line) and continuous concentration variation in the inset. The sum of the DNA and cage concentration is kept constant and equal to 24 µM in 10 mM $KClO_4$.

In order to gain better insight into the origin of the chiral recognition process for the different structures and topologies of G4s, the chiroptical response of the cage binding to different G4s was investigated. A convincing range of structural diverse G4s included 13 different unimolecular sequences (Figure 5.14 a), four tetramolecular (Figure 5.14 b) and three bimolecular ones (Figure 5.14 c), both in $KClO_4$ and $NaClO_4$ electrolyte-containing solutions.

In the experimental part of this chapter in Table 5.4, the full sequences, naming schemes and additional information of the DNA employed for this study are reported. In Figures 5.22-26 the CD and UV-Vis absorption spectra for each sequence of the G4 in pure water, G4 in 9:1 H_2O:DMSO mixtures, G4 and ligand **MB-Q** in a 1:4 ratio (same number of ligands as in the cage) in 9:1 H_2O:DMSO mixtures and G4 and cage [Pd_2(**MB-Q**)$_4$] in a 1:1 ratio in 9:1 H_2O:DMSO mixtures are reported. The measurements were performed at 25 °C, in 10 mM LiCaCO buffer (pH 7.2) in both $KClO_4$ and $NaClO_4$ electrolyte-containing solution (10 mM), containing 6 µM of the G4, if present 24 µM of ligand **MB-Q** and if present 6 µM of [Pd_2(**MB-Q**)$_4$].

The measured CD signatures arising from the interaction of the analyzed G4s with [Pd_2(**MB-Q**)$_4$] are reported in Figure 5.14. In the different insets of the figure, G4s formed by the same number of strands coming together (molecularity) are grouped: unimolecular (a), bimolecular (b) and tetramolecular (c) G4s. Within the unimolecular ones, different topologies are depicted in different colors, and different electrolyte conditions in different shades, to allow a better understanding of the respective results. G4s owing parallel topologies are reported in green (dark green with Na^+ and light green with K^+), antiparallel topologies in pink and hybrid topologies or G4s that can form multiple topologies (mixed topologies) in blue (dark blue with Na^+ and light blue with K^+). It can be directly observed that, independently from the molecularity of the G4, its topology, the loops orientation and length, sequence and therefore charge, the preferred enantiomer for most G4 structures is **M.** Only specific sequences in certain conditions, parallel unimolecular G4, resulted in the **P** enantiomer signature, with *c-Myc27* delivering the clearest effect in this respect (black curve in Figure 5.14 a). Within the unimolecular topologies, besides the parallel topologies that give rise to the **P** signature of the cage, a general trend connected to the CD band intensity can be observed. The highest ICD signal is given by hybrid/mixed topologies in K^+, followed by hybrid-mixed topologies in Na^+, followed by antiparallel topologies and at last parallel topologies. For tetramolecular G4s, the signal intensity is always relatively small except for (TGG GGT)$_4$ in K^+, probably indicating that the loop regions are important in the recognition process. Indeed, bimolecular G4, characterized by at least 2 loops, show higher CD intensities. However also the length and consequent charge of the oligonucleotide must be taken into consideration since the highest charge leads to the highest electrostatic contribution to the binding strength. On the other hand, the CD signature of the DNA (region between 240-350 nm) with or without the metallo-helicate were mostly not affected. Small differences were observed for G4s that form mixture of topologies (see controls in Figure 5.22-5.26).

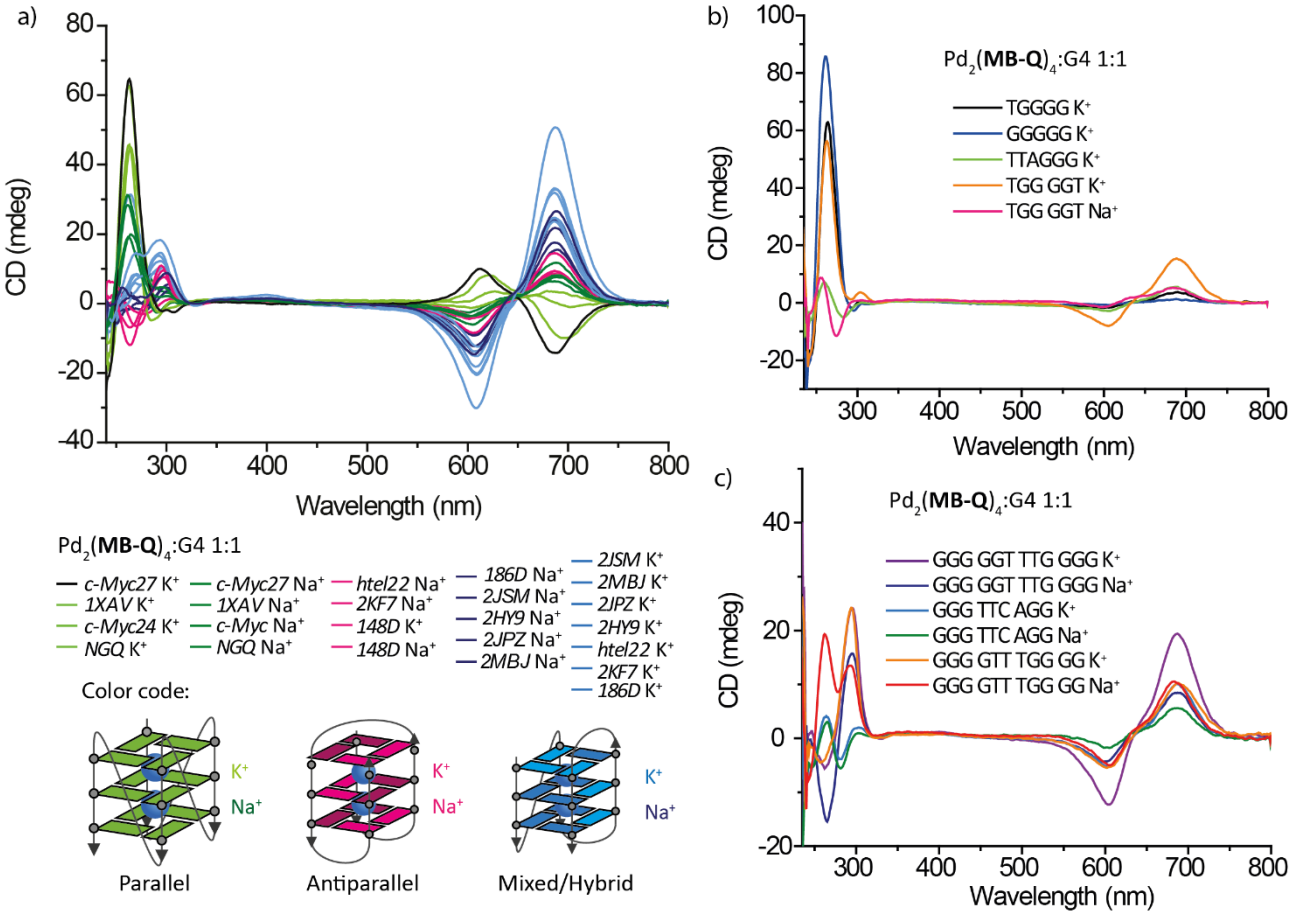

Figure 5.14: CD spectra of 9:1 H_2O:DMSO solutions with 10 mM LiCaCo buffer (pH 7.2), 6 µM [Pd_2(**MB-Q**)$_4$] and 6 µM G4 in 10 mM $KClO_4$ or 10 mM $NaClO_4$ as indicated. G4: a) Unimolecular G4s named after their PDB identification code and colored as indicated, b) tetramolecular G4s, c) bimolecular G4s.

5.2.3 ICD on MB-Q

The interaction of ligand **MB-Q** with the G4 DNA is expected since already multiple **MB** derivatives, also similar to **MB-Q** have been found to stack on top of G-tetrads and stabilize the overall structure.[53] In order to maximize the positive interaction, the binding of flat ligands to DNA, might also lead to the population of chiral conformations for the organic molecule, an effect which is measurable with CD spectroscopy. For most of the analyzed sequences, the chiral induction on ligand **MB-Q** is not significant or of very low intensity (Figure 5.15 for *2HY9* and *2KF7*). However, for one specific case, G4 *2JPZ* in Na^+ electrolyte solution, the extent of the chiral induction is much greater. The strong ICD signal with negative Cotton effect with minimum at 590 nm and maximum at 545 nm is indicative of a specific binding mode for **MB-Q** on the G4, different from the other G4s under study. Melting experiments, gel electrophoresis studies, together with NMR and mass spectroscopy, will bring important additional information in future research studies to deeper understand such binding mode. Here, we concentrate on the metallo-helicate interaction.

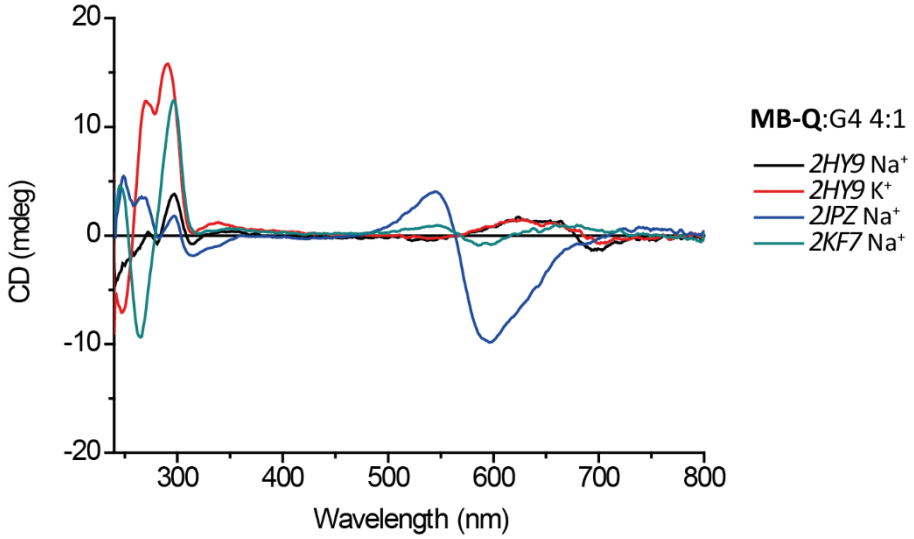

Figure 5.15: CD spectra of 9:1 H_2O:DMSO solutions, 10 mM LiCaCo buffer (pH 7.2) with 10 mM $KClO_4$ or $NaClO_4$ as indicated in the legend and 6 µM DNA (black line *2HY9* with Na^+, red line *2HY9* with K^+, blue line *2JPZ* with Na^+ and green line *2KF7* with Na^+) and 24 µM of ligand **MB-Q**.

5.2.4 Melting experiments

DNA melting experiments with *htel22* and *c-Myc27* in Na^+ and K^+ electrolyte solutions (Table 5.1) were performed to investigate the G4s stability in the presence of the cage and the single components. Not particularly surprising, since methylene blue derivatives are already known as G4 stabilizers, ligand **MB-Q** alone (in blue in Figure 5.16) has an overall stabilization effect on both G4s in both electrolyte conditions. Completely different results are observed for the Pd-assembly (in green). The cage shows a general tendency of destabilizing the DNA when the **M** enantiomer of the cage is the best binding partner (*htel22* K^+, *htel22* Na^+, *c-Myc27* Na^+). Interestingly, the opposite effect, a stabilization of the G4 is observed, when the **P** cage enantiomer is the better binder (*c-Myc27* K^+). The different stabilization effects are already an indication for different binding modes for the different G-quadruplexes: a not-specific and weak binding effect when the cage signature is **M** and a rather specific and more stable one then the **P** signature is present.

Table 5.1: Melting temperatures of the indicated G-quadruplexes with 10 mM $KClO_4$ or $NaClO_4$ electrolyte solutions in 6 µM concentration with 10 mM LiCaCo buffer (pH 7.2) in the following conditions: in pure H_2O, in 9:1 mixture of H_2O and DMSO, with 24 µM **MB-Q** in a 9:1 mixture of H_2O and DMSO and with 6 µM [Pd_2(**MB-Q**)$_4$] in a 9:1 mixture of H_2O and DMSO. The red signs indicate an increase in melting temperature, and the blue a decrease. The Figure on the right reflects the results reported in the last line of the Table and represents the CD spectral region between 500 and 800 nm where the methylene blue-based helicate absorbs and reports the cage signatures in interaction with the G4s.

	htel22 K^+	*htel22* Na^+	*c-Myc27* K^+	*c-Myc27* Na^+
H_2O	50 °C	40 °C	66 °C	33 °C
9:1 H_2O:DMSO	55 °C	45 °C	74 °C	39 °C
MB-Q	73 °C (+18)	48 °C (+3)	> 95 °C	71 °C (+32)
Pd_2(**MB-Q**)$_4$	52 °C (-3)	42 °C (-3)	> 95 °C	36 °C (-3)
CD signature	**M**	**M**	**P**	**M**

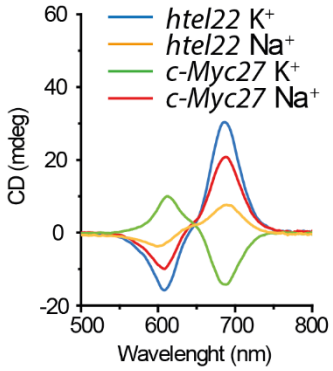

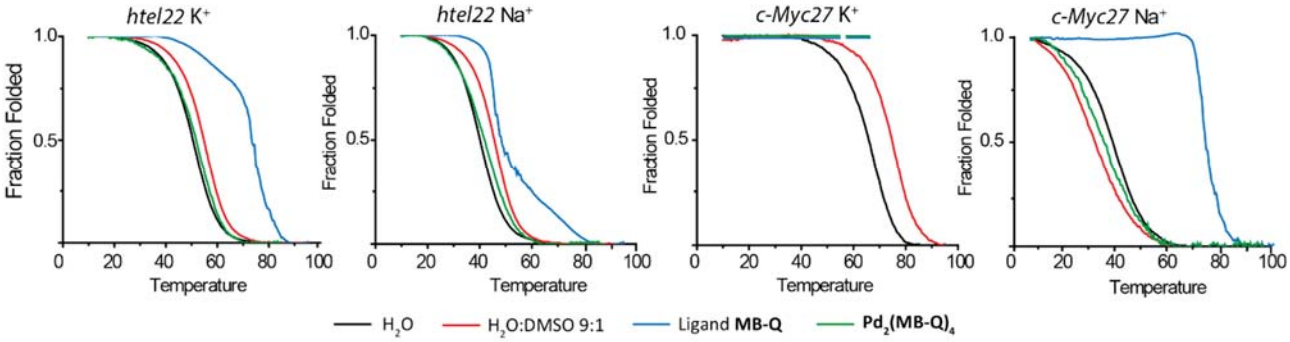

Figure 5.16: UV-based melting curves of G4s *htel22* and *c-Myc27* in the two electrolyte conditions of Na^+ and K^+ in pure water (black line), in 9:1 water:DMSO (red line), in 9:1 water:DMSO with ligand **MB-Q** (blue line) and in 9:1 water:DMSO with cage [Pd_2(**MB-Q**)$_4$] (green line). All measurements were performed in 10mM LiCaCo buffer (pH 7.2), 5mM $NaClO_4$ or $KClO_4$, if present 24 µM ligand **MB-Q** and 6 µM cage [Pd_2(**MB-Q**)$_4$]. Temperature range 10-95 °C.

5.2.5 Docking studies with AutoDock

Preliminary docking studies were performed using the software AutoDock Tools, implemented with the algorithm AutoDock Version 4.2,[58] on three chosen unimolecular G-quadruplex of parallel (*1XAV*), antiparallel (*143D*) and hybrid topology (*2JSM*) in combination with the **M** and **P** enantiomers of the cage. AutoDock is an automated procedure for predicting the interaction of ligands with biomacromolecular targets. The followed procedure is reported in detail in section 5.4.4 of the experimental part. AutoDock calculates several (exactly how many can be changed in the settings, for the presented studies 50 for each combination) docked conformations, assigning estimated energy of binding and highlighting the lowest energy conformations. The final energy values are composed of contribution from the final intermolecular energy (van der Waals, hydrogen bonds and desolvation energy), electrostatic energy, final total internal energy and torsional free energy.

In Figure 5.17, the lowest energy structural conformations obtained for the combination of the two enantiomers and the three G4 topologies are reported. The structures nicely show how the cages dock side to side (not through the palladium centers) along the sugar-phosphate backbone of the DNA, where the negative charge is localized. However, if looking for theoretical support in the different chiral recognition processes involved for the different structure, highlighting the best binder for *1XAV* to be the **P** enantiomer and the **M** enantiomer for the other two G4s, the simulations were not conclusive. In Table 5.2, the energy values for each of the six combinations are reported. A big difference between the two enantiomers of the cage with the same G4 could not be observed, and especially the results are not in line with the experimentally obtained ones.

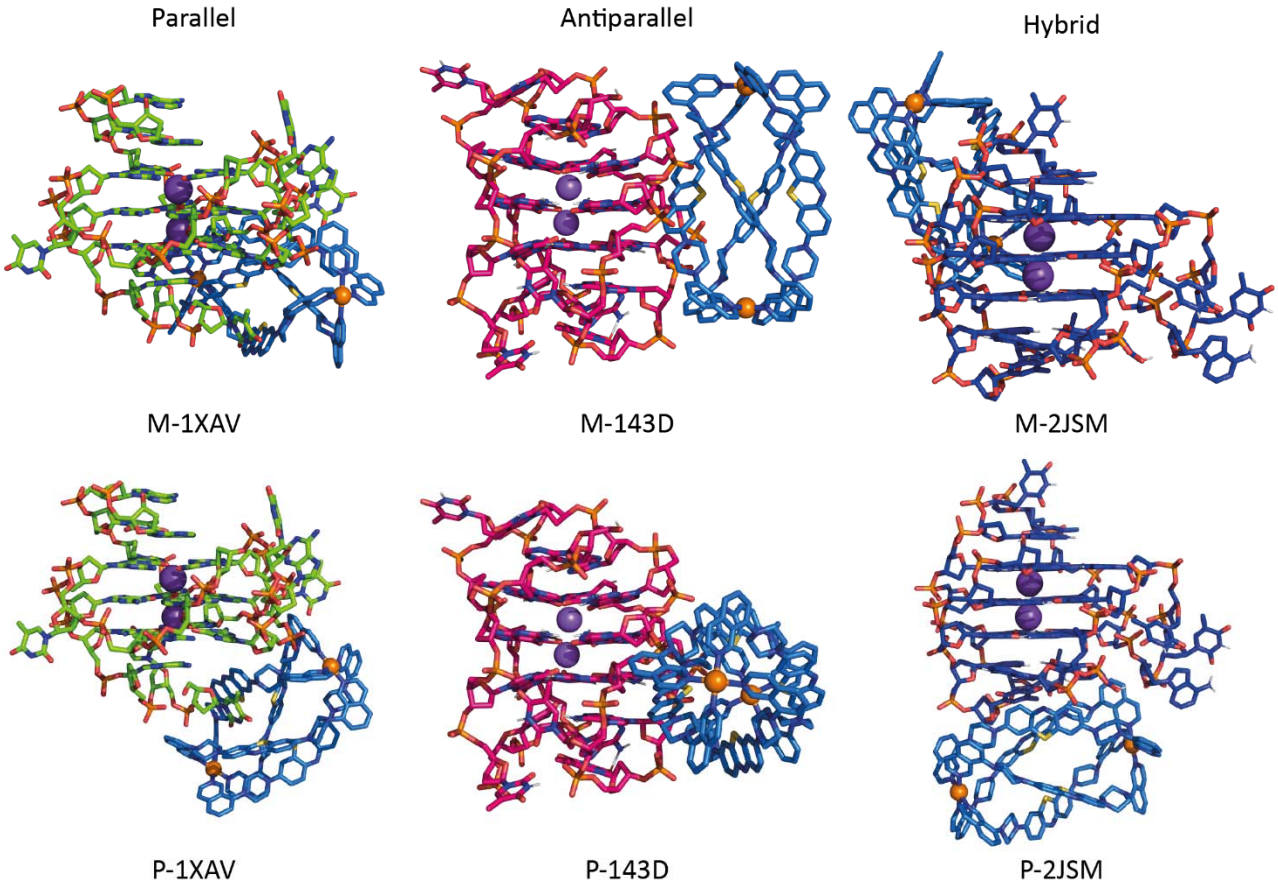

Figure 5.17: Lowest energy docked structural conformations for the combination of the **M** and **P** enantiomer of the helicate and the three G4 topologies *1XAV* (parallel topology in green), *143D* (antiparallel topology in pink) and *2JSM* (hybrid topology in blue).

Table 5.2: Energy values of the lowest energy conformations. The (**M**) or (**P**) in the name and topology field of the G4 indicates the measured CD signature for the preferred enantiomer of $[Pd_2(\mathbf{MB\text{-}Q})_4]$.

	1XAV Parallel (**P**)	*143D* Antiparallel (**M**)	*2JSM* Hybrid (**M**)
M	-9.29 kcal/mol	-10.35 kcal/mol	-9.00 kcal/mol
P	-9.00 kcal/mol	-9.74 kcal/mol	-9.07 kcal/mol

Naturally, the presented docking studies are still in their initial state and would require many more improvements until reliable information can be extracted. Only to name a few possible changes, a first option could be to manually change also the charges of the DNA structures with the most commonly used RESP charges; or an algorithm for *blind docking* (when the specific docking site is unknown) could be implemented rather than the preselected ones which are made for docking of small molecules in defined pockets. The chosen software, AutoDock, was initially created and optimized for different binding partners, like proteins and small neutral organic ligands, and might also not be the best possible choice in this context. Molecular Dynamics simulations might lead to deeper insights on the binding events.

5.2.6 C-Myc27 investigation

The special chiral recognition on *c-Myc27* combined with the high biological relevance of the G-quadruplex in the promoter region of MYC, led to deeper analysis of this particular sequence (Figure 5.18). *c-Myc27*, or more often named *Pu27* in the literature, is composed of 27 nucleobases with 6 guanine-tracks. The oligomer can fold in multiple ways and form different G4s, however most of them are characterized by a parallel topology. A great number of research groups tackled the structural elucidation problem of such sequence with the purpose of better designing selective drugs and specifically control the c-MYC gene expression. However, the high number of morphology that can originate from native sequence does not provide insights when studied with NMR spectroscopy since a mixture of all possible G4 conformations is observed and could not be crystallized for solid-state structure analysis. For the mentioned reasons, the general tendency in the literature is to "simplify" the sequence, by shortening it and exchanging guanine bases for bases that do not engage in G4 formation and to study the resulting single morphology. Several solution and solid-state structures have been obtained for the reported mutations that could lead to insights in the field and promising selective binders. [12,14,18,20,59–66]

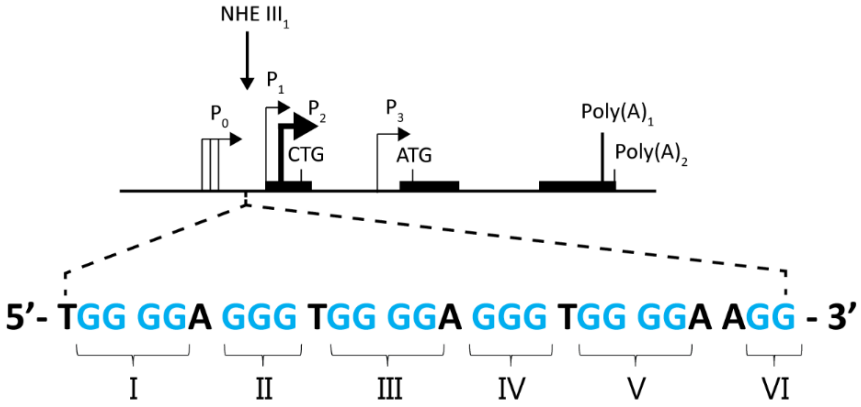

Figure 5.18: Promoter structure of the c-MYC gene and location of the NHE III_1.

In the original selection of G4s and topologies, beside *c-Myc27*, two more sequences, *1XAV* and *c-Myc24*, were chosen that are related to the same promoter region and can be accounted as modification of *c-Myc27*. *1XAV* is a NMR structure solution of what is considered the major G4 formed in the human c-MYC promoter, representing a parallel unimolecular G-quadruplex.[65] When interacting with [Pd_2(**MB-Q**)$_4$], it shows very similar results to *c-Myc27*, as in the CD spectral region around 600-700 nm, in K^+ electrolyte solutions, the negative Cotton effect signal of the **P** enantiomer of the cage can be observed, while in Na^+ electrolyte solution the **M** signature is detected. On the other hand, *c-Myc24*, is a truncated version of c-Myc27 in which the last three nucleotides, including two guanine residues and og VIth G-rich region, are missing. While in Na^+ condition it shows the typical **M** signature, in K^+ it shows almost no ICD.

Fascinated by these effects and wondering whether this could lead to an elucidation of where in *c-Myc27*, or with which of the multiple morphology, the supramolecular specific chiral recognition with the **P** enantiomer of the cage is occurring, 6 more shorter *c-Myc27* mutations and a longer *Pu47*, where 10 more nucleobases before and after the *c-Myc27* sequence are taken into account (Table 5.3), were investigated. The binding of the cage in both K^+ and Na^+ electrolyte conditions was analyzed, following the general measurement conditions and the CD signatures arising with [Pd_2(**MB-Q**)$_4$] compared with *c-Myc27*.

Table 5.3: c-Myc27 mutations and truncations most often found in the literature and investigated in this study.

c-Myc sequences: Literature name	Sequence 5´-3´	G regions	VI
Pu27, c-Myc27	TGG GGA GGG TGG GGA GGG TGG GGA AGG	I-VI	Y
1XAV (22)[65]	TGA GGG TGG GTA GGG TGG GTA A	II-V	N
Pu22[62]	TGA GGG TGG GGA GGG TGG GGA A	II-V	N
Pu24 [63,66]	TGA GGG TGG GGA GGG TGG GGA AGG	II-VI	Y
Pu21_2-5[64]	GA GGG TGG GGA GGG TGG GGA A	II-VI	N
Pu21_1-4[64]	A TGG GGA GGG TGG GGA GGG TG	I-IV	N
c-Myc24 (Pu27-3endnuc)	TGG GGA GGG TGG GGA GGG TGG GGA	I-V	N
c-Myc 25 (Pu27-2endnuc)	TGG GGA GGG TGG GGA GGG TGG GGA A	I-V	N
c-Myc 26 (Pu27-1endnuc)	TGG GGA GGG TGG GGA GGG TGG GGA AG	I-V	N
Pu47	C TAT GTA TAC- -TGG GGA GGG TGG GGA GGG TGG GGA AGG- -TTA GCG GCA C	I-V	Y

In Figure 5.19 the CD signatures of cage-G4 species are reported in both Na^+ and K^+ electrolyte conditions. The first important observation is that indeed all the sequences form parallel G4 which give the typical CD signature with a maximum at ca. 260 nm and a minimum at ca. 240 nm. Despite the very complicated systems under study and multiple interactions and effects involved, there is an observable trend in the results obtained. If the sequences are cathegorized based on what G-rich track they contain and whether they include or not the VIth region, which is composed of only two guanine residues, the following can be obtained:

a) Sequences *1XAV* and *Pu22* both truncate the Ist G-rich region and include regions II to V. Both, in combination with the cage, prefer the **P** enantiomer for K^+ solution and the **M** enantiomer for Na^+, similar to *c-Myc27*.
b) *Pu21_2-5* and *Pu24* include regions II to V with *Pu24* including also region VI. Both sequences in combination with the cage in both electrolyte conditions give the **P** enantiomer of the cage, with *Pu24* giving the highest answer of all.
c) *Pu21_1-4* include exclusively the first four regions and in both electrolyte conditions give the **M** enantiomer. Pu47 is a much longer sequence and also shows in both electrolyte conditions the enantiomer **M**.
d) *c-Myc24*, 25 and 26 are very similar to *c-Myc27*, the only difference lays in the presence of last 3 nucleotides and region VI. Extremely interestingly, also in this case, the cage answer is always **M**, even with *c-Myc26* which is only one guanine shorter than *c-Myc27*. This information directly indicates the importance of region VI in the binding mode that favors enantiomer **P** over the **M**.

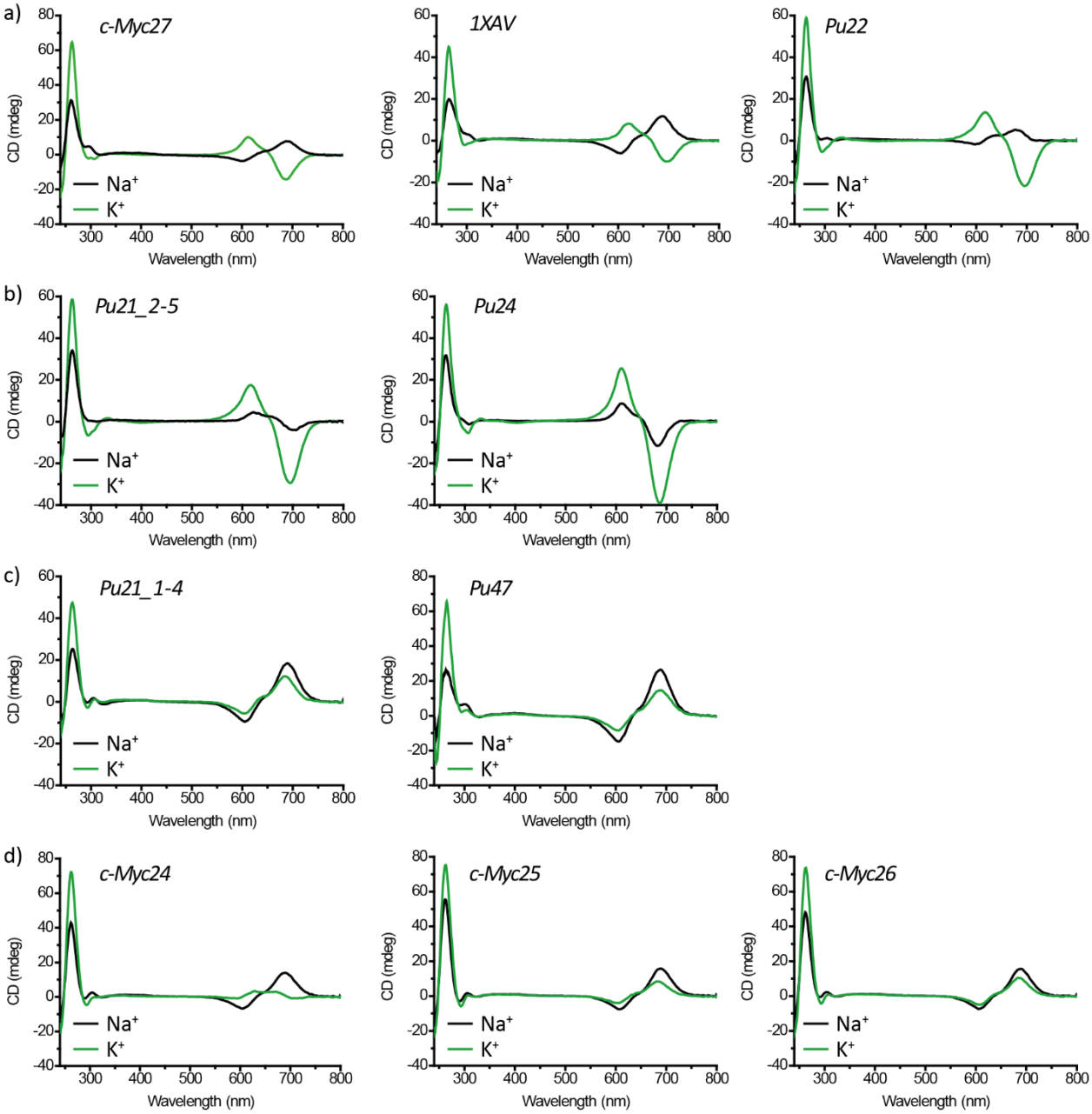

Figure 5.19: CD spectra of 9:1 water:DMSO solutions, 10 mM LiCaCo buffer (pH 7.2), 5 mM $NaClO_4$ (black lines) or 5 mM $KClO_4$ (green lines), 6 µM [Pd_2(**MB-Q**)$_4$] and 6 µM G4. G4: a) *c-Myc27*, *1XAV*, *Pu22*; b) *Pu21_1-4*, *Pu24*; c) *Pu21_1-5*, *Pu47*; d) *c-Myc24*, *c-Myc25* and *c-Myc26*.

It is strongly believed that in order to obtain full and exhaustive explanations of the behavior of such sequences in combination with [Pd_2(**MB-Q**)$_4$], much more experimental data (NMR, ESI-MS, melting experiments, gel electrophoresis, …) must be collected and analyzed, probably even with the support of calculations and atomic simulations. However, a theory can already be hypothesized: *c-Myc27* can fold into different topologies, all parallel, that generally have unspecific binding with the cage, leading to the general **M** signature, except for one, that will be named A that leads to the special chiral recognition with the **P** enantiomer of the cage. When only regions 1-4 or 1-5 are included in the studied sequences, the majority of G4 formed are not A. When only regions 2 to 5 are part of the sequence under study, at least two topologies can form, one of which is A, and the other(s) lead to the unspecific binding. A is stabilized by K^+ but not as much by Na^+, which leads to preferential formation of the other topologies. If region 6 is also part of the assembly, it helps to stabilize A even in Na^+ electrolyte solutions (see *Pu24*!).

5.2.7 Competition experiments

Most interestingly, the typical signature of the **P** enantiomer could be observed in the CD spectrum of a mixture of equimolar amounts of *htel22*, *c-Myc27* and Pd_2(**MB-Q**)$_4$ in K^+ buffer, indicating that the cage seems to selectively interact with the *c-Myc27* G-quadruplex. This selectivity was observed not only in mixtures of two different G-quadruplexes, but also when *c-Myc27*, *htel22* and G-quadruplex *148D*, giving a clean antiparallel topology in K^+ solutions, and *2JSM*, adopting a hybrid-3 topology in K^+ solution (and the strongest CD answer of the **M** enantiomer when examined alone), were mixed in different combinations. Again, only in those solutios in which *c-Myc27* is present, the **P** signature was observed, while the **M** enantiomer was found prevalent for every other combination excluding *c-Myc27*. This observation coincides with the strong stabilization found in the melting experiments.

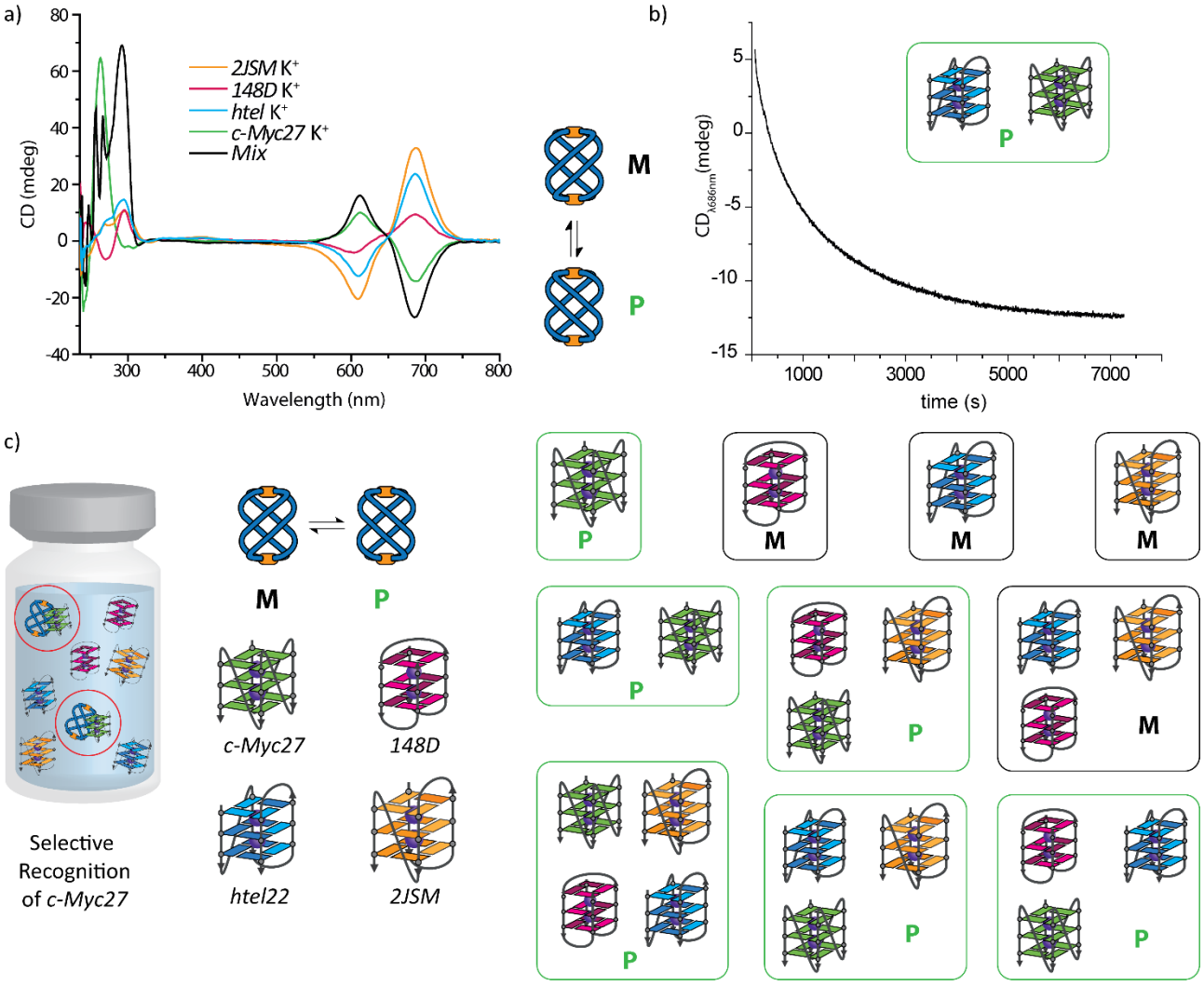

Figure 5.20: a) CD spectra of 9:1 water:DMSO solutions, 10 mM LiCaCo buffer (pH 7.2), 5 mM $KClO_4$, 6 µM [Pd_2(**MB-Q**)$_4$] and 6 µM G4. G4: *c-Myc27* (green line), *148D* (pink line), *htel22* (blue line), *2JSM* (yellow line), mixture of *c-Myc27*, *148D*, *htel22* and *2JSM* (black line). b) Evolution of CD signal over time at 686 nm for the mixture solution with *c-Myc27*, *htel22* and the cage. c) Schematic illustration of the selective recognition process for c-Myc27 with the already-defined color codes for the different G4s. Each box shows the combination of the four different G4s with [Pd_2(**MB-Q**)$_4$] and the enantiomer signature observed in the CD spectrum.

Time-dependent investigation of the cage-G4 complex formation offered further interesting observations. The intensity of the CD signal at 686 nm is indicative of the equilibrium position between the **M** and **P** enantiomer. In the first few seconds after mixing all components together, the sign of the signal is positive (as it could be expected in a situation where no preference on the G4 is shown by the cage), but over time it decays. After almost 60 minutes it gets constant on a negative CD value, indicative

for the **P** enantiomer (in Figure 5.20 b). The methylene blue-based helicate shows preferential binding to *c-Myc27 (thermodynamic product)*. However, initially, it binds with no specificity all G4s in solution driven by electrostatics (*kinetic products*) to than slowly shift to the preferred binding partner.

In order to answer some questions around the nature of the selectivity for *c-Myc27*, some further competition experiments were performed. Sequences of different lengths and therefore of different charge, were employed to ensure that the selectivity is not exclusively due to electrostatic reasons since *c-Myc27* is the longest sequence in the mixture. First *c-Myc27* with *2MBJ* were combined, both sequences are composed of 27 nucleotides and have the same charge. Upon addition of [Pd_2(**MB-Q**)$_4$], a CD signal with negative Cotton effect, with minimum at 686 nm and maximum at 609 nm, was observed, suggesting the **P** enantiomer of the cage. However, the signal showed a pronounced shoulder at 650 nm which was not typically observed for G4-**P** complexes. Such behavior probably indicates that the cage is interacting with both G-quadruplexes but still with a higher preference for *c-Myc27*. Similar results were observed when *1XAV*, considered the major G4 in the c-MYC promoter region, was mixed with *htel22*, both sequences have 22 nucleotides, with the shoulder signal even more pronounced.

It must be specified here, that even if in the overall discussion, the ICD signal was always assigned to either the **M** or **P** enantiomer of the cage, what is really measured is the difference in concentration between the diasteromers of the complexes G4-**P** or G4-**M**. Diasteromers, on the contrary of enantiomers, have different physical properties and therefore the CD signal maxima and minima could be different for each analyzed G4-cage complex. In most of the cases the exact same signal or negligible differences could be observed. But in competition experiments, especially when suspecting that the cage interacts with both G4s, the contributions of all formed complexes, might lead to more complicated spectra.

In the previous section it was learned that the sequence *Pu24*, 24 nucleotides long, is the sequence for which the recognition by the **P** enantiomer of the cage is the highest and probably better represents the core of the specific chiral recognition. This sequence was mixed with *2JSM*, which is only 23 nucleotides long. Not surprisingly, the resulting CD signature upon addition of [Pd_2(**MB-Q**)$_4$] corresponds to the **P** enantiomer. Much more exciting was to observe the same **P** signature when *Pu24* was mixed in solution in combination with *2MBJ*, 3 nucleotides longer and favored from an electrostatic point of view. This result proofs that, not only the cage has a stronger preference to interact with *Pu24* (and by extension with *c-Myc27*), but also that the binding, other than electrostatics, involves further reversible interactions.

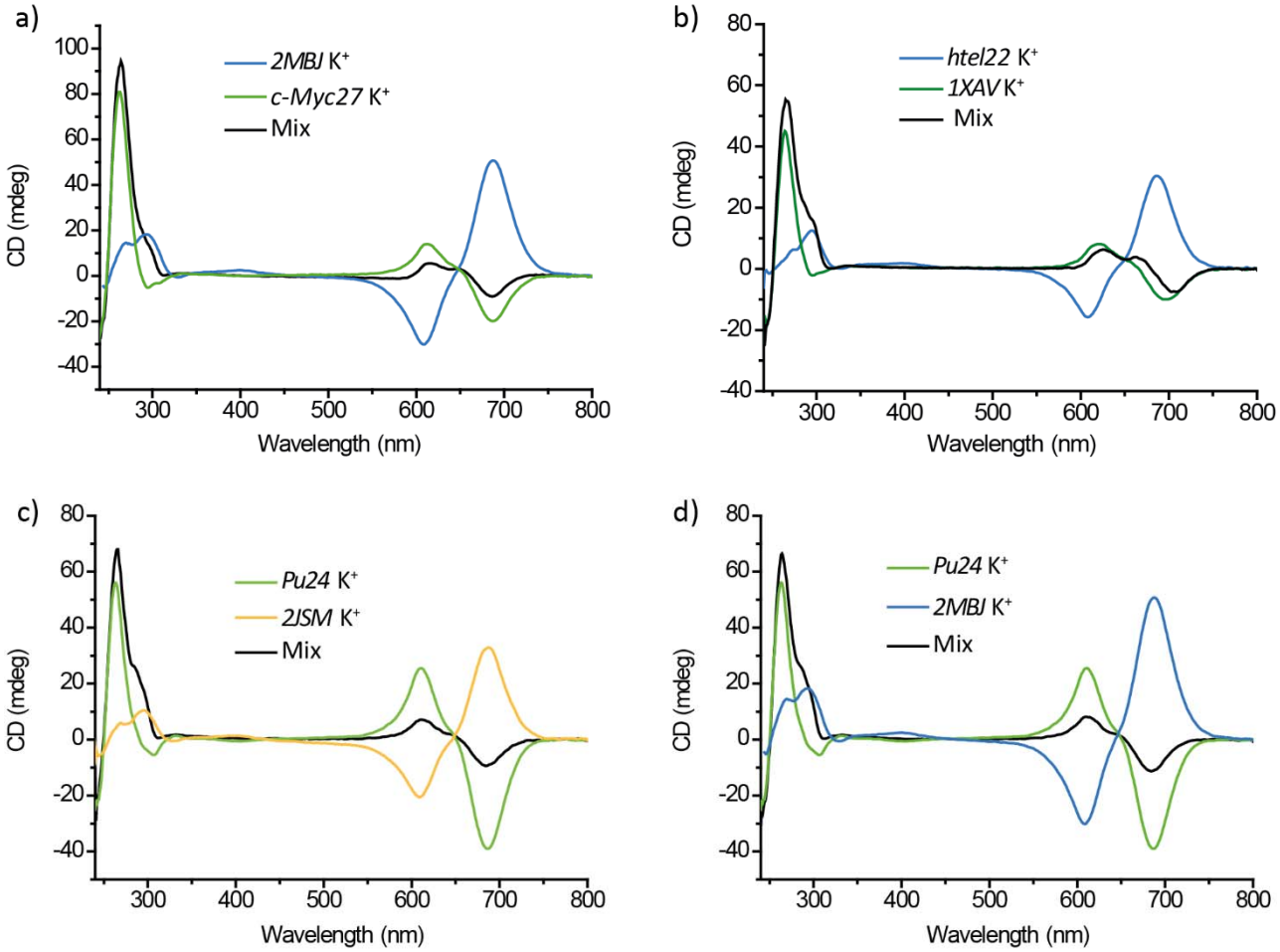

Figure 5.21: Competition experiments in mixture solutions of G4s. The black curve always represents the solution in which the other two G4s indicated in the legend are mixed. All measurements were performed in 9:1 water:DMSO solutions, 10 mM LiCaCo buffer (pH 7.2), 5 mM $KClO_4$, 6 µM $[Pd_2(\mathbf{MB\text{-}Q})_4]$ and 6 µM of each G4 indicated in the legends.

5.3 Conclusion and outlook

In conclusion, a new design of a metallo-helicate was shown, derived from the self-assembly of bis-monodentate isoquinoline ligands with backbones based on the methylene blue dye and palladium cations, that binds to DNA. The metallo-helicate exists as an equilibrium of interconverting enantiomers (**M** and **P**) and the interaction with the DNA is generally stronger with the **M** enantiomer. The cage absorption in the region around 600 nm was exploited to investigate the chiral induction from different DNA structures with special focus on the class of G-quadruplexes due to their high importance in gene regulation. It could be proven that, even if already ligand **MB-Q** alone strongly binds the G4 with an overall stabilization effect, the CD signal that originates from the interaction of the DNA with the cage is exclusively attributed to the cage-DNA complex formation. Most excitingly, the cage's enantiomeric preference of binding was found to be opposite for a specific sequence, *c-Myc27*, which was explored in its known mutations and truncations for simpler G4s topologies and some hypotheses on the specific location of the origin of the different binding could be postulated. Moreover, in competition experiments followed by CD spectroscopy, the **P** signature of the cage was detected when the *c-Myc27* G4 was present in the mixture highlighting recognition specificity for such G4.

The sequence *Pu24* was found as the most promising G4 to deeper analyze the specific recognition process. Since *Pu24* has already been investigated and its solution structure, also in combination with small molecules as binders, is reported in the literature,[63] future research will focus on the NMR solution structure of the G4-helicate complex. In order to understand which of the possible structures that can form from *c-Myc27* sequence is strongly binding the **P** enantiomer of the cage, ESI-MS studies

can offer a deeper insight and important information. Furthermore, crystallization attempts will be tried together with gel electrophoresis studies and melting behavior in order to assess the stabilization properties of the helicate on different topologies. Moreover, collaborative work on molecular dynamics simulation of the interaction will be established.

In parallel, in view of the high stabilization properties of ligand **MB-Q** encountered in the presented results, such effect will be explored on other different G4s and compared with the known methylene blue derivatives. Special focus will be put on the *2JPZ* sequence to understand the origin of the chiral induction.

The extraordinary affinity of the here presented binding agent [Pd_2(**MB-Q**)$_4$] for the sequence found in the promoter region of c-MYC, sparks the interest on how this would affect the highly important regulation role of the gene. For this reason, collaborative studies could be established to investigate the action of [Pd_2(**MB-Q**)$_4$] first in longer, *c-Myc27*-containing DNA sequences (for examples as PCR products), followed by in vitro cell studies. Since higher stability of the helicate might be required for these kinds of biological applications, the Pt-analogue of the methylene blue-based structure should be synthesized and employed.

5.4 Experimental Section

Table 5.4: Oligonucleotides used in this study.

ID	CD 686nm	M/P	bases	G		derivation		Sequence
15bp dsDNA	15.89	**M**	15	4			ds	TGCAAGCTTGGCACT
15b ssDNA A	3.48	**M**	15	4			ss	TGCAAGCTTGGCACT
15b ssDNA B	2.25	**M**	15	4			ss	AGTGCCAAGCTTGCA
10bp dsDNA	10.18	**M**	10				ds	TGCAAGCTTG
7bp dsDNA	9.00	**M**	7				ds	TGCAAGCT
5bp dsDNA	7.09	**M**	5				ds	TGCAA
htel22_K	23.69	**M**	22	12	X-ray	htel	uni	AGGGTTAGGGTTAGGGTTAGGG
htel22_Na	9.22	**M**	22	12		htel	uni	AGGGTTAGGGTTAGGGTTAGGG
c-Myc27_K	**-14.16**	**P**	27	20		c-Myc	uni	TGGGGAGGGTGGGGAGGGTGGGGAAGG
c-Myc27_Na	7.56	**M**	27	20		c-Myc	uni	TGGGGAGGGTGGGGAGGGTGGGGAAGG
186D_K	24.44	**M**	24	16	NMR	tetrahymena telomeric	uni	TTGGGGTTGGGGTTGGGGTTGGGG
186D_Na	15.24	**M**	24	16		tetrahymena telomeric	uni	TTGGGGTTGGGGTTGGGGTTGGGG
2HY9_K	33.17	**M**	26	12	NMR	htel	uni	AAAGGGTTAGGGTTAGGGTTAGGGAA
2HY9_Na	21.72	**M**	26	12		htel	uni	AAAGGGTTAGGGTTAGGGTTAGGGAA
2JSM_K	32.76	**M**	23	12			uni	TAGGGTTAGGGTTAGGGTTAGGG
2JSM_Na	23.88	**M**	23	12			uni	TAGGGTTAGGGTTAGGGTTAGGG
148D_K	9.35	**M**	15	8	NMR	Thrombin aptamer	uni	GGTTGGTGTGGTTGG
148D_Na	8.50	**M**	15	8		Thrombin aptamer	uni	GGTTGGTGTGGTTGG
2JPZ_K	31.84	**M**	26	12	NMR	htel	uni	TTAGGGTTAGGGTTAGGGTTAGGGTT
2JPZ_Na	17.52	**M**	26	12		htel	uni	TTAGGGTTAGGGTTAGGGTTAGGGTT
2KF7_K	24.72	**M**	22	12	NMR	htel	uni	GGGTTAGGGTTAGGGTTAGGGT
2KF7_Na	14.45	**M**	22	12		htel	uni	GGGTTAGGGTTAGGGTTAGGGT
T30175_K	0.37	**M**	17	12			uni	GTG GTG GGT GGG TGG GT
T30175_Na	6.35	**M**	17	12			uni	GTG GTG GGT GGG TGG GT
2MBJ_K	50.58	**M**	27	12		htel	uni	TTAGGGTTAGGGTTAGGGTTAGGGTTA
2MBJ_Na	26.38	**M**	27	12		htel	uni	TTAGGGTTAGGGTTAGGGTTAGGGTTA
1AXV_K	-8.44	**P**	22	13	NMR	c-Myc	uni	TGAGGGTGGGTAGGGTGGGTAA
1AXV_Na	11.70	**M**	22	13		c-Myc	uni	TGAGGGTGGGTAGGGTGGGTAA
Pu21_2-5_K	**-26.78**	**P**	21	15		c-Myc	uni	GA GGG TGG GGA GGG TGG GGA A
Pu21_2-5_Na	**-2.12**	**P**	21	15		c-Myc	uni	GA GGG TGG GGA GGG TGG GGA A

Pu21_1-4_K	12.20	**M**	21	15		c-Myc	uni	A TGG GGA GGG TGG GGA GGG TG
Pu21_1-4_Na	18.06	**M**	21	15		c-Myc	uni	A TGG GGA GGG TGG GGA GGG TG
Pu24_K	**-38.96**	**P**	24	17		c-Myc	uni	TGA GGG TGG GGA GGG TGG GGA AGG
Pu24_Na	**-11.28**	**P**	24	17		c-Myc	uni	TGA GGG TGG GGA GGG TGG GGA AGG
Myc22_K	**-19.03**	**P**	22	15		c-Myc	uni	TGA GGG TGG GGA GGG TGG GGA A
Myc22_Na	4.83	**M**	22	15		c-Myc	uni	TGA GGG TGG GGA GGG TGG GGA A
c-Myc24_K	3.46	**M**	24	18		c-Myc	uni	TGGGGAGGGTGGGGAGGGTGGGGA
c-Myc24_Na	8.03	**M**	24	18		c-Myc	uni	TGGGGAGGGTGGGGAGGGTGGGGA
c-Myc25_K	8.30	**M**	25	18		c-Myc	uni	TGGGGAGGGTGGGGAGGGTGGGGAA
c-Myc25_Na	15.66	**M**	25	18		c-Myc	uni	TGGGGAGGGTGGGGAGGGTGGGGAA
c-Myc26_K	10.36	**M**	26	19		c-Myc	uni	TGGGGAGGGTGGGGAGGGTGGGGAAG
c-Myc26_Na	15.53	**M**	26	19		c-Myc	uni	TGGGGAGGGTGGGGAGGGTGGGGAAG
Pu47_K	14.57	**M**	47	24		c-Myc	uni	C TAT GTA TAC-TGG GGA GGG TGG GGA GGG TGG GGA AGG-TTA GCG GCA C
Pu47_Na	26.15	**M**	47	24		c-Myc	uni	C TAT GTA TAC-TGG GGA GGG TGG GGA GGG TGG GGA AGG-TTA GCG GCA C
156DK_C	19.36	**M**	24	18			bi	GGGGGTTTGGGG
156D_Na_C	8.39	**M**	24	18			bi	GGGGGTTTGGGG
1F3S_K_C	10.08	**M**	18	10			bi	GGGTTCAGG
1F3S_Na_C	5.58	**M**	18	10			bi	GGGTTCAGG
2AVH_K_C	10.15	**M**	22	16			bi	GGGGTTTGGGG
2AVH_Na_C	10.34	**M**	22	16			bi	GGGGTTTGGGG
5C	3.56	**M**	20	16			tetra	TGGGG
6C	1.24	**M**	20	20			tetra	GGGGG
7C	5.47	**M**	24	12			tetra	TTAGGG
1S45_K_C	15.20	**M**	24	16			tetra	TGGGGT
1S45_Na_C	5.16	**M**	24	16			tetra	TGGGGT

5.4.1 Materials and Methods

Oligonucleotides were purchased from IBA or BIOMERS in 0.1 nmol or 1 nmol scale with HPLC purity and lyophilized state and stock solutions of the desired concentrations were prepared in pure water. Stock solutions of 50 µM double-stranded DNA were formed in 10 mM Sodium Cacodylate buffer (pH 7.2) containing 5 mM $Mg(ClO_4)_2$ and were heated to 85 °C and cooled down to 4 °C at 0.5 °C min^{-1}. Stock solutions of 50 µM G-quadruplex DNA were formed in 10 mM Lithium Cacodylate buffer (pH 7.2) containing either 10 mM $NaClO_4$ or 10 mM $KClO_4$ and were heated to 85 °C and cooled down to 4 °C at 0.5 °C min^{-1}. Samples of bimolecular and tetramolecular G-quadruplexes were then frozen at –20 °C for one hour to ensure full G-quadruplex formation.[65]

Solutions for CD and UV-Vis measurements were always prepared following the general procedure.

General Procedure for DNA-helicate complex formation

A 700 µM solution of $[Pd_2(\mathbf{MB\text{-}Q})_4]$ was formed in DMSO-d_6 by mixing 450 µL of a 3.11 mM solution of ligand **MB-Q** with 50 µL of a 15 mM solution of $Pd(NO_3)_2$ and heating the resulting solution for 15 min at 70 °C. After checking the assembly formation by ^{1}H NMR, 8.6 µL of this solution where mixed with 91.4 µL of pure DMSO to obtain 100 µL of a 60 µM helicate solution. The final solutions were then prepared as indicated in Table 5.5 for single-stranded and double-stranded DNA and in Table 5.6 for G-quadruplexes.

Table 5.5: Single- and double-stranded DNA solutions for interaction studies with $[Pd_2(\mathbf{MB\text{-}Q})_4]$. Buffer is sodium cacodylate (pH 7.2) and electrolyte $Mg(ClO_4)_2$.

	DNA (50 µM)	DMSO	**MB-Q** (240 µM)	$[Pd_2(\mathbf{MB\text{-}Q})_4]$ (60 µM)	Buffer (1 M)	Electrolyte (1 M)	H_2O
DNA H_2O	120 µL	-	-	-	8.8 µL	44 µL	827 µL
DNA 9:1 H_2O:DMSO	120 µL	100 µL	-	-	8.8 µL	44 µL	727 µL
MB-Q	-	-	100 µL	-	10 µL	50 µL	840 µL

$[Pd_2(\mathbf{MB\text{-}Q})_4]$	-	-		100 µL	10 µL	50 µL	840 µL
DNA:**MB-Q** 1:4	120 µL	-	100 µL	-	8.8 µL	44 µL	727 µL
DNA:$[Pd_2(\mathbf{MB\text{-}Q})_4]$ 1:1	120 µL	-	-	100 µL	8.8 µL	44 µL	727 µL

Table 5.6: G-quaduplexes DNA solutions for interaction studies with $[Pd_2(\mathbf{MB\text{-}Q})_4]$. Buffer is lithium cacodylate (pH 7.2) and electrolytes either $NaClO_4$ or $KClO_4$.

	DNA (50 µM)	DMSO	**MB-Q** (240 µM)	$[Pd_2(\mathbf{MB\text{-}Q})_4]$ (60 µM)	Buffer (1 M)	Electrolyte (0.1 M)	H_2O
G4 H_2O	120 µL	-	-	-	8.8 µL	88 µL	783 µL
G4 9:1 H_2O:DMSO	120 µL	100 µL	-	-	8.8 µL	88 µL	683 µL
MB-Q	-	-	100 µL	-	10 µL	100 µL	790 µL
$[Pd_2(\mathbf{MB\text{-}Q})_4]$	-	-		100 µL	10 µL	100 µL	790 µL
G4:**MB-Q** 1:4	120 µL	-	100 µL	-	8.8 µL	88 µL	683 µL
G4:$[Pd_2(\mathbf{MB\text{-}Q})_4]$ 1:1	120 µL	-	-	100 µL	8.8 µL	88 µL	683 µL

Nanodrop

Concentrations were individually determined using a Thermo Scientific Nanodrop One instrument under consideration of the revised extinction coefficient of the single nucleotides.[68]

UV-Vis

UV-vis absorption spectra were recorded on a DAD HP-8453 UV-Vis spectrometer. Cuvette path length 10 mm, wavelength: 240 nm – 800 nm, step size: 1 nm. Thermal denaturation experiments were carried out on a Jasco V-750 absorption spectrometer in quartz glass cuvettes to determine the thermal stability expressed in the melting temperature $T_{1/2}$. Therefore, the change in absorbance, as the temperature was increased with 0.5 °C min^{-1}, was followed at 295 nm indicative for G-quadruplex denaturation and at 350 nm as control. The spectrometer bandwidth was set to 2 nm. To control the temperature, a cuvette containing water was equipped with a temperature probe connected to the spectrometer. Water evaporation from the samples was avoided by addition of small amounts of silicon oil. To ensure equal heating rates between different experiments, always five samples were measured at a time. The measured absorbance was plotted against the temperature after the absorbance at 350 nm was subtracted to remove background absorption. Spectra were normalized to fraction folded values between 1 and 0 corresponding to fully folded or unfolded G-quadruplexes, respectively.[69]

CD spectroscopy

CD measurements were carried out on a Chirascan qCD spectrometer in black quartz-glass cuvettes, 10mm path length. The temperature was controlled using a Quantum Northwest temperature control attached to a sample probe. Spectra of solutions containing DMSO were recorded at 25 °C from 240 to 800 nm (120 nm min^{-1}) with a 1 nm interval and 0.5 nm bandwidth three times and averaged using the instrument-specific software. The averaged spectra were smoothed (adjacent averaging) with a factor of 5 and the smoothed background (sample containing only buffer, smooth factor 5) was subtracted. The background was recorded from 240 to 800 nm with the same settings as for the samples. Spectra of pure DNA in pure buffered water were recorded at 25 °C from 205 to 400 nm (120 nm min^{-1}) with a 1 nm interval and 0.5 nm bandwidth three times and averaged using the instrument-specific software. The averaged spectra were smoothed (adjacent averaging) with a factor of 5 and the smoothed background (sample containing only buffer, smooth factor 5) was subtracted. The background was recorded from 205 to 400nm with the same settings as for the samples.

5.4.2 CD controls with G-Quadruplexes

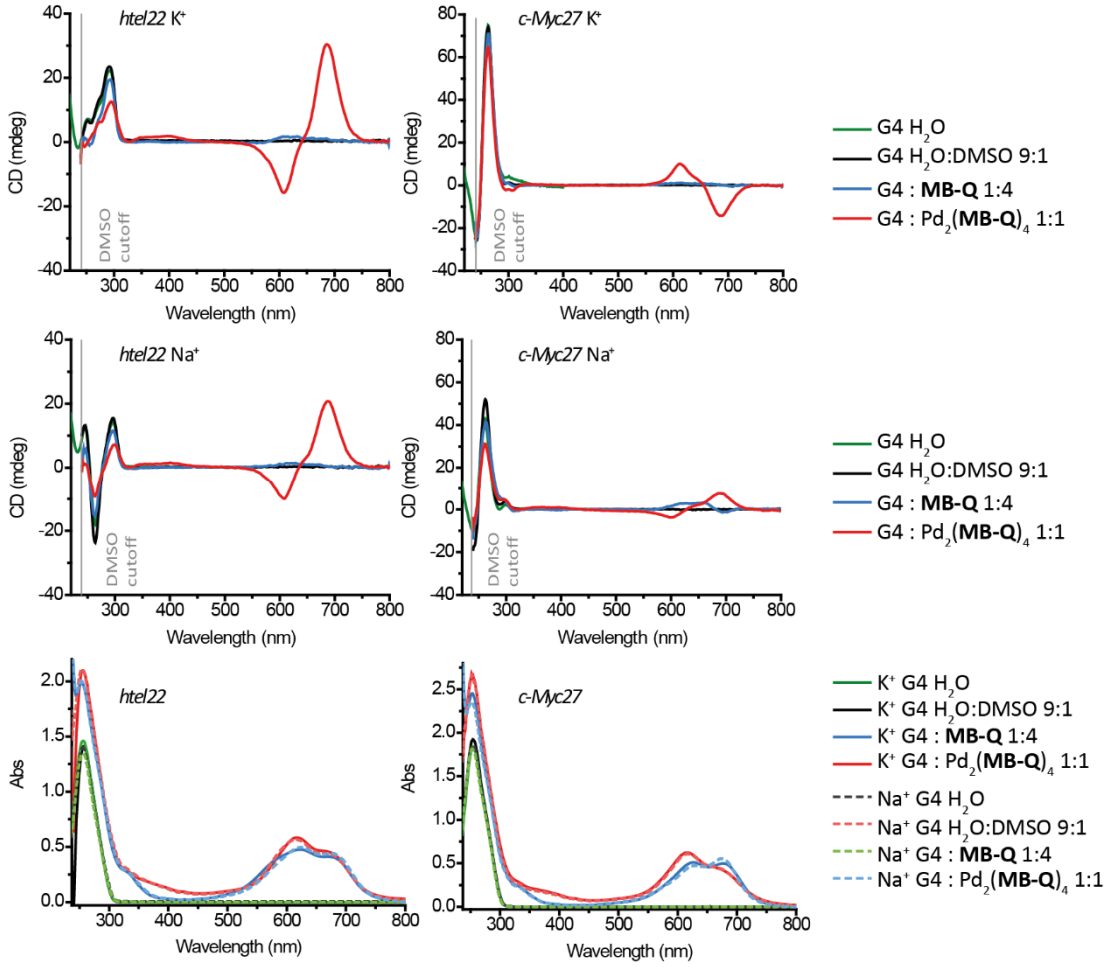

Figure 5.22: CD and UV-Vis absorption spectra of the sequences named in the insets. All measurement were performed at 25 °C, in 10 mM LiCaCO buffer (pH 7.2) in either 10 mM $KClO_4$ or 10 mM $NaClO_4$ electrolyte-containing solution (as indicated in the insets), 6 µM of the G4, when present 24 µM of ligand **MB-Q** and when present 6 µM of [Pd_2(**MB-Q**)$_4$].

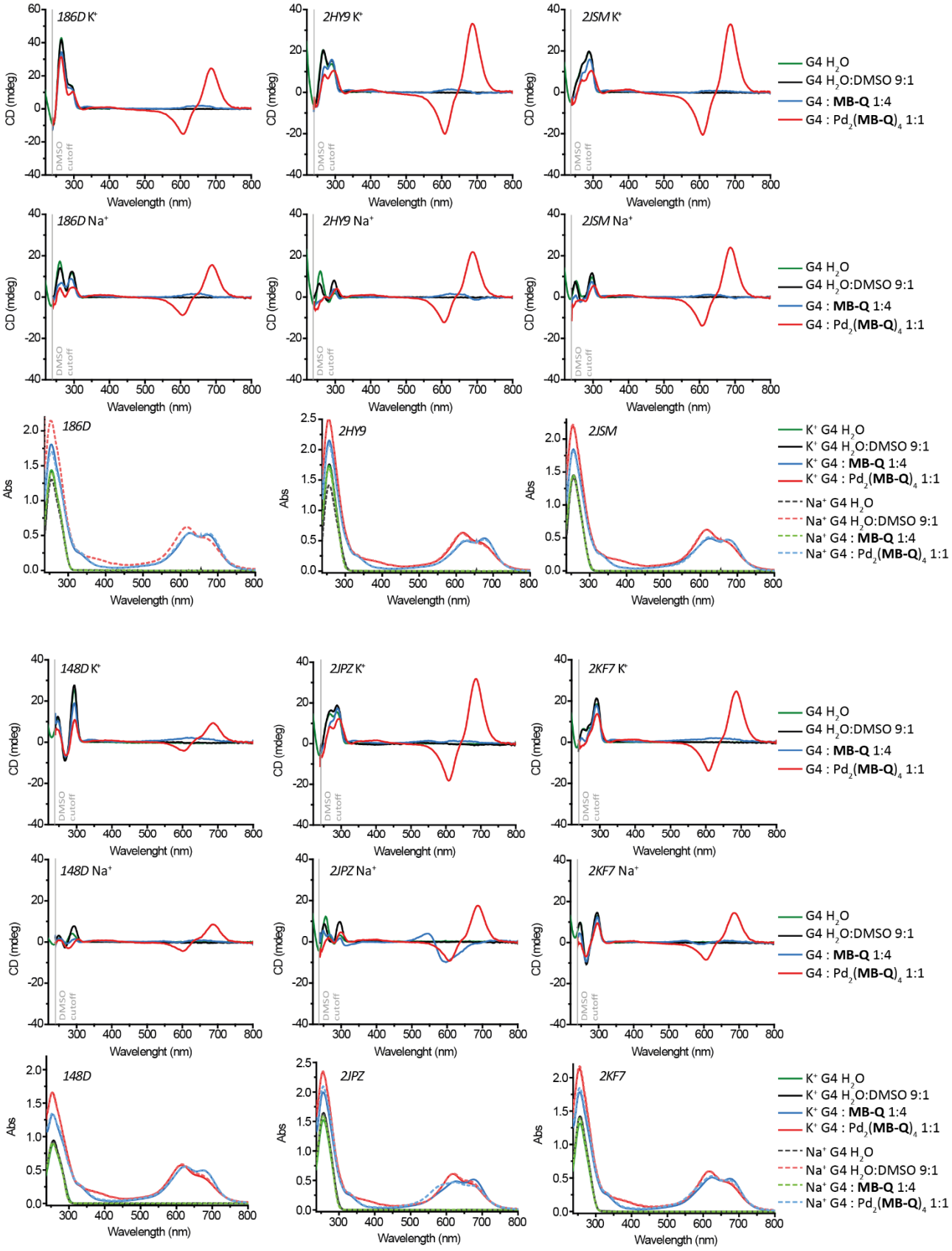

Figure 5.23: CD and UV-Vis absorption spectra of the sequences named in the insets. All measurement were performed at 25 °C, in 10 mM LiCaCO buffer (pH 7.2) in either 10 mM $KClO_4$ or 10 mM $NaClO_4$ electrolyte-containing solution (as indicated in the insets), 6 µM of the G4, when present 24 µM of ligand **MB-Q** and when present 6 µM of [Pd_2(**MB-Q**)$_4$].

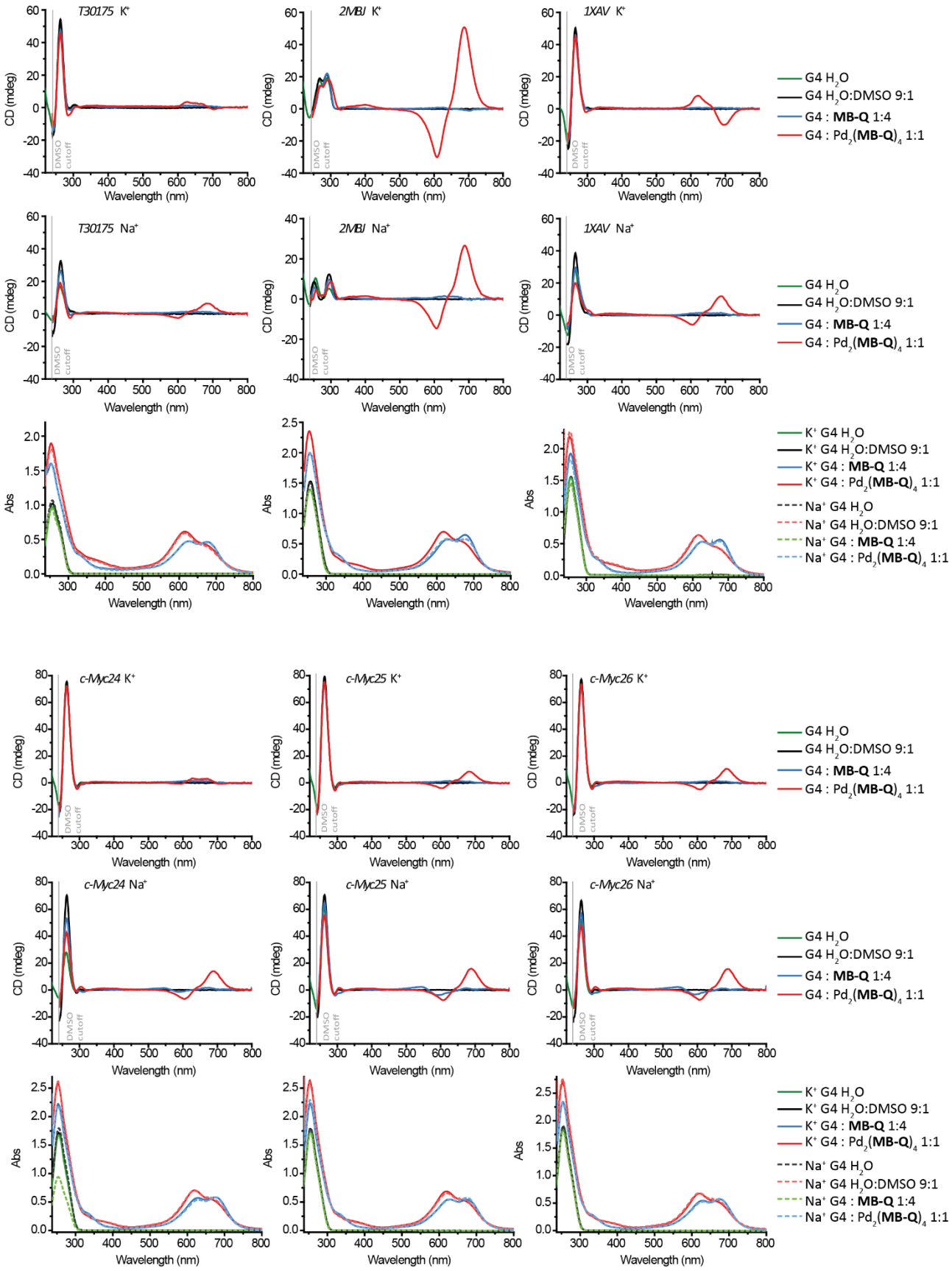

Figure 5.24: CD and UV-Vis absorption spectra of the sequences named in the insets. All measurement were performed at 25 °C, in 10 mM LiCaCO buffer (pH 7.2) in either 10 mM $KClO_4$ or 10 mM $NaClO_4$ electrolyte-containing solution (as indicated in the insets), 6 µM of the G4, when present 24 µM of ligand **MB-Q** and when present 6 µM of [Pd_2(**MB-Q**)$_4$].

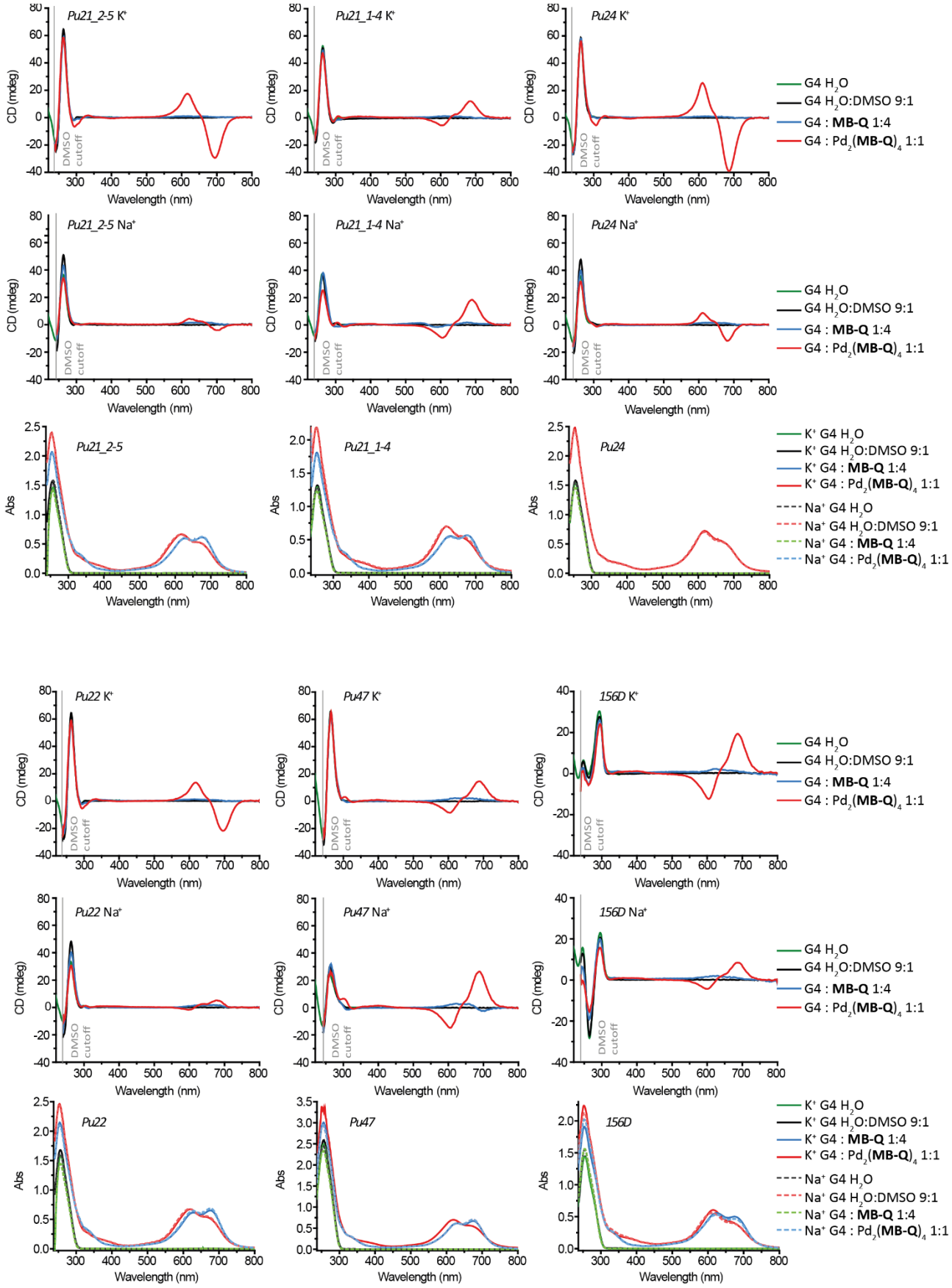

Figure 5.25: CD and UV-Vis absorption spectra of the sequences named in the insets. All measurement were performed at 25 °C, in 10 mM LiCaCO buffer (pH 7.2) in either 10 mM $KClO_4$ or 10 mM $NaClO_4$ electrolyte-containing solution (as indicated in the insets), 6 µM of the G4, when present 24 µM of ligand **MB-Q** and when present 6 µM of [Pd_2(**MB-Q**)$_4$].

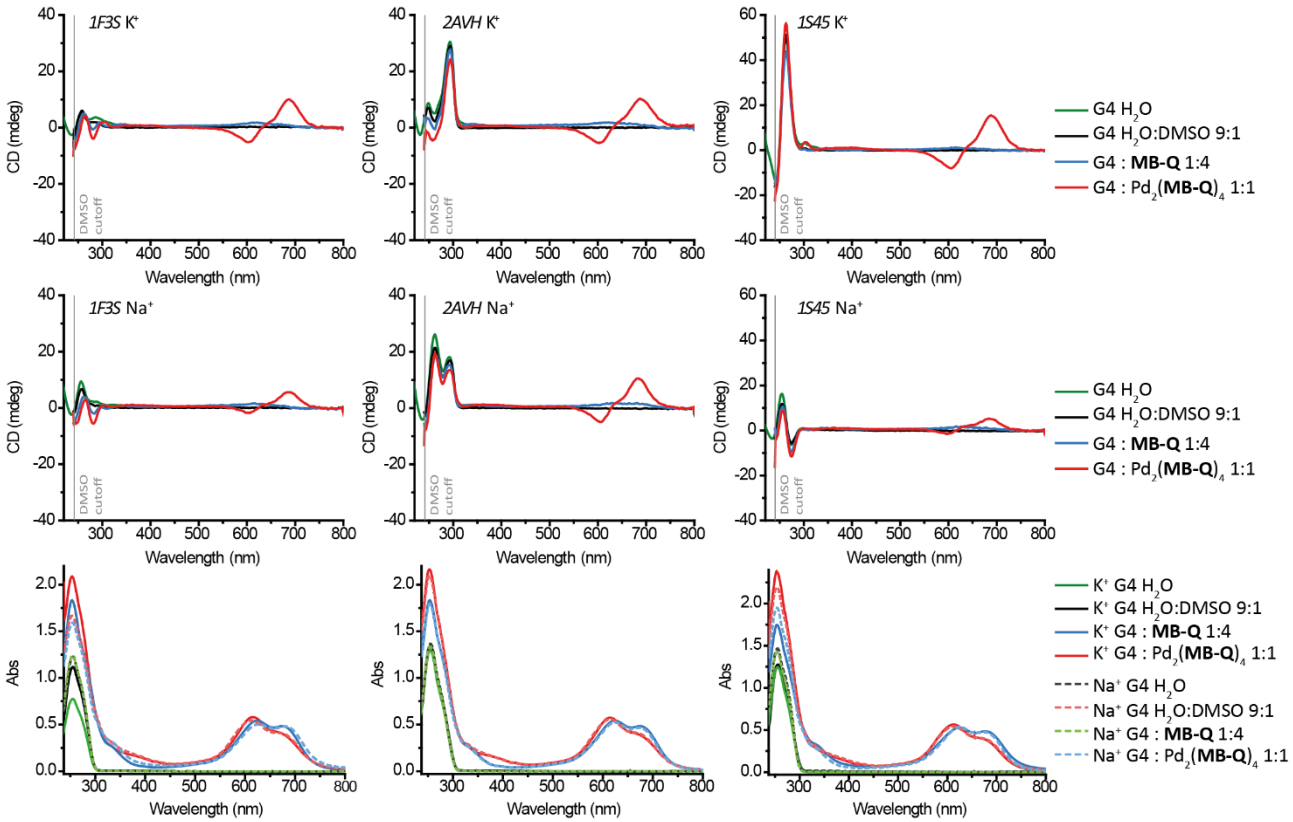

Figure 5.26: CD and UV-Vis absorption spectra of the sequences named in the insets. All measurement were performed at 25 °C, in 10 mM LiCaCO buffer (pH 7.2) in either 10 mM $KClO_4$ or 10 mM $NaClO_4$ electrolyte-containing solution (as indicated in the insets), 6 µM of the G4, when present 24 µM of ligand **MB-Q** and when present 6 µM of [Pd_2(**MB-Q**)$_4$].

5.4.3 ECD calculations

ECD calcuations were performed with Gaussian 16 software with a combination of functionals and basis set as indicated in Table 5.7. The calculations performed with 100 excited states were then compared and the general trend analyzed with the experimental CD spectra. As starting structure for the TD DFT calculation, a B3LYP/def2-SV(P) optimized model for (*M*)-[Pd_2(**MB-Q**)$_4$] has been employed and as it can be observed in Figure 5.27, however different the results from different calculations, a band with positive Cotton effect (at different wavelength range) can always be observed. From this result, the absolute configuration of the cage showing a positive Cotton effect was assigned to the (*M*)-[Pd_2(**MB-Q**)$_4$] enantiomer of the cage.

Table 5.7: ECD calculations performed with indicated the basis set, the functional and N stands for the number of excited states considerate.

B3LYP/def2-SV(P)	N=1,50,100
B3LYP/TZVP	N=1,50,100
CAM- B3LYP/def2-SV(P)	N=100
B3PW91/def2-SV(P)	N=100
WB97XD/def2-SV(P)	N=100

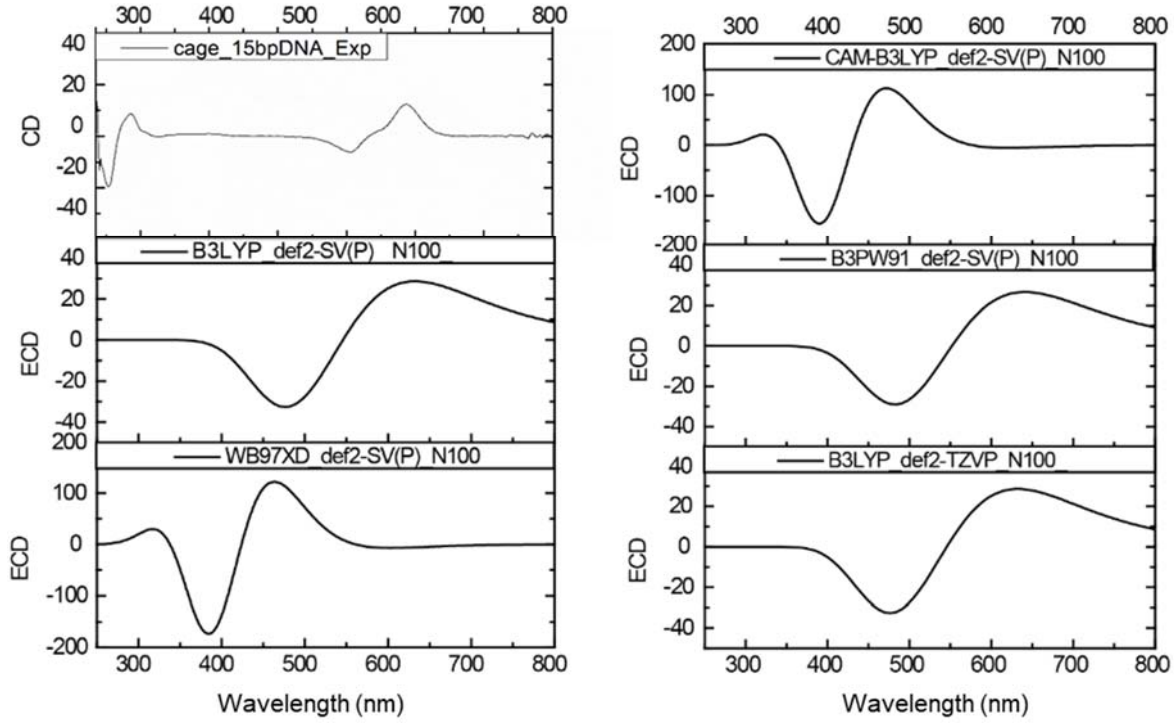

Figure 5.27: Experimental CD spectra obtained from the combination of cage [Pd_2(**MB-Q**)$_4$] with double-stranded DNA **15bp dsDNA** and different results of ECD calculations from the different functional-basis set combinations employed.

5.4.4 Docking studies with AutoDock Version 4.2

AutoDock is an automated procedure for predicting the interaction of ligands with biomacromolecular targets. Version 4.2 was employed and the manual procedures were followed.[58] The essential steps accomplished are the following:

- Preparation of coordinate files using **AutoDockTools:** AutoDock4.2 is parameterized to use a model of the protein and ligand that includes polar hydrogen atoms (hydrogen atoms that can potentially be involved in hydrogen bonding), but not hydrogen atoms bonded to carbon atoms. An extended PDB format, **PDBQT**, is used for coordinate files, which includes atomic partial charges and atom types. In order to originate input file for [Pd_2(**MB-Q**)$_4$], the .mol2 file of the DFT optimized and C4-symmetry constrained structures for both enantiomers was uploaded in the software, the torsional freedom set to 0 (otherwise the palladium coordination centers get compromised since such bonds are unknown to the used algorithms) and the corresponding .pdbqt file was created. The partial charges implemented in the software are Gasteiger charges, which have no parameters for coordination metal cations. Since nowhere in the process it was possible to indicate the total charge of the assembly, only after generation of the .pdbqt file, the partial charge on each atom were manually changed. The new charges were part of the result of the DFT optimized model and corresponds to Mulliken charges with hydrogens summed into heavy atoms. For the biological part, the structures were downloaded form the Protein Data Bank (RCSB PDB) database and where missing, the cations (potassium or sodium) that are part of the G-quadruplex structure were added. In this case, the charges that were automatically assigned by AutoDock were used.

- Before performing the actual docking calculation, it is necessary to calculate the atomic affinities using the software **AutoGrid**. AutoDock requires pre-calculated *grid maps*, one for each atom type present in the ligand being docked. Each point within the grid map stores the potential energy (as well as electrostatic and desolvation potentials) of a '*probe*' atom or functional group that is due to all the atoms in the macromolecule. Then, during the AutoDock calculation, **the energetics of a particular ligand configuration is evaluated using the values from the grids**.

AutoGrid requires parameters for all the atom types present in the '*ligand*' (intended as the molecule to dock to the receptor, in our case the two enantiomers of [Pd_2(**MB-Q**)$_4$]) and the macromolecules. Since in the default parameter file atoms types like Pd, K and Na are not present, they were manually added.

- Calculation of the docking *ligand* structures using **AutoDock.** AutoDock provides several methods for doing conformational search. The Lamarckian Genetic Algorithm provides the most efficient search for general applications. The Genetic Algorithm, Simulated Annealing and Local Search are further available algorithms. In all cases the search can be personalized for the specific systems. For the presented calculations, all default settings were unchanged except for the Number of Evaluations (how many docked structures were calculated) that was changed from 10 to 50.
- Analysis of results using **AutoDockTools/PyMOL.** The output structures are evaluated through a cluster analysis. In this process conformations with the same final energy are be part of the same cluster, weighted for how many conformations they are composed of and the lowest energy docked conformation was highlighted and plotted using PyMOL (Figure 5.17).

5.4.5 Competition experiments

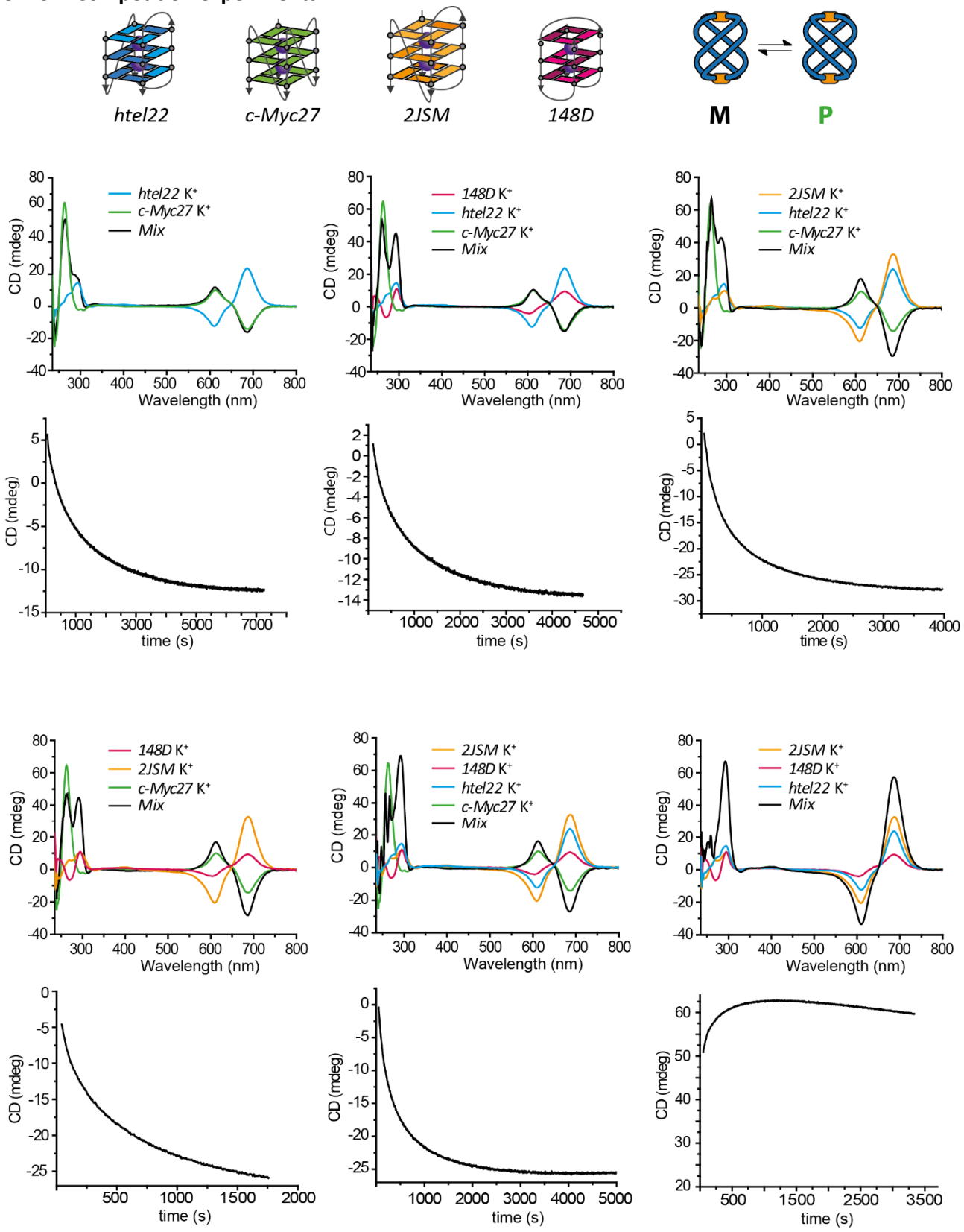

Figure 5.28: CD spectra of 9:1 water:DMSO solutions, 10 mM LiCaCo buffer (pH 7.2), 5 mM $KClO_4$, 6 µM $[Pd_2(\mathbf{MB\text{-}Q})_4]$ and 6 µM G4. G4: *c-Myc27* (green line), *148D* (pink line), *htel22* (blue line), *2JSM* (yellow line), mixture of G4 indicated in the figures (black line). Under every CD spectrum, the evolution of CD signal over time at 686 nm for the mixture solution with the G4s indicated in the figure and the cage (same sample as black line).

5.5 References

[1] J. M. Berg, L. Stryer, J. Tymoczko, G. Gatto, *Biochemistry*, Macmillan Education/Macmillan Learning, 2019.

[2] J. Choi, T. Majima, *Chem. Soc. Rev.* 2011, *40*, 5893–5909.

[3] J. Kypr, I. Kejnovská, D. Renčiuk, M. Vorlíčková, *Nucleic Acids Res.* 2009, *37*, 1713–1725.

[4] M. Vorlíčková, I. Kejnovská, K. Bednářová, D. Renčiuk, J. Kypr, *Chirality* 2012, *24*, 691–698.

[5] R. del Villar-Guerra, J. O. Trent, J. B. Chaires, *Angew. Chem. Int. Ed.* 2018, *57*, 7171–7175.

[6] D. Rhodes, H. J. Lipps, *Nucleic Acids Res.* 2015, *43*, 8627–37.

[7] T. Tian, Y.-Q. Chen, S.-R. Wang, X. Zhou, *Chem* 2018, *4*, 1314–1344.

[8] E. Ruggiero, S. N. Richter, *Nucleic Acids Res.* 2018, *46*, gky187-.

[9] A. L. Moye, K. C. Porter, S. B. Cohen, T. Phan, K. G. Zyner, N. Sasaki, G. O. Lovrecz, J. L. Beck, T. M. Bryan, *Nat. Commun.* 2015, *6*, 7643.

[10] S. Shi, S. Gao, T. Cao, J. Liu, X. Gao, J. Hao, C. Lv, H. Huang, J. Xu, T. Yao, *Plos One* 2013, *8*, e84419.

[11] S. Balasubramanian, L. H. Hurley, S. Neidle, *Nat. Rev. Drug Discov.* 2011, *10*, 261–75.

[12] A. Rangan, O. Y. Fedoroff, L. H. Hurley, *J. Biol. Chem.* 2000, *276*, 4640–4646.

[13] J. Seenisamy, E. M. Rezler, T. J. Powell, D. Tye, V. Gokhale, C. S. Joshi, A. Siddiqui-Jain, L. H. Hurley, *J. Am. Chem. Soc.* 2004, *126*, 8702–8709.

[14] A. Siddiqui-Jain, C. L. Grand, D. J. Bearss, L. H. Hurley, *Proc. Natl. Acad. Sci. U.S.A.* 2002, *99*, 11593–11598.

[15] S. Neidle, S. Balasubramanian, *Quadruplex Nucleic Acid*, RCS Publishing, 2006.

[16] G. N. Parkinson, M. P. H. Lee, S. Neidle, *Nature* 2002, *417*, 876–880.

[17] K. N. Luu, A. T. Phan, V. Kuryavyi, L. Lacroix, D. J. Patel, *J. Am. Chem. Soc.* 2006, *128*, 9963–9970.

[18] R. I. Mathad, E. Hatzakis, J. Dai, D. Yang, *Nucleic Acids Res.* 2011, *39*, 9023–9033.

[19] V. González, L. H. Hurley, *Annu. Rev. Pharmacol. Toxicol.*2010, *50*, 111–129.

[20] T. A. Brooks, L. H. Hurley, *Genes & Cancer* 2010, *1*, 641–649.

[21] M. J. Hannon, *Chem. Soc. Rev.* 2006, *36*, 280–295.

[22] B. Schoentjes, J. Lehn, *Helv. Chim. Acta* 1995, *78*, 1–12.

[23] M. J. Hannon, V. Moreno, M. J. Prieto, E. Moldrheim, E. Sletten, I. Meistermann, C. J. Isaac, K. J. Sanders, A. Rodger, *Angew. Chem. Int. Ed.* 2001, *113*, 903–908.

[24] A. Oleksi, A. G. Blanco, R. Boer, I. Usón, J. Aymamí, A. Rodger, M. J. Hannon, M. Coll, *Angew. Chem. Int. Ed.* 2006, *45*, 1227–1231.

[25] J. Malina, M. J. Hannon, V. Brabec, *Chem. Eur. J.* 2007, *13*, 3871–3877.

[26] G. I. Pascu, A. C. G. Hotze, C. Sanchez-Cano, B. M. Kariuki, M. J. Hannon, *Angew. Chem. Int. Ed.* 2007, *46*, 4374–4378.

[27] J. Malina, M. J. Hannon, V. Brabec, *Nucleic Acids Res.* 2008, *36*, 3630–8.

[28] S. Phongtongpasuk, S. Paulus, J. Schnabl, R. K. O. Sigel, B. Spingler, M. J. Hannon, E. Freisinger, *Angew. Chem. Int. Ed.* 2013, *52*, 11513–11516.

[29] J. Malina, M. J. Hannon, V. Brabec, *Chem. Eur. J.* 2015, *21*, 11189–11195.

[30] H. Yu, X. Wang, M. Fu, J. Ren, X. Qu, *Nucleic Acids Res.* 2008, *36*, 5695–5703.

[31] J. Wang, Y. Chen, J. Ren, C. Zhao, X. Qu, *Nucleic Acids Res.*2014, *42*, 3792–3802.

[32] A. Zhao, C. Zhao, J. Ren, X. Qu, *Chem. Commun.* 2015, *52*, 1365–1368.

[33] C. Zhao, H. Song, P. Scott, A. Zhao, H. Tateishi-Karimata, N. Sugimoto, J. Ren, X. Qu, *Angew. Chem. Int. Ed.* 2018, *57*, 15723–15727.

[34] S. E. Howson, A. Bolhuis, V. Brabec, G. J. Clarkson, J. Malina, A. Rodger, P. Scott, *Nat. Chem.* 2011, *4*, 31–36.

[35] V. Brabec, S. E. Howson, R. A. Kaner, R. M. Lord, J. Malina, R. M. Phillips, Q. M. A. Abdallah, P. C. McGowan, A. Rodger, P. Scott, *Chem. Sci.* 2013, *4*, 4407.

[36] A. D. Faulkner, R. A. Kaner, Q. M. A. Abdallah, G. Clarkson, D. J. Fox, P. Gurnani, S. E. Howson, R. M. Phillips, D. I. Roper, D. H. Simpson, P. Scott, *Nat. Chem.* 2014, *6*, 797–803.

[37] R. A. Kaner, S. J. Allison, A. D. Faulkner, R. M. Phillips, D. I. Roper, S. L. Shepherd, D. H. Simpson, N. R. Waterfield, P. Scott, *Chem. Sci.* 2016, *7*, 951–958.

[38] H. Song, N. J. Rogers, S. J. Allison, V. Brabec, H. Bridgewater, H. Kostrhunova, L. Markova, R. M. Phillips, E. C. Pinder, S. L. Shepherd, L. S. Young, J. Zajac, P. Scott, *Chem. Sci.* 2019, *10*, 8547–8557.

[39] D. H. Simpson, A. Hapeshi, N. J. Rogers, V. Brabec, G. J. Clarkson, D. J. Fox, O. Hrabina, G. L. Kay, A. K. King, J. Malina, A. D. Millard, J. Moat, D. I. Roper, H. Song, N. R. Waterfield, P. Scott, *Chem. Sci* .2019, *10*, 9708–9720.

[40] A. Zhao, S. E. Howson, C. Zhao, J. Ren, P. Scott, C. Wang, X. Qu, *Nucleic Acids Res.* 2017, *45*, gkx244.

[41] J. Zhu, C. J. E. Haynes, M. Kieffer, J. L. Greenfield, R. D. Greenhalgh, J. R. Nitschke, U. F. Keyser, *J. Am. Chem. Soc.* 2019, *141*, 11358–11362.

[42] W. Drożdż, A. Walczak, Y. Bessin, V. Gervais, X.-Y. Cao, J.-M. Lehn, S. Ulrich, A. R. Stefankiewicz, *Chem. Eur. J.* 2018, *24*, 10802–10811.

[43] F.-T. Zhang, J. Nie, D.-W. Zhang, J.-T. Chen, Y.-L. Zhou, X.-X. Zhang, *Anal. Chem.* 2014, *86*, 9489–9495.

[44] Y. Xiao, B. D. Piorek, K. W. Plaxco, A. J. Heeger, *J. Am. Chem. Soc.* 2005, *127*, 17990–17991.

[45] E. Bağda, E. Bağda, E. Yabaş, *J. Turk. Chem. Soc., Sect. A* 2017, *4*, 579-596.

[46] J. Jaumot, R. Gargallo, *Curr. Pharm. Des.* 2012, *18*, 1900–1916.

[47] T. Cao, F.-T. Zhang, L.-Y. Cai, Y.-L. Zhou, N. J. Buurma, X.-X. Zhang, *Analyst* 2017, *142*, 987–993.

[48] P. O. Vardevanyan, A. P. Antonyan, M. A. Parsadanyan, M. A. Shahinyan, L. A. Hambardzumyan, *J. Appl. Spectrosc.* 2013, *80*, 595–599.
[49] A. Głuszyńska, B. Juskowiak, B. Rubiś, *Molecules* 2018, *23*, 3154.
[50] D.-L. Ma, V. P.-Y. Ma, K.-H. Leung, H.-J. Zhong, H.-Z. He, D. S.-H. Chan, C.-H. Leung, 2013, DOI 10.5772/54809.
[51] S. H. Adjalley, G. L. Johnston, T. Li, R. T. Eastman, E. H. Ekland, A. G. Eappen, A. Richman, B. K. L. Sim, M. C. S. Lee, S. L. Hoffman, D. A. Fidock, *Proc. Natl. Acad. Sci. U.S.A.* 2011, *108*, E1214–E1223.
[52] W. Gai, Q. Yang, J. Xiang, H. Sun, Q. Shang, Q. Li, W. Jiang, A. Guan, H. Zhang, Y. Tang, G. Xu, *Sci. Bull.* 2013, *58*, 731–740.
[53] T. Mohammad, H. Morrison, *J. Photochem. Photobiol.* 2000, *71*, 369–381.
[54] Y. Wang, A. Zhou, *J. Photochem. Photobiol., A* 2007, *190*, 121–127.
[55] D. S.-H. Chan, H. Yang, M. H.-T. Kwan, Z. Cheng, P. Lee, L.-P. Bai, Z.-H. Jiang, C.-Y. Wong, W.-F. Fong, C.-H. Leung, D.-L. Ma, *Biochimie* 2011, *93*, 1055–1064.
[56] Z. Hu, C. Tong, *Anal. Chim. Acta* 2007, *587*, 187–193.
[57] R. Zhu, I. Regeni, J. J. Holstein, B. Dittrich, M. Simon, S. Prévost, M. Gradzielski, G. H. Clever, *Angew. Chem. Int. Ed.* 2018, *57*, 13652–13656.
[58] G. M. Morris, R. Huey, W. Lindstrom, M. F. Sanner, R. K. Belew, D. S. Goodsell, A. J. Olson, *J. Comput. Chem.* 2009, *30*, 2785–2791.
[59] L. Yuan, T. Tian, Y. Chen, S. Yan, X. Xing, Z. Zhang, Q. Zhai, L. Xu, S. Wang, X. Weng, B. Yuan, Y. Feng, X. Zhou, *Sci. Rep.* 2013, *3*, 01811.
[60] V. González, K. Guo, L. Hurley, D. Sun, *Biol. Chem.* 2009, *284*, 23622–35.
[61] S. Paul, S. S. Hossain, B. D. M, A. Samanta, *J. Phys. Chem. B* 2019, *123*, 2022–2031.
[62] F. Yang, X. Sun, L. Wang, Q. Li, A. Guan, G. Shen, Y. Tang, *RSC Adv.* 2017, *7*, 51965–51969.
[63] A. T. Phan, V. Kuryavyi, H. Y. Gaw, D. J. Patel, *Nat. Chem. Biol.* 2005, *1*, 167–173.
[64] J. Dickerhoff, B. Onel, L. Chen, Y. Chen, D. Yang, *Acs Omega* 2019, *4*, 2533–2539.
[65] A. Ambrus, D. Chen, J. Dai, R. A. Jones, D. Yang, *Biochemistry* 2005, *44*, 2048–2058.
[66] A. Tawani, S. K. Mishra, A. Kumar, *Sci. Rep.* 2017, *7*, 3600.
[67] Q. Zhai, M. Deng, L. Xu, X. Zhang, X. Zhou, *Bioorg. Med. Chem. Lett.* 2012, *22*, 1142–1145.
[68] M. J. Cavaluzzi, P. N. Borer, *Nucleic Acids Res.* 2004, *32*, e13–e13.
[69] Curr. Protoc. Nuleic Acid Chem. 2009, Chapter 17, 17.1.1-17.1.15.

6. Conclusion and perspectives

Ligands based on the functionalities of diketopyrrolopyrrole (**DPP**) dyes and coal-tar dyes Michler's ketone, methylene blue, rhodamine B, crystal violet, were successfully synthesized and included as ligands in Pd(II)-based supramolecular architectures. The dye-based supramolecules were fully characterized by a wide range of spectroscopic, spectrometric and diffraction techniques in order to evaluate their structural and optical properties. Interesting optical features were found for **DPP**-based homoleptic and heteroleptic assemblies and will be further investigated in future research projects. From the structural point of view, a new topology of homoleptic $[Pd_2L_4]$ cage has been identified with an atypical arrangement of the four ligands around the Pd-axis in order to promote π-stacking of the four chromophores. Furthermore, fascinating cage-to-cage transformations were observed for a combination of three ligands (one **DPP**-based, one carbazole-based and one dimethylfluorene-based functionality). In a future study, photoinduced electron/energy transfer processes between these functionalities will be explored.

The introduction of the coal-tar dye moieties into bis-pyridine or bis-isoquinoline ligands required a careful design to allow retainment of the of the functionality. Typically used alkyne bridges between donor groups and backbones would hamper the electronic structure of the parental dyes, therefore, the new ligand design exploits piperazine linkers. From coordination to the square-planar metal cations, lantern-shaped and helical twisted visible light-absorbing $[Pd_2L_4]$ cages formed. Their remarkable absorption properties were exploited for the recognition of small chiral molecules. Encapsulation or even only external association caused the chromophore-based cages to populate a chiral conformation and the effect was studied by CD spectroscopy. Moreover, promising results were obtained in the recognition of bio-relevant anionic molecules where one specific lantern-shaped cage, based on the rhodamine B dye, exhibited impressive ellipticities. A study comprising a wider selection of nucleotides mono-, di- and tri-phosphates as well as anionic phospholipids is currently ongoing.

In view of the optical, structural and physical properties of the methylene blue-based Pd-helicate, important results were obtained in the DNA supramolecular recognition field. Besides the preferential interaction of double-stranded DNA for one helical handiness of the artificial binding agent, focus was set on the class of G-quadruplexes. Several different topologies were analysed in combination with the helicate to understand the origin of different and selective structural recognition. A notable selectivity was found for the sequence *c-Myc27*, found in the promoter region of gene c-MYC, and its derivatives.

To conclude, the implementation of organic dye functionalities has proven to be a successful strategy to expand cage properties arising from the interaction with visible light. New structural motifs, with interesting optical properties and applicability in chiral recognition events of both small molecules and DNA have arisen. A direct expansion of this concept could include mixtures of multiple dye-based cages owning different structures and recognition features to implement a "finger-print-type" approach to recognise different guests in a multiplex approach. The cages, owing to their different inherent optical feature (wavelength of maximum absorption, CD answer…) would give distinct signals for each recognition process and this could be easily detected with optical spectroscopies. The different results would then create a specific array for each molecule detected. Furthermore, the presented research opens new possibilities of explorations in light-driven processes. For example, the photosensitizing ability of the new functional cages has not yet been exploited but promises to bring great advance in the field of photo-redox supramolecular catalysis. The beneficial effect of the cage would be ascribed to the encapsulation of substrates/intermediates, even if in quick exchange, leading to increasing proximity of substrate and catalytic centers, thereby increasing reaction rate as compared to the free ligand.

7. Abbreviations

BODIPY	boron-dipyrromethene
CH_3CN	acetonitrile
$CHCl_3$	chloroform
COSY	correlated spectroscopy
DFT	density functional theory
DMSO	dimethylsulfoxide
DOSY	diffusion ordered spectroscopy
DTE	diethienylethene
equiv.	equivalent
ESI	electrospray ionization
EtOAc	ethyl acetate
GPC	gel permeation chromatography
HMBC	heteronuclear multiple-bond correlation spectroscopy
HR-MS	high resolution mass spectrometry
HSQC	heteronuclear single-quantum correlation spectroscopy
ICD	induced circular dichroism
J	coupling constant
L	ligand
M	metal
m/z	mass-to charge ratio
Me	methyl group
$MeNO_2$	nitromethane
MeOH	methanol
NEt_3	triethylamine
NMP	*N*-methyl-2-pyrrolidone
NMR	nuclear magnetic resonance
NOESY	nuclear overhauser effect spectroscopy
ppm	parts per million
r.t.	room temperature
THF	tetrahydrofuran
Tims	trapped ion mobility spectrometry
TLC	thin layer chromatography
VT	various temperature

Acknowledgments

The first huge thank you goes to Prof. Dr. Guido H. Clever, my PhD supervisor. Your excitement for science is contagious and it is a real privilege to work in your team and learn from you. Thank you for offering me a PhD position and suggesting to apply to the FCI scholarship. Thank you for providing me with the best PhD project I could think of, I had a lot of fun! Thank you for sending me to so many scientific conferences and meetings where I had the opportunity of proudly showing my work and being inspired by excellent scientists while developing critical sense. Thank you for always supporting me, from assisting with my scientific work and showing me how to present results more effectively, for nominating me to the 70th Lindau Nobel Laureate Meeting and for giving me more and more responsibilities within your group. Thank you for the time dedicated to me with very nice talks about my future and all the encouraging words which I really appreciated. You made me a better scientist.

I would like to thank Prof. Dr. Christian Merten for being part of the PhD examination committee and for the fruitful discussion over the years in multiple occasions.

I wish to thank all the precious scientific collaborations and the scientific experts that supported my work. I particularly thank Laura Schneider for her effort in providing the best mass spectrometry measurements and Dr. Julian Holstein for sharing his knowledge in X-ray crystallography. I deeply acknowledge the Fonds der Chemischen Industrie (FCI) to select me for a PhD scholarship to finance my research and studies. I would like to especially thank Dr. Stefanie Kiefer for her nice words and believing in me.

The whole Clever LAB! Past and present! Thank you for the amazing time together, the support and the laughter! Our group trips were just perfect: rafting on the Ruhr, Edersee, Juist, sailing, hiking, Weihnachtsmarkts, Hamburg for measurement time at DESY (what happens in Hamburg stays in Hamburg), all the trips to Göttingen for the PhD defences…! Thanks to all the open-minded members, diverse in traditions and background. I have always believed it a fundamental element of a student's career to work in an international and multicultural context to spark intellectual growth and discovery. Thank you, Robin, for welcoming me in the first period and being the best lab partner ever! H-LAB! Thank you, Marcel, Robin (potato?), Thorben, Susi, Mark, Wit, Rongmei, Philip (ew), Lukas, Julian, Soham, Julia (for introducing me to the DNA world), Subhadeep, Bin (office mate!), Bo (BO?), Rujin (A B C D E E E E!!), Haeri (O Battaglia!!), Jacopo (caffe´? Italian crew), Sonja, Kristina (once you have been in India together, you are *** friends forever), Andre´, Qianqian, Kai, Simon, Hannah, Christoph, Hasi (room-mate!!), Pedro (que onda wey), Sudhakar (and Lavagna <3), Ananya, David, Alexandre and naturally, Birgit(chen <3), Laura (patata) and Maike. A special thanks goes to Gabi. There is no situation you can´t make better, talking with you has the power of changing a tear into a smile. You have a good heart and I appreciate all the time you dedicated to our talks.

Thank you, Sonja, Jacopo and Haeri, for being always available for scientific discussion and for your invaluable career suggestions and advice! Thank you, Lukas and Philip, for fundamental support, help and tutoring in DNA chemistry!

Thank you, Lukas, Philip, Thorben, Cristian, Giovanni, Sonja and Lukas (two times, yes) for correcting my thesis and much more!

Thanks to all the students that helped me in the lab or that I supervised. I am sure that I learned much more from you that you did from me!! Thank you, Armin, Lars, Kai, Eliza, Sandy, Lorenz and all the fun students I met in the practical courses and tutorials!

Thanks to all the professors I met during my education and who believed in me, the ones that still support me and motivate me, the ones that are proud of me and also the ones that told me I was not good enough. A special thank you goes to Betta, my Master Supervisor, that for some reason saw something in me and never let go. You still inspire me.

Thank you to all the new special friends that supported me in first line in these years here in Dortmund! Starting from the “Girls Night” girls, Susi, Rike, Isa and Renee´, you hugged me from the beginning and never made me feel alone. Thank you to my roommates Jan, Anjla, Carsten, Alisa and Steffen! My family in Dortmund! Thank you to the Italian gang, Caterina (invaluable books on colors and dyes) and Giovanni, Alice and Pippo (AH come si scrive bene nella vostra cucina! Siete splendidi!), Elena and Pino, Jacopo, Stefano Giorgio. Thank you, Pandas, for the constant support and getting excited about life with me! Thank you, Silvia, our love (based on food) is the strongest kind!

Thank you Brojli Cabernet Franc. E grazie Tulia per le salse!!

But also thanks to all my dearest Italian friends always on my side and always interested in what I have to tell! Thank you, Giulia, Sara, Raffi and Ilaria for trying to understand my research and always listening to me for the fun of seeing me excited about science (we will manage!). Thank you to Marina and Cristian, we share the love for Chemistry and the memories of the happiest times as young dumb nerds! Thank you, Marta, for being my pusher of theoretical chemists! Thank you to my high school incredibly-achieved friends, Renata, Chiara, Maria, Francesca, Giovanna, Claudia and Michele. We might be spread around the world and rarely see each other, but it always feels like not a second has passed.

I couldn´t have done any of this if it wasn´t for the unconditional support of my Mum and Dad. You have always put my interests and passion above everything else and there is no way to thank you enough for this. You know by heart the way Fiumicello-Dortmund and even at 1100 km distance I feel like I shared with you all the steps of my PhD. I love you, you are special. Non avrei mai potuto fare nulla di tutto ciò se non fosse per il supporto incondizionato della mia mamma e papa´. Avete sempre messo i miei interessi e le mie passioni al di sopra di tutto e non saprei da dove iniziare per ringraziarvi. Conoscete la strada per fare Fiumicello-Dortmund a memoria e anche a 1100 km di distanza, sento di aver condiviso con voi ogni singolo passaggio del mio dottorato. Vi voglio bene, siete speciali. Thank you, Alessandra, for taking care of us all. Grazie Ale per prenderti cura di tutti noi.

Lukas you are the best most patient person in my life. Thank you for always taking care of me, for making me happy, for making me angry (or hungry?), for scientific discussions in the middle of the night, for working with me during the weekends, for being my proof reader of all the documents I sent out, for correcting my thesis (!!! And for saying that I could do better :), you were right). I feel lucky to have found you, life will never be boring together with you! Of course, thank you for introducing me to the Schützenfests, making me your Queen and making me falling in love with your family and culture. Thank you for the support, Ulla, Christoph, Jonas, Sophie, Moritz, Annika, Silja and Alex! Vielen Dank für die Unterstützung, Ulla, Christoph, Jonas, Sophie, Moritz, Annika, Silja and Alex!

With this one, all three thesis I produced in my Chemistry studies are dedicated to you, Giulio. The first one was perfectly picturing our relationship based on jokes and mutual respect for each other´s passions. At your provocation “Your belief on atoms is a faith because you can´t see them” (quela nel atomo xe´ come una religion, no te pol vederli, te ga de far el salto de fede), I answered with STM images (pretty cool ones too). The second I dedicated to your memory. And the third I dedicate it to thank you. Thank you for always challenging me and being so different from me. Thank you for giving me the different perspective and the outside point of view. Thank you for teaching me that I can do everything I want and I should follow my interests finding the answer to all the questions I have, even if they might seem stupid to others (you in *primis*!!). I know you were with me during my whole PhD, supporting me during the hard times – Irene, deal with one thing at a time -, and while celebrating the achievements – I could hear you cheering for me. Thank you for having been the best brother I could ever ask for. Our love for research will never fade.